SCHLIEREN-INTERFEROMETRIC STUDY OF CIRCULAR AND SQUARE CYLINDER WAKES: EFFECT OF BUOYANCY AND OSCILLATION

Surendra kumar singh

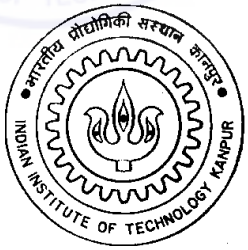

DEPARTMENT OF MECHANICAL ENGINEERING
INDIAN INSTITUTE OF TECHNOLOGY KANPUR
INDIA

December, 2010

भारतीय प्रौद्योगिकी संस्थान कानपुर
INDIAN INSTITUTE OF TECHNOLOGY KANPUR

SCHLIEREN-INTERFEROMETRIC STUDY OF CIRCULAR AND SQUARE CYLINDER WAKES: EFFECT OF BUOYANCY AND OSCILLATION

A *Thesis Submitted*
In Partial Fulfillment of the Requirements
for the Degree of

DOCTOR OF PHILOSOPHY

by

Surendra kumar singh

to the

DEPARTMENT OF MECHANICAL ENGINEERING
INDIAN INSTITUTE OF TECHNOLOGY KANPUR
INDIA

December, 2010

भारतीय प्रौद्योगिकी संस्थान कानपुर
INDIAN INSTITUTE OF TECHNOLOGY KANPUR

Certificate

It is certified that the work contained in the thesis entitled "**Schlieren-interferometric study of circular and square cylinder wakes: effect of buoyancy and oscillation**", by "Surendra Kumar Singh", has been carried out under my supervision and that this work has not been submitted elsewhere for a degree.

P. K. Panigrahi
Professor
Department of Mechanical Engineering
Indian Institute of Technology Kanpur
Kanpur 208016
India

December, 2010

भारतीय प्रौद्योगिकी संस्थान कानपुर
INDIAN INSTITUTE OF TECHNOLOGY KANPUR

Abstract

Flow past bluff bodies have extensive applications in aerodynamics, hydrodynamics and design of thermal systems such as heat exchangers, chemical reactors, nuclear reactor fuel rods and electronics cooling. Primary objectives of bluff body flow research have been elimination of flow-induced oscillations, drag reduction, mixing enhancement and heat transfer enhancement etc. The wake behind a bluff body displays characteristics that are distinct to the object shape, Reynolds number and distance from the object itself. The development of wake characteristics in the downstream direction is dependent on the instability modes and their amplification rates. When the body is heated with respect to the incoming flow, the buoyancy force is expected to play an additional role on growth rate of these instability modes. Such forces are usually negligible for forced flow, however for a highly heated body with low velocity, these forces may have significant influence on the wake structures. Therefore, heat addition to the near wake can be used as an effective strategy for control of wake instability. Small external energy input to the system can also greatly modify the growth and development of instability modes. Therefore, it is also possible to alter the vortex structures by controlled oscillations of the body, either normal (*transverse*) or parallel (*inline*) to the main flow direction. The bluff body surface motion can contribute to fluid acceleration and deceleration leading to re-organization of the vorticity field and significant change of flow structures. In a complex situation, the flow field behind the body can be under joint influence of buoyancy and forced oscillation of the body. The additive effect of heat input due to buoyancy and additional energy imparted to the flow by oscillations can have significant influence on wake instability and vortex formation process in the near-wake region.

Separate effect of buoyancy and oscillation on the wake characteristics have been reported as independent investigations in literature. No study on joint influence of buoyancy and oscillation is available to date. Similarly, no experimental study for flow past a heated square cylinder is available. Therefore, the present study investigates the wake characteristics behind heated stationary and oscillating cylinders (both circular and square) at low Reynolds numbers. The flow behavior is examined at Reynolds numbers range around Re = 100. Richardson number is varied in the range of 0.025 to 0.314 to cover both forced

and mixed convection regimes. Joint influence of buoyancy and oscillation on the vortical structures is examined at various frequencies (fundamental ($f_e/f_s = 1$), sub-harmonic ($f_e/f_s = 0.5$), super-harmonic ($f_e/f_s = 2$ and 3) and non-harmonic frequencies ($f_e/f_s = 1.5$)). The oscillation amplitude (a/d) is varied in the range of 0.02 to 0.10 in a small step of 0.02.

Experiments are carried out in a vertical flow facility with a low free stream turbulence (less than 0.3%). Circular and square cylinders are internally heated and maintained at precise constant temperature above the ambient temperature. Electromagnetic linear actuator is used to generate controlled oscillations of the cylinder. Laser schlieren-interferometry configured with a high-speed camera is used for quantitative flow imaging. Long sequence of schlieren images are recorded for visualization and analysis of spatial and temporal flow structures. Quantitative flow-field statistics obtained from the gray scale value of the fluctuating light intensity of schlieren images i.e. RMS fluctuations, power spectra, cross spectra, phase shift, Strouhal number, vortex formation length, coherence function and convection velocity results are reported.

Suppression of vortex shedding can be realized for both circular and square cylinders by heating i.e. increase in Richardson number. The critical Richardson number at which vortex shedding abruptly ceases is Reynolds number dependent and varies linearly with the Reynolds number. The critical Ri values for a circular cylinder are Ri = 0.122 and 0.157 for Re = 94 and 110, respectively. The critical Ri values for a square cylinder are equal to 0.107, 0.121, 0.140, 0.155, and 0.171 for Re = 87, 94, 103, 109, and 118, respectively. The Strouhal number is a function of both Reynolds number and Richardson number. The Strouhal number is higher at higher Reynolds numbers and slowly increases with an increase in Richardson number and becomes zero at critical Richardson number.

The details of flow mechanism that leads to suppression of vortex shedding can be visualized as follows. The length of the base region increases and the instant of vortex detachment from the cylinder is delayed with increase in Richardson number. This leads to an increase in the formation length and a decrease in convection velocity at a given stream wise location. Instantaneous visualization images show that shape, size and time-dependent movement of vortex structures are altered with increase in Richardson number. The shape of vortex structures become thin elongated slender-like at higher Richardson number. The absence of multiple peaks in the power spectra at cylinder centerline for higher Richardson number indicates the reduction in the circulation of these structures as well as interaction between neighboring vortex structures of the opposite shear layers. Owing to an increase in formation length, these structures only rub each other from the opposite sides and transverse interaction between the shear layers is insignificant.

The slender vortices subsequently reduce to a single plume oscillating at the shedding frequency. The plume becomes steady at the critical value of heat input leading to broadband spectra and suppression of shedding. RMS fluctuations of light intensity diminish to an insignificant magnitude at suppression of vortex shedding. The time-averaged stream wise velocity profiles across the wake shows a decrease in velocity deficit with an increase in Richardson number. With subsequent increase in Richardson number, the velocity deficit disappears and finally the velocity inside the wake exceeds that of the free stream velocity due to the additive effect of buoyancy in an aided flow configuration. Similarities in schlieren visualization images, vortex formation lengths, time traces and power spectra between circular and square cylinder geometries indicate similar flow mechanisms for the suppression of instability of both the cylinders.

The oscillation experiments show reappearance of vortex shedding at the critical Richardson number, where vortex shedding gets suppressed for a stationary cylinder. At the critical Richardson number, the power spectra for the oscillating cylinder at all frequency ratios show a dominant spectral peak at the excitation frequency (f_e) contrary to a broadband spectra without any clear peak for the stationary cylinders indicating reappearance of the vortex shedding. This reappearance of vortex structures can be attributed to amplification of natural instability by additional energy imparted to the wake by cylinder oscillations. The fluctuations level is very high at critical Richardson number for all oscillation frequency ratios as compared to insignificant value for the stationary cylinder due to the presence of sustained vortex structures. The power spectra for the oscillation case show presence of a single or multiple frequencies depending on the frequency ratio (f_e/f_s), Richardson number (Ri), stream wise location of the near-wake (x/d) and geometry of the cylinder. The observed frequencies include natural vortex shedding frequency (f_s), excitation frequency (f_e), super-harmonics ($2f_s$ and $2f_e$), sum ($f_e + f_s$) and differences ($f_e - f_s$) of these frequencies depending on the nature of interaction between the vortex structures.

When a sufficiently heated cylinder is oscillated, the lock-on of vortex shedding with the cylinder oscillation is a function of stream wise location of the wake (x/d), Richardson number (Ri), amplitude ratio (a/d), frequency ratio (f_e/f_s), and base geometry of the cylinder. Lock-on phenomenon is examined using power spectra, Lissajous trajectories, spectral coherence function, and instantaneous patterns of the near-wake vortex structures. Various types of locked-on states of vortex formation e.g. no lock-on (NLO), quasi lock-on (QLO) and lock-on (LO) have been identified. Spectral coherence has been used as a quantitative measure of the degree of lock-on of the shed vortices with the cylinder motion. A decreasing trend of the variation of the spectral coherence (Coh) in the stream-wise direction (x/d) indicates a lower degree of lock-on in the downstream region.

Spectral coherence (Coh) magnitude is higher at higher Richardson number indicating a higher degree of lock-on. The spectral coherence magnitude increases with increase in amplitude ratio indicating higher degree of lock-on for higher amplitude ratios. Fundamental Strouhal frequency ($f_e/f_s = 1$) is the most favoured frequency and sub-harmonic frequency ($f_e/f_s = 0.5$) is the least favoured frequency for occurrence of lock-on of both the geometries. At comparable Richardson numbers, the area enclosed by the envelope of lock-on regime in the contours of the spectral coherence is larger for the square cylinder compared to that of the circular cylinder. This indicates that square cylinder provides more favourable condition for lock-on as compared to the circular cylinder. These results clearly demonstrate the functional dependence of lock-on on the x/d, Ri, a/d, f_e/f_s, and cylinder geometry.

Acknowledgements

I express my profound gratitude, regards and thanks to my thesis supervisor Professor P.K. Panigrahi for excellent guidance and generous help throughout my research work. His critical evaluation of the data to get an insight and valuable comments were of immense help to produce quality results. His friendly behaviour has been comforting during most stressful times. I am very grateful to Professor K. Muralidhar for rendering an excellent professional training to produce high quality experimental setup and instrumentation. His continuous motivation and guidance has helped alot at all stages of my thesis. He has taught me about much more than just doing research in experimental fluid mechanics.

I am very thankful to Mr. Rajesh Kumar Singh and Mr. S. N. Sharma for dedicated help in the fabrication of my experimental setup. The technical approach of Mr. Rajesh Kumar Singh was the deciding factor in the fabrication of the high quality experimental setup. The support received from Mr. Manoj Kumar Sharma and Mr. Naresh has been of immense help and is acknowledged with deep regards.

I express my sincere thanks to Mr. Atul Srivastava for transferring his knowledge about schlieren apparatus to me. I take this opportunity to thank Ms. Anamika Sethia Gupta, Mr. Sushant Dutta, Mr. Andallib Tariq, Mr. Joytirmay Banerjee, Mr. Adnan Quyam, for giving me a friendly atmosphere during my stay at IIT Kanpur. I am thankful to them for their help and cooperation.

I am thankful to QIP scheme of the Government of India for providing me financial assistance. I am also thankful to my organization, J. N. Vyas University, Jodhpur for deputing me in the program for pursuing Ph.D.degree. I also extends my thanks to Dr. D.K.S. Gautam and other faculty members of my parental organization for their cooperation.

I also offer my sincere appreciation to my parents for their moral support, encouragement and blessings. I would like to give special thanks my brother, Ravendra for helping me in the initial programming and in incorporating the corrections in the thesis. My daughter, Swapnil and son, Priyansh have created an excellent environment in home.

I express my indebtness to them for their patience waiting of the completion of this work.

I am eternally grateful to my wife, Renu. Her unqualified support, patience and encouragement contributed immensely in the successful completion of the work. She always lent an ear of my excitements or disappointments and motivated all the times. Her help can not be expressed in words.

I am also thankful to all those friends and well-wishers who stood by me throughout this research work.

Surendra Kumar Singh

To my

FAMILY

for all the love, support and encouragement

भारतीय प्रौद्योगिकी संस्थान कानपुर
INDIAN INSTITUTE OF TECHNOLOGY KANPUR

Contents

भारतीय प्रौद्योगिकी संस्थान कानपुर
INDIAN INSTITUTE OF TECHNOLOGY KANPUR

List of Figures

List of Tables

Nomenclature

a	amplitude of cylinder oscillation, m
a/d	amplitude ratio
b	height of the light source remaining unobscured by the knife-edge, m
C	contrast in the schlieren image
C_p	specific heat of the fluid, kJ/kg°C
C_D	drag coefficient based on mean velocity profile
d	representative dimension of the cylinder (diameter for circular cylinder, edge for square cylinder), m
f	focal length, m
f_2	focal length of the second concave mirror, m
f_c	Nyquist critical frequency, Hz
f_s	frequency of vortex shedding for stationary cylinder, Hz
f_e	frequency of cylinder oscillation, Hz
f_v	dominant shedding frequency of oscillating cylinder , Hz
f_e/f_s	frequency ratio
g	gravitational acceleration, m/s^2
I	gray scale intensity value of the image
k	thermal conductivity of the fluid, W/m°C
L_f	formation length, m
L	length of the cylinder, m
n	refractive index of the working medium (air)
P_r	Prandtl number ($\mu C_p/k$)
Re	Reynolds number based on cylinder dimension ($U_\infty d/\nu$)
Ri	Richardson number ($dg\beta\Delta T/U_\infty^2$)

S	schlieren sensitivity
St	Strouhal number ($f_s d/U_\infty$)
t	time, s
T	temperature, °C
T_w	cylinder surface temperature, °C
T_∞	free-stream temperature, °C
T_{eff}	effective temperature ($T_\infty + 0.28(T_w - T_\infty)$), °C
T_{film}	film temperature, $(T_w + T_\infty)/2$, °C
T^*	temperature ratio $(T_w + 273)/(T_\infty + 273)$
Δt	time interval between two consecutive images
ΔT	$T_w - T_\infty$, °C
ΔT_ϵ	Temperature change per fringe shift, °C
u	cross stream velocity across the wake, m/s
U_∞	uniform free-stream velocity, m/s
u_c	stream wise convection velocity, m/s
x	stream wise dimension of coordinates, m
y	transverse dimension of coordinates, m
z	span wise dimension of coordinates, m

Greek Symbols

μ	dynamic viscosity, kg/m-s
ν	kinematic viscosity of the fluid, m^2/s
	(also frequency integer of discrete data)
β	Volume coefficient of thermal expansion, $°C^{-1}$
θ	nondimensional temperature $(T - T_\infty)/(T_w - T_\infty)$
ρ	density of the fluid, kg/m^3
λ	wavelength of the laser beam, m
ϕ	phase difference
τ	discrete time, s
ϵ	refraction angle

Subscripts

$crit$	critical
w	cylinder surface
rms	root mean square
eff	refers to conditions at effective temperature
$film$	refers to conditions at arithmetic mean film temperature
∞	free stream

भारतीय प्रौद्योगिकी संस्थान कानपुर
INDIAN INSTITUTE OF TECHNOLOGY KANPUR

Chapter 1

Introduction

Flow behind bluff bodies has received immense attention by numerical and experimental fluid dynamicists due to the aerodynamics applications in wind engineering and hydrodynamics applications in marine and ocean engineering. Interaction between flow and the bluff body leads to increased resistance to fluid motion. These flows consists of three regions, namely the boundary layer, the separated shear layer and the wake. The instability of these flows increases as Reynolds number is progressively increased. Fundamental wake instability results in the formation of the classical von Karman vortex street consisting of a regular pattern of alternately shed vortices. Large separation region behind the bluff body leads to big pressure difference between the front and rear surfaces resulting in high drag forces on the bluff body. The vortex formation and unsteadiness in the flow field is responsible for the drag forces to be unsteady with respect to magnitude and direction, thus generating vibrations of the body, known as flow-induced vibrations. In addition, the vortex structures present in the wake of a heated object have direct influence on mixing and heat transfer rates from the body. The thermal influence may arise from changes in density and viscosity, though buoyancy is expected to be dominant. Important instances of flow across heated bluff bodies can be found in the design of thermal systems such as heat exchangers, chemical reactors, nuclear reactor fuel rods and electronics cooling. It is possible to alter the strength of primary vortices by creating low amplitude vibration of the cylinder. The primary objective behind flow manipulation can be either elimination of flow-induced oscillations and reduction in the magnitude of drag by weakening vortex shedding or intensification of vortex shedding to enhance the mixing and heat transfer rates.

The wake behind a bluff body display characteristics that are distinct to the object shape, Reynolds number and distance from the object itself. When the surface temperature of the object is different from the temperature of the surrounding fluid, the wake characteristics are once again influenced. Properties that are affected by the object shape,

flow speed and temperature difference are the drag coefficient, Strouhal number, time-averaged and rms velocity fields, power spectra, vorticity generation, and the convection velocity of vortex structures. At high Reynolds numbers, the wake structure is complex owing to unsteadiness and turbulence. In the lower range of the Reynolds number, the flow field is complex owing to three-dimensionality even in nominally two-dimensional geometries. Common bluff body cross section are circular and rectangular (especially, square). Between the two, the circular geometry has received considerable attention compared to the rectangular. For square/rectangular cross-sections, the orientation with respect to the mean flow is another important parameter.

The present chapter describes the conceptual overview of the vortex shedding phenomenon behind a bluff body, effect of heating and oscillation of the bluff body and various engineering applications of bluff body flows. The theoretical background of optical measurement with special emphasis on schlieren technique is discussed. Against this background, the specific objectives of this study are presented.

1.1 Flow across a bluff body

According to Zdravkovich (1997), when a fluid flows past a stationary body or, equivalently, when a body moves in a fluid at rest, a region of disturbed flow forms around the body. The size of the disturbed flow region is largely dependent on the shape, orientation, and size of the body, the velocity and viscosity of the fluid, and also on a wide variety of small disturbances. A body in which flow, under normal circumstances, separates from large section of the body surface and creates a significant wake region downstream, is called bluff body. A particularly large and usually unsteady separated flow is generated behind a bluff body. Bluff bodies may have sharp edges on their circumference, such as flat plates, triangular, and rectangular/square cylinders, or may be rounded like circular, and elliptical cylinders. Flow separation points are usually fixed on sharp edged body, whereas they can move and adjust itself in response to the flow structure in the separated region for the rounded bodies.

The flows around all bluff bodies have many similarities, despite the differences in the body shape and the presence or absence of sharp edges. The common feature is the development of similar flow structures in the separated region. The general flow features of bluff body flows presented in the following sections are primarily based on the results available for circular cylinder in the literature.

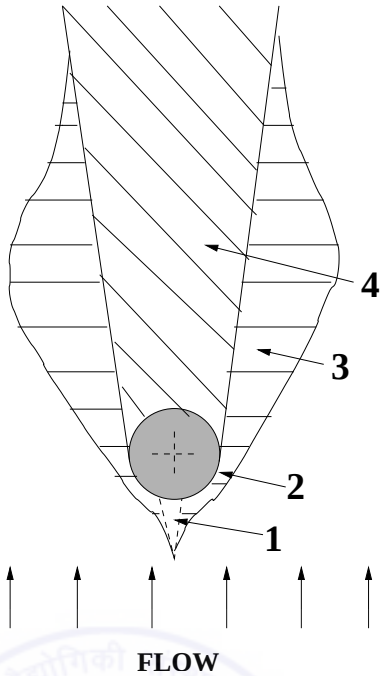

Figure 1.1: Regions of disturbed flow around a bluff body, Zdravkovich (1997).

1.1.1 Conceptual overview

Regions of disturbed flow : Disturbed flow around bluff body is characterized by the variation of a local time-averaged velocity (u), which may be greater than, equal to, or less than the free stream velocity (U_∞). According to Zdravkovich (1997), the disturbed flow field can be divided into four regions as shown in Figure 1.1.

1. one narrow region of retarded flow
2. two boundary layers attached to the surface of the cylinder
3. two sidewise regions of displaced and accelerated flow
4. one wide downstream region of separated flow called the wake

There are unexpected high fluctuations of velocity in the narrow upstream region of retarded flow. The boundary layers around the cylinder are subjected to a favourable pressure gradient followed by a small region of adverse pressure gradient before separation. The separated boundary layers continue to develop downstream as free shear layers. The region of displaced flow ($u > U_\infty$) is vigorously entrained by the low pressure in the wake. The extent of this displaced flow region may be affected by the vicinity of the confining walls parallel to the flow. This is known as blockage effect. In the downstream region

of the separated flow ($u < U_\infty$) large flow structures are formed in the near-wake region, which gradually decay along the wake. The formation and decay of the flow structures in the wake depend on the state of the flow which may be laminar, transitional, or turbulent.

State of flow : A particular feature of the flow around all bluff bodies is the succession of transitions in various regions of the disturbed flow. The Reynolds number is the primary *governing* parameter for description of the state of the flow. All transition states can be described by Reynolds number along with other relevant *influencing* parameters, such as free stream turbulence, surface roughness, wall blockage, aspect ratio, and free or forced oscillations. The state of flow may be fully laminar, transitional in the shear layer or fully turbulent. The laminar state of disturbed flow can be subdivided into three basic flow regimes namely (Zdravkovich, 1997):

1. Creeping flow or non-separation regime; $0 < \mathrm{Re} < 4$[1]
2. Steady separation regime; $4 < \mathrm{Re} <$ (40-48)
3. Periodic laminar regime; (40-48) $< \mathrm{Re} <$ (180-200)

In creeping flow regime, the flow smoothly divides and reunites around the cylinder and is firmly attached to the cylinder all around the circumference. At a Reynolds number of about 4, the separation initiates when a distinct, steady, symmetric, and closed near-wake is formed with the presence of two symmetrical steady eddies. These eddies, also called separation bubbles, grow in size but remains steady up to a Reynolds number of about 40. The steady, elongated closed near-wake becomes unstable for $\mathrm{Re} \geq 40$ and a sinusoidal oscillation of shear layer commences at the confluence point downstream. The eddies start to oscillate and thus bring asymmetry in the wake. The amplitude of oscillation increases with increasing Reynolds number. Subsequently, the shear layer rolls up and starts shedding of vortices into the stream i.e. the separation bubble detaches from the surface of the cylinder. The eddies periodically break off and shed from the two sides of the cylinder. The regular pattern of two staggered row of alternately shed clockwise and counter-clockwise toroidal vortices so formed is known as Von Karman vortex street. Due to alternate shedding of vortices of opposite circulation from the two sides, periodicity is induced in the flow field.

Frequency of eddy shedding (Strouhal number) : The periodicity of the wake is characterized by the frequency of the vortex-shedding, f_s. In non-dimensional form, it is normally expressed as $(f_s d/U_\infty)$, known as Strouhal number after V. Strouhal, a German engineer. The Strouhal number is determined by spectral analysis of the hot-wire signal

[1]The values of Reynolds number are specific for the flow over a circular cylinder

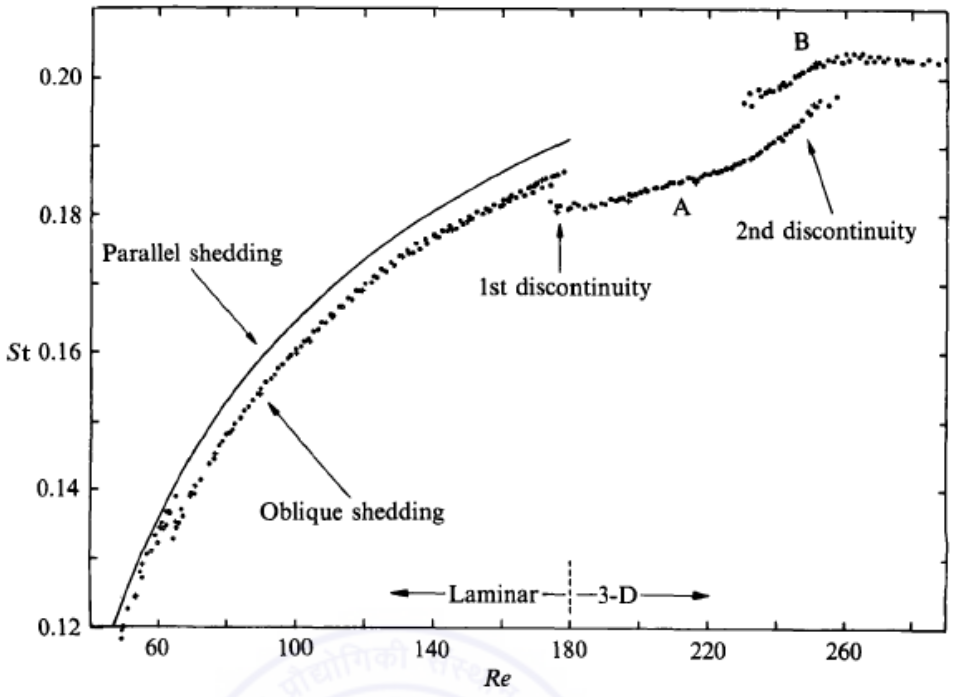

Figure 1.2: Variation of Strouhal number with Reynolds number for the flow over a circular cylinder, Williamson (1988).

from the unsteady velocity field near the edge of the separating shear layer or by spectral analysis of the temporal variation of drag or lift coefficient. However, because vortex shedding is associated with a *global* instability, any signal derived from measurements of the flow carries the signature of the vortex shedding frequency. The present work utilizes the time series of fluctuating light intensity of the schlieren images to determine the Strouhal number. The value of Strouhal number is dependent on bluff body shape.

The variation of Strouhal number with Reynolds number for the flow over a circular cylinder is shown in Figure 1.2 (Williamson, 1988). At low Reynolds number the flow is steady (St = 0) and symmetric about the centerline of the wake. At around Re = 48, the steady flow becomes unstable and bifurcates to a two-dimensional, time-periodic flow. The shedding frequency of the two-dimensional flow increases smoothly with Reynolds number along the curve as shown in Figure 1.2. For certain critical Reynolds number, the flow field is characterized by the initiation and growth of irregularities due to three-dimensional disturbances e.g. mode-A, mode-B instabilities and oblique shedding, which leads to discontinuities in the Strouhal-Reynolds number relationship.

Three dimensional effects : Above a certain value of Reynolds number, the vortex shedding from nominally two-dimensional bluff bodies exhibits certain three-dimensional characteristics. Two kinds of three-dimensionality are observed in the wake of two-

dimensional bluff bodies. One is due to *extrinsic* effects, such as due to end effects in conjunction with aspect ratio. The other is *intrinsic* three-dimensional motion arising from natural instabilities. The transition to three-dimensionality in the intrinsic form occurs over the range $190 < \mathrm{Re} < 260$, involving two distinct modes of vortex shedding (Williamson, 1988). This leads to two discontinuous changes in the Strouhal-Reynolds number relationship as shown in Figure 1.2. At the first discontinuity, which is hysteretic, the Strouhal frequency drops from the laminar shedding curve to the mode-A three-dimensional shedding curve, at around Re = 180-190. As Re is increased up to 230-260, another discontinuity manifests itself and the Strouhal number rises to mode-B three-dimensional shedding curve. This later discontinuity is, however, not hysteretic, but involves the gradual transfer of energy from mode-A to mode-B, as Re is increased. These two modes in the transition regime are characterized by the span wise wavelengths of the stream wise (secondary) vortices.

Figure 1.3 (Williamson, 1997) shows the instabilities involved in the development of wake turbulence as Reynolds number is progressively increased (from top to bottom). The fundamental wake instability results in formation of classical von karman vortex street. In the mode-A shedding, the primary vortices deform in a wavy fashion along their span during the shedding process. This results in the formation of vortex loops, which subsequently get stretched into stream wise vortex pairs. At a higher Re, when mode-B shedding manifests itself, finer scale stream wise vortex pairs are formed. The existence of the mode-A and mode-B small scale structures in the wake transition regime is complemented by the presence of much larger three-dimensional structures called vortex dislocations. At much higher Reynolds number, the instability in the shear layer occurs which is characterized by the formation of small scale vortices inside the shear layer having length and time scales much smaller than those of primary vortices.

At low Reynolds number ($49 < \mathrm{Re} < 190$), Williamson (1989) observed that vortex shedding is inclined to the cylinder axis and identified this as the oblique shedding. Oblique shedding is an extrinsic form of three-dimensionality. By using inclined end plates, parallel shedding is obtained, implying that end conditions play an important role in vortex shedding phenomenon. The phenomenon of oblique shedding provides an explanation for the observation of discontinuity in the variation of the St-Re curve near Re = 64. Figure 1.2 shows that completely continuous St-Re variation can be realized by manipulating the end conditions to produce parallel shedding.

Pressure and friction drag : A bluff body immersed in a flow field experiences a force in the direction of the flow. This force is called 'drag'. It mainly consists of viscous forces (due to fluid friction along the surface of the body) and form drag (due to the unsymmetric

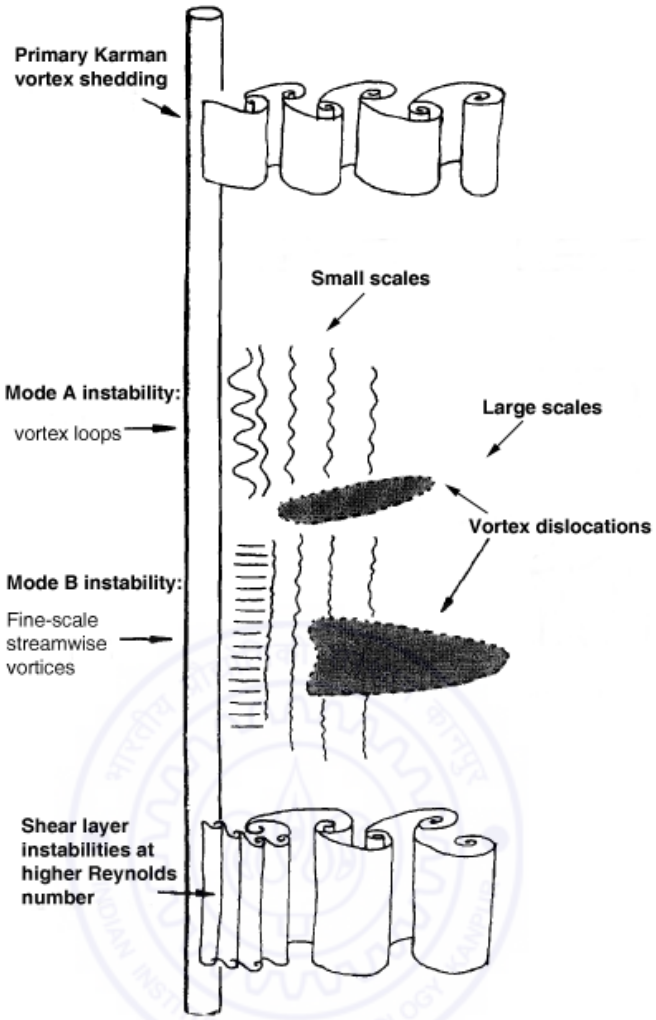

Figure 1.3: Summary of instability patterns in the wake of a cylinder, Williamson (1997).

distribution of surface pressure). In separated flows, the form drag is predominant and therefore constitutes major portion of the total drag. The span wise-averaged fluid force $F(t)$ is computed by integrating the shear stress and pressure over the surface of the cylinder. The component of the force $F(t)$ acting in the direction of the free-stream (x-direction) is called the drag force, while that acting in the perpendicular direction (y-direction) is called the lift force. These forces are normalized by the free-stream dynamic pressure and the projected area of the cylinder to produce force coefficients. The drag coefficient is defined as $C_D(t) = F_x(t)/\frac{1}{2}\rho U_\infty^2 dL$. The mean drag C_D is the time-averaged value of $C_D(t)$. Henderson (1997) stated that at the onset of vortex shedding about 1/3 of the total drag force is due to skin-friction and 2/3 is due to pressure drag. With increasing Reynolds number the skin-friction component continuously drops while the pressure drag steadily increases. At higher Reynolds number, the drag is almost entirely due to the variation in pressure around the surface of the cylinder.

1.1.2 Vortex dynamics of circular versus square cylinder

Circular and square cylinders are commonly encountered bluff body cross-sections. Flow past a square cylinder replicates flow past a circular cylinder in terms of instability and transition phenomena. But the separation mechanism and subsequent dependence of shedding frequency and aerodynamic forces on the Reynolds number differ significantly from that of a circular cylinder. Unlike a circular cylinder where the separation points vary with Reynolds number, the separation points are fixed for a square cylinder at the leading edge. It is also possible for the flow to reattach on the surface which subsequently separates at the rear corners of the cylinder, a trend seen at high Reynolds numbers. Furthermore, the width of the wake behind the square cylinder is at least one diameter whereas it is less than the cylinder diameter for a circular cylinder. The square cylinder tend to create a wider wake in comparison to the circular cylinder. Also, flat after body of a square cylinder somewhat stabilizes the separated shear layers. These differences indeed influence the formation and the dynamics of two-dimensional Karman vortices. The incidence angle of square cylinder also influences the wake structures behind the cylinder. Despite these differences, the disturbed flow behind these bluff bodies share certain similarities i.e. formation of a recirculation bubble in the near wake, a clear vortex shedding, variation of local velocity in term of magnitude and direction, flow fluctuations and statistical features that are geometry independent in the far-wake.

1.1.3 Flow past a heated cylinder

Most studies of bluff body wakes have focused on an isothermal fluid in which no temperature difference is maintained between the body and the ambient. However, quite a few engineering applications require the knowledge of flow behavior in the wakes of heated objects e.g. heat exchanger, chemical reactors, nuclear reactors, electronic cooling, and flow control applications. When the object is heated with respect to the incoming flow, temperature difference exist between the object and the ambient fluid resulting in a change of density and following possibilities arise as shown in Figure 1.4 (Oosthuizen and Naylor, 1999):

1. Forced convection, where effect of buoyancy forces are negligible and density changes are small.

2. Free convection, where the body forces that occur as a result of density changes entirely determine the flow field.

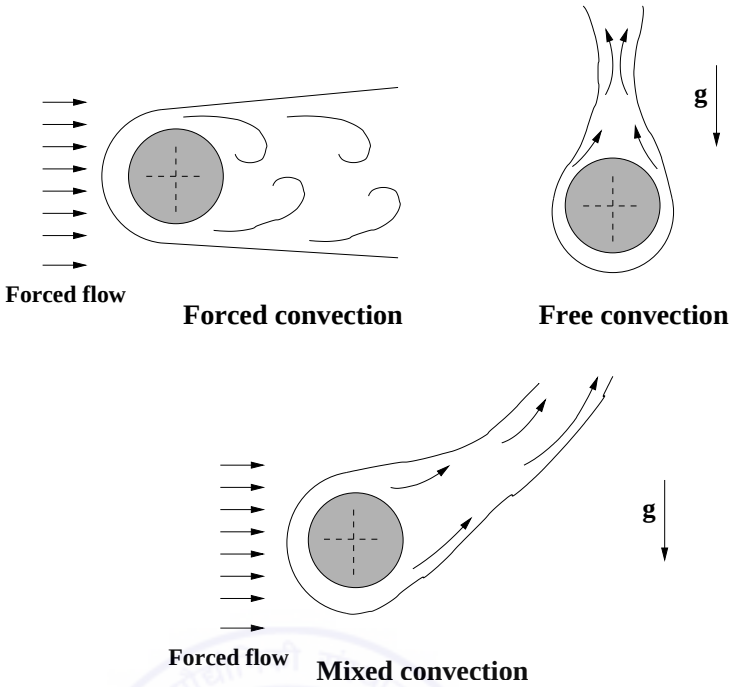

Figure 1.4: Various types of convection heat transfer, Oosthuizen and Naylor (1999).

3. Mixed convection, where the forced velocity exists and buoyancy forces have a significant influence on the flow.

In the mixed convection flows, free and forced convection effects are comparable and the forced flow is superimposed on the buoyancy driven flow. The interaction between two different sources of motion may result in enhanced mixing properties compared to purely forced convection case. Such mixed convection flows are normally associated with low flow velocity. Richardson number (Ri) is used to characterize the mixed convection flows. Its magnitude indicates the relative effect of buoyancy as compared to the forced flow. Limiting value of Ri is about 0.05 for considering buoyancy force to be negligible and the flow is termed as forced convection flow (Lecordier *et al.*, 2000). Above this limit of Ri, the flow is in the mixed convection regime. However, if Ri is of significantly greater order of magnitude than one, the buoyancy force predominates and the flow is termed as free convection flow.

In the mixed convection flows, the influence of heating depends on the orientation of the forced flow direction with respect to the direction of gravity (buoyancy force). Figure 1.5 (Oosthuizen and Naylor, 1999) shows aiding, opposing and cross-stream configurations based on angle (α) between the direction of forced flow and buoyancy force. When the angle α is 0°, the forced flow is in the same direction as the buoyancy force and the flow is termed as "aiding" or "assisting" flow. Upward forced flow over a heated

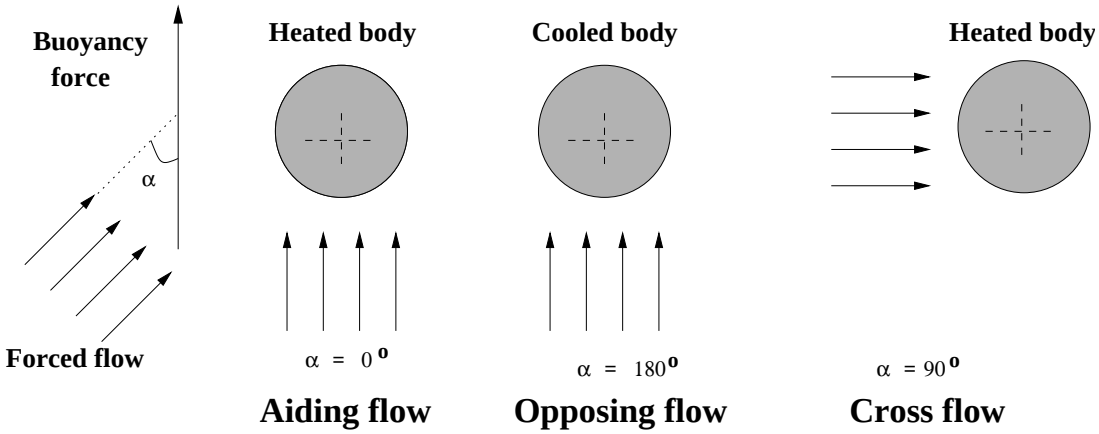

Figure 1.5: Angle between direction of forced flow and that of buoyancy force (Buoyancy force is assumed to be vertically up for the heated fluid and vertically down for the cooled one), Oosthuizen and Naylor (1999).

bluff body is an example of aiding flow. When α is 180°, the forced flow is in the opposite direction to the buoyancy force and the flow is referred as "opposing" flow. Upward forced flow over a cooled bluff body and downward forced flow over heated bluff body are the examples of opposing flow. When the forced flow is in perpendicular direction to that of buoyancy force i.e. α is 90°, the flow is termed as "cross-stream" flow, such as horizontal forced flow over a heated or cooled bluff body.

Mixed convection flow situations arise when the flow velocity is not very high and the temperature difference between the body surface and the ambient fluid is large. The vortex shedding characteristics is dependent on the magnitude of the heat input. Therefore, heating the surface of bluff body can be a method to disturb and control the vortex shedding process. In the present work, wakes behind heated cylinders of two extreme geometry, circular and square have been investigated at low Reynolds numbers. The effect of buoyancy on the wake instability of these cylinders has been studied in aiding buoyancy configuration.

1.2 Flow control

Gad-el-hak (2000) in his monograph stated that the ability to actively or passively manipulate a flow field to effect a desired change is of immense technological importance. The potential benefits of realizing efficient flow control systems include saving money in fuel cost for vehicles as well as achieving economically environmentally more competitive industrial processes involving fluid flows.

1.2.1 Need for flow control

The desired objectives of flow control may include drag reduction, lift enhancement, noise suppression, separation control, enhanced mixing and maximizing energy transfer etc. These requirements are adequately met by modifying the flow structures by the application of appropriate control method. The primary objective is either to eliminate the flow-induced oscillations and reduction in the magnitude of drag by weakening vortex shedding or to intensify the vortex shedding for enhancing the mixing and heat transfer rates.

1.2.2 Types of flow control

A variety of controlling techniques have been developed in the past, which can be roughly classified as passive and active controls.

Passive control : Passive technique requires no external energy input to the system and rely on modifying the geometry of the object with respect to the flow direction in such a way that the surface pressure is altered and desired effect is obtained. The examples are addition of vortex generators, grooves, or riblets to bluff bodies to affect the formation of vortex shedding. Passive control techniques tend to be simpler, less expensive, and easier to maintain. However, these may only be effective over a limited range of operating conditions.

Active control : In contrast to passive techniques, active techniques involve external energy input via actuators to bring about desirable change to the flow-structure. It may be implemented by using either independent external disturbance or a feedback controlled system. The former is often referred to as open loop control, whereas the latter is called the closed loop control. In both cases, the controlled performance strongly depends on activating mechanisms and, in the latter case, also on the control scheme.

1.2.3 Oscillating bluff bodies

For a stationary cylinder, the size and shape of the vortices determine the forces acting on it as well as the energy exchange between the solid surface and the flowing medium. It is possible to alter the strength of these primary vortices by creating low amplitude vibration of the cylinder. The surface motion contributes to the fluid acceleration and there is re-organization of the vorticity field resulting in significant change of wake structure. Different techniques are available for active control of the near wake: forced oscillation (transverse or in-line with respect to the flow direction), acoustic excitation, and flexibly

mounted cylinder. The basic difference between forced oscillation and flexibly mounted cylinder is that for the latter, fluid-structure coupling can occur in either direction i.e. structure to fluid and fluid to structure. In forced oscillation of a rigid cylinder, surface motion defines and hence controls the fluid motion. For this reason, forced cylinder oscillations are being effectively used as an active control strategy of bluff body wakes. Moreover, oscillations by using the feedback signal from the wake itself can have potential for suppression of vortex shedding. Preliminary studies show that a large variation in the flow field is possible if the cylinder motion is driven by the unsteadiness of the wake. This control strategy requires sensors, actuators and controller.

A few researchers have investigated flow structures and heat transfer from heated bluff body undergoing forced oscillation. The results indicate increase in heat transfer for the flow approaching the lock-in regime, which occurs when the cylinder oscillation frequency is near the natural vortex shedding frequency. In the present study, in-line and transverse oscillations of the heated cylinders have been considered and joint effect of buoyancy and in-line/transverse oscillation on the wake characteristics have been investigated.

1.3 Importance and technological applications

The flow around bluff body shows interesting features. When the body is heated, the buoyancy forces have a significant influence on the flow structures. In addition, natural/forced vibration give rise to a number of interesting phenomenon, such as vortex lock on, hysteresis and bifurcation, alteration of vortex shedding patterns etc. Importance of the bluff body flows can be seen in various engineering applications as described below:

Vehicle aerodynamics : The subject find its importance for energy conservation e.g. automobiles, ships, aircrafts, submarines must meet the stringent fuel-consumption requirements which translates into the need for reduced drag.

Flow-induced vibrations : High-rise buildings or large towers, chimneys or smoke-stacks, nuclear and conventional power plants, suspended cables for bridges, power transmission lines and other structures are subjected to wind-induced oscillations. Ocean pipelines or risers, offshore-platform structures, marine structures, bridge piers, tube banks in heat exchangers, steam generators, condensers and nuclear fuel rods are other examples of possible where flow-induced vibrations.

Aerodynamics generated acoustics : Aerodynamic noise is generated mainly by local unsteady flow separations causing the pressure fluctuations on the body surface.

Vortex flowmeter : Knowledge of vortex-shedding characteristics is also used in the design of vortex shedding flow meter for measuring the flow rates inside the close conduits. The idea is based on the assumption of constant strouhal number independent of the Reynolds number and a well-designed flowmeter shows flow rate directly proportional to the shedding frequency over a wide range of Reynolds number.

Signature analysis : Recent applications of bluff body dynamics is the detection of military objects (submarines, fighter aircrafts etc.), where the flow induced signature is suppressed to prevent the identification of objects. The other application is the dispersion of pollutants.

Electronics cooling : Miniaturization of electronic components has resulted in increased circuit densities with large heat flux from the components and the junction temperature exceeds the allowable limit of the device. As a consequence, efficient cooling of such components has gained importance recent times.

Thermal devices : Heated bluff bodies subjected to high temperature environment are observed in many thermal devices i.e. heat exchanger tubes, chemical reactors, nuclear reactor fuel rods etc.

Flow control : Proper understanding of wake instability mechanism is important for flow control applications. For a non-heated body the prime objective is to eliminate flow-induced oscillations and reduce the magnitude of drag. While for a heated body, the enhancement in the heat transfer from the body is of prime importance. For any thermal component, vibrations may lead to significant increase in heat transfer from the body. But, unaccepted vibrations may damage the structure. But, vibration can be used as one of the methods for enhancing heat transfer if the effect of small amplitude vibration could be accepted. In addition, any thermal device during its normal operation may encounter some degree of vibration. The vibration may be generated from the flow itself and/or other components in motion. These kinds of vibration usually have small amplitudes and relatively high or low frequency. These small amplitude vibrations may have significant effect on the flow structures and heat transfer. Moreover, the study of heat transfer from a cylinder under natural coupling with the fluid (fluid-induced vibration) has potential application in areas of passive cooling of the thermal components.

1.4 Flow imaging and optical techniques

To understand complicated thermo-fluid dynamic processes, detailed information of flow parameters with high spatial and temporal resolution is required. Traditionally, “flow vi-

sualization" provides qualitative information about the nature of flow field. Modern flow imaging, however, goes far beyond qualitative flow visualization and aims at obtaining quantitative information, simultaneously. The development of non-intrusive flow diagnostic techniques for measuring large number of flow variables such as density, temperature, pressure, concentration and velocity is an important area of experimental fluid mechanics research. Integrating new technological developments in various fields and evolving new technique of flow quantification is the current scope of research. Availability of intense coherent light sources, high-resolution, high-speed video cameras and computer-aided data processing of huge amount of digital image data have caused a revival of optical techniques over a wider horizon of fluid mechanics, heat and mass transfer processes in engineering applications.

Optical techniques for flow measurement employ a visible wavelength radiation source to probe the flow field. The major advantage is the non-intrusive properties i.e. no disturbance of the probe on the flow field and the investigated phenomenon. Also being inertia less, light beams can help in understanding rapid transient phenomena with high temporal resolution. A majority of optical techniques generate field information at a given time instant because entire cross-section of the physical region can be scanned as against the conventional mechanical probe methods, where only a point-wise data can be recorded. These techniques require the medium to be transparent. Optical techniques used in the measurement of flow include (Goldstein, 1996):

1. Direct visualization methods, where some types of marker such as smoke, particles, helium bubbles, dyes etc. are introduced along with the fluid which makes the flow patterns visible due to scattering of the incident light.

2. Scattering methods, in which light interacts with the matter and gets partially deflected from its incident direction. For inelastic scattering, the frequency of light changes during scattering. The intensity and the wavelength often yields the valuable information regarding the properties of the matter. Some of the techniques based on the scattering are laser-Doppler velocimetry, particle-image velocimetry and laser-induced fluorescence etc.

3. Index of refraction methods, that utilize refractive index variation of the medium due to change in density, concentration or temperature.

1.4.1 Laser-based measurements

Using laser light as the radiation source, laser-based measurement techniques have become popular and reached a high degree of maturity as a qualitative flow visualization tool as well as for quantitative measurements. Possible reasons for this development are:

1. Commercially available lasers have a high degree of coherence (both spatial and temporal) and therefore generates stable image patterns, which truly reflect the flow behavior.

2. Various types of cost-effective lasers are available, each suitable for a certain technique depending on its special characteristics, such as for observing high-speed flows, pulsed lasers could be used to freeze the motion.

3. Laser measurements in thermo-fluid sciences have been facilitated by the fact that most of the fluid media are transparent.

Laser measurements of flow and heat transfer in fluids are carried out with a variety of configurations: shadowgraph, schlieren, interferometry, PIV, LDV, LIF, and holography, to name a few. Laser Doppler velocimetry (LDV) and particle image velocimetry (PIV) have replaced traditional methods such as pitot tubes and hot-wire anemometry.

1.4.2 Index-of-refraction methods

The optical methods described in this section involve variation of the index of refraction. Such variations result from spatial and/or temporal change in the thermodynamic state, often only the density, of a gas or a liquid. These methods are based on the principle that the light rays travel in a straight path in a homogeneous medium with uniform refractive index. In an inhomogeneous optical medium the refractive index varies with position and time, on account of local non uniformities of density, pressure and/or temperature. As a consequence, the light ray is deflected from its original rectilinear direction and the phase of the disturbed light wave is shifted with respect to that of the undisturbed. This phenomena is used not only to visualize the flow but also to perform quantitative measurements. These optical methods require special optical devices and can be configured in many different ways. Three available routes are:

1. Interferometry, where the image formation is related to changes in the refractive index with respect to a reference environment.

2. Schlieren, where light deflection in a variable refractive-index field is captured.

3. Shadowgraphy, where the reduction in light intensity is employed.

Irrespective of the physical quantities being measured, the refractive index based optical techniques generate path integral information through the whole depth of the measurement region under study. Hence, they are well-suited for measurements in two-dimensional fields where the light beam crosses the gradients of the index of refraction of the flow field in a direction normal to the light beam and there is predominantly no change in the refractive index along the length of the light beam. Interferometers respond directly to differences in optical path length, thus giving the integrated index of refraction (or density) field within the flow. Schlieren systems, on other hand, are sensitive to the first derivative of the index of refraction in direction normal to the light beam. shadowgraphs respond to the index of refraction's second derivative normal to the optical path.

The phenomenon that causes density variations in the flowing fluid may be due to pressure gradient e.g. high-speed compressible flows or temperature gradient e.g. heat transfer and convection situations or due to concentration gradient in mass transfer situations where mixing of fluids of different densities is present. In the low speed flows where no inherent change in refractive index occurs naturally, an artificial density distribution can be introduced into a flow through local heating, often of a transient nature, from a heating wire or spark. The flow field is said to be visualized by marking it by heat energy addition, which behave like thermal "tracers" in the flow field.

The sensitivity of the three techniques can be quite different. Specifically, the interferometry is suitable for applications where the density gradients are small. Schlieren and shadowgraph find applications when large density gradients are present in the flow field such as studying shock and flame phenomenon. In view of interferometry detecting the refractive index field directly, it has found extensive usage in quantitative determination of local field values. In contrast, schlieren and shadowgraph have found utility as a flow visualization tools alone, in the past. Since, it is now possible to precisely quantify changes in light intensity, they are extended to quantify the measurements as well, provided an exact knowledge of the relation between refractive index and fluid density is known. In interferometry, one can measure refractive index values only at those points where fringes appear. The quantity of information is also limited by the number of fringes (infinite fringe setting). Schlieren and shadowgraph generate information of the refractive index field at every pixel of the image in the form of intensities.

1.4.3 Schlieren technique

Schlieren derives its name from the German word *schliere* that means gradient disturbances of inhomogeneous transparent medium and has been attributed to certain optical devices, that allows to visualize such optical inhomogeneities. Classical schlieren technique relies on variation of the index of refraction in transparent medium (usually gases or liquids) and provides qualitative visualization of density fluctuations. This technique requires a light source, collimating lenses or mirrors and an aperture such as knife-edge or filter to mask certain portion of light. The choice of light source of illumination, improvement in CCD technology for image acquisition and fast computers for data analysis has motivated researchers to use schlieren technique for quantitative information. Quantitative analysis relies on geometric-optical theory and associates pixel gray-scale values with source image displacement due to refractions in the test area. Diffraction effect limits the applicability of the geometric theory, especially at high schlieren sensitivity settings, where the light source image is almost entirely cutoff. Therefore, there is a trade off between the schlieren sensitivity and the quantitative accuracy. To overcome these limitations, new schlieren techniques such as phase-shift schlieren (Joannes, 2003 and Farinotti, 2005) and heterodyne schlieren system (Stricker, 2003 and 2005) have been evolved recently. Instead of knife edge, both technique utilizes a slit grating and relies on the estimation of phase value that is subsequently converted into beam deviation angle. In the past, schlieren interferometer has been devised by taking the advantages of schlieren optics and common path interferometry to get the quantitative information by the fringe analysis. Using modern high-speed video cameras, the schlieren technique opens new perspectives for the quantitative investigation of highly transient processes by recording a series of images with a very high temporal resolution. Fusion of schlieren with other technologies have flourished in recent past to get the quantitative information. Examples are:

1. Background oriented schlieren (Richard, 2001 and Meier, 2002) in which a time-dependent optical field is viewed against a detailed background. The distortion of the background is recorded and a standard PIV algorithm is applied to extract the displacement field that can be used for velocimetry or for the measurement of refractive-index gradient distribution .

2. Synthetic schlieren (Dalziel, 2000), that utilizes a background pattern through fluid medium and the perturbations in the density field lead to perturbations in the refractive index of the fluid that cause the pattern appearing to move. A pattern matching algorithm is applied to this apparent movement to determine the refractive index and hence density perturbations. Synthetic schlieren and background oriented

schlieren are essentially the same techniques with only the minor difference in the approaches they take towards pattern matching.

3. Schlieren image correlation velocimetry that utilizes consecutive high-speed schlieren images and determines displacement fields between two successive time separated images using correlation methods or gradient methods for subsequent velocity field determination.

In the present work, refractive index based optical technique, namely schlieren-interferometry have been employed to visualize and characterize convective fields set up around heated horizontal stationary and oscillating cylinders. Quantitative information has been obtained by spectral and statistical analysis of time-dependent fluctuations in light intensity obtained from the sequence of real-time schlieren images. The temporal variations in the light intensity distribution in the flow field necessarily correlate with the velocity field. Therefore, velocity of vortical structures of the wake flow field has been determined by the cross-correlation technique between the pairs of time-separated schlieren images.

1.5 Objectives of the present work

Flow past heated circular and square cylinders are considered in the present study. The literature reveals that detailed experimental study of buoyancy effect on the vortex shedding for heated circular and square cylinders is not available. The effect of oscillation on the wake characteristics have been reported for unheated bluff bodies only. However, no study on joint influence of buoyancy and oscillation is available for both circular and square cylinders. The present study investigates the influence of buoyancy on the wake instability for the stationary circular and square cylinders. Oscillations of heated cylinders have been considered separately and joint influence of buoyancy and oscillation on the vortical structures are examined. This knowledge can be useful for control of the wake pattern such as forces acting on the object and heat transfer from the object. Against this background, the specific objectives of the present study can be summarized as follows:

1. To study the influence of buoyancy on wake dynamics of stationary circular and square cylinders.

2. To carry out detailed quantitative analysis using Strouhal number, vortex formation length, power spectra, rms fluctuations, phase shift and convection velocity results for explaining the suppression of vortex shedding.

3. To study the joint influence of buoyancy and cylinder oscillation on vortex dynamics.

4. To carry out comprehensive parametric study on influence of relevant oscillation parameters i.e. oscillation frequency and oscillation amplitude at different Richardson number.

5. To carry out detailed analysis of lock-on mechanism between the near-wake and heated cylinder motion.

1.6 Thesis organisation

Subsequent chapters of the present thesis have been organized in the following sequence. Chapter-2 presents a literature review related to fundamental studies of flow past a circular and square cylinder, effect of buoyancy, effect of in-line and transverse oscillation on the wake behaviour of these cylinders. The review also emphasizes literature related to the schlieren imaging especially diffraction based schlieren-interferometry. The experimental setup, heated cylinders, laser schlieren system, imaging system, cylinder oscillation system and related instrumentations are discussed in chapter-3. Chapter-4 presents the procedure for data analysis along with uncertainty analysis. The validation of experiments and data analysis procedure are also presented. Chapter-5 presents results on the effect of buoyancy on the wake instability of heated circular and square cylinders. The results on combined influence of heating and transverse oscillation on the wake characteristics of heated circular and square cylinders are reported in Chapter-6. Chapter-7 summarizes the major conclusions drawn from the present study and scope for future work. Appendix-A presents preliminary results from in-line oscillation of heated circular cylinder.

भारतीय प्रौद्योगिकी संस्थान कानपुर
INDIAN INSTITUTE OF TECHNOLOGY KANPUR

Chapter 2

Literature Review

The literature related to flow past cylinders of circular and square cross-section is reviewed here. Fundamentals related to the basic mechanism of wake instability and vortex shedding have been discussed. Special emphasis is made on the effect of buoyancy and oscillation on the wake behaviour reported in the literature. Emphasis have been given to experimental studies, while numerical results are also included for comparison, where appropriate. Flow past a square cylinder resembles the flow past a circular cylinder as far as the instabilities are concerned. But the separation mechanisms and the consequent dependence of the shedding frequency and the aerodynamic forces on the Reynolds number differ significantly. For a circular cylinder, the points of separation depends on Reynolds number. Whereas, the separation points are fixed for a square cylinder. However, in low velocity flows, the nature of the boundary layer at the separation location is affected by thermal buoyancy forces arising due to heating of the cylinder and have significant influence on the flow structures. In addition, externally imposed vibration of the cylinder also influences the near-wake characteristics and the shedding mechanisms. A brief review on the sensitivity of the wake to these external factors have been undertaken. Literature related to schlieren imaging of convective flows with special emphasis to diffraction based schlieren-interferometry have been discussed. Literature related to data processing i.e. the image correlation and convection velocity of vortex structures is also presented.

The literature review has been presented in the following sequence: (i) Review of bluff body flows, (ii) Wake behaviour of heated cylinder, (iii) Wake dynamics of oscillating cylinder, and (iv) Optical measurement and schlieren technique. The summary from the literature review leading to the objectives of the thesis has been presented in the closure section.

2.1 Review of bluff body flows

Bluff body flows consists of more or less coherent structures, which form under certain conditions, get shed and advect downstream. These are primary responsible for the global characteristics eg. unsteady forces, mixing properties and heat transfer. A number of experimental and numerical investigations have been performed at low as well as high Reynolds number[1]. The focus of the present thesis is towards the low Reynolds numbers range of the order Re = 100. The Reynolds number referred here is based on the average incoming velocity and the cylinder diameter/edge. The present section reviews the flow over circular and square cylinders with reference to few fundamental studies to understand the mechanism of vortex shedding and its control.

2.1.1 Flow past a circular cylinder

The circular cylinder geometry has been extensively studied in the literature. Excellent review for the flow past circular cylinder has been written by Zdravkovich (1997). In fact, the current knowledge of bluff-body wakes stems from the research on flow past a circular cylinder. Despite its simple shape, a circular cylinder generates a wake that is dynamically complex.

Perry *et al.* (1982) studied flow behind a circular cylinder using different flow visualization techniques. Instantaneous streamline and streakline patterns during vortex shedding process were examined on the basis of flow visualization images, Figure 2.1 (a). The streamline patterns show that a closed cavity forms behind the cylinder at low Reynolds numbers. With an increase in Reynolds number, vortex shedding is initiated, the closed cavity becomes open and instantaneous *alleyways* (shown by cross-hatching, Figure 2.1 (b)) of fluid are formed which penetrate the cavity from either side of the cylinder at different times.

Roshko (1993) reviewed the fundamental aspects of the bluff body flows with powerful theoretical discussion regarding the near wake recirculation region. The variation of drag and base suction of circular cylinder and bluff plates over a range of Reynolds number from 10 to 10^7 were discussed. A model for flows with a wake splitter plate was proposed. Effects of three-dimensionality arising from natural instability as well as due to end effects were discussed.

[1]The low and high Reynolds number range vary somewhat as they are defined in the literature. Generally speaking, a value less than Re = 350 refers to the low Reynolds number regime and greater than Re = 350 refers to high Reynolds number regime (Griffin, 1995).

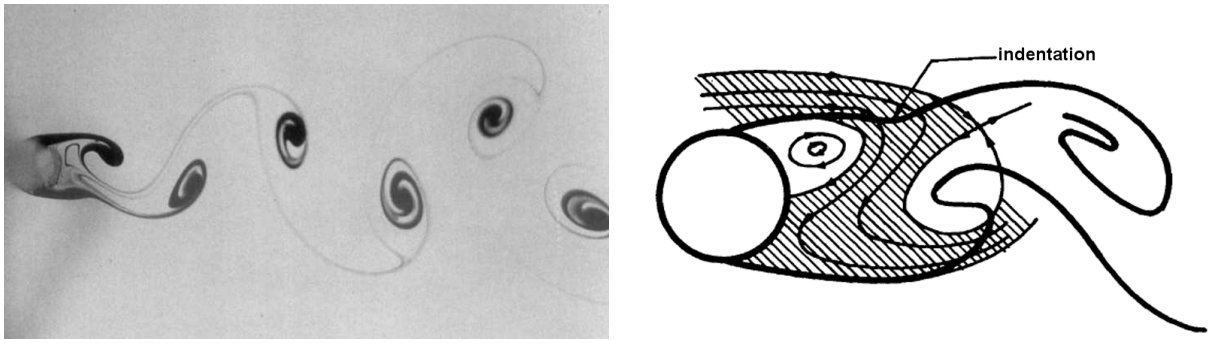

(a) (b)

Figure 2.1: (a) Typical dye traces in a Karman vortex street behind a circular cylinder at Re = 80, and (b) Interpretation using instantaneous streamlines, Perry *et al.* (1982).

Wu *et al.* (1994) performed an experimental study to visualize the three-dimensional structures in near wake of a circular cylinder at Re = 50 to 1800. The hydrogen-bubble flow visualization patterns were recorded with two CCD cameras placed in two orthogonal planes. A typical pattern presented in Figure 2.2 (a) shows that mushroom-type structures (indicated by the arrow) develop in the near wake behind the cylinder. Thus, implying the existence of the counter-rotating streamwise vortices superimposed on the nominally two-dimensional Karman vortex street along the span of the cylinder and interpreted in Figure 2.2 (b). The mean spanwise wavelength of the streamwise vortices was obtained using digital images and found to scale with the diameter of the cylinder.

Williamson (1997) presented an overview on the fundamental aspects of the vortex

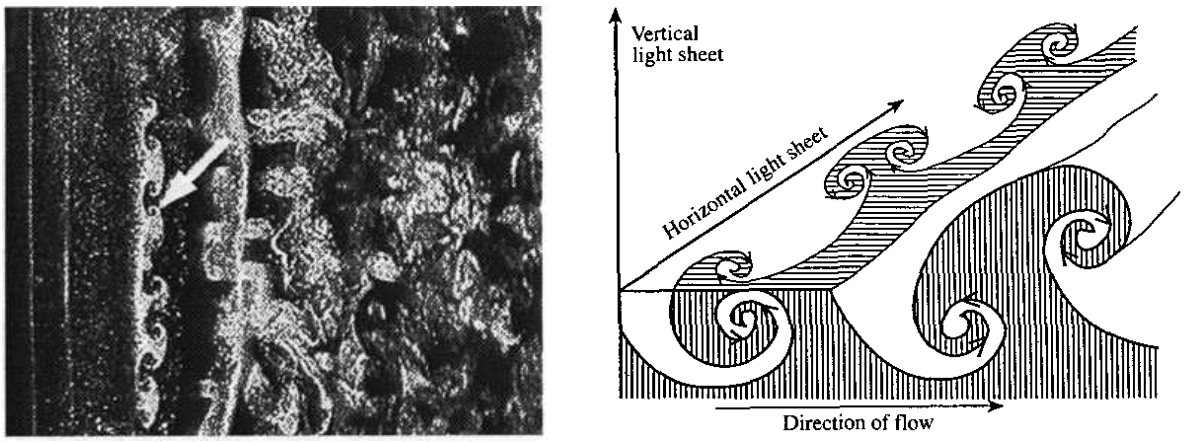

(a) (b)

Figure 2.2: Streamwise vortices embedded in the Strouhal vortices: (a) Flow visualization, flow from left to right and the cylinder is located at left, and (b) Conceptual diagram, Wu *et al.* (1994).

dynamics for flow past a circular cylinder over wide range of Reynolds numbers. Three dimensionality in laminar regime, transition regime and instability in the shear layer were discussed in great detail. Vortex dislocations, nonparallel or oblique shedding, vortex loops and streamwise vortex pairs were shown to be the major three-dimensional phenomenon in the wake of a nominally two-dimensional body. The vortex shedding patterns are either oblique or parallel to the cylinder axis in the laminar regime and are susceptible to end conditions.

Bearman (1997) studied the vortex formation and the near-wake dynamics behind two and three-dimensional bluff bodies. A brief review of the characteristic three-dimensional features found in the wakes behind two-dimensional geometries were presented. It was observed that three-dimensionality of the vortex structures have a strong influence on the level of fluctuating transverse force. Numerical simulation results showed that vortex formation length varies through lock in range for a circular cylinder oscillating transverse to the flow. The PIV results in the wake of a three-dimensional complex bluff body (car model) showed that the instantaneous flow field is quite different from the time-averaged field.

2.1.2 Flow past a square cylinder

For a square cylinder, the separation points are fixed, either at the leading edge or the trailing edge, depending on the Reynolds number. The square cylinder is a bluffer body as compared to the circular cylinder. Therefore, the vortex formation region is significantly broader and longer. In the following section, the literature on the flow past cylinders of square and rectangular cross-sections at zero incidence (flat face facing the flow) are reviewed.

Okajima (1982) has conducted an experimental study for the flow past a rectangular cylinder for a wide range of Reynolds number (70 to 2×10^4) and width-to-height ratios range of 1 to 4. Experiments were performed in air as well as in water with hotwire anemometer and flow visualisation (Figure 2.3). The dependence of Strouhal number on Reynolds number for different width-to-height ratios was brought out in the study. For a ratio of 2 and 3 there was a certain critical range of Reynolds number where the flow pattern changed abruptly with a sudden discontinuity in the Strouhal number. Below this critical range the flow separated from the leading edge reattaching at the side surfaces and beyond this range the flow fully detaches itself from the cylinder.

Davis and Moore (1982) performed two-dimensional numerical simulation for the flow past a rectangular cylinder in the Reynolds number range of 100 to 2800. The effects

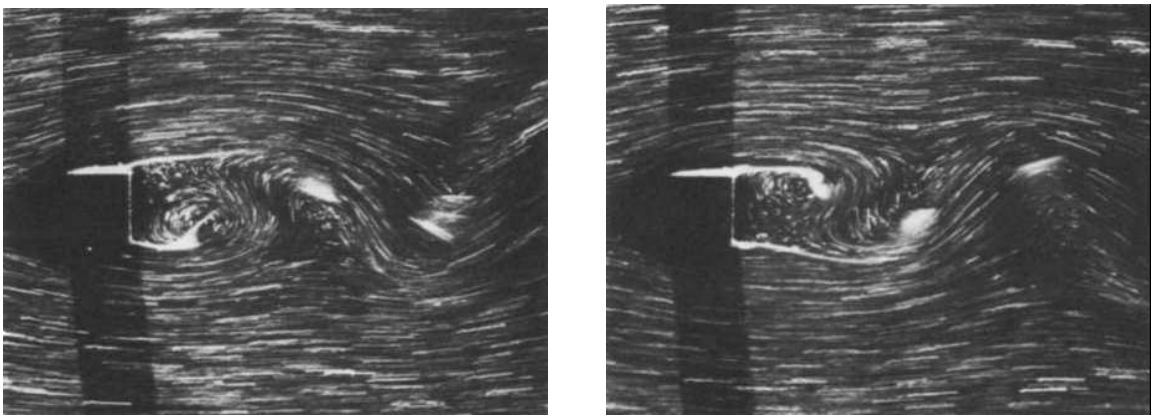

Figure 2.3: Flow visualization patterns in the near wake of a square cylinder at two different times in a shedding cycle for Re = 150, Okajima (1982).

of upstream velocity profile, angle of attack and variation in rectangle dimensions on the vortex shedding phenomenon have been studied. The results show that the lift and drag coefficients and Strouhal number depend strongly on the Reynolds number. For a square cross section, the Strouhal number increases with increase in the Reynolds number to a certain value beyond which further increase in Reynolds number results in decrease in Strouhal number reaching an asymptotic value. Within the Reynolds number considered, the average drag coefficient continuously increases with Reynolds number.

In a comparative study of flow past circular and square cylinders, Franke *et al.* (1990) carried out a two-dimensional numerical simulation (Re $\leq$ 5000 for the circular cylinder and Re $\leq$ 300 for the square cylinder). Reynolds number dependence of the Strouhal number and the drag coefficient were compared with the published experimental and numerical results and a good agreement was found. In the case of square cylinder, a relatively large discrepancy was seen in the variation of Strouhal number as a function of Reynolds number. The sharpness of cylinder corners in the experiments and the numerical treatment of these corners considerably influenced the shedding frequency.

In a numerical study to predict the onset of unsteadiness in the flow over a square cylinder, Kelkar and Patankar (1992) performed linear stability analysis and reported the critical Reynolds number at which the flow becomes unsteady. The two-dimensional linear stability analysis of the steady flow was carried out by computing the evolution of two-dimensional perturbations and the critical Reynolds number was determined by the growth of these perturbations. The study shows the critical Reynolds number to be 53. The periodic vortex shedding behind the cylinder at Re = 100 can be seen in instantaneous streamlines and isotherm patterns of Figure 2.4 at three different instants in a shedding cycle.

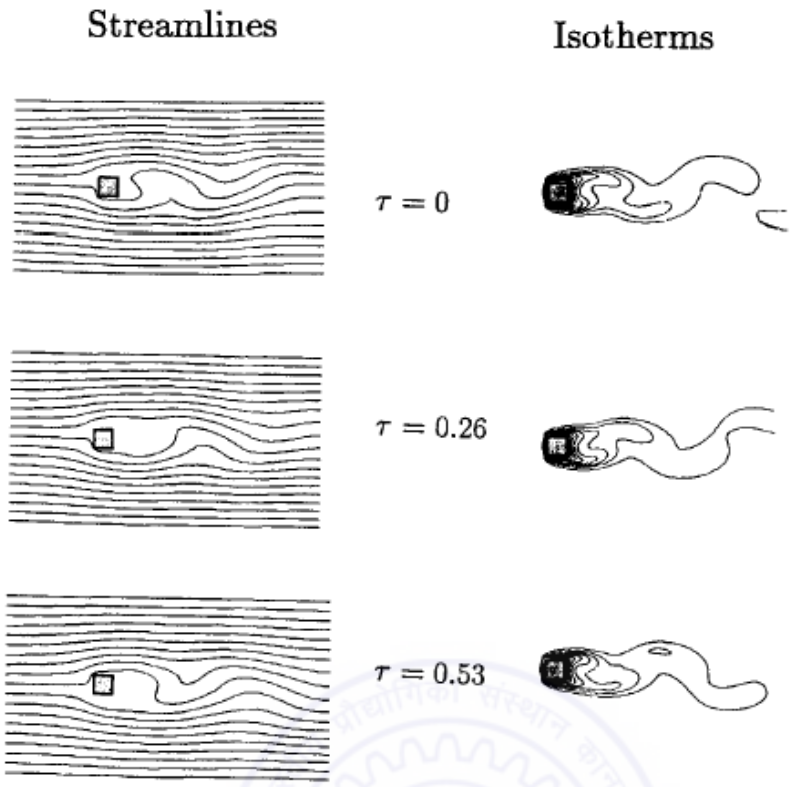

Figure 2.4: Instantaneous streamlines and isotherm patterns at different time instants during one cycle of periodic unsteady flow behind a square cylinder at Re = 100 with Pr = 0.7, Kelkar and patankar (1992).

Sohankar *et al.* (1998) carried out calculations of unsteady, incompressible 2D flow past a square cylinder at incidence (0°-45°) for Re = 45-250. The influence of Re and angle of incidence on quantities such as drag and lift coefficients and Strouhal number were shown. The critical Reynolds number for onset of vortex shedding decreased from 51 to 42, when the angle of incidence was varied from 0° to 45°.

In a later study, Sohankar *et al.* (1999) performed direct numerical simulations of 2D and 3D unsteady flow around a square cylinder for Re = 150-500 at a blockage ratio of 5.6%. The authors observed transition from 2D to 3D shedding flow between Re = 150 and 200. Both spanwise instability modes, namely A and B, were present in the wake transitional process, similar to that seen for a circular cylinder (see Figure 1.3). However, the transitional flow around a square cylinder exhibits a phenomenon of distinct low-frequency force pulsations (Re = 200-300). The phase shift between the shedding frequency and lift amplitude at the intiation of three-dimensional flow observed in the present calculations were suggested as a reason for these pulsations.

Robichaux *et al.* (1999) numerically investigated the onset of three-dimensionality in the wake of a square cylinder using Floquet stability analysis. A new mode of instability,

called mode 'S' was observed along with modes 'A' and 'B'. This mode is absent for a circular cylinder flow. Mode S is a rare occasion where a two dimensional flow with T period undergoes a period doubling bifurcation by becoming unstable to $2T$-periodic three- dimensional disturbances.

Saha *et al.* (2003) performed numerical simulation to study spatial evolution of vortices and transition to three-dimensionality in the wake of a square cylinder. Two modes of secondary vortex structures in the transition zone were discussed in terms of their influence on Strouhal number and time-averaged drag coefficient. At about Re = 175, the flow becomes three-dimensional, with Mode-A instability. The transitional route to three-dimensionality exhibits an intermittent low frequency modulation and flow at around Re = 250 reveals mode-B secondary vortices.

Luo *et al.* (2003) studied the characteristics of the wake transition regime for the flow past a square cylinder using dye and LIF flow visualization and hotwire anemometry. The authors observed the presence of two dominant transition modes similar to that of a circular cylinder. However, there are differences in spanwise wavelengths and Reynolds numbers at which the respective transitions occurs. For the square cylinder, the critical Reynolds numbers are lower while spanwise wavelengths are larger for both mode-A and mode-B transitions when compared to the circular cylinder. However, the structures of the streamwise vortices are similar to those of circular cylinder. No hysteresis is present for the square cylinder in the transition to mode-A instability contrast to that of a circular cylinder. Furthermore, the transition from mode-A to mode-B is not accompanied with discontinuous sudden jump in St-Re curve.

2.1.3 Mechanism of vortex formation and its control

The flow field in the vortex formation region of a bluff body is important to the overall development of the near-wake flow. A physical discussion on the mechanism of vortex street formation serve to introduce a relationship between the size of the formation region, the strength of the vortices and the frequency of vortex shedding. The present section reviews the literature on mechanism of vortex street formation and its control.

Gerrard (1966) studied the mechanism of vortex shedding from the circular cylinder and presented a model to describe it. According to this model, the growing vortex is fed by circulation from the separated shear layer until it is strong enough to roll up and draw the opposing shear layer across the wake. The vorticity of opposing sign cuts off further circulation to the growing vortex, which then is shed and moves away downstream. Figure 2.5 shows that vorticity 'a' is entrained into the growing vortex, vorticity 'b' is

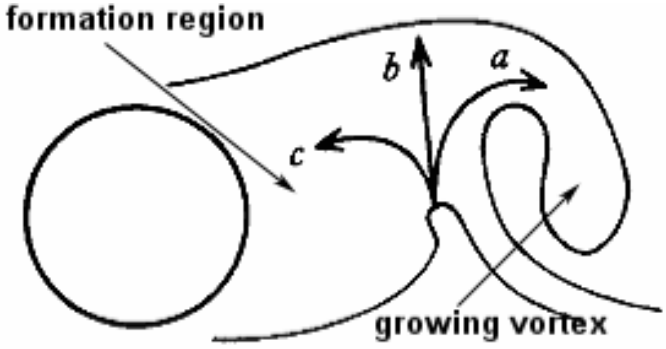

Figure 2.5: A sketch of the instantaneous filament lines in the formation region behind a circular cylinder. The arrows show entrainment, (a) and (b) and reversed flow, (c), Gerrard (1966).

entrained into the separated shear layer, and vorticity 'c' moves back into the formation region. Thus, the path of vorticity 'b' (i.e. interaction of the oppositely-signed shear layer) is of key importance for a vortex to be cutoff from its feeding shear layer and shed. Gerrard proposed the 'vortex street' formation to be a function of the formation length, specifically, the relative scales in the formation and diffusion regions. The model predicts that the vortex street is inhibited if vorticity in the shear layer diffuses over a critical diffusion length or the shear layers are prevented from interactions over a critical formation length.

Strykowski and Sreenivasan (1990) reported that vortex shedding behind a circular cylinder can be altered and suppressed altogether for Reynolds numbers upto about 80 by proper placement of a second, much smaller, cylinder in the near wake of the main cylinder. The authors studied the phenomenon through experimental and numerical investigations, including flow visualization. It was argued that properly placed control cylinder redistributes the vorticity in the shear layer in which it resides; a related effect is that the secondary cylinder diverts a small amount of fluid into the wake of the main cylinder. The suppression of the vortex street corresponds to the global decay of modes that would, under normal circumstances, be temporally amplified leading to vortex shedding.

Mori *et al.* (1986) studied the effect of heating of the wake with fine wires and the effect of using splitter plate or mesh behind a cylinder in uniform upward flow. The vortices behind the cylinder were gradually modified from the Karman vortex street to symmetrical vortices with increase of heat input and also by the increase of the splitter plate length or mesh number behind the cylinder. The shedding of the symmetrical vortices was caused by the instability of the free shear layer just behind the separation point.

The summary of the above review of bluff body flow shows that three-dimensionality is a prominent feature of flow past circular and square cylinder in the low Reynolds number regime. The cylinder of the square cross-section shares many of the transitional features of the circular cylinder such as onset of the vortex shedding, onset of three-dimensionality and structures of three-dimensional streamwise vortices. There are points of difference as well such as the dependence of the Strouhal number and drag coefficient on the Reynolds number. The mechanism of formation and suppression of vortex shedding strongly depends on the distribution of vorticity in the formation region as well the interaction of the opposed shear layers.

2.2 Wake behaviour of heated cylinder

When the cylinder is heated with respect to the incoming flow, the buoyancy forces arise as a result of temperature difference between the cylinder surface and the ambient fluid. For forced convection problems, the magnitude of buoyancy force is comparatively small and thus negligible. The forced convection limit has received considerable attention in the literature. However, the literature on wakes of heated bluff bodies that are influenced by significant changes in fluid density is less common and is reviewed below.

2.2.1 Effect of buoyancy

When the flow velocity is not very high and the temperature difference is large, the buoyancy forces have a significant influence on the flow structures and consequently on the heat transfer rate. The wake behaviour is physically more complicated due to buoyancy effects added in the forced flow. For these mixed convection flows, the interaction between two different sources of motion may result in enhanced mixing properties compared to purely forced convection case. Richardson number, Ri ($dg\beta\Delta T/U_\infty^2$) is an important parameter for characterization of buoyancy effects at a given Reynolds number.

In an earlier work, Oosthuizen and Madan (1971) studied unsteady mixed convection flow past a cylinder over Reynolds number range of 100-300. The authors interest was on the average heat transfer coefficient and not on the behavior of the near wake vortices. Merkin (1977) studied the thermal boundary layer over a horizontal circular cylinder in a stream flowing vertically upwards for differentially heated and cooled cylinders. It was observed that heating delayed separation of the boundary layer and separation was completely suppressed at a higher heating level. Cooling the cylinder was seen to bring the separation point closer to the forward stagnation point and for a sufficiently cold

cylinder, the boundary layer on the cylinder disappears. Jain and Lohar (1979) reported an increase in vortex shedding frequency with an increase in cylinder temperature.

Badr (1984) performed a numerical study for laminar mixed convection heat transfer from an isothermal horizontal circular cylinder. Two cases of external flow directed vertically upward (aiding buoyancy) and vertically downward (opposing buoyancy) were considered. The streamlines and isotherms were plotted as function of Reynolds number and Grashof number. The study was limited to the mixed convection with Reynolds number up to 40. The effect of increasing Grashof number on vorticity generation and Nusselt number distribution was brought out.

Noto *et al.* (1985) experimentally observed the breakdown of unsteady vortex street for heated horizontal circular and triangular cylinders. The breakdown phenomenon was demonstrated from the flow visualization by smoke wire method, power spectra and Strouhal number. By adding natural convection to neutrally buoyant wake, the Struouhal number increases gradually and then decreases abruptly. As causes of the breakdown, an acceleration of velocity in the wake is more dominant than a shift of the separation points.

Chang and Sa (1990) performed a detailed numerical study of the phenomenon of vortex shedding from a heated/cooled circular cylinder in the mixed, natural and forced convection regimes at a Reynolds number of 100 and -1 $<$ Ri $<$ 1. According to their results, cooling of the cylinder surface activates the roll up process and promotes the generation of the Karman street. Heating the cylinder impedes the roll up process with subsequent degeneration of the vortex street into steady twin vortices at a critical Richardson number of 0.15. Figure 2.6 show the time sequence of streamlines and isotherms for periodic flow with vortex shedding at Re = 100, Ri = 0.10. Purely periodic flow degenerates into steady flow with twin vortices for Ri $\geq$ 0.15, Figure 2.7. The heating of the cylinder was found to accelerate the wall boundary layer and increase the velocity in the wake region. As the Richardson number increased, the thinner boundary layer caused the shedding frequency to increase, while the weakened roll-up process reduced entrainment of the ambient flow into the wake cavity until the vortices finally ceased to shed from the cylinder surface.

In similar numerical studies performed at a Reynolds number of 100, Hatanka and Kawahara (1995) and Singh *et al.* (1998) established that vortex shedding ceases at a critical Ri value of 0.15. Flow was seen to become steady with symmetric twin vortices attached to the cylinder. Hatanka and Kawahara (1995) also showed that Strouhal number increases as the Richardson number increases owing to positive buoyancy force whereas it reduces as the cylinder surface is cooled below the fluid temperature, Figure 2.8.

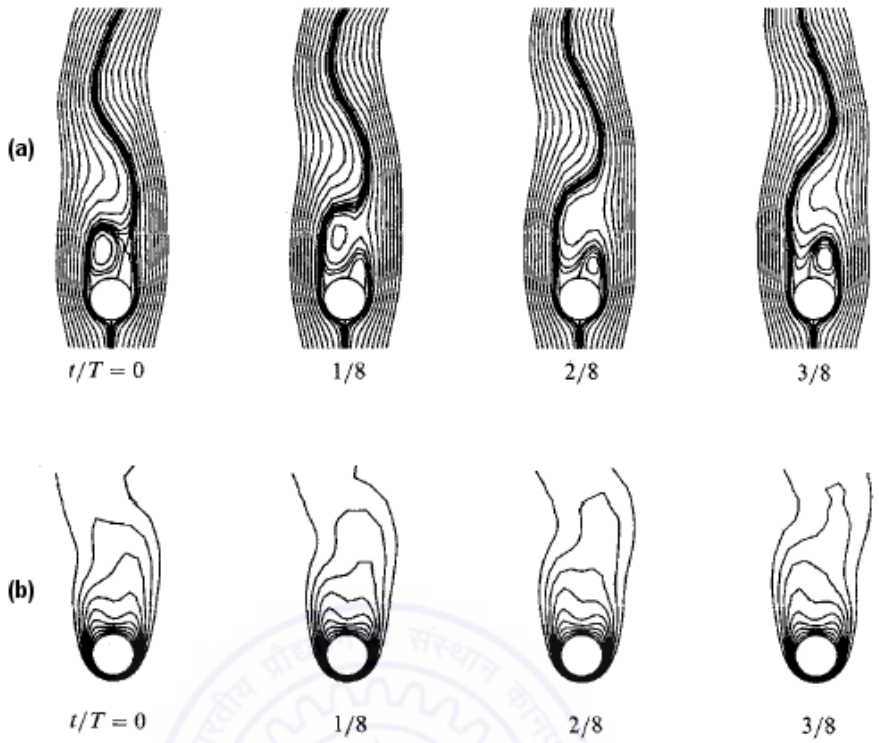

Figure 2.6: (*a*) Streamlines and (*b*) Isotherms in periodic flow with vortex shedding at Re=100, Ri=0.10, Chang and Sa (1990).

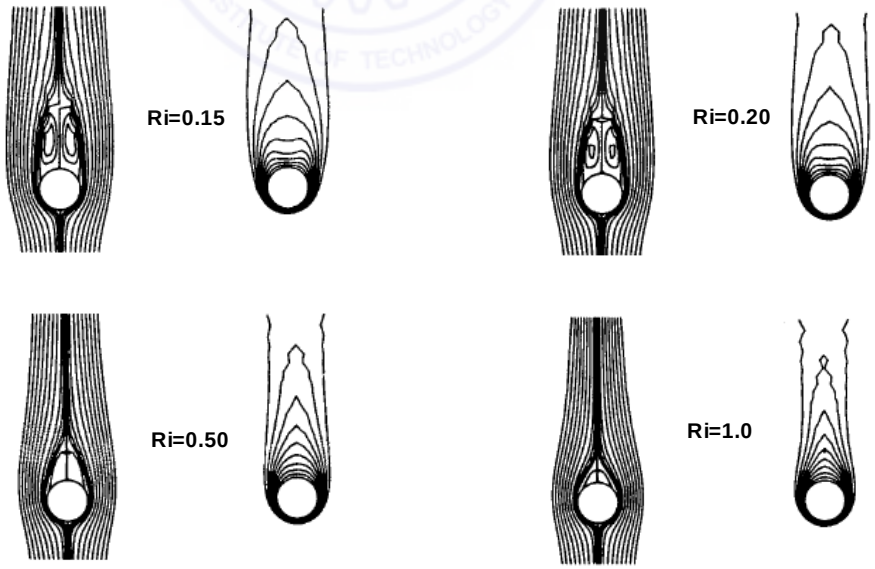

Figure 2.7: Streamlines and isotherms in steady flow with twin vortices at Re=100, Ri=0.15, 0.20, 0.50 and 1.0, Chang and Sa (1990).

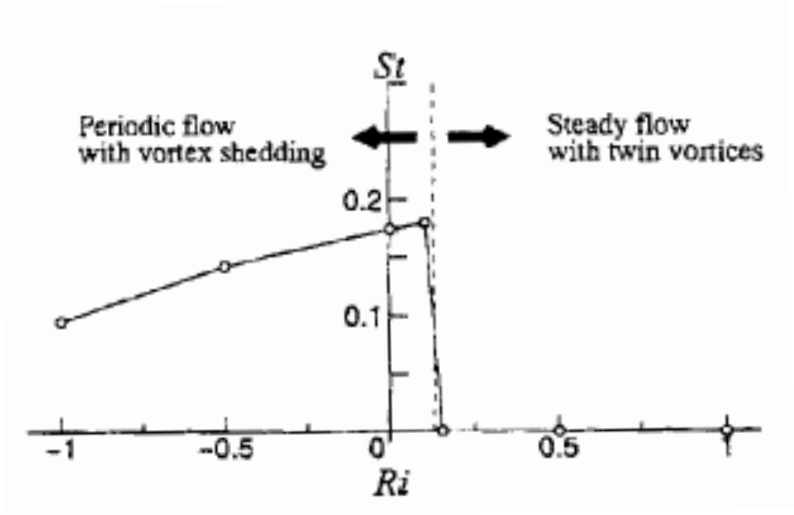

Figure 2.8: Strouhal number versus Richardson number, Hatanka and Kawahara (1995).

Michaux-Leblond and Belorgey (1997) experimentally performed an investigation of the mean flow velocities in the near wake region of a heated circular cylinder. Velocity and temperature fields were obtained respectively by laser Doppler velocimetry and thermocouples. The role of heating was found to accelerate the wall boundary layer and to increase the velocity in the near-wake region. The critical value of the heat input needed for the suppression of the vortex street was determined. The heat input required for suppression increases with increase in Reynolds number.

In a numerical study, Patnaik *et al.* (1999) confirmed the suppression of vortex shedding and found the critical Richardson number to be 0.12 at Re = 100 for a circular cylinder. The effect of buoyancy on the Nusselt number, Strouhal number, structures of the wake, temporal lift and drag forces were reported. Under the influence of buoyancy opposing the flow, vortex shedding could be triggered even at a low Reynolds number of 20-40.

Sharma and Eswaran (2004) have numerically studied the flow structure and heat transfer characteristics of a heated square cylinder in upward cross flow considering the effect of aiding and opposing buoyancy at Re = 100, Pr = 0.7 and -1 $\leq$ Ri $\leq$ 1. The disappearance of vortex shedding was reported at a critical Richardson number of 0.15. Cooling the cylinder increases the strength of the shear layer and roll-up of the isotherms downstream of the cylinder is activated. In contrast, heating weakens the shear-layer and the roll up process as seen in Figure 2.9. The influence of buoyancy on the recirculation length, drag and lift coefficients, Strouhal number and time-averaged Nusselt number has been investigated. The mean recirculation length increases with an increase in Richardson number in the periodic flow regime and decreases in the steady flow regime.

Figure 2.9: Isotherms near the square cylinder as a function of Richardson number at Re = 100, Sharma and Eswaran (2004).

2.2.2 Concept of effective temperature

When a horizontal circular cylinder is exposed to parallel cross flow of air and level of heating is not strong enough to generate buoyancy effects, the heated cylinder operates in the forced convection regime. However, temperature differences within the fluid lead to variations of its properties e.g. viscosity and density. Lecordier *et al.* (1991) showed that at low Reynolds number, the characteristics of vortex shedding can be significantly altered by heating the cylinder and a total suppression can be achieved by sufficient heat input. The authors suggested that this control could be a result of a slight change of the separation point location due to an increase in the dynamic viscosity. Based on the reduction in Reynolds number due to increase in dynamic viscosity of air with increase in temperature, the authors proposed an effective temperature concept. The effective temperature was defined as the temperature needed to increase the air kinematic viscosity in order that the effective Reynolds number (Re_{eff}) at the suppressed heating

is equal to critical Reynolds number for the onset of vortex shedding. Dumouchel *et al.* (1998), working in the same group extended this concept and calculated the effective temperature, $T_{eff} = T_\infty + C(T_w - T_\infty)$, with $C = 0.24 \pm 0.02$ for a temperature ratio, T^* $((T_w + 273)/(T_\infty + 273))$ less than 1.5. The effective temperature is lower than the usual film temperature, $T_{film} = T_\infty + 0.5(T_w - T_\infty)$.

Wang *et al.* (2000) used the similarity concept that the onset of vortex shedding begins at the same value of effective Reynolds number for all the cylinder temperatures, if the Reynolds number is defined with a kinematic viscosity computed from an effective temperature. The authors proposed a modified value of $C = 0.28$ in the range $1.1 \leq T^* \leq 1.8$. Although, the vortex shedding frequency decreases with increasing cylinder temperature, the relationship between the Strouhal number and effective Reynolds number is found to be "universal" as seen in Figure 2.10.

Although the study of Lecordier *et al.* (1991) relates the suppression of instability to viscosity, this phenomenon has also been related to density change in the near wake (Yu and Monkewitz, 1990; Schumm *et al.*, 1994). Yu and Monkewitz (1990) concluded that change in the stability characteristics brought about by heating is the result of a slightly modified interaction between the two mixing layers via inertial effects and not related to viscous forces; No significant discrepancy between computations based on constant and temperature dependent dynamic viscosity was obtained. Schumm *et al.* (1994) showed the suppression of vortex shedding by steady heating upto twice the critical Reynolds number (based on the cold free stream properties) for a circular cylinder. The authors related the instability mechanism to the ratio of average density in the recirculation region to free stream density. Apart from wake heating, the authors also investigated the other methods of controlling the vortex shedding in the near wake such as base bleed and forced transverse oscillations.

In a later study, Lecordier *et al.* (2000) reported suppression of vortex shedding in airflow and related it to changes in viscosity and density with temperature. An opposite trend was found in water, suggesting a dominance of change in viscosity as compared to change in density with temperature. The shape of the velocity profile is coupled with temperature field, i.e. the changes in viscosity and density due to temperature variation relate to the velocity profile and hence the instability characteristics.

In a numerical study, Shi *et al.* (2004) separately computed the effect of the dynamic viscosity and density variations with heating for laminar flow of air past a horizontal circular cylinder. The authors concluded that both the viscous effect and inertia effect have an essential influence on the shedding frequency and other heat transfer characteristics.

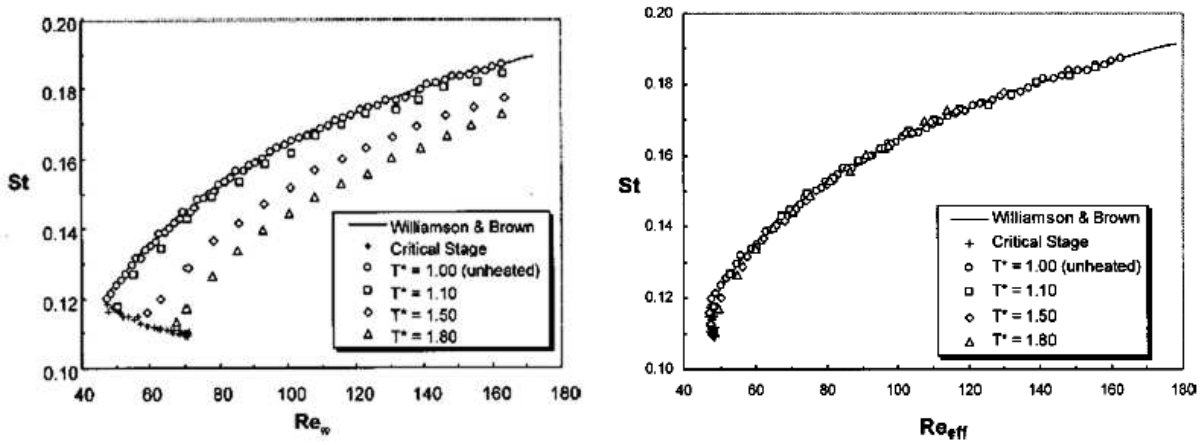

(a) (b)

Figure 2.10: (*a*) St vs Re_∞, and (*b*) St vs Re_{eff} relationship for the unheated and heated cylinder, Wang *et al.* (2000).

In a flow visualization study using electrochemical tin precipitation method, Maas *et al.* (2003) reported heat-induced 3D-transition of the vortex street in the wake of a horizontal heated circular cylinder, immersed in water. The wake became three-dimensional for a Richardson number greater than 0.3 at Re = 117. For these Richardson numbers 3D vortical structures are observed near the cylinder wall.

Vit *et al.* (2007) investigated laminar vortex shedding behind heated circular cylinder in the forced convection regime for water and air. The effective temperature concept was used for discussion of the St-Re data from the hotwire measurement. The evaluation of effective temperature was based on fitting of all St-Re data onto one $St - Re_{eff}$ curve instead of evaluation by means of the flow similarity at the onset of vortex shedding. The authors reported a universal relationship between Strouhal number and effective Reynolds number for both air and water. The effective temperature was found to be $T_{eff} = T_\infty + C(T_w - T_\infty)$, with $C = 0.97$ or 0.28 for water and air, respectively.

The above review of literature reveals that suppression of shedding for the flow past a circular cylinder is possible by heating the cylinder and has been demonstrated by numerical simulations. However, detailed experimental study of buoyancy effect on the wake behavior of a heated cylinder is limited. Moreover, no experimental study on vortex shedding mechanisms for flow past a heated square cylinder is available. The square cylinder is fundamentally different from that of the circular cylinder due to its fixed separation point. Therefore, it is of interest to compare the effect of heating on the vortex shedding mechanism of the circular cylinder with that of the square and is the focus of the present study.

2.3 Wake dynamics of oscillating cylinder

The interest on the near-wake structures of an oscillating cylinder has arisen to simulate the practical consequences of flow-induced vibrations. With a view to control the wake or to simulate the problem of vortex-induced oscillations, a rigid cylinder submerged in steady flow can be oscillated in a predefined direction (transverse or in-line with respect to the mean flow direction) at defined frequency and amplitude of oscillation. The nonlinear interaction of the body motion and the incident flow leads to a number of interesting phenomenon, such as vortex lock-on, hysteresis and bifurcation, alteration of vortex shedding patterns, chaotic behaviour of the wake and many more. Of these, the focus has been on the phenomenon of 'lock-on' also known as 'phase-locking' or 'synchronization', where vortex shedding is entrained by the cylinder motion. Here, the vortex shedding frequency changes to match with the forced oscillation frequency. Investigators have studied lock-on phenomenon both for the forced simple-harmonic oscillation of a cylinder as well as for an elastically mounted cylinder. Griffin and Hall (1991) presented an extensive review of vortex shedding lock-on in the near-wake of bluff bodies due to body oscillations both in-line and transverse direction with respect to the mean flow and rotational oscillations of the body. The effect of sound on the vortex lock-on was also studied. For vortex-induced vibrations, investigators have observed that in certain range of reduced velocities (defined in next paragraph), the flow causes the cylinder to oscillate at its natural frequency and a peak of amplitude is reached. The cylinder oscillation frequency is thus different from the Strouhal frequency that would be obtained if the cylinder was supposed to be fixed. With the proper understanding of flow structures modification by the cylinder oscillation and their role in determining fluid forces and mixing process, an active flow control strategy can be effectively proposed.

For a cylinder subjected to forced simple-harmonic oscillations, the relevant governing parameters are: (i) Reynolds number, $\mathrm{Re} = U_\infty d/\nu$; (ii) amplitude ratio, a/d; (iii) frequency ratio, f_e/f_s; (iv) reduced frequency, $f_e D/U_\infty$, or reduced velocity, $U_\infty/f_e D$; where U_∞ is the free stream velocity, d is the diameter/edge of the cylinder, ν is kinematic viscosity of the fluid, and a is the oscillation amplitude and f_e frequency is the frequency of cylinder oscillation. The vortex shedding frequency for the stationary cylinder (Strouhal frequency) is denoted by f_s, while for the oscillating cylinder it is denoted by f_v.

2.3.1 Forced transverse oscillations

In most of the flow control applications, controlled transverse oscillation is applied to counteract the instantaneous transverse forces due to vortex shedding. For transverse oscillations, 'lock-on' occurs at a frequency close to the fundamental Strouhal frequency of vortex shedding i.e. at a frequency ratio, $f_e/f_s \approx 1$. Investigators have determined bounds of *lock-on* regime in a frequency-amplitude plane as a function of frequency ratio (f_e/f_s) and amplitude ratio (a/d). In the fundamental lock-on regime, as f_e approaches f_s, an abrupt jump in the magnitude and phase of the fluctuating lift force has been observed by the investigators. The changes in the patterns (mode) of vortex shedding as well as the phase (timing) of initially shed vortices with respect to the cylinder displacement have been identified as the causes of this abrupt jump. Literature review related to the changes in the overall patterns of vortex formation due to transverse oscillations with the aim to determine origin of loading on the cylinder is presented below.

In an earlier work, Koopmann (1967) investigated the effect of forced transverse oscillations of a circular cylinder on vortex shedding at Re = 100, 200 and 300 and determined a threshold (minimum) oscillation amplitude, $a/d = 0.05$ required for lock-

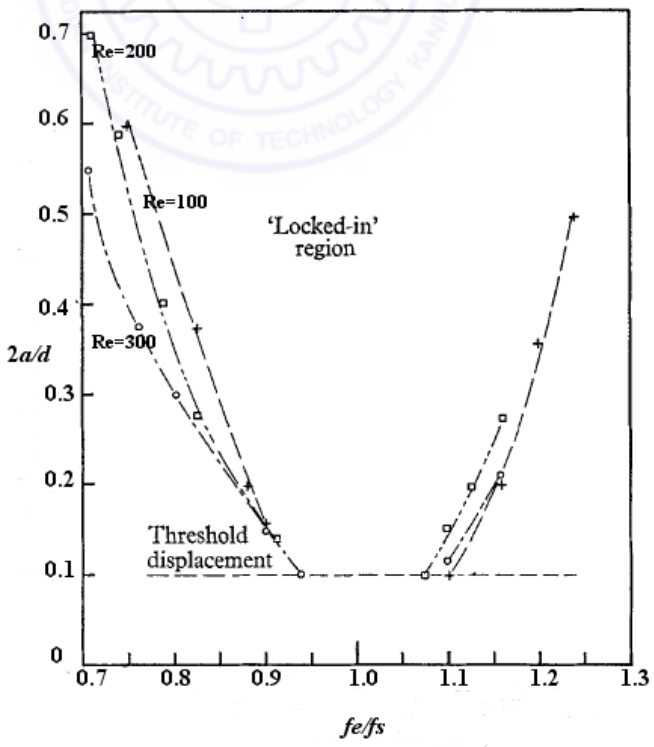

Figure 2.11: Limits of lock-on regime as a function of frequency ratio (f_e/f_s) and amplitude ratio (a/d) for transverse oscillations of the circular cylinder, Koopmann (1967).

on. It was observed that lock-on changed the angle of vortices with respect to the cylinder axis and a slant-wise vortex shedding was replaced by parallel vortex shedding. The limits of lock-on regime as a function of frequency ratio (f_e/f_s) and amplitude ratio (a/d) is shown in Figure 2.11.

Griffin and Votaw (1972) studied the effect of forced transverse oscillations on the wake behind a vibrating cylinder at Re = 144. The authors observed that vibrations at the Strouhal frequency in lock-on range reduce the vortex formation length by 50% ($3.2d$ to $1.7d$) when amplitude (peak to peak) of vibration was increased to half a diameter. In a later study, Griffin and Ramberg (1974) obtained the vortex formation length, vortex strength and vortex spacing for the similar experimental conditions. The authors found an inverse relation between the vortex strength and the formation length inside the lock-on range. An increase of 65% in the initial circulation (or strength) of the vortices was observed at an oscillation amplitude (peak to peak) 50% of the cylinder diameter. Increasing the amplitude of oscillation reduces the lateral spacing of the vortices.

Zdravkovich (1982) analyzed the flow visualization results of Den Hartog (1934) and concluded that within the synchronization range, the change of conditions from below Strouhal frequency to above it, the timing (phase) between the initially shed vortices and cylinder displacement changes by the order of π. Within the synchronization range, two modes of vortex shedding was seen for the frequencies of oscillation above and below the natural shedding frequency. For frequencies of oscillation above the Strouhal value, the vortex formed on one side of the cylinder was shed when the cylinder was near the maximum amplitude on the opposite side. On decreasing the frequency of oscillation, the timing changed suddenly and the vortex of the same circulation as before was shed when the cylinder reached the maximum amplitude on the same side.

Ongoren and Rockwell (1988a) visualized near wake flow structures of transversely oscillating cylinders of circular, triangular and square cross-sections using hydrogen-bubble visualization technique. A wide range of oscillation frequencies from sub-harmonic to super-harmonic over a range of Reynolds numbers from 584 to 1300 were studied. Two basic forms of lock-on was seen. At a frequency equal to one-half of the Strouhal frequency, a sub-harmonic form of lock-on take place, where initially formed vortex is always from the same side of the cylinder, irrespective of the cylinder movement toward extreme positive or negative position. The second form of fundamental synchronization occurs at excitation frequencies near the Strouhal frequency where successive vortex shedding from either side of the cylinder alternately moves towards its maximum negative and maximum positive positions during an oscillation cycle. In passing through $f_e/f_s \approx 1$, a shift in the phase of vortex shedding relative to cylinder displacement was observed for circular

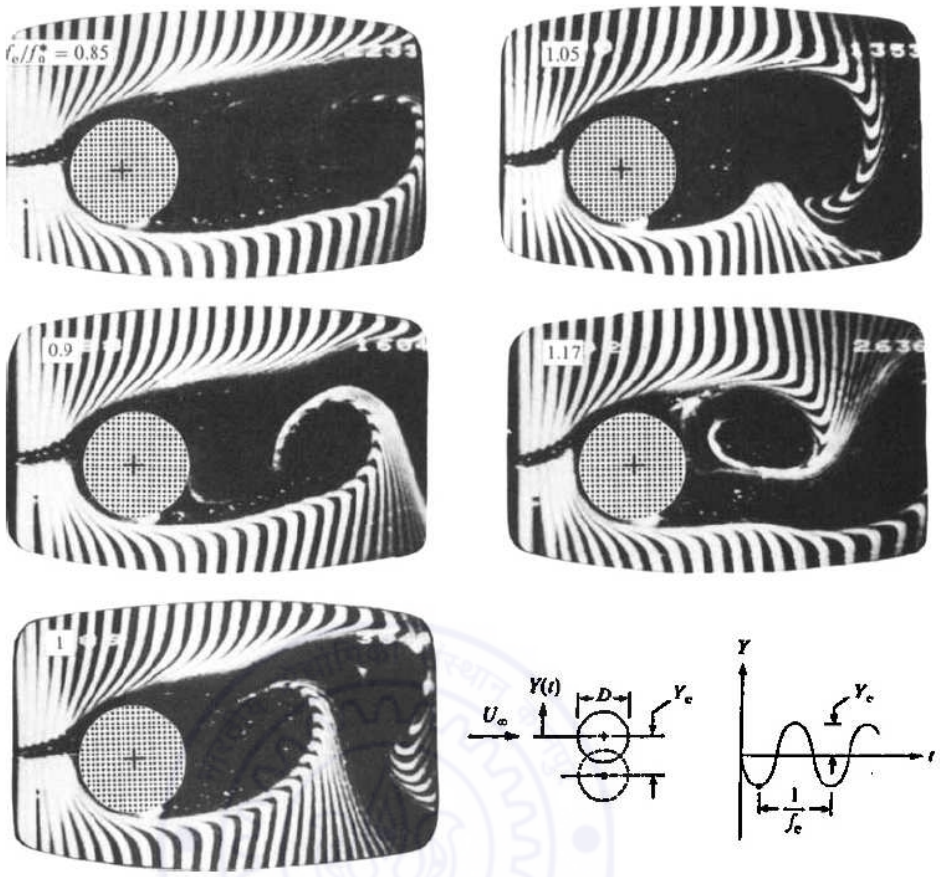

Figure 2.12: Effect of frequency ratio (f_e/f_s= 0.85, 0.9, 1.0, 1.05 and 1.17) on the near-wake structure. All photos taken at maximum negative displacement of cylinder, Ongoren and Rockwell (1988a).

(Figure 2.12) and triangular cylinders. However, the presence of after body in a square cross section cylinder appears to induce reattachment and prevents phase switching. Figure 2.12 shows that for the frequency ratios (f_e/f_s) of 0.85, 0.9 and 1.0, the vortex is shed for the lower side of the cylinder, as opposed to upper side for f_e/f_s values of 1.05 and 1.17. The perturbed near-wake was observed to recover rapidly to an antisymmetric Karman vortex street over a wide range of excitation frequencies, varying from sub-harmonic to super-harmonic forcing. However, the frequency of the recovered vortex street can depart substantially from the natural shedding frequency.

Williamson and Roshko (1988) visualized the vortex patterns behind a towed circular cylinder subjected to transverse forcing for a range of Reynolds number between 300 to 1000. A regime map based on visualized wake patterns was developed for a wide range of parameters ($0.2 < a/d < 5$ and $1.0 < U_\infty/f_eD < 15.0$). The authors labeled different shedding modes in terms of number of vortex-pairs ('P') or single vortices ('S') shed during each cycle of cylinder oscillation. The major vortex patterns near the fundamental lock-on

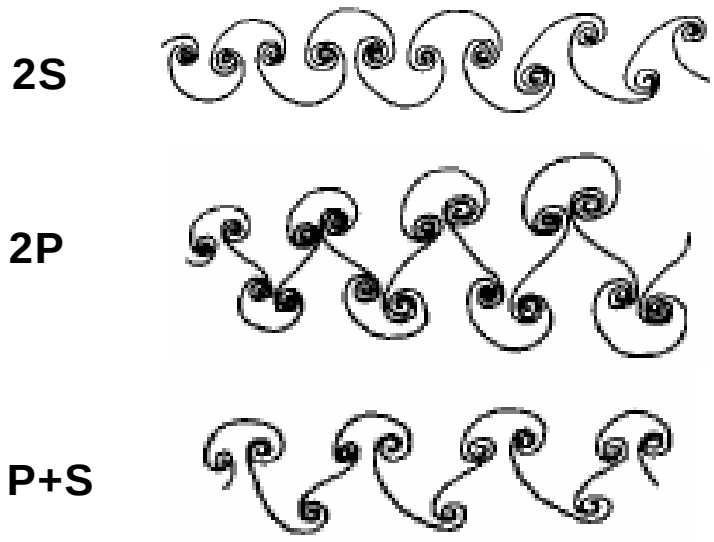

Figure 2.13: Sketch of vortex shedding patterns found in the map of vortex synchronization regions, Williamson and Roshko (1988).

regime were '2S', '2P' and 'P+S' modes as shown in Figure 2.13. The designation '2S' means two single vortices (one of each sign of vorticity) shed per cycle; '2P' means two vortex-pairs shed per cycle; 'P+S' means an asymmetric pattern with one vortex-pair and a single vortex shed in each cycle. The authors explained that due to transverse oscillations, the cylinder is continually accelerating and decelerating along its trajectory through the fluid. In the fundamental lock-on regime, the acceleration phase of every half oscillation cycle induces vortex roll up from each shear layer. Thus, four vortices are formed from the shear layers for each cycle of the oscillation. Below a critical trajectory wavelength, two like-sign vortices coalesce during each half cycle and results in two vortices of opposite vorticity per cycle of cylinder oscillation ('2S' mode). When, the trajectory wavelength exceeds a critical value, vortices of opposite sign pair up to give rise two vortex pairs per cycle ('2P' mode). In the fundamental lock-on regime, as U_∞/f_eD is increased, a sudden change in synchronized vortex shedding from '2S' mode to '2P' mode is observed at $U_\infty/f_eD \approx 5$ (or $f_e/f_s \approx 1$). This abrupt change in the dynamics of the wake vortices is associated with the sharp jump in the phase of the lift force. At the critical value of the trajectory wavelength (i.e. at critical oscillation frequency), the four regions of vorticity are not formed. However, each shear layer is rolled into one of the vortices which began its life in the previous half cycle. The resulting pattern consists of two appositively signed vortices for each cycle ('2S' type) and the wake vorticity is more concentrated. This wake condition is referred to as 'resonant synchronization'. The change in phase switching observed by Ongoren and Rockwell (1988a) was not accompanied by a change

in shedding mode and only Karman mode or '2S' mode was observed on both sides of the phase switch in their experiments.

Gu *et al.* (1994) studied the phase switch phenomenon by measurement of near-wake vorticity fields using particle image velocimetry. Two Reynolds number, Re = 185 and 5000 were studied for a cylinder oscillating at $a/d = 0.2$. With an increase in excitation frequency to the order of natural shedding frequency, the initially formed concentration of vorticity moves closer to the cylinder until a limiting position is reached; at this position, the vorticity concentration abruptly switches to the opposite side of the cylinder. For Re = 185, the phase switch occurred between $f_e/f_s = 1.10$ and 1.12, while it occurred between 0.85 and 0.90 for Re = 5000. In a similar study, Lu and Dalton (1996) computationally examined the phenomenon of vortex switching at Re = 185, 500 and 1000. Increasing the Reynolds number decreases the frequency ratio (f_e/f_s) at which the switching occurs.

Blackburn and Henderson (1999) conducted a 2-D numerical simulation for flow past a transversely oscillating circular cylinder at Re = 500 and a fixed amplitude ratio of 0.25. When the wake was in a periodic state prior to the phase switch ($f_e/f_s = 0.875$), energy transfer from the fluid to the cylinder, averaged over a cycle, was shown to be positive. For periodic states of the wake after the phase switch ($f_e/f_s = 0.975$), the energy transfer was negative. Therefore, phase switching was associated with a change of sign of mechanical energy transfer between the cylinder and the flow.

Krishnamoorthy *et al.* (2001) conducted flow visualization experiments in a water tunnel for an oscillating circular cylinder at Reynolds number ranging from 1250 to 1500 and $a/d = 0.22$. The oscillation frequencies were varied ranging from $\frac{1}{3}$-subharmonic excitation to 3-superharmonic excitation. Within the fundamental lock-on regime, as f_e was incremented, both the sudden transition from '2P' to '2S' synchronization and the phase switching phenomenon within the '2S' regime were observed. However, the frequency (f_e) corresponding to the transition from the '2P' to '2S' regimes is lower (between 1.0 and 1.1 Hz) than that corresponding to the phase switch (between 1.1 and 1.2 Hz). Between the two transitions, the vortex formation length was a minimum. A similar minimum in vortex formation length was also attained when f_e was increased to a 3-superharmonic synchronization.

Carberry *et al.* (2001) studied various wake modes and forces generated when the cylinder was oscillated at around the Karman frequency. With an increase in the frequency ratio (f_e/f_s), transition from a small amplitude lift force (out-of-phase with the cylinder oscillations) to a large amplitude lift force (in-phase with the cylinder oscillations) with a phase shift of order of 180° was observed. The corresponding change in the mode of vortex shedding involves an alteration in both the timing of the vortices initially shed

form the cylinder and change in overall pattern of vortices from '2P' to '2S'.

Zheng and Zhang (2008) performed unsteady fluid dynamic simulations to study the effect of oscillation frequencies on the lift and drag of a transversely oscillating circular cylinder. The Reynolds number was fixed at Re = 200 and frequency range included from $\frac{1}{2}$-subharmonics to 3-superharmonics of the natural von karman shedding frequency. Based on the spectral analysis of time histories of lift and drag, the effects of frequency lock-on, superposition and demultiplication on lift and drag were discussed. Near the natural shedding frequency, frequency lock-on occurred, resulting in significant peak at the forcing frequency in the spectra of lift coefficient. However, at the 1.5-, 2- and 3-superharmonic excitations, the frequency demultiplication leads to large-amplitude coherent components at fractions of the excitation frequencies. Therefore, peaks both at the natural shedding frequency and the excitation frequencies in the lift coefficient spectrum were observed.

Placzek *et al.* (2009) performed a numerical simulation for flow past a circular cylinder oscillating transversely to the incident stream at Reynolds number, Re = 100. The frequency content and vortex shedding modes have been studied as a function of frequency and amplitude of the imposed oscillations. The well-known lock-on zone has been highlighted and characterized with the analysis of power spectral densities (PSDs) and phase portraits of the cylinder displacement and lift coefficient. Simulations involving free vibrations (vortex-induced vibrations) were also carried out to investigate amplitude and frequency response of the cylinder over a wide range of reduced velocities.

2.3.2 Forced inline oscillations

Most of the investigation of vortex-induced oscillations and their forced-body analogues have concentrated upon vibrations transverse to the incident flow. In air, the shedding of vortices produces the periodic forces which act primarily in cross-flow direction at a frequency near the strouhal value. The in-line component of the periodic forces is less in magnitude than the cross-flow component and, owing to small density of air, does not excite the structure. With the increased use of cylindrical structures in water, the importance of in-line oscillations has increased because of larger fluid forces in that medium and lower velocities at which the in-line vibrations are initiated. These classes of flow have practical applications relating to design of offshore and underwater structures. In-line oscillations of a cylinder in steady uniform flow is distinctly different from transverse oscillation case. In this case, the disturbances produced by the forced oscillating cylinder is symmetric in nature, while vortex formation process produced by the natural instability is antisymmetrical. Therefore, a competition between symmetrical and antisymmetrical

mode is expected. The literature related to forced inline oscillating cylinder at small amplitude is less common and is reviewed below.

Tanida *et al.* (1973) measured fluctuating lift and drag forces to study the stability of a circular cylinder oscillating either in a uniform flow (single cylinder) or in a wake (tandem arrangement) over a range of Reynolds number ($40 < Re < 10^4$). The forces were measured using strain gauges. Both inline and transverse oscillations of the cylinder were considered. In the case of a single cylinder, the cylinder oscillation causes synchronization in a frequency range near the Strouhal frequency for transverse oscillation and around double the Strouhal frequency for inline oscillation. For tandem arrangement, no vortex shedding occurred from the upstream cylinder if down stream cylinder is placed before a critical separation between cylinders. Hence, down-stream cylinder suppresses the vortex shedding from the upstream and plays a role like a splitter plate behind a cylinder. However, the transverse oscillation of the down stream cylinder forces vortex shedding and brings about synchronisation, but no vortex shedding is observed in case of inline oscillation of the downstream cylinder.

Griffin and Ramberg (1976) visualized the wake of a circular cylinder oscillating in-line with the incident steady flow at Reynolds number of 190. The excitation frequencies were in the range from $f_e/f_s = 1.74$ to 2.2 and peak to peak amplitude ratio between 0.06 to 0.22. Vortex shedding was synchronized at oscillation frequencies in a range near twice the strouhal frequency. Two different asymmetric modes of vortex formation were observed. In the first regime, one vortex was shed for each cycle of the cylinder oscillation (Figure 2.14 (a)). In the second regime, two vortices of opposite sign were shed for each cycle of cylinder oscillation and resulted in a wake with two rows of vortices, one on each

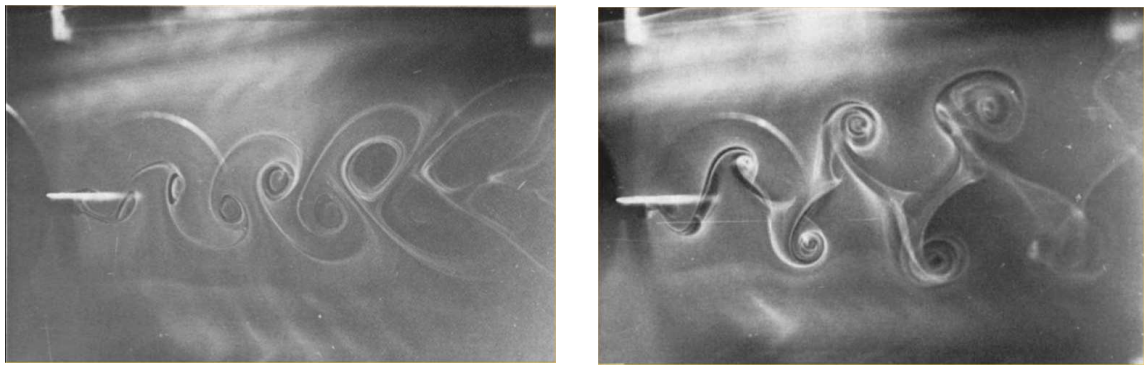

(a) (b)

Figure 2.14: Vortex shedding from an inline vibrating cylinder at Re = 190. During each cycle of the cylinder's vibration, (a) A single vortex was shed, and (b) Two vortices were shed, Griffin and Ramberg (1976).

side of the cylinder containing pairs of opposite signed vortices (Figure 2.14 (b)). These two different flow patterns in effect correspond to A-I and A-IV modes, respectively as categorized later by Ongoren and Rockwell (1988b). The longitudinal and lateral spacing of the vortices were seen to depend on the oscillation frequency and amplitude.

Ongoren and Rockwell (1988b) studied the near-wake flow structures for a circular cylinder oscillating at an angle with respect to the free stream using same instrumentation as were employed in the work of Ongoren and Rockwell (1988a). The frequency ratio (f_e/f_s) was varied from 0.5 to 4.0 and amplitude ratio was fixed at 0.13. Two basic modes i.e. symmetrical and antisymmetrical vortex formation were identified. The authors further classified the two basic modes into five sub-modes: the S mode for the symmetric vortex formation and A-I, A-II, A-III, A-IV modes for the antisymmetric vortex formation. Depending on the excitation frequency, the two basic modes of vortex formation either synchronizes with the cylinder motion or compete with each other. When mode competition occurs, near-wake structures successively locks-on to each mode over a defined number of cycles, abruptly switching between modes. The A-II mode did not occur in the case of a streamwise oscillating cylinder.

Minewitsch *et al.* (1994) performed a systematic numerical study of the flow past an inline oscillating square cylinder at Re = 200. Depending on the frequencies and amplitudes of the cylinder oscillation, the authors identified three sub regimes with different flow behaviour e.g. regime of superposition, lock-on regime and transition regime beyond lock-on. Due to the nonlinear interactions between the natural and imposed oscillations, a variety of combination frequencies e.g. $(f_e + f_s)$ and $(f_e - f_s)$ occur in the spectra of the lift coefficient.

Cetiner and Rockwell (2001) investigated the flow past a circular cylinder subjected to forced streamwise oscillation using PIV and instantaneous force measurements. The relationship between the fluid forces and the patterns of vorticity and streamline topology in the near wake was studied over a range of the Reynolds numbers $405 \leq \mathrm{Re} \leq 2842$ at frequency ratios $0.37 \leq f_e/f_s \leq 2.27$. Based on the time trace and spectra of the transverse force coefficients, the authors pointed out that it is possible to attain either locked-on or quasi locked-on states due to streamwise oscillations at f_e/f_s close to 0.5, 1.0 and 2.0.

Guilmineau and Queutey (2002) obtained numerical solution of the unsteady two-dimensional Navier-Stokes equations to study flow over an oscillating circular cylinder in two configurations. First case is the flow induced by harmonic inline oscillations of the cylinder in water at rest for a Re = 100 and Keulegan-Carpenter number, KC = 5. The second problem is the transverse oscillations of cylinder in uniform flow at Re = 185

and f_e/f_s varying between 0.8 and 1.20; the oscillation amplitude fixed at 20% of the cylinder diameter. The authors calculated drag coefficient, formation length, vorticity contours, streamlines and velocity profiles. The calculations pedict that vortex switching occurs slightly earlier in the f_e/f_s range of 1.00-1.10 as compared to 1.10-1.12 in the experimental results reported in literature.

Nishihara *et al.* (2005) performed flow visualization and measurements of fluid forces on a circular cylinder forced to oscillate in the stream-wise direction in cross flow. The relation between the unsteady drag force and the wake patterns at subcritical Reynolds numbers were investigated. Two ranges of the reduced velocity with distinct flow phenomena were identified. In the first range, wake breathing and typical symmetric vortex shedding was observed, while in the second range, combined pattern of wake breathing and alternate vortex shedding was realized. The authors observed a well organized alternate shedding pattern when the forcing frequency was twice the natural shedding frequency.

Xu *et al.* (2006) studied the wake of a streamwise oscillating circular cylinder using LIF flow visualization, PIV and hot-wire techniques for Re = 100 to 600. Five distinct modes of the flow structures were identified for f_e/f_s = 0-3.1 and a/d = 0.5-0.67. These modes were designated as S-I, A-I, A-III, A-IV, and S-II. Ongoren and Rockwell (1988b) reported four of them (S-I, A-I, A-III and A-IV), though at a different combination of f_e/f_s and a/d. The S-II mode was observed experimentally for the first time. It consists of two rows of binary vortices symmetrically arranged about the wake centerline. Each binary vortex contains two counter rotating vortices shed from the same side of the oscillating cylinder, in distinct contrast with the counter-rotating vortex pairs of A-III and A-IV modes, which are shed from different sides of the cylinder.

Nobari and Naderan (2006) performed 2D numerical simulation for flow past an oscillating circular cylinder for Reynolds number up to 300, using finite element method. Both cross flow and inline oscillations were studied for various frequencies and amplitudes and bounds of the lock-on region were determined. For cross flow oscillations, lock-on occurred near the strouhal frequency, whereas it occurred near twice the strouhal frequency for inline oscillations. With frequency, the time-averaged drag coefficient first increases to a peak and then decreases, which is higher for higher amplitudes. For both cases, the increase in amplitude of oscillation decreases lateral spacing of vortices till they become collinear as row of opposite sign vortices. Further increase in amplitude results in change of wake pattern and formation of secondary vortices. The former pattern is referred as 2S and the later as P+S according to terminology by Williamson and Roshko (1988).

Al-Mdallal *et al.* (2007) numerically investigated the flow structures and lock-on

phenomena in the near-wake of a forced streamwise oscillating cylinder placed in uniform stream. The simulations were conducted for a fixed Reynolds number, Re = 200; f_e/f_s = 0.5 to 3 and a/d = 0.1, 0.3 using spectral finite-difference method. The near-wake vorticity contours and Lissajous patterns of unsteady lift coefficient were used to analyze the lock-on phenomenon. Both symmetric and antisymmetric modes of vortex formation were observed, depending on the frequency ratio, f_e/f_s.

2.3.3 Bluff body in oscillating flow

The problem of wave-cylinder interaction in ocean engineering can be effectively represented by an incident mean flow with periodic component superimposed upon a stationary cylinder. Griffin and Hall (1991) stated that this perturbed flow is equivalent to in-line oscillations of the cylinder in a steady incident flow when the perturbation wavelength is large compared to the cylinder diameter. The relevant governing parameters for this flow are: (i) Reynolds number, Re = U_mD/ν, where U_m is the maximum oscillatory velocity, and D is the cylinder diameter; (ii) Keulegan-Carpenter number, KC = U_m/f_eD, where f_e is the frequency of the oscillatory flow; (iii) Frequency parameter, β = Re/KC. For a harmonic oscillation with A as the amplitude of oscillatory flow, the Keulegan-Carpenter number can be written as KC = $2\pi A/D$.

Hall and Griffin (1993) simulated the oscillatory flow around a fixed circular cylinder using spectral element method and estimated the bounds of the lock-on region (Fig-

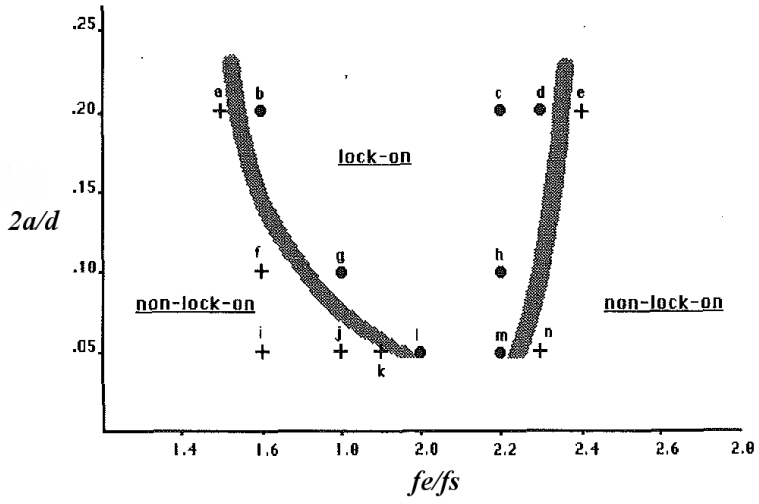

Figure 2.15: Limits of the lock-on regime for perturbed flow around a fixed circular cylinder at Re = 200, Hall and Griffin (1993).

ure 2.15). At peak to peak amplitude ratio, $2a/d = 0.2$, perturbation frequencies in the range $1.6f_s$ to $2.3f_s$ result in lock-on, and the extent of this frequency range decreases with decreasing perturbation amplitude.

Konstantinidis *et al.* (2003) performed experiments in a water tunnel using Laser Doppler velocimeter to study the near wake characteristics of a circular cylinder in perturbed approach flow at Re = 2150. The fluctuations, wave length of the vortex street, vortex formation length, and recirculation bubble length were measured. Lock-on was observed for perturbation frequencies around two times the natural vortex shedding frequency. In the limits of the lock-on regime, the recirculation bubble and the vortex formation region shrink systematically in size and attain minimum values near the middle of the lock on range at $f_e/f_s = 2$.

Kim *et al.* (2006) studied the dynamics of vortex lock-on behind a circular cylinder in a oscillatory flow with nonzero mean velocity using a time resolved PIV at Re = 360. The behaviour of wake regions i.e. mean recirculation and zone of vortex formation, dynamic behavior of shed vortices, phases of vortex evolution, and the Reynolds stress fields were investigated. Lock-on which occurring at twice the natural shedding frequency considerably reduces mean circulation and vortex formation region and concentrates kinetic energy closer to the cylinder base.

2.3.4 Heated oscillating bodies

The process of heat transfer from a body surface to the surrounding fluid is of technological importance in the design of thermal systems. Vibration of the body significantly alters the wake structures which in turn affects the heat transfer from the body. All thermal devices under normal operations encounter some degree of small amplitude vibrations which are generated from the flow itself and/or other components in motion. In practical design of thermal systems, the effect of these vibrations on thermo-fluid behaviour has to be considered. Selected recent reviews relating to the enhancement of heat transfer by small amplitude transverse/in-line oscillations of the cylinder are presented below.

Gau *et al.* (1999) performed experiments to study flow structures and heat transfer over a heated circular cylinder oscillating at small amplitudes ($a/d = 0.016$, 0.032, and 0.064) in the direction transverse to the mean flow. Flow visualization using a smoke-wire and local heat transfer measurements around the cylinder were made for Reynolds number, Re = 1600, 3200, and 4800. The excitation frequencies of the cylinder were selected at $f_e/f_s = 0$, 0.5, 1, 1.5, 2, 2.5, and 3. It was observed that synchronization of vortex shedding with the cylinder oscillation occurs not only at $f_e/f_s = 1$ but also at

$f_e/f_s = 3$, which greatly enhance the heat transfer in the wake region due to rapid growth of vortices and their intense interactions. The authors pointed out that as long as the instability mode in the wake region is amplified by excitation of the cylinder, enhancement in heat transfer can be obtained.

Gau *et al.* (2001), later performed experiments at small amplitude oscillations in the streamwise direction for Reynolds numbers between 1600 and 3200. Two different types of vortex formation namely, symmetric and antisymmetric mode were observed. At $f_e/f_s = 2$, the synchronized pattern of vortex formation occurred in the antisymmetric mode and resulting in maximum enhancement of heat transfer, while at $f_e/f_s = 2.5$ and 3, the vortex formation appeared in the symmetric mode leading to smaller enhancement in the heat transfer. At $f_e/f_s = 1$, the vortex formation frequently switches over between the two modes and the average enhancement in heat transfer of the two modes is not significant.

Park and Gharib (2001) performed an experimental investigation to examine the effect of forced transverse oscillations on heat transfer from a circular cylinder in water at Re = 550, 1100, 3500. A range of forced oscillation frequencies ($1 < f_e/f_s < 5$) and two oscillation amplitudes, ($a/d = 0.1$ and 0.2) were considered. Increase in heat transfer for oscillation at fundamental Strouhal frequency and certain super-harmonics were observed. A closer inspection of the flow field using digital particle image velocimetry/thermometry (DPIV/T) revealed that increase in the heat transfer rate depends on the distance at which vortices roll-up behind the cylinder. It was observed that large amount of vorticity flux results in shorter formation length and closely rolled-up vortices, which are more effective in removing of the stagnant and low heat convecting fluid from the base of the cylinder. Therefore, when the wake is synchronized with the cylinder oscillation and vortices roll-up close to the cylinder, a large increase in surface heat transfer was observed.

Pottebaum and Gharib (2006) performed an experimental study using DPIV/T to see the effects of transverse oscillations on heat transfer from a circular cylinder in water at Re = 687. A wide range of oscillation frequencies from $\frac{1}{3}$-sub-harmonic to 5-super-harmonic and oscillation amplitudes in the range $0.1 \leq a/d \leq 1$ were considered. The heat transfer was significantly enhanced by small amplitude oscillations at frequencies near the Strouhal frequency and its harmonics. In addition to the vortex formation length reasoning of Park and Gharib (2001), the vortex roll up processes in the form of wake modes (2S or 2P) and transverse cylinder velocity were shown to play a significant role in determining heat transfer coefficient.

The above literature review shows that the wake of an oscillating cylinder differ significantly from that of a stationary cylinder. Depending on the direction of oscillation

with respect to the incident flow (i.e. transverse or inline), frequency and amplitude of oscillation, a variety of flow structures (e.g single vortices or paired vortices) and shedding patterns (e.g. antisymmetric or symmetric) are observed. Lock-on of the vortex shedding with the cylinder motion occur near the Strouhal frequency for the transverse oscillations and near twice the Strouhal frequency for inline oscillations. For a heated cylinder in forced convection regime, oscillation of the cylinder results in the enhancement of heat transfer from the cylinder.

2.4 Optical measurement and schlieren technique

Optical methods are versatile tool for making non-invasive, quantitative measurements in thermo-fluid sciences. In convective flow investigations, optical methods have gained significant attention as far as heat and mass transfer are concerned. Now, these techniques are being evolved as to measure scalar and vector fields simultaneously. Refractive index based optical techniques e.g. shadography, schlieren and interferometry are used to study nonuniform density fields in transparent medium e.g. gas or liquid. Among these, the schlieren technique deserves special attention for its simplicity (alignment is straight forward), ease of applications, relatively low cost and satisfactory accuracy level. In schlieren system, the first derivative (normal to the beam direction) of the index of refraction determines the intensity distribution. To obtain quantitative information, ray deflection angle have to be evaluated. A review of the published literature on imaging convective fields using optical techniques is presented below. The emphasis is on the literature related to quantitative schlieren methods with special attention to diffraction based schlieren-interferometry.

2.4.1 Imaging of thermally buoyant flows

Buoyancy driven convection is encountered in a large number of engineering applications such as cooling of electronic components, solar ponds, stratified fluid layers in water bodies, and material processing to name a few. Studying convection patterns is also important in nuclear power plants such as passive heat removal in advanced reactor systems, stratification phenomenon in steam vessels in which hot and cold water streams mix. A survey of optical methods as applied to thermally induced buoyancy flows is presented below.

In an earlier work using schlieren method, Richardson (1967) estimated the distribution of temperature in the thermal boundary layer of heated horizontal circular cylinder for natural convection, using ray deflection approach. To measure the deflection of light

rays, a straight edge body has been inserted in the light path optically upstream of the convection body under study. An excellent agreement between the measured ray deflections and those predicted from the analysis was found. A transcendental temperature profile approximation function was also shown to give good quantitative agreement with measured ray deflections.

Zhong and Squire (1995) used double-pulse, diffuse-illumination interferometry to evaluate organized structures in the wake of a circular cylinder for high-speed compressible flow at a Mach number of 0.6. The authors reported similarities in the features of the compressible wake as compared to low-speed incompressible wake deduced from separate visualization techniques. They also confirmed the similarities in their turbulent structures.

Tanda and Devia (1998) performed a quantitative schlieren study of laminar free convective heat transfer in air from a heated vertical plate and a vertical channel (formed by a pair of parallel plates). The channel was either symmetrically heated (both plates kept at constant temperature) or asymmetrically heated (one plate kept at constant temperature and the other adiabatic). The authors employed a schlieren system using focal filament method to identify regions of fluid that deflect light rays by the same amount. In this method, a movable opaque filament is located in the cutoff plane, which intercepts the disturbed rays having a given angular deflection (i.e. known position of the filament). Therefore, a shadow is formed on the image plane; this shadow defines the locus of the images of the test section points deflecting the light by the same amount. Temperature profiles and heat transfer coefficients were obtained by processing the light ray deflection measurements.

Muralidhar (2001) described temperature field measurements in fluids using laser interferometry technique. By interpreting the interferograms as path integrals of the field variable, it was shown that the three-dimensional field can be reconstructed using tomography algorithms. Principles of laser interferometry, image processing, evaluation of fringe patterns and computerized tomography have been discussed. Experimental results of buoyancy-driven convection in three configurations namely, a protruding heater, a two-dimensional square cavity, and a differentially heated horizontal fluid layer was presented.

Yildirim and Agrawal (2005) studied flow structures of momentum-dominated helium jets discharged vertically into ambient air using a high-speed rainbow schlieren deflectometry. To map the helium concentration field, the authors used a calibrated rainbow filter and quantified the angular displacement of light ray by the measurement of hue in the color schlieren image. Jet oscillations were characterized by power spectra of the hue value of the consecutive schlieren images. A cross-correlation technique was applied to track the structures to get convection velocity.

2.4.2 Diffraction based schlieren-interferometry

In a two-beam interferometer, a pair of coherent, collimated light beams originally from the same source are recombined to create an interference pattern. Changes in optical path of one of the light beams shift the phase of that beam with respect to the other, producing interference pattern on an imaging plane. Other variants, such as schlieren-interferometer have also been suggested in the literature for the flow measurement. This system is self referencing and the two interfering beams originate in the test region itself. Literature related to the aspects of diffraction based schlieren-interferometry have been presented below.

Gayhart and Prescott (1949) were first to describe a schlieren-interference system as an attempt to obtain quantitative temperature measurements on a vertical heated plate. The authors observed that, with partially-coherent schlieren illumination and either a standard knife-edge or a filament cutoff, fringes are seen in boundary layers perpendicular to cutoff orientation due to interference of direct and cutoff diffracted light. It was demonstrated that, these are functionally the same fringes as obtained in a standard interferometer and the temperature of the plate can be inferred from the fringe count. However, no attempt to plot the temperature distribution was reported.

Temple (1957) discussed the effect of placing obstacles in the focal plane. It was demonstrated that a small absorbing object (filament wire) has the effect of subtracting a coherent beam from every point in the image plane. Therefore, it can be replaced for the purpose of analysis as a coherent source differing in phase with the initial beam by 180° and playing a role analogous to that of reference beam of a standard interferometer. Resulting interference pattern can be used for quantitative evaluation, but the interference region is of limited extent near solid boundaries rather than whole field interferometry.

Oppenheim *et al.* (1966) discussed the use of coherent light for schlieren imaging and described three difficulties for laser-illuminated schlieren imaging: (i) the hypothesis of geometrical-optics is not applicable, (ii) point light source produces very small focal spot at the schlieren cutoff, and (iii) high energy density burns the optics in the cutoff plane. Therefore, coherent laser light in knife-edge schlieren system fails to achieve partial cutoff of the source image yielding uniform darkening of the schlieren image. Instead, diffraction at the schlieren cutoff leads to fringing effects in the schlieren images and such system becomes schlieren-interferometers. The authors suggested a less-severe cutoff such as graded-filter as a solution to this problem.

Brackenridge and Peterka (1967) reported that in a laser schlieren system, when an obstacle, such as a vertical wire was introduced into the focal plane of the light beam,

an interference pattern is observed. When the wire is removed from the focal plane, uniform illumination on the screen was seen. A distribution of intensity, similar as with a Mach-Zehnder interferometer was observed when the wire was inserted into the middle of the focal plane. Unlike the principle of two-beam interferometry, the conversion of phase variation to amplitude variation was accomplished without separating the beam into two distinct portions. The authors used a fine wire of diameter 16 μm in their studies and reported that the diameter of the wire plays a significant role in adjusting the fringe contrast on the screen. Temperature distributions near a heated vertical plate and a heated horizontal cylinder in air have been presented.

Anderson and Milton (1989) reported that a double pass schlieren system and Z-type concave mirror schlieren system can be converted to an interferometer by using a laser source and a suitable cutoff filter. It is known that Z-type concave mirror schlieren layout results in astigmatic image of the source due to the difference in the path lengths along the optical centerline and mirror periphery due to off-axis tilt. Therefore, for the laser source, instead of the image of a point, two line images perpendicular to one another appear near the gaussian focus of the second mirror. Good results were obtained when either of the line images were blocked but with a slight degradation of fringe visibility.

Goldmeer *et al.* (2001) evaluated the performance of a point diffraction interferometry (PDI) by replacing knife-edge with a PDI disk consisting of circular pin-hole. The interaction of the transmitted wave front with the diffracted wave front created the fringe pattern. Temperature profiles in thermal boundary layers and diffusion flames for both two-dimensional and axisymmetric geometries were measured and compared with thermocouple measurements and published analytical solutions.

Raj kumar *et al.* (2007) demonstrated that Knife-edge diffraction pattern is due to the interference of two superimposing waves: geometrical wave from the primary source of light and the boundary diffraction wave from the secondary source (knife-edge). They have shown that, as the knife-edge is moved towards the focus, the observed diffraction fringe pattern starts broadening and ultimately results in an infinite fringe mode. At this point the setup converges to a schlieren diffraction interferometer. This bears a similarity to that of any known two-beam interferometer and can be used to study the phase objects using diffraction-limited optics.

The review of the literature shows that schlieren technique is an efficient tool for thermal convection studies. Self-referencing schlieren-interferometer bears the similarity to a two-beam interferometer and can be used for measurement of temperature distribution by analyzing the interferograms. Due to inherent difficulties in conducting experiments with a hot-wire probe for a strongly heated cylinder, schlieren technique is better suited.

2.5 Image correlation and convection velocity

Estimation of flow velocity from the correlation of two successive scalar images has been used by many researchers in many fields ranging from fluid mechanics to computer vision research. The most common methods for measuring flow velocities uses seeding particles, that can be easily imaged and tracked. In this method, the extraction of velocity information involves subdividing the two images into smaller subimages and quantifying the average spatial shift of particles from subimages in the first image to the subimages in the second image, using cross-correlation technique. An extensive review of this technique is presented by Adrian (1991) and Keane *et al.* (1992). Besides velocity vectors of the flow field, the estimation of convection velocity of large structures from the time-correlated images has also been reported in the area of jet flows, turbulent boundary layer flows and wake flows. In the present section, literature related to the estimation of convection velocity of large eddies from time-correlated images is reviewed, especially for the vortex structures in the near wake of a circular cylinder.

Zhou and Antonia (1992) estimated convection velocity of vortices in the wake of a circular cylinder for a wide ranges of streamwise distance ($10 \leq x/d \leq 60$) and Reynolds number (Re = 80-13,700) using two different approaches. In the first method, the velocity at the vortex center is estimated directly. For this, a detection scheme based on vorticity concentration, circulation and vortex size was used to identify vortices with respect to time and position. The second method is based on the time taken by a characteristic feature of the vortex such as the leading or trailing edge of the dye concentration to travel a certain distance. Several variant of the second method including conditional average, cross-correlation, phase, and flow visualisation were used. The results show that the ratio of convection velocity to the free-stream velocity is almost independent of the Reynolds number. In the laminar wake, its value is in the range of 0.84 to 0.87 for $10 \leq x/d \leq 60$. In the turbulent wake, it slowly increase from about 0.86 at $x/d = 10$ to 0.92 at $x/d = 60$.

Tokumaru and Dimotakis (1995) proposed a method for flow velocity estimation which locally correlates a pair of convected scaler images for displacements, rotations, deformations, and higher order displacement gradient fields. This method employs an integral form of the equation of the motion and applies a global minimization procedure to ensure a global consistency in the results. The method is appropriate for both continuous-scalar as well as discrete-particle-image data. As an example, the results in the wake of a circular cylinder has been demonstrated.

Smith and Dutton (1999) presented a fully automated procedure to determine con-

vection velocity of large-scale turbulent structures from the time-correlated image data. The scheme was based on cross-correlation algorithm for plane laser imaging of high-speed compressible shear layers. A systematic procedure to determine optimum window size and time delay between initial and delayed image was discussed. The dimensions of the window should be large enough to contain eddy pattern but small enough to maintain maximum spatial resolution. Longer time delays allows the structure to convect farther, therefore reducing uncertainty in convection velocity calculations. However, shorter time delays reduce the amount of deformation and rotation as the structure convects. Therefore, an optimum time delay was determined using a wide range of time delays.

Ben-yakar and Hanson (2002) used an ultra-fast-framing imaging system to study the time evolution and convection properties of large-scale structures present in the shear layer of the jet/free-stream interface in supersonic crossflows via schlieren imaging. The exposure time of the schlieren images was determined by optimizing the four main factors, including schlieren sensitivity, spatial resolution, dynamic range and signal-to-noise ratio. To compute the convection characteristics of the large scale eddies, each individual structure was tracked with a cross-correlation method using FFT, Figure 2.16. The size of the interrogation window was manually selected as 128×128 pixels.

Lin and Hsieh (2003) experimentally determined convection velocity of vortex structures in the near wake of a circular cylinder over the region, $1.6 \leq x/d \leq 12.0$ for Re = 160-12,000. A dye injection technique of flow visualisation for Re ≤ 320 and two laser doppler velocimeter systems for Re ≥ 400 were used. In flow visualisation technique, the streamwise displacement of the tip of the dye-marked streaklines of shed vortices is measured in a given time interval. For LDV systems, the mean path of the vortex cores was identified, along which spatial correlation measurements were performed to determine

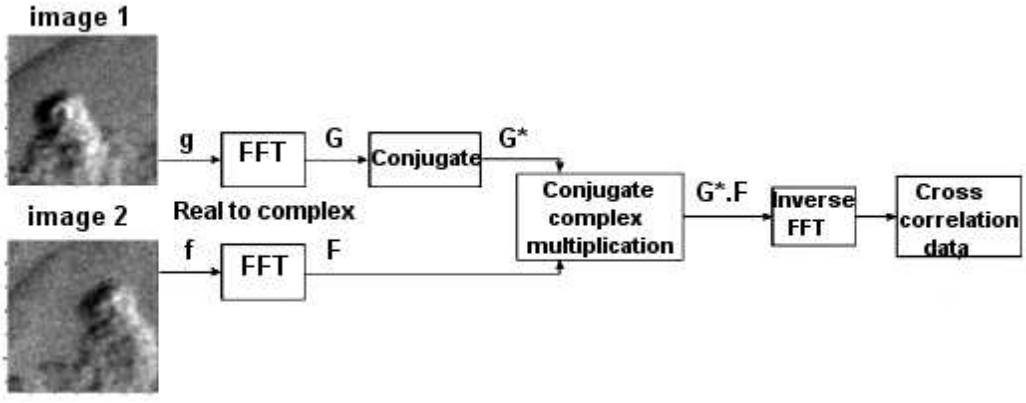

Figure 2.16: Implementation of cross-correlation using FFT to measure convection characteristics of large eddies, Ben-yakar and Hanson (2002).

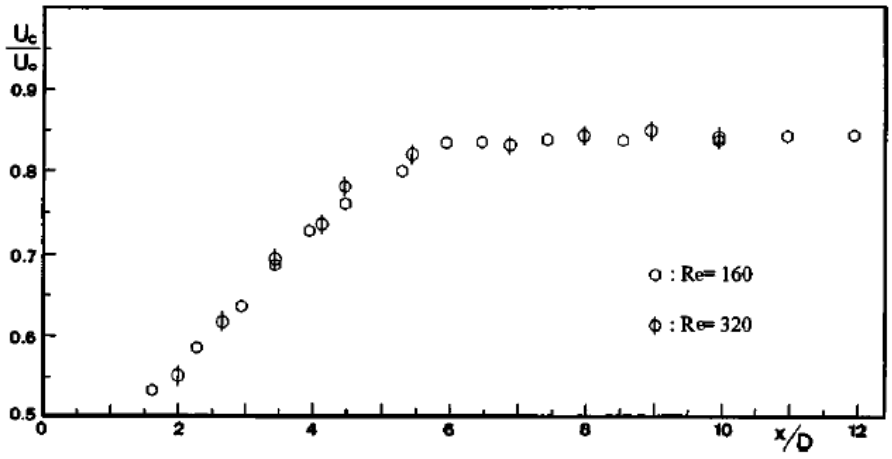

Figure 2.17: Dependance of u_c/U_∞ on x/d at Re = 160 and 320, Lin and Hsieh (2003).

the mean elapsed time for maximum cross-correlation of the streamwise velocity signals. For the low Reynolds numbers (Re = 160 and 320), the behaviour of u_c/U_∞ verses x/d was quite similar. Its value increased from 0.53 to 0.84 over a region $1.6 \leq x/d \leq 6.0$ and became constant at 0.84 for $x/d \geq 6.0$ as seen in Figure 2.17. For the turbulent wake (Re = 400-12,00), the ratio of convection velocity to the free-stream velocity increased from a certain value (0.55-0.75 depending upon Reynolds number) and reached to a mean value of about 0.86 in the region $x/d \cong$ 5.0-6.0, and then changed little with increase of x/d.

The above review of literature shows the use of cross-correlation technique for tracking individual structures in time-correlated images and is an efficient method to get convection velocity. The vortex structure in the near-wake of a circular cylinder attain an asymptotic speed of around 80-90% of the free stream speed.

2.6 Closure

The above literature review shows extensive research carried on bluff body flow dynamics till date. However, there are still more unresolved issues, which can be broadly categorized as follows:

1. Independent investigations on effect of buoyancy and oscillation on bluff body flows are available. However, no study on joint influence of buoyancy and oscillation is available in literature.

2. Few numerical studies on effect of buoyancy on vortex structures for the flow past a circular and square cylinders are available. No detailed experimental study of

buoyancy effect on the vortex shedding for circular and square cylinder is available till date.

3. The synchronization or lock-on phenomenon of unheated oscillating cylinder is available in literature. The influence of heating or buoyancy on synchronization of vortex shedding with cylinder oscillation is not available till date.

Therefore, the present study attempts to answer the above unanswered issues related to bluff body flows. Traditionally, hot-wire is used for investigation of flow fluctuations, which is intrusive in nature and is a point measurement technique. The proper characterization of spatial and temporal structures require instantaneous measurement of the flow field. Hence, optical techniques are ideal for investigation of heated bluff body flows. In addition to above benefits, the availability of high-speed camera can facilitate characterization of temporal structures. Laser schlieren-interferometry has been used in the present study for characterization of the heated wake of circular and square cylinders. The schlieren technique along with a high-speed camera enables visualization of the spatial and temporal structures in the flow field. Schlieren signal have been used for statistical analysis to get quantitative information. The effect of buoyancy on the wake structures of heated stationary cylinders and the mechanisms involved in the heat-induced changes of vortex structures have been explored. Richardson number is varied in a wide range to cover forced and the mixed convection regimes. Joint influence of buoyancy and oscillation on the vortical structures has been examined by using controlled cylinder oscillations at various frequencies and amplitudes. Detailed quantitative analysis is carried out using fluctuating light intensity signal from Laser schlieren-interferometry images to explain the synchronization and lock-on states of the near-wake region.

Chapter 3

Apparatus and Instrumentation

The experiments for the present investigation were carried out in the Fluid Mechanics Laboratory of Indian Institute of Technology, Kanpur. A photograph of the lab with the experimental setup used is shown in Figure 3.1. A vertical flow facility to characterize the wake properties of heated circular and square cylinders has been fabricated for the present study. This testcell resembles an open-circuit vertical wind tunnel, in which low velocity steady air flow is maintained in upward direction. The vertical flow arrangement facilitates the convenient transmission of light and imaging of the test area. The cylinder is internally heated and a precise control of cylinder surface temperature is achieved to maintain isothermal boundary condition. Laser schlieren apparatus with high speed CMOS camera is primarily used for the quantitative flow imaging. The cylinder is oscillated with the help of electromagnetic linear actuators at small amplitudes for study of wake sensitivity to forced oscillations. This chapter describes the details of the experimental setup and instrumentation used in the present study. The details of the experimental conditions are provided. The precaution issues related to measurements are discussed. The experiments for calibration of electromagnetic actuators and testing of flow quality to check flow parallelism and turbulence intensity have been presented.

3.1 Experimental setup

The schematic diagram of the experimental setup and the optical measurement system used in the present study are shown in Figure 3.2. The setup comprises a vertical flow facility, a horizontal heated oscillating cylinder, a laser schlieren apparatus and image acquisition system. The details of the flow facility with instrumentation used are discussed in the following section. The details of the heated cylinder arrangement, laser schlieren system, data acquisition and imaging system, hot-wire anemometry, cylinder oscillation

Figure 3.1: A photograph of the lab with experimental facility used in the present work.

system and details of other auxiliary instruments have been presented in the subsequent sections.

3.1.1 Flow facility

The experiments were performed in a vertical flow facility (to be called as *vertical test-cell*). The testcell has been kept in a large conditioned lab to ensure constant ambient conditions. Testcell provides an open-loop air flow system and resembles an open-circuit wind tunnel (Figure 3.3 (a)). The testcell is made of plexiglas and consists of honeycomb structure, settling chamber, anti-turbulence wire screens, contraction section, test section and outflow section. The function of the honeycomb section is to straighten the flow by damping the transverse components of velocity, and to reduce the turbulence level by suppressing the turbulence fluctuations that are larger than the size of a honeycomb cell. Fine wire screens are mounted in the settling chamber to suppress the small disturbances generated at the outlet tips of the honeycomb and make the flow velocity profile more uniform by imposing a static pressure drop. The screen also refracts the incident flow towards the local normal and reduces the turbulence intensity in the whole flow-field. The contraction section guides the flow from the settling chamber to the test section with an

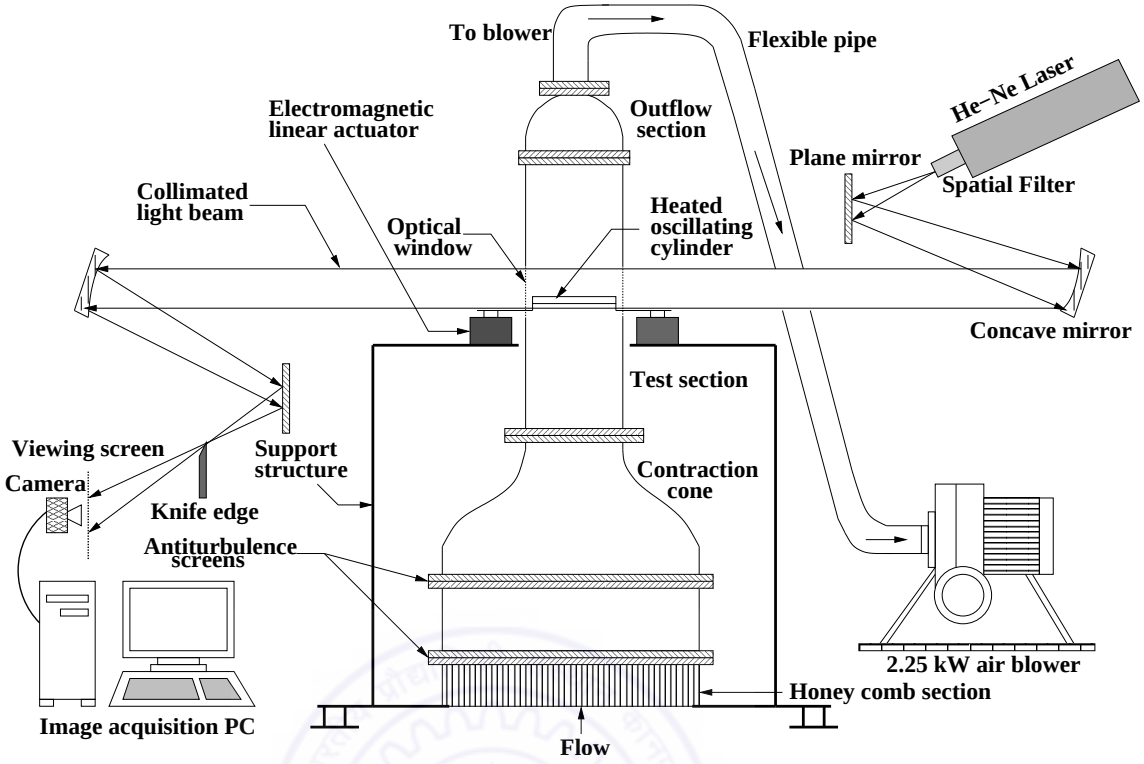

Figure 3.2: Schematic diagram of the experimental setup with Z-type laser schlieren apparatus.

area contraction ratio of 4:1. The contraction section increases the mean velocity in the test section. The honeycomb and the screens are placed in the low speed region, thus reducing pressure losses. The overall objective of these flow conditioners is to obtain a spatially uniform steady stream of air throughout the volume of the tunnel test section. The cross-section of the test section is 0.4×0.4 m^2 square section with an overall length of 0.95 m. The test section has been provided with a removable side panel for ease in installation of the cylinder in the test section.

A 2.25 kW centrifugal blower, (Figure 3.3 (c), *Azad factory*) is used to maintain steady air flow in the test section[1]. The suction side of the the blower is connected to the outflow section of the test cell through a flexible PVC pipe. The blower is mounted on a suitably dampened base with rubber sheet padding for vibration isolation. The speed of the blower motor is regulated by a frequency-based inverter drive (VICTOR G1000, *Kirloskar Electric*) having a maximum variation of ± 1 RPM. Very low stable velocities in the range of 0.13-0.27 m/s could be realized in the test section. These values correspond to a low Reynolds number range near 100 for both circular and square cylinders. The free-stream velocity in the test section is measured by a pitot-static tube connected to a

[1]Names in italics indicate the make of the device.

Figure 3.3: Photograph of the (a) Vertical flow facility, (b) Frequency-based inverter drive and, (c) Blower, connected through a flexible pipe at the end of the outflow section.

differential pressure digital micromanometer (FC012, *Furness Controls* : 1.999 pascals) with a resolution of 0.001 Pascal; it translates to an error in the Reynolds number of about ± 1. The free-stream velocity is continuously monitored during the experiment for any velocity fluctuations in the approach flow to ensure its constant value.

A one wire hot wire probe (5μm diameter, platinum-plated tungsten wire) in conjunction with a constant temperature anemometer (CTA, Model 56C17, *DANTEC*) is used to measure turbulence intensity of the test section. The hot wire signal integrated over a time interval of 20 seconds at 1 kS/s was acquired via a PC through a 12-bit A/D card (PCI-MIO-16E-4, *National instruments*). LabVIEW was used for data collection. The free-stream turbulence level in the approach flow is quite small i.e. less than 0.3% for the velocity range used in the present study. The flow uniformity is better than 1%

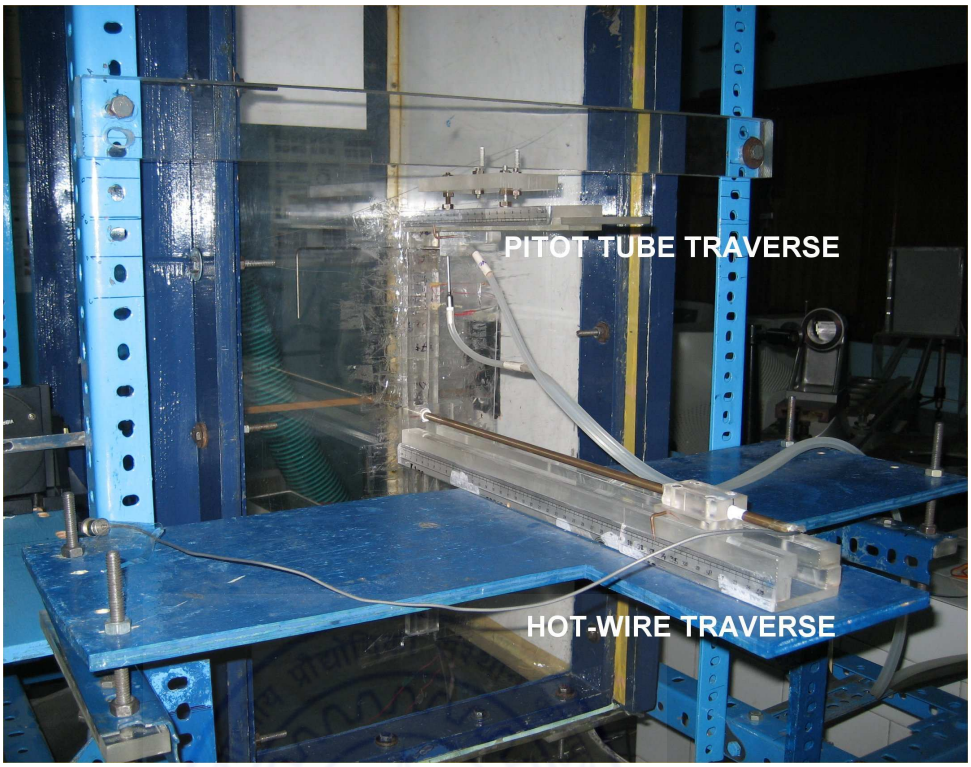

Figure 3.4: Photograph of the pitot tube and Hot-wire traverse.

over 95% of the width of the test cell (outside the wall boundary layers) for the velocity range considered. The details of the test cell for flow quality has been discussed in a later section of the present chapter.

Traverses for hotwire and pitot-static tube : An important accessory during measurements is the traversing mechanism. Manually controlled traverse mechanisms with graduated scales has been designed and used in the present investigation. These are used for the mounting and accurate positioning of pitot-static tube and hotwire probe (Figure 3.4). The linear resolution of the transverse motion is ± 1 mm. To insert the pitot-static tube and hotwire probe in the test section, the removable side panel has been provided with a narrow slot. This slot has been suitably plugged and proper care has been taken to ensure minimal disturbance to the flow by surface non-uniformity and leakage. The plugs have holes for insertion of the probes at suitable streamwise locations.

Support structure : The testcell is placed on a rigid support structure made of slotted angles. This support structure consists of four stiff plastic wheels at each corner to enable the testcell to move and align with the light beam. This support structure provide necessary fixtures for mounting probe traverses and platforms of the electromagnetic linear actuators.

3.2 Heated test cylinders

Figure 3.5 shows the picture of the heated cylinders used in the present investigation. Complete details of the heated cylinders, their heating arrangement and control are discussed in the present section.

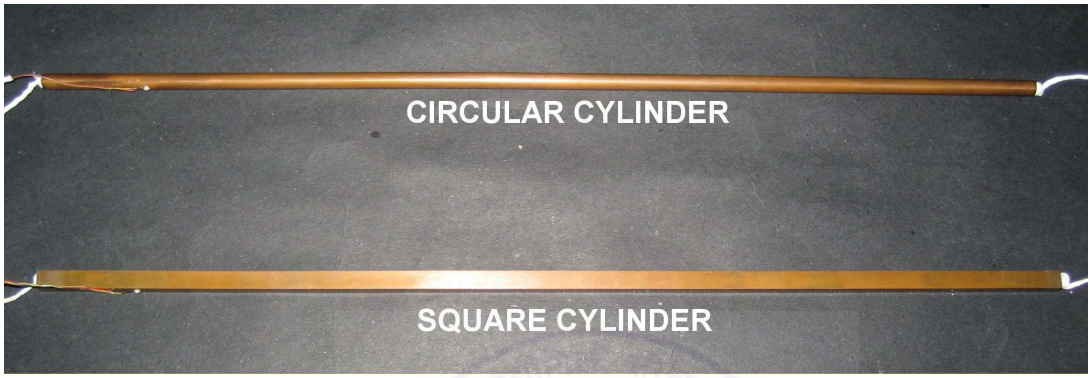

Figure 3.5: Photograph of the circular and square cylinders used in the present experiments.

3.2.1 Geometry, dimensions and material

Two test cylinders, one of circular cross-section and the other of square cross-section were used for study of buoyancy and oscillations effects. The circular cylinder has an outer diameter of 6.2 mm and a length of 390 mm, while the square cylinder have an edge of 6.7 mm and a length of 390 mm (Figure 3.6 (a)). Each cylinder was placed horizontally with its major axis at right angle to the main flow direction. For the square cylinder one of its faces was kept perpendicular to the main flow. The cylinders spanned the full width of the test section resulting an aspect ratio of 65 for the circular cylinder and 60 for the square cylinder. The corresponding blockage ratio was 1.55% and 1.68% for the circular and square cylinders respectively.

The choice of the material was based on the thermal conductivity because perfectly conducting cylinders are required for modeling isothermal surfaces. Copper was selected amongst due to its high thermal conductivity and availability of different gauges tubes. The copper cylinders were well polished to remove oil and dust build-up. The square cylinder was carefully machined to produce a square section with sharp edges. Figure 3.6 (b) shows a schematic to fabricate the square section of 6.7 mm edge from a thick gauge copper tube with 9.5 mm outer diameter and 4 mm internal diameter. The rounded material from the four sides was carefully removed by milling and then finished to generate

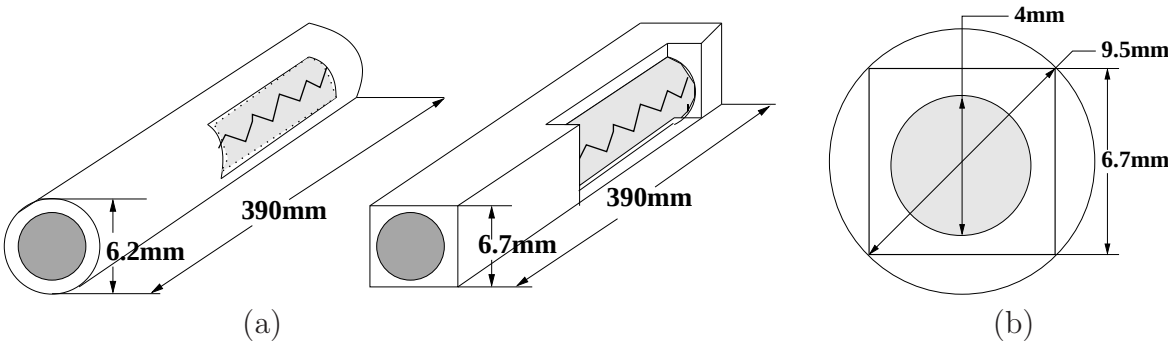

Figure 3.6: (a) Dimensions of the circular and square cylinders and, (b) Fabrication of square section cylinder from circular cylinder.

perfect square section. Proper thickness of the cylinder was selected to permit adequate straightness to the surface and to ensure uniform temperature distribution.

3.2.2 Flow geometry and coordinate system

The flow direction and coordinate system with respect to the cylinder are shown in Figure 3.7 for both circular and square cylinders. The origin of the wake coordinate system is fixed on the top surface of the cylinder at the midspan. The x-axis is directed downstream (the stream wise direction) along the vertical. The y-axis is perpendicular (the transverse direction) to the flow and the cylinder axis. The z-axis lies on the top surface of the cylinder parallel to its own axis (the span wise direction).

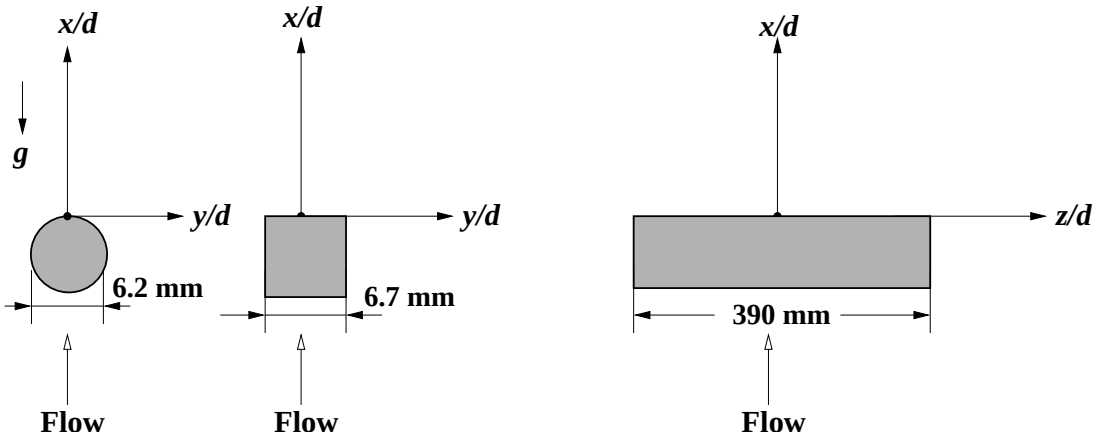

Figure 3.7: Flow geometry around a heated horizontal circular and square cylinder.

3.2.3 Heating arrangement and control

The inside details of a heated cylinder with its heating arrangement for temperature control have been shown in Figure 3.8. Both cylinders are internally heated by passing direct current through a nichrome wire, positioned at the axis of the cylinder tube and through out the length of the cylinder. The resistance of the nichrome wire is equal to a constant value of 15 Ω. The wire is insulated from the copper body by packing mica powder in the gap. The mica has good thermal conductance to conduct heat to the cylinder walls from the nichrome wire with poor electrical conductance, which provide electrical insulation between the cylinder body and nichrome wire. For oscillation experiments, the weight of the cylinders should be as small as possible. The mica powder serves this additional advantage by adding almost negligible weight to the cylinder's own weight. During filling, the powder was uniformly rammed into the gap to have uniform heating throughout the length of the cylinder. The power to the heater was supplied by a regulated DC power supply. To reduce end heat losses to the wall of the test section, two small Teflon plugs of approximately 5mm length were attached to the ends of the cylinder. Two pointed metallic holders wrapped with teflon insulation tape support the cylinder at each plug through small openings in the tunnel. Temperature resistance sleeve is used to cover nichrome wire coming out of the cylinder ends. Care was taken to ensure excellent electric contact at the wire ends to minimize any power loss through the electric circuit.

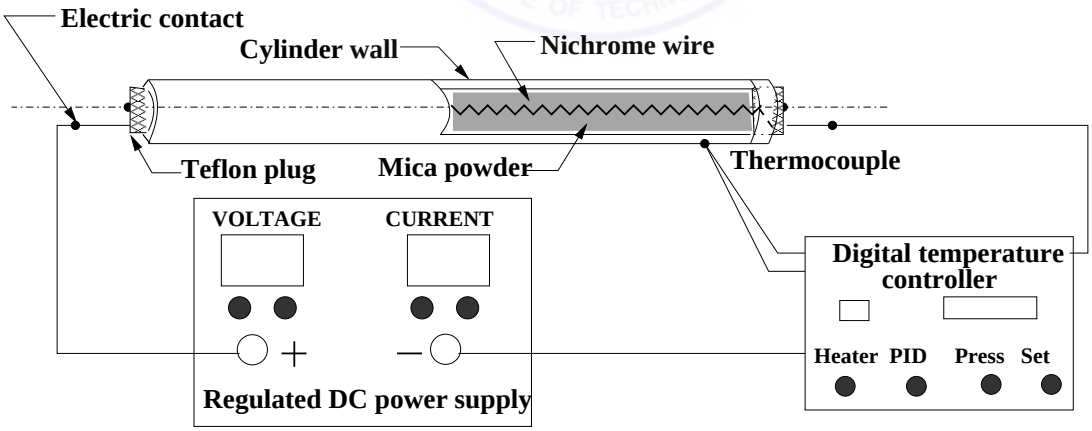

Figure 3.8: Schematic diagram of a heated cylinder assembly and its heating arrangement.

3.2.3.1 Fine wire thermocouple

The surface temperature of the cylinder was measured using a pre-calibrated, 36-gage (AWG, 0.127 mm) chromel-alumel (type K) thermocouple (TT-K-36-SLE, *Omega En-*

(a)

(b)

Figure 3.9: Photograph of the (*a*) Regulated DC Power supply, and (*b*) Digital PID temperature controller.

gineering). Special limits of error (SLE) wire has a better accuracy as compared to the standard wire. The thermocouple was flushed on the cylinder surface using a heat-conducting epoxy (OMEGABOND® 101), which offers high thermal conduction and poor electric conduction characteristics.

3.2.3.2 Regulated DC power supply

The electrical power to heat the cylinder was provided using a regulated DC power supply (9000 series, *ELNOVA*), Figure 3.9 (a). The unit provides stable voltage and current in the range of 0-60 V and 0-30 A respectively. Depending on the temperature level required, both voltage and current were precisely regulated and monitored by separate front panel meters.

3.2.3.3 Digital PID temperature controller

A digital PID temperature controller (*Raagaa Industries*) in closed-loop with solid state relay circuit and DC power supply was used to maintain constant cylinder surface temperature with an accuracy of ±0.2°C. Thermocouple fixed to the outer cylinder surface provides feedback to the controller (Figure 3.9 (b)) and the power to the heater is controlled by the solid state relay. The controller can be set at any temperature ranging from 30-200°C with a resolution of 0.1°C. The cylinder surface temperature was measured at various axial and circumferential locations to check the uniformity of the cylinder surface temperature. The temperature was uniform to within 0.1°C around the cylinder circumference and at all faces of the square cylinder. This is expected as the wall of the cylinder is quite thin and thermal conductivity is quite high. Temperature non-uniformities of up to ±0.3°C were recorded along the cylinder axis for the highest temperature consid-

ered. Experiments were conducted over a period of several months during which the room temperature was maintain at 21-25°C.

3.3 Laser schlieren system

The flow field has been quantitatively imaged using a monochrome schlieren technique. Light patterns due to a variable refractive index field generated by temperature variation has been captured in the schlieren image. The sequence of time separated schlieren images has been recorded using a high-speed camera. The intensity distribution in the images indicates an integrated property of the flow field over the length of the heated cylinder. The details of the light source, optical setup, its alignment and related precautions have been discussed in the present section.

3.3.1 Light source

A 35 mW, continuous wave He-Ne laser (Model 127-35, *Spectra-physics*) is employed as the coherent light source for the laser schlieren system (Figure 3.10 (a)). The laser emits red colour light radiation with Gaussian intensity distribution at a wavelength of 632.8 nm. This laser is sturdy in construction, economical, and stable in operation. The diameter of the original laser beam is 1.25 mm, which has been expanded to allow illumination of larger field of view. For this, a spatial filter (Model 332, *Spectra-physics*) is mounted at the laser outlet by the use of mounting threads. The spatial filter blocks out the random fluctuations (spatial noise) from the intensity profile of the laser beam and passes only the central most bright portion of the laser beam. This filter is a lens-pinhole arrangement in which the micron size pin hole is placed at the focus of the objective lens. The pinhole is provided with x and y motion adjustment knobs and the distance between the pinhole and objective lens is adjusted by z motion adjustment ring. The adjustment knobs and the ring are carefully adjusted so that the small size laser beam is precisely focused on the pin hole and the outgoing beam is expanded with highest intensity output.

Optical windows : The expanded laser beam is used to illuminate the flow field that is being scanned. Two circular optical windows (BK-7, 60 mm diameter, 5 mm thickness, $\lambda/4$ flatness, *Standa*) have been installed in the flow channel to facilitate passage of the laser beam through the test section. Commercially available laser grade BK-7 is highly transmissive to visible and near infrared radiations. Therefore, the optical windows permit the passage of laser beam without reflection. The windows are mounted on accurately cut seats in Plexiglas frames. The frames are made of two pieces with screw tightening the

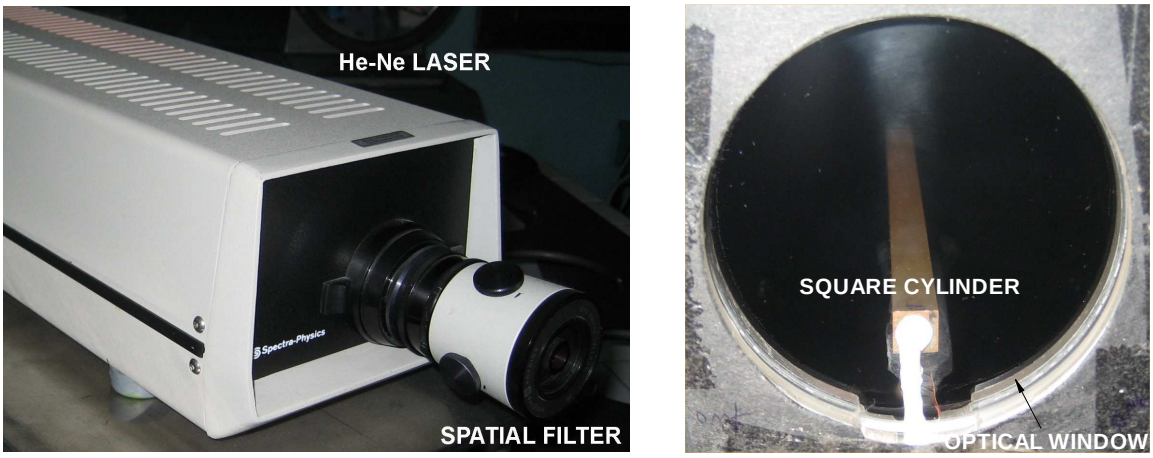

(a) (b)

Figure 3.10: Photograph of the (*a*) He-Ne laser, and (*b*) circular optical window with square cylinder inside the testcell.

two pieces and placing the window in the seat with Teflon tape sealing the circumference. The Plexiglas frames fit in the 10×8 cm^2 size rectangular slots, cut on opposite sides of the test section walls and flush with the internal surfaces of the walls. A photograph of the circular optical window with square cylinder inside the test section is shown in the Figure 3.10 (b). Considerable care has been taken to ensure parallelism between two optical windows placed at the entrance and the exit of the laser beam, which is critical for generating meaningful images.

3.3.2 Optical configuration of schlieren setup

The optics used in the present study consists of a Z-type 2-mirror schlieren system as shown in the layout drawing of Figure 3.11. The optical setup comprises a laser light source, a pair of plane and concave mirrors, a knife-edge and a viewing screen. Twin $f/8$, 20-cm diameter and 160-cm focal length oppositely-tilted concave mirrors (*Unertl optical co.*) are used to illuminate the test region placed in between the two mirrors. The sensitivity of a schlieren system is defined as the rate of change of image contrast with respect to refraction angle, $S = dC/d\epsilon = f_2/b$ (Settles, 2001). Where f_2 is the focal length of the second concave mirror and b is the height of the light source remaining unobscured by the knife-edge. Therefore, relatively large focal lengths (160-cm) of the concave mirrors make the optical system more sensitive to the thermal gradients. Two plane beam folding mirrors one each in incoming diverging beam and outgoing converging beam are used to shorten the overall length of the schlieren setup and to keep the test region free from interference with the optics. All the optical components and the laser light source are

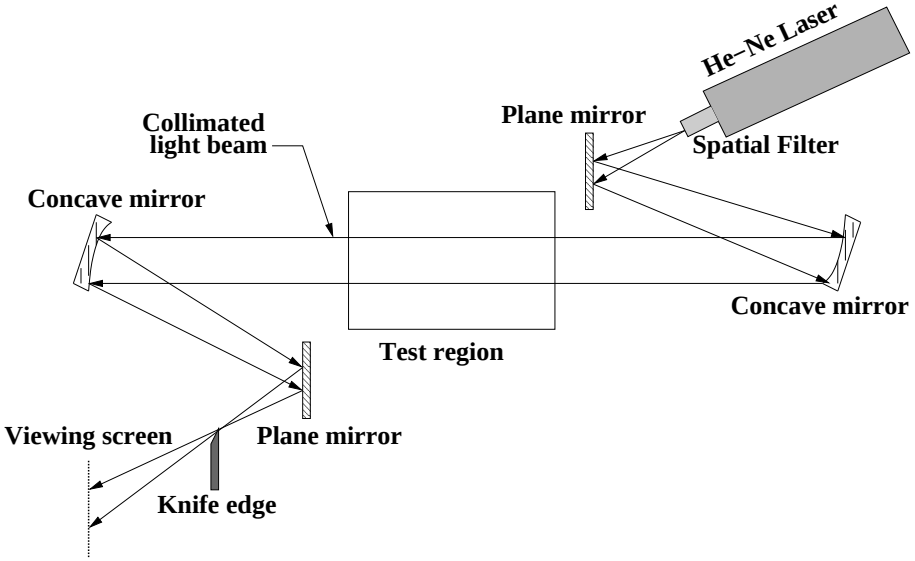

Figure 3.11: Schematic diagram of Z-type 2-mirror laser schlieren system.

kept on a common centerline elevation above the ground level. The elevation is at the level of the heated cylinder in the test section of the flow facility. The original laser beam is diverged by a spatial filter and after expansion, only the core region of the expanded beam falls on a plane mirror that directs a square shaped beam onto the first concave mirror which collimates it into a beam of uniform size. This collimated beam pass through the test region and falls on the second concave mirror which refocuses the beam to an image of the point source in the plane of the knife-edge via a plane mirror. The mirrors are provided with rotation and tilt control knobs and hence slight misalignments in the schlieren optics with respect to the laser beam can be taken care off by adjusting these knobs. The knife-edge is a good quality new razor blade, placed at the focal length of the second concave mirror. It is positioned to cutoff a part of the light focused on it, so that, in the absence of any optical disturbance, the illumination on the screen is uniformly reduced (ideally). In the test region, flow past the heated cylinder results in a heated wake and hence density gradients prevail. The density field results in a refractive index field and therefore a light intensity distribution at the image plane is obtained. Depending upon the orientation of the density gradients, the beam may be refracted away from the knife-edge or in the direction of the knife-edge and corresponding image will be brighter or darker as compared to the undisturbed image. Hence, the knife-edge cuts off a part of the incident light for observing the schlieren effect in the form of an intensity contrast. The initial percentage cutoff is adjusted in such a way that the thermal field is imaged with good contrast but without saturating the camera. The knife-edge is mounted on a graduated traverse that permits the movement of the knife-edge with a fine vernier

adjustment in the cutoff direction to mask light intensity to the extent required (% cut-off). The mount holding the knife-edge has an arrangement to change cutoff orientation i.e. either vertical or horizontal depending upon the gradients one wishes to visualize. In practice, the knife-edge is set perpendicular to the direction of the density gradients to be observed. In the present study, the gradients are predominantly in the vertical direction, and therefore the knife-edge is kept horizontal.

At the viewing screen the real inverted image of the test region is formed. Although it is desirable to focus the schlieren image directly on the camera sensor plane, we have used screen made of translucent material to avoid too much laser light reaching onto the sensor and damage it. Due to its diffusing nature, the light intensity and image contrast get effected. However, it does not influence the dominant dynamic features of the flow field. For the present work, textured plastic sheet in combination with the tracing paper sheet has been used as viewing screen to display the images and the camera is focused at the image formed on the screen.

3.3.3 Optical alignment procedure

Mirror-based schlieren apparatus is difficult to align and a stringent alignment is essential to get meaningful images. Before starting the experiments, the schlieren setup has been aligned using the following procedure:

1. The spatial filter is precisely adjusted using x, y and z adjustment knobs so that the diffraction rings in the expanded beam vanish and only central bright spot of the expanded beam falls on the plane mirror.

2. The light source (the pin hole of the spatial filter) is placed exactly at the focus of the first concave mirror because placing at an incorrect focal length leads to a non-parallel beam reflected from the mirror.

3. It is ensured that second concave mirror lies on a common centerline with the first, so that the parallel beam fills exactly the same region as in the first mirror. The two concave mirrors should be tilted at equal angles in opposite directions from the central optical axis.

4. All the optical components are adjusted so that the light beam falls on the central region of all the mirrors. The rotation and tilt control knobs of the first concave mirror are adjusted to render horizontal parallel beam along the optical centerline and for the second concave mirror these knobs are adjusted to bring the light-source image to bear upon the knife edge.

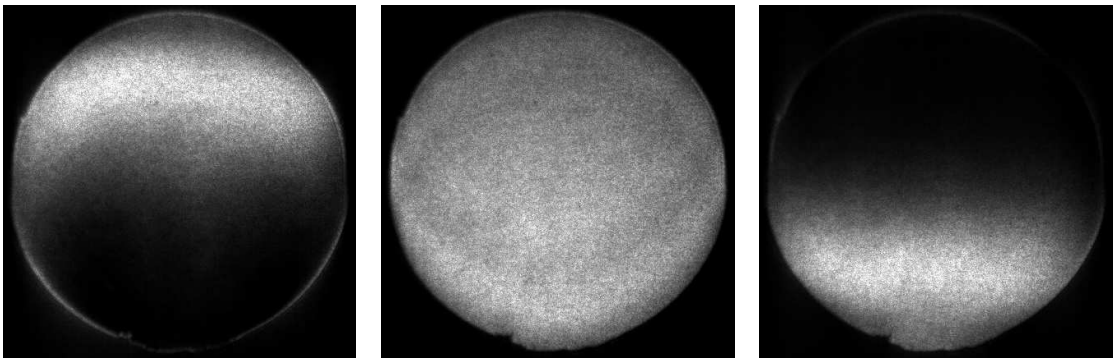

(a) (b) (c)

Figure 3.12: Effect of axial displacement of the knife-edge on the schlieren image, for a horizontal knife-edge entering the beam from below. (*a*) knife-edge too close to the mirror, (*b*) correct adjustment, and (*c*) knife-edge too far from mirror, Settles (2001).

5. The size of the collimated laser beam is checked at various locations along the direction of propagation by using a clean sheet of white paper and scale. The size should be constant at all the locations for a proper collimated laser beam.

6. Position of the knife-edge plays very important role in the alignment of the schlieren system. Best results are obtained when the knife-edge is placed exactly at the focus of the second concave mirror. At the focus, the expanded laser beam converges to an image of the point source. Any shift in the position of the knife-edge from the focal point of second concave mirror results in non-uniform illumination on the screen. To determine the exact position of the knife-edge, first the approximate position of the knife-edge is determined. Then it is inserted from one side into the beam path. If the image on the viewing screen (placed beyond the knife edge) becomes darker from the same side as the knife-edge is moved into the beam path, the knife-edge must be moved away from the second mirror. The opposite happens, if the knife-edge is too far from the mirror. The knife-edge position is exact when the screen darkens uniformly as the knife-edge is gradually inserted in the beam path. This effect is demonstrated in Figure 3.12 (Settles, 2001), which shows the distribution of intensity on the screen as a function of the position of the knife-edge with respect to the second concave mirror and the horizontal knife-edge is entering the beam from below. Figure 3.12 (a) and (c) show the nonuniform distribution of light intensity when the knife-edge is either too close or too far away from the mirror, respectively. Figure 3.12 (b) demonstrates correct position of the knife-edge where, light intensity uniformly changes with the advancement of the knife-edge into the beam.

7. The final step in the alignment procedure of a schlieren setup is to adjust the percent cutoff of the knife-edge in order to obtain the desired sensitivity. Too low

cutoff results in poor contrast of the schlieren images whereas a high percentage of light intensity cutoff blocks a portion of the useful information. The initial percent cut-off is adjusted in such a way that the thermal field is imaged with good contrast but without saturating the camera.

3.3.4 Noise sources

The noise in optical signal at any stage of the experiment can be due to internal and external disturbances such as vibration, thermal current along the optical path outside the test region and presence of any stray light due to reflection or ambient room light. The sources of these disturbances and precautions are discussed below, (Settles, 2001).

Vibration and mechanical stability : The mechanical stability of the optical set-up is essential for the good quality images. Since the optical components are sensitive to vibrations, they are mounted on a self-contained framework linking the components rigidly. Two such frames containing the optics for the incoming and outgoing beams are placed on two separate concrete platforms above the ground level and the testcell is placed in the middle of the platforms. The possible sources of vibration include floor vibrations, regular vibrations from adjacent heavy machinery and the room air-conditioners itself. These may also be due to the movement of laboratory personnel in the vicinity of the experimental area. Schlieren vibration problems directly affect the desired level of sensitivity. Therefore, utmost care has been taken to eliminate these disturbances during the entire period of the experiments and more importantly at the time of recording schlieren images.

Stray light : Stray light problems are attributed to the ambient room light and some other unwanted light such as that from the LED of the nearby electronic instruments. They pose severe problem in high speed imaging as the capturing speed of the camera is much higher than the frequency of illumination of these stray lights. Hence, they appear as fluctuating light in the image sequence. Therefore, during the time of recording schlieren images, all room lights are switched off and masking is used to block any stray light entering the optical path.

Ambient airflows : External convection patterns along the optical path outside the test region also influence the sensitive schlieren experiments. The possible sources include air currents from the cooling fans of electronic hardwares, stirup of the ambient air due to human motion, flow from the room air-conditioners etc. These ambient currents and drafts pose a severe problem particularly for schlieren imaging of low velocity air-flow. Since, the schlieren apparatus is kept in a conditioned lab, turning off the air-conditioners

is used as first line of defense and movement of the people were restricted during sensitive schlieren work. Electronic hardwares were kept at a far place so as to eliminate any warm-air draft directly striking the optical beam path.

The errors in the optical measurements can also be due to the misalignment of the apparatus with respect to the light beam. Therefore, horizontal alignment of the testcell and cylinder with respect to the laser beam is ensured. The quality of the optical components in term of imperfections and inhomogeneities also need careful consideration. This is also required in order to maintain high sensitivity. Experiments are conducted with due considerations to above mentioned precautions and repeatability of the data have been ensured from many experiments performed under practically identical test conditions.

3.4 High speed imaging system

The present study utilizes a high-speed digital imaging system capable of recording consecutive schlieren images at frame rates up to several thousand frames per second depending on image resolution. It consists of a high speed camera (Figure 3.13) connected to a PC-based image acquisition system through a 64-bit frame grabber card and video capture software.

3.4.1 High speed CMOS camera

A high speed CMOS sensor based monochrome camera (MC1302, *Mikrotron*) with 8-bit dynamic resolution (0-255 gray scale) has been used to capture the sequence of schlieren images. It is a high resolution megapixel camera with a resolution of 1280(H)×1024(V) pixel (pixel size, 12 × 12 μm^2). Contrary to CCD-sensor, CMOS-sensor offers high resolution, extremely high data rates, random access to pixels with free programmability and low power. Free programmability means that the user is free to define the region of interest by size and position and the speed of data output. The configuration of the camera is carried out via camera-link interface. Maximum video data rate at the 2×8-bit base camera-link connector is 132 Mb/sec. Camera can be configured at different frame rates and resolution in the limit of video data width and therefore easily adapts to any specific requirements. It can grab with a maximum frame rate of 4956 frames per second at a resolution of 100×100 pixels. With maximum spatial resolution of 1280×1024 pixel, it can grab at a rate of 100 frames per second. Eight sets of camera configuration schemes can be stored in non-volatile memory of the camera micro controller. The camera is

Figure 3.13: Photograph of the high speed CMOS camera used in present experiments.

mounted on a leveled tripod and uses a standard 25 mm C-mount lens system.

Spatial and temporal resolution : The term spatial resolution is used to describe the number of pixels utilized in rendering a digital image. Temporal resolution is termed as the interframing time between two consecutive images. Spatial and temporal resolution requirements are utmost important in imaging of the unsteady wake flows. In schlieren imaging, a high knife-edge cut-off increases the sensitivity of schlieren apparatus in the sense that small density gradients in the flow can be detected. However, this setting diminishes the amount of light reaching to the camera. Short exposure time in high-speed imaging requires high light intensity to cover the full dynamic range. Hence, to balance exposure time for proper light intensity with high-speed imaging, an optimum is arrived at between knife-edge cut-off and frame speed to cover the full dynamic range of the camera. After various trials, the flow field was recorded at a speed of 250 frames per second and a spatial resolution of 512×512 pixels. This frame speed is well above the Nyquist criterion limit to capture the vortex-shedding frequency and resolve the other events occurring during the development of the wake flow structures.

3.4.2 Acquisition hardware

The analog output signal from the camera sensor is converted to the digital format by an analog to digital converter, known as frame grabber located in the PCI slot of the host computer. A 64-bit camera-link frame grabber card (X64-CL, *Coreco Imaging*) in conjunction with the sapera LT software (*Coreco Imaging*) have been used for high-speed imaging. X64-CL is a full size single-slot PCI bus image capture card (operated in 64-

bit, 66 mHz PCI slot) with an on board frame buffer memory of 2 Gb. It consists of an acquisition control unit (ACU) to control the rapid image acquisition rates up to 396 Mb/s for base camera-link standard and a data transfer engine (DTE) to deliver fast sustained image data transfer between the board and host computer with almost zero CPU usage. These two units use on board memory to transfer images from the acquisition control unit to local frame buffer memory or transfer the same images to multiple addresses in the host PC memory. Special image acquisition PC powered with SUPER P4SCT (*supermicro computer*) with 64-bit, 66 mHz PCI-X expansion slots and 128 Mb AGP graphics card in combination with 19" SVGA monitor (1920×1440 pixel) have been used for image display and processing.

3.4.3 Imaging software

Sapera LT software development libraries has been used to support X64-CL frame grabber card, thus enabling applications to be developed under Windows environment. This provides an interactive environment to create a new or modify an existing camera configuration file. CamExpert, an advanced configuration utility supported by sapera library has been used as camera interfacing tool for the frame grabber board. This generates different camera configuration files based upon timing and control parameters selected. Sapera LT applications need to load appropriate configuration file before acquiring images from the camera. After loading the configuration file and clicking grab button, the live digitized video of the focused region is displayed in CamExpert window. A single frame can be freezed and saved as tiff format image file. For recording a movie, sequential grab demo program of Sapera demo applications has been used. Frame buffer count is selected first, which determines the duration of the movie depending upon frame rate. For making a movie of 5 seconds duration at a rate of 250 frames per second, the frame buffer count of 1250 images have been selected. Subsequently, the sequence of images is recorded as movie and saved as avi file.

3.5 Hot-wire anemometry

In the present work, a multi-channel hot-wire anemometer (*DANTEC*) was used for validation experiments and also to measure turbulence intensity, Figure 3.14. Hot-wire anemometry (HWA) is based on the principle of convective heat loss from a small electrically heated metallic wire exposed to flow. Any change in fluid flow rate affects the heat transfer from the filament. Therefore, there is a change in the resistance of the filament. The variation of resistance is monitored by a feedback circuit which passes ad-

Figure 3.14: Photograph of the Hotwire anemometer used in present experiments.

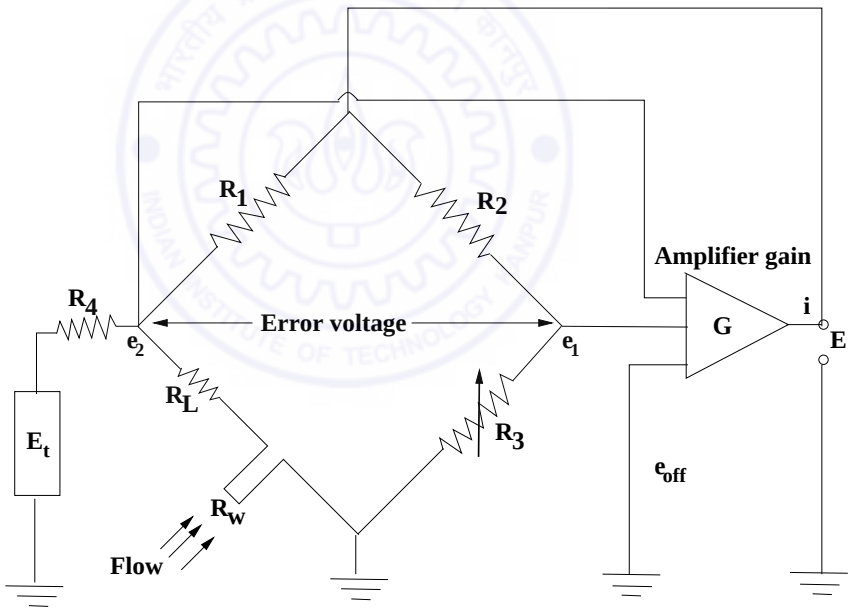

Figure 3.15: Circuit diagram of a Constant Temperature Anemometer (CTA).

ditional current till the wire 'temperature' is maintained constant independent of the flow velocity.

The hot-wire in combination with feedback circuit is termed as a Constant Temperature Anemometer (CTA). It consists of a Wheatstone bridge and servo-amplifier, Figure 3.15. The hot-wire probe (R_w) is placed in one arm of the Wheatstone bridge. When the probe is heated to its normal operating temperature, no voltage difference exists between the two arms of the bridge and input to the servo-amplifier is zero. As

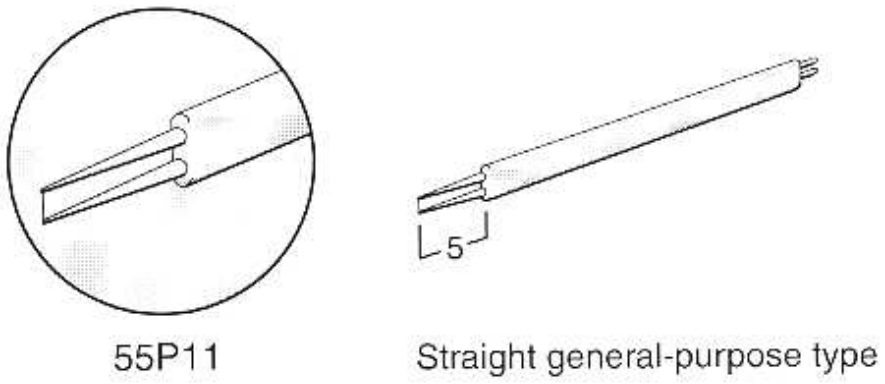

Figure 3.16: Miniature Wire Probe – 5μm diameter, platinum-plated tungsten wire, welded at the ends of prongs to provide active sensor length of 1.25 mm.

the flow condition varies, the sensor tends to cool appropriately with a resulting change in resistance. The change in resistance leads to an error voltage $e_2 - e_1$ and forms the input to the servo-amplifier. The amplifier has an output current, i, which is inversely proportional to the change in the resistance of the hot-wire sensor. Feeding this current back to the top of the bridge will restore the sensor's resistance and temperature to its original value. Higher gain of the servo-amplifier is desirable to have its fast response. The output of the feedback circuit is a measure of the fluid velocity. After proper calibration of the probe, it is possible to measure fluid velocities with an accuracy of 0.05% or better, depending upon the measurement range and the quality of calibration. In view of the high frequency response of the hot-wire anemometer[2], it can follow transients in the flow field without practically any time delay. The anemometer output voltage can be passed through signal conditioning unit to filter out noise and improve the Signal-to-noise ratio.

3.5.1 Hot-wire probe

A one wire hot-wire probe (Type-55P11, *DANTEC*) was used to measure the power spectra of the velocity fluctuations in the wake. It is a miniature wire probe of 5μm diameter, 1.25 mm long platinum-plated tungsten wire sensor (Figure 3.16). The wire is welded directly to the prongs and the entire wire length acts as a sensor.

The operating temperature of the hot-wire is set at higher temperature compared to the room temperature, typically, 150-250°C in air flow measurements. In the present experiments, the probe is operated at a temperature of around 160°C to minimize mixed convection and radiation errors. Higher temperature enhances the sensitivity of wire but make the wire fragile. Additionally, to avoid oxidization it is essential that the wire

[2]in excess of 100 kHz

temperature at any point along the wire element is kept well below 350°C. To illustrate these points, consider the hotwire probe used in the present investigation (DANTEC 55P11) for which electrical properties are $R_{20} = 3.5\Omega$ and $\alpha_{20} = 0.0036°C^{-1}$. For an overheat ratio of 1.5, the operational resistance of the wire will be $1.5 \times 3.5\Omega$. The corresponding mean wire temperature can be evaluated from equation

$$R = R_{20} + \alpha_{20} R_{20} (T_{sensor} - T_{20})$$

as being equal to about 160°C, which is well below the oxidization temperature.

3.5.2 CTA Bridge and accessories

The hot-wire probe was connected to a commercially available DANTEC 56C17 constant temperature Wheatstone bridge circuit. The 56C17 CTA bridge is supplied as a plug-in module for an existing 56C01 CTA system. The main unit 56C01 CTA delivers the servo-voltage as the output of the instrument. This voltage is a measure of fluid velocity. The 56C01 circuits contains servo amplifiers, filters, protective circuits, and a square-wave generator for dynamic balancing of the bridge. The 56C01 CTA contains a function switch with three modes for operation, namely TEMP, STD.BY and FLOW. In TEMP position the resistance of the connected probe can be measured in terms of a current supplied to it. In STD.BY position no current flows through the bridge. In FLOW setting the CTA starts operating with the active function of the servo amplifier.

A setting named BRIDGE ADJ enables the adjustment of bridge balance for measurement of probe resistance and setting of the desired overheat resistance. This BRIDGE ADJ has a switch pair for coarser adjustment of overheat resistance and a screw for fine adjustment. Resistance settings ranging from 0-30Ω in steps of 0.001Ω are possible. This adjustment is crucial for adjusting the overheat resistance for the calibration procedure. CTA in TEMP mode produces a voltage proportional to resistance of the wire. Here it functions as a constant current anemometer, CCA, and measures the wire resistance.

The main frame of the anemometer unit is fitted with the DANTEC 56N20 signal conditioner unit, which is designed to amplify the AC output signals from 56C01 CTA up to a level suitable for PC based data acquisition. The filter circuit of the 56N20 unit comprises high-pass and low-pass filters as well as an amplifier. The filter setting were determined by examining the complete power spectrum of the velocity components. A DANTEC 56N22 Mean value unit is used to measure the DC component of the output signal from 56C01 CTA. It is a 5.5 digit display voltmeter having a 100 μV resolution, 1-1000 seconds integration times and switch selectable 14 inputs.

3.6 Data acquisition system

The HWA output is a continuous analog voltage signal, which is sampled as a time series consisting of discrete values by an analog-to-digital converter (A/D board). The accuracy of the analog output signal is determined by the quality of the anemometer hardware. The accuracy of the digitized time series depends on the choice of the A/D board, the selection of *sampling rate* (SR), *number of samples* (N), and the extent of digitization. The level of digitization is specified as n-bit, where the resolution is the ratio of the full-scale reading (which is selectable by the program) and 2^n. The range, resolution and gain available on a A/D board determine the smallest detectable change in voltage, known as least significant bit (LSB). Smaller voltages can be measured by using a higher gain setting of the board. The values of *sampling rate* and *number of samples* depend primarily on the specific experiment, the type of data analysis (time-averaged or spectral analysis), the available computer memory and the acceptable level of uncertainty. Time-averaged analysis, such as the determination of the time-averaged velocity and rms of velocity fluctuations requires uncorrelated samples. It can be achieved when the time elapsed between individual samples is at least two times larger than the integral time scale of the fluctuations. On the other hand, spectral analysis requires the sampling rate to be at least twice the highest frequency component in the signal. The sampling rate requirement is based on the Nyquist criterion to accurately represent a signal without distortion (aliasing).

In the present experiments, the hot-wire signal was acquired *via* a PC through a 12-bit A/D DAQ card (PCI-MIO-16E-4, *National instruments*) and 68 pins SCB-68 termination I/O connector (*National instruments*). The DAQ board has 8 differential analog input channels and two analog output channels (D/A conversion). The SCB-68 is a shielded I/O connector block for easy signal connection to DAQ card. The A/D card was configured in the differential mode to avoid unwanted noise in the measured signal. The signal is amplified prior to digitization. The gain, ranges and resolution are selected on the basis of the characteristics (amplitude and spectral) of the input signal. A long signal, integrated over a time duration of 20 seconds and with a sampling rate of 1 kS/s was recorded from the hot-wire anemometer.

DAQ card software consists of drivers and application software. Drivers include a set of commands that the device accepts and the application software sends the commands to the drivers to acquire, display and analyze the data. In the present work, *LabVIEW Software* has been used for programming the DAQ card for data collection. *LabVIEW (Laboratory Virtual Instrument Engineering Workbench)* delivers a powerful graphical development environment for signal acquisition, measurements, analysis, and data pre-

sentation. It includes a set of programs (VIs) to configure, acquire data from, and send data to DAQ system. The data acquisition was done using traditional intermediate VIs.

3.7 Cylinder oscillation system

Two electromagnetic linear actuators (SP2, *Spranktronics*) driven by a dual channel power oscillator were used to generate controlled oscillations of the cylinder. The arrangement of the cylinder in the test section with actuators for forced oscillations is shown in Figure 3.17. The actuators are mounted on the wooden platforms fixed to the support structure of the test cell. Two sharp metallic holders rigidly support each end of the cylinder through small openings in the optical window frames. These holders are fixed to the actuators located outside the side walls of the test section. Proper care has been taken to ensure no leakage at the small opening of the optical window frames. The details of the actuators and the drive unit are discussed below.

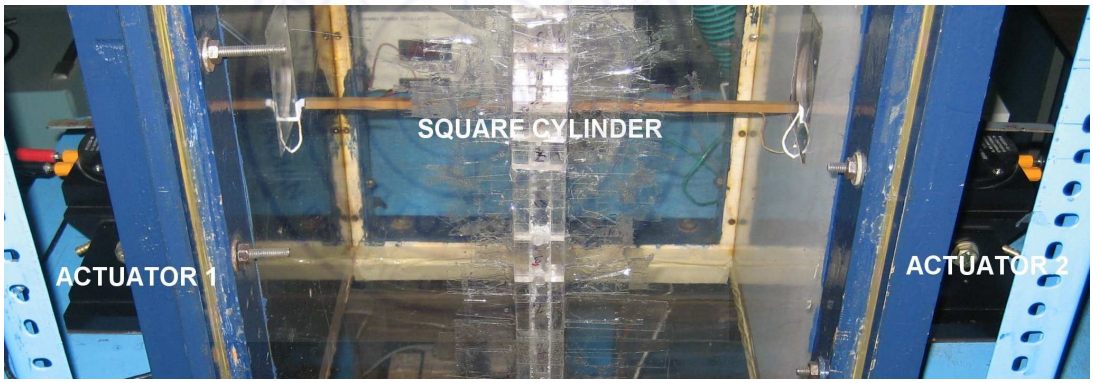

Figure 3.17: A photograph of the arrangement of the cylinder with electromagnetic actuators.

3.7.1 Electromagnetic linear actuator

Electromagnetic actuator (Figure 3.18 (a)) also termed as electrodynamic shaker has been used to oscillate the cylinder. This consists of a pair of permanent magnets and an electromagnet made-up of a soft-iron core with a coil wound around it. The coil is suspended in the radial magnetic field generated by the permanent magnets and is allowed to move axially. The actuator works by virtue of the interaction between the magnetic field and an oscillating current flowing in the coil. Under such circumstances, a longitudinal force is generated at right angles to the line of flux and to the conductor carrying the

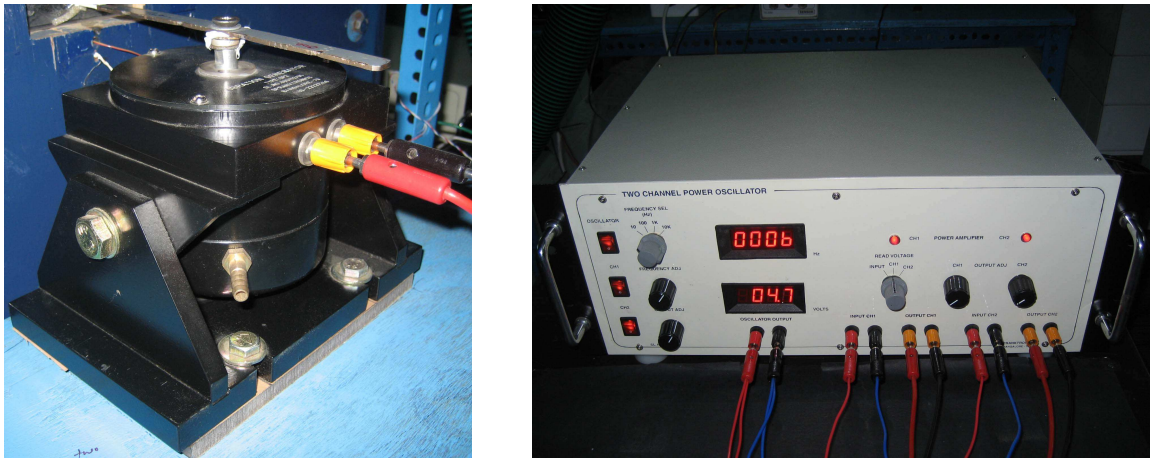

(a) (b)

Figure 3.18: Photograph of the (*a*) Electromagnetic actuator and (*b*) Dual channel power oscillator.

current. This force is proportional to the instantaneous current and is transmitted to a moving assembly to which the test cylinder is affixed. The actuators may be driven by sinusoidal, random or transient signals and therefore suitable for either open loop arrangement with sinusoidal signal or feedback arrangement where the signal is random. The useful frequency range of the actuator (SP2) is equal to 1-200 Hz. The maximum amplitude in this frequency range under unloaded condition is 1.7 mm, corresponding to approximately 25% of the cylinder size.

3.7.2 Dual channel power oscillator

Dual channel power oscillator (Figure 3.18 (b)) consists of a built-in oscillator to generate sinusoidal activation signal and a drive unit having two power amplifiers. The output of the oscillator is supplied to the power amplifiers and the amplified signal is used to drive two electromagnetic actuators. Since, both the actuators are driven from a single power source, identical phase of oscillation at both ends is ensured. During experiments, the shedding frequency of the stationary cylinder is first measured. The cylinder is subsequently excited at various harmonics around the shedding frequency using the frequency adjustment knob of the oscillator. The amplitude of the excitation is varied by adjustment of the voltage input to the electromagnetic actuator. To ensure identical oscillation amplitude, both the amplifiers are kept at the maximum potentiometer settings and output of the oscillator is varied to change the voltage applied. The calibration experiments relating the voltage applied and the amplitude of oscillation are presented in a later section of the present chapter.

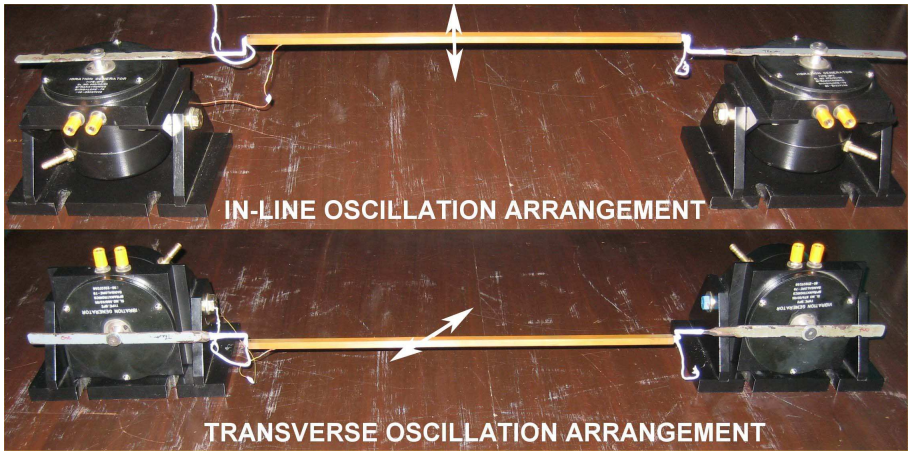

Figure 3.19: Photograph of the actuator orientations for inline and transverse oscillations.

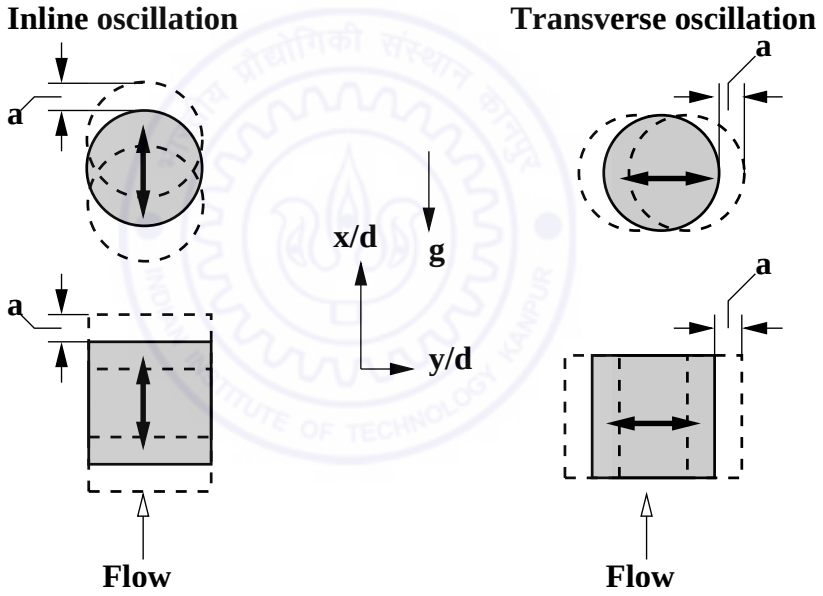

Figure 3.20: Schematic of the oscillation geometry for circular and square cylinders. The symbol 'a' is the amplitude of oscillation and the arrow indicates the direction of motion of the cylinder.

3.7.3 Inline and transverse oscillations

The cylinder has been oscillated in both streamwise (in-line) and transverse (crossflow) directions to the main flow direction. A photograph illustrating the orientation of actuators for the Inline and crossflow oscillations is shown in Figure 3.19. For achieving transverse oscillation, the actuator assembly is tilted at 90° to the base plate as compared to inline arrangement. Figure 3.20 shows the schematic of the oscillation geometry for the inline and transverse oscillation of both circular and square cylinders. The dotted

line is the extreme position of the cylinders with 'a' being the amplitude of oscillation. The arrow direction for the movement of the cylinder is same as that of the direction of mean flow for the inline oscillation case. For transverse oscillation, the cylinder oscillates normal to the mean flow direction.

3.8 Auxiliary instruments

Starting from the initial validation experiments to the final measurements, various other instruments have also been used. They are directly or indirectly being used for measurements or testing purposes. A brief introduction of each of them is presented below.

3.8.1 Digital micromanometer

The free-stream velocity in the test section and velocity distribution across the wake is measured by a pitot-static tube. The pitot-static tube is carefully aligned with the main flow direction. It is connected to a high resolution digital micromanometer (FC012, *Furness Controls*) using twin flexible tubing. The micromanometer uses a capacitance-type differential pressure transducer and can measure differential pressures upto 1.999 pascals with a resolution of 0.001 Pascal. It has a pre-calibrated velocity output and is equipped with a temperature correction chart to account for changes in the room temperature. The micromanometer can measure a maximum velocity upto 5.6 m/s. The pitot-static tube in conjunction with digital micromanometer (Figure 3.21) have also been used for calibration experiments of the hotwire anemometer.

(a) (b)

Figure 3.21: Picture of the (a) Micromanometer and (b) Pitot-static tube used during the experiments.

3.8.2 Digital storage oscilloscope

A two-channel digital storage oscilloscope (*Caddo* 9100) with an operating frequency of 100 MHz has been used, Figure 3.22 (a). This can operate in storage as well as real time mode with each channel having 16k memory to store and open a large number of datum. It have VGA colour LCD display that helped to observe and analyse the signals of two different channels with different colour. One FFT module is connected to the oscilloscope and is realised from the MATH function of the oscilloscope. This apply Fast Fourier transform (FFT) algorithm to perform real time spectral analysis of the hot wire signal for computing the power spectrum and determining vortex-shedding frequency. In the oscillation experiments, to ensure identical amplitude and phase of the input signal to the two actuators, the oscilloscope was used to continuously monitor this signal on-line.

3.8.3 Function generator

Figure 3.22 (b) shows the picture of a 15 MHz Funtion / Arbitrary Waveform Genrator (HP33120A, *Hewlett packard*). It can generate five standard waveforms including sine, square, triangle, ramp and noise. The generator can also create and store arbitrary waveforms using the front panel. There are five in-built arbitrary waveforms stored in non-volatile memory. Function generator is used to generate the sinusoidal signal of known frequency and amplitude, amplified to the required voltage level by the power amplifier of the actuator drive unit, and finally sent to the actuators to oscillate the cylinder. The sinusoidal signal is also used to check the analogue phase shift circuit for its amplitude

(a) (b)

Figure 3.22: Photograph of the (*a*) Digital storage oscilloscope, and (*b*) Function generator.

and phase response to the input signal. The stored arbitrary waveform signals are also used to check the behaviour of the actuators to arbitrary signals.

3.8.4 Digital multimeter

A versatile digital multimeter (HP3457A, *Hewlett packard*) is also used in the measurements. It can measure DC voltage, AC voltage, AC and DC currents and the resistance over a wide range of values. Presently, this has been used to measure resistance of the nichrome wire used for heating the cylinder. The resistance is measured by sourcing a known current through the unknown resistance. The range of resistance measurement is 10Ω to 3GΩ.

3.9 Test-section flow quality

For an empty test-section, the velocity of air flow at each plane (normal to the centerline) should be uniformly parallel to the centerline and should have minimal flow fluctuations. Therefore, the inlet flow turbulence level and the flow parallelism have been checked for the flow quality, to characterize the testcell. The turbulence intensity has been measured

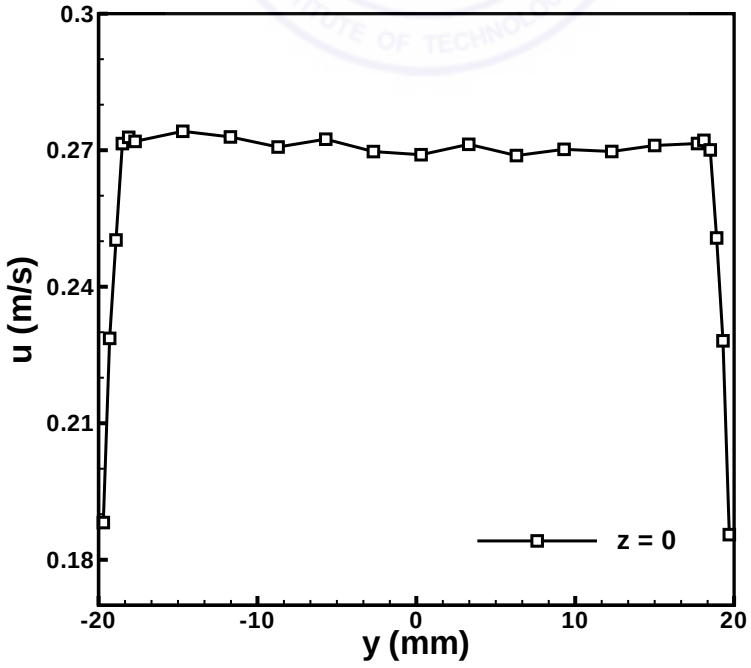

Figure 3.23: Velocity profile inside the testcell from hotwire measurements at vertical mid-plane ($z = 0$).

from the hotwire signal. The free-stream turbulence level in the approach flow is quite small i.e. less than 0.3% at the test region for the velocity range used in the present work. The flow uniformity is better than 1% over 95% of the width of the test cell (outside the wall boundary layers) for the velocity range considered. Uniform and stable free-stream velocities in the range of 0.13-0.27 m/s were realized in the testcell for the present study. The test cell flow parallelism for the vertical mid-plane of the testcell has been presented in Figure 3.23.

3.10 Calibration of electromagnetic actuators

In order to set the proper amplitude of oscillation, the relation between the voltage applied to the actuators and the corresponding displacement of the cylinder has to be known. To determine this relation, calibration experiments have been performed without loading the actuators and loading with circular and square cylinder subsequently. The experiments were performed for a set of frequencies at various harmonics of the Strouhal value. Without inserting the knife-edge, the schlieren optics is merely a projector, imaging opaque objects in the test region as silhouettes on the screen and the cylinder shadow is seen in the image. Therefore, the cylinder size can be correlated to the size of the shadow in the magnified images in terms of the number of pixels. A typical calibration value for the present set of images has been estimated to be 0.14 mm/pixel. Actual displacement of the cylinder can be estimated by scaling the number of pixels moved by the moving opaque boundary of the cylinder shadow from one extreme position to the other in an oscillation cycle. Horizontal and vertical alignment of the cylinder with respect to the laser beam is very crucial for measuring the cylinder size from its shadow in the image.

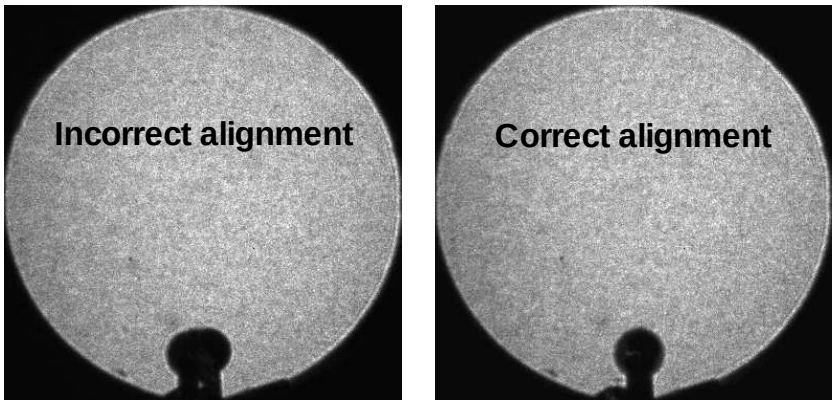

Figure 3.24: Images showing incorrect and correct alignment of the cylinder with respect to the laser beam.

For correct alignment, the shadow of both ends of the cylinder should merge and produce exact circular/square shape with identical size across horizontal and vertical dimensions of the cylinder. This was ensured with due care as shown in Figure 3.24, showing the shadow of the circular cylinder with incorrect and correct alignment.

3.10.1 Without loading

The cylinder is oscillated by mounting it on two electromagnetic actuators driven by two channel power oscillator. Both actuators should produce identical displacement for the similar input signal. Therefore, performance of each actuator has been individually tested for different actuator-channel combinations under no load condition. For this, a small countersunk screw (having smooth flat surface) was screw fixed to the actuator and displacement of its surface was measured as a function of the amplitude and frequency of the input voltage. Figure 3.25 (a) shows a sequence of such calibration images separated by a time interval of one eighth of the time period of the oscillation. In the figure 'a' and 'i' are the lowest positions and 'e' is the highest position in the oscillation cycle. A datum line clearly shows the progressive movement of the surface from 'a' to 'e' position and then from 'e' to 'i' position; the displacement between two extreme positions corresponds to two times the amplitude of oscillation. Exactly identical displacement is observed for different cycles of oscillation validating precise performance of the actuators.

3.10.2 With loading

Figure 3.25 (b) and (c) shows a sequence of calibration images with circular and square cylinder mounted on the actuator for inline and transverse oscillations respectively. For inline oscillations, the movement of the upper surface of the cylinder is considered to measure the displacement. Whereas, for transverse oscillations, either the right extreme position (marked as e) or the left extreme position (marked as a, i) is considered. The boundary of the cylinder surface can be estimated within one pixel value. Figure 3.26 shows the variation of cylinder displacement with the voltage applied to the actuators at fundamental Strouhal frequency. A linear variation is observed for all the cases and highest amplitude is obtained at no load condition. Whereas, lowest amplitude of oscillation is obtained for inline oscillating square cylinder. In general, at a particular voltage, the amplitude of oscillation is higher for the transverse case as compared to inline case with almost equal amplitude for both circular and square cylinder. However, there is a considerable difference between the amplitudes for circular and square cylinder for inline oscillation. This is probably due to higher power requirement for oscillating heavier weight

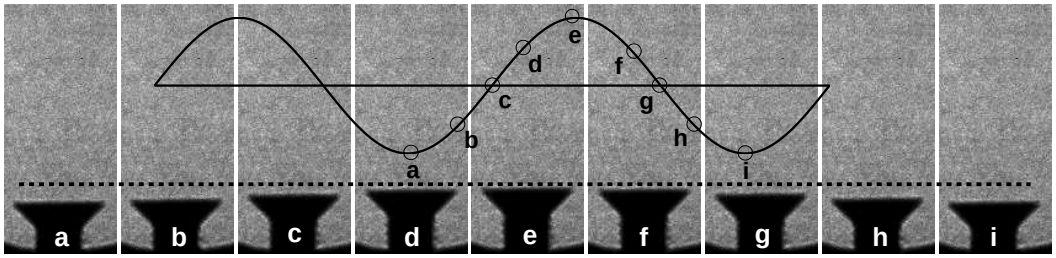

(a)

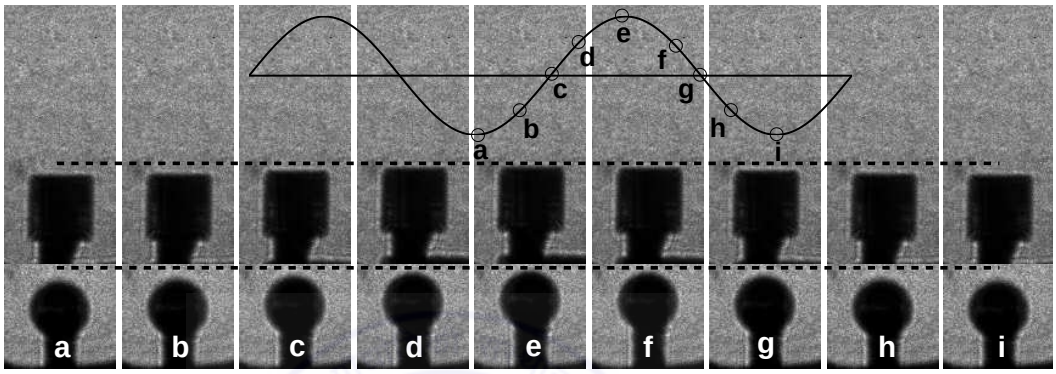

(b)

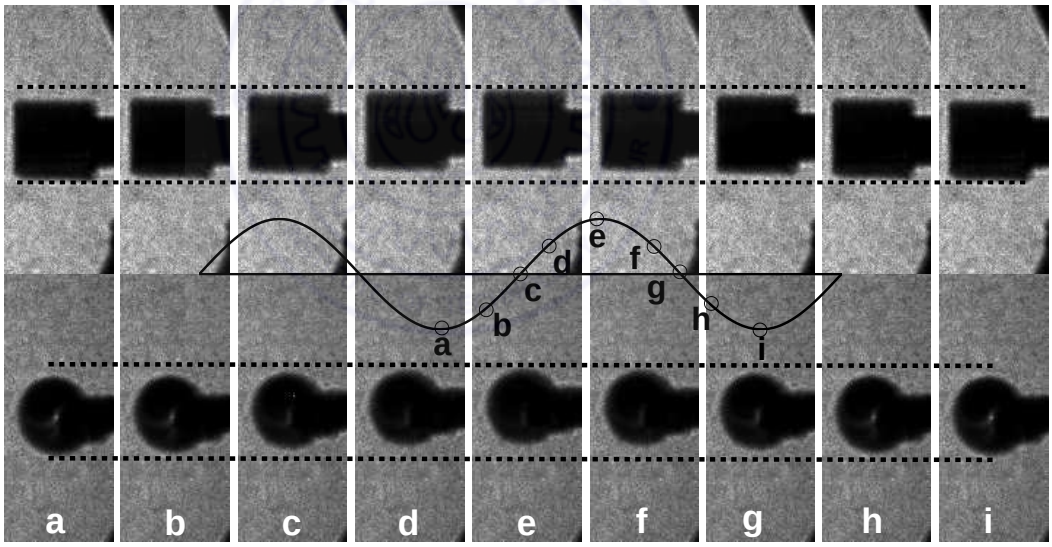

(c)

Figure 3.25: Calibration images showing progressive movement of the surface in an oscillation cycle. (*a*) without load, (*b*) Inline oscillations, and (*c*) Transverse oscillations (Images rotated 90°).

of the square cylinder compared to the lighter weight of the circular cylinder against gravity. Similar calibration curves showing the variation of the cylinder displacement with the voltage applied to the actuators were generated at different oscillation frequencies. At a particular frequency, the precise values of the voltage required to oscillate the cylinder for different oscillation amplitudes were obtained from these calibration curves.

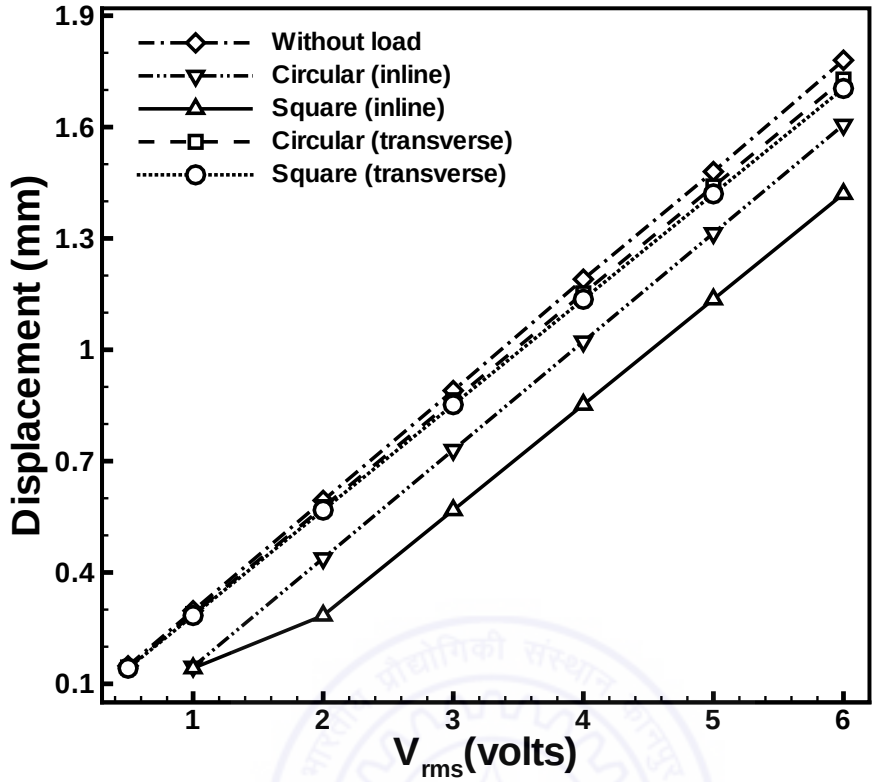

Figure 3.26: Variation of the cylinder displacement with the voltage applied to the actuators at fundamental Strouhal frequency (6 Hz).

3.11 Details of the experimental conditions

In the present work, the effect of buoyancy on the wake characteristics of circular and square cylinders have been investigated for stationary cylinders. Subsequently, the wake behavior under combined influence of buoyancy and inline/transverse oscillations have been explored. The operating parameters, i.e. Reynolds number, Richardson number, oscillation frequency, and oscillation amplitude are varied to examine flow behavior over a range of experimental conditions. Complete details of the conditions at which these experiments have been performed are given in the following sections.

For the range of Reynolds numbers studied, three-dimensional flow can be expected in the test cell. The cylinder length is quite large with respect to the cylinder diameter/edge (aspect ratios being 65 and 60 for circular and square cylinders respectively). Therefore, wall effects are not expected to be an important factor in determining the wake behavior. The maximum Richardson number at Re = 118 is 0.171, a value less than 0.3 needed for heat-induced 3D-transition (Maas *et al.* 2003).

Table 3.1: Experimental conditions for a stationary circular cylinder.

Test case	Cylinder diameter (mm)	Flow velocity (m/s)	Reynolds number (Re)	Free stream temperature, °C
1	6.2	0.13	53	23
2	6.2	0.23	94	21
3	6.2	0.27	110	21

Set no.	Cylinder surface temperature °C	Richardson number (Ri) Case 1 (Re=53)	Richardson number (Ri) Case 2 (Re=94)	Richardson number (Ri) Case 3 (Re=110)	Set no.	Cylinder surface temperature °C	Richardson number (Ri) Case 3 (Re=110)
1	30	0.084	0.035	0.025	11	55	0.091
2	35	0.143	0.053	0.039	12	60	0.104
3	40	0.201	0.072	0.052	13	65	0.116
4	43	0.235	-	-	14	70	0.128
5	45	-	0.090	0.065	15	75	0.140
6	46	0.269	-	-	16	77	0.145
7	50	0.314	0.108	0.078	17	79	0.150
8	52	-	0.115	-	18	80	0.152
9	53	-	0.119	-	19	81	0.154
10	54	-	0.122	-	20	82	0.157

3.11.1 Stationary cylinder

The details of the experimental conditions for stationary circular and square cylinders are compiled in Tables 3.1 and 3.2 respectively. Experiments were conducted at three Reynolds numbers for both circular and square cylinders. One Reynolds number, Re = 53 for circular cylinder corresponds to the laminar steady flow regime. The other Reynolds numbers are within the vortex shedding regime i.e. Re = 94 and 110 for circular cylinder and Re = 87, 109 and 118 for square cylinder. To study the effect of heating at different Reynolds numbers, a total of 60 (29 for circular and 31 for square) sets of experiments were performed for different cylinder temperatures ranging from 30°C to 85°C. The ambient temperature was in the range 21-23°C during experiments. The Richardson number range was large enough to cover forced and mixed convection regimes. The highest Reynolds number in this study is limited to Re = 118 because of the higher temperature requirement of the heated cylinder for study of vortex shedding suppression.

Table 3.2: Experimental conditions for a stationary square cylinder.

Test case	Cylinder edge (mm)	Flow velocity (m/s)	Reynolds number (Re)	Free stream temperature, °C
1	6.7	0.20	87	23
2	6.7	0.25	109	23
3	6.7	0.27	118	23

Set no.	Cylinder surface temperature °C	Richardson number Case 1 (Re=87)	Richardson number Case 2 (Re=109)	Richardson number Case 3 (Re=118)	Set no.	Cylinder Surface temperature °C	Richardson number Case 2 (Re=109)	Richardson number Case 3 (Re=118)
1	32	0.049	-	-	13	58	0.117	-
2	35	0.065	0.042	0.036	14	59	-	0.103
3	40	0.092	0.059	-	15	60	0.124	-
4	41	0.097	-	-	16	63	0.133	-
5	43	0.107	-	0.059	17	65	0.139	0.119
6	44	0.113	-	-	18	67	0.146	-
7	45	-	0.075	-	19	70	0.155	-
8	47	0.128	-	-	20	71	-	0.135
9	48	0.133	-	-	21	73	0.164	-
10	50	0.143	0.092	-	22	76	0.173	0.148
11	51	-	-	0.081	23	82	-	0.163
12	55	-	0.108	-	24	85	-	0.171

3.11.2 Transverse oscillations

The details of the experimental conditions for the study of combined influence of buoyancy and transverse oscillations are presented in Tables 3.3 and 3.4 for circular and square cylinders respectively. The airflow speed was set at 0.26 m/s and 0.27 m/s for circular and square cylinders respectively. These correspond to Reynolds number equal to 105 and 116 in the laminar vortex shedding regime. Four different cylinder surface temperatures for the circular cylinder and five for the square cylinder in the range from 35°C to 86°C were maintained to cover forced and mixed convection regimes. The ambient temperature was in the range 24-25°C during experiments. For a particular heating level, first the experiments were performed without oscillating the cylinder and schlieren movies were recorded. At lowest heating level, the vortex shedding frequency (f_s) for both circular and square cylinders were estimated to be nearly equal to 6 Hz . Subsequently, the cylinder was oscillated at a frequency ratio (f_e/f_s) of 0.5, 1, 1.5, 2 and 3. These correspond to oscillation at subharmonic frequency, fundamental Strouhal frequency, nonharmonic at

Table 3.3: Experimental conditions for a circular cylinder subjected to transverse oscillations.

Test case	Cylinder diameter (mm)	Flow velocity (m/s)	Reynolds number (Re)	Free stream temperature, °C
1	6.2	0.26	105	24

Set number	Cylinder surface temperature, °C	Richardson number (Ri)	Frequency ratio (f_e/f_s)	Amplitude ratio (a/d)
			0	-
1	37	0.038	0.5	0.02, 0.04, 0.06, 0.08, 0.1
2	51	0.078	1.0	0.02, 0.04, 0.06, 0.08, 0.1
3	68	0.124	1.5	0.02, 0.04, 0.06, 0.08, 0.1
4	76	0.145	2.0	0.02, 0.04, 0.06, 0.08, 0.1
			3.0	0.02, 0.04, 0.06, 0.08, 0.1

Table 3.4: Experimental conditions for a square cylinder subjected to transverse oscillations.

Test case	Cylinder edge (mm)	Flow velocity (m/s)	Reynolds number (Re)	Free stream temperature, °C
1	6.7	0.27	116	25

Set number	Cylinder surface temperature, °C	Richardson number (Ri)	Frequency ratio (f_e/f_s)	Amplitude ratio (a/d)
			0	-
1	35	0.030	0.5	0.02, 0.04, 0.06, 0.08, 0.1
2	55	0.086	1.0	0.02, 0.04, 0.06, 0.08, 0.1
3	68	0.121	1.5	0.02, 0.04, 0.06, 0.08, 0.1
4	86	0.167	2.0	0.02, 0.04, 0.06, 0.08, 0.1
			3.0	0.02, 0.04, 0.06, 0.08, 0.1

1.5 times the Strouhal frequency, first harmonic and second harmonic respectively. The cylinder was oscillated at small amplitudes ranging from 0.02-0.10 times the diameter/edge of the cylinder for each of the excitation frequency. A total 26 sets of experiments were performed for a particular heating level (cylinder temperature). These experiments were repeated for all the heating levels considered for circular and square cylinders.

3.11.3 Inline oscillations

The experimental conditions for the study of combined influence of buoyancy and inline oscillations is given in Tables 3.5 for circular cylinder. The experiments were performed

Table 3.5: Experimental conditions for a circular cylinder subjected to inline oscillations.

Test case	Cylinder diameter (mm)	Flow velocity (m/s)	Reynolds number (Re)	Free stream temperature, °C
1	6.2	0.26	104	25

Set number	Cylinder surface temperature, °C	Richardson number (Ri)	Frequency ratio (f_e/f_s)	Amplitude ratio (a/d)
1	34	0.027	0	-
2	45	0.058	1.0	0.02, 0.04, 0.06, 0.08, 0.1
3	63	0.108	1.5	0.02, 0.04, 0.06, 0.08, 0.1
4	77	0.144	2.0	0.02, 0.04, 0.06, 0.08, 0.1

at an airflow speed of 0.26 m/s with Reynolds number equal to 104. Four different heating levels for the circular cylinder from 34°C to 77°C were maintained to cover forced and mixed convection regimes. The ambient temperature was maintained at 25°C during experiments. Initial experiments were performed without oscillating the cylinder. Subsequently, the cylinder was oscillated at a frequency ratio (f_e/f_s) of 1, 1.5 and 2. The cylinder was oscillated at small amplitudes ranging from 0.02-0.10 times the diameter of the cylinder for each of the excitation frequency. For a particular heating level, a total 16 sets of experiments were performed.

Chapter 4

Data Analysis

In the present study, laser schlieren-interferometry has been primarily used for visualization and analysis of the instantaneous flow structures. The spatial and temporal characteristics of the flow field have been evaluated from a long sequence of schlieren images. Quantitative flow-field statistics are obtained from the measurement of fluctuations in the light intensity (referred to as schlieren signal) of real-time schlieren image. These measurements have been used to describe the statistical quantities of the flow field, i.e. the time-averaged flow field, phase-averaged flow structures , RMS fluctuations, power spectra, cross spectra, phase shift, Strouhal number, vortex formation length and convection velocity of vortex structures. The details of the data analysis procedures for these quantities have been discussed in the present chapter. Fluctuation results from the schlieren measurements have been validated with the Strouhal number data in the published literature and hotwire measurements. The evaluation of interference fringe pattern of the schlieren images for evaluation of temperature field have been discussed in great detail in schlieren-interferometry section. The uncertainty in the measurements has been reported in a separate section.

4.1 Schlieren-interferometry

In general, fluid flow with variable density represents an optical disturbance, which changes the phase of a transmitted light wave with respect to an undisturbed wave. The interferometer displays such alterations in the optical phase by creating interference between the disturbed wave that has passed through the test field with a second wave that propagates along a different undisturbed optical path to the recording plane. This class of interferometers is classified as “two-beam interferometers”. In a typical schlieren system, a parallel beam of light brought to a focus on an obstacle that cuts off most of the beam

with the exception of the small portion that is diffracted around the obstacle. The introduction of an optical inhomogeneity (schliere) into the beam will produce a deflection of the rays, causing them to miss the obstacle and forming a shadow image of the disturbance region at the image plane. In addition to the deflection, the portion of the beam passing through the schliere undergoes a phase change relative to the undisturbed light, whose magnitude depends upon the gradients of index of refraction present in the schlieren. Therefore, when this light arrives at the focal plane of the camera, interference occurs between the disturbed and undisturbed light. The system bears some similarity to that of a two-beam interferometer, but two interfering beams originate in the test region itself and the system is self-referencing. Self-referencing interference is more prominent, when high temperature gradients are present in the flow field and phase object is sufficiently long. Schlieren-interferometer enjoys the advantage of both schlieren optics and common path interferometry, making it much simple, easier to align and much less vibration-sensitive than the classical Mach-Zehnder interferometer. Diffractive disturbances in the schlieren system, formation of the schlieren interferograms and evaluation of interferograms for the determination of fringe temperature are discussed in the following headings.

4.1.1 Diffraction effects and geometric-optics limitations

Diffraction, now recognized as an integral part of the schlieren-image formation process appear more pronounced for highly coherent light source; some of these disturbances will average out for the different wavelengths of a white light source. According to Settles (2001), two diffraction effects are of main concern: the diffraction of light by an opaque edge in the test area that diffracts light in a direction perpendicular to that edge and second is the diffraction of the light-source image at the knife-edge. As the knife-edge cutoff is advanced, fringing effect is seen in the whole field which broadens with the cutoff. A narrow bright diffraction band or halo appears around all opaque edges in the test area that have components parallel to the knife-edge. Figure 4.1 shows the appearance of the diffraction effects with increasing knife-edge cutoff for a flow field without the presence of any optical disturbance. Fringing effects are clearly seen in Figure 4.1 (b-e). In the Figure 4.1 (e) a bright diffraction band appear at the top surface of the cylinder due to the diffraction of light by the opaque edge. These diffractive disturbances puts a natural limit for increasing sensitivity ($S = f_2/b$) indefinitely by increasing knife-edge cutoff. Nonuniform image illuminance due to diffraction shadows restricts quantitative measurements based on the analysis by geometrical-optics theory especially at high schlieren sensitivity settings.

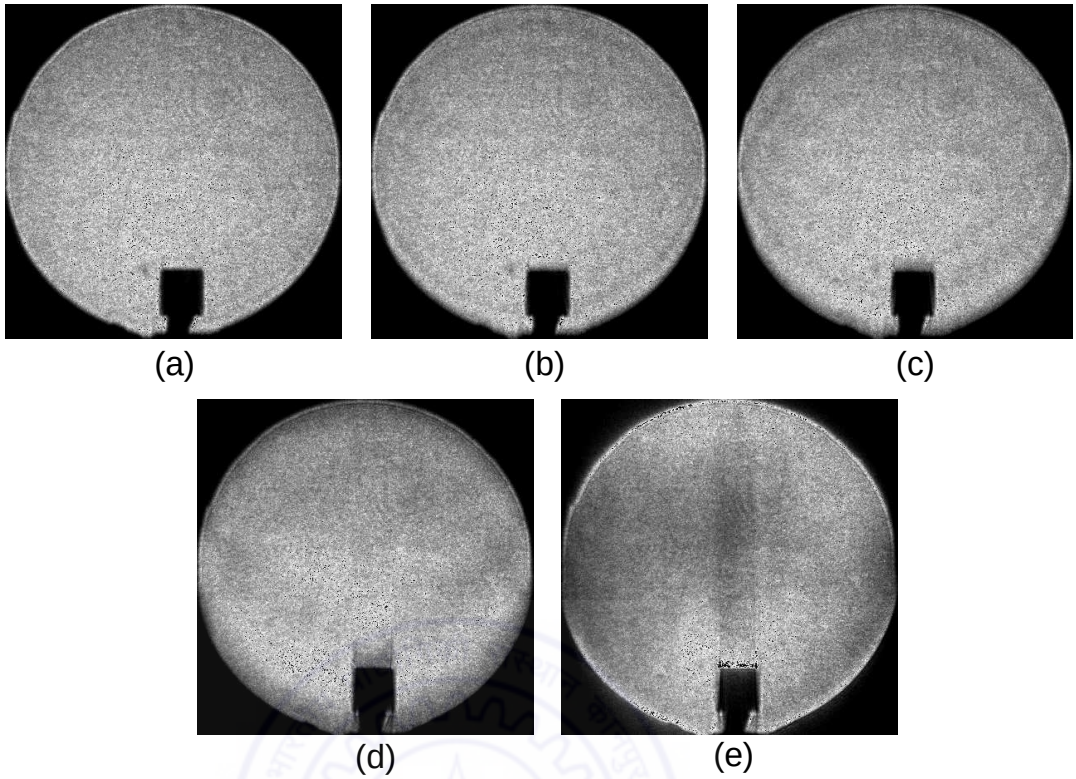

Figure 4.1: Diffraction halos in the schlieren image by increasing knife-edge cutoff. (*a*) 0% cutoff, (*b*) 39% cutoff, (*c*) 49% cutoff, (*d*) 56% cutoff, and (*e*) 61% cutoff.

4.1.2 Formation of schlieren-interferograms

In the schlieren technique, the light beam closer to the cylinder is refracted due to gradients in refractive index because of the temperature field, thus generating an intensity distribution on the imaging plane. Away from the cylinder surface, temperature gradients are small and the object beam passes with a small deflection through the test medium. Hence, if sufficiently long phase objects are available, the light beam away from the cylinder can act as a reference beam (undisturbed) with which the test beam (disturbed) closer to the cylinder can interfere. When high temperature gradients appear in the flow field, the interference effect is more prominent. Interference between the distributed and undistributed light beam results in interferometric fringes. Fringes are the lines of constant optical path length. As discussed by Goldstein (1996), if the index of refraction varies only in a plane perpendicular to the beam, fringes are also contours of constant index of refraction. In ideal gas at constant pressure and constant gas composition the fringes are lines of constant temperature averaged in the viewing direction within the test cell. Thus, schlieren-interferograms provide additional information in the form of isotherms in the wake.

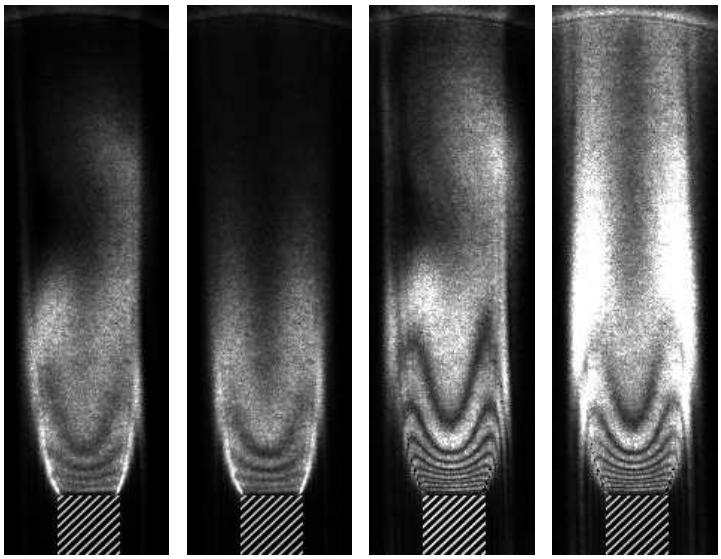

Figure 4.2: (*a*) Instantaneous, (*b*) time averaged, (*c*) mean removed phase averaged, and (*d*) mean removed time averaged schlieren interferograms for a square cylinder at Re=109 and Ri=0.059.

Schlieren interferograms are prone to errors due to the inhomogeneous distribution of the background light intensity in the image plane and the reference beam non-uniformity. Therefore, all fringes are not clearly visible in the image. Brackenridge and Peterka (1967) reported that the knife-edge positioned at maximum contrast could not produce a correct total fringe count. Anderson and Milton (1989) reported that Z-type concave mirror schlieren system results in astigmatic image of the source. They observed a slight degradation of fringe visibility. as one of the reason for uneven schlieren background illuminance, Settles (2001) showed that use of concave mirrors configured for on-axis use in an off-axis mirror-type schlieren system lead to errors in the faithful production of light source image in the cutoff plane. This arises from differences in path lengths along the optical centerline and the mirror periphery. To minimize this, mirrors with large f/number (6 or greater) should be used and tilted at equal small angles in opposite directions from the central optical axis. In addition to uneven distribution of the background light intensity, the problem of fringe visibility can be more serious for imaging of a time dependent flow field, where both the test beam and to an extent the reference beam fluctuate with time, as in the present case. According to the present study, all fringes can be recovered by working with the mean-removed intensity distribution of the schlieren images. The averaging has the effect of eliminating the time-dependent oscillations in the background intensity. The effect of different processing procedure on the schlieren interferogram of the wake of a square cylinder heated to 40°C in an ambient at 23°C is shown in Figure 4.2. The Reynolds number in this experiment is 109. Figure 4.2 (a) and (b) show

the instantaneous and time-averaged schlieren images respectively. The time-averaged schlieren interferograms have been generated from 1250 instantaneous schlieren images, consisting of total 27 vortex-shedding cycles. Figures 4.2 (c) shows the mean removed phase averaged (over 27 vortex-shedding cycles) schlieren interferogram at the time instant corresponding to Figure 4.2 (a). The procedure of phase averaging is similar to that discussed in Section 4.2.8. The number of fringes in Figure 4.2 (c) is higher than that in Figure 4.2 (a) indicating the reduction of background noise due to phase averaging. Figure 4.2 (d) shows the mean removed time averaged schlieren interferograms, involving the subtraction of averaged intensity from the instantaneous schlieren images. This improve the contrast leading to clear interferograms in Figure 4.2 (d). We evaluate the accuracy of schlieren interferogram by comparing the actual temperature difference between the cylinder surface and the free stream with the predicted temperature difference from the number of fringes in a later section.

4.1.3 Interferogram evaluation and its validation

Evaluation of interferograms for the determination of fringe temperature is discussed in the present section. The test beam records information about the variation of the refractive index of the fluid. for temperature measurement, the refractive index variation must be related to that of temperature. This relationship between the refractive index n and temperature T is established as follows. For a transparent medium, refractive index and density have a unique relationship, known as Lorenz-Lorentz formula (Goldstein, 1996)

$$\frac{n^2-1}{\rho(n^2+2)} \quad = \quad \text{constant} \tag{4.1}$$

Where n is the refractive index and ρ is the density. For air and other gases, the refractive index is close to unity and the above expression reduces to the Gladstone-Dale equation

$$\frac{n-1}{\rho} \quad = \quad \text{C} \tag{4.2}$$

Hence, $dn/d\rho =$ constant. The constant C, called the Gladstone-Dale constant, is a function of the particular gas and varies slightly with wavelength. Instead of using constant C directly, it is common to use the index of refraction n_o at a standard condition. Hence

$$n-1 = \frac{\rho}{\rho_o}(n_o-1) \tag{4.3}$$

or

$$\rho = \rho_o \frac{n-1}{n_o-1} \tag{4.4}$$

For moderate changes in temperature and nearly uniform bulk pressure, density varies linearly with temperature as

$$\rho = \rho_o(1 - \beta(T - T_o)) \tag{4.5}$$

Accordingly, refractive index varies linearly with temperature (within limits). It follows that dn/dT is also a constant, being purely a material (fluid) property. For the discussion presented below, it is taken to be constant, independent of temperature.

Let $n(x, y)$ and $T(x, y)$ be the refractive index and temperature fields respectively, the physical domain being a two-dimensional plane. Let n_o and T_o be the reference values of n and T respectively as encountered by the reference beam. Let L be the total geometric path length covered by the test and reference beams. The interferogram is a fringe pattern arising from the optical path difference

$$\Delta PL = \int_0^L (n(x, y) - n_o)ds \tag{4.6}$$

Differences between $n(x, y)$ and n_o occur only over the length of the cylinder. Hence L can be taken directly to be the length of the cylinder. In terms of temperature, the difference in the path lengths can be expressed as

$$\Delta PL = \frac{dn}{dT} \int_0^L (T(x, y) - T_o)ds \tag{4.7}$$

The integral is evaluated along the path of a light ray given by the coordinate s. Neglecting refraction effects, this path will be a straight line and the integral evaluation is greatly simplified. The fringes seen on the interferograms are a locus of points having equal optical path difference. Hence on any given fringe the optical path difference ΔPL is a constant and

$$\int_0^L (T(x, y) - T_o)ds = \frac{\Delta PL}{dn/dT} = \text{constant} \tag{4.8}$$

Hence

$$\int_0^L (T(x, y)ds - T_oL = \text{constant} \tag{4.9}$$

The integral $\int_0^L T(x, y)ds$ is defined as $\overline{T}L$, where $\overline{T}$ is the average value of $T(x, y)$ over the length L of the laser beam along the length of cylinder. This is also the line integral of the function $T(x, y)$. Hence

$$L(\overline{T} - T_o) = \text{constant} \tag{4.10}$$

Equation 4.10 holds good for all fringes. When L is constant for all rays, Equation 4.10 implies that $\overline{T}$ is a constant over the fringe and hence each fringe represents a locus of

points over which the average of the temperature field along the direction of the ray is a constant; in this sense, fringes are isotherms.

Let the length of each ray through the test cell is not a constant. The line integral of the function $T(x,y)(=\overline{T}_2)$ at a location which corresponds to a length L_2 of the ray can be related to the line integral of the function $T(x,y)(=\overline{T}_1)$ at some other location corresponding to a ray length L_1 as

$$\overline{T}_2 \;=\; T_o + \frac{L_1}{L_2}(\overline{T}_1 - T_o) \tag{4.11}$$

Since the change in path length per fringe shift is a constant, the temperature drop per fringe shift is also a constant. Defining the function $L(\overline{T}-T_o)$ in Equation 4.10 as $f(\overline{T},L)$, the fringe temperature on two successive fringes for a given value of L can be given as

$$\text{fringe 1} \qquad f_1(\overline{T},L) \;=\; \frac{\Delta PL}{dn/dT}$$

$$\text{fringe 2} \qquad f_2(\overline{T},L) \;=\; \frac{(\lambda+\Delta PL)}{dn/dT}$$

where λ is the wavelength of the laser beam. From these two equations, the temperature change per fringe shift can be calculated as

$$\Delta T_\epsilon \;=\; \frac{1}{L}(f_2(\overline{T},L) - f_1(\overline{T},L)) = \frac{\lambda/L}{dn/dT} \tag{4.12}$$

The interferograms thus incapsulate analytically the equation

$$\Delta PL \;=\; \frac{dn}{dT}\int_0^L (T-T_o)ds \tag{4.13}$$

This shows that the fringe patterns contain information about the line integral of the temperature field. The set of line integrals in a plane defines a projection of the temperature field. The interferograms can be numerically processed so that the left hand side of the above equation is a known quantity. One can then proceed for the calculation of temperature distribution from the known temperature at the boundary.

The above derivation of temperature difference between successive fringes will be modified in the presence of a strong refracting field. In the present case, a strong refracting field will arise when a large transverse temperature gradient is present. The light ray will not travel in single horizontal plane, and the ray will bend in the vertical plane owing the to refraction effects. Refraction, thus will introduce an additional path length to the test beam. Refraction effects can be precisely computed and accounted for. An estimate of the increase in path length due to refraction has been developed by Muralidhar (2001)

and the formula for calculating the temperature drop per fringe shift (including refraction effects) is given as

$$\Delta T_\epsilon = \frac{1}{Ldn/dT}\left(\lambda - \frac{1}{\overline{6n}}\left(\frac{dn}{dT}\right)^2\left(\left(\frac{\partial T}{\partial y}\bigg|_2\right)^2 - \left(\frac{\partial T}{\partial y}\bigg|_1\right)^2\right)L^3\right) \qquad (4.14)$$

subscripts 1 and 2 refers to the fringe 1 and fringe 2 respectively. The predicted temperature difference between the cylinder surface and the free stream can be obtained by multiplying the number of fringes and the temperature difference per fringe shift. The temperature difference per fringe shift can be calculated using the Equation 4.14. Since the gradient in the temperature field is not known prior to the calculation of the fringe temperature, the factor $\left(\frac{\partial T}{\partial y}\Big|_2\right)^2 - \left(\frac{\partial T}{\partial y}\Big|_1\right)^2$ must be calculated from a guessed temperature field. The formula neglecting refraction effects for temperature difference per fringe shift $\Delta T_\epsilon = \frac{\lambda/L}{dn/dT}$ can be used as an initial guess. The final calculation of ΔT_ϵ relies on a series of iterative steps with improved estimates of the temperature gradients. The refraction contribution in the present set of experiments is found to be quite small. For the following numerical values: $\lambda = 632.8$ nm, $L = 0.39$ m, dn/dT for air at 20°C and 1 atm = -0.927×10^{-6}(°C)$^{-1}$ and refractive index for air at 20°C = 1.0, a typical value of ΔT_ϵ is calculated to be 1.8°C.

Figure 4.3 and Figure 4.4 show the mean removed time averaged schlieren interferograms for circular and square cylinders at different cylinder temperatures, respectively. They are shown for Reynolds number of Re = 53, 94 and 110 for circular cylinder and Re = 87, 109 and 118 for square cylinder. The predicted temperature difference between the cylinder surface and the free stream has been calculated by multiplying the number of fringes with the temperature difference per fringe shift. The predicted temperature based on schlieren interferograms for various cylinder temperatures at different Reynolds numbers are compared with the actual temperature difference in Table 4.1 and Table 4.2 for circular and square cylinders, respectively. These can be used for validation of the schlieren interferogram analysis and experimental procedure. A maximum difference of 8% between the actual temperature difference with that from the interferograms seen in Table 4.1 and Table 4.2. This small difference can be attributed to the experimental uncertainty arising from errors in the measurement of cylinder surface temperature, effectiveness of the temperature controller, optical misalignment, and digitization error. Measurement of the centerline wake temperature using a thermocouple also compared well with the schlieren interferogram data. Overall, Table 4.1 and table 4.2 confirm the accuracy of the schlieren-interferometry technique and data analysis procedure.

Figure 4.5 shows the mean removed time averaged schlieren interferograms for circular and square cylinders at no flow condition (natural convection). Two cases for the

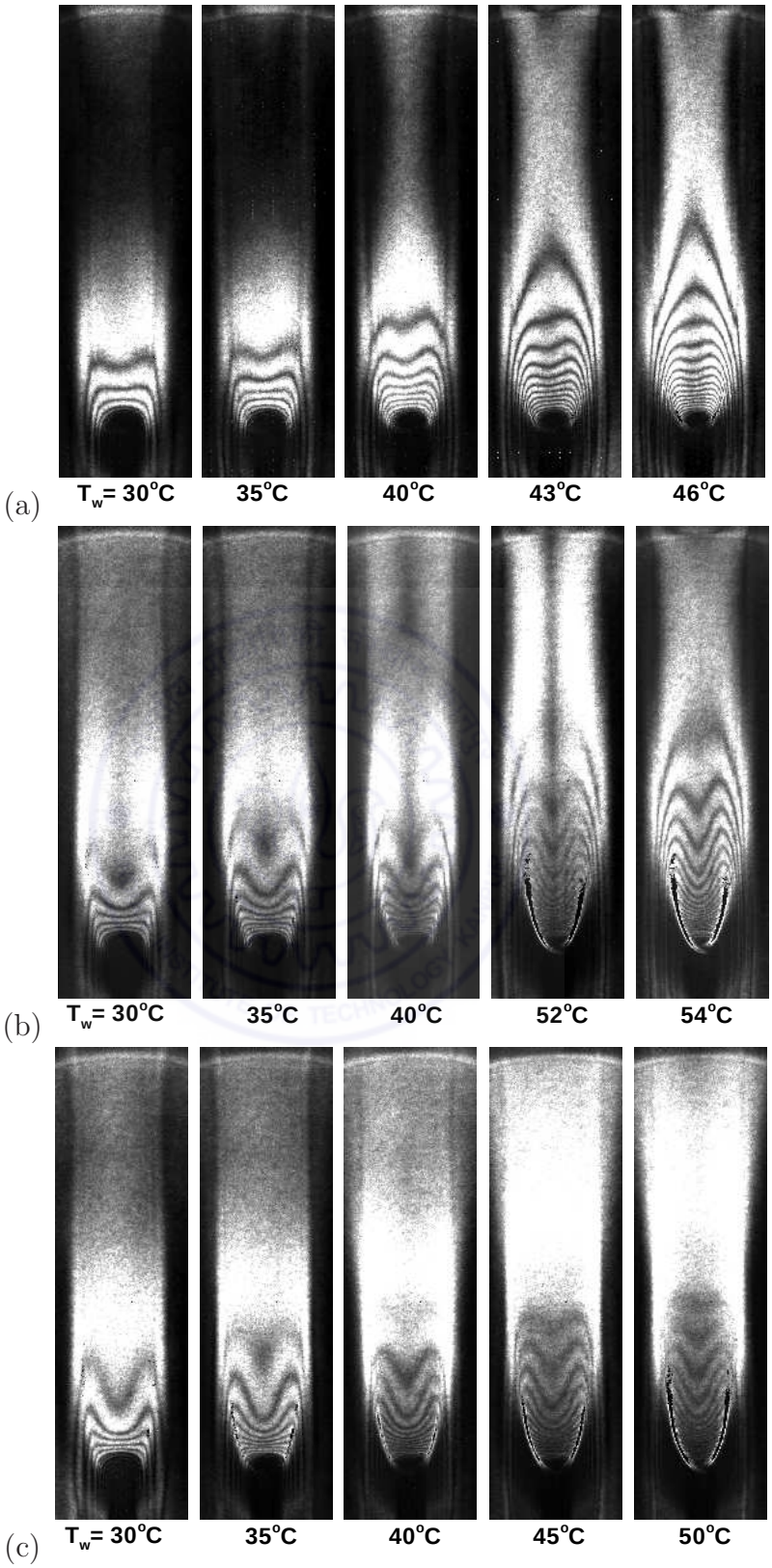

Figure 4.3: Mean removed time averaged schlieren interferograms for a circular cylinder at (*a*) Re=53, (*b*) Re=94, and (*c*) Re=110 for different cylinder surface temperatures.

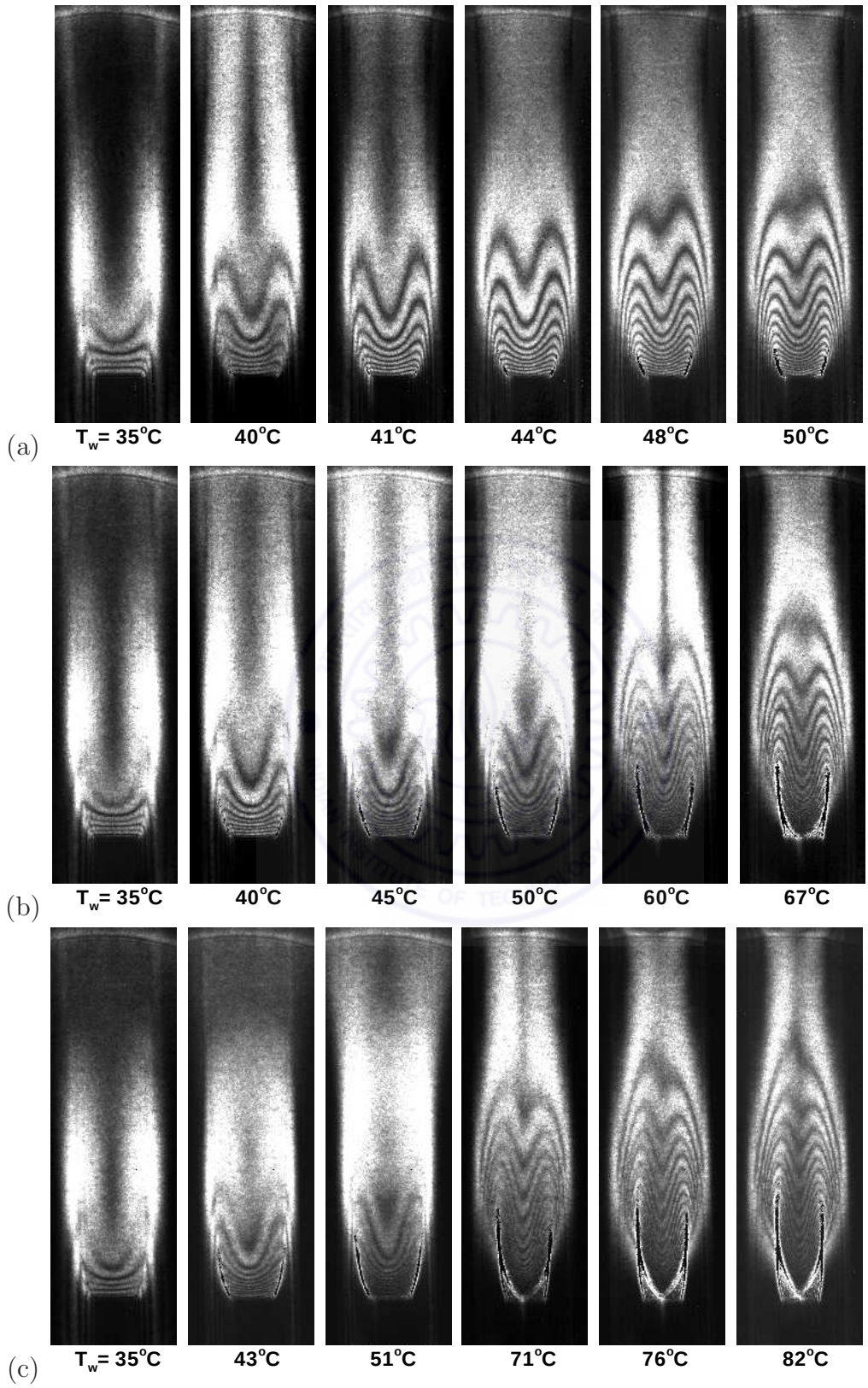

Figure 4.4: Mean removed time averaged schlieren interferograms for a square cylinder at (*a*) Re=87, (*b*) Re=109, and (*c*) Re=118 for different cylinder surface temperatures.

Table 4.1: Comparison of the predicted temperature difference between the circular cylinder surface and the free stream from the evaluation of schlieren interferograms with that of the actual temperature difference.

S.N. & Re	Cylinder surface temperature T_w, °C	Free stream temperature T_∞, °C	Measured ΔT $(T_w - T_\infty)$ °C	Number of fringes	Temperature change per fringes shift ΔT_ϵ,°C	ΔT from schlieren interferograms °C
1.	30	23	**7**	4	1.8	**7.2**
Re=53	35	23	**12**	7	1.8	**12.6**
	40	23	**17**	10	1.8	**18.0**
	43	23	**20**	12	1.8	**21.6**
2.	30	21	**9**	5	1.8	**9**
Re=94	35	21	**14**	8	1.8	**14.4**
	40	21	**19**	11	1.8	**19.8**
3.	30	21	**9**	5	1.8	**9**
Re=110	35	21	**14**	8	1.8	**14.4**
	40	21	**19**	11	1.8	**19.8**

Table 4.2: Comparison of the predicted temperature difference between the square cylinder surface and the free stream from the evaluation of schlieren interferograms with that of the actual temperature difference.

S.N. & Re	Cylinder surface temperature T_w, °C	Free stream temperature T_∞, °C	Measured ΔT $(T_w - T_\infty)$ °C	Number of fringes	Temperature change per fringes shift ΔT_ϵ,°C	ΔT from schlieren interferograms °C
1.	40	23	**17**	9	1.8	**16.2**
Re=87	44	23	**21**	11	1.8	**19.8**
	48	23	**25**	14	1.8	**25.2**
	50	23	**27**	15	1.8	**27**
2.	40	23	**17**	9	1.8	**16.2**
Re=109	45	23	**22**	12	1.8	**21.6**
	50	23	**27**	15	1.8	**27**
3.	35	23	**12**	7	1.8	**12.6**
Re=118	43	23	**20**	11	1.8	**19.8**
	51	23	**28**	15	1.8	**27**

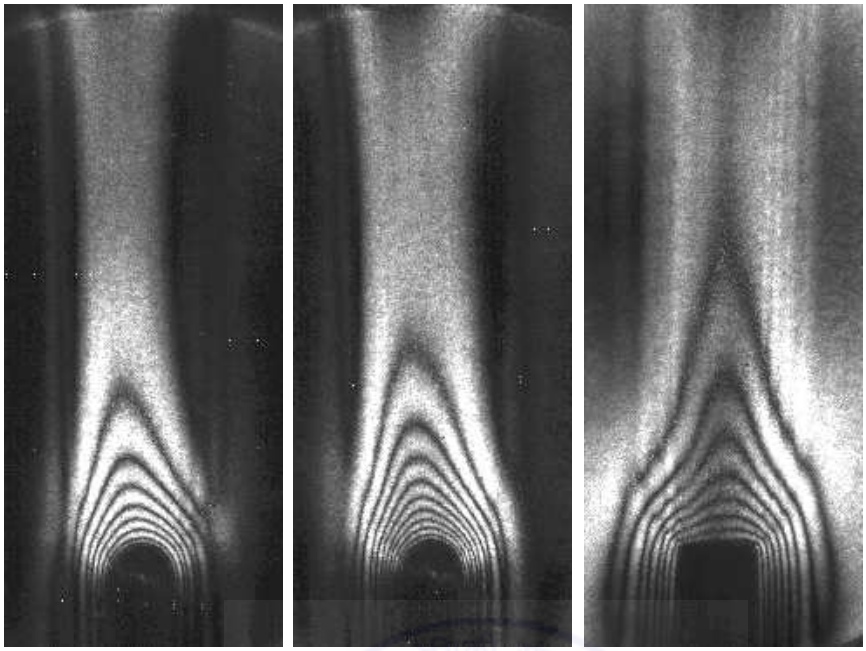

Figure 4.5: Mean removed time averaged schlieren interferograms for circular cylinder (a) & (b) and square cylinder (c), at no flow condition (natural convection).

circular cylinder at the cylinder surface temperature of 35°C and 40°C at ambient temperature of 23°C and one case for the square cylinder at a cylinder surface temperature of 45°C at an ambient temperature of 30°C have been shown. The predicted temperature difference between the cylinder surface and ambient from the fringe count analysis is 12.6, 18 and 14.4°C for the case a, b and c, respectively. These value compares well with the actual temperature difference for all the cases considered; the values being 12, 17 and 15°C for the case a, b and c, respectively. Therefore, these result also validates the usefulness of schlieren-interferometry technique.

4.1.4 Temperature distribution

Temperature variation in the wake of a heated cylinder has been obtained by analyzing the schlieren-interferograms and using Equation 4.12. The center of the dark fringe is assumed to be the location of the isotherm. To a closest approximation isotherms can be located by plotting the locus of points connecting all minimum intensity pixels within the dark band.

4.2 Statistical analysis of schlieren signal

The quantitative information about the flow structures can be related to the time-dependent fluctuations of the light intensity (schlieren signal). The gray scale value of the fluctuating light intensity obtained from the time-sequence of schlieren images has been used as time varying signal. To study the global picture of the wake, a number of sequences has been extracted from different specific locations in the image. This is useful in understanding the detailed dynamical characteristics of the vortex structures. The details of the schlieren signal statistical analysis procedure are discussed in the following sections.

4.2.1 Instantaneous traces

The time history of the fluctuating light intensity in schlieren images at various streamwise and transverse locations provide the basic nature of flow fluctuations. For stationary cylinders, these traces are presented as a function of Richardson number. Three streamwise locations, namely x/d= 2, 3.5 and 5 and three transverse locations, y/d= 0.0, 0.35 and 0.70 (0.75 for square cylinder) in the near wake region are considered. At these locations, the light intensity is averaged over 4×4 pixels to filter out the pixel level noise.

4.2.2 Power spectra

Power spectral analysis provides information about how the energy of a fluctuating signal is distributed with respect to frequency and to find out the dominant frequency content. Periodic shedding of vortices will produce a sharp peak in the light intensity spectrum at a frequency corresponding to the vortex shedding frequency. Other peaks may also appear owing to vortex interactions, three dimensionality and plume movement in the direction transverse to the main flow. Interaction between the shear layers shed from each side of the cylinder can in fact, give rise to multiple peaks. This interaction plays an important role in characterizing the vortex shedding mechanisms. Therefore, the power spectra can be useful in understanding the mechanism responsible for suppression of vortex shedding as a function of Richardson number. For an oscillating cylinder, the dominant components of the power spectra can illustrate the synchronisation of the wake with the cylinder oscillation. For no synchronization, the appearance of additional peaks is an indication of mode competition between the natural instability and imposed excitation. Power spectra is calculated at same streamwise and transverse locations as that of time traces for correlating the two in terms of flow structures.

The power spectra of the discrete schlieren signal has been computed using fast Fourier transform (FFT) algorithm. Direct evaluation using DFT method requires N^2 arithmetical operations for 'N' number of data points, which is very time consuming. However, the same result can be obtained in only $N\log N$ operations by using the fast Fourier transform (FFT) algorithm. Thus, for a periodic data sampled at sufficiently small time intervals, the FFT is an efficient tool for evaluating discrete Fourier transform (DFT) and its inverse. By definition a sequence of samples, $f(\tau)$ possesses a discrete Fourier transform $F(\nu)$ given by

$$F(\nu) = \frac{1}{N}\sum_{\tau=0}^{N-1} f(\tau)e^{-i2\pi(\nu/N)\tau} \qquad \nu = 0, 1, 2, \ldots, N-1.$$

The quantity ν/N is analogous to frequency measured in cycles per sampling interval. Given the discrete transform $F(\nu)$, one may recover the time series $f(\tau)$ with the aid of inverse DFT defined as

$$f(\tau) = \sum_{\nu=0}^{N-1} F(\nu)e^{i2\pi(\nu/N)\tau} \qquad \tau = 0, 1, 2, \ldots, N-1.$$

As the image acquisition has been performed at a rate of 250 Hz, therefore the maximum frequency (Nyquist frequency, f_c) that can be interpreted uniquely is equal to 125 Hz ($f_c = 1/(2\Delta t)$). Here Δt is the time interval between two consecutive images.

4.2.3 Strouhal number

An important parameter in unsteady periodic flow is the vortex shedding frequency expressed in non-dimensional form as the Strouhal number (St)

$$\mathrm{St} = \frac{f_s d}{U_\infty} \qquad \text{(where } f_s \text{ is the frequency of vortex shedding).}$$

It indicates the time scale of the unsteady forces and the nature of flow induced vibrations. Traditionally, spectral analysis of the hotwire signal placed inside the wake or spectral analysis of the temporal variation of drag or lift coefficient is used for obtaining the vortex shedding frequency of bluff bodies. However, the use of hotwire anemometry is prone to large error for the heated cylinder due to influence of temperature distribution inside the wake on the hot wire signal. Therefore, we have obtained the vortex shedding frequency of the heated cylinder from the light intensity fluctuations of schlieren images. Temporal changes in light intensity scale with those in temperature gradients. Since the Prandtl number of air is of the order of unity, it can be assumed that temporal changes in temperature are correlated to those in velocity. This approximation enables

the calculation of Strouhal number from time traces of light intensity. A fast Fourier transform (discussed in preceding section) of the time series of light intensity in the schlieren images is used to determine shedding frequency and hence the Strouhal number. The light intensity is averaged in a zone of 4×4 pixel to diminish the pixel-level noise. The location of this zone has been chosen based on the visualization image to obtain clear vortex shedding frequency and is located at $2d$ in the stream wise and $0.75d$ in the transverse direction.

4.2.4 Cross-spectrum

The cross-spectrum represents discrete Fourier transform of the cross-correlation function. It is a complex valued function whose magnitude and phase information are used to indicate the degree of correlation the between two signals. As stated by Kay (1988), the magnitude of the cross-spectrum describes whether frequency components of one signal are associated with large or small amplitudes at the same frequency in the second signal, while the phase of the cross-spectrum indicates the phase lag or lead of one signal with respect to the second signal for a given frequency component.

Let the fluctuating signal, $f(\tau)$ and $g(\tau)$ are expressed in frequency domain using discrete Fourier transforms $F(\nu)$ and $G(\nu)$ as:

$$\begin{aligned} F(\nu) &= Re_f(\nu) + iIm_f(\nu) \\ G(\nu) &= Re_g(\nu) + iIm_g(\nu) \end{aligned}$$

The Fourier transform of the cross-correlation of two sequences $f(\tau)$ and $g(\tau)$ is the product of their Fourier transform with one of them conjugated. Therefore, cross-spectrum can be given as:

$$S_{gf}(\nu) = G(\nu)F^*(\nu)$$

The cross-spectrum consists of complex numbers that can be divided into a real and an imaginary part given as:

$$S_{gf}(\nu) = (Re_f Re_g + Im_f Im_g) + i(Re_f Im_g - Im_f Re_g) = Re(\nu) + iIm(\nu)$$

$|S_{gf}(\nu)|$ is the magnitude function called amplitude cross-spectrum given as:

$$|S_{gf}(\nu)| = \sqrt{Re^2(\nu) + Im^2(\nu)}$$

Amplitude cross-spectrum can be interpreted as a measure of covariance between the respective frequency components of the two series. Frequencies with correlated signals present in both spectra will lead to large amplitude in the cross-spectrum.

4.2.5 Phase shift

The phase difference (ϕ) between the two signals at a frequency (ν) is obtained from the real $Re(\nu)$ and imaginary parts $Im(\nu)$ of the cross-spectrum as:

$$\phi(\nu) \;=\; \tan^{-1}\left[\frac{Im(\nu)}{Re(\nu)}\right]$$

In the present work, the cross-spectra and phase shift calculations have been performed between schlieren signals extracted at different locations of the same sequence of schlieren images as follows.

1. The signals of the wake at two streamwise locations, such as $x/d = 2$ and 5 (for the same transverse location) have been used to get the phase shift of equal frequency vortex structures at two different spatial locations and its variation as a function of Richardson number.

2. The signals from the right and left side of the shear layers i.e. at opposite sides of the cylinder centerline for same streamwise and transverse locations can indicate the nature of vortex shedding process i.e. symmetric or alternate.

3. The cross spectra between the signal from a specific location of the wake and the cylinder oscillation signal provide information about the phase of the vortex-shedding process, relative to the displacement of the oscillating cylinder.

Cylinder oscillation signal : Cylinder oscillation signal have been extracted from a location in the schlieren image fixed at the boundary of the cylinder when it is in the mean position of oscillation (or stationary). This location was selected at the top surface of the cylinder for inline oscillation and at the right or left boundary of the cylinder for transverse oscillations. In the schlieren images, the cylinder portion is dark and its outside boundary is bright. When cylinder oscillates about the mean position of oscillation, the selected location experiences a dark and bright signal alternatively. The time trace of dark and bright intensity gray scale values is referred as cylinder oscillation signal.

The actual oscillation frequency of the cylinder is also determined by the spectral analysis of the above cylinder oscillation signal. This has been used to cross-check the imposed oscillation frequency set by the function generator. The signal has also been used to determine the synchronization of vortex shedding with the oscillation of the cylinder. The cylinder oscillation signal has also been used to fix the reference phases for computing the phase-averaged informations for an oscillating cylinder. Since both the wake signal and cylinder oscillation signal have been extracted from the same sequence of instantaneous

schlieren images, the practical limitation of phase variation of two signals obtained from two different sensors is eliminated.

4.2.6 Averaged coherence function

Coherence is a measure of the degree of relationship between two time series signals. It is a unitless quantity which varies from 0 to 1 for a particular frequency. The coherence value of 1 indicates the two signals to be identical with each other. The coherence magnitude equal to zero indicates the two signals to be completely random with respect to one another. For two sequences of samples $f(\tau)$ and $g(\tau)$ with discrete Fourier transforms $F(\nu)$ and $G(\nu)$, respectively, the averaged cross spectrum and auto spectrum are:

$$\begin{aligned}
\overline{S}_{gf}(\nu) &= \frac{1}{N}\sum_{k=0}^{N-1}[G_k(\nu)F_k^*(\nu)] \\
\overline{S}_{ff}(\nu) &= \frac{1}{N}\sum_{k=0}^{N-1}[F_k(\nu)F_k^*(\nu)] \\
\overline{S}_{gg}(\nu) &= \frac{1}{N}\sum_{k=0}^{N-1}[G_k(\nu)G_k^*(\nu)]
\end{aligned}$$

Here identical subscript indicates auto spectrum ($\overline{S}_{ff}$ and $\overline{S}_{gg}$) and different subscript indicates cross spectrum ($\overline{S}_{gf}$). The averaged magnitude squared coherence can be computed as:

$$\left|\overline{C}(\nu)\right|^2 = \frac{\left|\overline{S}_{gf}(\nu)\right|^2}{(\overline{S}_{ff}(\nu))(\overline{S}_{gg}(\nu))}$$

The square of the cross-amplitude value divided by the product of the spectrum density estimates for each series results in squared coherence function. In the present work, the averaged coherence function has been estimated between the wake signal and cylinder oscillation signal to determine the degree of relation between similar frequency components.

4.2.7 Instantaneous and time-averaged flow patterns

The instantaneous schlieren images have been used to visualize the vortical structures in the wake of the heated cylinder. The initial image recorded on the screen is one of uniform darkness. Under heated conditions, bright streaks are created around the cylinder. An increase in light intensity at a point is a measure of the local temperature gradient in the plane of the paper. Thus, the brightest light streaks are to be found in the shear layers originating from the cylinder corners. The wake as a whole is brighter than the background

indicating thermal gradients distributed within. For a stationary cylinder, the changes in the organized wake structures, namely its shape, size and time-dependent movement is readily perceived from the instantaneous images before the wake degenerates into a steady plume. For an oscillating cylinder, these images clearly depict different patterns of vortex formation such as symmetrical or antisymmetrical. Therefore, instantaneous schlieren images have been used to visually illustrate the detailed dynamical characteristics of vortex structures as a function of different experimental parameters. These images are presented as a sequence of eight images separated by a fixed time interval. For stationary cylinder, the time interval between two consecutive images is equal to one-eighth of the time period of vortex shedding and for oscillating cylinder, the time interval is equal to one-eighth of the time period of cylinder oscillation.

The time-averaged schlieren images are generated by averaging the instantaneous schlieren images. These time-averaged schlieren images provide information about the streamwise and transverse extent of the heated cylinder wake and can be used as an indicator of the wake mixing. The time-averaged schlieren images for the stationary circular and square cylinders have been generated from 1250 instantaneous schlieren images. This represents approximately 25-30 vortex shedding cycles depending upon the Reynolds number and Richardson number. The time-averaged schlieren image, $\overline{I}(x, y)$ is determined by averaging the instantaneous intensity $I(x, y, t)$ using the formula:

$$\overline{I}(x, y) = \frac{1}{N} \sum_{i=1}^{N} I(x, y, t)$$

Where, N is the number of images and $\overline{I}(x, y)$ is the average intensity at a particular pixel with (x, y) denoting its position (pixel location) in the image.

4.2.8 Phase-averaging

The *phase-averaging* is the averaging of large ensemble of points having the same phase with respect to a reference phase position. In the present work, phase-averaging of the instantaneous schlieren images have been performed to study the flow structures in the wake of an oscillating cylinder. The reference phases have been fixed at different phases of the cylinder oscillation cycle. The formula for the phase-averaging of the measured time-varying intensity signal $I(x, y, t)$ is written as:

$$\langle I(x, y, t) \rangle = \lim_{N \to \infty} \frac{1}{N} \sum_{n=0}^{N-1} I(x, y, t + n\tau)$$

Here $\langle I(x, y, t) \rangle$ is the phase averaged quantity, $I(x, y, t+n\tau)$ is the instantaneous intensity distribution, t is the reference time corresponding to a specific phase and τ is the time

period of the cylinder oscillation cycle. In practice, the phase-averaging is determined over a finite number of cycles (N) and the corresponding estimation of $\langle I(x,y,t)\rangle$ is

$$\langle I(x,y,t)\rangle \;=\; \frac{1}{N}\sum_{n=0}^{N-1} I(x,y,t+n\tau)$$

Number of cycles N should be sufficiently large for correct phase-average estimation. In the present case, the phase-averaged statistics were generated from 3000 instantaneous schlieren images, representing roughly 72 vortex shedding cycles. When the vortex shedding is synchronized with the cylinder oscillation, the phase-averaging is performed by dividing the cylinder oscillation cycle to eight evenly spaced phases over one oscillation period. In some cases, the flow synchronization may be present over multiple oscillation cycles i.e. period doubling with respect to the cylinder oscillation period for harmonic oscillation and period tripling for nonharmonic oscillation at 1.5 times the Strouhal frequency. For these cases the phase-averaging were extended over appropriate number of cycles, with eight evenly spaced phases over one oscillation period.

4.2.9 RMS fluctuations

Since light measurements are inertia free, time-dependent fluctuations in light-intensity from schlieren interferograms are essentially due to the temperature fluctuations. As the working fluid is air with Prandtl number of the order of unity, these can be further correlated to velocity fluctuations outside the recirculation zone, where advection effects are expected to be much larger than diffusion. These fluctuations are a measure of the flow fluctuations and depends on the nature of vortex formation and their interactions. In the present work, RMS fluctuations of light-intensity in the wake of circular and square cylinders have been presented as a function of the Richardson number and oscillations parameters. For periodic unsteady flows, the measured time-varying intensity signal, $I(x,y,t)$ can be decomposed into mean part $\overline{I}(x,y)$ and fluctuating part $I^{'}(x,y,t)$ as:

$$I(x,y,t) \;=\; \overline{I}(x,y) + I^{'}(x,y,t)$$

The root mean square (rms) fluctuations of light-intensity has been calculated using the formula:

$$I_{\text{rms}} \;=\; \sqrt{\frac{1}{N}\sum_{i=1}^{N}\left[I(x,y,t)-\overline{I}(x,y)\right]^2}$$

The summation extends over N samples, N being the number of instantaneous schlieren images.

4.2.10 Vortex formation length

When vortices are shed from the cylinder, a quantity of interest is the maximum length of the shear layer before it detaches from the point of separation. This quantity exhibit the characteristics of the shed vortices and is called the vortex formation length. In literature, it has been determined from the location of peak in the streamwise velocity fluctuation along the wake centerline. Konstantinidis (2003) have presented the vortex formation length defined by the peak position in the u_{rms} distribution along the cylinder centerline. It is assumed that the intensity fluctuation in schlieren images is directly related to the temperature fluctuation and indirectly related to velocity fluctuation. These fluctuations in turn scale with the local fluctuation in the light intensity. Therefore, streamwise location where the rms intensity magnitude along the centerline of a cylinder rises to a peak value can be taken to correspond to the location where the vortex just detaches itself from the cylinder. The corresponding x/d location is termed as the vortex formation length. In the present work, vortex formation length has been obtained based on the peak position in the light intensity fluctuation at small offset location (i.e. y/d=0.30 or 0.45 depending upon Richardson number) from the cylinder centerline for better accuracy due to higher overall magnitude of the rms fluctuations. The vortex formation length has been evaluated as a function of cylinder surface temperature and oscillation parameters.

4.3 Convection velocity

The convection velocity, u_c is defined as the average traveling velocity of the vortex structures. It is useful for observing the flow field in a frame of reference which translates with the vortices. In the near wake region, the flow structures develop in the streamwise direction and experience a drastic change due to the formation of vortices and the growth of the von karman street. Therefore, convection velocity is not constant and varies with the streamwise distance in the near wake region. The value of convection velocity is governed by entrainment, shear layer growth rates and mixing characteristics of the wake. In the present work, convection velocity of vortex structures has been determined from a pair of time separated schlieren images as discussed in the following headings.

4.3.1 Cross-correlation of image pairs

Convection velocity of the vortex structures in the near wake region is obtained as follows. A two-dimensional cross-correlation technique is used to track individual structures as they convect downstream. This procedure has been employed earlier by several researchers

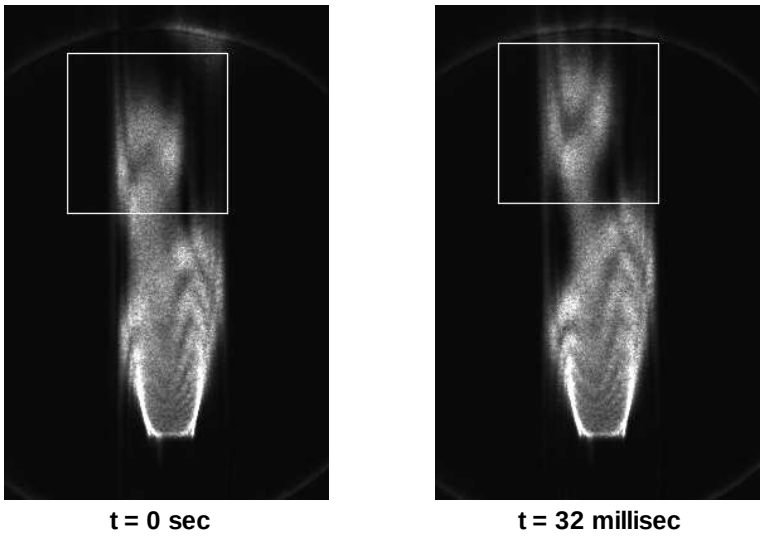

(a)

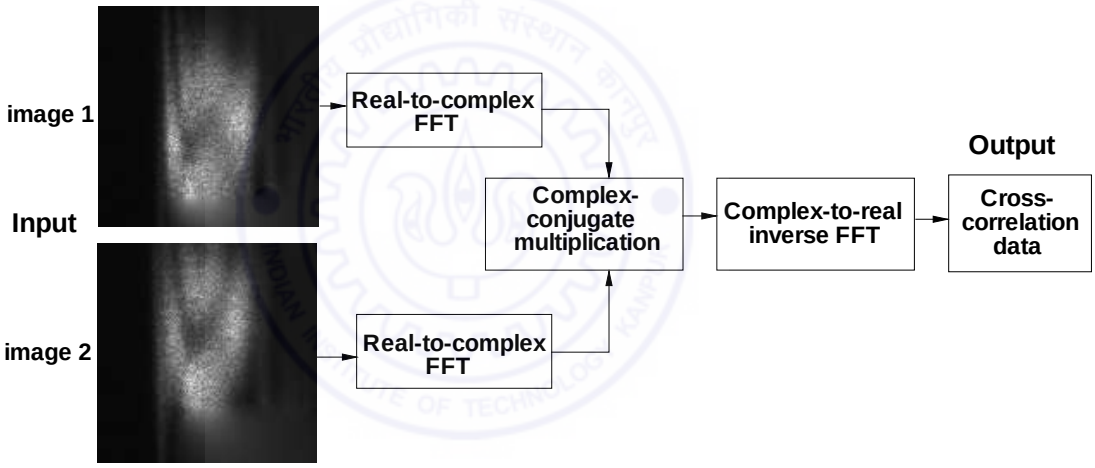

(b)

Figure 4.6: (*a*) Selection of the interrogation window, and (*b*) Implementation of cross-correlation using FFT to measure convection velocity of vortex structures.

e.g. Ben-yaker and Hanson (2002), and Smith and Dutton (1999) on image pairs. The large structure (vortex) is identified within a specified window in the first image and is tracked within the specified window in the time delayed image. Figure 4.6 (a) shows the selection of the interrogation window from two schlieren images separated by a time delay of 32 milli seconds. The interrogation window is selected such that the vortex is located almost at the center of the window. The cross-correlation function is calculated at each pixel location of the second image. The point of highest cross-correlation magnitude corresponds to displacement of the structure (Δx) over the time interval considered (Δt). Once displacement is known, the large-scale convection velocity is determined by the

formula

$$u_c = \frac{\Delta x}{\Delta t}$$

Here Δt is the interframing time between images. For a streamwise location, a specified window of certain shape and size is extracted from the source image. Let $I(i, j, t)$ is pixel-wise $(i = 1 \ldots m; j = 1 \ldots n)$ light intensity distribution of the specified window at time t. It is cross correlated with the corresponding sample window $I(i + \Delta x, j + \Delta y, t + \Delta t)$ at time $t + \Delta t$. The spatial cross-correlation function between these interrogation windows is given by

$$R(\Delta x, \Delta y) = \sum_{i=1}^{m} \sum_{j=1}^{n} I(i, j) I(i + \Delta x, j + \Delta y)$$

Cross-correlation function has been computed in the frequency domain using FFT algorithm. FFT performs faster calculations and decreases the image processing time. A schematic presentation of the cross-correlation estimation using FFT analysis is shown in Figure 4.6 (b). The cross-correlation of the two functions is equivalent to a complex conjugate multiplication of their Fourier transforms. This cross-correlation is inverse-transformed back to the physical space. The resulting displacement corresponding to maximum correlation function value over the interrogation window is regarded as displacement of the vortex structure. In the present work, the large-scale structures convect mainly in the streamwise direction and the convection velocity is based on the streamwise displacement of the structure. The displacement (Δx) has an uncertainty of ± 1 pixel and its actual value ranges from $0.5d$ to $0.8d$ depending on the streamwise location. Three shedding cycles have been considered for tracking vortical structures to ascertain cycle-to-cycle variations. The convection velocity was observed to be equal for each oscillation cycle with an uncertainty of 4.8%.

4.3.2 Determination of window dimensions

The actual implementation of the convection velocity calculation procedure is non-trival owing to the difficulty involved in identifying and tracking the specific flow structure during a given time delay. For correct displacement estimation, location of vortex structure in the interrogation window is critical. Therefore, size of the interrogation window depends on the size of the vortex structures. In the present work, square shaped interrogation window of size 128×128 pixels is manually selected. This size was large enough to include the vortex structure in the initial window and its later location in the time delayed window. For streamwise locations away from the cylinder, the displacement was large and therefore the time delayed window was shifted by certain % of the displacement in the streamwise direction such that the vortex structre is almost at the centre of the window.

4.3.3 Selection of time delay

The time separation between initial and delayed images influences the accuracy of the convection velocity calculation. Smith and Dutton (1999) observed that longer time delays allows the structure to convect farther, therefore reducing uncertainty in convection velocity calculations. However, shorter time delays reduce the amount of deformation and rotation as the structure convects. In the present work, the time separation between two consecutive images is 4 milliseconds. Therefore, a wide range of time delays in a step of 4 milliseconds were considered and a time delays of 32 milliseconds was selected for the computation of convection velocity. This separation time was large enough to predict the smaller displacements in the nearer streamwise locations while maintaining the criterion for maximum displacement (Keane and Adrian, 1990) in the farther streamwise locations based on the interrogation window size; a maximum displacement (without window offset) of 30 pixels is observed for the window size of 128×128 pixels.

4.3.4 Image calibration and velocity extraction

To obtain the velocity of vortical structures from the image data, calibration from image space to physical space was carried out. The cylinder size in terms of number of pixels is known by the size of the shadow of the cylinder in the magnified images. This corresponds to the exact physical size of the cylinder in the test region. Therefore, a linear relationship between the actual object size and the pixel size is established. Actual displacement of the vortex structure is calculated by scaling the number of pixels moved by the structure from first image to the time delayed image using this linear relationship. The convection velocity of vortex structures is obtained by dividing the actual displacement by the interframing time between two images.

4.3.5 Frame-by-frame analysis

The convection velocity determined by the cross-correlation algorithm has been manually verified by frame-by-frame analysis of the digitized frame sequences. This procedure involves visual inspection of the vortex structures in the image pairs and manual estimation of the structure displacement during the time separation. The intensity contour of the identified vortex structure is plotted for the initial and time delayed images. The streamwise displacement of the leading edge of the intensity contour of vortex structure is measured in a given time interval by visual inspection. Maximum deviation of 2.4% in convection velocity was observed between the frame-by-frame analysis and the cross-

correlation algorithm. The midpoint of the intial and time delayed position of the leading edge of the contour of vortex structure is taken as the streamwise location of the structure.

4.4 Hotwire measurements

The measurement of velocity fluctuations in the wake and turbulence intensity in the approach flow were carried out using commercially available *DANTEC* hot-wire anemometer. The one wire hot-wire probe was calibrated in the testcell itself and the calibration curve was curve fitted using a fourth order polynomial. A pitot-static tube connected to a digital micromanometer (Section 3.8.1) was used for the calibration. In the low velocity regime, measurements with the pitot-static tube as well as the hotwire anemometer are prone to errors. These can arise from higher order physical phenomena as well as probe interference effects. The errors can be controlled by using a pitot-static tube of small diameter (3.3 mm in the present study); in addition the hotwire in the present work was operated at a lower temperature (of around 160°C). It was felt that the lower wire temperature minimized free convection and radiation errors, without excessive loss of sensitivity.

Before the start of measurements, the stability of the CTA bridge as well as the signal conditioner setup was checked. This consists of overheat setting in the CTA hardware and adjustment for the filtering and the amplification of the CTA signal in 56N20 amplifier/filter unit prior to digitizing. Voltage signal was low-pass filtered at 1 kHz with high-pass filtered at 0.1 Hz and a gain factor of 10 was used for amplifying the input signals. The continuous output voltage from the anemometer was acquired *via* a PC through an analog to digital (A/D) converter (Section 3.6).

4.4.1 Calibration methodology

Calibration establishes a relation between the CTA output voltage and the flow velocity. The calibration of a hotwire involves two important steps, namely data generation and curve fitting. Calibration data are generated by exposing the probe to a flow with a known velocity at low turbulence levels and recording the output of the anemometer voltage. The curve fitting between the points of known velocities and voltages represents the transfer function for converting voltage data into velocities. In principle, specially designed apparatus is used to generate high quality flow with uniform velocity, temperature and very low turbulence level (say $< 0.1\%$). However, a testcell that has clean approach flow conditions can also be used to carry out an *in situ* calibration (Perry, 1982). In the present study, calibration has been performed in the testcell itself, very close to the inflow

plane. A much wider range of expected velocity variation was covered during calibration. Air velocity was directly measured using a pitot-static tube mounted along the centerline of the test section.

Small changes in room temperature can occur between the calibration and experiment. It is necessary to correct the CTA data records for temperature variations. For changes up to $\pm$ 1^{o}C, the recorded data can be compensated through the use of a correction formula that assumes a constant heat transfer coefficient (Bearman, 1971). The anemometer output voltage is corrected as

$$E_{corr} = \left(\frac{T_w - T_o}{T_w - T_a}\right)^{0.5} . E_a \tag{4.15}$$

Here E_a is the acquired voltage, T_w the sensor hot temperature, T_o the ambient reference temperature at which calibration data is available, and T_a is the ambient temperature during the experiment.

4.4.2 Curve fitting

A number of functions for curve fitting of the hotwire calibration data have been proposed in the literature. The most commonly used functions are (Bruun, 1995): polynomials, power laws (King's law [1]) and look-up tables. The fourth- and fifth-order polynomials do not show an oscillatory trend between calibration points and gives less error as compared to power law fits. Therefore polynomial curve fits are preferable and normally recommended.

In the present work, polynomial curve fitting approach has been adopted and the data points are fitted with fourth order polynomial functions. With C_0 - C_4 as calibration parameters, the fourth order polynomial is of the form

$$U = C_0 + C_1 E + C_2 E^2 + C_3 E^3 + C_4 E^4 \tag{4.16}$$

Here, U is velocity and E is voltage. Typical calibration data with the 4^{th} order polynomial curve fit is shown in Figure 4.7.

4.4.3 Signal analysis

The digitized time-series of the hotwire signal consists of N evenly distributed and statistically independent samples[2]. The time-series data from the sensor is converted into

[1] Originally proposed by King (1914). King's evaluation suggested that the relationship $E = F(U)$ may be assumed to be of the form $E^2 = A + BU^n$, where $n = 0.5$.

[2] If the signal is obtained for total time of T seconds at a sampling rate of SR per second, then $N = SR \times T$.

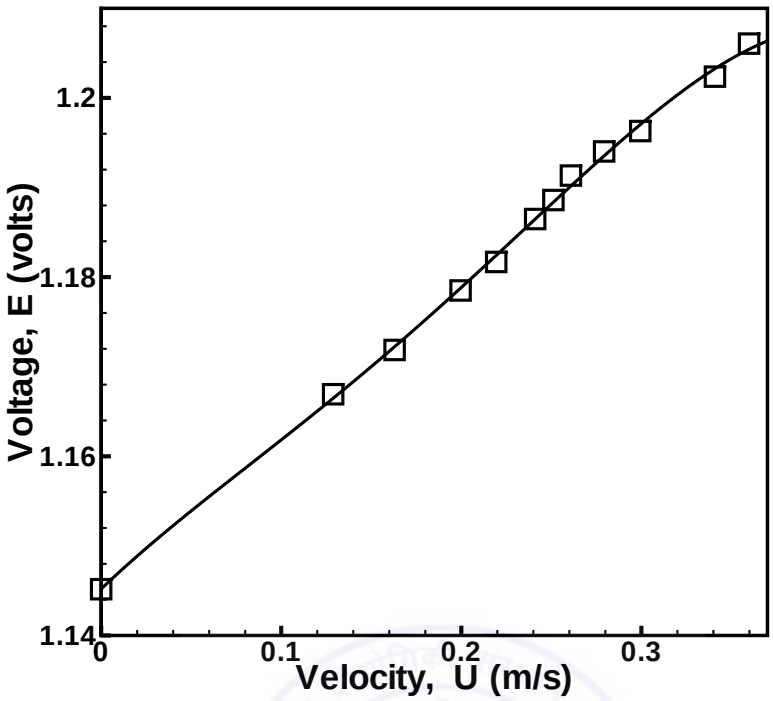

Figure 4.7: Calibration data for hotwire probe (symbols) compared with a polynomial curve fitting of the fourth order (line).

velocity time-series which provides mean, mean square and higher order moments. The mean value of the velocity, U can be evaluated as the average of the velocity signal $u(t)$, i.e.

$$U = \frac{1}{N}\sum_{i=1}^{N} u \tag{4.17}$$

Subsequently, the velocity fluctuation, $u'(t)$ is calculated by subtracting the mean component of velocity from the velocity signal $u(t)$. Hence

$$u'(t) = u(t) - U \tag{4.18}$$

The root mean square components of velocity and the turbulence intensity have been evaluated as:

$$u_{rms} = \left[\frac{1}{N}\sum_{i=1}^{N}(u')^2\right]^{1/2} \tag{4.19}$$

$$Tu(\%) = \left(\frac{u_{rms}}{U}\right) \times 100 \tag{4.20}$$

For validating schlieren measurements, hotwire measurements have been carried out in the wake of square cylinder. The frequency of the vortex shedding has been measured by the spectral analysis of the hotwire signal. Different locations of the hotwire probe have

been examined and the location showing sharpest peak in the spectra has been selected. The hotwire probe was placed at the midspan ($z = 0$) of the cylinder and at a distance of $2d$ downstream from the top face of the square cylinder, offset by $0.75d$ to one side of the wake center plane. The power spectra of the velocity fluctuations were determined using the FFT algorithm. The sampling frequency used set equal to 1000 Hz; the signal length being 20 seconds. The validation results are presented in the next section.

4.5 Validation experiments

The validation of the experiment and data analysis procedure has been carried out in two ways: (i) Comparison between the data obtained from different measurement techniques, and (ii) Comparison with the data in the published literature. Strouhal number is an important parameter in unsteady periodic flow and therefore have been used for validation of schlieren measurements. For this study, a separate set of experiments have been conducted for the flow over square cylinder. The details of the experimental conditions are compiled in Table 4.3. The square cylinder is mildly heated to a temperature of 30°C in an ambient at 23°C for obtaining reasonable schlieren signal under forced convection conditions. Considerable attention has been paid towards realizing the uniform temperature boundary condition along the cylinder span for the duration of the experiment. This is an important requirement because the schlieren image is an average obtained along the length of the cylinder. The flow velocity is varied between 0.24 and 0.60 m/s to investigate a range of Reynolds number from 105 to 262 with corresponding Richardson number in the range of 0.026 to 0.004. Buoyancy effects can thus be neglected

Table 4.3: Experimental conditions for validation study.

Set number	Flow velocity (m/s)	Reynolds number (Re)	Richardson number (Ri)
1	0.24	105	0.026
2	0.27	118	0.021
3	0.32	140	0.015
4	0.36	157	0.012
5	0.40	175	0.010
6	0.44	192	0.008
7	0.49	214	0.006
8	0.54	236	0.005
9	0.60	262	0.004

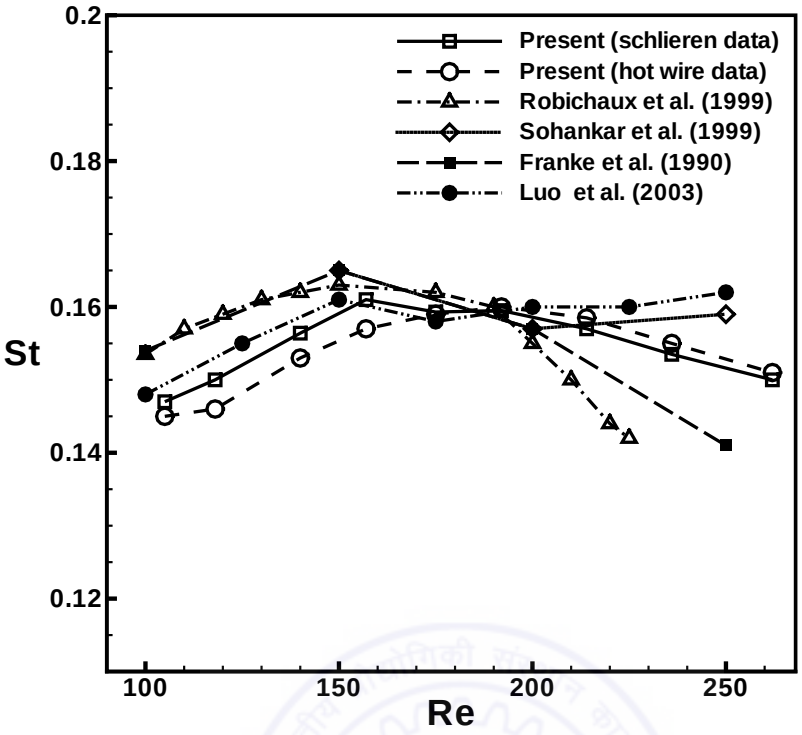

Figure 4.8: Variation of Strouhal number with Reynolds number for a square cylinder and comparison with the literature.

for the validation study. Experiments for the hotwire measurement have been conducted at identical flow velocities for no cylinder heating. Strouhal number has been obtained from the data analysis procedures discussed in Section 4.2.3 and 4.4.3. The variation of Strouhal number with Reynolds number and a comparison with the published literature is presented in Figure 4.8. Figure 4.8 shows that at low Reynolds number, the Strouhal number increases continuously with Re, and at Re=157, the Strouhal number reaches its local maximum. Beyond this Reynolds number, there is reduction in its value. The magnitude and nature of variation of Strouhal number with respect to Reynolds number from hotwire measurements is in close agreement with the schlieren data.

4.5.1 Comparison of hotwire and schlieren signal

Figure 4.9 shows a comparison of the power spectra of the hotwire and the schlieren signal at three different Reynolds number. The peak in the spectra is almost at the same locations (frequency) for both the signals. Thus one can conclude that the non-intrusive schlieren technique can accurately measure the instability characteristics in the wake.

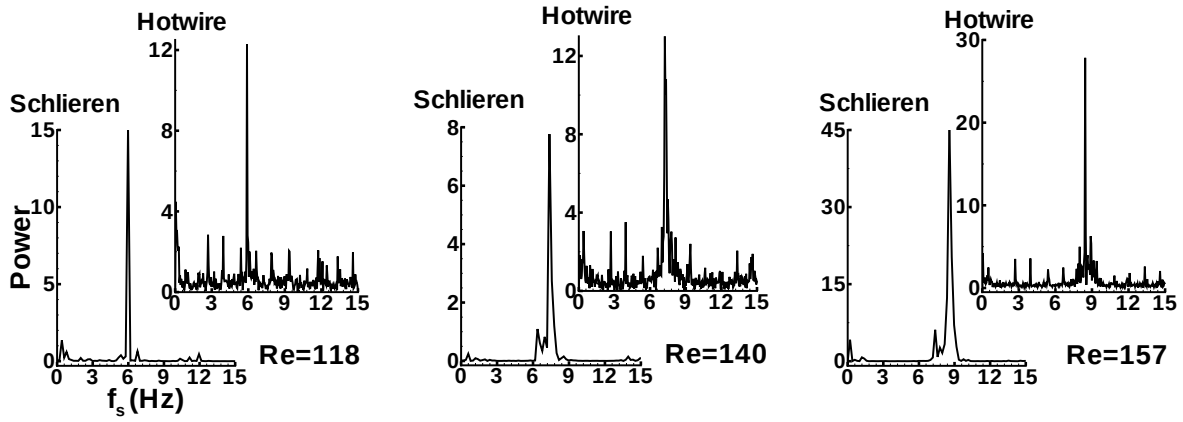

Figure 4.9: Comparison of power spectra of the hotwire and schlieren signal.

4.5.2 Validation based on Strouhal number

The results from the present experiments are in agreement with the experimental data of Luo *et al.* (2003) and numerical results of Sohankar *et al.* (1999) (see Figure 4.8). An exception is seen in the form of deviation from the results of Robichaux *et al.* (1999) in which low Re data appear to be higher and higher Re data appear to be lower. The deviation is more significant for Reynolds number greater than 200 with the largest deviation being nearly 7%. Possible explanation for this discrepancy can be attributed to the aspect ratio of the model, blockage and upstream conditions. The present experiments have been performed at a Reynolds number about Re=100. Therefore, the comparison of Strouhal number data from the present work with that of the literature at Re=100 have been carried out and presented in Table 4.4. A maximum deviation of $\pm 5\%$ between the present work and that of other investigations is indicated in Table 4.4. Therefore, Figure 4.8 and Table 4.4 broadly validate the present experimental and data analysis procedure.

4.5.3 Validation based on drag coefficient

The x-component of velocity (u) Measurements have been carried out using a pitot static tube with a high-resolution differential pressure digital micromanometer (Section 3.8.1). The average drag coefficient has been calculated from the mean velocity profile across the wake and compared with the published literature. The mean velocity profile at a streamwise location of x/d=13 have been measured for no cylinder heating. Drag coefficient has been calculated by a momentum integration approach over a control volume. It is also called the *wake survey method*, and has been extensively discussed (Schlichting, 1979).

Table 4.4: Comparison of Strouhal number with the published literature for flow past a square cylinder at Re=100.

Authors	Nature of study	Reynolds number (Re)	Strouhal number (St)
Okajima (1982)	Experimental	100	0.14
Davis *et al.* (1982)	Numerical	100	0.15
Franke *et al.* (1990)	Numerical	100	0.154
Sohankar *et al.* (1998)	Numerical	100	0.146
Robichaux *et al.* (1999)	Numerical	100	0.154
Luo *et al.* (2003)	Experimental	100	0.148
Present (Schlieren)	Experimental	105	0.147
Present (Hotwire)	Experimental	105	0.145

The drag coefficient C_D can be written as the sum of two integrals:

$$C_D = 2\int_{-\infty}^{\infty} \frac{u}{U_\infty}\left(1-\frac{u}{U_\infty}\right) d\left(\frac{y}{d}\right) + 2\int_{-\infty}^{\infty} \left(\frac{\overline{v'^2}-\overline{u'^2}}{U_\infty^2}\right) d\left(\frac{y}{d}\right) \tag{4.21}$$

The first term is the momentum deficit of the time-averaged flow field and the second term is the contribution of the turbulent fluctuations. Here u is the local mean velocity; U_∞ is the free stream velocity, assumed to remain constant in x direction; u' and v' are longitudinal and lateral velocity fluctuations; and d is the projected area of the cylinder normal to the flow direction (per unit length along the cylinder axis). To maintain uniformity with the nomenclature in the published literature, the projected dimension has been taken to be equal to the edge of the cylinder. At sufficiently large distance from the body, contributions from the turbulent fluctuations is zero and the value of C_D can be obtained only from mean velocity profile by simplified formula:

$$C_D = 2\int_{-\infty}^{\infty} \frac{u}{U_\infty}\left(1-\frac{u}{U_\infty}\right) d\left(\frac{y}{d}\right) \tag{4.22}$$

It is clear from the above expression that the drag coefficient can be interpreted simply as a momentum loss coefficient. In the Equation 4.22, the integration is performed over a width of the control volume at which the local velocity attains the free stream value and the drag coefficient is calculated. Table 4.5 presents a comparison of time-averaged drag coefficient of a square cylinder from the present experiments with that of other investigations at similar Reynolds number. The experimental value pertain to the mid-plane of the cylinder that divides equally the cylinder length, obtained by a *wake survey*

Table 4.5: Comparison of drag coefficient with the published literature for flow past a square cylinder.

Authors	Nature of study	Reynolds number (Re)	Drag coefficient ($\overline{C}_D$)
Davis *et al.* (1982)	Numerical	100	1.63
Franke *et al.* (1990)	Numerical	100	1.61
Sohankar *et al.* (1998)	Numerical	100	1.478
Robichaux *et al.* (1999)	Numerical	100	1.53
Saha *et al.* (2003)	Numerical	100	1.5
Present	Experimental	119	1.31

method. The drag coefficient from all studies are in the range of 1.478 to 1.63 and are comparable to each other. The drag coefficient obtained from the present experiments is equal to 1.31, which is slightly lower than that of the published results. The difference can be attributed to neglecting the turbulent fluctuations at x/d=13 as reported by Antonia and Rajagopalan (1990) in determining drag of a circular cylinder. They observed that contribution of the turbulent fluctuations at x/d=20 is only 5% to the value of C_D, while at x/d=10, they contribute approximately 15% to the value of C_D.

4.6 Uncertainty analysis

Uncertainties are inherent in the experimental results due to the error in measurements and its propagation during calculation. The uncertainty attributed to a measurement is an estimate of the possible residual error in that measurement after all proposed corrections have been made. Uncertainty analysis is the statistical interpretation of the errors in well-replicated experimental results. In the present work, quantitative assessment of uncertainty has been made for different flow parameters. Let the variables p, q, r, $\cdots$ provide the result R through a functional relationship

$$\mathrm{R} = \psi(p, q, r, \cdots)$$

Then the general expression for uncertainty in the result R can be given as:

$$\delta\mathrm{R} = \sqrt{\left(\frac{\partial \mathrm{R}}{\partial p}\delta p\right)^2 + \left(\frac{\partial \mathrm{R}}{\partial q}\delta q\right)^2 + \left(\frac{\partial \mathrm{R}}{\partial r}\delta r\right)^2 + \cdots}$$

Where δp, δq, δr, $\cdots$ are the uncertainties or errors in the measurement of independent variables p, q, r, $\cdots$ and δR is the error in the result.

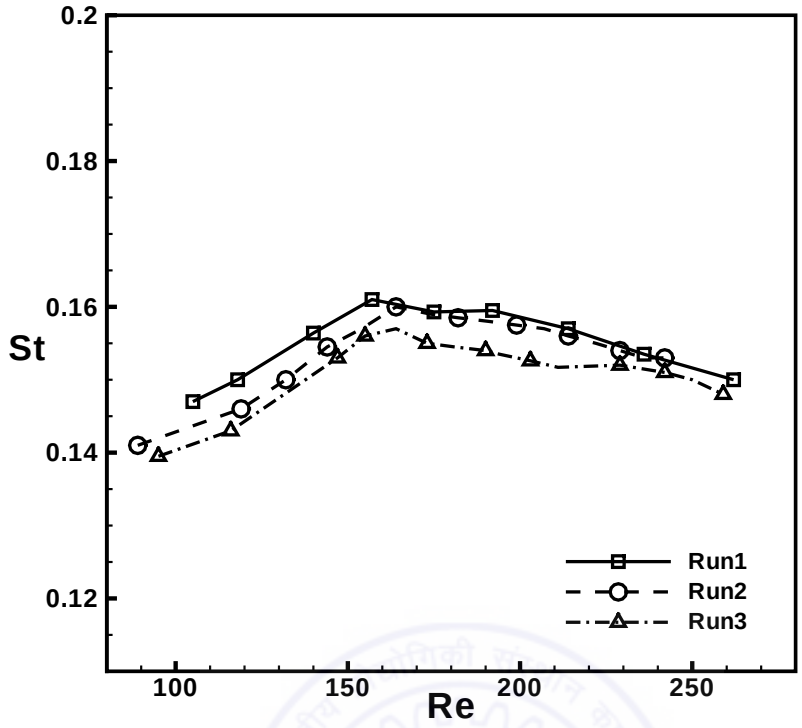

Figure 4.10: Variation of Strouhal number with Reynolds number for a square cylinder. Experiments were conducted at three different times under nominally similar conditions.

The digital micromanometer used for measuring free-stream velocity has a resolution of 0.001 Pascal in pressure measurement, which introduces an uncertainty of 1.1% in the velocity calculation for a free-stream velocity of 0.27 m/s at which most of the experiments were conducted. Change in density of air due to change in ambient temperature may also introduce error in velocity calculation. The uncertainty in velocity translates to an uncertainty in Reynolds number of about 1.1%, assuming negligible uncertainty in the measurement of the cylinder diameter. There are 250 frequency components obtained from a sequence of schlieren images and the uncertainty in frequency calculation is estimated to be 0.08 Hz. From above, the uncertainty in the estimation of the Strouhal number ($f_s d/U_\infty$) was calculated using the formula:

$$\delta \mathrm{St} = \sqrt{\left(\frac{\partial \mathrm{St}}{\partial f_s}\delta f_s\right)^2 + \left(\frac{\partial \mathrm{St}}{\partial d}\delta d\right)^2 + \left(\frac{\partial \mathrm{St}}{\partial U_\infty}\delta U_\infty\right)^2}$$

The uncertainty in the estimation of the Strouhal number was calculated to be 1.6%.

The thermocouple has been used for surface temperature measurement and its error is estimated to be ± 0.1°C. The uncertainty in the Richardson number ($dg\beta\Delta T/U_\infty^2$) has been calculated to be roughly 2.2% for the highest temperature considered. Accuracy in calculating convection velocity based on the repeatability study for different shedding cycles is estimated to be equal to 4.8%.

The uncertainty in the Strouhal number calculation have been evaluated by repeating the validation experiments at different times with nominally similar experimental conditions. In a classical sense, it is not possible to repeat precisely the identical experiments, mainly due to establishing identical velocity and ambient conditions. Instead, the approach adopted is to perform the experiments at a nearby Reynolds number. A comparison of three different sets of data i.e. variation of Strouhal number with Reynolds number for a square cylinder has been presented in Figure 4.10. The agreement is found to be good with a maximum deviation of Strouhal number equal to 3.1%. In this sense, the Strouhal number reported in the present work have a high degree of repeatability. In general, the data presented in the present study have been ensured from many experiments performed under practically identical test conditions.

भारतीय प्रौद्योगिकी संस्थान कानपुर
INDIAN INSTITUTE OF TECHNOLOGY KANPUR

Chapter 5

Circular and Square Cylinder Wakes: Influence of Buoyancy

This chapter presents results for flow past stationary circular and square cylinders maintained at constant temperature above the ambient temperature. The wake characteristics as a function of cylinder temperature have been investigated in detail at low Reynolds numbers. In these flows, thermal buoyancy forces have a significant influence on the flow structures. Therefore, the main focus of the present investigation is understanding the processes and mechanisms involved in the heat-induced changes of the vortex structures under the influence of buoyancy. The approach is towards active control of wake instability by heat addition in the near wake, ultimately resulting in suppression of vortex shedding. Two operating parameters, i.e. Reynolds number and Richardson number have been varied to examine the flow behavior from near-forced flow conditions to the mixed convection regime. Reynolds number in the range of 53 to 118 and Richardson numbers from 0.025 to 0.314 are considered. The detailed dynamical characteristics of the vortical structures i.e. their size and shape, Strouhal number, power spectra, convection velocity, phase shift, vortex inception length and RMS fluctuations are presented. The flow physics that leads to the suppression of vortex shedding in heated wakes has been explored. The evolution of the vortex structures during vortex shedding suppression of a heated cylinder has been visually presented by the instantaneous flow visualization images. Previous numerical studies have focused on circular cylinder which is essentially different from the square cylinder having fixed separation points at the leading edge. However, nature of the boundary layer at the separation location is influenced by heating of the cylinder. Therefore, attention is directed toward the comparison of the effect of heating on the vortex shedding mechanism of the circular cylinder with that of the square.

The physical picture of vertical flow around a heated cylinder can be visualized as follows. The fluid particles accelerate in the boundary-layers around the cylinder. Increase

in kinetic energy delays the point of inception, thus raising the average base pressure. Consequently, the vortices formed in the wake are weakened by heating, ultimately resulting in complete suppression of vortex shedding. At elevated cylinder temperatures, vortices are weak and thus result in diminishing cross-stream transport. It is a minimum when vortex shedding is absent. The progression towards the state of no vortex shedding is, however, not monotonic. At mild heating levels, the acceleration of the fluid particles in the shear layers enhances vortex strength and moderately increases cross-stream diffusion. These trends are discussed in great detail in the present chapter.

The detailed results of the circular and square cylinders have been jointly presented and compared in the following sections: (1) Suppression of vortex shedding, (2) Instantaneous visualization images, (3) Time-averaged schlieren images, (4) Vortex formation length, (5) Distribution of light intensity fluctuations, (6) Time traces and power spectra, (7) Velocity profiles, (8) Temperature distribution, (9) Convection velocity, (10) Phase shift, and (11) Instability mechanism.

5.1 Suppression of vortex shedding

When the cylinders are heated to a certain higher temperatures, the suppression of vortex shedding for cylinders of both circular and square cross-sections have been observed. This has been demonstrated by schlieren image visualization, time traces of light intensity, corresponding power spectra, and Strouhal number. The lowest flow velocity achieved in the test section is 0.13 m/s, corresponding to a Reynolds number of 53. At this Reynolds number, no vortex shedding is seen for Richardson number ranging from 0.084 to 0.314. Therefore, the Strouhal number is zero. Regular vortex shedding and a definite Strouhal number is noted at other Reynolds numbers namely, Re = 94 and 110 for the circular cylinder and Re = 87, 109, and 118 for the square cylinder. At these Reynolds numbers, vortex shedding is suppressed at an elevated Richardson number, the corresponding Strouhal number becoming zero.

5.1.1 Strouhal number: effect of heating

The Strouhal number variation with respect to Richardson number for fixed Reynolds numbers is presented in Figure 5.1 (a) and (b) respectively for circular and square cylinders. Both figures show a small initial increase in Strouhal number with Richardson number at each Reynolds number. The Strouhal number is higher at higher Reynolds numbers. In this Reynolds number range, the Strouhal number follows an identical trend

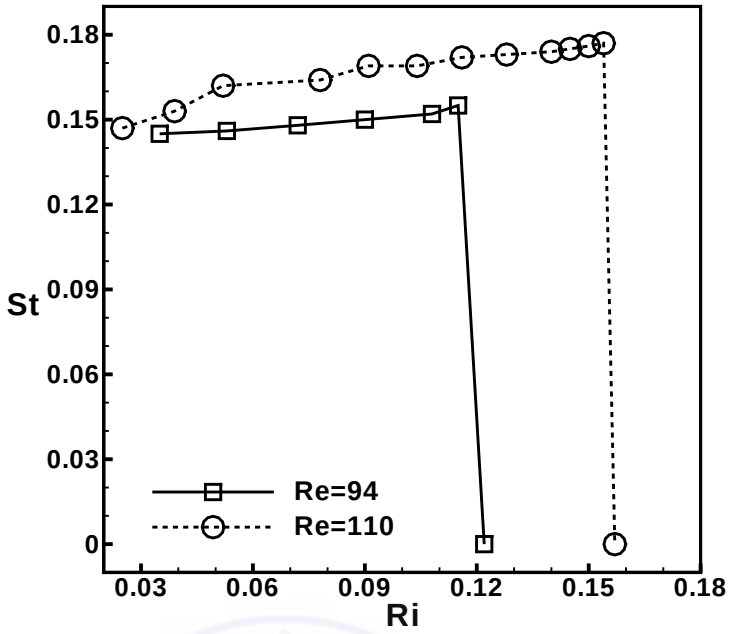

(a)

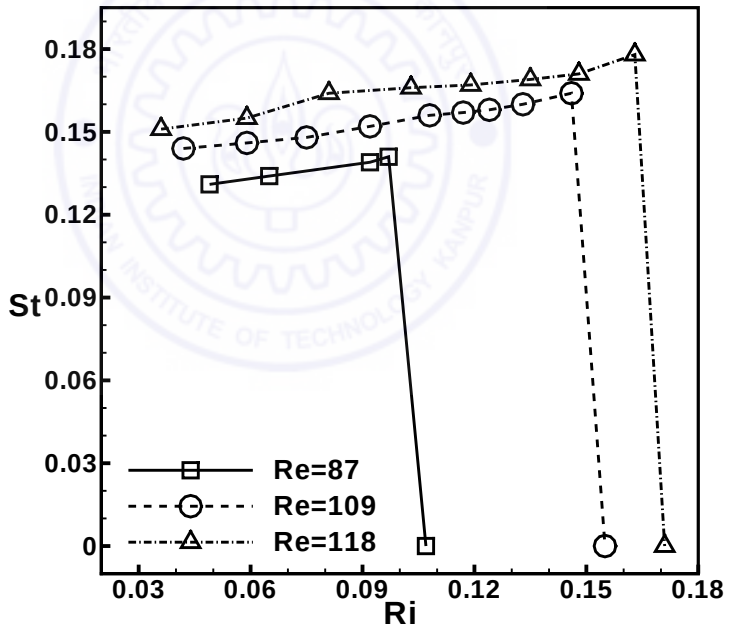

(b)

Figure 5.1: Variation of Strouhal number with Richardson number for a (a) circular cylinder, and (b) square cylinder.

with respect to Reynolds number for the heated cylinder as for an unheated cylinder, Figure 4.8 (Luo *et al.* (2003); Sohankar *et al.* (1999); Robichaux *et al.* (1999)). Hence, it is seen that the effect of Reynolds number on Strouhal number is not affected by heating till the critical point is reached. The increase in Strouhal number with increase in heating level, i.e., increase in Richardson number takes place for both circular and square cylinder

(Figure 5.1 (a) and (b)) till a critical value of Richardson number is reached. After the critical Richardson number, vortex shedding stops abruptly and Strouhal number falls to zero. Earlier numerical studies (Chang and Sa (1990); Hatanaka and Kawahara (1995); Singh *et al.* (1998); Patnaik *et al.* (1999)) have shown an increase in Strouhal number with increase in Richardson number, followed by a singular decay at critical Richardson number. These studies pertain to a fixed Reynolds number Re = 100 for a circular cylinder. The present experimental study confirms similar trends for both circular and square cylinders and for a Reynolds numbers range near 100.

5.1.2 Critical Richardson number: effects of Reynolds number

The critical Richardson number at which suppression of vortex shedding takes place depends on Reynolds number. It is higher at higher Reynolds numbers as depicted from the points of zero Strouhal number in Figure 5.1 (a) and (b). This is an indication that the critical Richardson number is not a universal property for the suppression of vortex shedding and is Reynolds number dependent. Table 5.1 presents critical Richardson number as a function of Reynolds number for both circular and square cylinders. The disappearance of vortex shedding takes place at Ri = 0.122 for Re = 94 and at Ri = 0.157 for Re = 110 for circular cylinder. The critical Ri values for a square cylinder are equal to 0.107, 0.121, 0.140, 0.155, and 0.171 for Re = 87, 94, 103, 109, and 118, respectively. The variation of the critical Richardson number as a function of Reynolds number is plotted in Figure 5.2 for a square cylinder. Linear curve fitting of the data shows goodness of fit equal to 0.997 indicating linear relationship between the critical Richardson number and

Table 5.1: Critical Richardson number and critical Reynolds number (Re_w, Re_{film} and Re_{eff}) calculated using kinematic viscosity of air at T_w, T_{film}, and T_{eff} at different free stream velocities for circular and square cylinders.

S.N.	Cylinder geometry	U_∞ (m/s)	Re_∞	Ri_{crit}	T_∞, °C	T_w, °C	T^*	T_{film}, °C	T_{eff}, °C	Re_w	Re_{film}	Re_{eff}
1.	Circular	0.23	94	0.122	21	54	1.11	37.5	30.2	78	85	89
2.	Circular	0.27	110	0.157	21	82	1.21	51.5	38.1	79	92	100
3.	Square	0.20	87	0.107	23	43	1.07	33	28.6	78	82	84
4.	Square	0.22	94	0.121	26	54	1.09	40	33.8	80	87	90
5.	Square	0.24	103	0.140	26	65	1.13	45.5	36.9	82	92	96
6.	Square	0.25	109	0.155	23	70	1.16	46.5	36.2	84	95	101
7.	Square	0.27	118	0.171	23	85	1.21	54	40.4	84	99	107

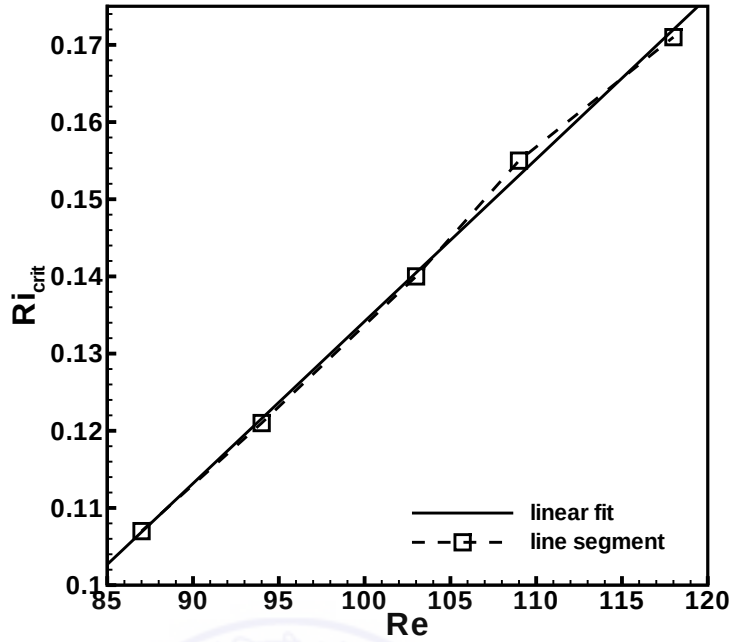

Figure 5.2: Variation of critical Richardson number with Reynolds number for a square cylinder.

Reynolds number. The equation of linear fit is: Y = A + B*X, where A = -7.58E-002 and B = 2.1E-003.

The critical Richardson numbers for a square cylinder are quite close to those of a circular cylinder at comparable Reynolds numbers (Table 5.1). This indicates that both circular and square cylinders share similar flow phenomena for vortex shedding suppression. From numerical simulation, Merkin (1977) reported delay in separation location over circular cylinder due to heating. For a square cylinder, the separation location is fixed at the edge of the cylinder. Identical critical Richardson number for both circular and square cylinder indicates that shift in separation location is not an important criterion responsible for suppression of vortex shedding. Noto *et al.* (1985) from the comparison of circular and triangular cylinder also attributed the vortex street breakdown to acceleration of velocity in the wake and not the shift in separation points.

5.1.3 Effective Reynolds number

An effective Reynolds number using the kinematic viscosity calculated at effective temperature has been used in the literature for characterization of the heated cylinder wake. Lecordier *et al.* (1991) defined the effective temperature as the temperature needed to increase the air kinematic viscosity in order that the effective Reynolds number (Re_{eff})

at the suppressed heating is equal to critical Reynolds number for the onset of vortex shedding. Wang *et al.* (2000) showed a universal relationship between Strouhal number and effective Reynolds number. The above two experimental studies were carried out in the forced convection regime (Ri $\leq$ 0.012 and 0.02, respectively) for a circular cylinder in horizontal flow configuration. In the present study, the cylinder is mounted in a vertical flow configuration i.e. buoyancy force adds to the main flow and suppression of vortex shedding takes place in the mixed convection regime. Therefore, the concept of effective temperature normally applied in forced convection regime has been extended to check its validity in the mixed convection regime. For this, the critical Reynolds number has been calculated based on three characteristic temperatures when vortex shedding is suppressed; the cylinder surface temperature (T_w), mean film temperature (T_{film}), and effective temperature (T_{eff}).

Table 5.1 compares the critical Reynolds number based on the three characteristic temperatures for both circular and square cylinders at different free stream velocities. For a circular cylinder, the range of variations i.e. scatter in the critical Reynolds number calculated using the kinematic viscosity at temperatures T_w, T_{film}, and T_{eff}, respectively is equal to 1, 7, and 11. Similarly, the scatter in the critical Reynolds number of a square cylinder is equal to 6, 17, and 23, respectively, for temperatures based on T_w, T_{film}, and T_{eff}. The greatest variation in critical Reynolds number for both circular and square cylinders is observed when T_{eff} is used for kinematic viscosity calculation. It may be noted that the effective temperature (T_{eff}) used here has been obtained based on the instability characteristic of heated circular cylinder in horizontal mean flow configuration. The buoyancy effect on the wake characteristics of a heated cylinder in horizontal and vertical configurations is not identical. Therefore, a large deviation in critical Reynolds number is observed at T_{eff} for the vertical cylinder configuration. The present study indicates that the cylinder surface temperature (T_w) is a better estimate of effective temperature for calculation of fluid properties in the mixed convection regime. The corresponding critical Reynolds number for vortex shedding suppression behind a heated cylinder is around 81.

The importance of cylinder surface temperature can be seen from the following discussion. The instability of the separating shear layer is influenced by the curvature of the velocity profile. Close to the cylinder surface, the inertia term is negligible ($u = v = 0$) and therefore from the boundary layer equation, the curvature ($\delta^2 u/\delta y^2$) of the velocity profile is primarily dependent on pressure gradient and viscous force. Hence, the viscous force calculated using the viscosity at cylinder surface temperature properly represents the wake instability. For the horizontal mean flow configuration, the overall wake instability is influenced by the contribution of buoyant flow from the lower shear layer to the upper shear layer. In contrast, for a vertical flow configuration, both the

shear layers are primarily influenced by the upstream conditions, i.e. the cylinder surface temperature.

5.2 Instantaneous visualization images

The changes in the organized wake structures with respect to their shape, size and time-dependent movement is readily perceived from instantaneous schlieren images before the wake degenerates into a steady plume. In the present study, three Reynolds numbers (Re = 53, 94, and 110) for the circular cylinder and three Reynolds numbers (Re = 87, 109, and 118) for the square cylinder are considered. Of these six cases, the instantaneous schlieren images for two comparable Reynolds numbers (Re = 110 for the circular cylinder and Re = 109 for the square cylinder) are presented and compared first. Subsequently, the images for other Reynolds numbers are also presented as a supplement.

5.2.1 Circular (Re = 110) versus square (Re = 109) cylinder

Figure 5.3 and Figure 5.4 show the instantaneous schlieren images as a function of Richardson number for the circular and square cylinders respectively. The corresponding Reynolds numbers being equal to 110 and 109 for circular and square cylinder respectively. For a given Richardson number, the images are separated by a time interval of one eighth of the time period of vortex shedding.

Figure 5.3 (a) presents instantaneous images at a temperature of 40°C (Ri = 0.052). The heated wake zones, i.e. the bright zones behind the cylinder extend to a downstream distance of about $x/d = 6.0$. The near field region ($x/d < 1$) close to the cylinder shows very small variation with time and is practically stationary during the complete vortex shedding cycle. The far field region shows a stronger time-dependence. Thus, the base region of the wake shows very low levels of velocity and temperature fluctuations. The growth of the heated shear layer on both sides of the cylinder takes place asymmetrically at different phases of the vortex shedding cycle. The instability of the growing shear layers results in the shedding of two alternate rows of vortices from the opposite side of the cylinder. Figure 5.3 (b) shows instantaneous images of the cylinder wake at a surface temperature of 60°C (Ri = 0.104). Vortex shedding at this higher Richardson number is more distinct. Clear fringes are visible within the near-wake indicating the presence of temperature variation inside the vortex. Figure 5.3 (c) shows the time-sequence of schlieren interferograms behind the circular cylinder at a surface temperature of 75°C (Ri = 0.140). Regular vortex shedding with a higher number of fringes when compared to

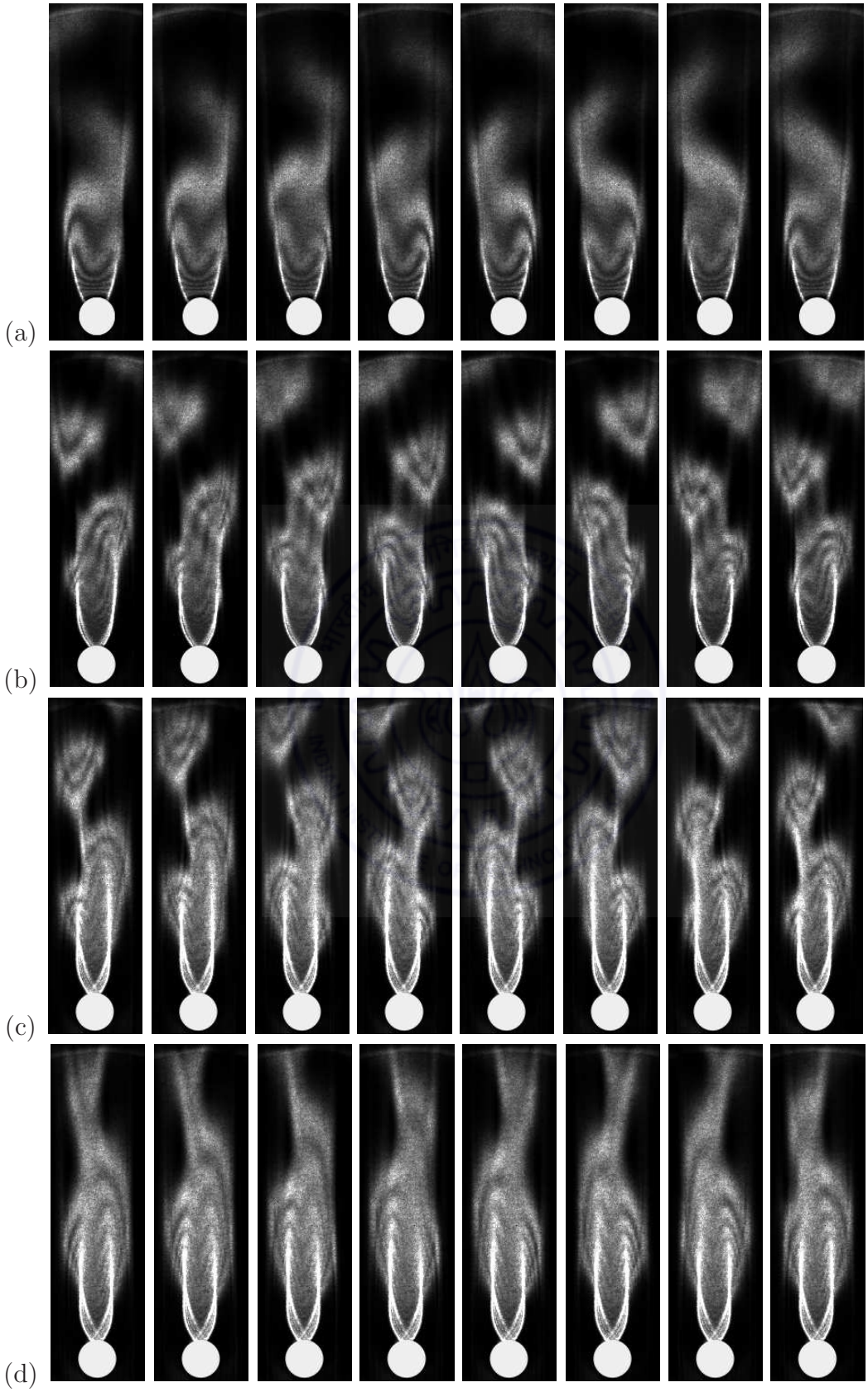

see caption on the facing page

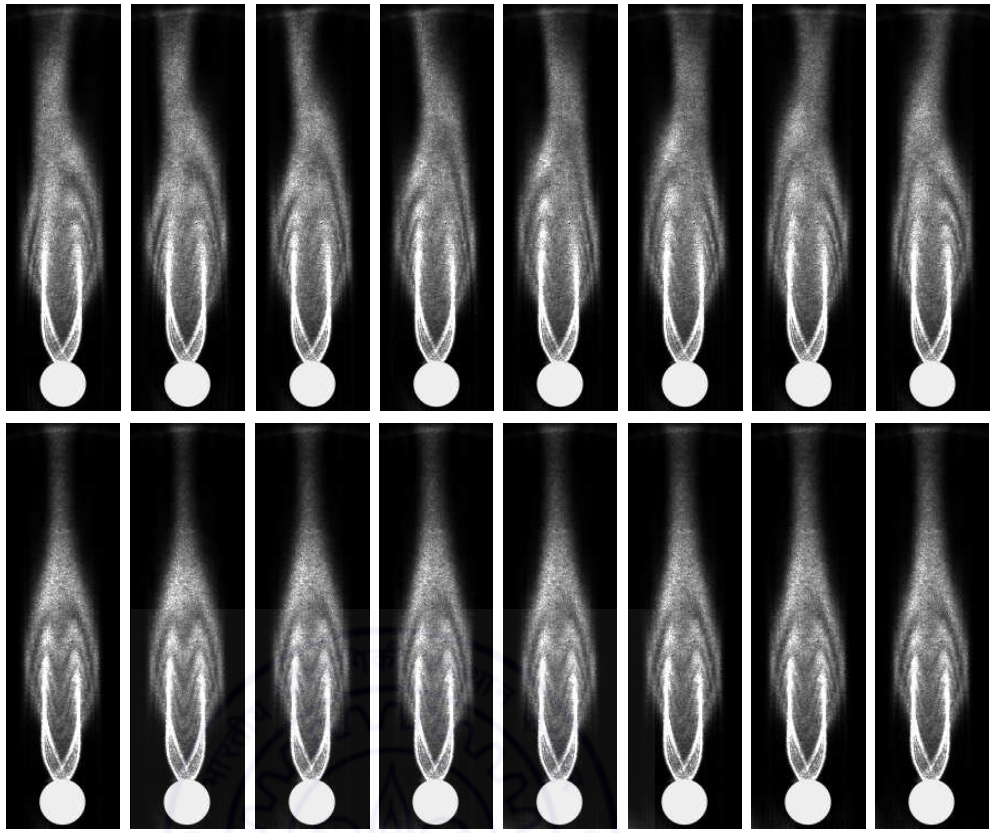

Figure 5.3: Instantaneous schlieren images (a-f) for a circular cylinder separated by a time interval of one eighth of the time period of vortex shedding at Re=110 for different heating level i.e. Richardson number. (a) Ri=0.052, (b) Ri=0.104, (c) Ri=0.140, (d) Ri=0.145, (e) Ri=0.150, and (f) Ri= 0.157. For Ri $\geq$ 0.157, images show steady state.

the smaller temperature level (Ri = 0.104) is seen here. This indicates that vortex is not an isothermal packet of fluid; rather it is the recirculation bubble with a temperature distribution within. With increasing Richardson number, the increase in the number of fringes is a consequence of a higher overall temperature difference on one hand and large localized temperature gradients, on the other. These gradients arise from the structure of a shear layer, with thermal gradients correlating with velocity gradients at the limit of near-unity Prandtl number. The instability mechanisms that result in the detachment of the vortex continue to be quite similar at Richardson numbers up to 0.140. Figure 5.3 (d) shows instantaneous images at a surface temperature of 77°C (Ri = 0.145). The vortex shedding structure starts transforming at this Richardson number compared to the earlier cases. The big vortex structures are converted to small and thin elongated structures interacting from either sides of the wake. The visualization images during one shedding cycle for the cylinder temperature of 79°C (Ri = 0.150) are shown in Figure 5.3 (e). The vortex shedding structure is completely altered at this Richardson number. The alternate shedding pattern observed at lower Richardson numbers is now replaced by a

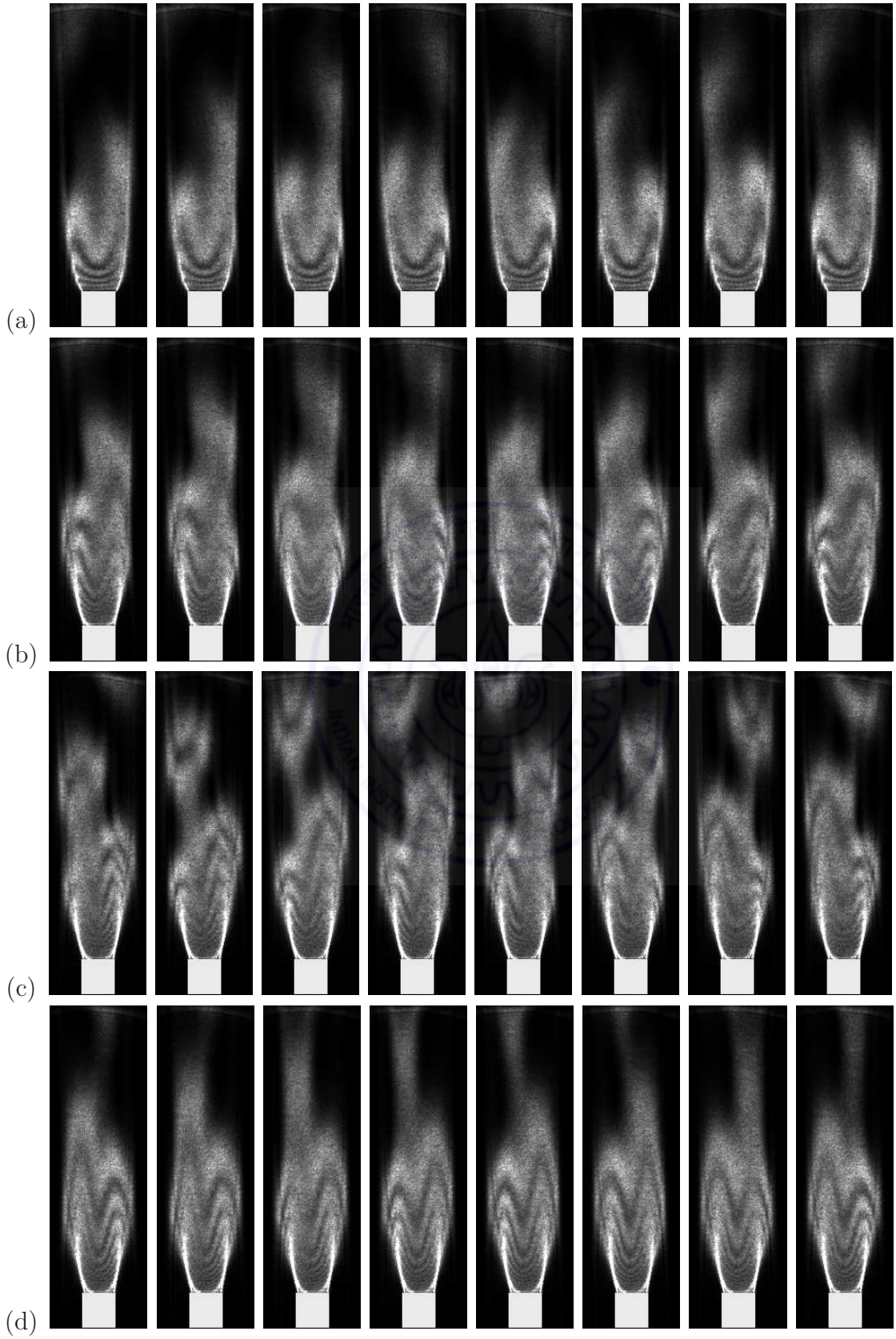

see caption on the facing page

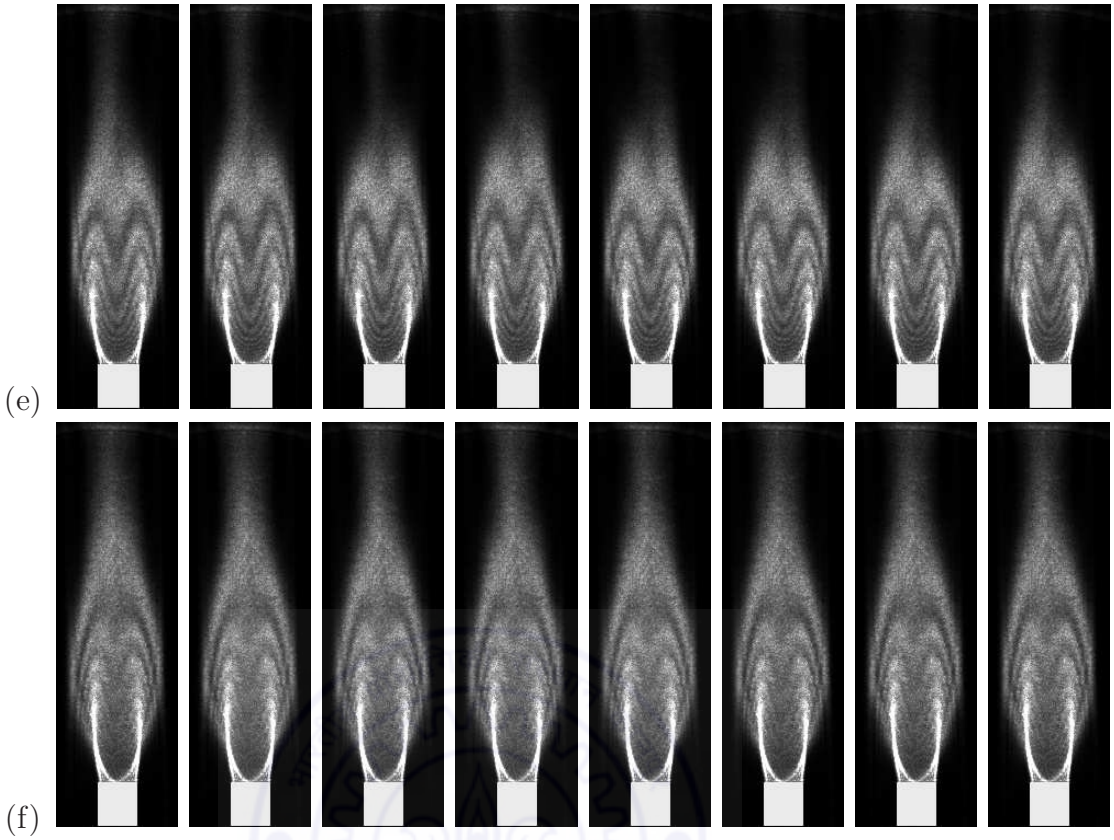

Figure 5.4: Instantaneous schlieren images (a-f) for a square cylinder separated by a time interval of one eighth of the time period of vortex shedding at Re=109 for different heating level i.e. Richardson number. (a) Ri=0.059, (b) Ri=0.108, (c) Ri=0.117, (d) Ri=0.124, (e) Ri=0.133, and (f) Ri=0.155. For Ri $\geq$ 0.155, images show steady state.

thin plume, which slowly oscillates in the transverse direction. The interferograms in the near field region of the cylinder fluctuate in phase with the cross-stream oscillation of the thin plume region. The schlieren-interferograms at a higher surface temperature of 82°C (Ri = 0.157) are presented in Figure 5.3 (f). The thin plume in the far field region is now steady, aligned with the cylinder mid-plane. The plume is thinner compared to that at Ri = 0.150. The interferograms do not oscillate any longer and the wake can be termed as steady.

Figure 5.4 (a) presents the visualization images for a square cylinder when its surface temperature is equal to 40°C (Ri = 0.059). The oscillation in the far field region with vortex shedding from the opposed shear layers is visible. Figure 5.4 (b) shows the instantaneous schlieren images at a surface temperature of 55°C (Ri = 0.108). Compared to the lower Richardson number, the images show vortex shedding with greater clarity. The size of the detached shear layer is bigger at the higher Richardson number. Vortex shedding here is less distinct for the square cylinder when compared to the circular cylinder

(Figure 5.3 (b)). The schlieren-interferograms at the cylinder temperature of 58°C (Ri = 0.117) for the square cylinder in Figure 5.4 (c) show distinct and regular vortex shedding. The interferometric fringes are visible inside the detached vortices. Hence, the increase in heating level regularizes the vortex shedding process, though mixed convection influences the interaction among the shed vortices. Figure 5.4 (d) shows schlieren-interferograms for a cylinder temperature of 60°C (Ri = 0.124). The shape and size of the detached shear layer at this Richardson number is distinctly different from that at the lower Richardson number (Ri = 0.117). The detached shear layer arising from the vortex shedding process is more elongated at the higher Richardson number. The instantaneous images at higher cylinder temperature of 63°C (Ri = 0.133) in Figure 5.4 (e) indicate mild unsteadiness of the shear layer. Figure 5.4 (f) shows the schlieren images at cylinder temperature of 70°C (Ri = 0.155). Here, two shear layers have merged into one leading to a single steady plume at the center of the cylinder. The interferograms in the near field region are also steady in time, indicating complete steadiness of the wake. However, the plume extends farther downstream for the higher Richardson number (Ri = 0.155) when compared to the lower (Ri = 0.133).

The schlieren interferograms of both circular and square cylinder show similar vortex structures as a function of heating level i.e. Richardson number. The mechanism for suppression of vortex shedding can be identified from the schlieren images as follows: Heating reduces fluid density and a small increase in cylinder surface temperature accelerates fluid particles, feeds vorticity to the shear layer, which leads to regular vortex shedding. Thus, the first effect of cylinder heating is to increase the Strouhal number with Richardson number. With further increase in heating level, the diffusion of thermal energy in the near wake creates stabilizing buoyant forces with respect to the fluid at ambient temperature contained in the shear layer. This suppress vortex shedding when the Richardson number exceeds the critical value. Wake unsteadiness (and mixing) is now diminished and a nearly steady plume is observed. The corresponding schlieren images have a uniform spread of light intensity over the wake region.

5.2.2 Circular cylinder (Re = 53)

One experiment at a lower Reynolds number (Re = 53) have been carried out to observe the wake structures in the steady flow regime before the onset of vortex shedding. Figure 5.5 shows instantaneous schlieren images at different Richardson numbers. For a given Richardson number, the time interval between two consecutive images is equal to 4 milliseconds. The images show the recirculation bubble to be attached to the cylinder at all the heating levels. At low Richardson numbers (Ri = 0.084 and 0.143), the recircula-

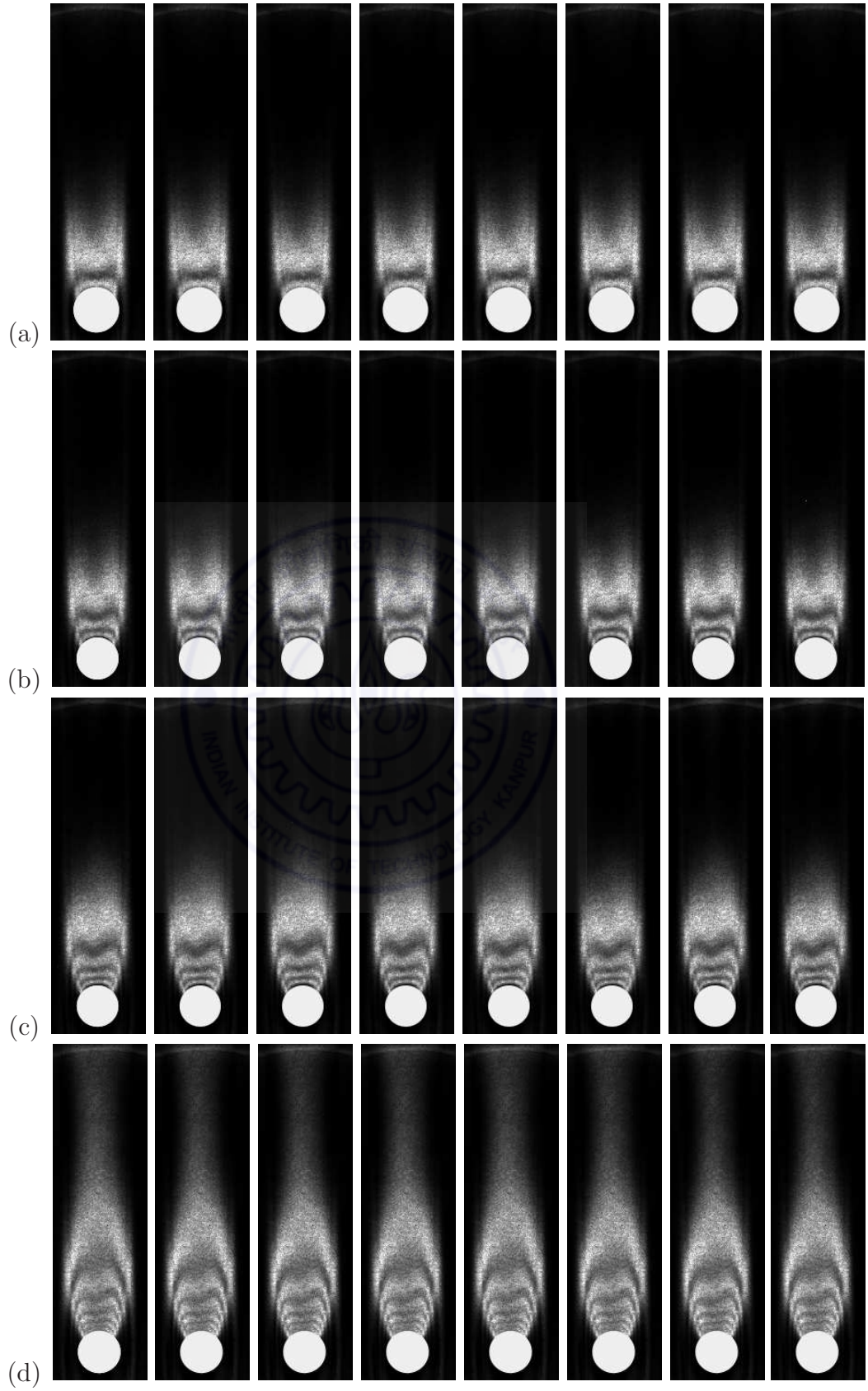

see caption on the next page

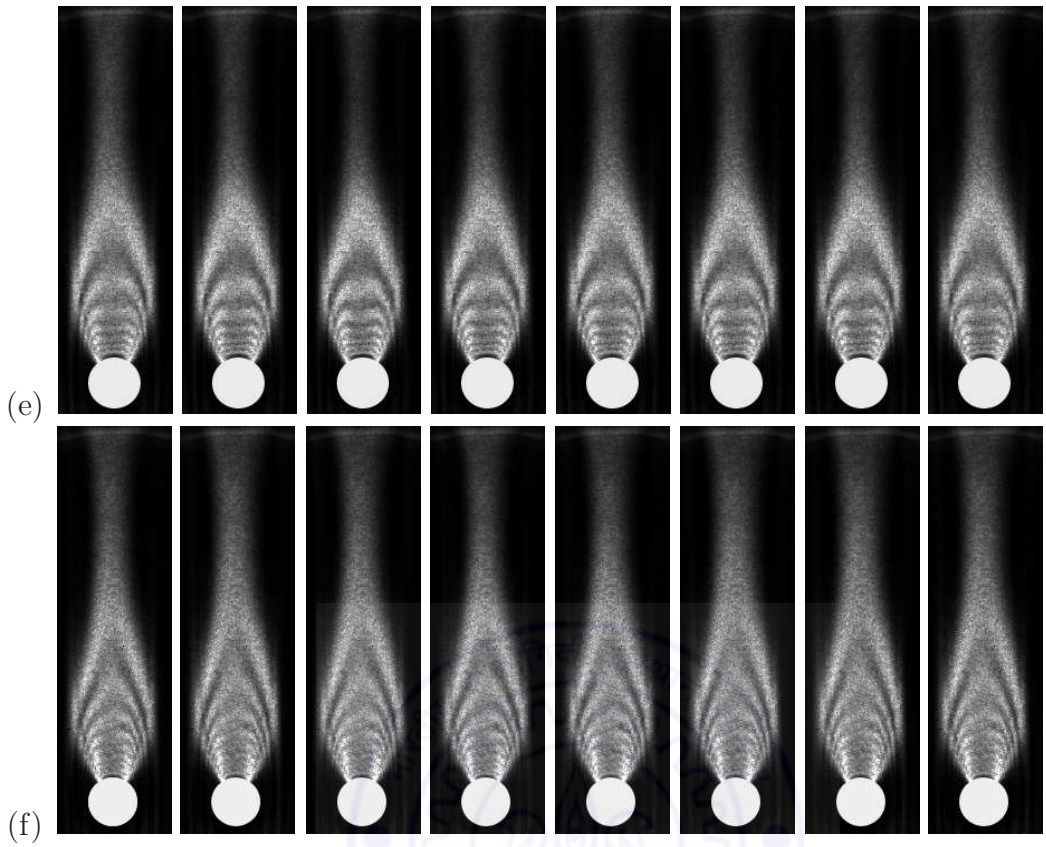

Figure 5.5: Instantaneous schlieren images (a-f) for a circular cylinder separated by a time interval of 4 milliseconds at Re=53 for different heating level i.e. Richardson number. (a) Ri=0.084, (b) Ri=0.143, (c) Ri=0.201, (d) Ri=0.235, (e) Ri=0.269, and (f) Ri= 0.314. For all Richardson numbers, images show steady state.

tion bubble on both sides of the cylinder can be distinguished from each other. With an increase in Richardson number, the two recirculation bubbles merge to a single plume-like structure which becomes thinner with further increase in Richardson number. No shedding or detachment of the two recirculation bubbles take place at any of the Richardson numbers, indicating a steady laminar flow at Re = 53. The corresponding effective Reynolds number is equal to 51. Literature reveals that the flow past a circular cylinder changes from steady to unsteady flow regime at a Reynolds number just below 50. The present work shows that the steady flow was realized at a Reynolds number just higher than 50. The slight heating of the cylinder could have enforced steadiness just beyond the critical Reynolds number. The steadiness may also be attributed to the extremely low turbulence intensity in the flow approaching the cylinder, being less than 0.3% (the smallest value measured by the hotwire anemometer).

5.2.3 Circular cylinder (Re = 94)

Figure 5.6 shows instantaneous schlieren images as a function of Richardson number for a circular cylinder at Re = 94. For a given Richardson number, the images are separated by a time interval of one eighth of the time period of vortex shedding. Figure 5.6 (a) presents the visualization images at a surface temperature of 35°C (Ri = 0.053). The alternate shedding of vortices from the opposite shear layers is clearly visible. The detachment and shedding of vortices become more distinct at a higher surface temperature of 45°C (Ri = 0.090) as shown in Figure 5.6 (b). Fringes are visible inside the detached vortices similar to that observed earlier for Re = 110. Figure 5.6 (c) presents the schlieren images at a surface temperature of 50°C (Ri = 0.108). The shape of the vortex structures start altering at this Richardson number and look like thin elongated slenders. The location of vortex detachment from the cylinder shifts towards a downstream location. Figure 5.6 (d) shows instantaneous images at a cylinder temperature of 53°C (Ri = 0.119), where the two shear layers have merged into a thin plume, which slowly oscillates in the transverse direction. The thin plume in the far field region becomes steady, aligned with the cylinder mid-plane at a temperature of 54°C (Ri = 0.122) as shown in Figure 5.6 (e). The overall trend of the vortex structures development with Richardson number at Re = 94 is similar to that observed for Re = 110 earlier; the only difference being the critical Richardson number at which the wake becomes steady.

5.2.4 Square cylinder (Re = 87)

Figure 5.7 shows instantaneous schlieren images as a function of Richardson number for a square cylinder at Re = 87. For a given Richardson number, the images are separated by a time interval of one eighth of the time period of vortex shedding. The visualization images at a surface temperature of 40°C (Ri = 0.092) are presented in Figure 5.7 (a). The images show alternate shedding of vortices from opposite sides of the wake centerline. But the interaction between opposite shear layers is absent. Instantaneous schlieren images at a surface temperature of 43°C (Ri = 0.107) are shown in Figure 5.7 (b). At this Richardson number, no shedding of vortices or oscillation of the two shear layers is seen and hence the wake is treated as steady. This shows that suppression of instability is brought about by weakening of the non-interacting shear layers, so that no detachment of shear layers and shedding takes place. Figure 5.6 (c) presents the schlieren images at a surface temperature of 48°C (Ri = 0.133). At this Richardson number, the two steady shear layers starts merging into a steady plume, but still can be distinguished from each other. A complete merging into a single steady plume at the centre of the cylinder occurs at a cylinder temperature of 50°C (Ri = 0.143) as shown in Figure 5.7 (d).

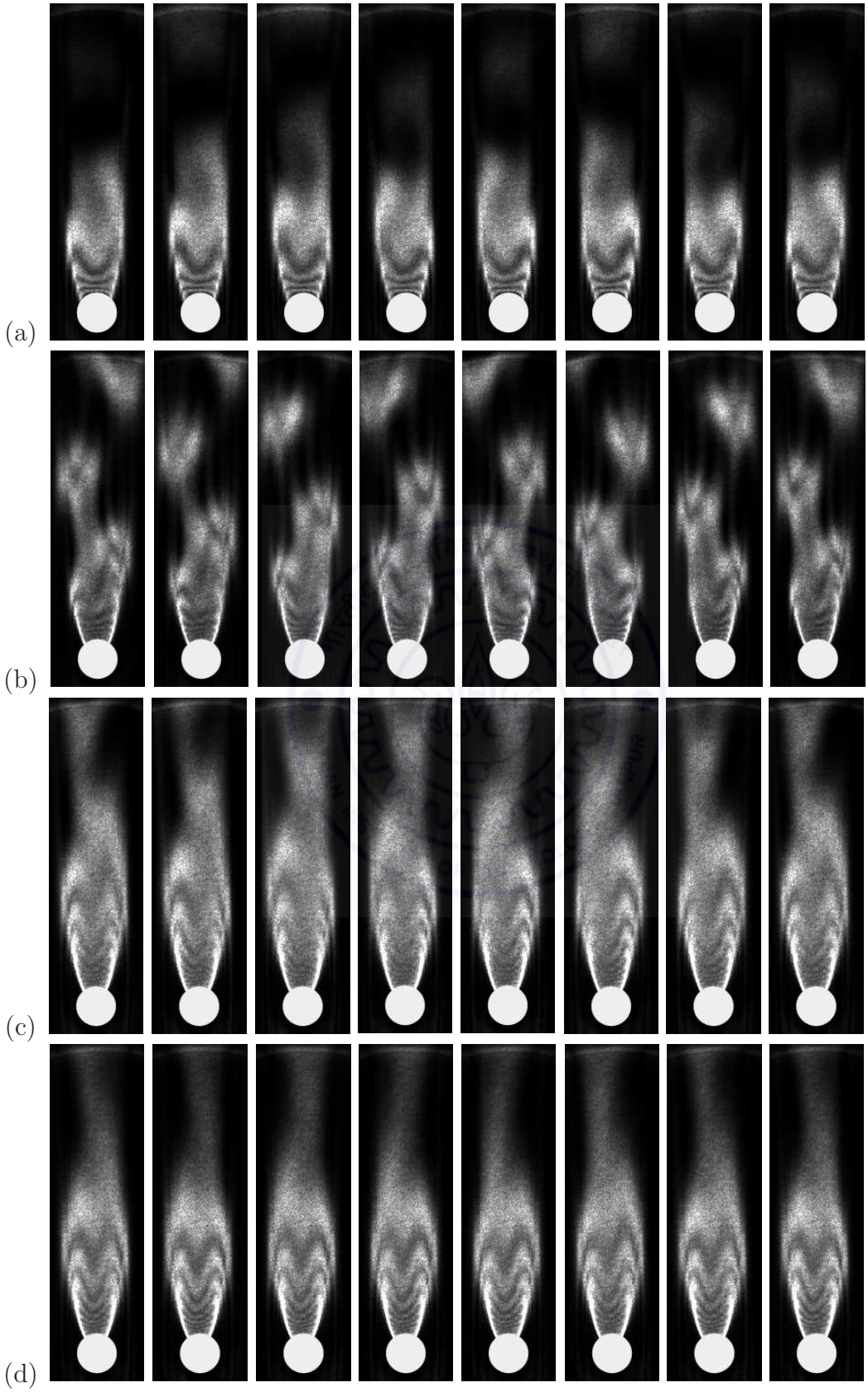

see caption on the facing page

(e) 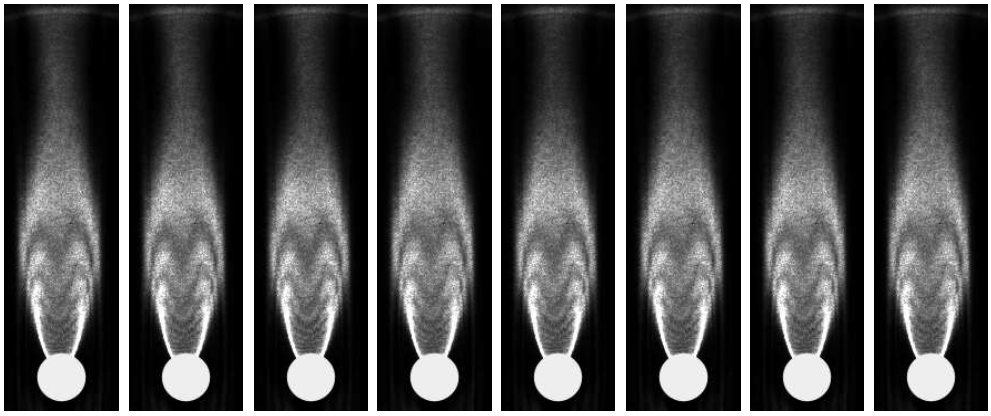

Figure 5.6: Instantaneous schlieren images (a-e) for a circular cylinder separated by a time interval of one eighth of the time period of vortex shedding at Re=94 for different heating level i.e. Richardson number. (a) Ri=0.053, (b) Ri=0.090, (c) Ri=0.108, (d) Ri=0.119, and (e) Ri=0.122. For Ri $\geq$ 0.122, images show steady state.

5.2.5 Square cylinder (Re = 118)

Figure 5.8 shows instantaneous schlieren images at different Richardson numbers for a square cylinder at Re = 118. For a given Richardson number, the images are separated by a time interval of one eighth of the time period of vortex shedding. Figure 5.8 (a) presents instantaneous images at a temperature of 35°C (Ri = 0.036). The instability of the growing shear layers results in the shedding of two alternate rows of vortices from the opposite sides of the cylinder. Figure 5.8 (b) shows instantaneous images at a surface temperature of 51°C (Ri = 0.081). The oscillation in the far field region with vortex shedding from the opposite shear layers is visible. With increase in heat input, the length of the base region increases and the vortex detachment location from the cylinder is delayed. The schlieren images at the cylinder temperature of 65°C (Ri = 0.119) in Figure 5.8 (c) show distinct and regular vortex shedding. Hence, the increase in heating level regularizes the vortex shedding process. Figure 5.8 (d) shows the instantaneous schlieren images at cylinder surface temperature of 71°C (Ri = 0.135). The vortex shedding structure is altered at this Richardson number compared to the earlier cases. The alternate shedding pattern observed at lower Richardson numbers is now replaced by a thin elongated plume, which slowly oscillates in the transverse direction. Figure 5.8 (e) shows the schlieren images at cylinder temperature of 85°C (Ri = 0.171). Here, two shear layers have merged into one leading to a single steady plume at the center of the cylinder. The interferograms in the near field region are also steady in time, indicating complete steadiness of the wake. Hence a small increase in cylinder surface temperature leads to regular vortex shedding initially due to the added flow by buoyancy forces. Further increase in the heating level leads to the appearance of plume-like structures, ultimately resulting in suppression of vortex

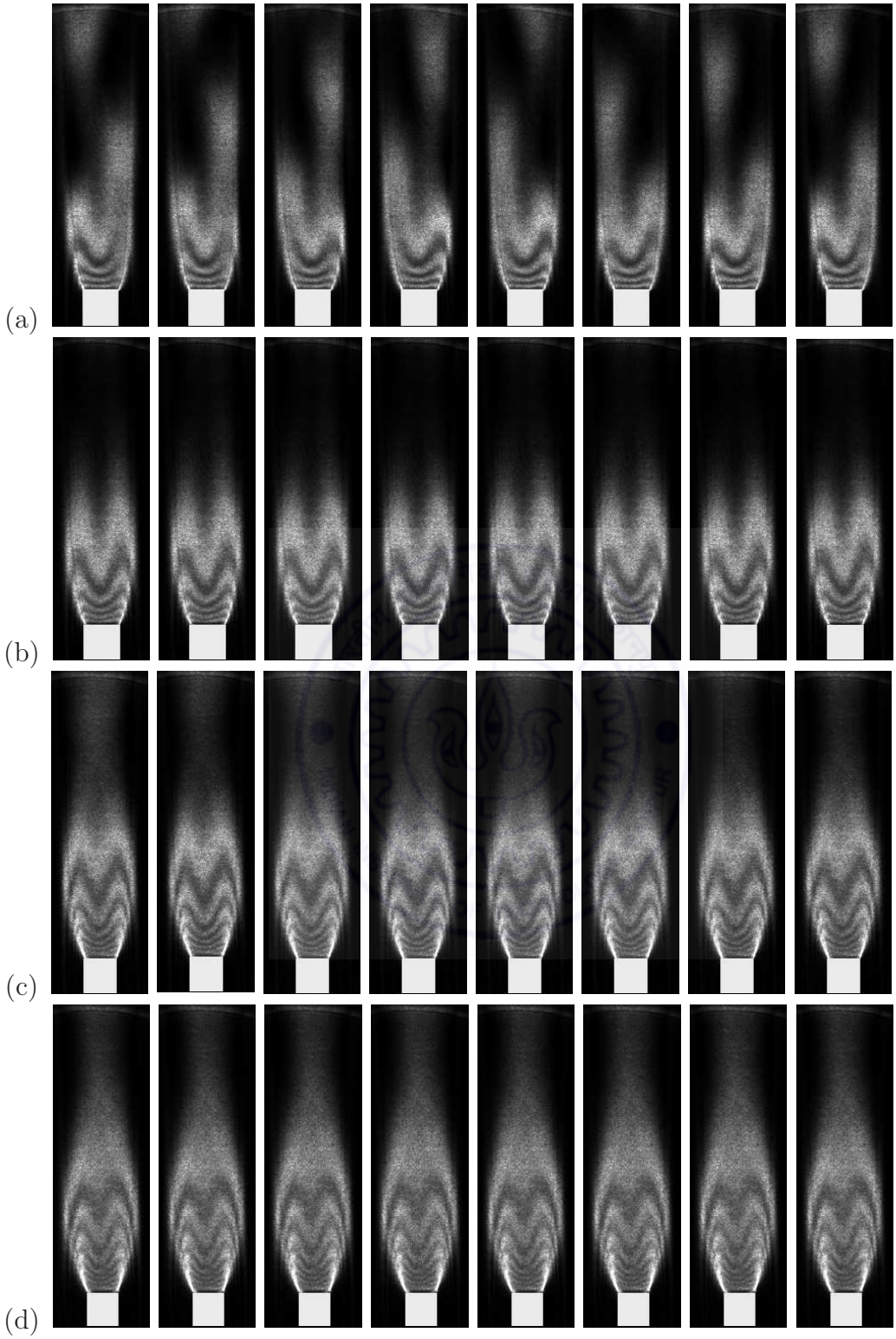

Figure 5.7: Instantaneous schlieren images (a-d) for a square cylinder separated by a time interval of one eighth of the time period of vortex shedding at Re=87 for different heating level i.e. Richardson number. (a) Ri=0.092, (b) Ri=0.107, (c) Ri=0.133, and (d) Ri=0.143. For Ri $\geq$ 0.107, images show steady state.

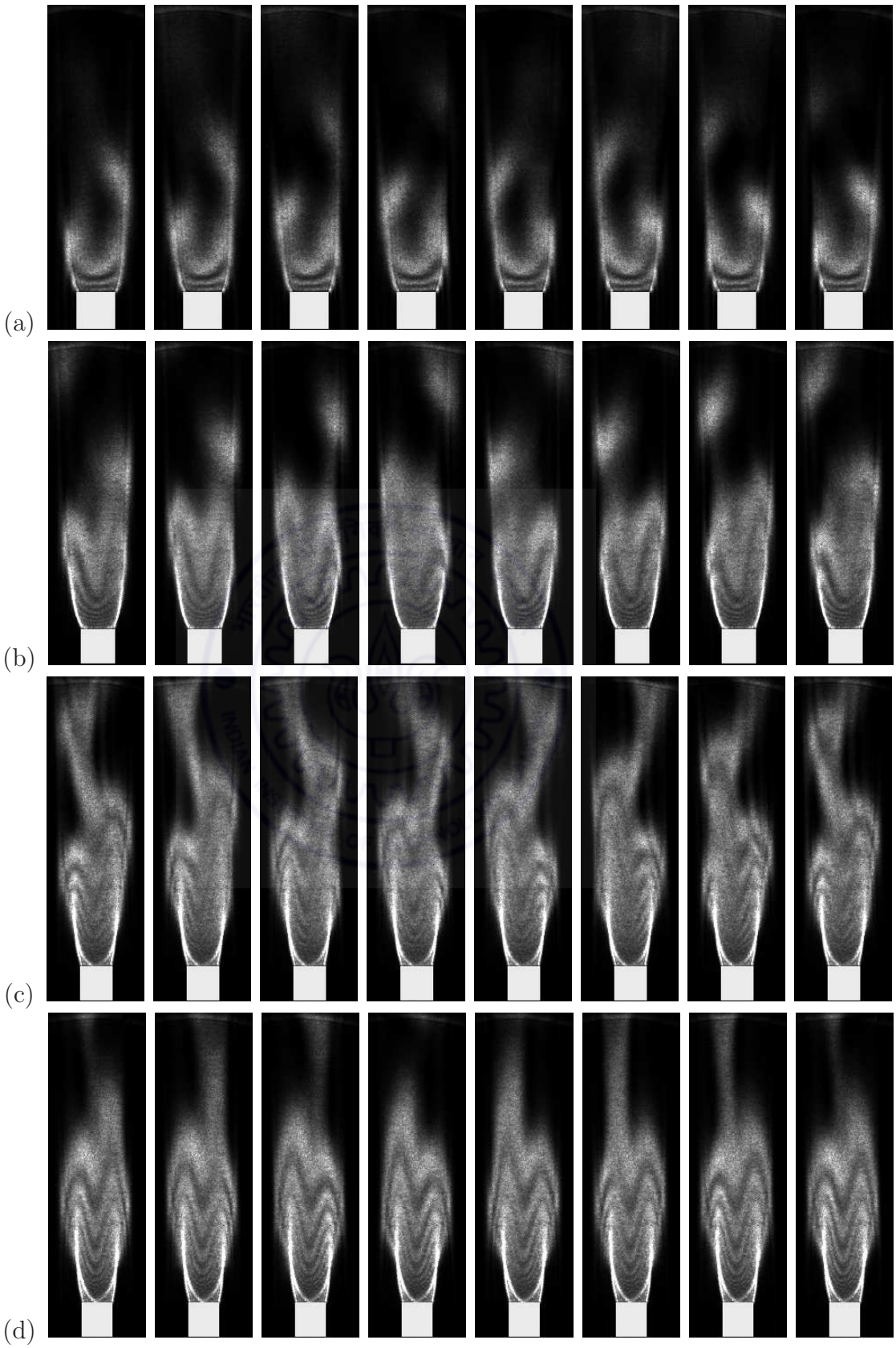

see caption on the next page

(e) 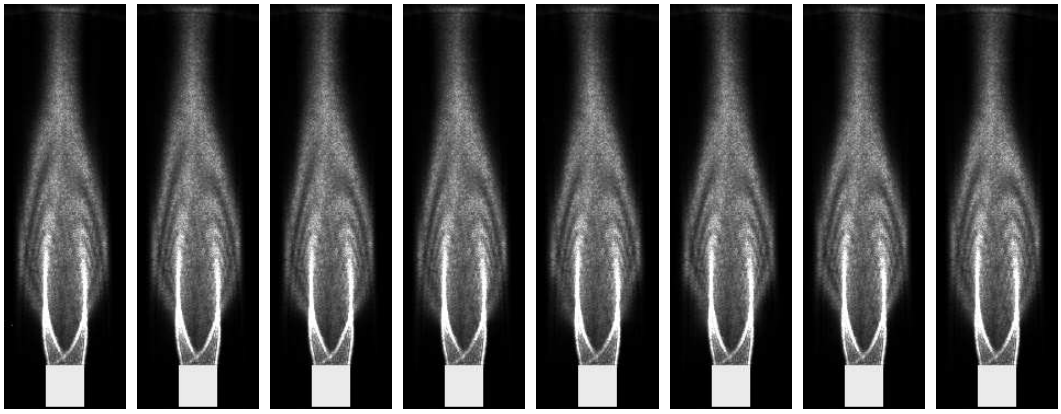

Figure 5.8: Instantaneous schlieren images (a-e) for a square cylinder separated by a time interval of one eighth of the time period of vortex shedding at Re=118 for different heating level i.e. Richardson number. (a) Ri=0.036, (b) Ri=0.081, (c) Ri=0.119, (d) Ri=0.135, and (e) Ri=0.171. For Ri $\geq$ 0.171, images show steady state.

shedding. The overall trend of the alteration of the vortex structures with Richardson number for Re = 118 is similar to that observed for Re = 109 earlier.

5.3 Time-averaged schlieren images

The time-averaged schlieren images provide information about the streamwise and transverse extent of the heated cylinder wake and can be used as an indicator of wake mixing. The time-averaged schlieren images for the circular and square cylinders are presented in Figures 5.9 and 5.10, respectively as a function of Reynolds number and Richardson number.

(a) 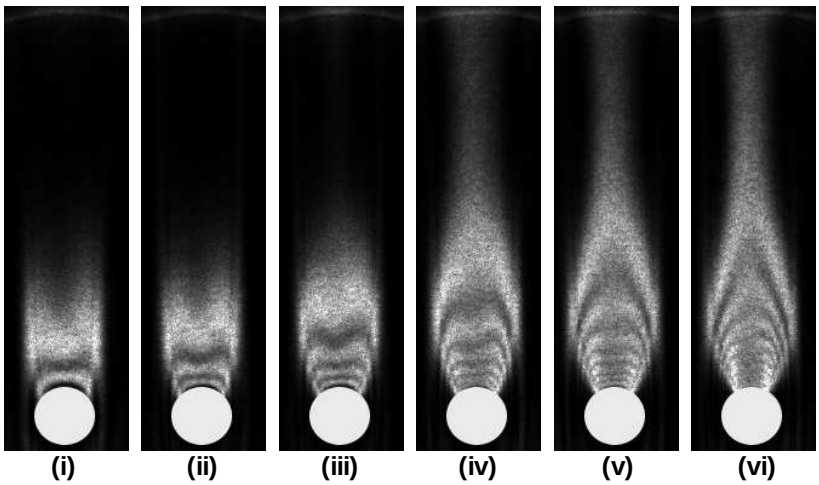

see caption on the facing page

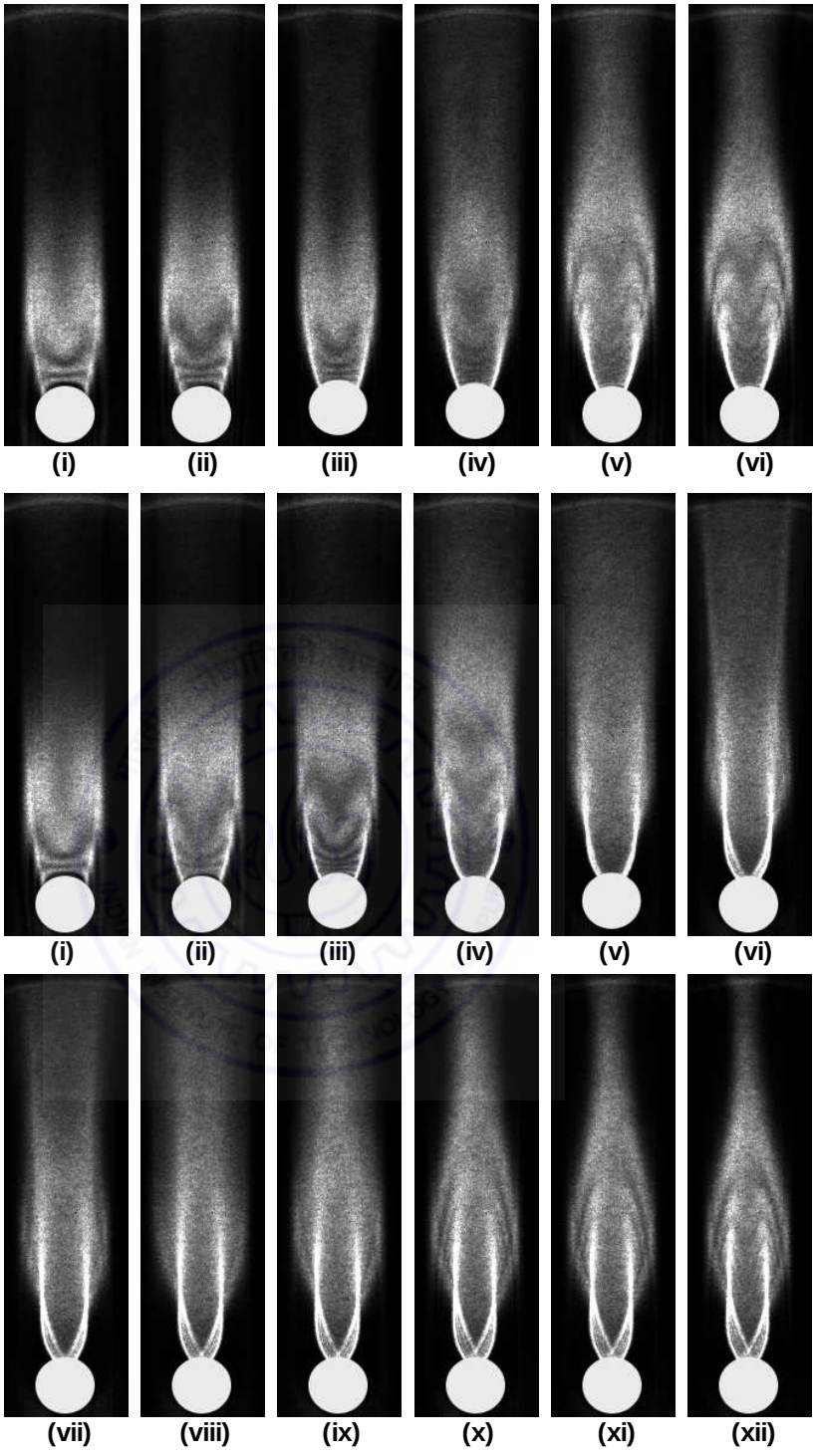

Figure 5.9: Circular cylinder: time-averaged schlieren images as a function of Reynolds number and Richardson number. (a) Re=53: (i) Ri=0.084, (ii) Ri=0.143, (iii) Ri=0.201, (iv) Ri=0.235, (v) Ri=0.269, and (vi) Ri=0.314; (b) Re=94: (i) Ri=0.035, (ii) Ri=0.053, (iii) Ri=0.072, (iv) Ri=0.090, (v) Ri=0.115, and (vi) Ri=0.122; (c) Re=110: (i) Ri=0.025, (ii) Ri=0.039, (iii) Ri=0.052, (iv) Ri=0.078, (v) Ri=0.091, (vi) Ri=0.116, (vii) Ri=0.128, (viii) Ri=0.140, (ix) Ri=0.145, (x) Ri=0.150, (xi) Ri=0.154, and (xii) Ri=0.157.

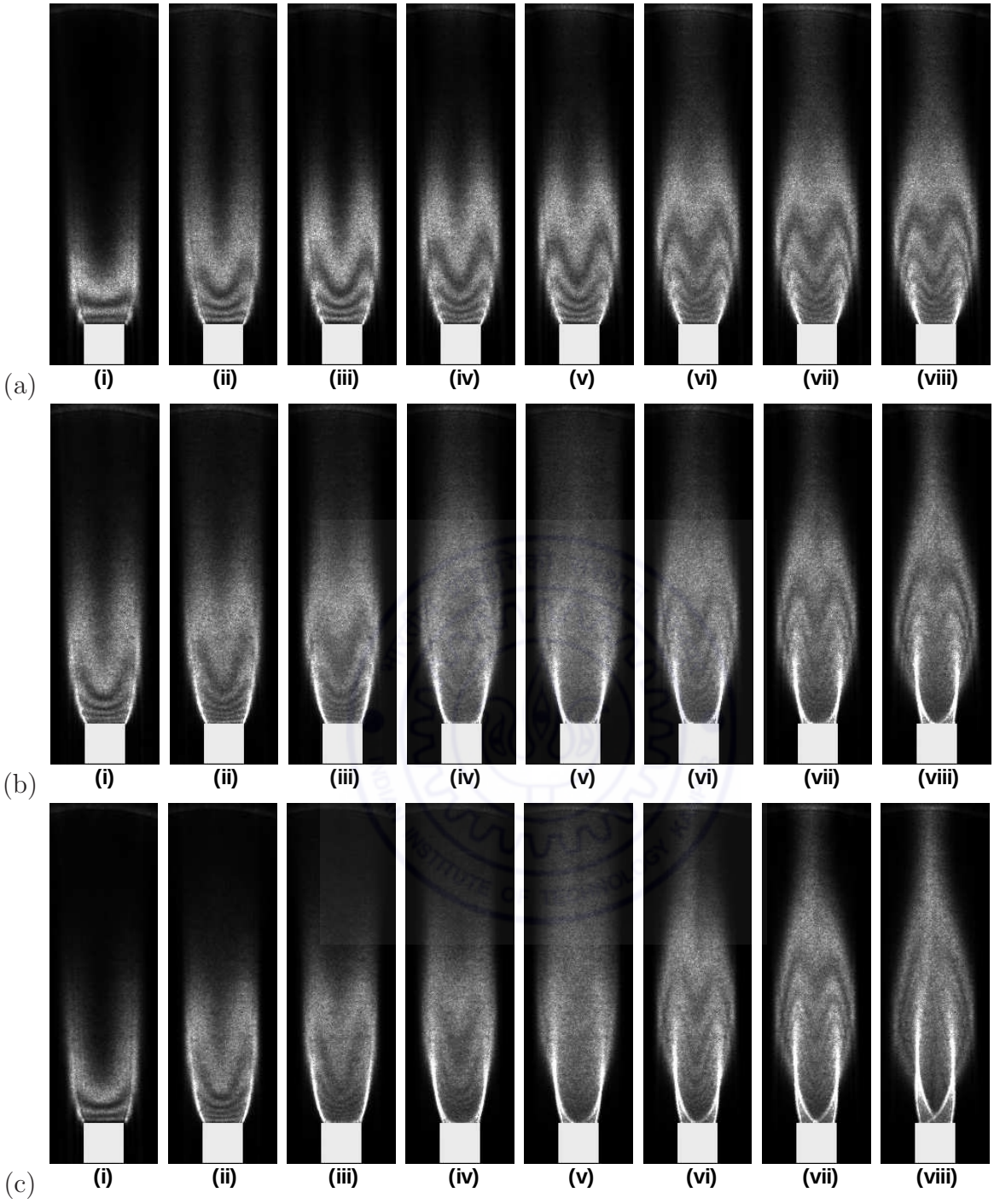

Figure 5.10: Square cylinder: time-averaged schlieren images as a function of Reynolds number and Richardson number. (a) Re=87: (i) Ri=0.065, (ii) Ri=0.092, (iii) Ri=0.097, (iv) Ri=0.107, (v) Ri=0.113, (vi) Ri=0.128, (vii) Ri=0.133, and (viii) Ri=0.143; (b) Re=109: (i) Ri=0.059, (ii) Ri=0.075, (iii) Ri=0.092, (iv) Ri=0.108, (v) Ri=0.117, (vi) Ri=0.124, (vii) Ri=0.133, and (viii) Ri=0.155; (c) Re=118: (i) Ri=0.036, (ii) Ri=0.059, (iii) Ri=0.081, (iv) Ri=0.103, (v) Ri=0.119, (vi) Ri=0.135, (vii) Ri=0.148, and (viii) Ri=0.171.

For a circular cylinder, the streamwise dimension of the wake zone increases with an increase in Richardson number for all Reynolds numbers (Figure 5.9). For Re = 53, the time-averaged schlieren images look identical to the instantaneous images (Figure 5.5) because the wake is steady. At this Reynolds number, the length of the base region increases with Ri. For other Reynolds numbers, heating also increases the length of the base region. The transverse extent of the wake in the far field region also increases with an increase in Richardson number but subsequently reduces. The transverse spread of the wake indicates the lateral movement of the shear layer during vortex shedding. The suppression of vortex shedding leads to a reduction in the growth of the shear layer and a thinner plume in the far field region at the centerline of the cylinder is obtained.

Time-averaged schlieren images for the square cylinder at various Reynolds numbers are compared in Figure 5.10 as a function of Richardson number. Heat transfer from the cylinder to the fluid is initially by the vortices arising from the roll-up of the shear layers and is a function of time. In a time-averaged sense, it leads to a high temperature gradient at the vortex boundary as heat is carried away by convection from the cylinder surface. The presence of a dark zone between the two opposite shear layers at the lower Richardson number indicates only a small time-dependent interaction between the two. The transverse extent of the plume in the far field region increases with an increase in Richardson number. This is due to an increase in the transverse diffusion of the shear layers by buoyancy in the regular vortex shedding regime. The increase in the wake width is to be correlated to the slight increase in Strouhal number with Richardson number. Subsequent increase in the cylinder temperature leads to vortex suppression and an abrupt reduction in the wake width. Hence, at a higher Richardson number, the shear layers from the two upstream corners interact, merge, and form a single plume-like structure. The wake is now a well-mixed zone with a uniform distribution of light intensity within.

The general shape and structure of the wake of the square cylinder is similar to that of the circular cylinder. The only difference is seen in the forced convection regime where buoyancy effects are not much significant. Here, the individual shear layers of the square cylinder are non-interacting due to the definite points of separation. For a circular cylinder the points of separation move closer with an increase in Richardson number. The transitional behavior towards the mixed convection regime and finally to suppression of shedding are however, quite similar.

5.4 Vortex formation length

The characteristics of the shed vortices and its length scale can be correspond to the location where the vortex just detaches itself from the cylinder. In the present work, the vortex formation length is estimated as being the streamwise (x/d) location where the maximum magnitude in rms fluctuation of light-intensity is observed. The rms fluctuation is minimum at the centerline among all radial locations inside the wake and the shear layer. This leads to an occasional noisy peak in the rms fluctuation distribution along the center-line. However, this effect is not seen at the offset location due to an improved signal-to-noise ratio in the light-intensity fluctuations. Therefore, small offset location (i.e. y/d= 0.30 or 0.45 depending upon Richardson number) is chosen for better accuracy due to higher overall magnitude of the rms fluctuations.

The vortex formation lengths, (L_f/d) obtained in various experimental conditions are compared in Tables 5.2 and 5.3 for the circular and square cylinders respectively. The vortex formation length is a function of cylinder surface temperature and hence Richardson number. Once vortex shedding is suppressed, the vortex formation length is no longer defined. For a low Richardson number i.e. at 30°C and 35°C cylinder surface temperature, the vortex formation length, L_f/d = 2.0 and 1.8 for the circular and square cylinder respectively. Konstantinidis *et al.* (2003) and Kim *et al.* (2006) reported L_f/d to be in the range of 1.5-2.3 for a circular cylinder, which is comparable to the above values obtained in our study. For both cylinders, the formation length increases with Richardson number and approaches an asymptotic value at each Reynolds number. The asymptotic formation lengths (L_f/d) are 2.9, 3.9 and 4.3 for Re = 87, 109 and 118 for the square cylinder. For circular cylinder, the formation length values are 3.6 and 4.0 at Re = 94 and Re = 110 respectively. Similar values of the asymptotic formation length for circular

Table 5.2: Vortex formation length as a function of Reynolds number and cylinder surface temperature for a circular cylinder. Here 'NS' indicates no shedding of vortices.

Cylinder surface temperature, °C	L_f/d Re=94	L_f/d Re=110	Cylinder surface temperature, °C	L_f/d Re=110
30	2.0	2.0	60	3.7
35	2.4	2.5	70	3.8
40	2.5	2.9	75	3.9
45	3.0	3.6	77	4.0
50	3.6	3.7	79	4.0
52	3.6	-	81	4.0
54	NS	-	82	NS

Table 5.3: Vortex formation length as a function of Reynolds number and cylinder surface temperature for a square cylinder. Here 'NS' indicates no shedding of vortices.

Cylinder surface temperature, °C	L_f/d Re=87	L_f/d Re=109	L_f/d Re=118	Cylinder surface temperature, °C	L_f/d Re=109	L_f/d Re=118
35	1.8	1.8	1.8	59	-	3.1
40	2.7	2.4	-	60	3.9	-
41	2.9	-	-	63	3.9	-
43	NS	-	2.4	65	3.9	3.6
45	-	2.6	-	67	3.9	-
47	NS	-	-	70	NS	-
50	NS	3.1	-	71	-	3.9
51	-	-	2.9	76	NS	4.3
55	-	3.5	-	82	-	4.3
58	-	3.6	-	85	-	NS

and square cylinders at around equal Reynolds numbers indicate similarity in the vortex shedding mechanisms of the heated square and circular cylinders. This is supported by similarity in the power spectra, time traces and schlieren visualization images of heated circular and square cylinder. Vortex formation is suppressed at near-equal critical points by the action of buoyancy (Figures 5.1 (a) and (b)).

The critical Richardson number at which suppression of vortex shedding takes place is higher at higher Reynolds numbers. Simultaneously, the Strouhal number prior to suppression is also higher. Hence, the formation length seems to be correlated to both critical Richardson number and Strouhal number. An increase in fluid speed in a highly buoyant flow field can explain longer distances traversed (increase in formation length, L_f) as well as a lower time period (increase in Strouhal number upto critical point). Beyond the critical Richardson number, vortex shedding itself is suppressed. The increase in size of the vortex formation region with an increase in the heating level can be related to the delay in transition of the separating shear layer. Buoyancy has the effect of diffusing the vorticity content inside the shear layer and the buoyant plume reduces the interaction between the opposite shear layer at both sides of the cylinder.

5.5 Distribution of light-intensity fluctuations

Since light measurements are inertia free, time-dependent fluctuations in light intensity from schlieren interferograms are essentially due to the temperature fluctuations. As the

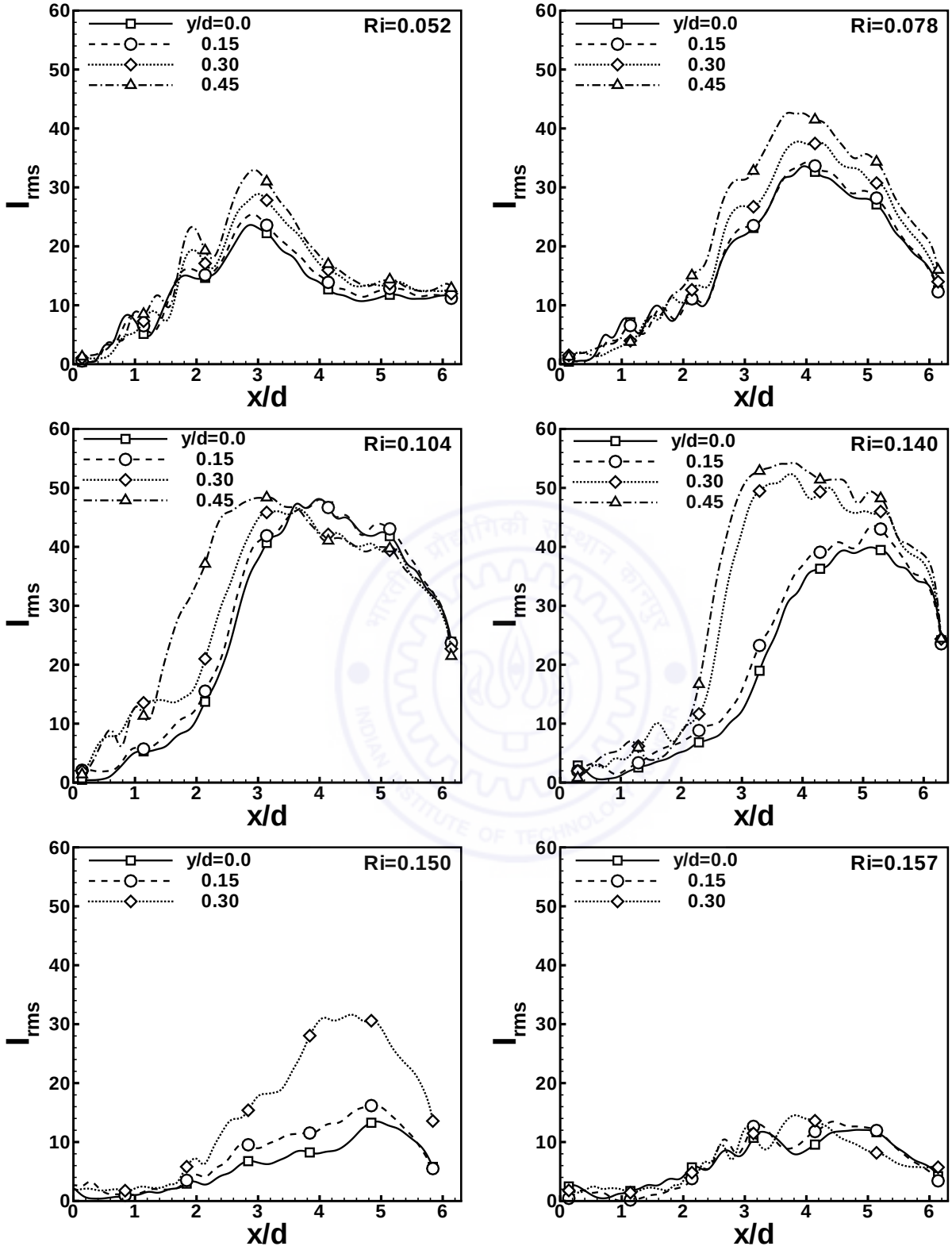

Figure 5.11: Circular cylinder: Evolution of the RMS intensity (I_{rms}) in the streamwise direction at various transverse locations, (y/d = 0.0, 0.15, 0.30 and 0.45), Re=110 . Functional dependence on Richardson number is shown.

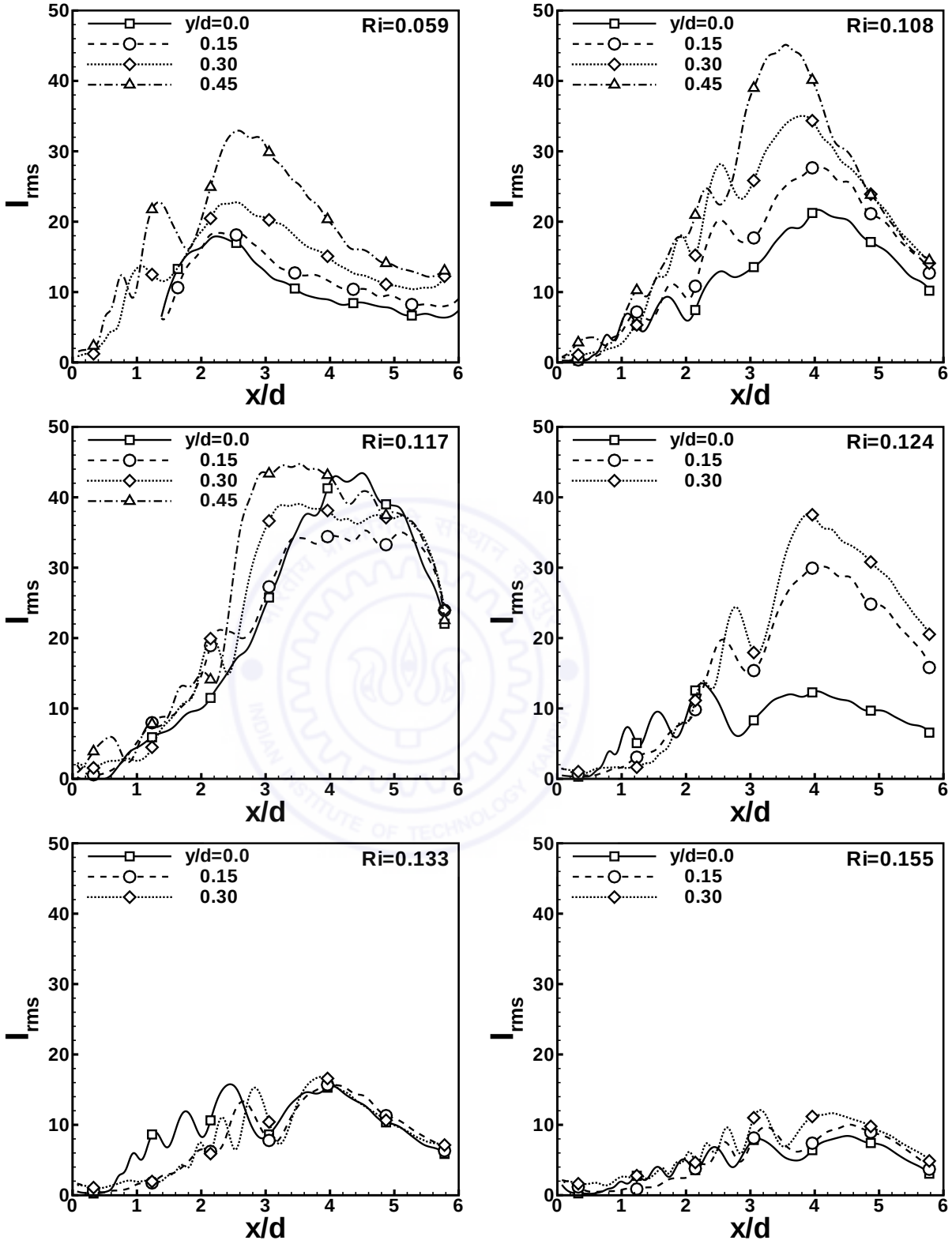

Figure 5.12: Square cylinder: Evolution of the RMS intensity (I_{rms}) in the streamwise direction at various transverse locations, ($y/d = 0.0$, 0.15, 0.30 and 0.45), Re=109. Functional dependence on Richardson number is shown.

working fluid is air with a Prandtl number of the order of unity, these can further be correlated to velocity fluctuations. The correlation is meaningful outside the recirculation zone, where advection effects are much larger than diffusion. The influence of heating on wake fluctuations of stationary circular and square cylinders is of interest in the present section.

The RMS (mean-removed) profiles of the fluctuating light intensity in the streamwise direction (x/d) at different transverse locations (y/d) are presented in Figures 5.11 and 5.12 for the circular and square cylinders, respectively. The corresponding Reynolds numbers for these cases are 110 and 109. Figures 5.11 and 5.12 indicate strong fluctuations in case of vortex shedding, which diminish to a small level due to vortex suppression. For both the cylinders, the intensity of fluctuations is small in the near field region ($x/d \leq 2$) i.e. very close to the cylinder surface. The instantaneous images in Figure 5.3 and 5.4 also show steady fringes in the near field region, supporting the trends in RMS intensity of Figures 5.11 and 5.12. The jump in the rms intensity magnitude is due to inception of vortex shedding. Therefore, RMS values are higher in the far field region where the flow is driven by sustained vortex shedding. The unsteadiness of this region was also observed in the schlieren images of Figure 5.3 and Figure 5.4. The RMS light intensity increases from a small value to a maximum in the streamwise direction, and subsequently reduces with distance. The streamwise location of the peak value of rms intensity fluctuation from the surface of the cylinder is termed as the vortex formation length. The fluctuation in light intensity is higher inside the shear layers ($y/d = 0.45$) and reduces towards the cylinder centerline ($y/d = 0$). These trends are supported by the RMS profiles of light intensity fluctuations in the transverse direction (y/d) at different streamwise locations (x/d) in Figures 5.13 and 5.14 for the circular and square cylinders respectively.

Figures 5.11 and 5.12 show the maximum RMS intensities to be functions of the Richardson number. At lower Richardson numbers (Ri = 0.052 for the circular and Ri = 0.059 for the square cylinder) the intensity of fluctuations are small for both the cylinders. The moderate increase in the cylinder temperature enhances the vortex strength accompanied by regular and strong vortex shedding. Therefore, maximum RMS intensity is high for sub-critical Richardson numbers when compared to lower Richardson number. At elevated cylinder temperature, the vortices become weak and thus result in reduced interactions between the vortices from the opposite shear layers. Therefore, RMS intensity is again low at the Richardson number just below the critical Richardson number of suppression. At the highest Richardson number of Ri = 0.157 for the circular and Ri = 0.155 for the square cylinder, the RMS values of fluctuations are insignificant due to the complete suppression of vortex shedding.

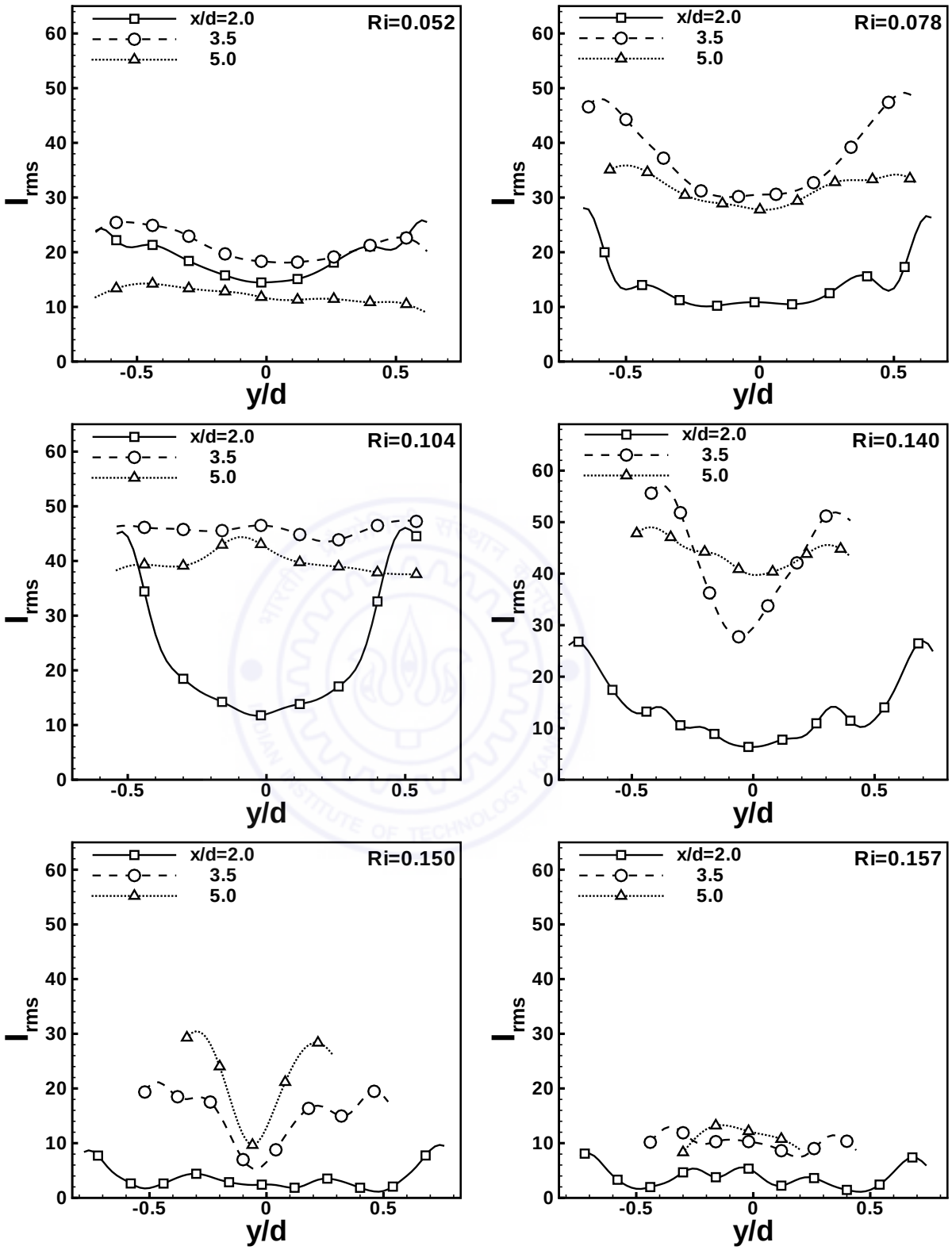

Figure 5.13: Circular cylinder: Evolution of the RMS intensity (I_{rms}) in the transverse direction at various streamwise locations, (x/d = 2.0, 3.5 and 5.0), Re=110. Functional dependence on Richardson number is shown.

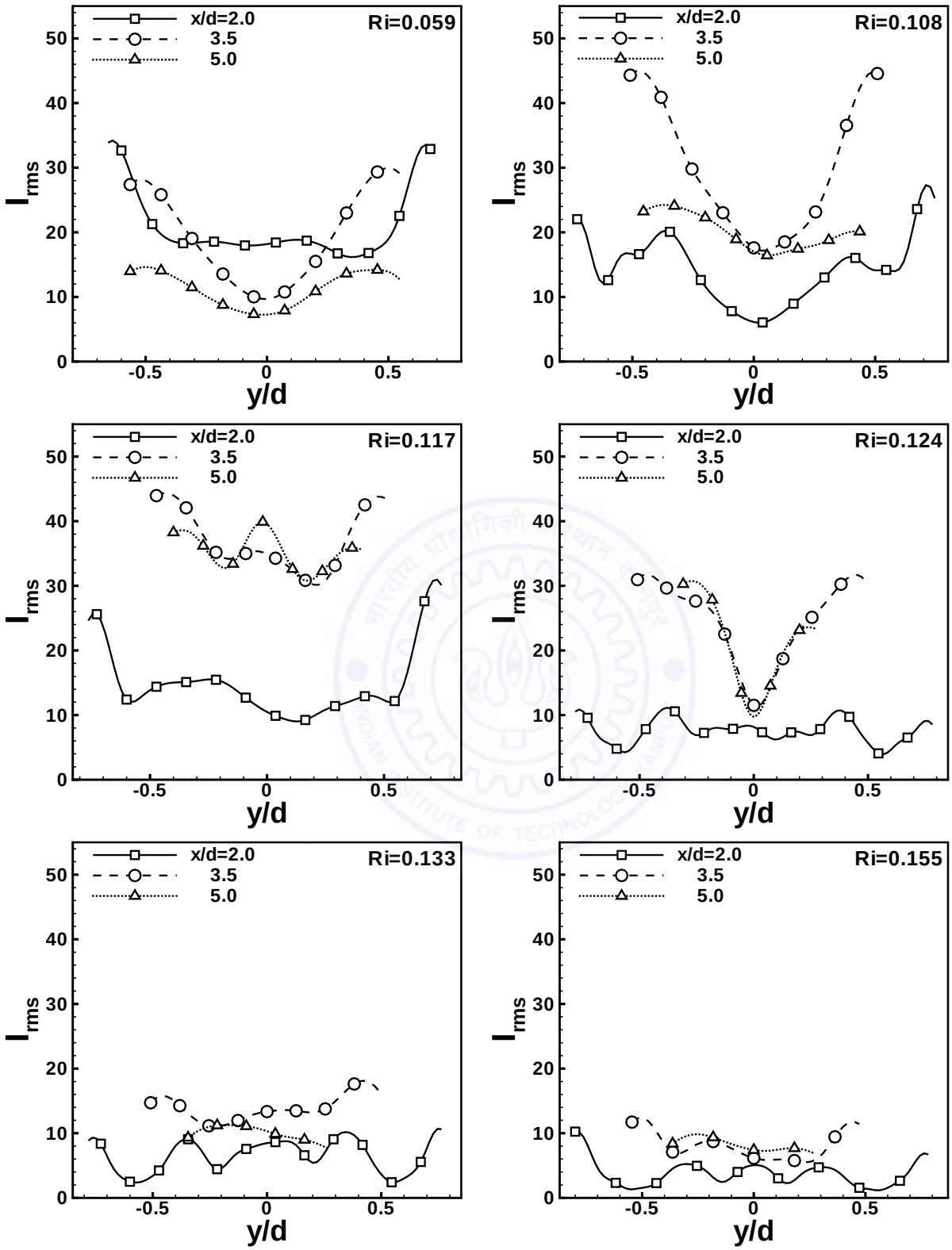

Figure 5.14: Square cylinder: Evolution of the RMS intensity (I_{rms}) in the transverse direction at various streamwise locations,(x/d = 2.0, 3.5 and 5.0), Re=109. Functional dependence on Richardson number is shown.

Figures 5.13 and 5.14 show the rms intensity distribution in the transverse direction at different streamwise locations. In the vortex shedding regime, the RMS intensity increases in the transverse direction away from the centerline. Factors that determine the flow fluctuation levels in the wake are (a) the average size of the shed vortex, (b) interaction between opposite shear layer vortices, and (c) the average fluid speed in the shear layers. The relative difference in magnitude of the RMS intensity between different transverse locations (y/d) is an indicator of the size and shape of the detached vortices. At lower Richardson number (Ri = 0.052 and 0.078 for the circular and Ri = 0.059 and 0.108 for the square cylinder), the maximum RMS intensity at the center locations is lower than that inside the shear layer. At Ri = 0.104 for the circular and Ri = 0.117 for the square cylinder, the maximum RMS intensity does not vary significantly in the transverse (y/d) direction. For these cases, almost uniform distribution of RMS intensity is seen in Figures 5.13 and 5.14 at $x/d = 3.5$ location. For these Richardson number, the size of the detached shear layer is bigger with symmetrical shape of the vortices compared to the lower Richardson number. In contrast, at Ri = 0.150 for the circular and at Ri = 0.124 for the square cylinder, the maximum RMS intensity at $y/d = 0.0$ is significantly lower compared to that inside the shear layer. Figure 5.3 and 5.4 shows the reversal to slender vortex structures at these Richardson numbers. This is also an indication of reduced interaction between neighboring shear layers at higher heating level. Lower interaction between the vortices shed from the opposite shear layers reduces the wake fluctuations. Figures 5.11 and 5.12 accompanied by Figures 5.13 and 5.14 show that buoyancy influences the nature of vortex shedding and the interaction between the two shear layers leading first to a reduction in fluctuation levels and then to the suppression of vortex shedding. After the suppression of vortex shedding, the RMS light intensity distribution is primarily related to the small scale vorticity production due to shear within the recirculation zone, bound on each side by the shear layers.

5.6 Time traces and power spectra

To show the transition of the cylinder wake from a clear vortex shedding mode to its final suppression, the time traces and corresponding power spectra of the light intensity fluctuation in the schlieren images are shown in Figure 5.15 and 5.16 for circular and square cylinders, respectively. These are presented for three different stream-wise locations namely, $x/d = 2$, 3.5 and 5 and three transverse locations, $y/d = 0$, 0.35 and 0.7 (0.75 for square cylinder) as a function of Richardson number. The power spectra have been calculated using 1250 images acquired over 5 seconds at a rate of 250 frames per second. The time traces are drawn from 250 successive schlieren images for total of one

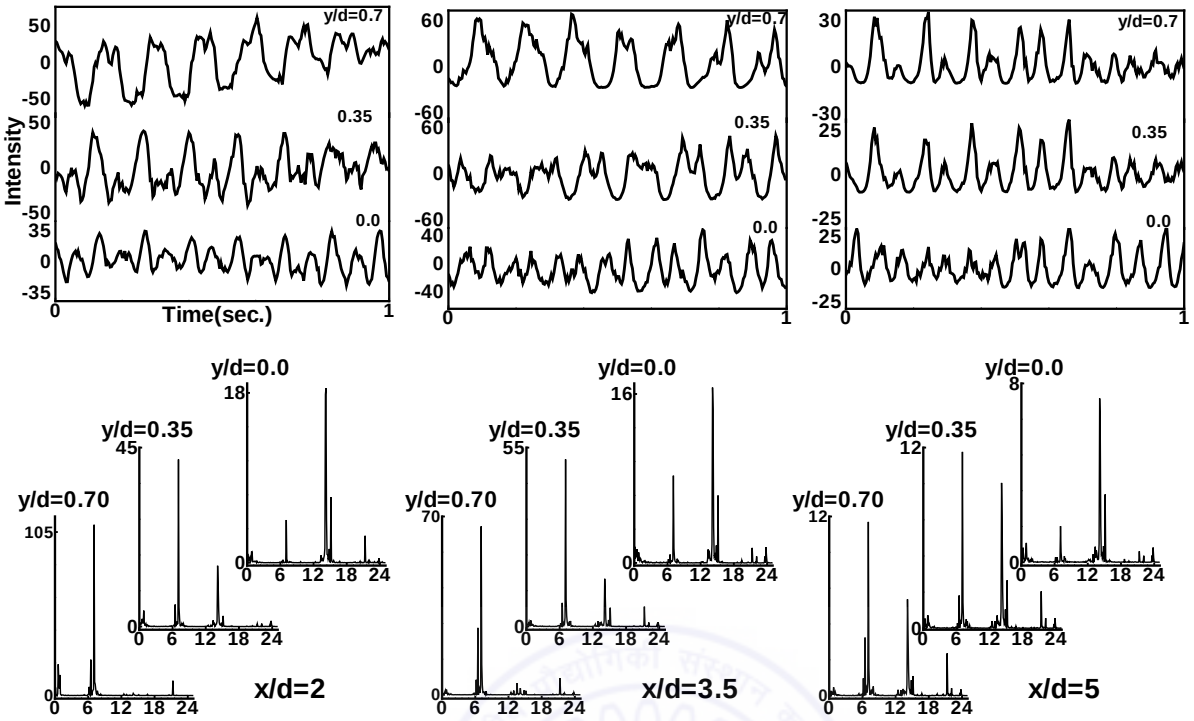

(a)

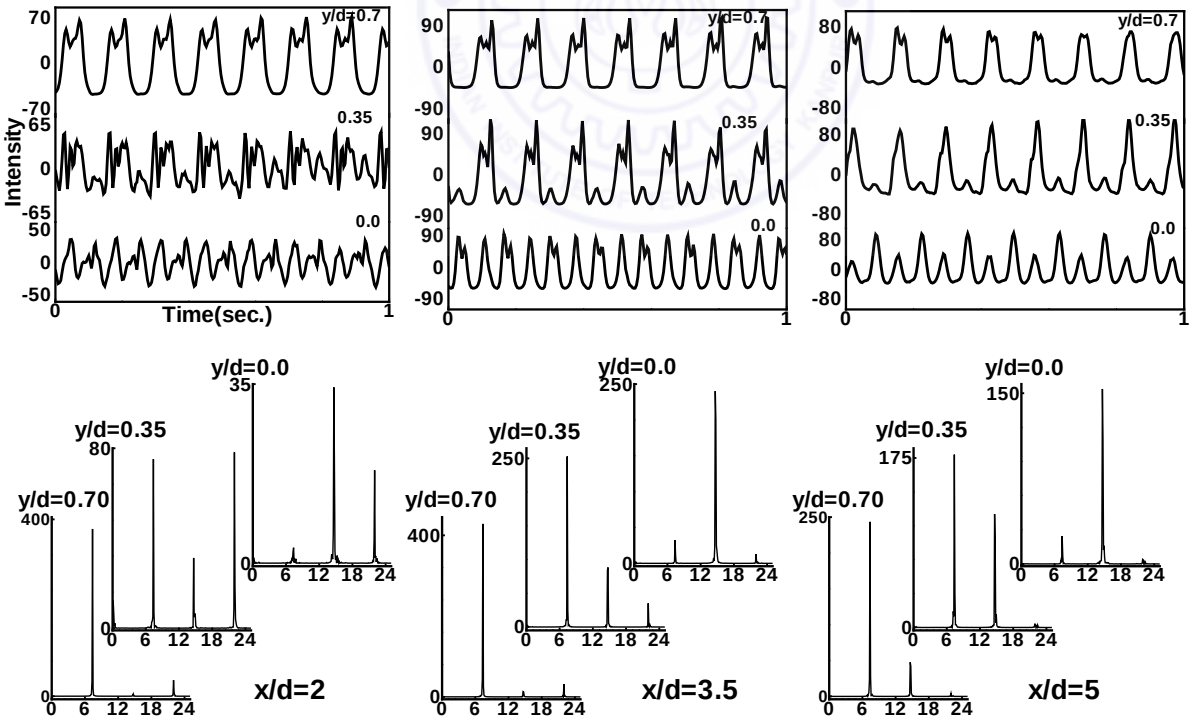

(b)

see caption on the facing page

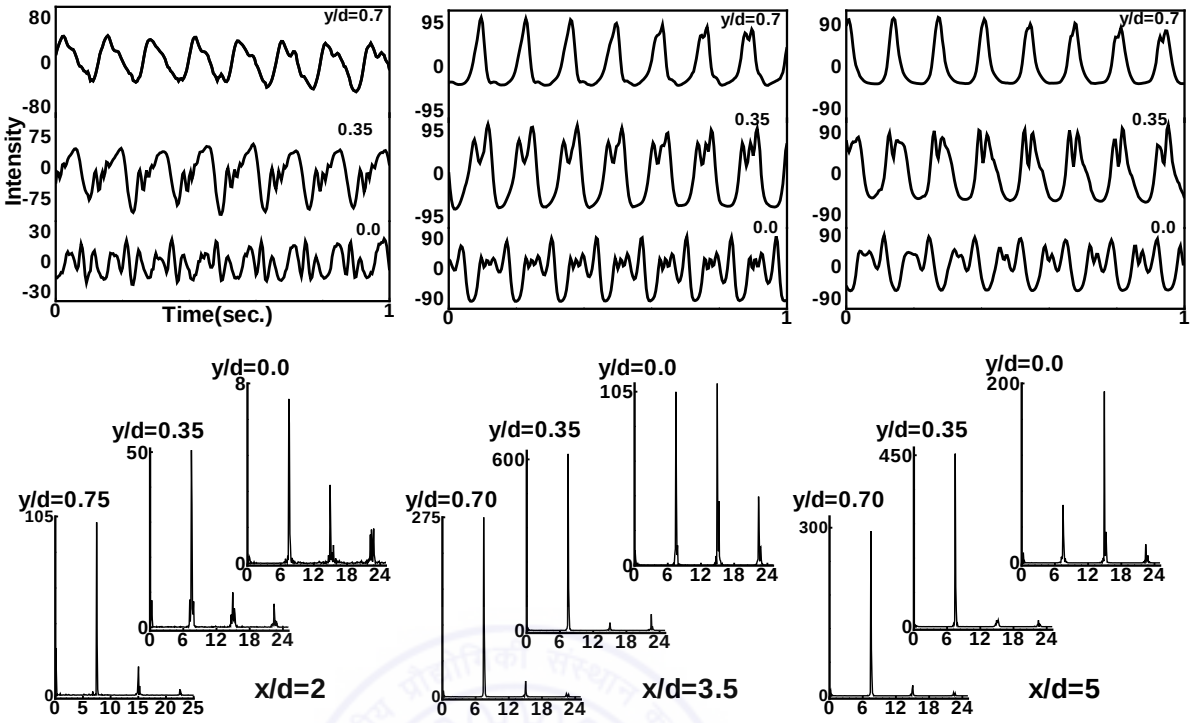

(c)

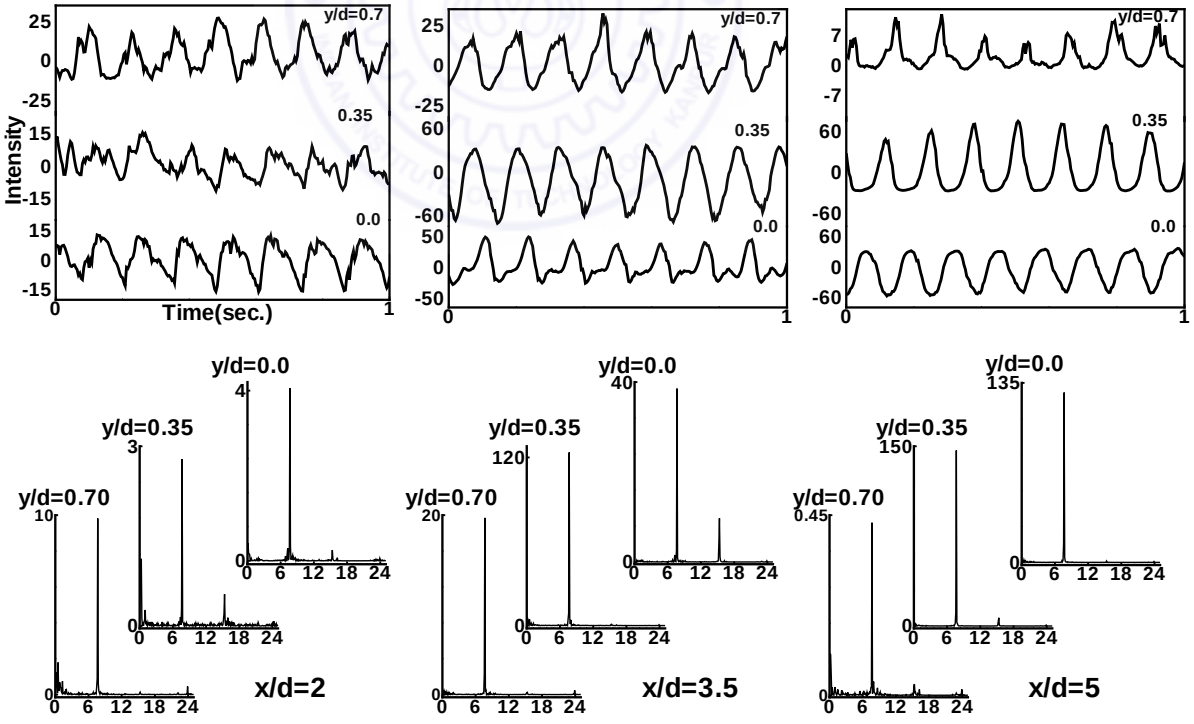

(d)

see caption on the next page

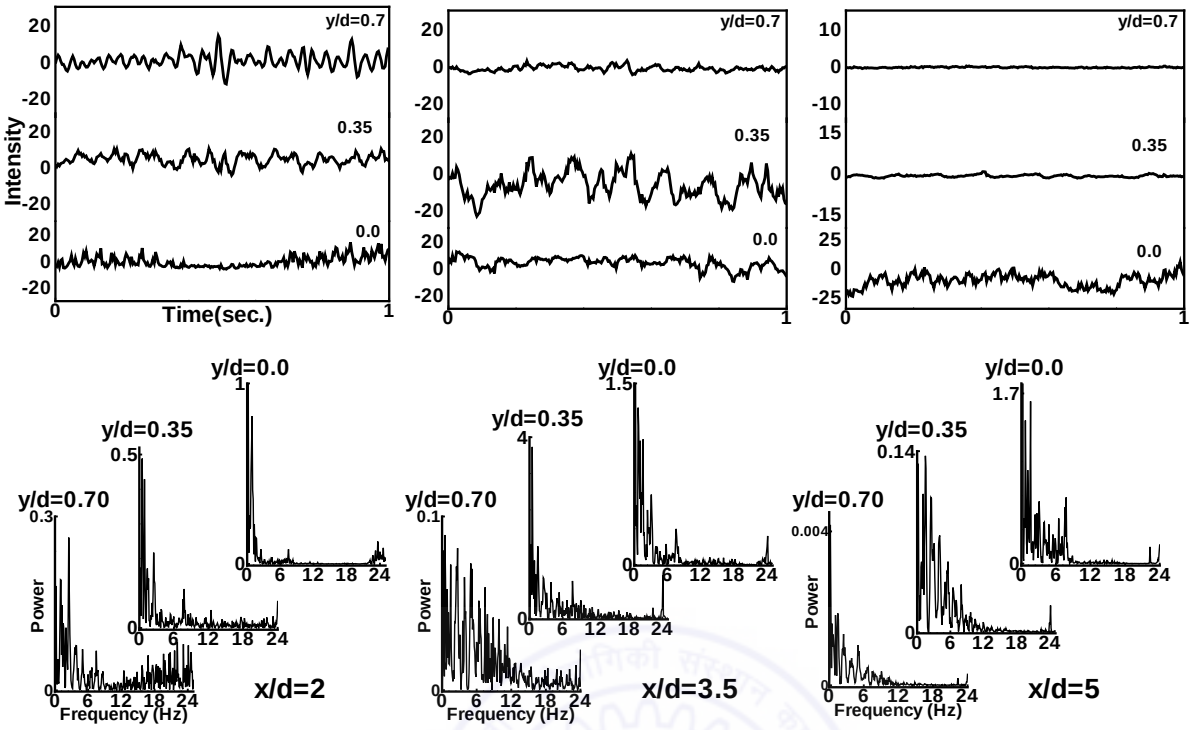

(e)

Figure 5.15: Time traces and power spectra of light intensity at various streamwise and transverse locations for a circular cylinder at Re=110. (a) Ri=0.052, (b) Ri=0.104, (c)Ri=0.140, (d)Ri=0.150, and (e) Ri=0.157. Time traces are shown for one second.

second duration. At all locations, the light intensity is averaged over 4×4 pixels to diminish pixel level noise.

In Figure 5.15 (a), for Ri=0.052, a clear dominant frequency is observed inside the shear layer at $y/d = 0.7$ for all streamwise locations and is an indication of the vortex shedding. The time traces show regular variation of intensity with some amount of aperiodicity. At the central region of the cylinder ($y/d = 0.0$), a clear spectral peak at twice the shedding frequency is observed. This can be attributed to the influence of the vortex interactions from the opposite shear layers. At an intermediate location, $y/d = 0.35$, both fundamental and harmonic modes are significant. At these locations, the time traces also show higher harmonics superimposed over the regular large-scale intensity variation. Overall, the nature of spectra properly corresponds to the trend observed in the respective time traces. Figure 5.15 (b) shows that with an increase in Richardson number (Ri=0.104), the intensity variation become regular and less noisy, indicating that initial heating strengthens the vortex shedding mechanism. The harmonics at the inner regions (close to the cylinder centerline) get strengthened due to the increased interaction between the neighboring vortices from the opposite shear layers. The power spectra

at Ri = 0.104 shows a similar trend as that observed for Ri = 0.052, i.e. a dominant fundamental mode inside the shear layer at $y/d = 0.7$ location, both fundamental and harmonic modes at $y/d = 0.35$ location and influence of the first harmonic in the central region at $y/d = 0.0$. The subsequent increase in Richardson number at Ri = 0.140 in Figure 5.15 (c) shows the absence of the harmonic mode at $y/d = 0.35$ location. The fundamental mode alone is significant similar to that observed for $y/d = 0.70$ location. This can be attributed to reduced interactions between the vortices from opposite shear layers at the elevated cylinder temperature of 75°C (Ri = 0.140). The subsequent increase in Richardson number to 0.150 in Figure 5.15 (d) shows only fundamental mode to be significant for all streamwise and transverse locations. There is no significance of harmonics in the inner region, in contrast to that at smaller Richardson numbers. The time trace also confirms regular periodicity in intensity variation at all stream-wise and transverse locations for Ri = 0.150. No higher harmonics are present near the centerline, $y/d = 0$. This trend can be attributed to the modification of shedding from symmetric to straight slender structures, Figure 5.3 (e). The power spectra at large Richardson number (Ri = 0.157) in Figure 5.15 (e) correspond to vortex suppression and show absence of any clear peak. The spectra are of the broadband type with small amplitude indicating an overall suppression of unsteadiness as confirmed by the appearance of steady plume in the visualization images in Figure 5.3 (f). Simultaneously, the time traces show irregular small-scale variation. The spectra, thus, evolve from being highly peaked at the vortex shedding frequency to broadband with the disappearance of vortex shedding. The overall trend of the spectral magnitude for all locations show that it increases with Richardson number but drops subsequently. The initial increase in the spectral magnitude at mild heating levels is due to enhanced vortex strength and moderate increase in cross-stream diffusion. The subsequent decrease in the spectral amplitude at elevated Richardson numbers can be attributed to the weakened vortices and a result of diminished cross-stream transport.

For the square cylinder, Figure 5.16 (a) shows a dominant frequency inside the shear layer at $y/d = 0.75$ for Ri = 0.059 indicating clear vortex shedding. The time trace of intensity shows regular variation of intensity with respect to time. The first harmonic is significant at the central region ($y/d = 0$) for x/d =3.5 and 5.0. This may be attributed to the interaction between the vortices in the opposite shear layer. Both fundamental and harmonic modes are significant at the intermediate location ($y/d = 0.35$). The time traces also shows higher harmonics superimposed over the regular large-scale intensity variation. The power spectra at Ri = 0.108 in Figure 5.16 (b) shows a similar trend as that for Ri = 0.059, i.e. a dominant fundamental mode inside the shear layer and influence of the first harmonic in the central region. The time trace of intensity shows periodic intensity

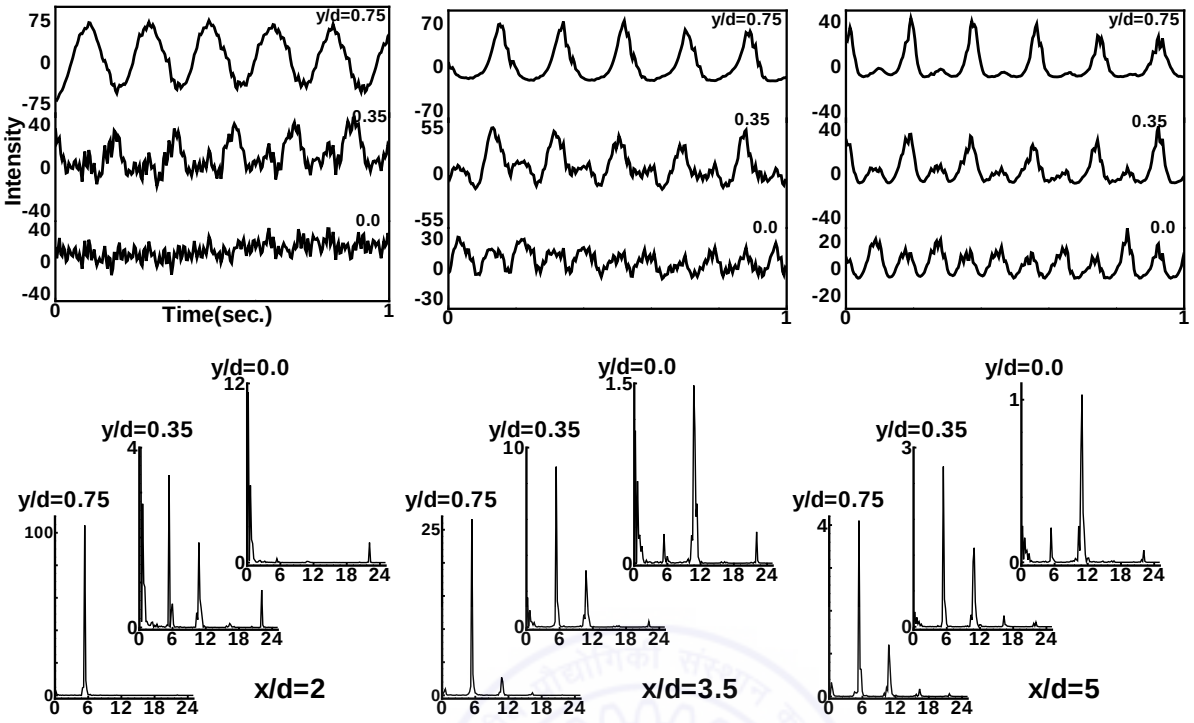

(a)

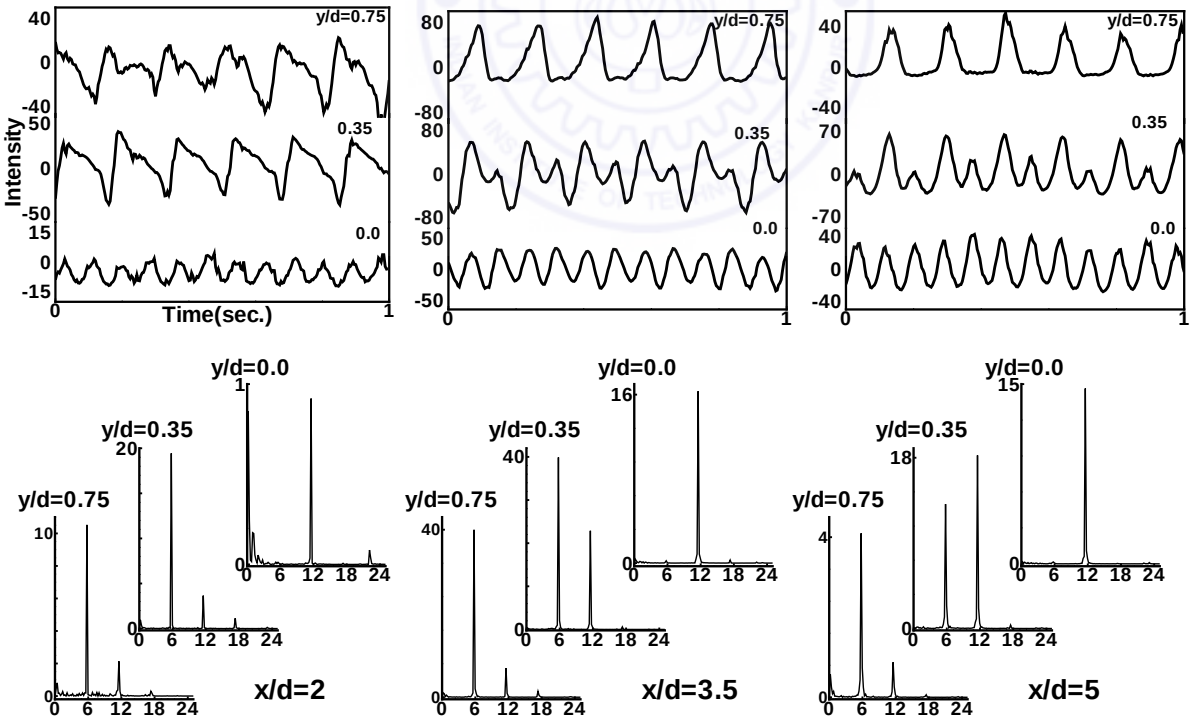

(b)

see caption on the facing page

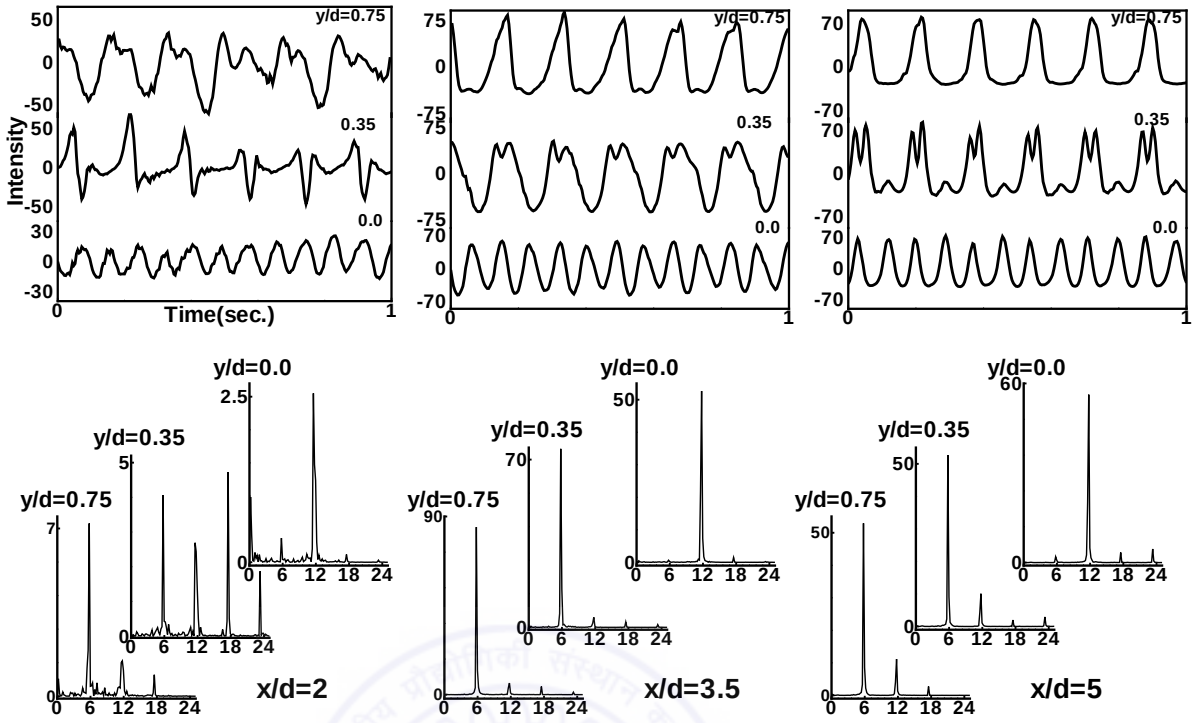

(c)

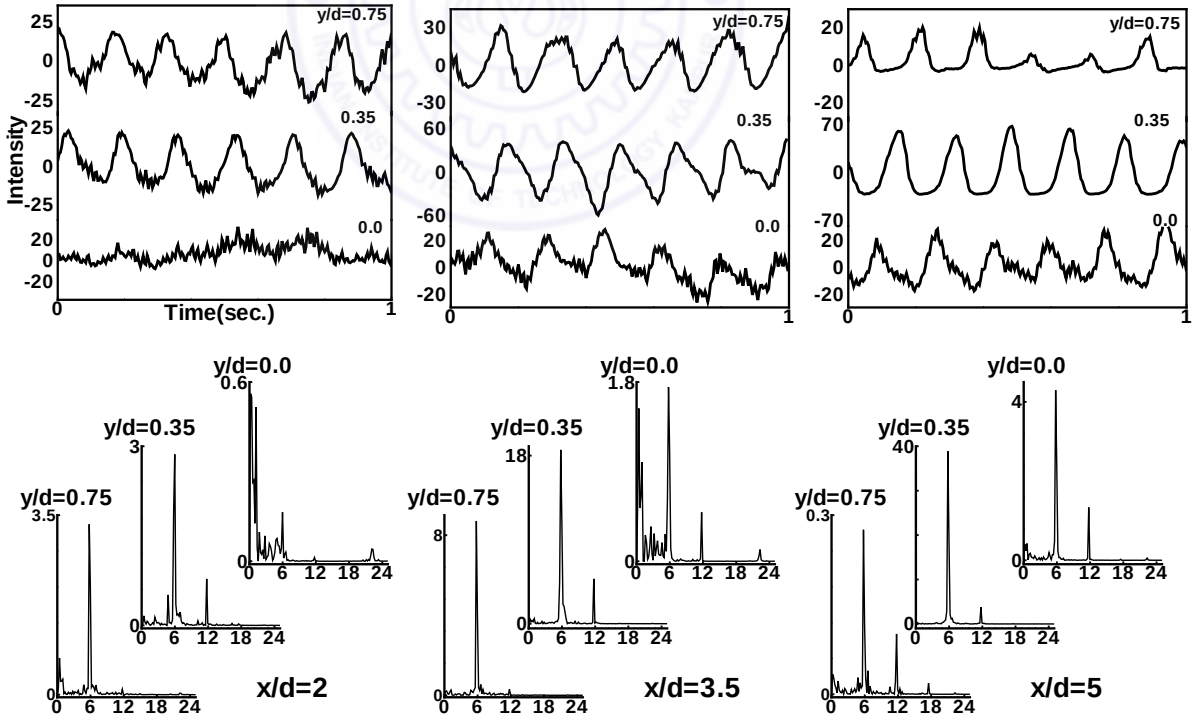

(d)

see caption on the next page

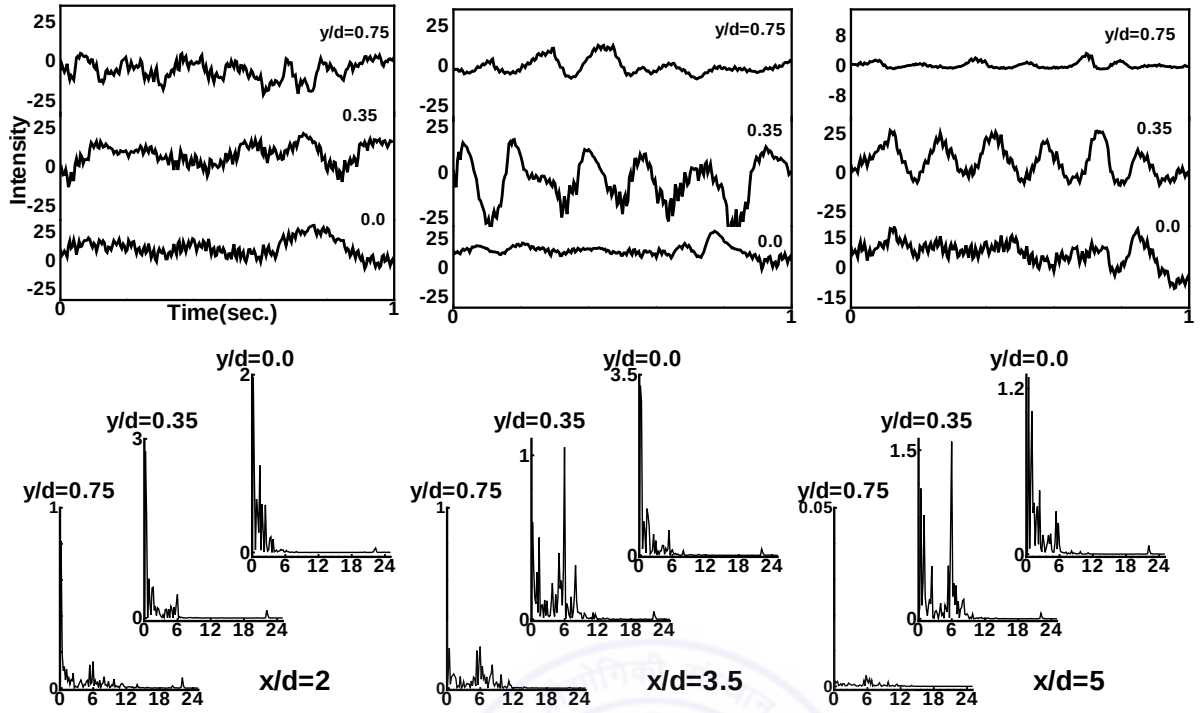

(e)

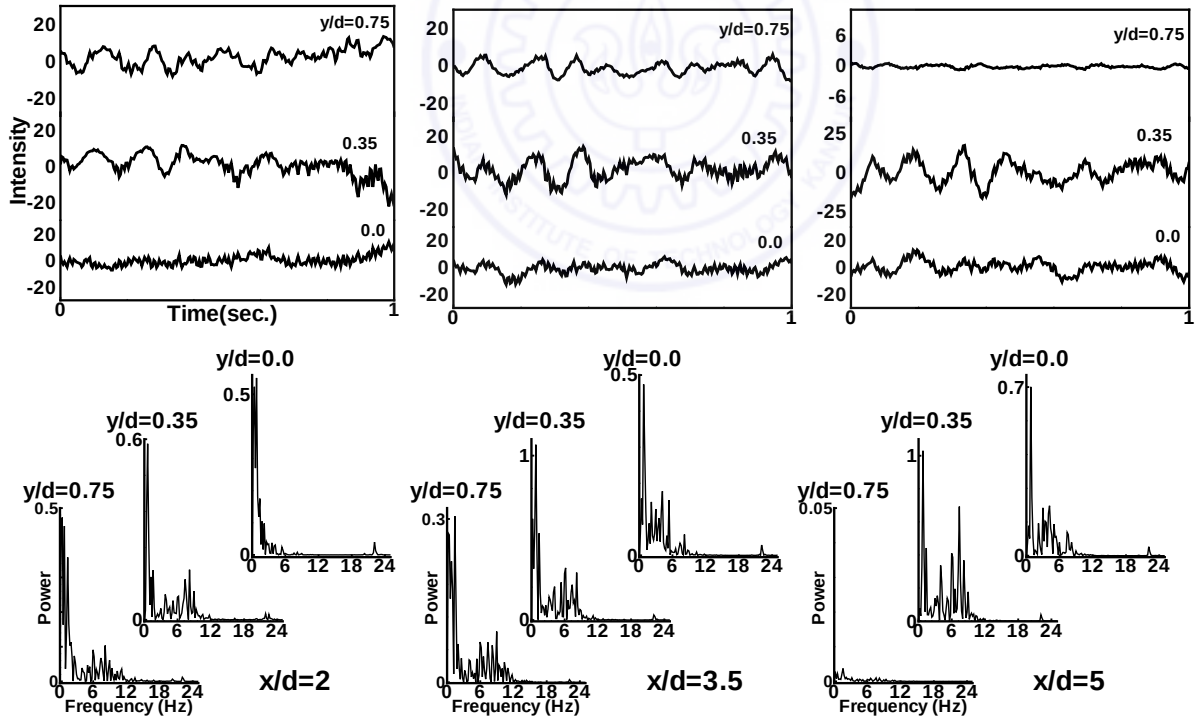

(f)

Figure 5.16: Time traces and power spectra of light intensity at various streamwise and transverse locations for a square cylinder at Re=109. (a) Ri=0.059, (b) Ri=0.108, (c)Ri=0.117, (d)Ri=0.124, (e)Ri=0.133, and (f) Ri=0.155. Time traces are shown for one second.

distribution corresponding to vortex shedding frequency at $y/d = 0.35$ and its half-time period at $y/d = 0$. The subsequent increase in Richardson number to 0.117 in Figure 5.16 (c) shows the fundamental mode alone to be significant at $y/d = 0.35$ location for $x/d =$ 3.5 and 5.0 locations. This is in contrast to the combined presence of fundamental and harmonic mode at $y/d = 0.35$ location at lower Richardson numbers. Multiple peaks are still seen near the cylinder at $x/d = 2.0$ and $y/d = 0.35$ location. At this location, the time trace results show the irregular shape of the periodic intensity fluctuation distribution. The frequency doubled periodic structures are seen in the central region of the cylinder. With further heating, Figure 5.16 (d) shows that fundamental mode alone is significant at all locations for Ri = 0.124. There is no significance of harmonics in the inner region, in contrast to that at smaller Richardson number. The time trace also confirms regular periodicity in intensity variation at all stream-wise and transverse locations for Ri = 0.124. No higher harmonics are present near the centerline, $y/d = 0$. This can be attributed to the modification of shedding from symmetric to straight slender structures and absence of vortex interaction between the two opposite shear layers, Figure 5.4 (d). Similar trend in the power spectra without frequency doubled harmonics are observed for the circular cylinder at Ri = 0.150 in Figure 5.15 (d), indicating identical influence of buoyancy. The power spectra at Ri = 0.133 in Figure 5.16 (e) shows the fundamental mode to be significant at $y/d = 0.35$ and $x/d = 3.5$ and 5.0 location. The time traces show the intensity fluctuation to be aperiodic in nature at Ri = 0.133. The flow visualization images at this Richardson number in Figure 5.4 (e) shows mild unsteadiness of the shear layer without any regular shedding. Hence, the increase in the Richardson number leads to inhibition of shedding process and oscillation of the shear layer. The power spectra at Ri = 0.155 show absence of any clear peak and there is a broadband spectra, Figure 5.16 (f). Regular vortex shedding is now suppressed at this Richardson number. The time traces show irregular small scale random variation. The spectra evolving from being highly peaked at the vortex shedding frequency to a broadband appearance show the disappearance of vortex shedding. The visualization images in Figure 5.4 (f) show that two shear layers have merged into one leading to a single steady plume at the center of the cylinder. A similar overall trend of the spectral magnitude with Richardson number is observed for the square cylinder as that of the circular cylinder.

The similar overall behavior of the power spectra for both square and circular cylinders indicate identical influence of buoyancy. A comparison of the time traces of the circular cylinder with that of the square shows that the shedding characteristics of the two are similar. Frequency doubled harmonics are seen in each set of experiments close to the midplane above the cylinder at lower Richardson numbers. At an elevated Richardson number, the harmonic mode disappears and only fundamental mode prevails at all the

locations for both cylinders. This is due to similar modifications in the shape of the vortex structures and absence of interactions for both the geometries.

5.7 Velocity profiles

The time-averaged streamwise velocity profiles across the wake of the heated square cylinder as a function of Richardson number are presented in Figure 5.17. Data has been presented at a streamwise location of $x/d = 13$. Measurements have been carried out using a pitot static tube with a high-resolution differential pressure digital micro-manometer. The Reynolds number based on the undisturbed flow condition is 110. The velocity measurements can be influenced by changes in temperature of the fluid due to the density variation. This leads to a possible error in the velocity measurement unless proper corrections are implemented for the change in temperature. To quantify the maximum error in the velocity measurement (at $x/d = 13$) on account of high fluid temperature in the wake, temperature measurement has been carried out by placing a thermocouple at the wake center-plane. A maximum increase of 2.0°C in the centerline temperature was observed at the highest heating level. The related maximum uncertainty in velocity measurement at Ri =0.155 is shown as an error bar in the centerline data in Figure 5.17. The maximum uncertainty in velocity measurement is found to be less than 0.3%.

Velocity profile at cylinder surface temperatures of 45, 60, 67, and 80°C (Ri = 0.053, 0.098, 0.118, and 0.155, respectively) are compared in Figure 5.17 with the unheated cylinder. The maximum heating level with Richardson number of 0.155 corresponds to the suppression of vortex shedding. The velocity deficit of the wake decreases with an increase in Richardson number. The wake size i.e. the transverse extent of the low velocity region reduces with an increase in Richardson number. At a Richardson number of 0.118, the velocity deficit disappears and the velocity profile is close to uniform. At this condition, the buoyancy forces add enough momentum to cancel the momentum deficit due to the cylinder blockage. With subsequent increase in the Richardson number, the velocity inside the wake exceeds that of the free stream velocity.

Michaux-Leblond and Belorgey (1997) observed increase in velocity and decrease in wake width behind a circular cylinder in a water tunnel with increase in cylinder temperature. They reported complete suppression of recirculation bubble at higher heat inputs. With an increase in heat input, the increase in the wake velocity can be attributed to the additive effect of buoyancy in an aided flow configuration. The heated cylinder acts as an effective pump or a self propelled body. Therefore, the suppression of vortex shedding can be related to the cancellation effect of thermal pumping and fluid inertia,

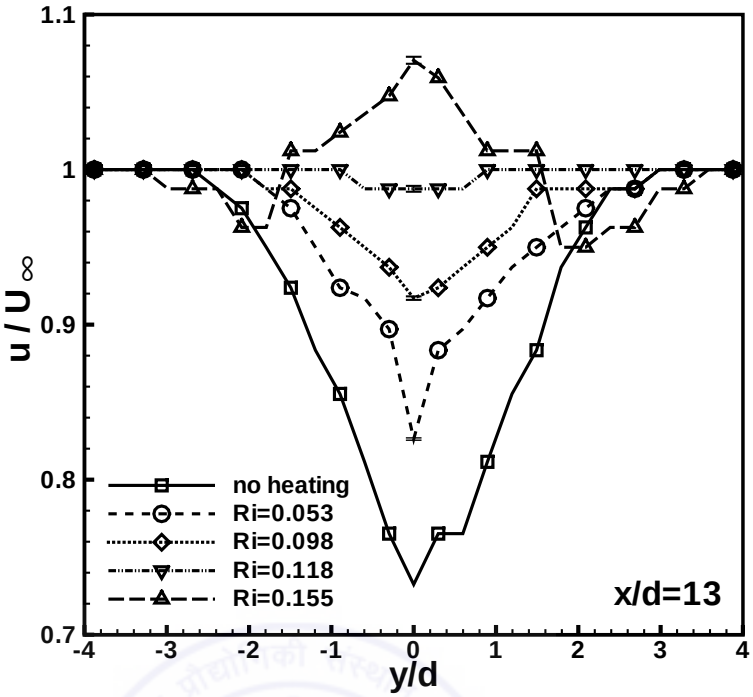

Figure 5.17: Streamwise velocity profile across the wake of a heated square cylinder as a function of Richardson number. The streamwise location selected for the plot is $x/d = 13$ and the Reynolds number, Re = 110.

leading to the disappearance of the velocity deficit. The curvature of the velocity profile in the wake changes due to heating of the cylinder. This modifies the wake instability characteristics. It provides an alternative explanation to elimination of vortex shedding at high Richardson number. The above trends were seen for a circular cylinder as well.

5.8 Temperature distribution

Temperature variation in the wake of a heated square cylinder has been obtained by analyzing schlieren-interferograms. The center of the dark fringe corresponds to the location of the isotherm. The time-averaged temperature distribution in the wake of a heated square cylinder is shown in the form of dimensionless profile ($\theta = (T - T_\infty)/(T_w - T_\infty)$) in the streamwise direction. The Reynolds number for the present experiment is 109. Temperature profiles are presented in Figure 5.18 (a) and (b) as a function of Richardson number at cylinder centerline ($y/d = 0.0$) and an offset location ($y/d = 0.35$), respectively. It is seen that temperature decreases continuously in the streamwise direction for both y-locations and at all Richardson numbers. The increase in Richardson number reduces the slope of the dimensionless temperature profile. Therefore, the heated zone spreads over a

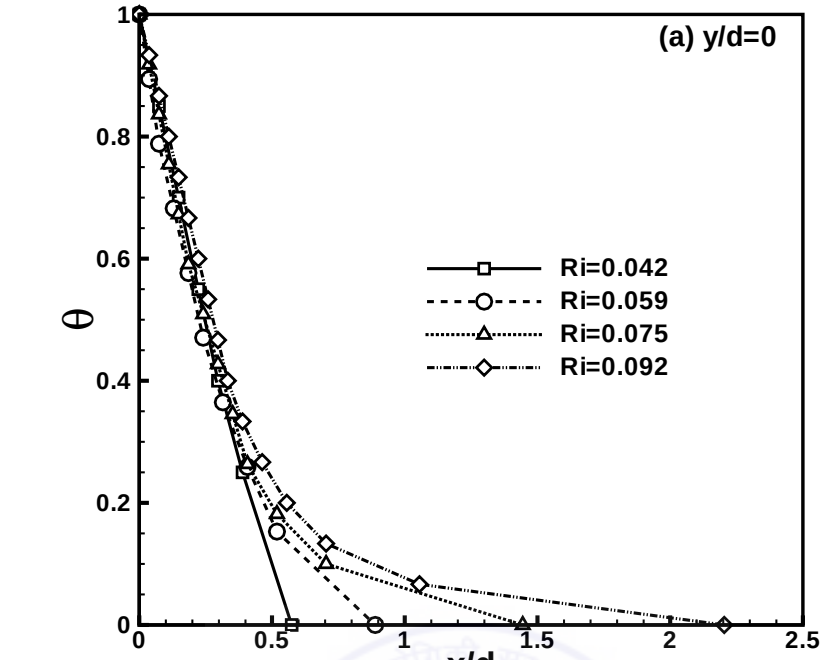

(a)

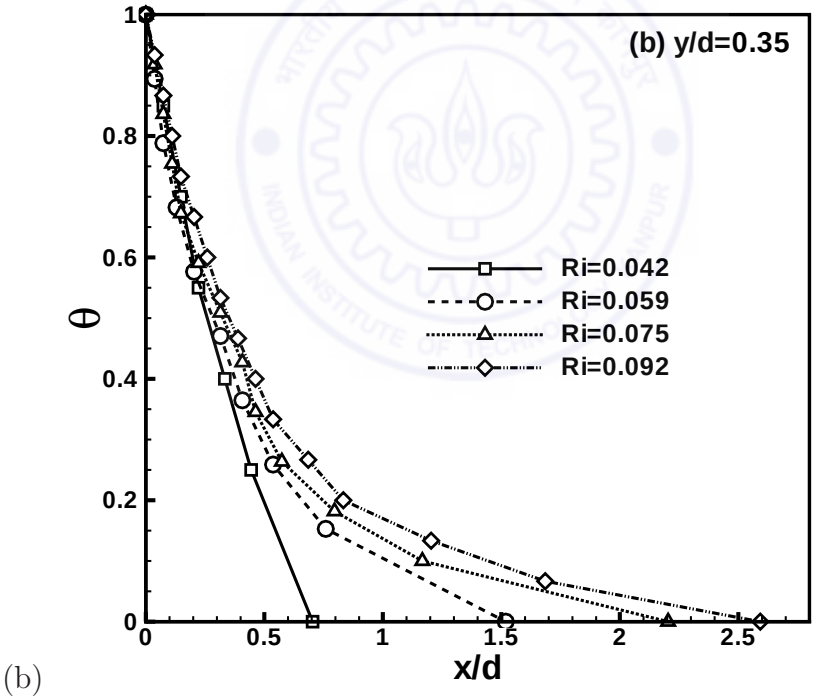

(b)

Figure 5.18: Dimensionless temperature profiles in the wake of a heated square cylinder as a function of Richardson number. Re=109. (*a*) $y/d = 0$, and (*b*) $y/d = 0.35$.

longer distance downstream. For the centerline data ($y/d = 0$), the temperature profiles at various Richardson numbers merge over a distance of x/d = 0-0.4. This indicates that heat transfer in the near field region of the cylinder is primarily by diffusion. When y/d = 0.35, the overlap occurs only upto $x/d = 0.2$. This can be attributed to greater influence of the external flow field inside the shear layer than that at the centerline.

5.9 Convection velocity of vortices

The convection velocity, u_c, defined as the average traveling velocity of vortex structures has been determined from a pair of time separated schlieren images as discussed in Section 4.3. Figure 5.19 (a) and (b) show the variation of the non-dimensional streamwise convection velocity behind a square cylinder as a function of the dimensionless streamwise coordinate and Richardson number. The data is presented at Reynolds numbers of 109 and 118. For the range of parameters considered, it is clear that u_c/U_∞ increases from 0.35 to 0.85 over $2.7 \leq x/d \leq 5.2$. The increase in the heating level increases the length of the base region i.e. the inception of vortex shedding and the instant of vortex detachment from the cylinder is delayed. Subsequently, when shedding is initiated, structures attain similar asymptotic speeds. The convection velocity at a given streamwise location is, however lower for a higher Richardson number. The convection velocity falls to zero beyond the critical Richardson number, when shedding has been suppressed.

For small Richardson number i.e. at Ri = 0.059, the nature of convection velocity variation in the streamwise direction is similar to that observed in a circular cylinder wake (Lin and Hsieh (2003)). Lin and Hsieh (2003) observed the convection velocity to increase from $0.5 \times U_\infty$ to $0.8 \times U_\infty$ at Re = 160. In present case (Figure 5.19 (a)), the convection velocity increases from $0.44 \times U_\infty$ to $0.74 \times U_\infty$ at Re = 109 for square cylinder. The variation of convection velocity in the streamwise direction changes with an increase in Richardson number. In the near field region ($x/d < 4$), the slope of the convection velocity variation is lower when compared to that in the far field at higher Richardson numbers (Ri = 0.075, 0.117 and 0.124). This indicates that the wake can be broadly categorized into two zones; the near field zone, in which diffusion due to viscosity and thermal effects influence the vortex motion and the far field zone, in which inertia and buoyancy effects dominate. Therefore, differing slopes in the convection velocity variation are observed at two Reynolds number (Re = 109 and 118), Figure 5.19. Overall, heating influences the dynamics of vortex structures in the wake of the heated cylinder when compared to that of an unheated cylinder.

5.10 Phase shift

The evolution of phase shift of vortex structures between two streamwise locations is reported in Figure 5.20 as a function of Richardson number. The phase difference between streamwise locatins, x/d = 2-3.5 and x/d = 2-5 at transverse location, $y/d = 0.75$ as a function of Richardson number is reported for Re = 109 and 118. The streamwise locations

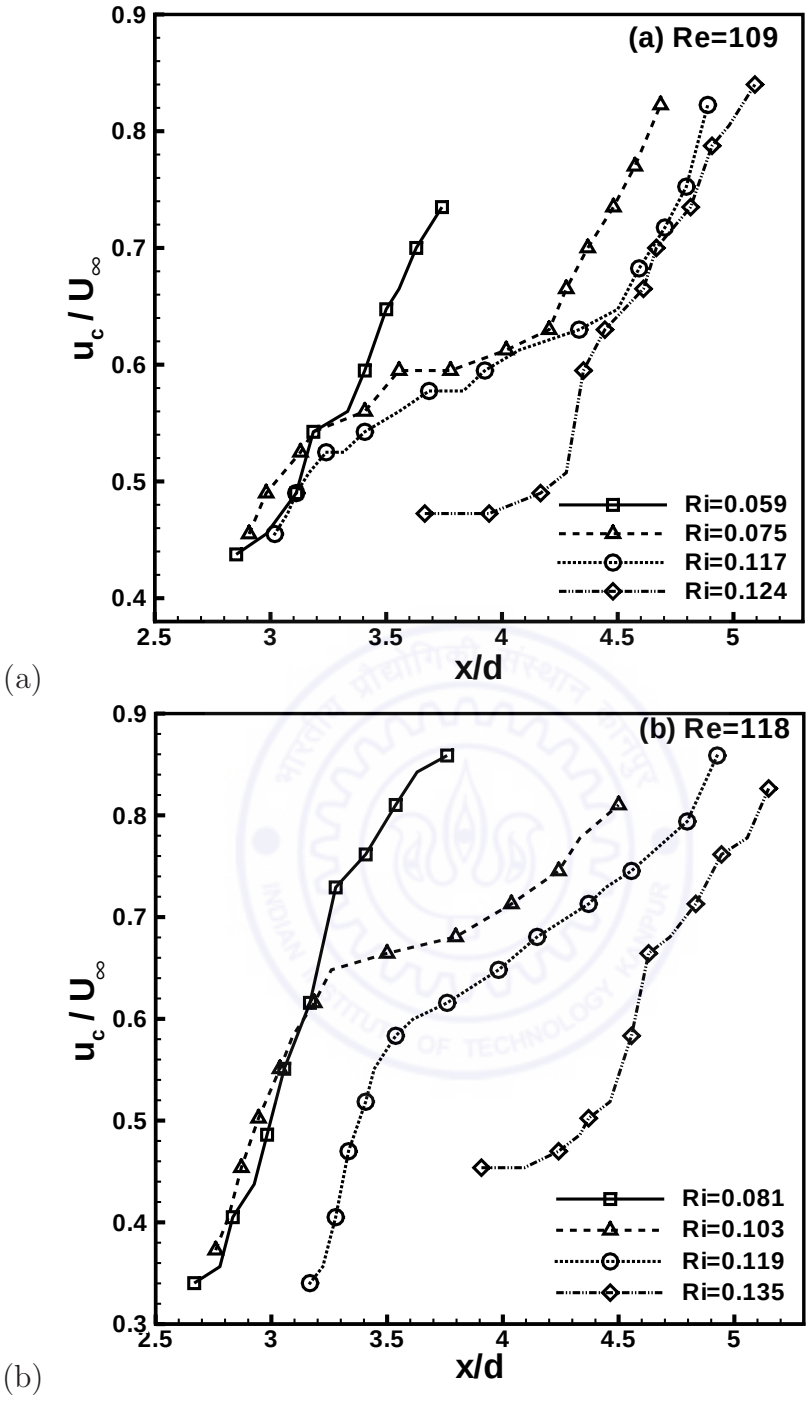

Figure 5.19: Non-dimensional convection velocity of vortex structures as a function of the streamwise coordinate in the wake of a heated square cylinder. (a) Re = 109, and (b) Re = 118.

(x/d = 2, 3.5 and 5) have been selected to investigate the coherence of vortical structures in the near field and far field region. As expected, the phase difference between $x/d = 2$ and 5 is higher than that between $x/d = 2$ and 3.5 locations. It is seen that an increase in Richardson number increases the phase difference of the vortex structures. Equivalently,

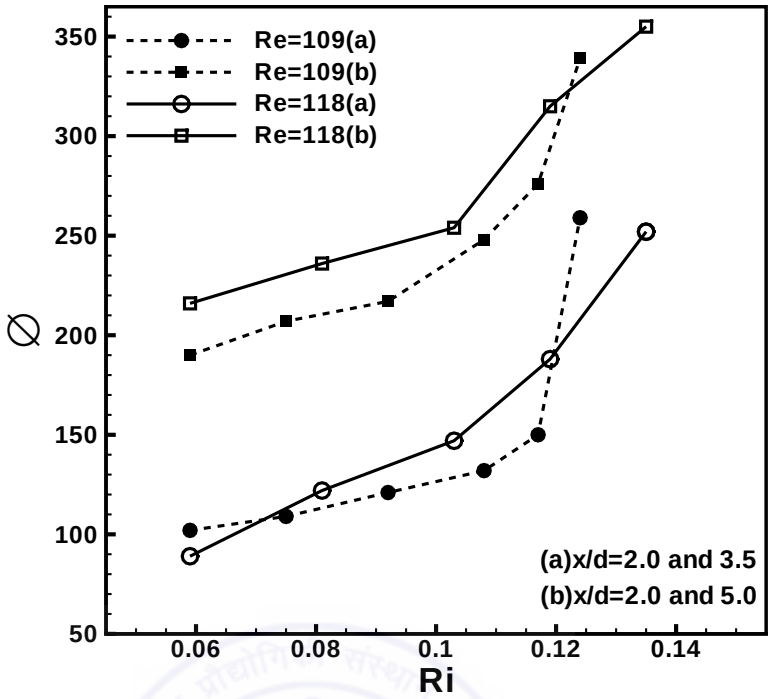

Figure 5.20: Variation of phase shift between two streamwise locations in the wake of a heated square cylinder as a function of Richardson number at two Reynolds number, Re = 109 and 118. The transverse location selected is $y/d = 0.75$.

it reduces the convection velocity of vortices (see Figure 5.19). The increase in phase difference of vortex structure is gradual at lower Richardson numbers, but shows a sharp increase at higher Richardson numbers. This indicates that in the near field region, the phase evolution is primarily related to the temperature dependent fluid properties. In the far field, the buoyancy induced vortex interaction influences the evolution of vortex structures. the increase in Richardson number leads to greater phase decorrelation of vortex structures resulting in higher dissipation and hence suppression of regular vortex structures.

5.11 Instability mechanism

To understand the mechanism of vortex shedding suppression by heat input, the physics of vortex formation needs to be understood. Gerrard (1966) proposed the 'vortex street' formation to be a function of the formation length, specifically, the relative scales in the formation and diffusion regions. According to this model, the separated shear layer feeds the circulation to the growing vortex until it becomes strong enough to draw the opposite shear layer across the wake. At this point, the approach of oppositely-signed vorticity

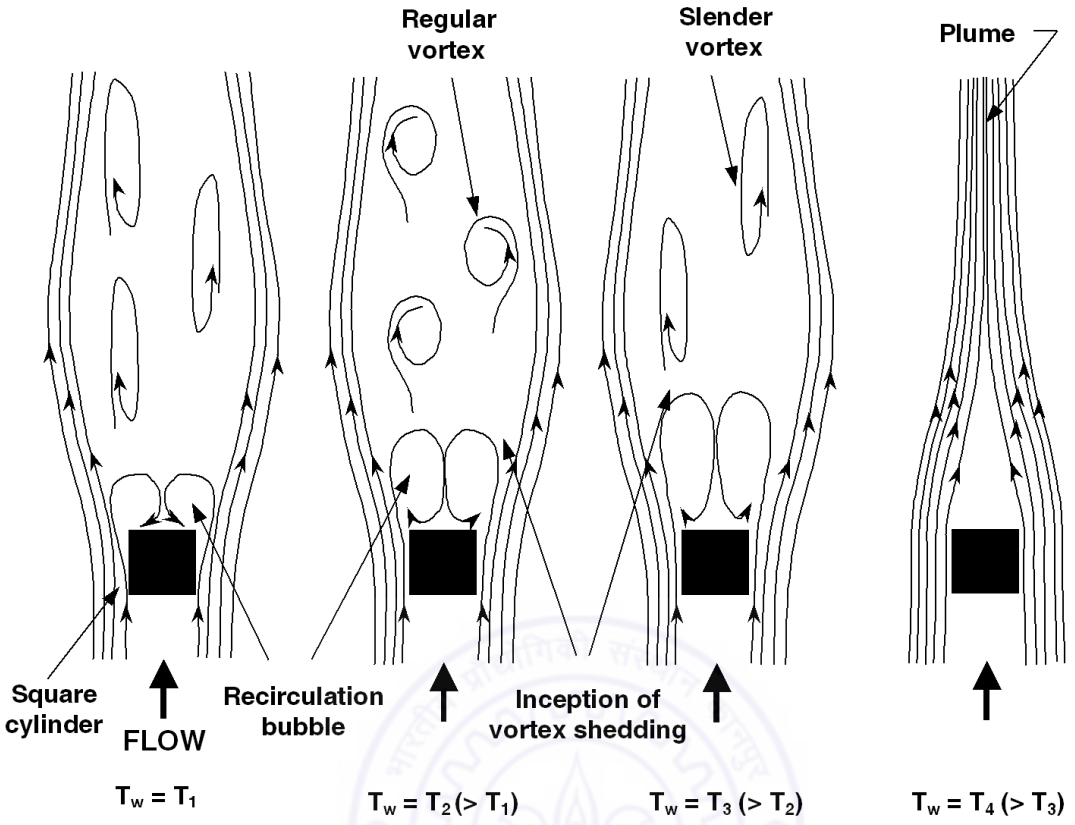

Figure 5.21: Schematic sketch of flow patterns showing the progressive suppression of vortex shedding behind a heated square cylinder.

in sufficient concentration cuts off further supply of circulation to the growing vortex, which then ceases to increase in strength and is shed. For a vortex to be cutoff from its feeding shear layer and shed, the interaction of the oppositely-signed shear layer plays an important role. Strykowski and Sreenivasan (1990) explained that according to Gerrard's model, the circulation in the shear layer must be sufficient to draw the opposite shear layer across the wake center-plane. Further, this interaction must take place before the formation length is reached. The vortex street is inhibited if vorticity in the shear layer diffuses over a critical diffusion length or the shear layers are prevented from interactions over a critical formation length. The time-averaged images of the present work (Figures 5.9 and 5.10) show that with an increase of heat input, the length of the base region increases and the instant of vortex detachment from the cylinder is delayed, leading to an increase in the formation length. The instantaneous visualization images show that the shape of vortex structures become slender-like at a higher Richardson number. The power spectra show absence of multiple peaks in the cylinder centerline at higher Richardson number (Figure 5.15 and 5.16). This indicates the reduction in the circulation of these structures as well as interaction between neighboring vortex structures of the opposite shear layers.

Owing to an increase in formation length, these structures rub each other from opposite sides. The transverse interaction between the shear layers is however insignificant. The slender vortices behave as a single plume oscillating at the shedding frequency. The plume becomes steady at the critical value of heat input. The u-velocity profile in the wake shows that buoyancy forces accelerate the fluid in the boundary layer and balance the deceleration of fluid caused by an adverse pressure gradient. Buoyancy adds enough momentum to reduce and finally stop the entrainment of the ambient fluid into the wake.

A schematic describing the mechanism of vortex formation and its evolution behind a heated cylinder is shown in Figure 5.21. At a lower heating level, the size of the recirculation bubble and the formation length of vortex shedding increase with increase in Richardson number. This may be attributed to the cancellation of inertial vorticity content by the baroclinic vorticity production due to density gradient. However, additional momentum of buoyancy regularizes the vortex shedding initially at lower Richardson numbers. With subsequent increase in Richardson number, the formation length of vortex shedding is higher and there is a transformation to slender vortical structures. At this heating level, there is minimal interaction between the vortices of opposite shear layers in the sense that there is no feeding of circulation between these shear layers for the growing vortex bubble before commencement of shedding. With subsequent increase in Richardson number, the recirculation bubble disappears due to sufficient momentum injected by buoyancy. The flow field behind the cylinder appears as a natural convection plume.

5.12 Summary

This chapter reports the effect of buoyancy on wake instability of heated circular and square cylinders. Temporally resolved schlieren imaging is used for flow visualization and quantitative characterizations. The effect of heating level i.e. Richardson number in the range of 0.025-0.314 on the characteristics of vortex structures are investigated at various Reynolds numbers near Re = 100. Some key observations from this study are summarised below.

Vortex shedding behind circular and square cylinders is a function of both Reynolds number and Richardson number. The similarities in schlieren visualization images, vortex formation lengths, time traces and power spectra between the two geometries indicate that both experience similar flow mechanisms for instability i.e. vortex shedding. The Strouhal number is higher at higher Reynolds numbers and slowly increases with an increase in Richardson number. Beyond a certain critical Richardson number, the vortex shedding abruptly ceases and Strouhal number falls to zero. There is a linear relationship

between critical Richardson number and Reynolds number. Instantaneous visualization images show that the shape, size and time-dependent movement of vortex structures are altered with increase in Richardson number. Before suppression of vortex shedding, the regular vortex structures are transformed to thin elongated structures of slender shape with minimal interaction between the vortices from opposite sides of the wake centerline. These patterns are subsequently replaced by a single and steady plume-like structure during suppression. The power spectra show a clear dominant frequency inside the shear layer and frequency doubled harmonic at the central region of the wake. At elevated Richardson number, the harmonic mode disappears and only fundamental mode prevails at all locations due to minimal interaction between the vortices and modification of shedding to slender structures. At the vortex suppression, the spectra show absence of any clear peak and there is a broadband spectra indicating an overall suppression of unsteadiness.

RMS fluctuations of light intensity is high for sub-critical Richardson numbers due to regular vortex shedding. The fluctuations increase to a maximum in the streamwise direction upto vortex formation length and subsequently reduces in downstream direction. RMS fluctuations is higher within the shear layers and reduces towards the cylinder centerline. Before suppression of vortex shedding, the fluctuation level diminishes due to lower interactions between the vortices of opposite shear layer and the fluctuation magnitude is insignificant at complete suppression of shedding. For both cylinders, the vortex formation length increases with an increase in Richardson number and approaches an asymptotic value. Similar values of asymptotic formation length at around equal Reynolds numbers for heated circular and square cylinders indicate similarity in the suppression mechanisms by the action of buoyancy.

For a vertical mean flow configuration, the cylinder surface temperature (T_w) provides best estimate of instability characteristics in the mixed convection regime for calculation of fluid properties. This observation is in contrast to the horizontal mean flow experiments in the forced convection regime, where an effective temperature based on initiation of vortex shedding successfully characterizes the wake instability. The time-averaged streamwise velocity profiles across the wake shows a decrease in velocity deficit with an increase in Richardson number. This trend continues till the velocity deficit disappears and the velocity profile is close to uniform. At this point, the buoyancy forces add enough momentum to cancel the momentum deficit due to cylinder blockage. With subsequent increase in Richardson number, the velocity inside the wake exceeds that of the free stream velocity due to the additive effect of buoyancy in an aided flow configuration. The convection velocity of vortex structures is a function of Richardson number and streamwise location. It increases in the streamwise direction for all Richardson numbers. The convection velocity at a given streamwise location is however lower for a higher Richardson

number. The convection velocity falls to zero after shedding has been suppressed. Phase shift of vortex structures between two streamwise locations increases with an increase in Richardson number. This increase in phase shift is attributed to the momentum provided by the aided buoyancy due to heating.

भारतीय प्रौद्योगिकी संस्थान कानपुर
INDIAN INSTITUTE OF TECHNOLOGY KANPUR

Chapter 6

Circular and Square Cylinder Wakes: Influence of Buoyancy and Transverse Oscillation

Flow past heated circular and square cylinders subjected to forced simple-harmonic oscillations in the transverse direction is investigated at low Reynolds number. The wake characteristics under combined influence of buoyancy and controlled cylinder oscillations have been presented. The approach is towards active manipulation of the near-wake flow field by simultaneous heat addition and small amplitude cylinder oscillations. Previous researchers have investigated the effect of forced cylinder oscillations on vortex shedding characteristics for an unheated circular cylinder and heat transfer characteristics for a heated circular cylinder in forced convection regime. These studies reveal that controlled cylinder oscillations influence the strength and interactions of the primary Von-karman vortices, which brings about desirable changes in the flow structures and heat transfer from the cylinder. The underlying mechanism is believed to be re-organization of the vorticity field in the presence of surface actuations. Apart from the effect of oscillations, the wake behaviour of non-oscillating cylinders have also been reported individually as a function of buoyancy. A detailed experimental study of buoyancy effect on the wake instability of circular and square cylinders have been presented in the previous chapter. The results show that vortex shedding is regular at lower Richardson number similar to that of unheated cylinder. The increase in Richardson number influences the circulation and the interactions of the vortex structures and finally results in ultimate suppression of vortex shedding at an elevated Richardson number. The experiments reported in this chapter depict that transverse oscillations of the cylinder excite the vortex structures to reappear at this Richardson number. The reappearance of the structures can be attributed to re-amplification of natural instability by additional energy imparted to the wake by cylinder oscillations. This indicates that additive effect of heat input due to

buoyancy as well as additional energy imparted to the flow by forced cylinder oscillations have significant influence on wake instability and hence vortex formation process in the near-wake region. The combined influence of buoyancy and controlled cylinder oscillations has not been studied earlier and forms the basis of present investigation. Such a study is important in the context of flow control and electronics cooling applications. The operating parameters i.e. Richardson number, frequency and amplitude of oscillations are varied to study the flow behaviour in forced and mixed convection regimes over a range of excitation frequencies from sub-harmonic to super-harmonic and for a small range of oscillation amplitudes above and below the threshold value for lock-on.

Cylinder oscillation provides a coupling between the unsteady flow field and the body motion. Blackburn and Henderson (1999) discussed the difference in fluid-structure interaction behaviour of free and forced oscillations. In the former, fluid-structure coupling can occur in both directions, as opposed to forced oscillations, where the fluid motion is coupled to the body motion but not *vice-versa*. Compared to free oscillations, forced oscillation helps in regularizing and idealizing every aspect of vortex induced oscillations and leads to almost repeatable wake states. The body motion can control the instability mechanism i.e. the vortex shedding process and thus the flow field can be manipulated according to the desired objectives.

When the cylinder is forced to oscillate, two periodic motions interact: the natural vortex-shedding motion with frequency f_s and the forced cylinder motion with frequency f_e. Due to the nonlinear interactions between the two oscillations, a variety of combination frequencies may be potentially excited. Minewitsch *et al.* (1994) using their numerical simulation showed that the forces acting on the cylinder oscillate not only with the frequencies f_e and f_s but also with the combination frequencies e.g. $(f_e + f_s)$ and $(f_e - f_s)$. Several of these frequencies correspond to new vortex shedding patterns which are essentially different than the naturally occurring vortex street. Williamson and Roshko (1988) observed a number of vortex shedding modes designated as '2S', '2P' and 'P+S' etc. in their visualization study. Ongoren and Rockwell (1988a) showed that excitation of the cylinder initially induce small-scale vortices at the excitation frequency (f_e), which interact themselves and coalesces to eventually form large-scale recovered vortices at f_v. In addition to the dominant spectral component f_v, a number of other interaction components $f_v^{'}$ were also present in the recovered wake frequencies. The patterns of vortex formation in the near-wake are functions of frequency ratio (f_e/f_s) and amplitude ratio (a/d). Here, a is the amplitude of the cylinder oscillation and d is the diameter/edge of the cylinder. At specific parameter combinations of f_e/f_s and a/d, the so called *lock-on* phenomenon or synchronization of the two periodic motions can be observed. Blackburn and Henderson (1999) described the phenomenon of lock-on as the result of an entrain-

ment process, in which vortex shedding is entrained by the cylinder motion, so that the vortex shedding frequency changes to match the cylinder oscillation frequency. When a sufficiently heated cylinder is oscillated, then in addition to frequency ratio (f_e/f_s) and amplitude ratio (a/d), Richardson number (Ri) is also a potential parameter to jointly influence the *lock-on* phenomenon. The geometry of the cylinder e.g. circular (oscillating separation points) or square (fixed separation points) may also play a role in phase-locking of the vortex structures with the cylinder oscillations. Moreover, it is also possible that oscillations of the cylinder only synchronizes the near-wake closer to the cylinder (vortex formation region) and near-wake away from the cylinder (beyond the vortex formation region) remains unsynchronized.

In this chapter, we address these unresolved issues by subjecting heated cylinders to controlled oscillations at defined frequency and amplitude. The concept of synchronization have been examined as a function of Richardson number (Ri), excitation frequency (f_e/f_s), excitation amplitude (a/d), stream wise location of the wake (x/d), and base geometry of the cylinder. Several representations including power spectra, lissajous trajectories, spectral coherence function, and instantaneous patterns of the near-wake vortex structures have been considered to define lock-on. In addition to these, the variation of f_v/f_s versus f_e/f_s is also presented to graphically demonstrate the *lock-on* behaviour. With the present approach, various types of locked-on states of vortex formation (e.g. no lock-on, quasi lock-on and lock-on) have been identified in the near-wake region. The essential features of these locked-on states are presented over significant portions of the parameter space containing Ri, a/d, f_e/f_s, x/d, and cylinder geometry. One salient feature of the present work is the quantitative characterization of phase-locking of the shed vortices with the cylinder oscillation and heating. The physics related to joint effect of buoyancy and transverse cylinder oscillations on the wake characteristics in a steady current is quite complex. The present study investigates the physical aspects of these classes of flow-structure interaction problem using quantitative schlieren imaging.

Experiments have been conducted over a wide range of buoyancy as well as oscillation parameters for the cylinders of both circular and square cross-sections. The Reynolds numbers are set at 105 and 116 for the circular and square cylinders, respectively. Four different heating levels i.e. Ri = 0.038, 0.078, 0.124 and 0.145 for circular cylinder and Ri = 0.030, 0.086, 0.121 and 0.167 for square cylinder are considered. These Richardson numbers correspond to both forced and mixed convection regimes. For a particular Richardson number, initial experiments were performed without oscillating the cylinder to determine the natural vortex shedding frequency (f_s) and use them for comparison with the oscillation results. Subsequently, the experiments were performed with the cylinder oscillating at different frequencies in the multiples of the natural vortex shedding fre-

quency, i.e. at f_e/f_s = 0.5, 1, 1.5, 2 and 3. These include excitations at fundamental, sub-harmonic, super-harmonic and non-harmonic frequencies. The oscillation amplitude (a/d) is varied from 0.02 to 0.10 in a small step of 0.02. This takes into account a small range above and below the threshold value of amplitude of oscillation for lock-in (namely, threshold value of a/d = 0.05 for a circular cylinder, Koopmann (1967)). It may be remembered from previous chapter that for the highest Richardson number, Ri = 0.145 for the circular cylinder and Ri = 0.167 for the square cylinder, vortex shedding is suppressed for the stationary cylinder and corresponding vortex shedding frequency (f_s) falls to zero. Therefore, at this critical Richardson number, multiples (i.e. 0.5, 1, 1.5, 2 and 3) of a representative vortex shedding frequency (f_s) are used to oscillate the cylinder at different frequency ratios (f_e/f_s). This symbolic vortex shedding frequency (f_s) is obtained at a cylinder surface temperature slightly less than the critical suppression temperature at which vortex shedding have not disappeared.

The detailed results of the effect of oscillations on the wake characteristics of heated circular and square cylinders have been jointly presented below in the following sequence: (1) Phase-referenced visualization images, (2) Power spectra, (3) RMS fluctuations of light intensity, and (4) Synchronization of vortex formation.

6.1 Phase-referenced visualization images

Phase-referenced visualization images have been used to visually illustrate the detailed dynamical characteristics of the vortex structures, relative to the cylinder motion for heated oscillating cylinders. The cylinder oscillation signal extracted from a time sequence of schlieren images has been used to fix the reference phases corresponding to the mechanical oscillation of the cylinder. When the cylinder is forced to oscillate, vortex formation process from the shear layers is modified by the cylinder motion. As a result, the vortices from the two shear layers interact in the near-wake through processes such as pairing and coalescence. The process of vortex evolution, near-wake vortex-vortex interactions and the distribution of vortex structures in near-wake is clearly depicted by phase-referenced schlieren images. The size, shape, patterns and time period of vortex structures behind an oscillating cylinder vary significantly compared to that of the stationary cylinder. The vortex formation patterns either repeat after one cycle or over multiple (e.g. two or three) cycles of the cylinder oscillation depending on the oscillation frequency and Richardson number. Therefore, the total time period for phase referencing of schlieren images was set according to the number of cylinder oscillation cycles required to observe repetition of vortex patterns. The phase-referencing is performed by dividing the cylinder oscillation cycle into eight evenly spaced phases over one oscillation period for

the shedding patterns repeating every cycle of cylinder oscillation. When the shedding patterns repeat over multiple oscillation cycles i.e. two or three cycles of the cylinder oscillation, the phase-referencing was extended over appropriate number of cycles, with eight evenly spaced phases over one oscillation period. The instantaneous schlieren images for stationary circular and square cylinders as a function of Richardson number have been presented first as a reference case for comparison with the oscillating results. Subsequently, phase-referenced schlieren images for oscillations cylinder have been presented for different excitation frequencies as a function of Richardson number at an oscillation amplitude, $a/d = 0.08$.

6.1.1 Stationary cylinder ($f_e/f_s = 0$)

Stationary cylinder corresponds to the limiting case of amplitude ratio, $a/d = 0$. Therefore, experiments for heated stationary cylinders were performed first for comparison with different oscillating cylinder results. For a heated stationary cylinder, the changes in the organized wake structures, namely its shape, size and time-dependent movement is readily perceived from the instantaneous images before the wake degenerates into a steady plume. Therefore, instantaneous schlieren images as a function of Richardson number for the circular and square cylinders have been presented in Figure 6.1 and 6.2, respectively. The corresponding Reynolds numbers being equal to 105 and 116 for circular and square cylinder respectively. For a given Richardson number, the images are separated by a time interval of one eighth of the time period of vortex shedding.

Figure 6.1 (A) shows the vortex formation process in the near-wake region at a cylinder temperature of 37°C (Ri=0.038). Regular alternate vortex shedding from opposite sides of the circular cylinder is observed at this temperature. Figure 6.1 (B) show the vortex shedding at a higher temperature of 51°C (Ri=0.078). Images show a increase in the length of the heated zone with higher number of interference fringes at Ri=0.078 compared to that at Ri=0.038. Schlieren images at cylinder temperature of 68°C (Ri = 0.124) in Figure 6.1 (C) show different vortex structures as compared to earlier cases. The interference fringes, which were confined within the shear layers are now visible inside the vortex structures. This indicates the presence of temperature distribution inside the detached vortices also. Figure 6.1 (D) shows the schlieren images at cylinder temperature of 76°C (Ri = 0.145). Here, two shear layers have merged into one leading to a single plume at the center of the cylinder depicting the suppression of vortex shedding at this temperature and the wake degenerates into a steady plume.

Figure 6.2 (A) presents the visualization images for a square cylinder when its surface temperature is equal to 35°C (Ri = 0.03). The instability of the growing shear

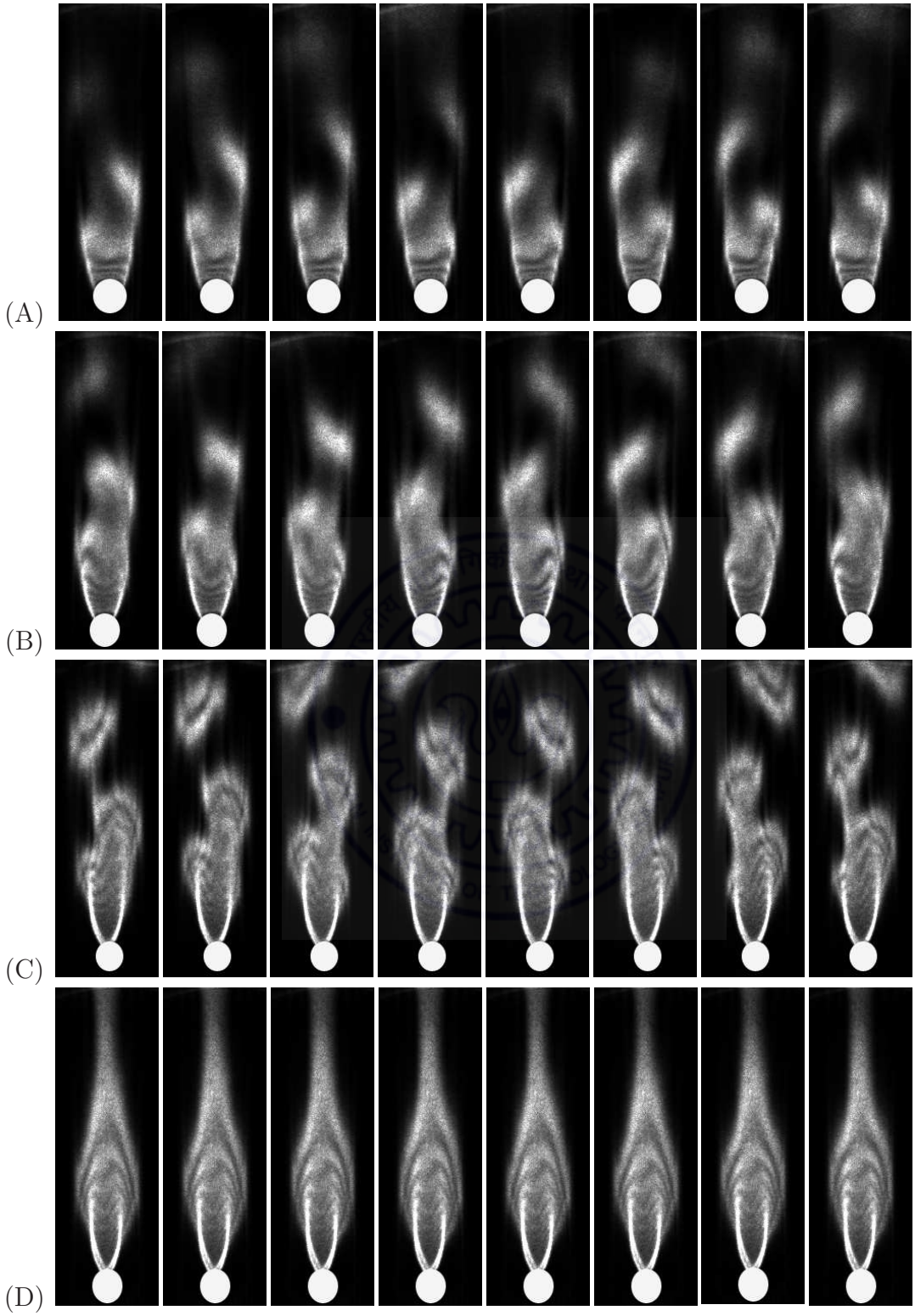

Figure 6.1: Time sequences of instantaneous schlieren images for a stationary circular cylinder separated by a time interval of one eighth of the time period of vortex shedding at Re=105 for different Richardson number: (A) Ri=0.038, (B) Ri=0.078, (C) Ri=0.124, and (D) Ri=0.145. For Ri $\geq$ 0.145, images show steady state.

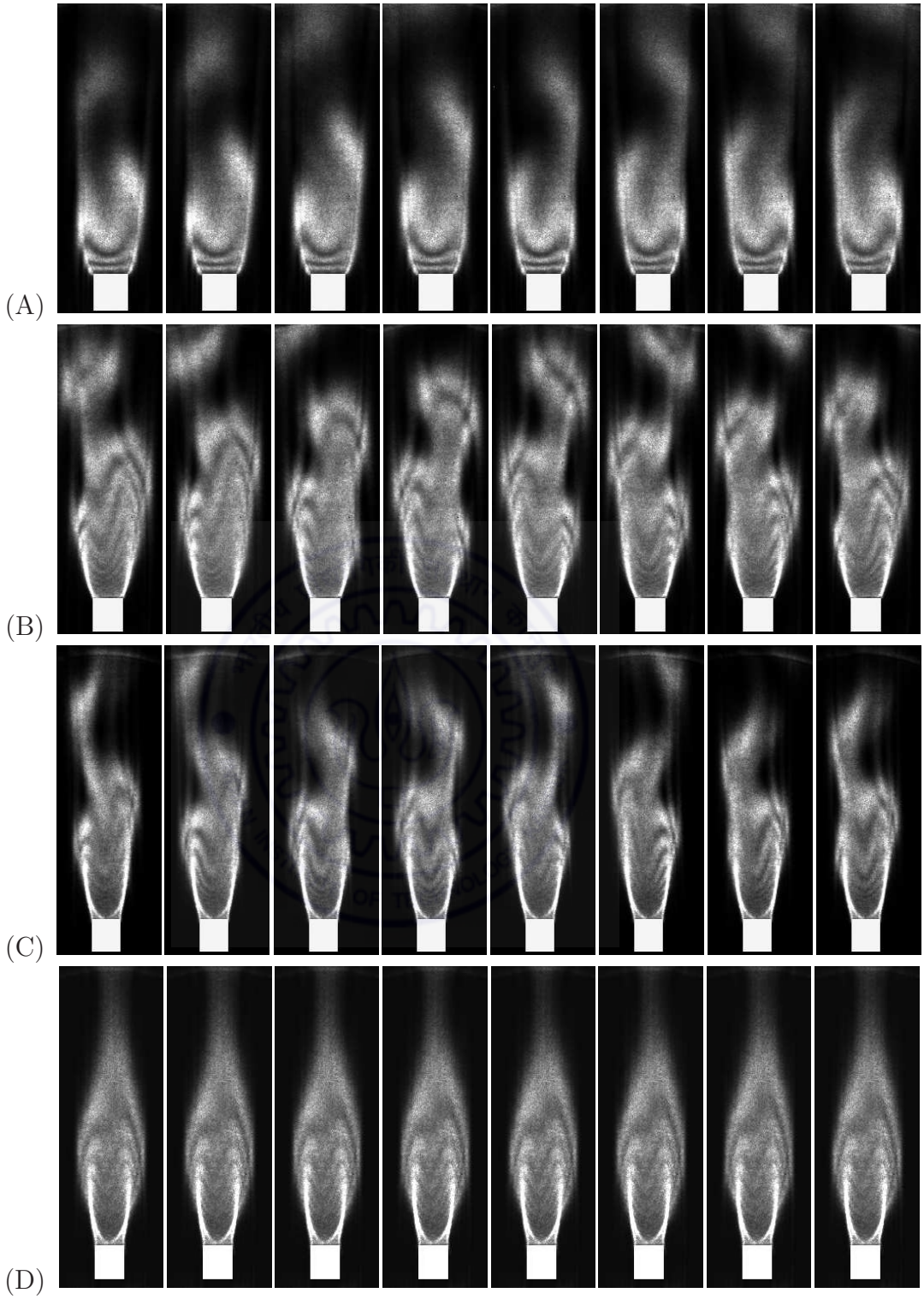

Figure 6.2: Time sequences of instantaneous schlieren images for a stationary square cylinder separated by a time interval of one eighth of the time period of vortex shedding at Re=116 for different Richardson number. (A) Ri=0.030, (B) Ri=0.086, (C) Ri=0.121, and (D) Ri=0.167. For Ri $\geq$ 0.167, images show steady state.

layers results in the shedding of two alternate rows of vortices from the opposite sides of the cylinder. Figure 6.2 (B) show the vortex shedding at a higher temperature of 55°C (Ri=0.086). The size of the detached shear layer is bigger at the higher Richardson number. Schlieren images at cylinder temperature of 68°C (Ri = 0.121) in Figure 6.2 (C) show distinct and regular vortex shedding. Hence, the increase in heating level regularizes the vortex shedding process. Figure 6.2 (D) shows the schlieren images at cylinder temperature of 86°C (Ri = 0.167). Here, the alternate shedding pattern observed at lower Richardson numbers is now replaced by a thin elongated steady plume at the center of the cylinder ultimately resulting in the suppression of vortex shedding at this temperature.

The overall comparison of Figure 6.1 and 6.2 indicates similar behaviour of vortex shedding for both circular and square cylinder geometry. The vortex patterns initially regularizes with increase in Richardson number and subsequent transform to plume like structures due to further increase in Richardson number.

6.1.2 Fundamental oscillation ($f_e/f_s = 1$)

Figure 6.3 shows different phases during oscillation cycle of a cylinder used for presentation of phase-reference schlieren images. Figure 6.4 and 6.5 show the sequence of phase-referenced schlieren images as a function of Richardson number for transversely oscillating circular and square cylinders respectively. For each Richardson number, the cylinder is oscillated at the corresponding vortex shedding frequency (i.e. $f_e/f_s = 1$) of the stationary cylinder. The amplitude of oscillation is fixed at 0.08 times the diameter/edge of the cylinder (i.e. $a/d = 0.08$). For each Richardson number, the images are presented corresponding to different phases (a-h) during one oscillation cycle as shown in Figure 6.3. The time interval between two consecutive images in the sequence is equal to one eighth of the time period of cylinder oscillation. The first image in the sequence (marked as 'a')

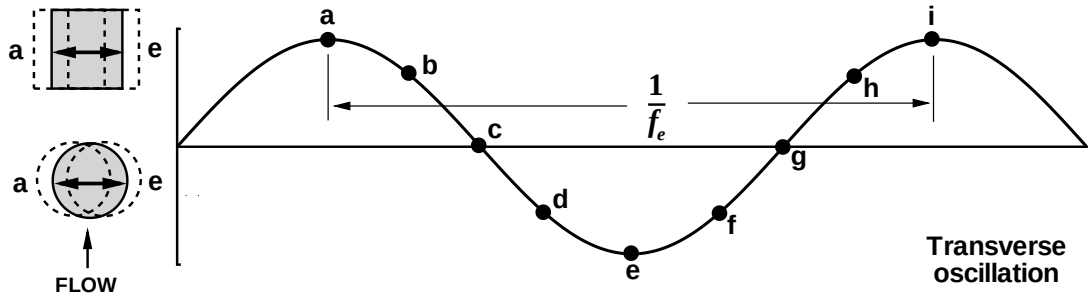

Figure 6.3: Different phases (a-i) during one oscillation cycle of transverse oscillation of circular and square cylinders.

corresponds to the maximum displacement of the cylinder on the left side whereas image marked as 'e' corresponds to the maximum displacement of the cylinder on the right side (see Figure 6.3). Therefore, these images provide an overview of the near-wake structures relative to the instantaneous displacement of the cylinder during one oscillation cycle.

Figure 6.4 (A) shows the sequence of images for oscillating circular cylinder at a cylinder temperature of 37°C (Ri = 0.038). The sequence of images show that during one oscillation cycle, one vortex of each sign of vorticity is alternatively shed from each shear layers of opposite side. The vortex from the left side shear layer grows to near its maximum size when cylinder reaches to the extreme left position ('a') in the oscillation cycle and then sheds as the cylinder reverses its direction towards right. The vortex from the right side shear layer starts growing at the position 'a' and attains its maximum size at the extreme right position ('e') in the oscillation cycle. The vortex then sheds as the cylinder reverses its direction towards the left. The wake pattern in the image at phase 'a' is seen as the mirror image of the wake pattern in the image at phase 'e'. The overall vortex shedding pattern is similar to the classical wake pattern behind the stationary cylinder. However, inclination of the vortices with wake centerline is greater compared to that of the stationary cylinder in Figure 6.1 (A). Gerrard (1966) has postulated that a growing vortex is fed by the circulation from the shear layer, which after attaining sufficient strength rolls up and draws other shear layer across the wake. For transverse oscillation, the motion of the cylinder forces the attached shear layer to be carried away with the cylinder. Therefore, roll up of the shear layer towards the wake axis with simultaneous outward movement at the cylinder base region induces a couple in the shear layer. This supplies additional circulation to the vortices which increases their strength and angle of inclination at the base region. Therefore, vortices of opposite shear layers roll up more quickly with enhanced interactions as compared to that of the stationary cylinder. The inspection of long sequences of images show that the vortex shedding pattern repeats itself for every cycle of the cylinder oscillation.

Ongoren and Rockwell (1988a) based on a flow visualization study reported that at a frequency ratio of $f_e/f_s = 1$, the vortex-formation is synchronized to the cylinder motion. The flow pattern involves successive vortex shedding from either side of the cylinder, as it alternately moves towards its maximum negative and maximum positive positions during an oscillation cycle. Figure 6.6 shows a comparison of the near-wake structures observed in the present schlieren images (at Re = 105, $a/d = 0.08$ & Ri = 0.038) with the flow visualization results of Ongoren and Rockwell (1988a) (at Re = 855 & $a/d = 0.13$) for the two phases 'a' and 'e' during an oscillation cycle of circular cylinder at $f_e/f_s = 1$. It should be noted that the present experiment is performed for mildly heated cylinder (Ri = 0.038, forced convection conditions) compared to unheated cylinder (isothermal flow

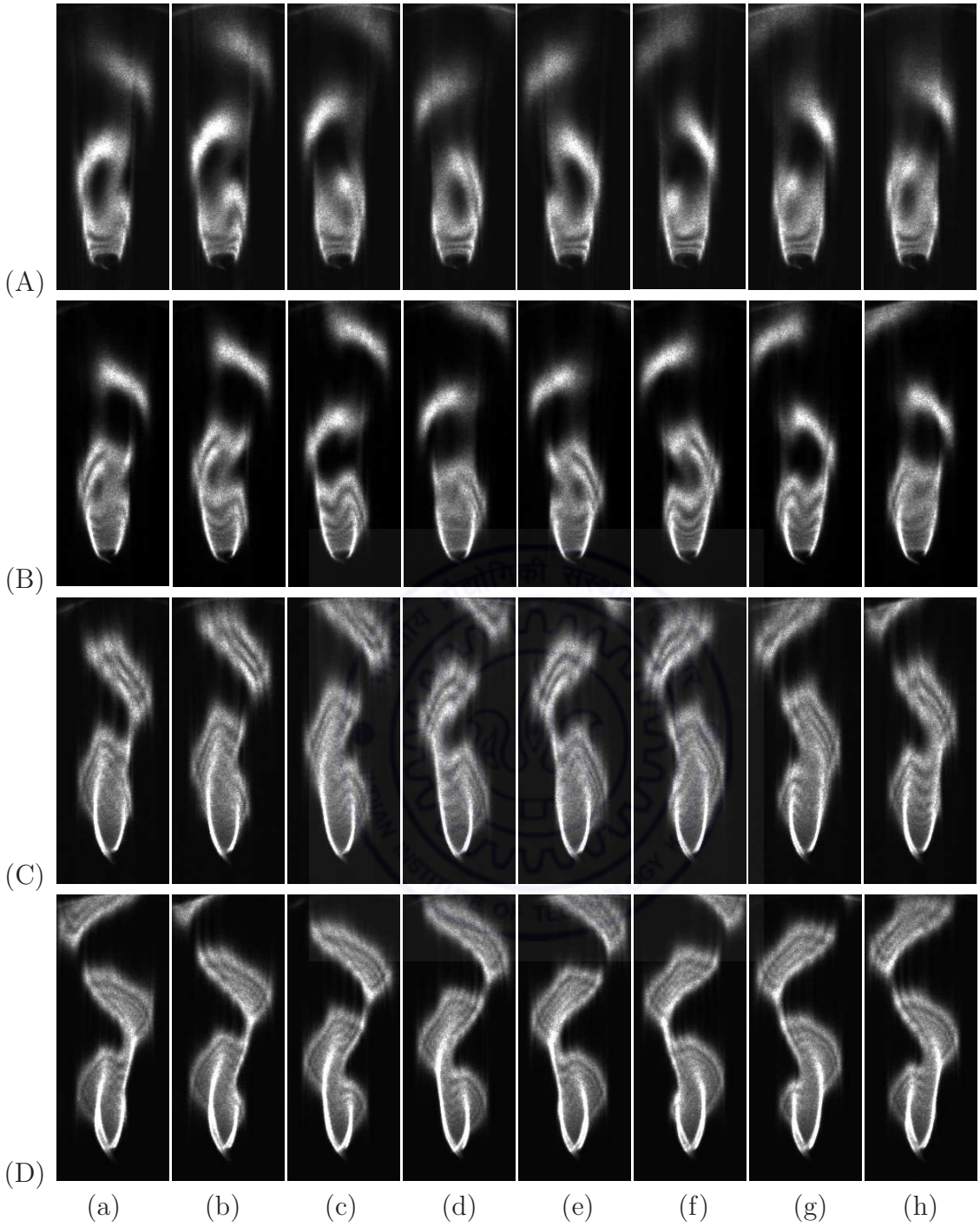

Figure 6.4: Phase-referenced schlieren images for a circular cylinder corresponding to different phases (a-h) of cylinder oscillation (Figure 6.3) at fundamental Strouhal frequency ($f_e/f_s = 1$) and amplitude, $a/d = 0.08$ as a function of Richardson number: (A) Ri=0.038, (B) Ri=0.078, (C) Ri=0.124, and (D) Ri=0.145.

conditions) in the case of Ongoren and Rockwell (1988a). The images show remarkable similarity between the near-wake structures of the present study with that of Ongoren and Rockwell (1988a). Figure 6.6 for both studies shows that at phase 'a', the initial vortex is

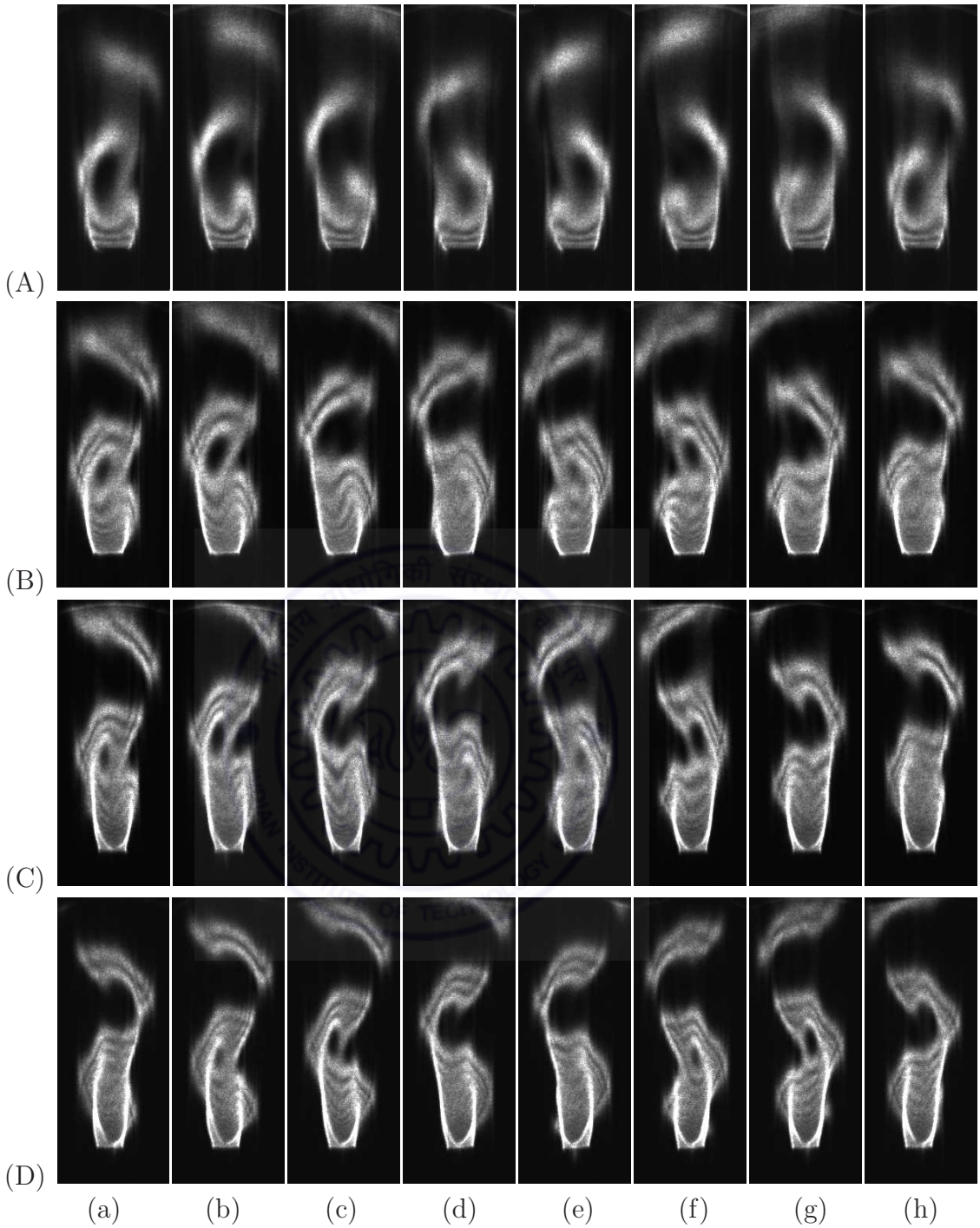

Figure 6.5: Phase-referenced schlieren images for a square cylinder corresponding to different phases (a-h) of cylinder oscillation (Figure 6.3) at fundamental Strouhal frequency ($f_e/f_s = 1$) and amplitude, $a/d = 0.08$ as a function of Richardson number:(A) Ri=0.030, (B) Ri=0.086, (C) Ri=0.121, and (D) Ri=0.167.

on the left side and the cylinder is at extreme left position while at phase 'e', the cylinder is at extreme right position and the initial vortex appears on the right side. Williamson and Roshko (1988) observed that at the critical oscillation frequency in fundamental lock-

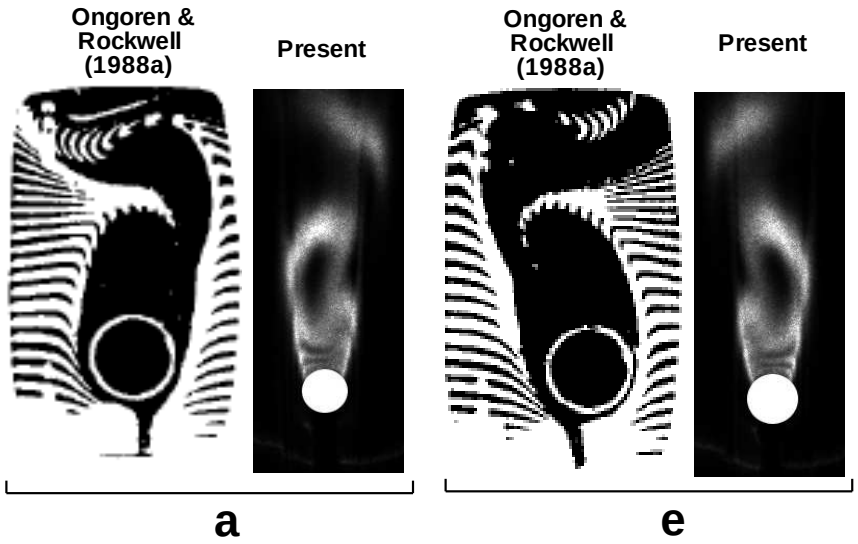

Figure 6.6: Comparison of the near-wake structures from present schlieren images with the flow visualization results of Ongoren and Rockwell (1988a) for the two phases 'a' and 'e' (Figure 6.3) during an oscillation cycle of a circular cylinder at fundamental excitation, $f_e/f_s = 1$.

in regime, the timing of vortex formation is such that two regions of opposite vorticity are fed into the wake per oscillation cycle ('2S' mode). The shed vortices are highly coherent and the wake condition is referred to as 'resonant synchronization'. Krishnamoorthy *et al.* (2001) also reported that at the critical oscillation frequency near $f_e/f_s \approx 1$, the wake is in the state of 'resonant synchronization' with shedding of exactly two vortices for each oscillation cycle. In a recent simulation study by Zheng and Zhang (2008), the flow field at $f_e/f_s = 1$ revealed the same '2S' vortex patterns as demonstrated in the experimental studies above. The '2S' type wake pattern is similar to the classical wake pattern behind the stationary cylinder. Karman street-type wake manifests its presence in the '2S' mode which coupled with the cylinder motion lead to a more dynamic and organized motion of the vortices.

Figure 6.4 (B) presents sequence of schlieren images at a higher temperature of 51°C (Ri=0.078). The vortex shedding pattern is similar to that observed for lower Richardson number (Ri = 0.038) except the higher number of interference fringes within the base region for higher Richardson number due to higher temperature wake region. Now, the fringes are visible inside the vortices which are at the verge of detachment from either side of the shear layer. However, the fringes are absent inside the detached vortices at downstream locations. This can be attributed to the drop in temperature of detached vortices due to the influence of external flow field in the far field region away from the heated base region. At a surface temperature of 68°C (Ri = 0.124), sequence of schlieren

images in Figure 6.4 (C) show alternate vortex shedding from both sides of the shear layer during each cycle of cylinder oscillation similar to that observed at lower Richardson numbers (Ri = 0.038 and 0.078). However, due to strong heating level, interference fringes are visible inside the whole near-wake region (bright zone) as well as inside the large size detached vortices. For a stationary cylinder in Figure 6.1 (C), the increase in heating level increases the length of the base region and detachment of shear layer takes place at a farther location from the cylinder. For an oscillating cylinder, the vortex structures have larger inclination angle with respect to the wake centerline as a result of transverse movement of the base region along with the cylinder oscillation. Therefore, due to larger base region and increase in the inclination angle, a large portion of the shear layer is effectively rolled-up to form larger size vortices as shown in Figure 6.4 (C). At a higher surface temperature of 76°C (Ri = 0.145), Figure 6.4 (D) shows alternate shedding of coherent structures from either side of the cylinder during one oscillating cycle. However, at this Richardson number, the vortex shedding was suppressed for the stationary cylinder and only a single steady plume was seen at the center of the cylinder in Figure 6.1 (D). The shedding behaviour of the re-appeared structures is similar to that observed for lower Richardson number (Ri = 0.124). However, the length of the base region is shortened and roll-up of vortices from the shear layers come closer to the cylinder. The re-appearance of vortex structures can be attributed to the additional energy imparted to wake by small amplitude transverse oscillations of the cylinder.

Figure 6.5 (A) shows sequence of schlieren images for oscillating square cylinder at a cylinder temperature of 35°C (Ri = 0.03). Two vortices are alternatively shed from the cylinder when it reaches its extremum positions on the left ('a') and right ('e') side during an oscillation cycle. The vortex formation patterns are similar to those observed for oscillating circular cylinder at Ri = 0.038. Thus shedding characteristics of the oscillating cylinders are identical for both the geometries. For the stationary square cylinder in Figure 6.2 (A), the vortices from both shear layers remain close (almost parallel) to the wake centerline as they propagate downstream. However, due to forced oscillations, the vortices become more inclined with the wake centerline resulting in greater penetration towards opposite side of the wake and an enhanced vortex activity in the vicinity of the cylinder. Figure 6.5 (B) and (C) present the sequence of schlieren images at higher temperatures of 55°C (Ri = 0.086) and 68°C (Ri = 0.121) respectively. The vortex shedding patterns are similar to those observed for lower Richardson number (Ri = 0.03) i.e. alternate vortex shedding from both sides of the shear layer during each cycle of cylinder oscillation. However, due to increase in the temperature, higher number of interference fringes are seen inside the whole base region; fringes are also visible inside the large size detached vortical structures. At a surface temperature of 86°C (Ri = 0.167), Figure 6.4

(D) shows clear vortex shedding from either side of the cylinder during one oscillation cycle. However, at this Richardson number, the vortex shedding was suppressed for the stationary cylinder as shown in Figure 6.2 (D). The re-appeared structures are quite similar to those observed for the lower Richardson number (Ri = 0.121). But, the length of the base region is shortened and vortices roll-up closer to the cylinder.

The schlieren images corresponding to fundamental oscillation of circular and square cylinders show similar patterns of vortex formation in the near-wake. For all Richardson numbers, two vortices are alternatively shed from either side of the cylinder during one oscillation cycle. The size of the detached vortices is larger at the higher Richardson numbers compared to that at lower Richardson number. For stationary cylinder, the vortex shedding is suppressed at a certain critical Richardson number. However, clear vortex structures are observed for oscillating cylinders of both the geometries at this critical Richardson number. In isothermal flows past a stationary cylinder, the formation of vortex is due to exponential growth of small disturbances occurring in the shear layer. When stationary cylinder is heated to critical Richardson number, the additive buoyancy force creates a stabilizing effect by cancellation of the vorticity content inside the shear layer. Thus, growth of the small disturbances in the shear layer is inhibited resulting in disappearance of the vortex shedding. However, when cylinder is oscillated, the excitation energy of the cylinder is readily transmitted into the small disturbances of the shear layer. This causes the amplification of the instability modes in the near-wake, which were suppressed by buoyancy forces for the stationary cylinder case. Due to the re-amplification of instability, dynamic equilibrium between the buoyancy force and inertia of the forced flow is disturbed and vortex shedding reappears for the oscillating cylinder at the critical Richardson Number case.

6.1.3 Sub-harmonic oscillation ($f_e/f_s = 0.5$)

Figures 6.7 and 6.8 show the sequence of phase-referenced schlieren images as a function of Richardson number for transversely oscillating circular and square cylinders, respectively. For each Richardson number, the cylinder is oscillated at sub-harmonic i.e. 0.5 times the fundamental Strouhal frequency ($f_e/f_s = 0.5$) at an amplitude ratio, $a/d = 0.08$. For each Richardson number, the images are presented corresponding to eight evenly spaced phases (a-h) during one oscillation cycle as shown in Figure 6.3.

Figure 6.7 (A) shows the sequence of images for oscillating circular cylinder at a cylinder temperature of 37°C (Ri = 0.038). The sequence of images show that four vortices (two from each side of the shear layer) are shed from the cylinder during one oscillation cycle. The vortex from the left side shear layer is fully formed when the cylinder is at the

extreme left position ('a') in the oscillation cycle (in-phase relationship with the cylinder motion) and subsequently when the cylinder is at the extreme right position ('e') in the oscillation cycle (out-of-phase relationship with the cylinder motion). The vortices from the right side shear layers are fully formed when the cylinder is at the mean positions ('c' and 'g') in the oscillation cycle. The phase relationship between body motion and shedding of vorticity is such that the initial vortex consistently forms on the same side (left side) of the cylinder irrespective of the cylinder displacement to either the maximum left or right positions. This aspect of $\frac{1}{2}$-subharmonic excitation was also observed by Ongoren and Rockwell (1988a) from their flow visualization images. The authors reported that the vortex-formation is synchronized to the cylinder motion in such a manner that shedding of vortices is always from the same side of the body at maximum negative and positive positions of the cylinder in an oscillation cycle. A comparison of the vortex formation patterns in the present schlieren images (at Re = 105, $a/d = 0.08$ & Ri = 0.038) with the flow visualization images of Ongoren and Rockwell (1988a) (at Re = 855 & $a/d = 0.13$) is shown in Figure 6.9 for the two phases 'a' and 'e' during an oscillation cycle for circular cylinder at $f_e/f_s = 0.5$. The images show that patterns of vortex shedding in the present study are identical to those observed by Ongoren and Rockwell (1988a). The cylinder is at extreme left position for phase 'a' and at extreme right position for phase 'e'. However, at both phases of the cylinder displacement, the vortex formation is consistently from the left side of the cylinder. Krishnamoorthy *et al.* (2001) also observed similar vortex shedding characteristics and reported that wake vortices are coherent during certain phases of the cylinder oscillation cycle. In a numerical study, Zheng and Zhang (2008) showed that four vortices are shed from the cylinder for each oscillation cycle similar to the above experimental findings. The long sequences of the present schlieren images show that the vortex shedding pattern repeats itself for every half-cycle of the cylinder oscillation (i.e. periodic per half cycle) and corresponds to natural vortex shedding frequency. It will be shown later that near-wake is not locked with the cylinder oscillation (Section 6.4) and dominant peak is observed at the natural shedding frequency in the power spectra (Section 6.2).

Figure 6.7 (B) and (C) present sequences of the schlieren images at higher temperatures of 51°C (Ri = 0.078) and 68°C (Ri = 0.124), respectively. The vortex shedding patterns are similar to that observed at the lower Richardson number (Ri = 0.038) i.e. shedding of two vortices from the left side of the cylinder at the two extreme positions of the cylinder, 'a' and 'e' in one oscillation cycle. However, comparison of the images at two phases, 'a' and 'e' in the oscillation cycle shows that the images are not exactly similar in terms of the shape and size of the structures. The images in Figure 6.7 (C) at 68°C (Ri = 0.124) show that due to strong heating level, interference fringes are visible inside the

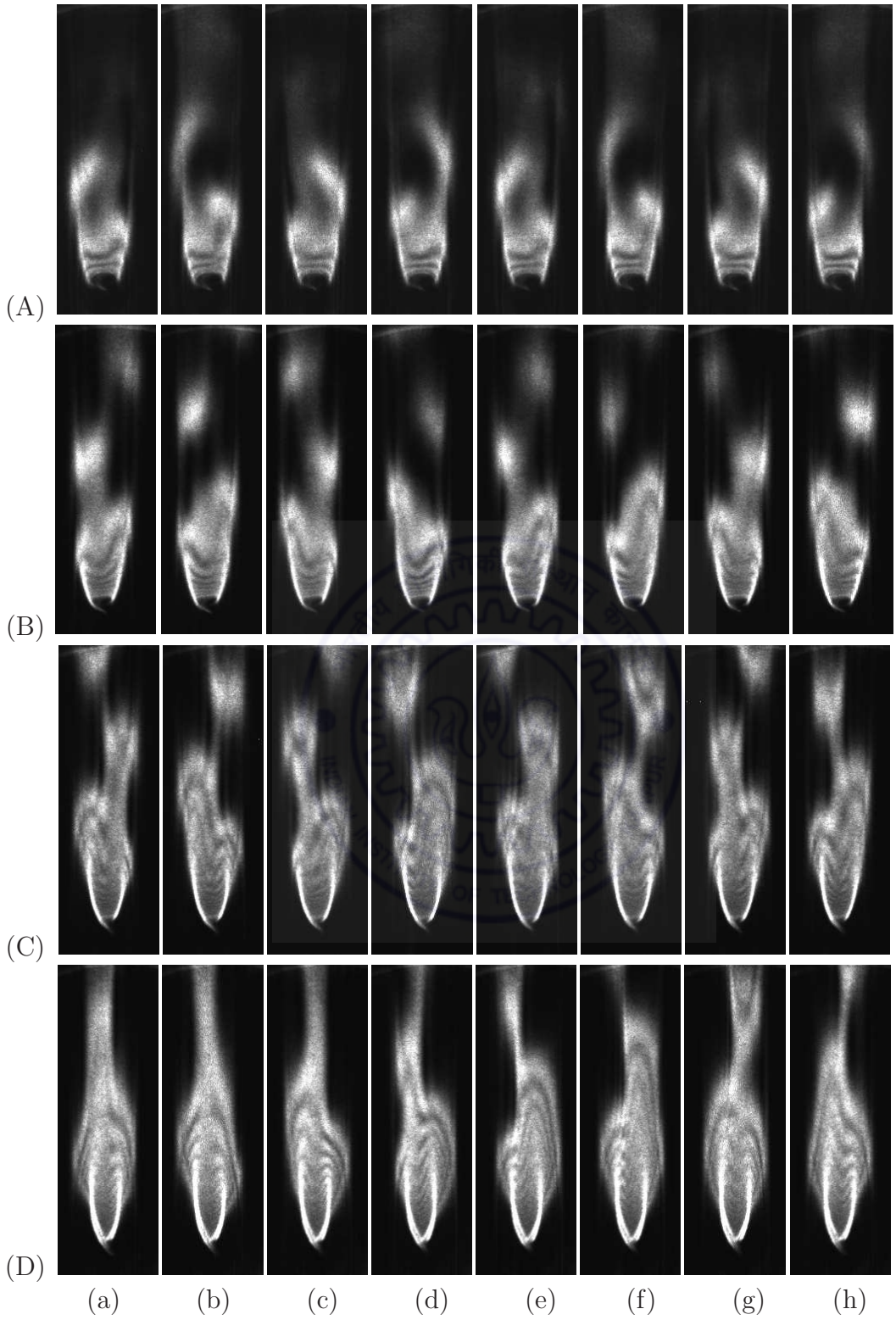

Figure 6.7: Phase-referenced schlieren images for a circular cylinder corresponding to different phases (a-h) of cylinder oscillation (Figure 6.3) at sub-harmonic of the Strouhal frequency ($f_e/f_s = 0.5$) and amplitude, $a/d = 0.08$ as a function of Richardson number:(A) Ri=0.038, (B) Ri=0.078, (C) Ri=0.124, and (D) Ri=0.145.

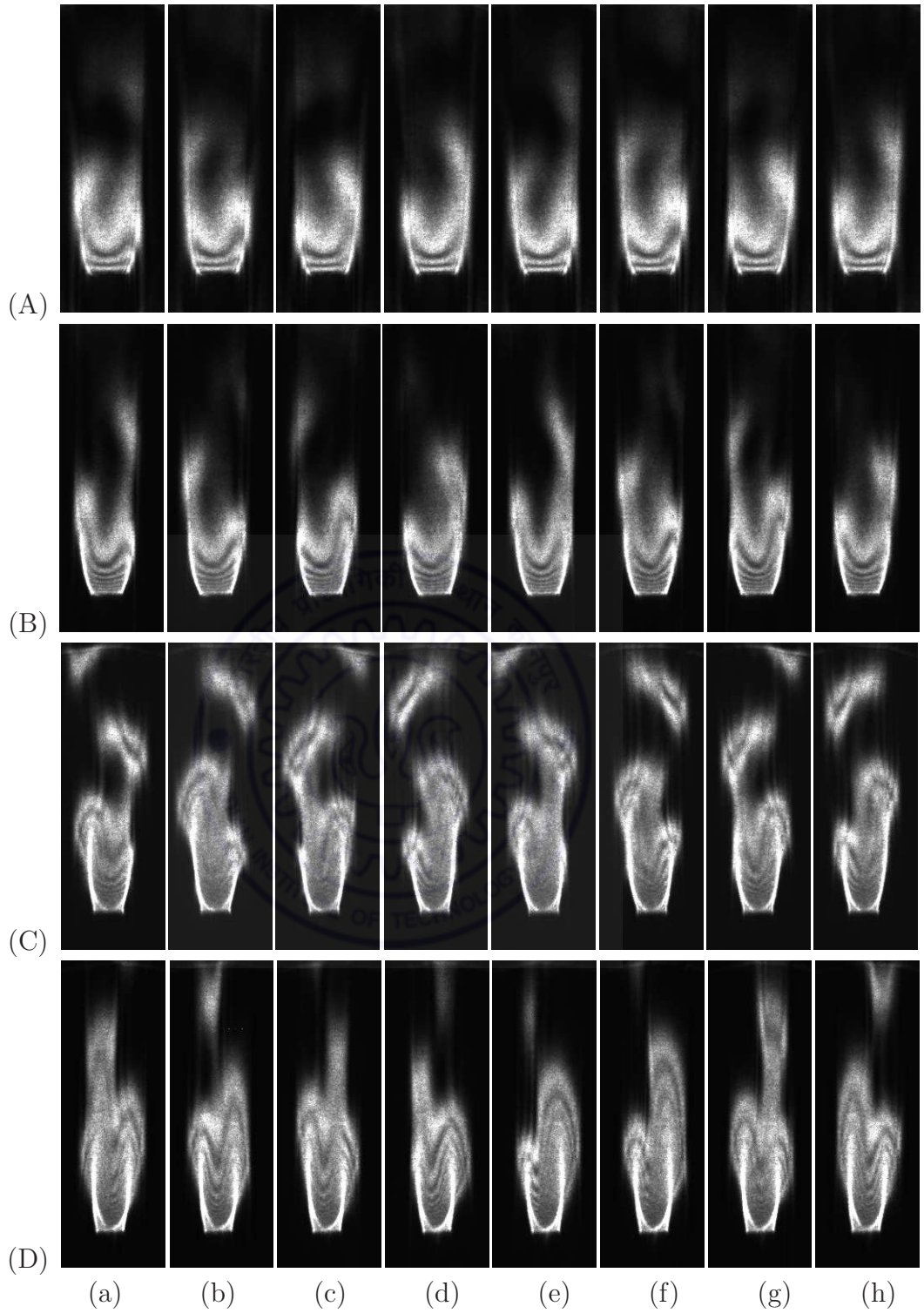

Figure 6.8: Phase-referenced schlieren images for a square cylinder corresponding to different phases (a-h) of cylinder oscillation (Figure 6.3) at sub-harmonic of the Strouhal frequency ($f_e/f_s = 0.5$) and amplitude, $a/d = 0.08$ as a function of Richardson number: (A) Ri=0.030, (B) Ri=0.086, (C) Ri=0.121, and (D) Ri=0.167.

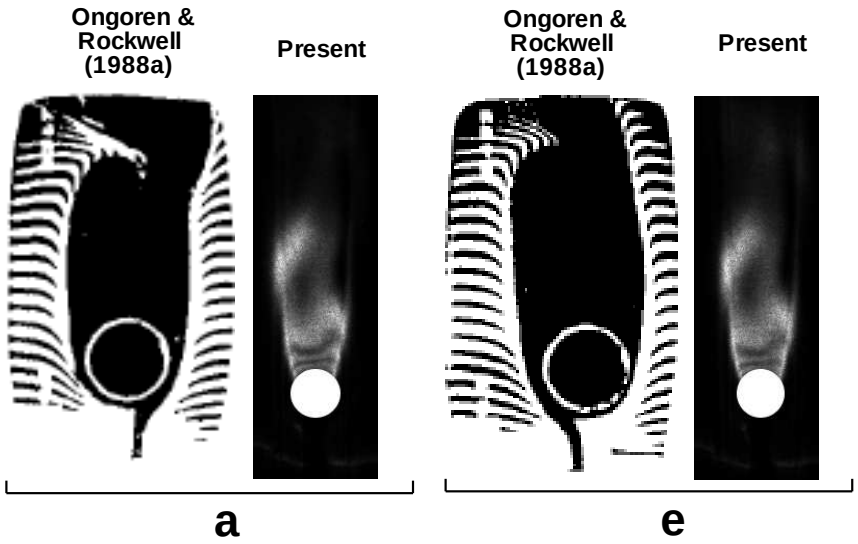

Figure 6.9: Comparison of the near-wake structures from present schlieren images with the flow visualization results of Ongoren and Rockwell (1988a) for the two phases 'a' and 'e' (Figure 6.3) during an oscillation cycle of a circular cylinder at sub-harmonic excitation, $f_e/f_s = 0.5$.

whole near-wake region and inside the detached vortices. At a higher surface temperature of 76°C (Ri = 0.145), Figure 6.7 (D) shows that one vortex from each side of the cylinder is shed during one oscillation cycle and follows the periodicity of the excitation frequency. This is in contrast to the patterns observed for the lower Richardson numbers, Ri = 0.038, 0.078 and 0.124. At this Richardson number (Ri = 0.145), the vortex shedding was suppressed for the stationary cylinder and only a single steady plume was seen at the center of the cylinder as shown in Figure 6.1 (D). The small amplitude perturbation at sub-harmonic oscillation ($f_e/f_s = 0.5$) of the cylinder imparts additional energy to wake and results in re-appearance of the vortex structures.

Figure 6.8 (A) and (B) show the sequences of the schlieren images for oscillating square cylinder at a surface temperature of 35°C (Ri = 0.03) and 55°C (Ri = 0.086), respectively. In both the sequences, the vortex from the left side shear layer is fully formed at the extreme left position ('a') and subsequently at the extreme right position ('e') of the cylinder in an oscillation cycle. This indicates that shedding patterns are similar to that observed for the oscillating circular cylinder at Ri = 0.038. Figure 6.8 (C) present the sequence of schlieren images at a higher temperature of 68°C (Ri = 0.121). Two vortices from the same side of the cylinder are shed during one oscillation cycle similar to those observed for the lower Richardson numbers (Ri = 0.030 and 0.086). However, due to increase in the temperature, higher number of interference fringes are seen inside the base region and fringes are also visible inside the detached vortical structures. At a

surface temperature of 86°C (Ri = 0.167), Figure 6.8 (D) shows that one vortex from each side of the cylinder is shed during one oscillation cycle and is periodic with the excitation frequency. However, at this Richardson number, the vortex shedding was suppressed for the stationary cylinder and single steady plume was observed at the center of the cylinder as shown in Figure 6.2 (D).

The schlieren images corresponding to sub-harmonic oscillation ($f_e/f_s = 0.5$) of circular and square cylinders show similar patterns of vortex formation in the near-wake. Two vortices from the same side shear layer are shed during one oscillation cycle except at the highest Richardson number for both the cylinders,. At the highest Richardson number (Ri = 0.145 for the circular cylinder and Ri = 0.167 for the square cylinder), only one vortex from each side shear layer is shed during one oscillation cycle. overall significant effect of heating on vortex shedding phenomenon is observed at high Richardson number.

6.1.4 Non-harmonic oscillation ($f_e/f_s = 1.5$)

Figures 6.11 and 6.12 show the sequence of phase-referenced schlieren images for transversely oscillating circular and square cylinders, respectively as a function of Richardson number at non-harmonic (1.5 times) of the fundamental Strouhal frequency (i.e. $f_e/f_s = 1.5$) for an amplitude ratio, $a/d = 0.08$. At this excitation frequency, phase-referencing is extended over three cylinder oscillation cycles with eight evenly spaced phases during each oscillation cycle. A schematic diagram representing different phases (a-y) during three consecutive cycles of transverse oscillation for circular and square cylinders is shown in Figure 6.10. For each Richardson number, the images corresponding to different phases (a-x) of the cylinder oscillation are presented where the images in first, second and third row respectively, corresponds to phases (a-h) of the first cycle, phases (i-p) of the second successive cycle and phases (q-x) of the third consecutive cycle. In each row, the images are separated by a time interval of one-eighth of the time period of cylinder oscillation. First image of the sequence in each row (marked as 'a', 'i' and 'q') corresponds to the extremum location of the cylinder on the left side whereas images marked as 'e', 'm' and 'u' corresponds to the extremum location of the cylinder on the right side (see Figure 6.10).

Figure 6.11 (A) shows the sequence of schlieren images for oscillating circular cylinder at a cylinder temperature of 37°C (Ri = 0.038). The images show that two vortices from each side shear layer are shed for every three cycles of the cylinder oscillation. The vortex from the left side shear layer is fully formed when the cylinder is at the extreme left position ('a') in the first oscillation cycle and subsequently when the cylinder is at the extreme right position ('m') in the second consecutive cycle (i.e. after 1.5 cycles). The vortex from the right side shear layer is fully formed when the cylinder is at the mean

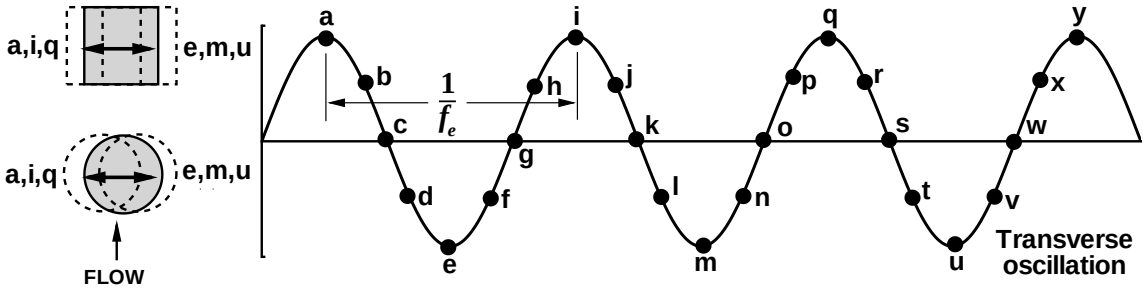

Figure 6.10: Different phases (a-y) during three consecutive cycles of transverse oscillation of circular and square cylinders.

position ('g') in the first oscillation cycle and subsequently when the cylinder is at the mean position ('s') in the third consecutive cycle (i.e. after 1.5 cycles). Therefore, one vortex from each shear layer is formed for every 1.5 cycles of the cylinder oscillation and follows the periodicity of fundamental Strouhal frequency. It will be shown later that near-wake is not locked with the cylinder oscillation (Section 6.4) and natural shedding frequency is still dominant amongst the multiple frequencies present in the power spectra (Section 6.2). The presence of multiple frequencies cause the vortex structures to be irregular in subsequent shedding after 1.5 cycles. However, the inspection of long sequences of images show that vortex structures repeat itself after every three cycles of the cylinder oscillation. This can be attributed to the presence of $f_e - f_s$ (Theoretically equal to $f_e/3$) component in the schlieren signal of the near-wake. This will be shown later using power spectra. Krishnamoorthy *et al.* (2001) experimentally observed that corresponding to 1.5-nonharmonic excitation, a coherent pair of vortices was observed at a dimensionless time, $t^* = 0$ just downstream of the formation region and subsequent coherent vortex pairs occurred only at $t^* = 3$, 6, 9 etc. (i.e. after 3, 6, 9 cycles and so on). In a simulation study performed by Zheng and Zhang (2008), no obvious synchronization was observed at 1.5-nonharmonic excitation. However, a large-amplitude coherent component at $f_e/3$ was observed in the C_D spectrum that corresponds to the structures repeating every three cycles of the cylinder oscillation. The flow structures resemblance after 3-cycles of the cylinder oscillation was shown in the vorticity contours.

Figure 6.11 (B) present sequence of schlieren images at a higher temperature of 51°C (Ri = 0.078). The sequence of images show that one vortex from each side shear layer is formed for every cycle of the cylinder oscillation and follows the periodicity of excitation frequency (f_e). The formation of vortices in the formation region ($x/d \approx 2$) is regular in the subsequent oscillation cycles. However, shed vortices loose their coherence at the downstream locations (beyond the vortex formation region) and show irregularity in the structures in successive oscillation cycles. It is shown later in Section 6.4 that near-wake

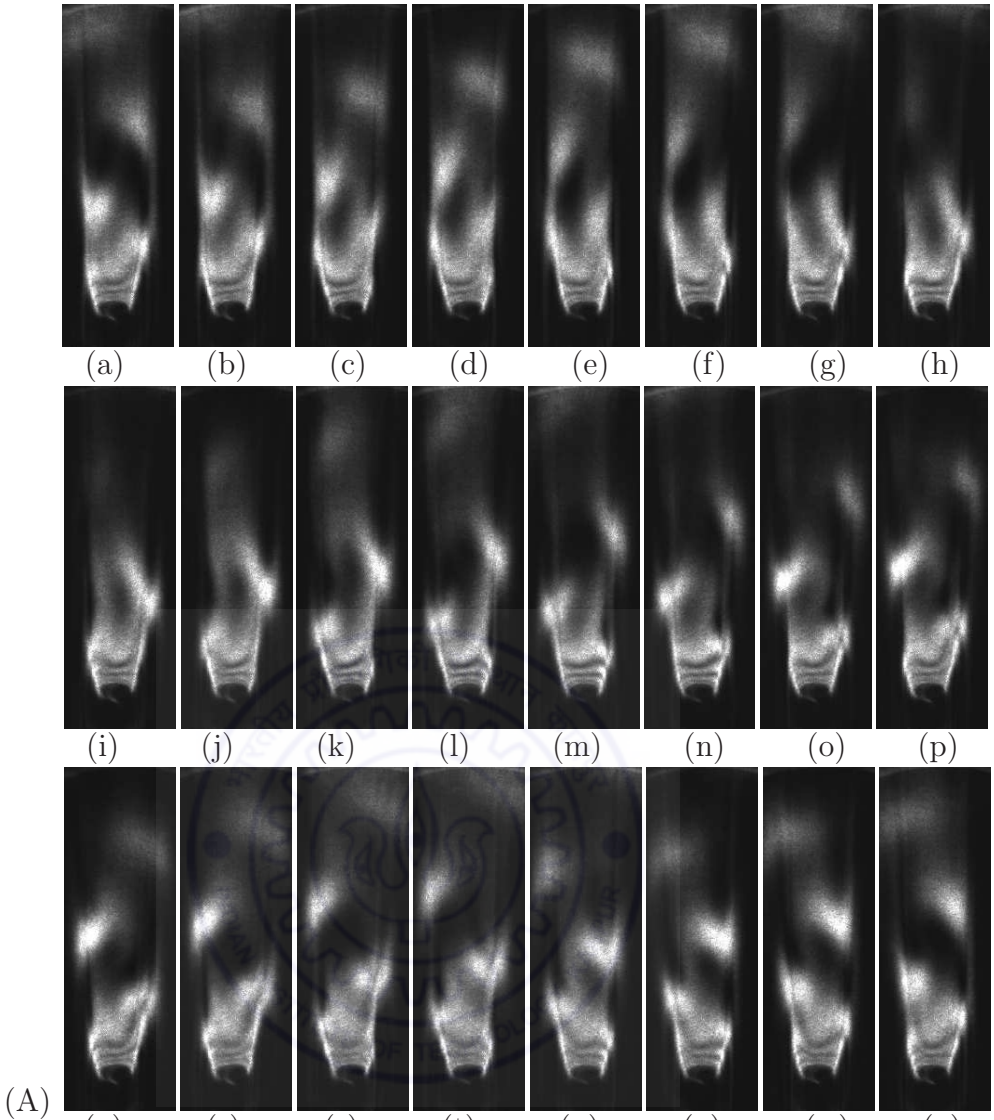

Figure 6.11 (A) : *see caption on the page number 200.*

is not locked with the cylinder oscillation at downstream locations, $x/d = 3.5$ and 5 and locked-on with the cylinder motion at $x/d = 2$ location. At a surface temperature of 68°C (Ri = 0.124), sequence of schlieren images in Figure 6.11 (C) shows alternate shedding of vortices from both sides of the shear layer during each cycle of the cylinder oscillation. The vortex from the left side shear layer is fully formed when cylinder reaches to the extreme left position ('a' or 'i' or 'q') in the oscillation cycle. The vortex from the right side shear layer is fully formed when cylinder reaches to the extreme right position ('e' or 'm' or 'u') in the oscillation cycle. The images in Figure 6.11 (C) show that due to strong heating level, interference fringes are visible inside the whole near-wake region (bright zone) as well as inside the detached vortices. The process of vortex formation is regular and shed vortices maintain their coherence at the downstream locations contrast to that at lower

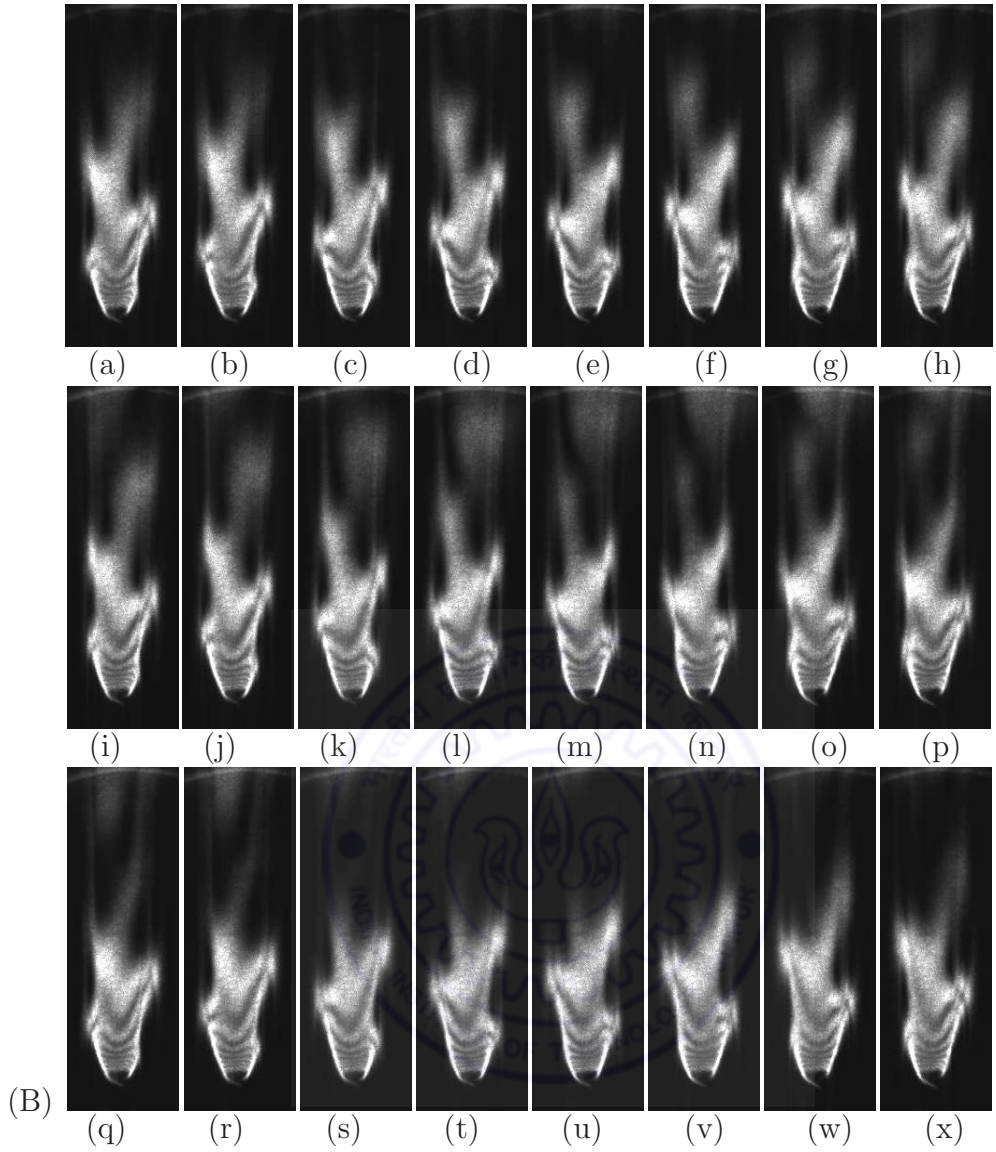

Figure 6.11 (B) : *see caption on the page number 200.*

Richardson number, Ri=0.078. However, comparison of the corresponding images in the consecutive oscillation cycles(three rows) show a small intermittency in the shape of the vortex structures at the downstream locations. It has been shown later in Section 6.4 that near-wake is locked-on with the cylinder oscillation at $x/d = 2$ location while it is quasi locked-on with the cylinder oscillation at $x/d = 3.5$ and 5 locations. At a higher surface temperature of 76°C (Ri = 0.145), Figure 6.4 (D) shows alternate shedding of coherent vortices from either side of the cylinder during each oscillating cycle similar to that observed for the lower Richardson number (Ri = 0.124). However, at this Richardson number, the vortex structures retain exactly similar shapes in the successive oscillation cycles at all stream wise locations. It has been shown later in Section 6.4 that near-wake is locked-on with the cylinder oscillation at all stream wise locations. It may be noted

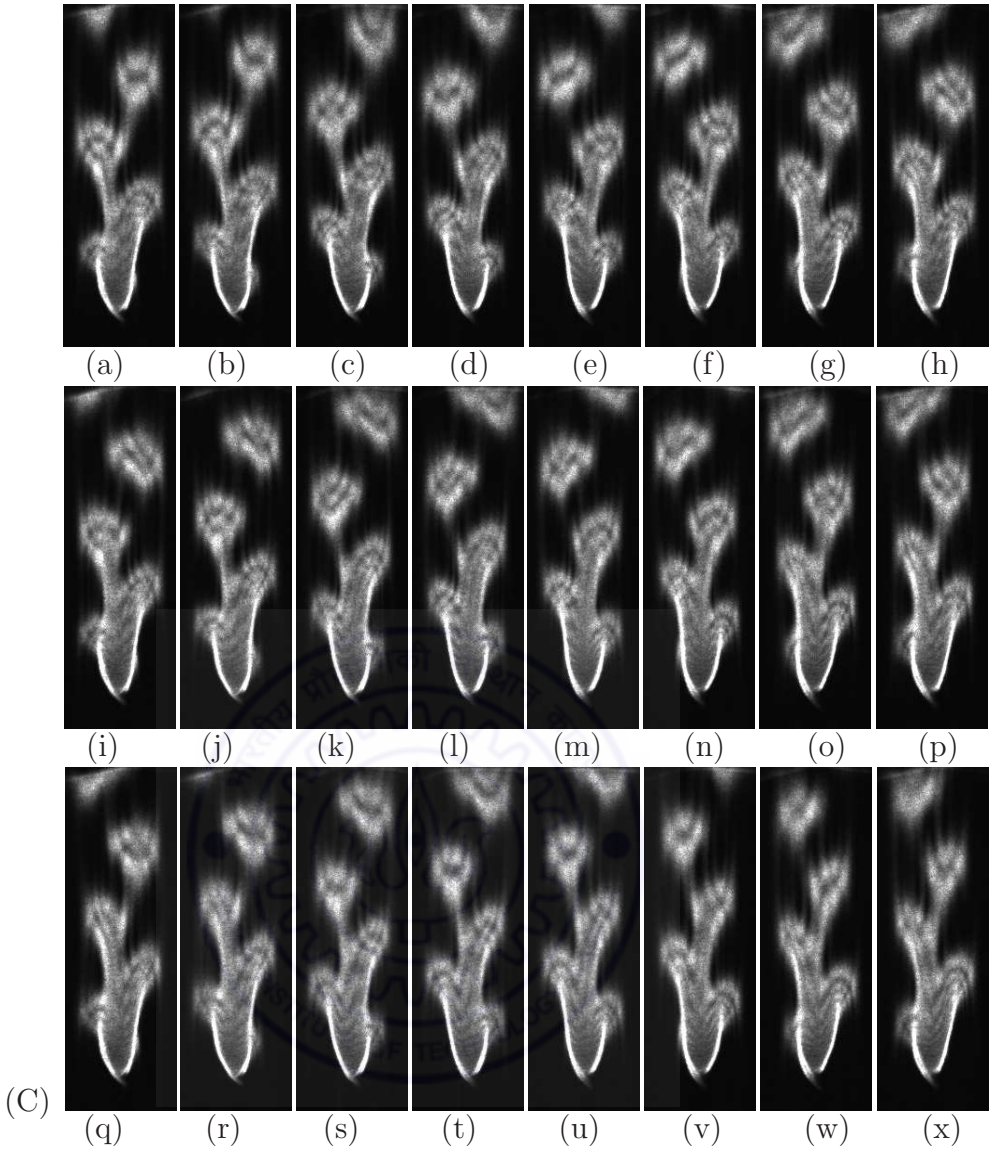

Figure 6.11 (C) : *see caption on the page number 200.*

that at this Richardson number, the vortex shedding was suppressed for the stationary cylinder and only a single steady plume was seen at the center of the cylinder as shown in Figure 6.1 (D). However, additional energy imparted to the wake by small amplitude transverse oscillations of the cylinder leads to reappearance of the vortex structures.

Figure 6.12 (A) shows the sequence of schlieren images for oscillating square cylinder at a cylinder temperature of 35°C (Ri = 0.03). The images show that one vortex from each side of the shear layer is alternatively formed when the cylinder reaches the maximum displacement position (left side, 'a', 'i', 'q' or right side, 'e', 'm', 'u') in an oscillation cycle. Therefore, formation of vortices follows the periodicity of the excitation frequency (f_e). This is in contrast to the case of a circular cylinder at comparable Richardson number

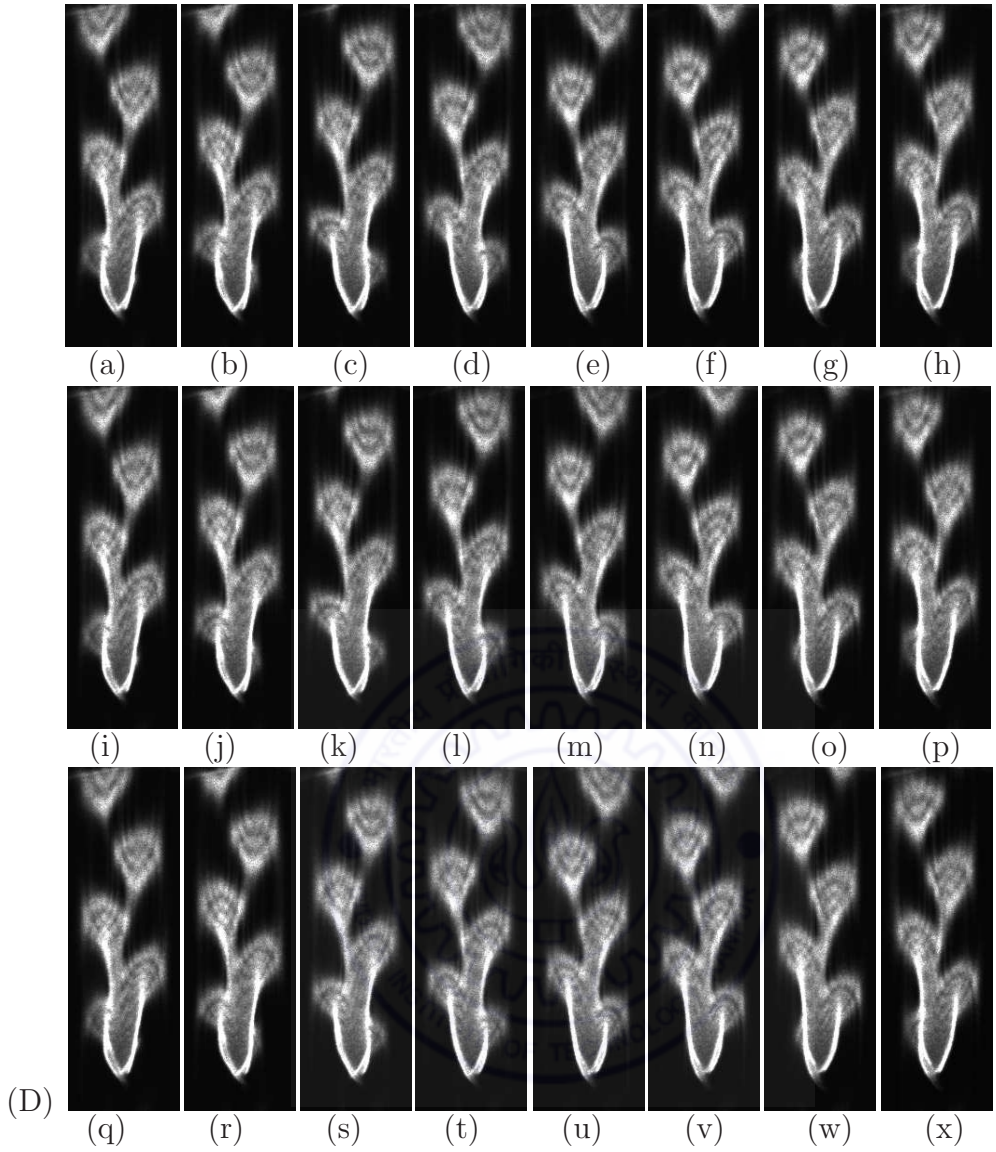

Figure 6.11: Phase-referenced schlieren images for a circular cylinder corresponding to different phases (a-x) of cylinder oscillation (Figure 6.10) at non-harmonic of the Strouhal frequency ($f_e/f_s = 1.5$) and amplitude, $a/d = 0.08$ as a function of Richardson number: (A) Ri=0.038, (B) Ri=0.078, (C) Ri=0.124, and (D) Ri=0.145.

(Ri = 0.038) where vortex formation is periodic with the natural shedding frequency (f_s) (Figure 6.11 (A)). This indicates higher sensitivity of the square cylinder wave to imposed oscillation compared to that of the circular cylinder at lower Richardson number possibly due to fixed separation location of the former case. The formation of vortices is regular in the formation region ($x/d \approx 2$) for every oscillation cycle. However, at the downstream locations (beyond the vortex formation region), the detached vortices show irregularity in subsequent oscillation cycles and repeat themselves after every three cycles of the cylinder oscillation. This can be attributed to the presence of $f_e - f_s$ component in the schlieren

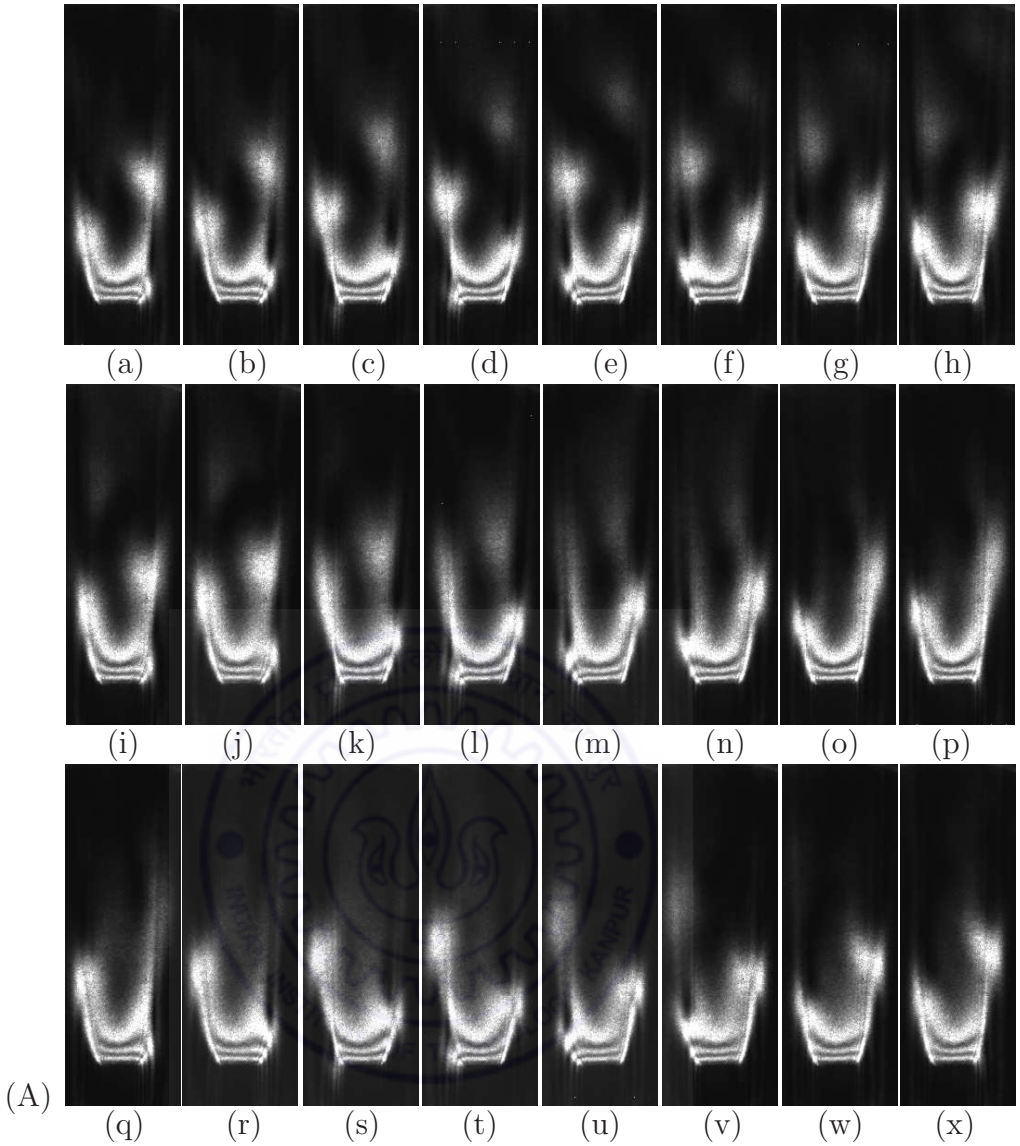

Figure 6.12 (A) : *see caption on the page number 204.*

signal at downstream locations ($x/d = 3.5$ and 5) as shown later in Section 6.2. It has been shown later in Section 6.4 that near-wake vortices are quasi locked-on with the cylinder oscillation at $x/d = 2$ location while not locked-on with the cylinder oscillation at $x/d =$ 3.5 and 5 locations. Figures 6.12 (B) and (C) show the sequence of schlieren images at higher temperatures of 55°C (Ri = 0.086) and 68°C (Ri = 0.121) respectively. For both the Richardson numbers, the sequence of images show that one vortex is alternatively formed from each side of the shear layer in one cycle of the cylinder oscillation. The vortex from the left side shear layer is fully formed when cylinder reaches to the extreme left position ('a' or 'i' or 'q') in the oscillation cycle. Similarly, the vortex from the right side shear layer is fully formed when cylinder reaches to the extreme right position ('e' or 'm' or 'u') in the oscillation cycle. For both the Richardson numbers, the formation and shedding

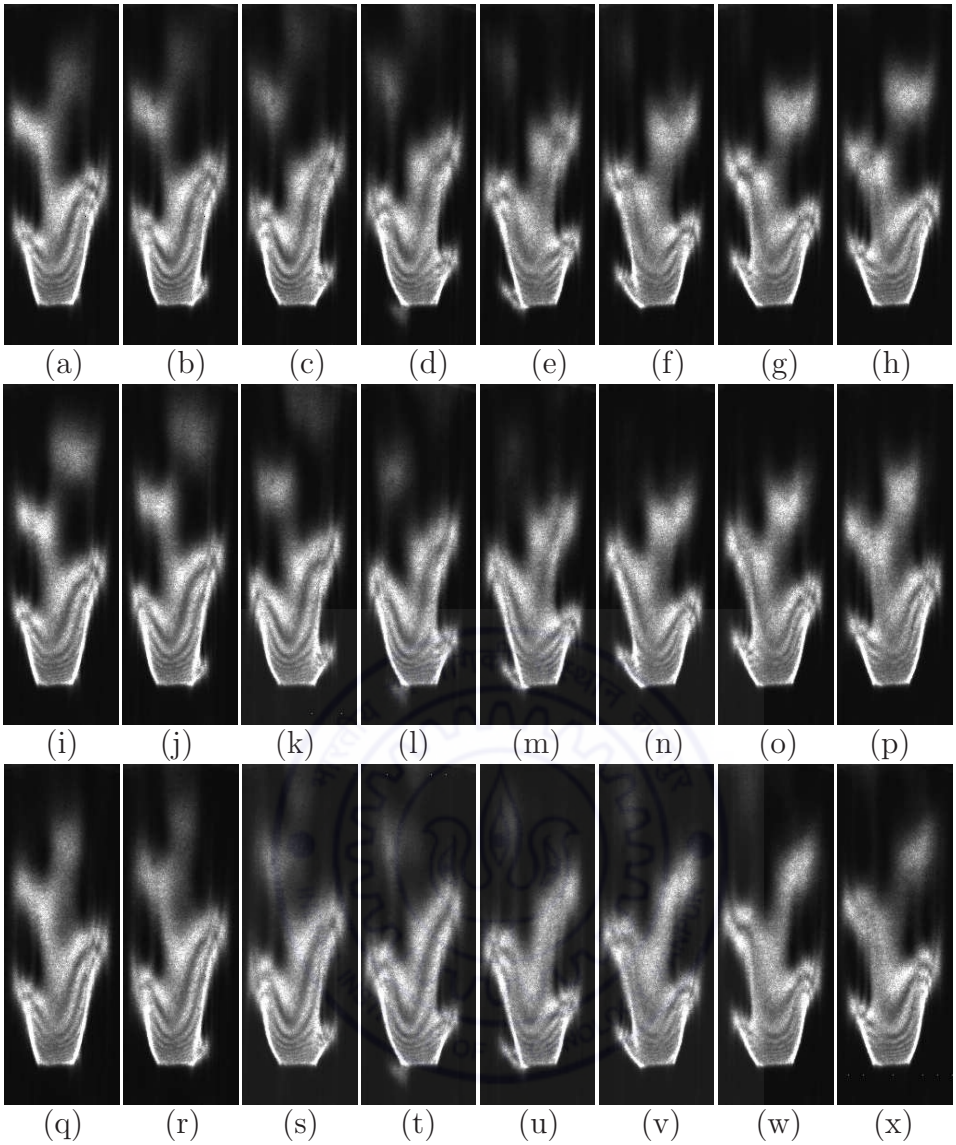

Figure 6.12 (B) : *see caption on the page number 204.*

of the vortices is regular in the subsequent oscillation cycles. However, comparison of the corresponding images between the successive oscillation cycles (three rows) show a small irregularity in the size and shape of the detached structures at the downstream locations. It has been shown in Section 6.4 that near-wake vortices are locked-on, quasi locked-on and not locked with the cylinder oscillation at x/d = 2, 3.5 and 5 locations respectively. Thus, the locked-on characteristics of the cylinder enhances with increase in Richardson number to 0.086 and 0.121 from 0.03. At a higher surface temperature of 86°C (Ri = 0.167), Figure 6.12 (D) shows alternate shedding of two vortices from the cylinder as it reaches its extremum left and right positions during an oscillation cycle. In contrast to lower Richardson numbers (Ri = 0.086 and 0.121), no irregularity in the shed vortices is observed in subsequent cycles at the downstream locations. The vortex

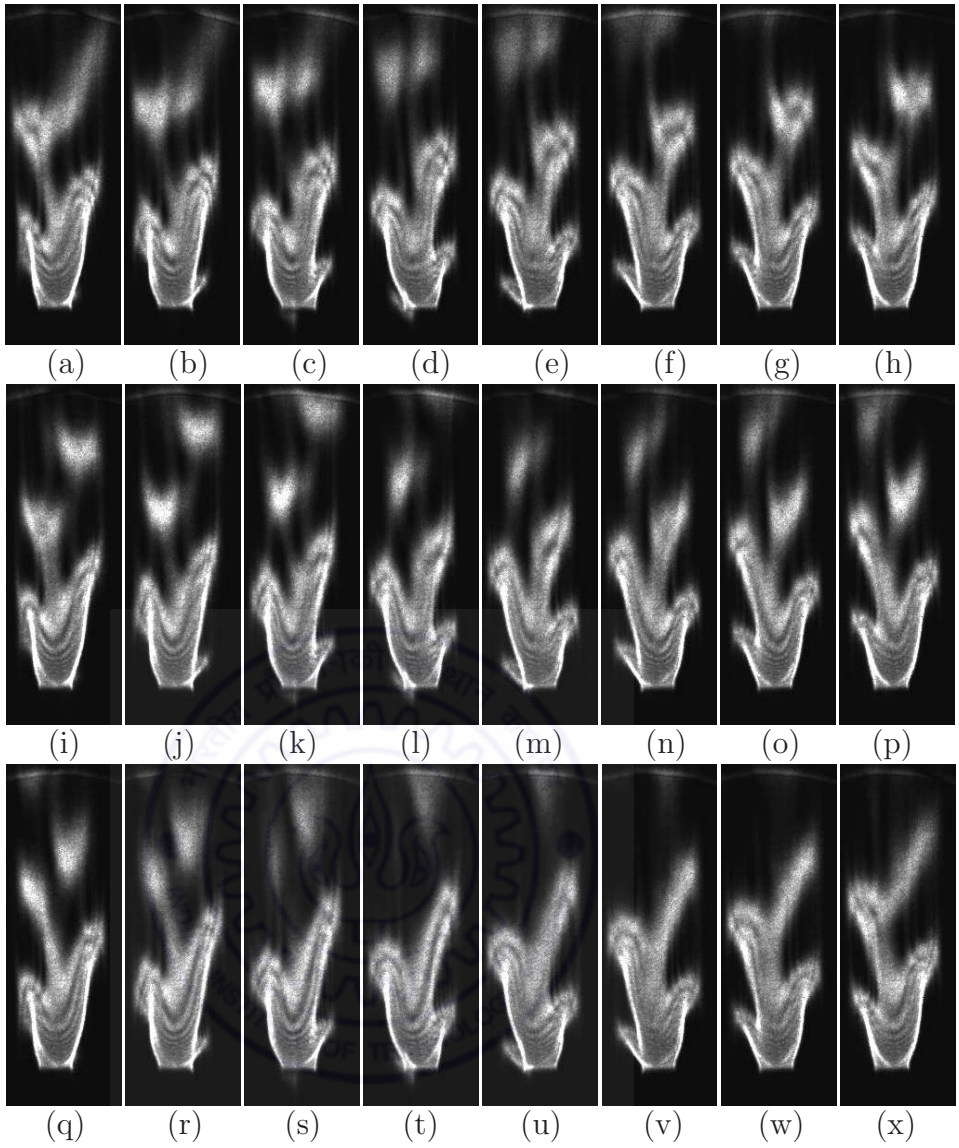

Figure 6.12 (C) : *see caption on the page number 204.*

structures in consecutive oscillation cycles (three rows) are exactly similar. It has been shown later in Section 6.4 that near-wake is locked-on with the cylinder oscillation at all stream wise locations. It may be noted that at this Richardson number, the vortex shedding was suppressed for the stationary cylinder as shown in Figure 6.2 (D). However, small amplitude transverse oscillations of the cylinder imparts additional energy to the near-wake resulting in appearance of vortex structures.

The schlieren images corresponding to non-harmonic oscillation ($f_e/f_s = 1.5$) of circular and square cylinders show similar patterns of vortex formation in the near-wake except at the lowest Richardson number. At the lowest Richardson number (Ri = 0.038 for the circular cylinder and Ri = 0.030 for the square cylinder), the formation of vortices for a circular cylinder follows the periodicity of the fundamental Strouhal frequency (f_s),

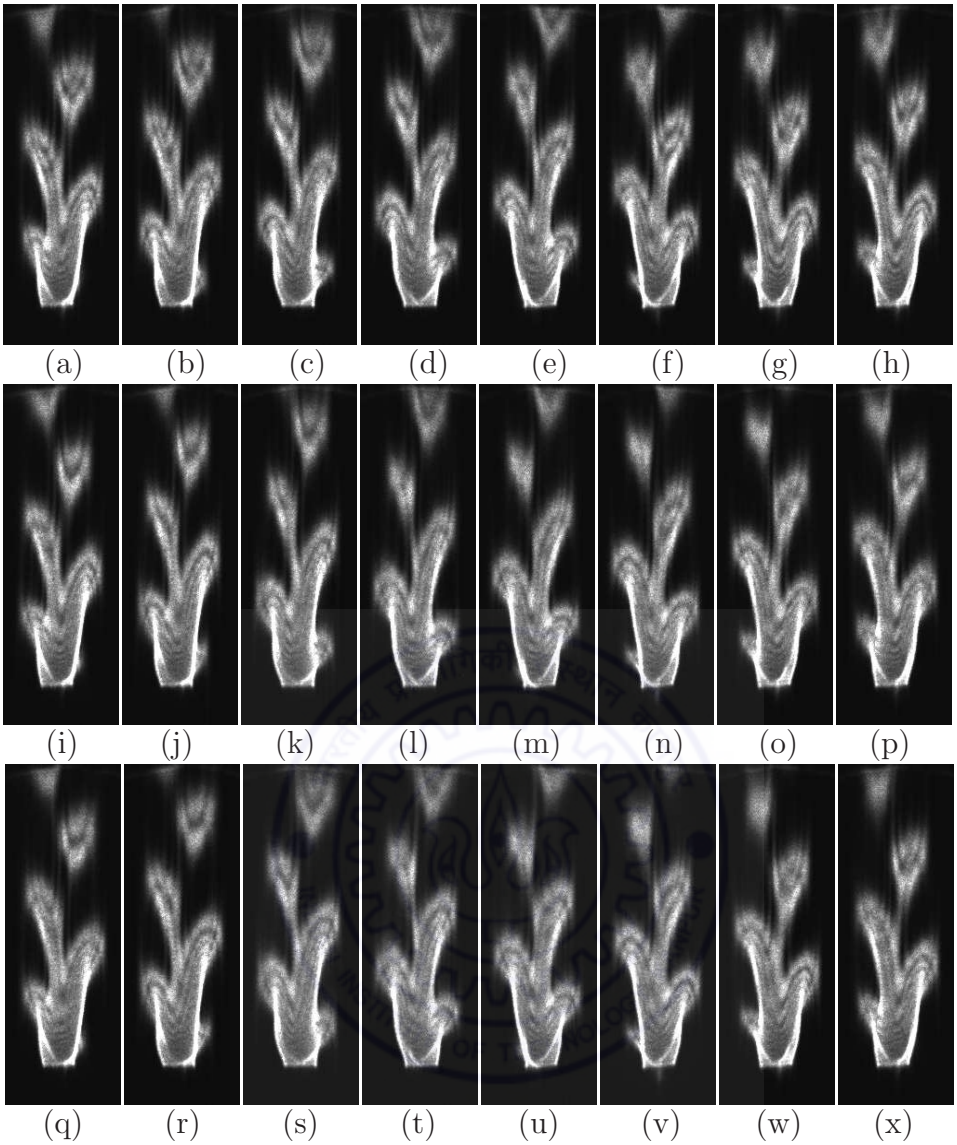

Figure 6.12: Phase-referenced schlieren images for a square cylinder corresponding to different phases (a-x) of cylinder oscillation (Figure 6.10) at non-harmonic of the Strouhal frequency ($f_e/f_s = 1.5$) and amplitude, $a/d = 0.08$ as a function of Richardson number:(A) Ri=0.030, (B) Ri=0.086, (C) Ri=0.121, and (D) Ri=0.167.

while square cylinder follows the periodicity of the excitation frequency (f_e). The effect of perturbation on near-wake vortex structures become more pronounced with increase in Richardson number. Therefore, formation of vortices is regularized and become periodic with the cylinder oscillation in the formation region for both the cylinders. However, at the downstream locations, the detached vortices show irregularity and loss of coherency in subsequent oscillation cycles. No irregularity in shape, size and coherency of the shed vortices is observed at the downstream locations in subsequent oscillation cycles with further increase in the Richardson number.

6.1.5 Super-harmonic oscillation ($f_e/f_s = 2$)

Figures 6.14 and 6.15 show the sequence of phase-referenced schlieren images for transversely oscillating circular and square cylinders, respectively as a function of Richardson number at super-harmonic (2 times) of the natural vortex shedding frequency (i.e. $f_e/f_s = 2$) at an amplitude ratio, $a/d = 0.08$. At this excitation frequency, phase-referencing is extended over two successive cycles of the cylinder oscillation with eight evenly spaced phases during each oscillation cycle. A schematic diagram representing different phases (a-q) during two successive cycles of transverse oscillation of circular and square cylinders is shown in Figure 6.13. The images corresponding to different phases (a-p) for two consecutive cycles of the cylinder oscillation are presented in two rows i.e. the images in first and second row corresponds to phases (a-h) of the first cycle and phases (i-p) of the second cycle, respectively. In each row, the images in the sequence are separated by a time interval of one-eighth of the time period of cylinder oscillation. First image of the sequence in each row (marked as 'a' and 'i') corresponds to the extremum of the cylinder on the left side whereas images marked as 'e' and 'm' corresponds to the extremum location of the cylinder on the right side (see Figure 6.13).

Figure 6.14 (A) shows the sequence of schlieren images for oscillating circular cylinder at a cylinder temperature of 37°C (Ri = 0.038). The vortex from the left side shear layer is fully formed when the cylinder is at the extreme left position ('a') in the first oscillation cycle. The vortex from the right side shear layer is fully formed when the cylinder is at the extreme left position ('i') in the second consecutive cycle. In the similar manner, subsequent vortices of respective sign of vorticity are formed when the cylinder is at the extreme left positions in alternate cycles. Therefore, one vortex from each shear layer is formed for every 2 cycles of the cylinder oscillation and follows the periodicity of fundamental Strouhal frequency. The vortex structures repeat itself after every two

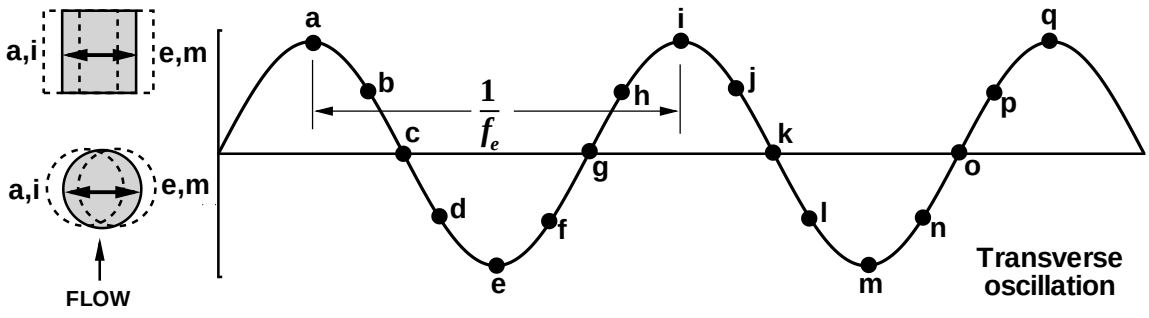

Figure 6.13: Different phases (a-q) during two consecutive cycles of transverse oscillation of circular and square cylinders.

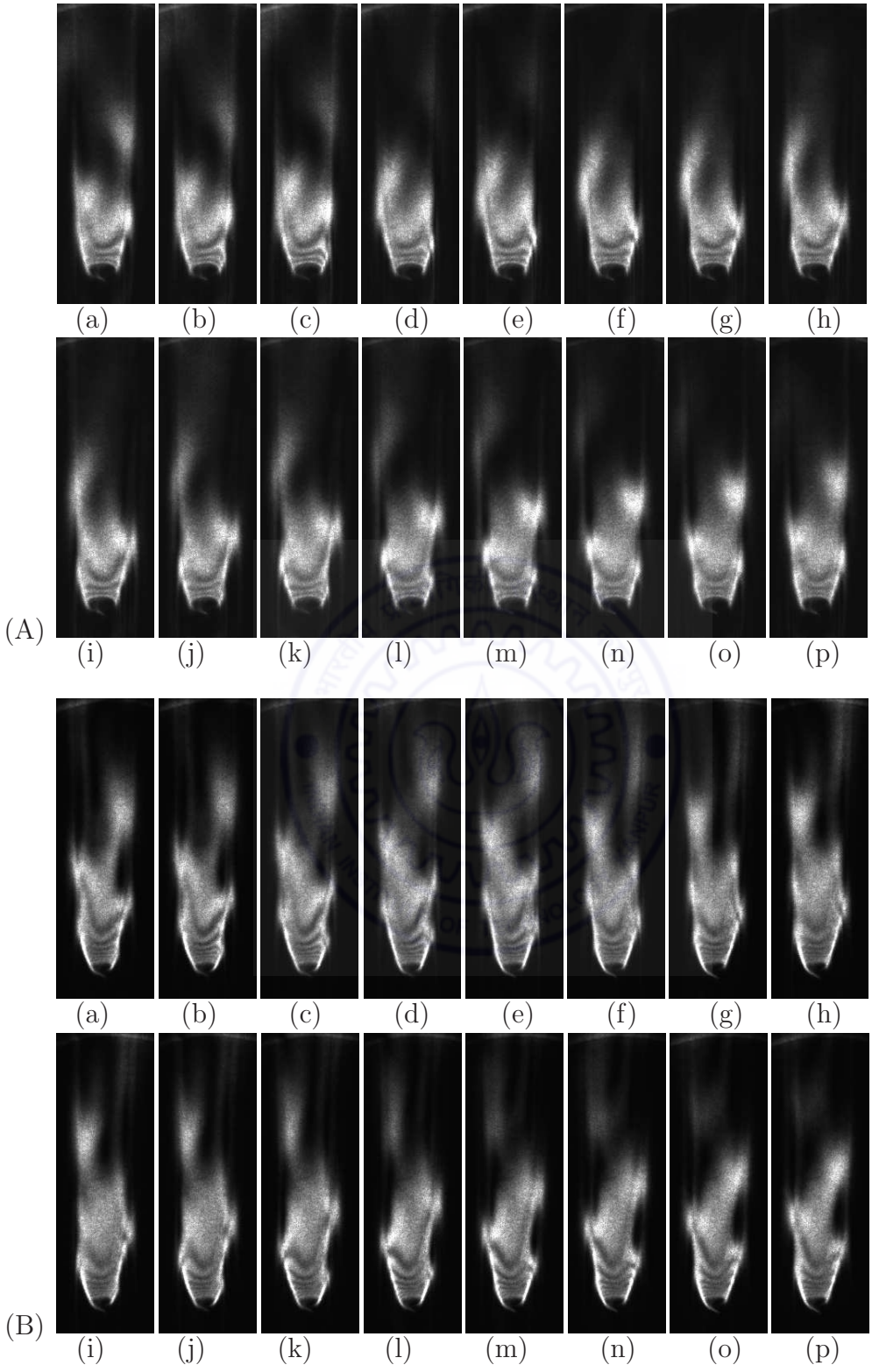

see caption on the facing page

cycles of the cylinder oscillation. It will be shown later that near-wake is not locked with the cylinder oscillation (Section 6.4) and the power spectra contains sharp peak at the natural vortex shedding frequency (f_s) (Section 6.2). Based on the results of the flow

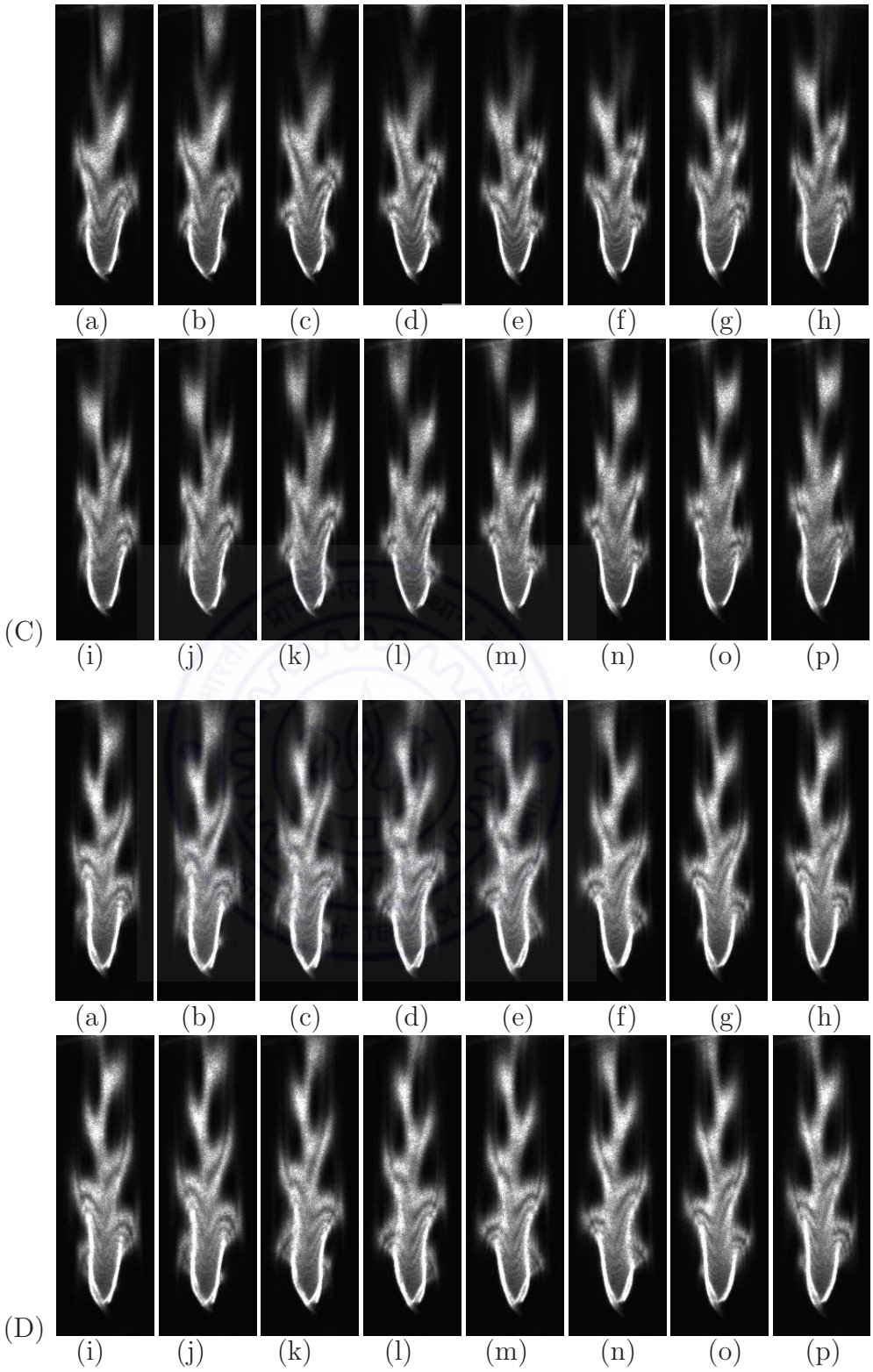

Figure 6.14: Phase-referenced schlieren images for a circular cylinder corresponding to different phases (a-p) of cylinder oscillation (Figure 6.13) at super-harmonic of the Strouhal frequency ($f_e/f_s = 2$) and amplitude, $a/d = 0.08$ as a function of Richardson number: (A) Ri=0.038, (B) Ri=0.078, (C) Ri=0.124, and (D) Ri=0.145.

visualization and hot film experiments, Krishnamoorthy *et al.* (2001) pointed out that synchronization of the near-wake does not occur for 2-superharmonic excitation. However, in a simulated flow visualization study, Zheng and Zhang (2008) observed $\frac{1}{2}$-cycle coherence at this excitation frequency. The vorticity contours show that every complete cycle of the entrained frequency of natural vortex shedding contains exactly 2 cycles of the oscillation frequency.

Figure 6.14 (B) present sequence of schlieren images at a higher temperature of 51°C (Ri = 0.078). The sequence of images show that one vortex from each side shear layer grows in the formation region ($x/d \approx 2$) for every cycle of the cylinder oscillation. However, vortex from only one side propagates to the downstream region for every oscillation cycle and the vortex from other side propagates to the downstream region in the successive oscillation cycle. Therefore, pattern of vortex structures is repeated after every two cycles of the cylinder oscillation. At a temperature of 68°C (Ri = 0.124), the sequence of schlieren images in Figure 6.14 (C) show that one vortex is alternatively formed from the left side and right side shear layers when the cylinder reaches to the extreme left position ('a' or 'i') and the extreme right position ('e' or 'm'), respectively in the oscillation cycle (see the near field region of the images). The images show that due to strong heating level, interference fringes are visible inside the whole near-wake region as well as inside the detached vortices. The process of vortex formation is regular in the formation region. However, comparison of the corresponding images in two rows of the consecutive oscillation cycles show a small intermittency in the vortex structures at the downstream locations. It has been shown later in Section 6.4 that near-wake is locked-on and quasi locked-on with the cylinder oscillation at $x/d = 2$ and 3.5 locations, respectively, while not locked with the cylinder oscillation at $x/d = 5$ location. At a higher surface temperature of 76°C (Ri = 0.145), Figure 6.4 (D) shows alternate shedding of coherent vortices from either side of the cylinder during each oscillating cycle similar to that observed for the lower Richardson number (Ri = 0.124). However, in contrast to Ri = 0.124, exactly matching vortex structures are observed in the successive oscillation cycles at all stream wise locations. It has been shown later in Section 6.4 shows that near-wake is locked-on with the cylinder oscillation at all stream wise locations. It may be noted that at this Richardson number, the vortex shedding was suppressed for the stationary cylinder and only a single steady plume was seen at the center of the cylinder as shown in Figure 6.1 (D).

Figure 6.15 (A) shows the sequence of schlieren images for oscillating square cylinder at a cylinder temperature of 35°C (Ri = 0.03). The images show that one vortex from each side of the shear layer is alternatively formed when the cylinder reaches to the extreme position on the respective side in one oscillation cycle. Therefore, formation of vortices

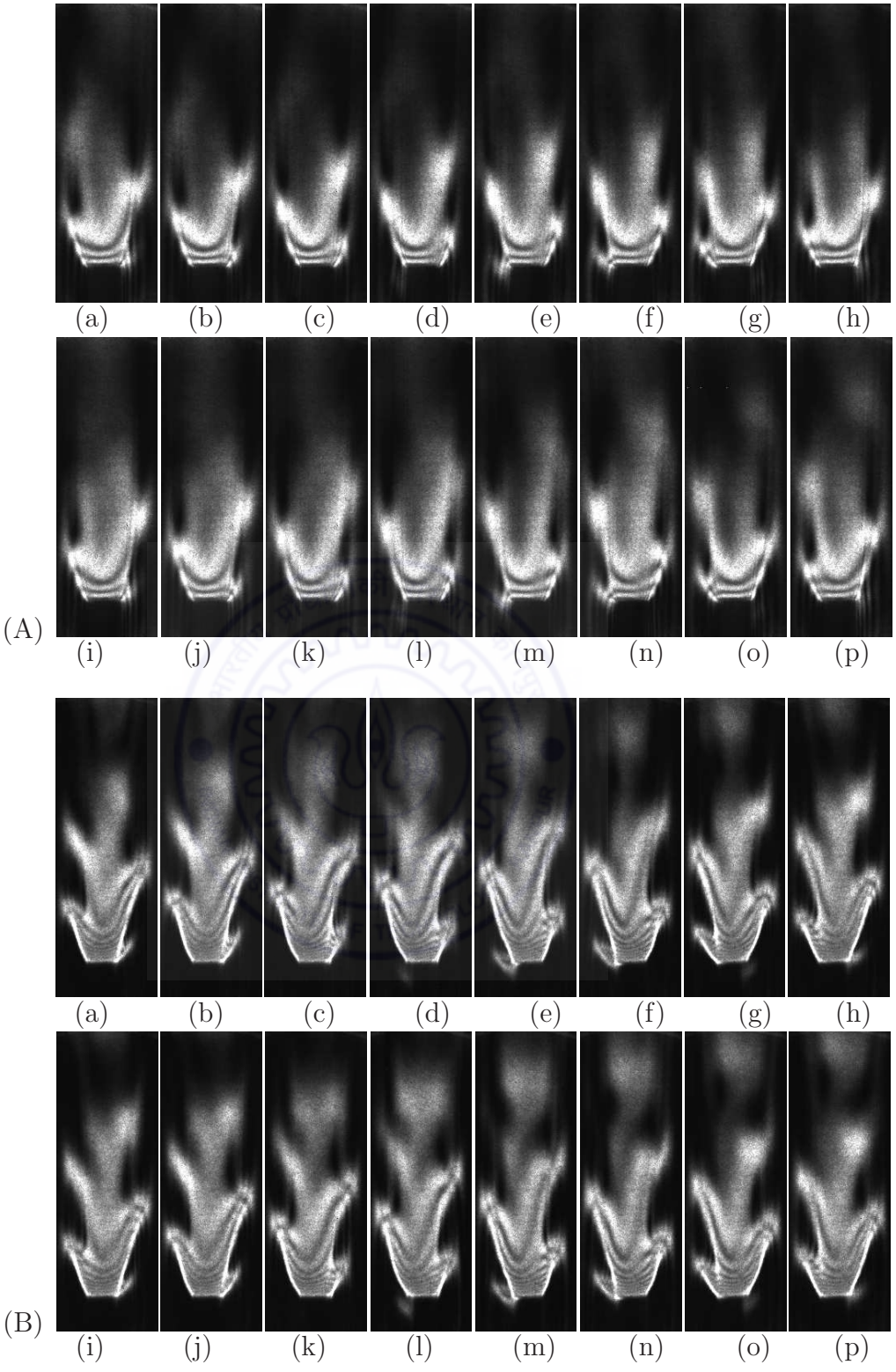

see caption on the next page

follows the periodicity of the excitation frequency (f_e). This is in contrast to the case of a circular cylinder at comparable Richardson number (Ri = 0.038) where one vortex from each side shear layer is formed for every two cycles of the cylinder oscillation i.e.

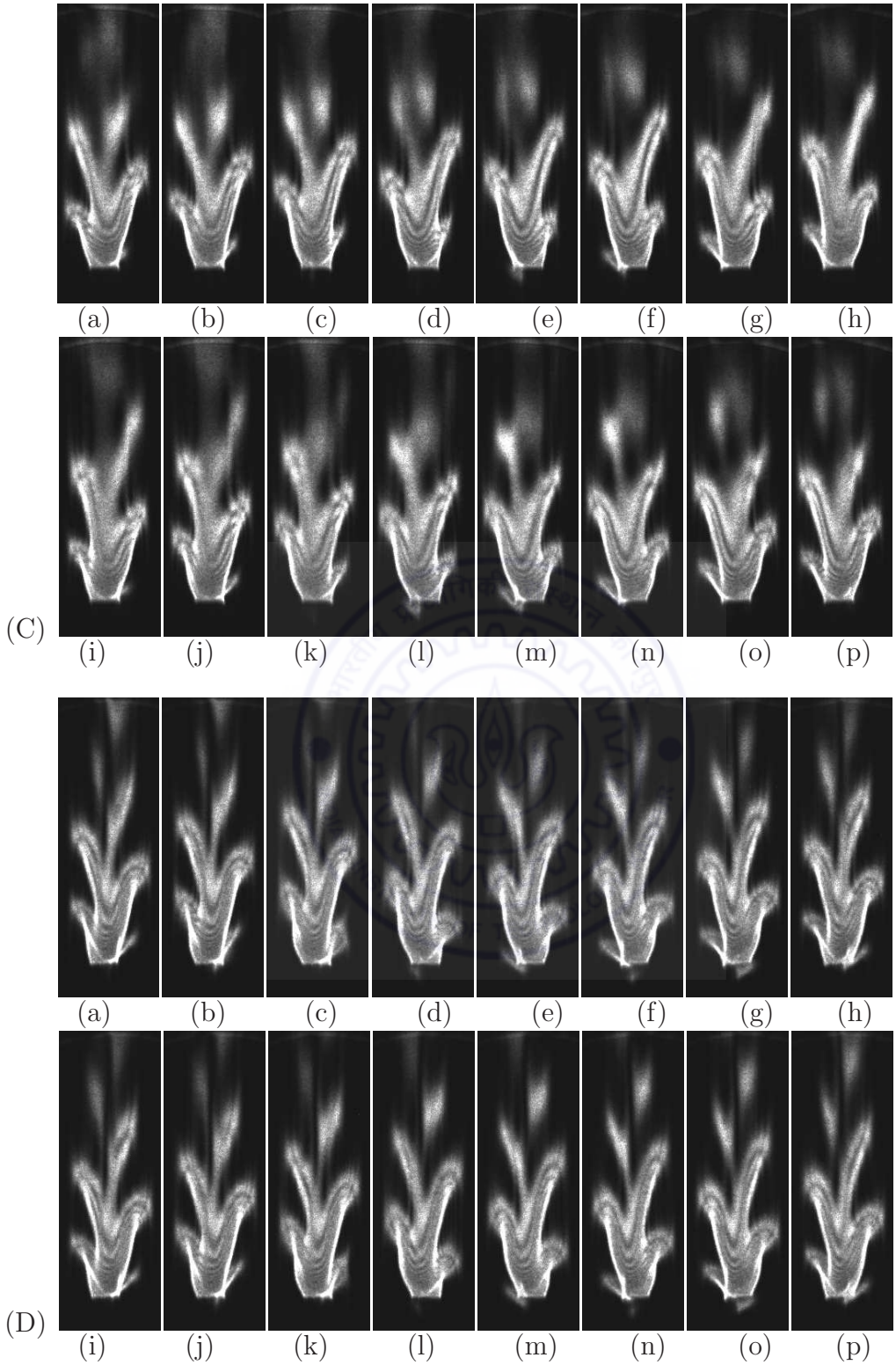

Figure 6.15: Phase-referenced schlieren images for a square cylinder corresponding to different phases (a-p) of cylinder oscillation (Figure 6.13) at super-harmonic of the Strouhal frequency ($f_e/f_s = 2$) and amplitude, $a/d = 0.08$ as a function of Richardson number: (A) Ri=0.030, (B) Ri=0.086, (C) Ri=0.121, and (D) Ri=0.167.

periodic with the natural vortex shedding frequency (f_s). Figure 6.15 (B) and (C) present the sequence of schlieren images at higher temperatures of 55°C (Ri = 0.086) and 68°C (Ri = 0.121), respectively. For both Richardson numbers, the sequence of images show that one vortex is alternatively formed from each side of the shear layer in one cycle of the cylinder oscillation. The vortex from the left side shear layer is fully formed at the extreme left position of the cylinder ('a' or 'i') in the oscillation cycle. Similarly, the vortex from the right side shear layer is fully formed at the extreme right position of the cylinder ('e' or 'm') in the oscillation cycle. For both Richardson numbers, the formation and shedding of the vortices is regular in the formation region ($x/d \approx 2$) in successive oscillation cycles. However, detached structures at the downstream locations show small irregularity in the successive oscillation cycles (see corresponding images in two rows of the sequences) and repeat themselves after every two cycles of the cylinder oscillation. This can be attributed to the presence of natural vortex shedding (f_s) in addition to the excitation frequency (f_e) in the schlieren signal at downstream locations ($x/d = 3.5$ and 5) as shown later in Section 6.2. At the surface temperature of 86°C (Ri = 0.167), Figure 6.15 (D) shows alternate shedding of two vortices from each side of the shear layer as the cylinder reaches to its extremum positions on the respective side during an oscillation cycle. In contrast to lower Richardson numbers (Ri = 0.086 and 0.121), no irregularity in the detached structures is observed in subsequent cycles at the downstream locations and exactly matching structures are repeated after every cycle. It has been shown in later section that near-wake is locked-on with the cylinder oscillation (Section 6.4) at all stream wise locations and power spectra contains a large amplitude sharply defined peak at the excitation frequency (Section 6.2). However, it may be remembered that at this Richardson number, the vortex shedding was suppressed for the stationary cylinder as shown earlier in Figure 6.2 (D).

The schlieren images corresponding to super-harmonic oscillation ($f_e/f_s = 2$) of circular and square cylinders show almost similar patterns of vortex formation in the near-wake except at the lowest Richardson number where periodicity of vortex formation is different for the two cylinders. For both the cylinders, the effect of perturbation on near-wake vortex structures become more pronounced with an increase in Richardson number. Therefore, at the higher Richardson numbers, the vortices are formed on a regular basis with a periodicity of the cylinder oscillation for both the cylinders.

6.1.6 Super-harmonic oscillation ($f_e/f_s = 3$)

Figures 6.16 and 6.17 show the sequence of phase-referenced schlieren images for transversely oscillating circular and square cylinders, respectively as a function of Richardson

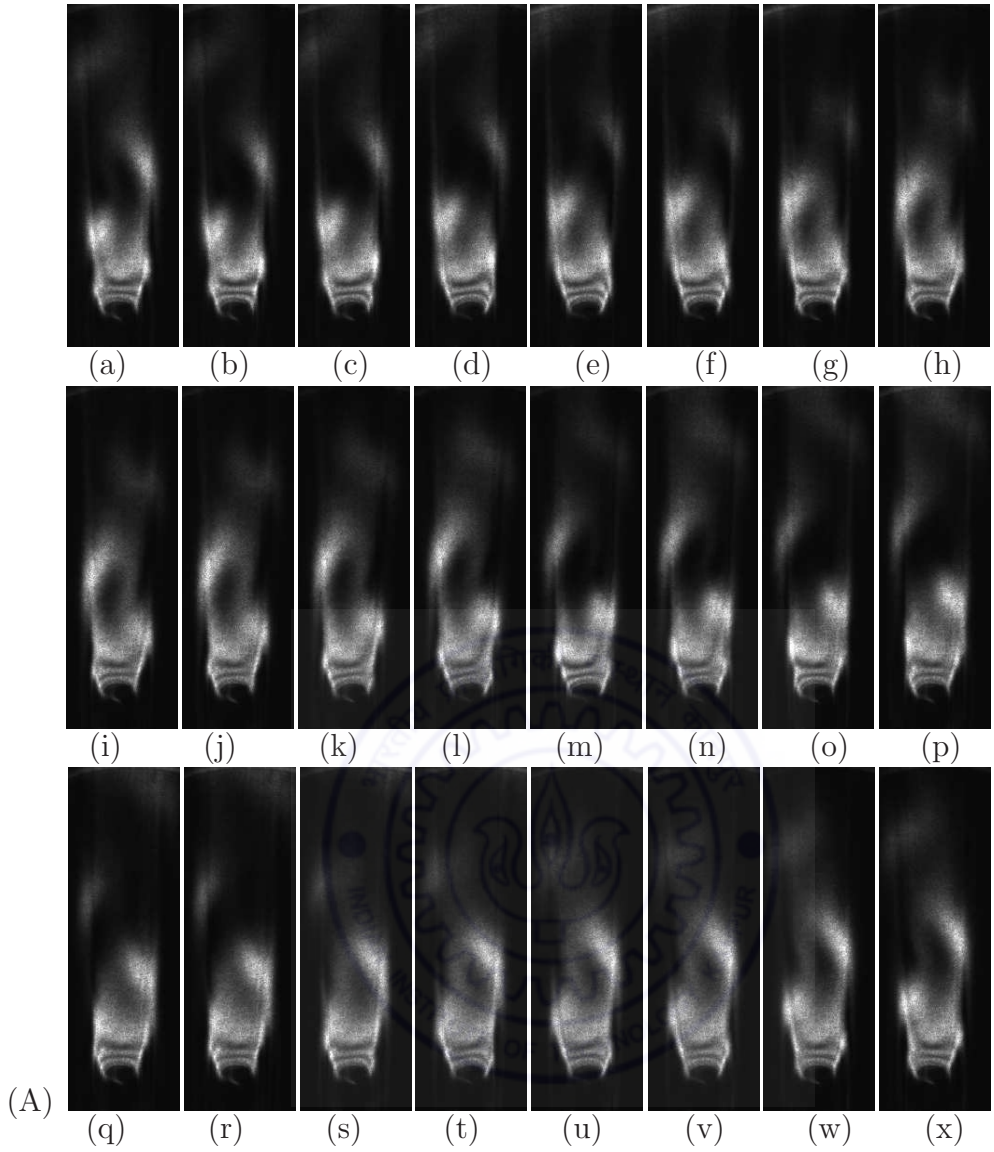

Figure 6.16 (A) : *see caption on the page number 215.*

number at super-harmonic (3 times) of the natural vortex shedding frequency (i.e. $f_e/f_s = 3$) at an amplitude ratio, $a/d = 0.08$. At this excitation frequency, phase-referencing is extended over three successive cycles of the cylinder oscillation with eight evenly spaced phases during each oscillation cycle as shown in Figure 6.10. For each Richardson number, the images corresponding to different phases (a-x) for three consecutive cycles of the cylinder oscillation are presented in three rows of the sequences. The images in first, second and third row corresponds to phases (a-h) of the first cycle, phases (i-p) of the second successive cycle and phases (q-x) of the third consecutive cycle, respectively. First image of the sequence in each row (marked as 'a', 'i' and 'q') corresponds to the extremum location of the cylinder on the left side whereas images marked as 'e', 'm' and 'u' corresponds to the extremum location of the cylinder on the right side (see Figure 6.10).

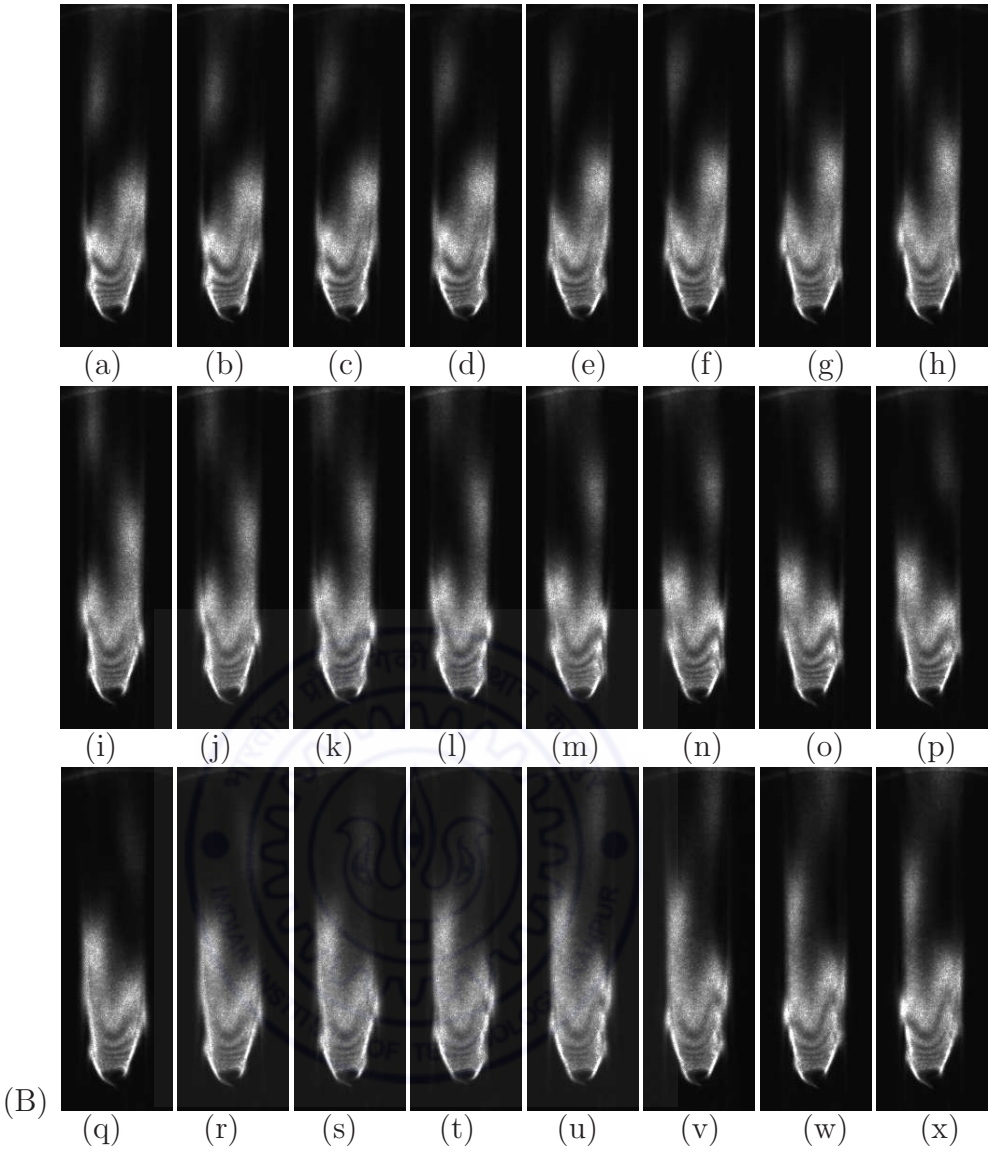

Figure 6.16 (B) : *see caption on the page number 215.*

Figure 6.16 (A) shows the sequence of schlieren images for oscillating circular cylinder at a cylinder temperature of 37°C (Ri = 0.038). The images show that one vortex from each side shear layer is shed for every three cycles of the cylinder oscillation. The vortex from the left side shear layer is fully formed when the cylinder is at the extreme left position ('a') in the first oscillation cycle. The vortex from the right side shear layer is fully formed when the cylinder is at the extreme right position ('m') in the second consecutive cycle. This indicates that vortex from one side shear layer is formed exactly after 1.5 oscillation cycles from the formation of the vortex of the other side shear layer. Therefore, formation of vortices follows the periodicity of the fundamental Strouhal frequency. The inspection of long sequences of images show that vortex structures repeat itself after every three cycles of the cylinder oscillation. It has been shown later that near-wake is

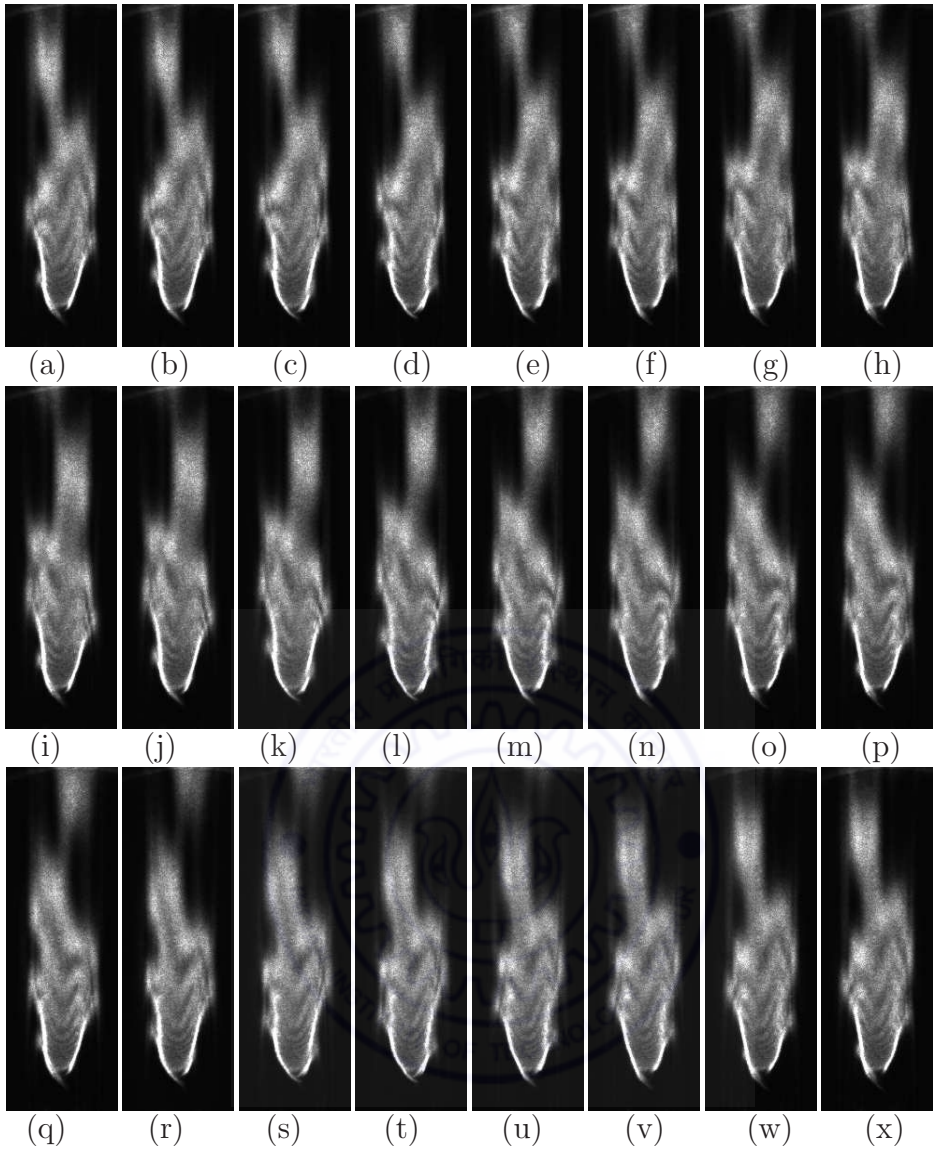

Figure 6.16 (C) : *see caption on the page number 215.*

not locked with the cylinder oscillation (Section 6.4) and the power spectra contains sharp spectral peak at the natural vortex shedding frequency f_s (Section 6.2). Krishnamoorthy *et al.* (2001) observed that for the 3-superharmonic excitation, the near-wake dynamics repeated itself every third cycle of cylinder motion, and a coherent, synchronized wake pattern was formed. The size of the formation region was substantially reduced at this excitation frequency. In a recent numerical study, Zheng and Zhang (2008) observed that every complete cycle of the entrained frequency of natural vortex shedding contains exactly 3 cycles of the oscillation frequency.

Figures 6.16 (B) and (C) present sequence of schlieren images at higher temperatures of 51°C (Ri = 0.078) and 68°C (Ri = 0.124) respectively. The sequence of images show

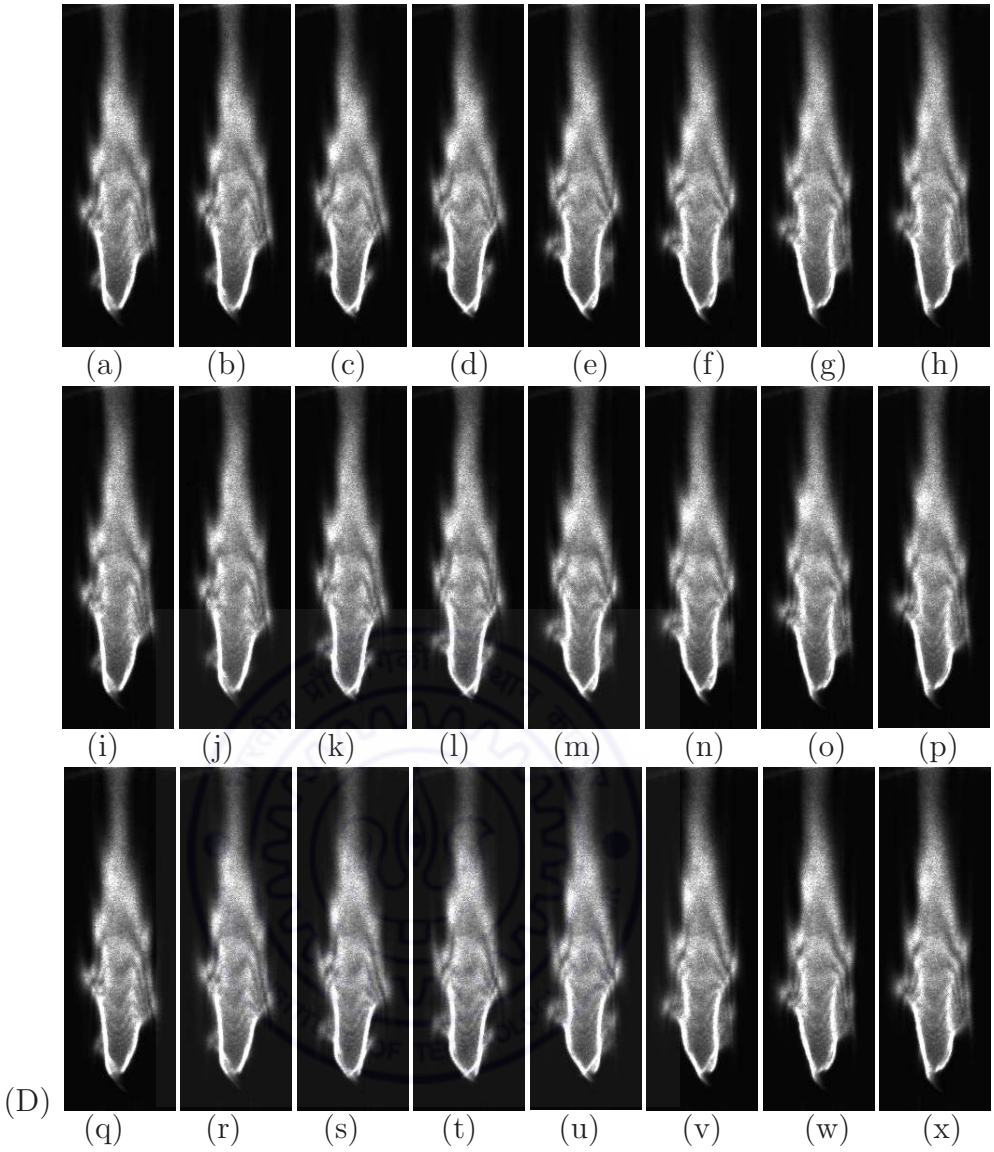

Figure 6.16: Phase-referenced schlieren images for a circular cylinder corresponding to different phases (a-x) of cylinder oscillation (Figure 6.10) at super-harmonic of the Strouhal frequency ($f_e/f_s = 3$) and amplitude, $a/d = 0.08$ as a function of Richardson number: (A) Ri=0.038, (B) Ri=0.078, (C) Ri=0.124, and (D) Ri=0.145.

that one vortex is alternatively formed from the left side and right side shear layers when the cylinder reaches to the extreme left position ('a' or 'i' or 'q') and the extreme right position ('e' or 'm' or 'u') respectively in the oscillation cycle. However, detached structures from both sides of the shear layer at the downstream locations are repeated only after three cycles of the cylinder oscillation. The patterns of vortex structures follows the periodicity of the natural vortex shedding frequency. It has been shown later in Section 6.4 that for both the Richardson numbers, near-wake vortices are quasi locked-on with the cylinder oscillation at $x/d = 2$ location, while not locked with the cylinder

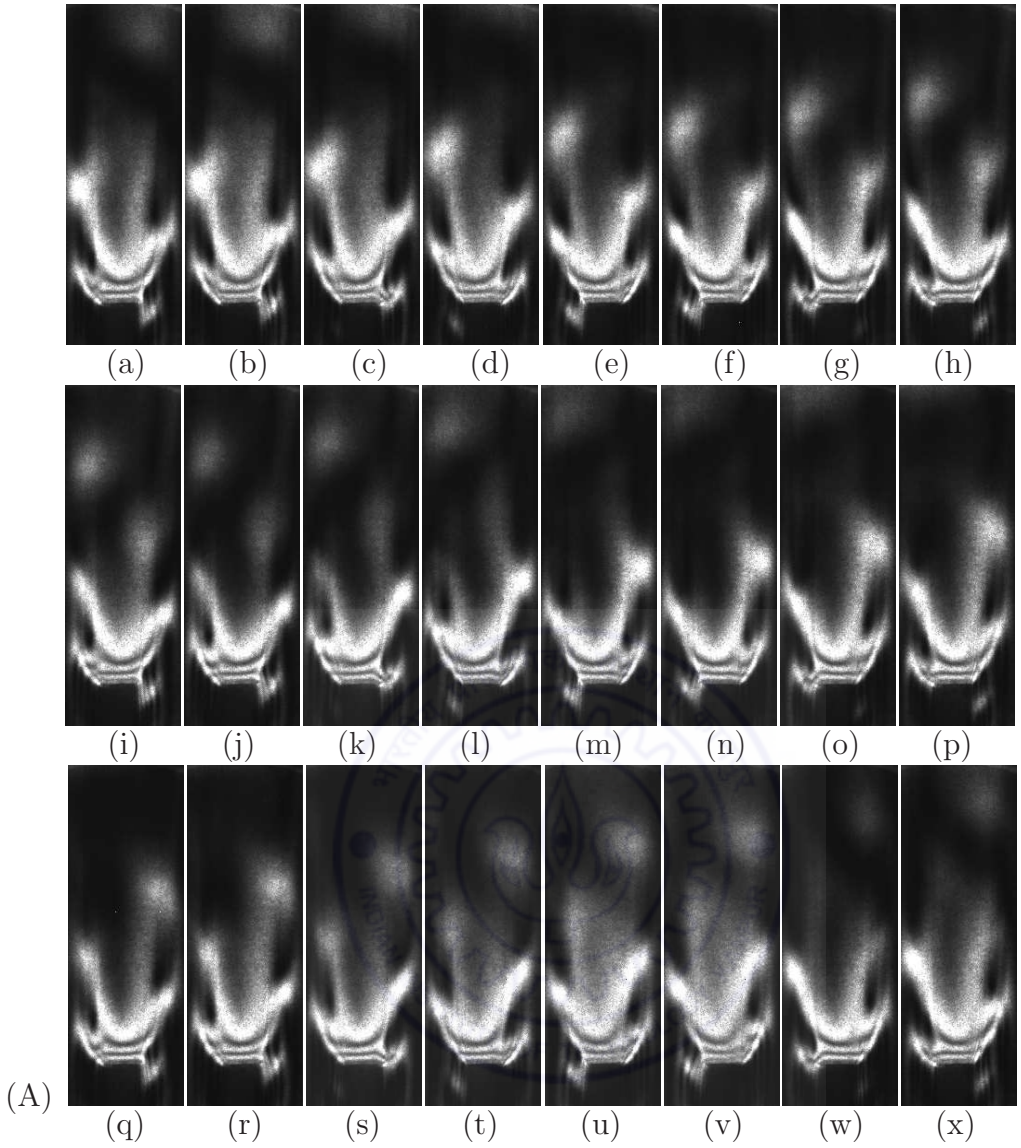

Figure 6.17 (A) : *see caption on the page number 219.*

oscillation at $x/d = 3.5$ and 5 locations. At a higher surface temperature of 76°C (Ri = 0.145), Figure 6.16 (D) shows that vortices are alternatively formed from either side of the cylinder during each oscillating cycle. However, the structures from both sides propagate to the downstream direction without detaching from the shear layer and merges with the plume at the centerline of the cylinder. The three rows of the sequences show that exactly similar patterns of the vortex structures are observed in the successive oscillation cycles. It may be remembered that vortex shedding was suppressed for the stationary cylinder and only a single steady plume was seen at the center of the cylinder (Figure 6.1 (D)) at this Richardson number.

Figure 6.17 (A) shows the sequence of schlieren images for oscillating square cylinder at a surface temperature of 35°C (Ri = 0.03). The images show that one vortex is

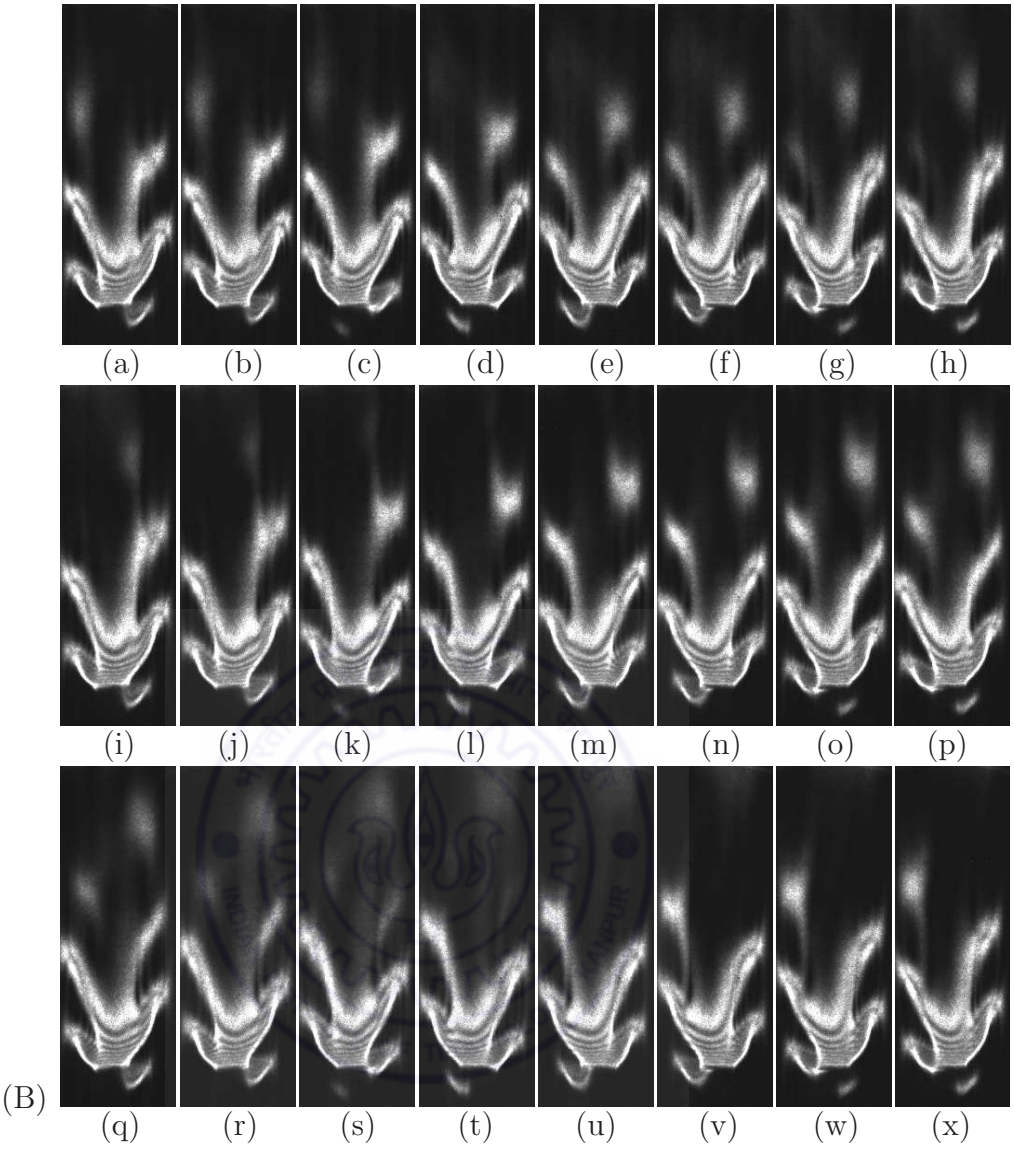

Figure 6.17 (B) : *see caption on the page number 219.*

alternatively formed from each side of the shear layer in the formation region when the cylinder reaches to the extremum positions on the respective sides in one oscillation cycle. Therefore, formation of vortices follows the periodicity of the excitation frequency (f_e). This is in contrast to the case of a circular cylinder at comparable Richardson number (Ri = 0.038) where one vortex from each side shear layer is formed for every three cycles of the cylinder oscillation. The sequence of schlieren images at the higher temperatures of 55°C (Ri = 0.086) and 68°C (Ri = 0.121) are presented in Figure 6.17 (B) and (C), respectively. One vortex is formed from each side of the shear layer in one oscillation cycle for both Richardson numbers. The vortex from the left side shear layer is formed at the extreme left position of the cylinder ('a' or 'i' or 'q') in the oscillation cycle. Similarly, the vortex from the right side shear layer is formed at the extreme right position of

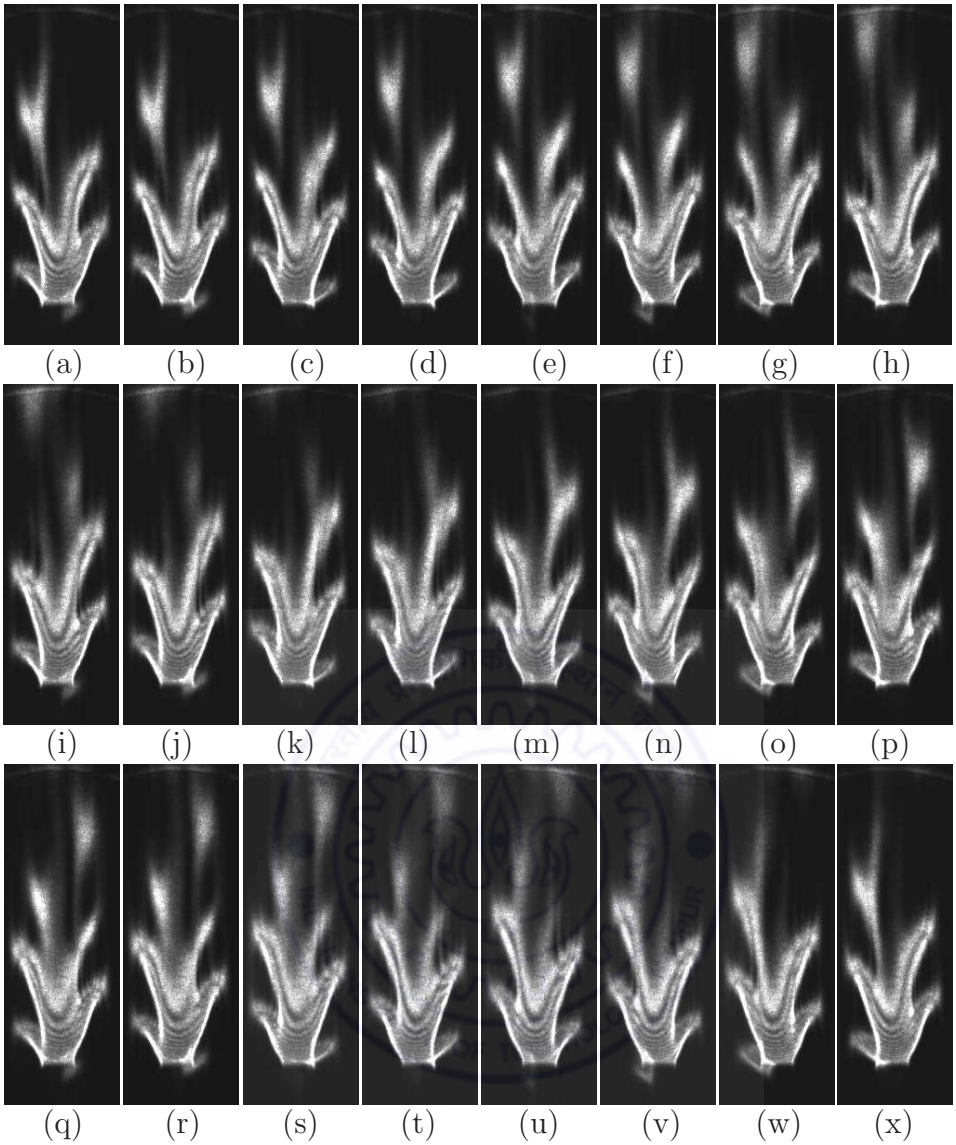

Figure 6.17 (C) : *see caption on the page number 219.*

the cylinder ('e' or 'm' or 'u') in the oscillation cycle. The formation and shedding of the vortices is regular in the formation region ($x/d \approx 2$) of successive oscillation cycles for both Richardson numbers. However, detached vortices at the downstream locations show small irregularity in their structures as seen in three rows of image sequences in the successive oscillation cycles. The structures repeat themselves after every three cycles of the cylinder oscillation. This can be attributed to the presence of natural vortex shedding (f_s) in the schlieren signal at the downstream locations ($x/d = 3.5$ and 5) as shown later in Section 6.2. At the surface temperature of 86°C (Ri = 0.167), Figure 6.17 (D) shows that two vortices are alternatively shed from each side of the shear layer as the cylinder reaches to the extreme positions on the respective side during an oscillation cycle. In contrast to lower Richardson numbers (Ri = 0.086 and 0.121), no irregularity in

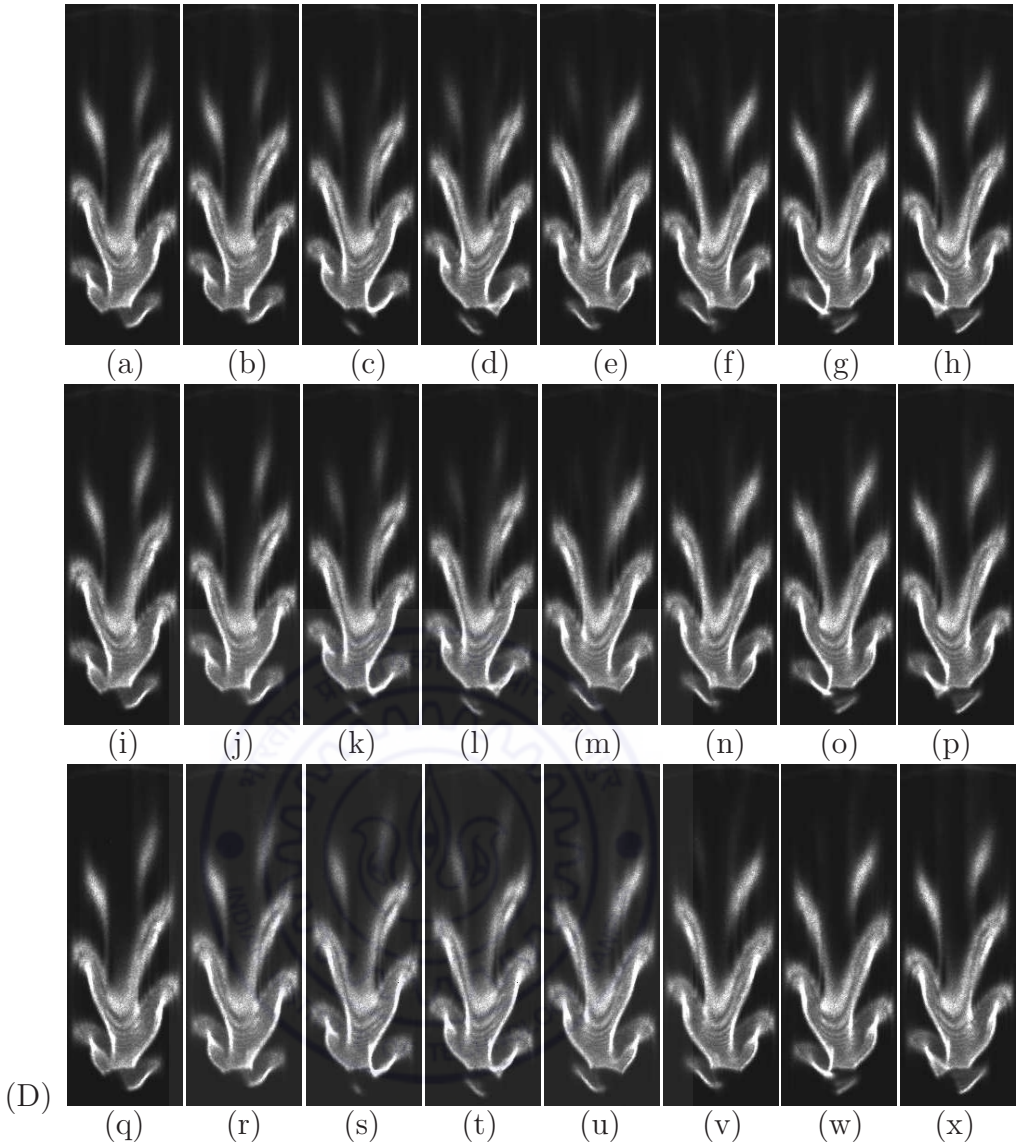

Figure 6.17: Phase-referenced schlieren images for a square cylinder corresponding to different phases (a-x) of cylinder oscillation (Figure 6.10) at super-harmonic of the Strouhal frequency ($f_e/f_s = 3$) and amplitude, $a/d = 0.08$ as a function of Richardson number: (A) Ri=0.030, (B) Ri=0.086, (C) Ri=0.121, and (D) Ri=0.167.

the detached vortices is observed in subsequent cycles at the downstream locations and exactly matching structures are repeated after every cycle. It has been shown in later section that near-wake is locked-on with the cylinder oscillation (Section 6.4) at all stream wise locations and power spectra contains a large amplitude sharply defined peak at the excitation frequency (Section 6.2). It may be remembered that at this Richardson number, the vortex shedding was suppressed for the stationary cylinder as shown in Figure 6.2 (D).

The schlieren images corresponding to super-harmonic oscillation ($f_e/f_s = 3$) of circular and square cylinders show a difference in the periodicity of the vortex formation

at the lowest Richardson number. At lowest Richardson number (Ri $\approx$ 0.03) the vortices are observed at oscillation frequency for the square cylinder contrary to that at the vortex shedding frequency for the circular cylinder. At the intermediate Richardson numbers, the vortices are formed on a regular basis with a periodicity of the cylinder oscillation for both the cylinders. However, much difference in the structures i.e. shape of the detached vortices are seen between the two cylinders.

6.2 Power spectra

Periodic shedding of vortices produce a dominant peak in the light intensity spectrum at a frequency corresponding to the vortex shedding frequency for a stationary cylinder. However, when the cylinder is forced to oscillate, multiple peaks occur in the spectrum as an outcome of nonlinear interactions between the natural instability and imposed excitation. Therefore, besides the natural shedding frequency (f_s) and the excitation frequency (f_e), a combination of these frequencies e.g. sum ($f_e + f_s$) and differences ($f_e - f_s$) appear in the spectra. A clean spectra with large-amplitude sharply defined peak at the excitation frequency suggest the *lock-on* of vortex shedding with the cylinder oscillation. The power spectra of the light intensity fluctuations in the schlieren images are presented in Figure 6.18 and 6.19 for oscillating circular and square cylinders, respectively to characterize the vortex shedding mechanism and relate it to various locked-on states discussed later in Section 6.4. For each frequency ratio i.e. f_e/f_s = 0, 0.5, 1, 1.5, 2, and 3, the power spectra are presented as a function of Richardson number (Ri) at the amplitude ratio, a/d = 0.08. Three stream-wise locations, namely x/d = 2, 3.5 and 5 in the near-wake region are considered. Outer edge of the shear layer is selected as the transverse location for each stream wise locations, which is determined as the boundary of the transverse spread of the bright zone in time-averaged schlieren images. Depending upon the excitation frequency, Richardson number and cylinder geometry, it ranges from y/d = 0.6 to 1.0. Ongoren and Rockwell (1988a) determined the phase of the vortex-shedding process relative to the displacement of the cylinder by placing a hot-film probe just at the outer edge of the mean shear layer at $y/d = 1$ and $x/d = 3$. Krishnamoorthy *et al.* (2001) mounted the hot film probe in the near-wake region at $y/d = 0.5$ and $x/d = 4.6$ for measuring shedding frequencies in the near-wake. These investigations rely on the data from the fixed transverse locations (i.e. either $y/d = 0.5$ or 1). The Shear layer locations depend on the oscillation parameters. Therefore, the present approach is advantageous as the outer edge of the shear layer can be precisely determined for different stream-wise locations (x/d) and for various operating conditions (i.e. f_e/f_s, Ri and cylinder geometry). The power spectra have been calculated using 3000 images acquired over 12 seconds at a

rate of 250 frames per second. For all locations, the light intensity is averaged over 4×4 pixels to diminish pixel level noise.

Stationary cylinder **($f_e/f_s = 0$)** : The power spectra for stationary cylinders have been included to determine the natural vortex shedding frequency and for comparison with the oscillation results. Figure 6.18 (A) and 6.19 (A) show the power spectra for stationary circular and square cylinders, respectively as a function of Richardson number. The scale of the abscissa is non-dimensionalized with the corresponding vortex shedding frequency (f_s). i.e. 1, 2 and 3 value on the abscissa denote the vortex shedding frequency and its superharmonics, respectively. At critical Richardson numbers i.e. Ri = 0.145 for the circular cylinder and Ri = 0.167 for the square cylinder, vortex shedding is suppressed. Therefore, for these Richardson numbers, the abscissa scale is normalized by a representative vortex shedding frequency (f_s) obtained at a cylinder surface temperature slightly less than the temperature at which vortex shedding is suppressed. Figure 6.18 (A) show that for the lower Richardson numbers of Ri = 0.038 and 0.078, at $x/d = 2$ location, the dominant frequency in the spectrum is the vortex shedding frequency, f_s. At the downstream locations, $x/d = 3.5$ and 5, the harmonics at twice the shedding frequency ($2f_s$) are present with the fundamental mode. The presence of harmonics can be attributed to the interaction between vortices of opposite shear layers. For higher Richardson number, Ri = 0.124, the power spectra are less noisy as compared to that at lower Richardson numbers and clean peak at the Shedding frequency (f_s) is observed at all stream-wise locations. The power spectra at Ri = 0.145 show the absence of any clear peak and there is a broadband spectra depicting suppression of the vortex shedding. The visualization images in Figure 6.1 (D) show the merging of two shear layers into a single steady plume conforming the suppression of unsteadiness at this Richardson number. For square cylinder, at the lower Richardson numbers of Ri = 0.030 and 0.086, a single peak at the vortex shedding frequency (f_s) is seen in the spectra at $x/d = 2$ location (see Figure 6.19 (A)). At the downstream locations, $x/d = 3.5$ and 5, the influence of harmonics at twice the shedding frequency ($2f_s$) is also observed. However, compared to the circular cylinder at Ri = 0.038 and 0.078 (Figure 6.18 (A)), the spectral power of the harmonic mode relative to the fundamental mode is smaller. This may be attributed to the wider wake of the square cylinder compared to that of a circular cylinder. Thus, the wake signal extracted from a location in the outer edge of the shear layer experiences comparatively lesser influence of the opposite side vortices. For a higher Richardson number, Ri = 0.121, the power spectra show clean peak at the Shedding frequency (f_s) for all the stream-wise locations except $x/d = 5$, where harmonics are also seen along with the fundamental mode. The spectra with a clear peak at the vortex shedding frequency (f_s) for Ri = 0.030, 0.086 and 0.121 transforms to a broadband spectra for Ri = 0.167 indicating the inhibition

of the vortex shedding process. At this Richardson number, the visualization images in Figure 6.2 (D) show the appearance of a single steady plume at the center of the cylinder depicting suppression of vortex shedding. The overall behavior of the power spectra are similar for both circular and square cylinders indicating identical influence of buoyancy.

Figures 6.18 (B-F) and 6.19 (B-F) show power spectra of the schlieren signal for oscillating circular and square cylinders, respectively as a function of Richardson number. For each Richardson number in Figures 6.18 (and 6.19) (B), (C), (D), (E) and (F), the cylinder is oscillated at 1, 0.5, 1.5, 2 and 3 times the corresponding vortex shedding frequency of the stationary cylinder (i.e. f_e/f_s = 1, 0.5, 1.5, 2 and 3). The amplitude ratio is kept at a value, a/d = 0.08. For all frequency ratios (f_e/f_s), the scale of abscissa is non-dimensionalized with the corresponding cylinder excitation frequency (f_e). Therefore, integers 1, 2 and 3 on the abscissa denote the excitation frequency (f_e) and its superharmonics, respectively. The dominant vortex shedding frequency (f_v) of the oscillating cylinder and other interaction components are non-dimensionalized with the corresponding cylinder excitation frequency (f_e). The results of the power spectra have been explained in the following paragraphs.

Fundamental oscillation **(f_e/f_s = 1)** : A dominant spectral peak is observed at the excitation frequency (f_e) for all stream-wise locations with fundamental oscillation (f_e/f_s = 1) of the circular cylinder, at a Richardson number of Ri = 0.038 in Figure 6.18 (B). Smaller peaks at twice ($2f_e$) and thrice ($3f_e$) of the excitation frequency are also seen at the downstream locations (x/d = 3.5 and 5) due to the interactions of the shed vortices at frequency, f_e from opposite side shear layers. The presence of natural vortex shedding frequency (f_s) along with its harmonics is seen as very small peaks at the base region. It has been shown later in Section 6.4 that due to this intermittency, the vortex shedding is quasi locked-on with the cylinder oscillation despite the presence of dominant peak in the power spectra at excitation frequency (f_e) for all stream-wise locations. For the higher Richardson numbers of Ri = 0.078 and 0.124, a dominant peak at the excitation frequency (f_e) along with the smaller peak at its harmonic ($2f_e$) occur in the spectra at x/d = 2 location. For the downstream locations, x/d = 3.5 and 5, three sharp peaks at f_e, $2f_e$ and $3f_e$ are evident in the spectra and power of the harmonic mode ($2f_e$) is similar relative to that of the dominant mode (f_e). This can be attributed to the greater interaction between the vortices shed at frequency, f_e from opposite side shear layers at further downstream locations. It has been shown earlier in visualization images (Figures 6.4 (B) and(C)) that increase in heating level shifts the point of vortex detachment to a farther downstream location and oscillation of the cylinder increases the inclination of the vortices with the wake centerline. Therefore, vortices from the opposite shear layers are more active at the downstream locations. Contrary to the lower Richardson number (Ri = 0.038), a

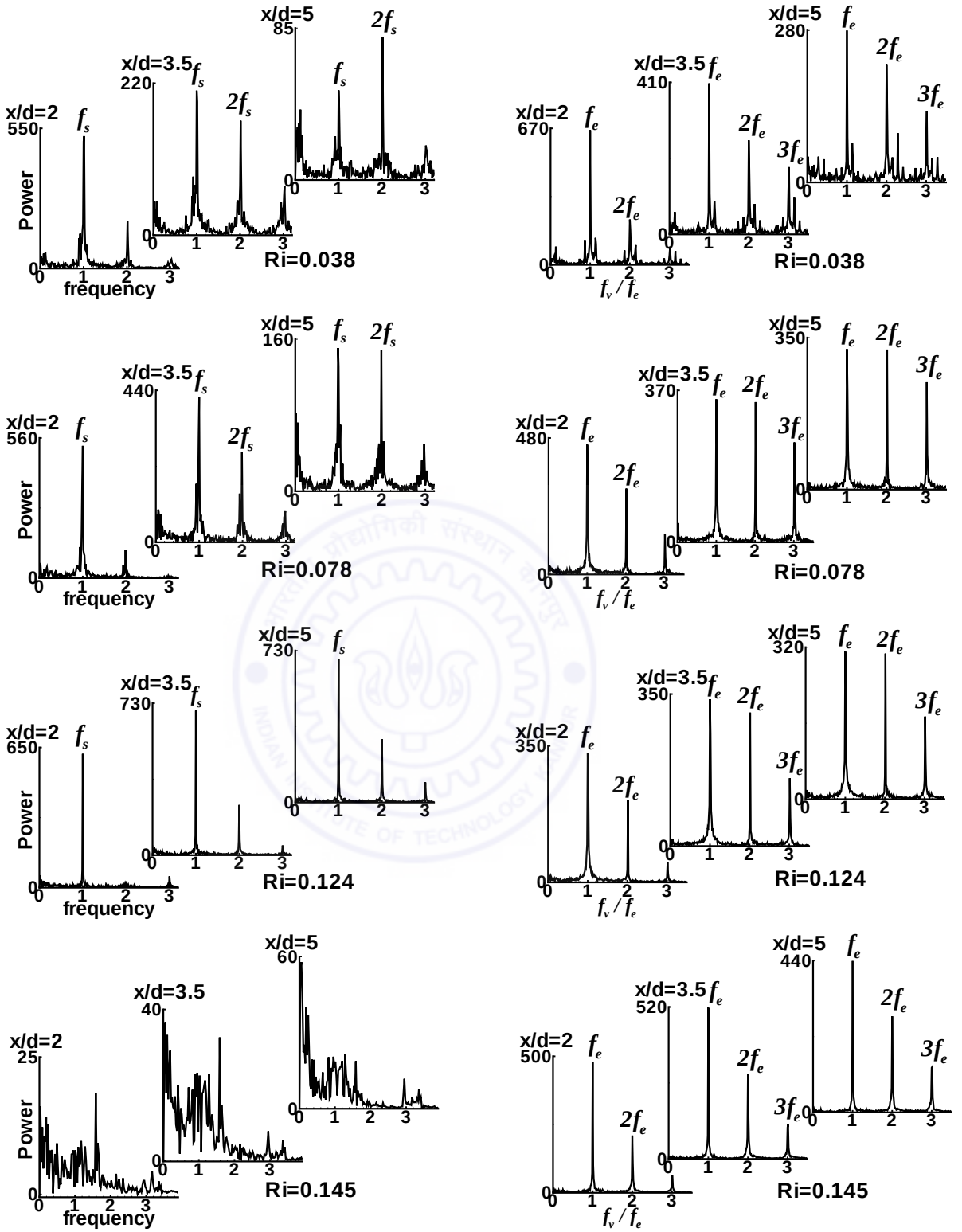

(A) (B)

Figure 6.18 (A) and (B): *see caption on the page number 225.*

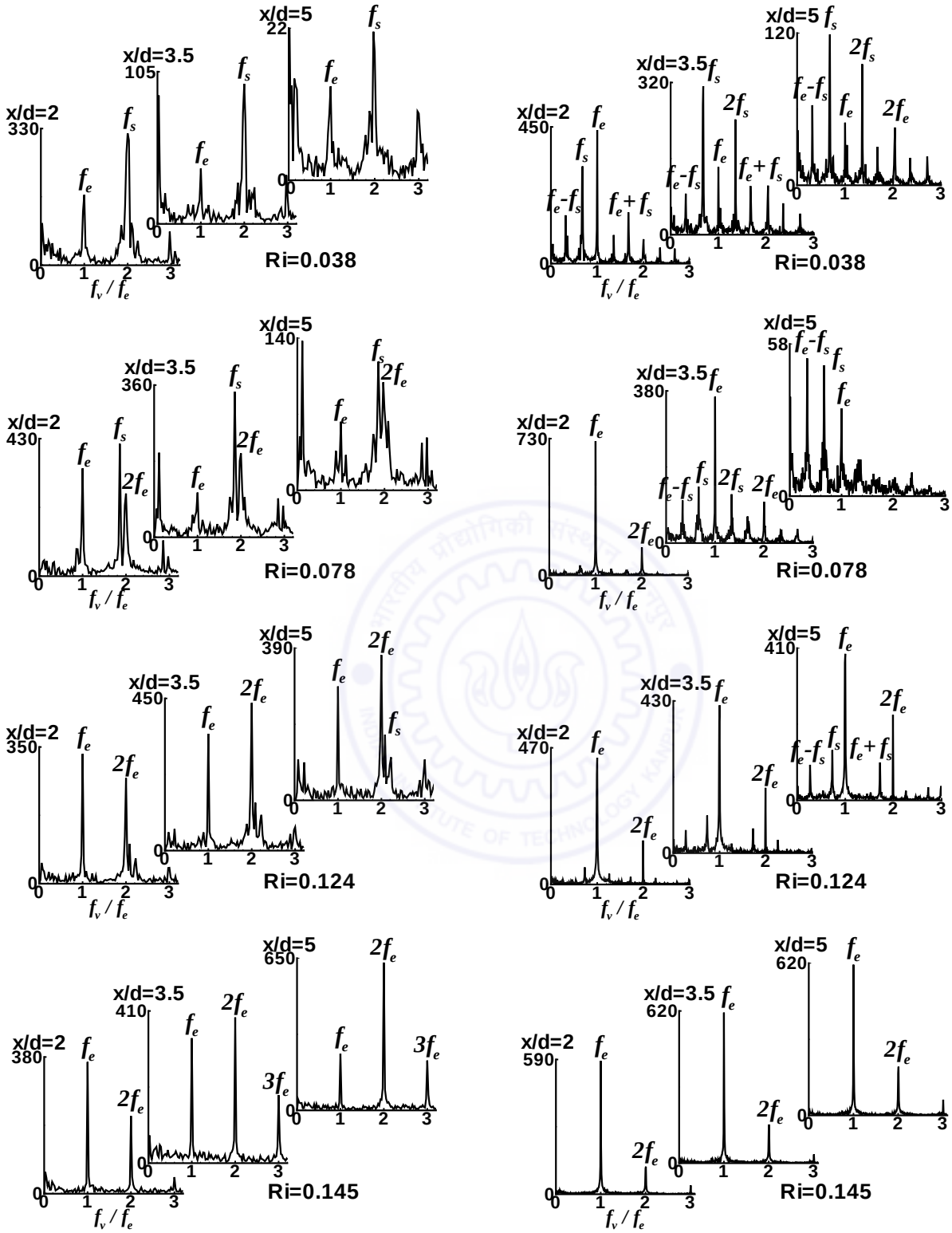

Figure 6.18 (C) and (D): *see caption on the page number 225.*

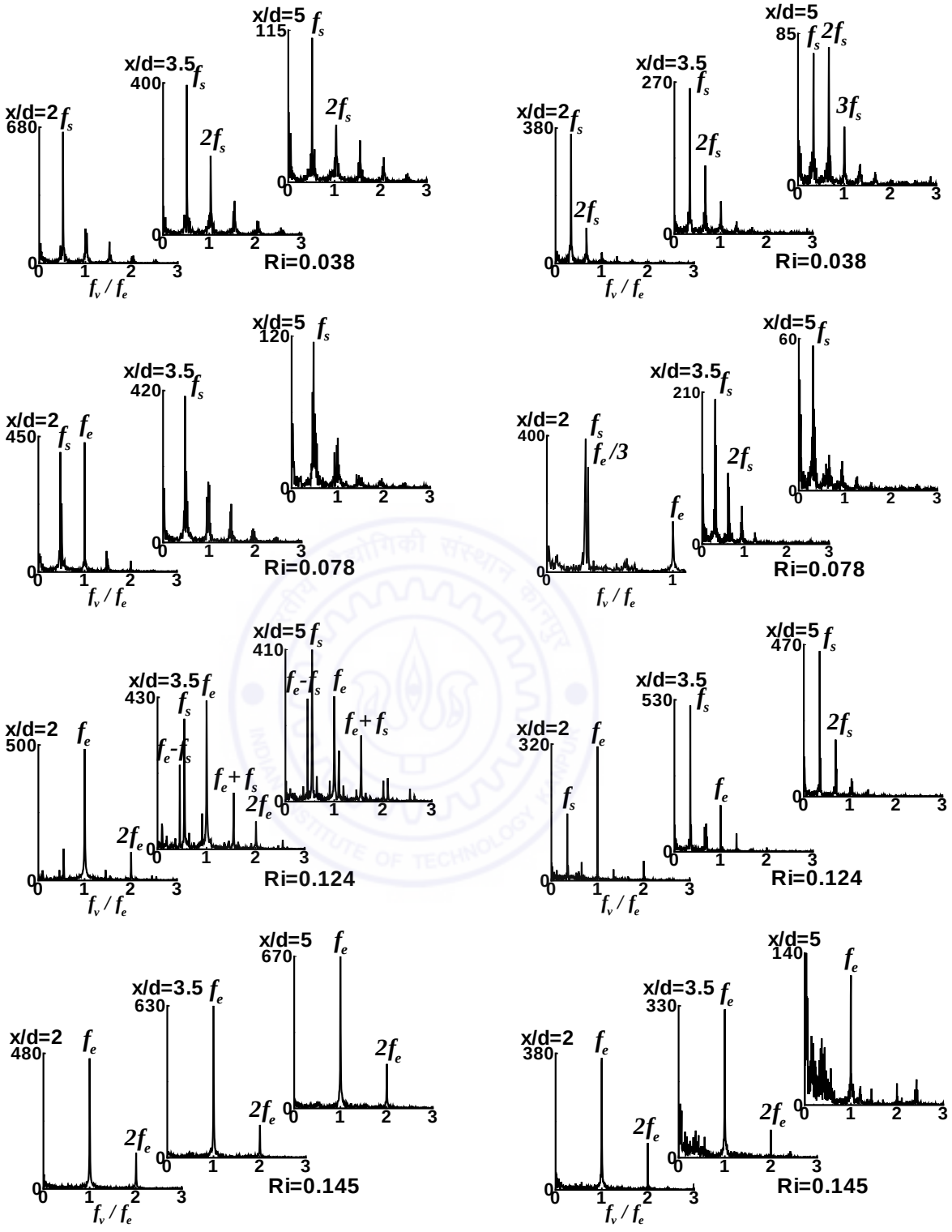

Figure 6.18: Power spectra of light intensity at various stream wise locations (x/d = 2, 3.5 and 5.0) for the oscillating circular cylinder at Re = 105. Functional dependence on Richardson number is shown for different excitation frequencies at $a/d = 0.08$: (A) $f_e/f_s = 0$, (B) $f_e/f_s = 1$, (C) $f_e/f_s = 0.5$, (D) $f_e/f_s = 1.5$, (E) $f_e/f_s = 2$, and (F) $f_e/f_s = 3$.

cleaner spectra without side band noise is observed for all stream-wise locations at higher Richardson numbers (Ri = 0.078 and 0.124). The flow structures in the near-wake are strongly synchronized with cylinder oscillation for all stream wise locations. At a higher Richardson number of Ri = 0.145, a spectral peak at the excitation frequency (f_e) is evident for all stream-wise locations. It may be remembered that, at this Richardson number, the power spectra for stationary cylinder in Figure 6.18 (A) shows a broadband spectra without any clear peak depicting suppression of the vortex shedding. The existence of clean peak at the excitation frequency (f_e) and comparison with visualization images in Figure 6.4 (D) indicates that the near-wake is strongly synchronized with the cylinder oscillation.

The power spectra for square cylinder at a Richardson number of Ri = 0.03 show the dominance of sharply defined peak at the excitation frequency (f_e) for all stream-wise locations in Figure 6.19 (B). The presence of harmonics (i.e. $2f_e$ and $3f_e$) at downstream locations (x/d = 3.5 and 5) show the interaction between shed vortices from opposite side shear layers. It has been shown in a later Section 6.4 that near-wake is locked-on with the cylinder oscillation at x/d = 2 location. However, it is quasi locked-on at x/d = 3.5 and 5 locations as evident from the small amplitude fluctuations i.e. noise of the power spectra. A dominant peak at the excitation frequency (f_e) with smaller peak at its harmonic ($2f_e$) are seen in the spectra at x/d = 2 location for the higher Richardson numbers of Ri = 0.086 and 0.121. At the downstream locations, x/d = 3.5 and 5, three sharp peaks at f_e, $2f_e$ and $3f_e$ occur in the spectra similar to those observed for the circular cylinder at comparable Richardson numbers (Ri = 0.078 and 0.124) in Figure 6.18 (B). However, contrary to the circular cylinder, spectral power of the harmonic mode ($2f_e$) relative to the dominant mode (f_e) is smaller. This can be attributed to a wider wake for the square cylinder as compared to that of a circular cylinder. Thus, the wake signal extracted from a location in the outer edge of the shear layer experiences comparatively lower influence of the opposite side vortices. It has been shown in a later section that the vortices in the near-wake are locked-on with the cylinder oscillation for all stream wise locations. At a higher Richardson number of Ri = 0.167, a dominant spectral peak at the excitation frequency (f_e) is observed for all stream-wise locations. Harmonical peaks at $2f_e$ and $3f_e$ are also seen at the downstream locations (x/d = 3.5 and 5). However, at this Richardson number, the power spectra for non-oscillating cylinder in Figure 6.19 (A) does not display any clear peak depicting absence of the vortex shedding process. Therefore, existence of clean peaks at the excitation frequency (f_e) and its harmonics show that vortices have reappeared in the near-wake. It will be shown in a later Section 6.4 that reappeared structures are completely locked-on with the periodicity of the cylinder motion for all stream-wise locations. The overall behaviour of the power spectra for fundamental

oscillation of the circular and square cylinders is almost similar. The only differences are that the interaction of the opposite shear layer is smaller for the square cylinder resulting in lower magnitude harmonics compared to the circular cylinder and the square cylinder is more responsive to imposed oscillation compared to the circular cylinder as evident from the spectra at critical Richardson number.

Sub-harmonic oscillation **($f_e/f_s = 0.5$)** : The power spectra at a Richardson number of Ri = 0.038 show a dominant peak at the natural vortex shedding frequency (f_s) along with smaller peak at the excitation frequency (f_e) for all stream-wise locations for sub-harmonic oscillation ($f_e/f_s = 0.5$) of the circular cylinder (Figure 6.18 (C)). In a later section (Section 6.4), it has been shown that vortex shedding is not locked with the cylinder oscillation for all stream-wise locations. Zheng and Zhang (2008) observed that for $\frac{1}{2}$-subharmonic excitation, single peak at the natural vortex shedding frequency (f_s) occur in the C_L spectrum, while significant peaks both at f_s and f_e were observed in the C_D spectrum. The authors related the occurrence of the peaks, both at f_s and f_e to incomplete synchronization. At a higher Richardson number of Ri = 0.078, the harmonic mode of the excitation frequency ($2f_e$) along with dominant peak at the natural vortex shedding frequency (f_s) is evident for all stream-wise locations. Extremely small difference between f_s and $2f_e$ value is evident from the power spectra. Smaller magnitude peak at the excitation frequency (f_e) is also observed . Due to dominance of the natural vortex shedding frequency (f_s), near-wake is not locked with the cylinder motion at all stream wise locations (Section 6.4). With further increase in Richardson number to Ri = 0.124, two sharp spectral peaks, one at the excitation frequency (f_e) and other at its harmonic ($2f_e$) are seen in the spectra at all stream wise locations. Minor contribution at the natural shedding frequency (f_s) is observed at $x/d = 5$ location. In a later section (Section 6.4) it has been shown that the vortex structures are quasi locked with the cylinder motion at $x/d = 2$ and 3.5 locations, while not locked at $x/d = 5$ location. At the highest Richardson number of Ri = 0.145, sharp spectral peaks at the excitation frequency (f_e) and its super-harmonics are present in the spectra for all stream wise locations. At x/d = 2 location, the dominant peak occurs at the excitation frequency (f_e), while at x/d = 3.5 and 5 locations, the dominant peak occur at its harmonic, $2f_e$. At this Richardson number, the existence of sharp spectral peaks show the re-appearance of vortex structures in the near-wake as opposed to the broadband spectra in Figure 6.18 (A) for the stationary cylinder. These structures are quasi locked with the cylinder oscillation for all stream wise locations (Section 6.4).

For square cylinder, at a Richardson number of Ri = 0.03, a dominant peak at the excitation frequency (f_e) along with smaller peak at the natural vortex shedding frequency (f_s) is observed in the spectra at $x/d = 2$ location. At the downstream locations, x/d

= 3.5 and 5, the dominant peak is observed at f_s along with smaller peak at f_e. At the higher Richardson number of Ri = 0.086, the dominant peak is observed at $2f_e$ for x/d = 2 location, both at $2f_e$ and f_s for x/d = 3.5 location and at f_s for x/d = 5 location. Smaller peak at the excitation frequency (f_e) is also observed at all the stream wise locations. For both the Richardson numbers, Ri = 0.030 and 0.086, the vortex structures are quasi locked with the cylinder motion at x/d = 2 location, while not locked at x/d = 3.5 and 5 locations (Section 6.4). At a higher Richardson numbers of Ri = 0.121, a large-amplitude spectral peak at the harmonic of the excitation frequency, $2f_e$ occur in the spectra at all stream wise locations. As compared to the lower Richardson numbers (Ri = 0.030 and 0.086), the spectra is cleaner without any broadband noise. Section 6.4 has shown that near-wake is quasi locked with the cylinder oscillation at all stream wise locations. At the highest Richardson number of Ri = 0.167, a dominant spectral peak at the excitation frequency (f_e) along with smaller harmonical peak at $2f_e$ is observed for all stream-wise locations. The existence of clean peak at the excitation frequency (f_e) and its harmonic ($2f_e$) shows that vortices have reappeared in the near-wake. It has been shown later in section 6.4 that reappeared structures are locked-on with the cylinder motion for all stream-wise locations. The overall behaviour of the power spectra for sub-harmonic oscillation (f_e/f_s = 0.5) of the circular and square cylinders is almost similar.

Non-harmonic oscillation **(f_e/f_s = 1.5)** : Figure 6.18 (D) shows additional frequencies in the power spectra for all stream-wise locations besides natural vortex shedding frequency (f_s) and imposed excitation frequency (f_e) for non-harmonic oscillation (f_e/f_s = 1.5) of the circular cylinder at a Richardson number of Ri = 0.038. These include super-harmonics ($2f_s$ and $2f_e$), sum ($f_e + f_s$) and differences ($f_e - f_s$) of the natural and imposed frequencies. At x/d = 2 location, the magnitudes of spectral power of the natural shedding frequency (f_s) and the excitation frequency (f_e) are comparable due to competition between these two modes of frequencies in the formation region. However, at the downstream locations, x/d = 3.5 and 5, the effect of excitation is less pronounced and the dominant peak occurs at the natural shedding frequency (f_s). In a later section (Section 6.4), it has been shown that vortex shedding is not locked with the cylinder oscillation for all stream-wise locations. Park and Gharib (2001) computed the power spectra from the time-trace of transverse velocity at the location of maximum fluctuations on the wake centerline and found that at f_e/f_s = 1.5 and a/d = 0.1, the dominant frequency is at the natural shedding frequency (f_s) and there is little sign of wake excitation at the oscillation frequency (f_e). The shedding of large-scale vortices is unaffected by the cylinder oscillation and near-wake is not synchronized with the motion of the cylinder. In a numerical study, Zheng and Zhang (2008) observed that for 1.5-nonharmonic excitation, C_L spectrum shows dominant peaks both at f_s and f_e. However, multiple peaks at

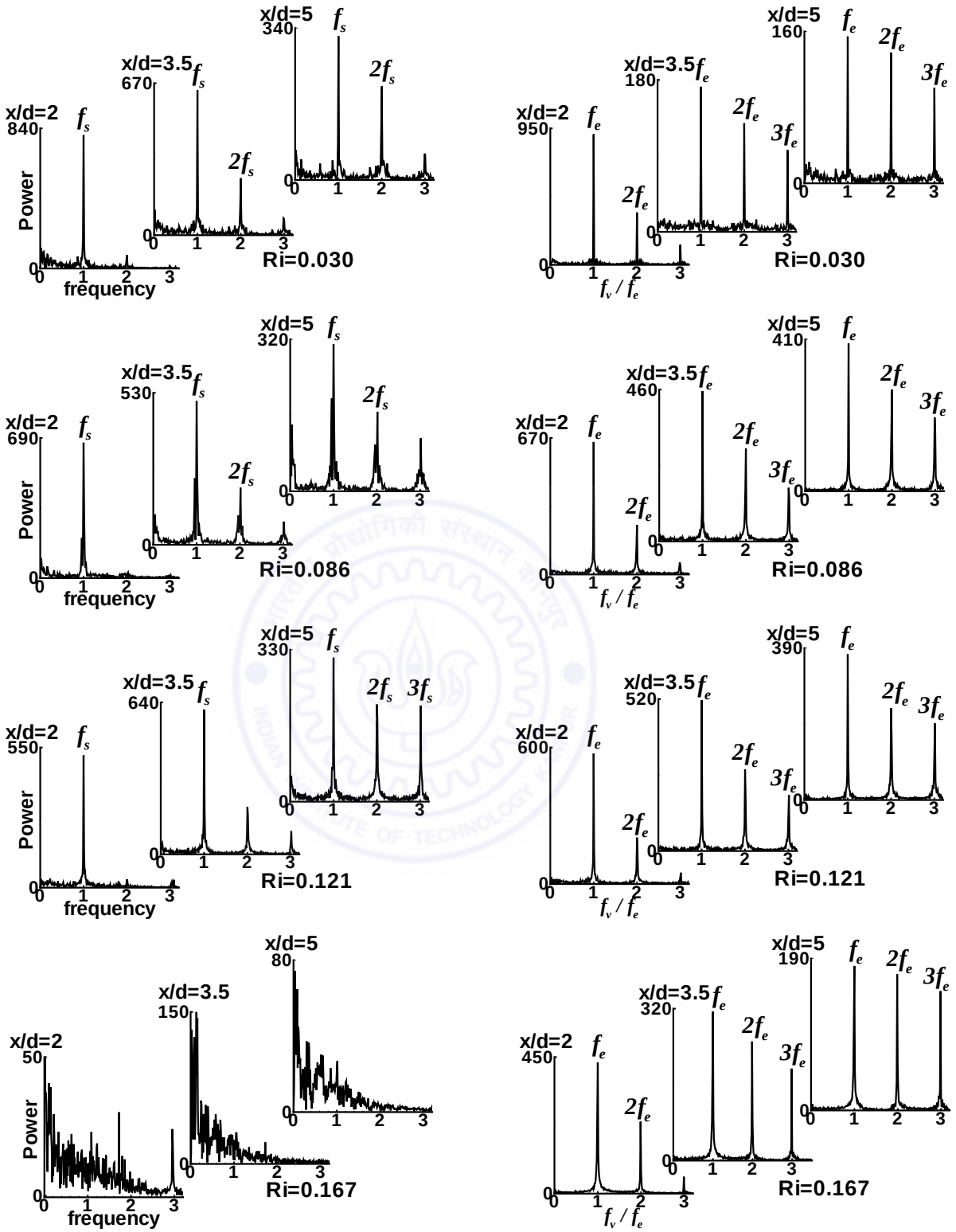

(A) (B)

Figure 6.19 (A) and (B): *see caption on the page number 231.*

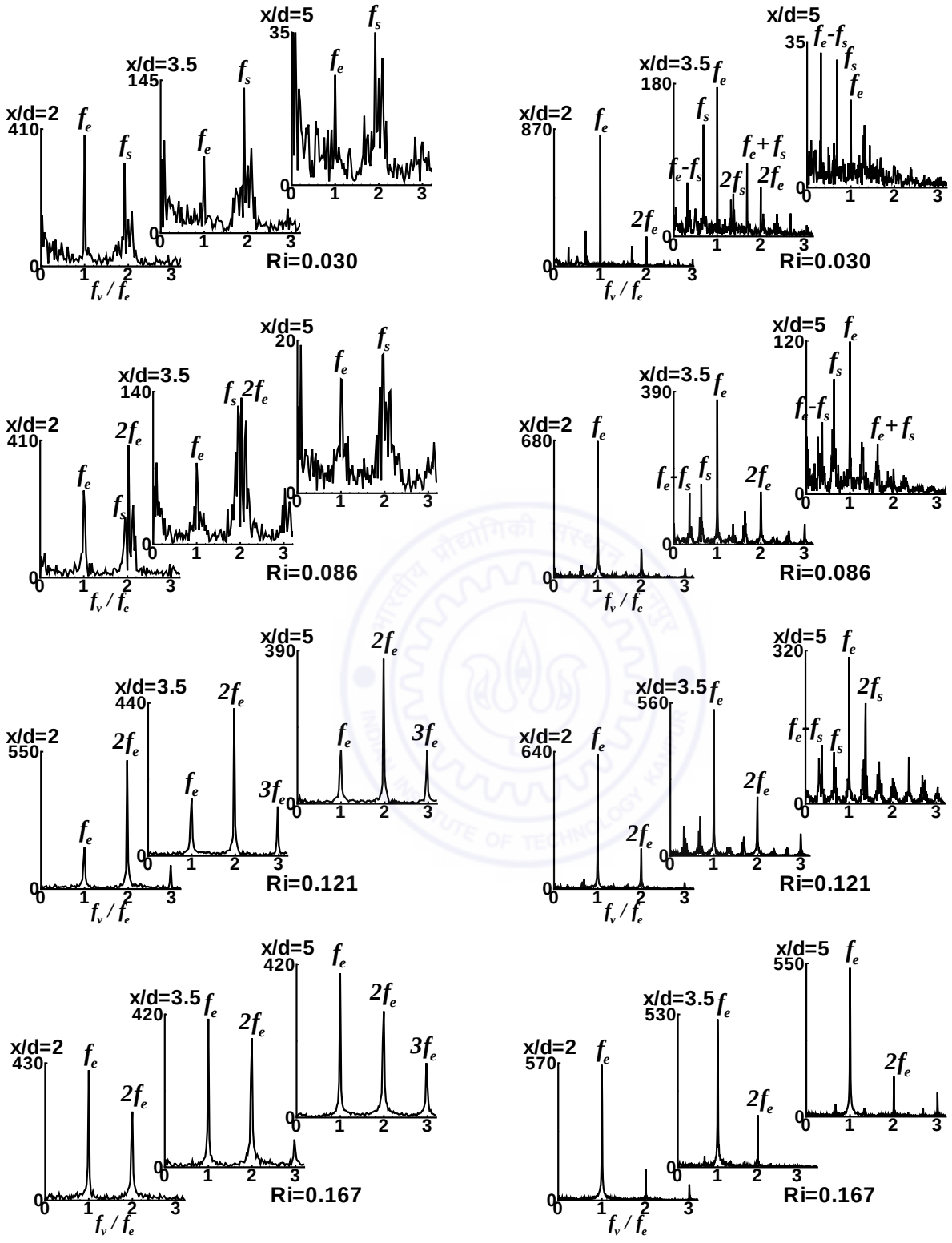

(C) (D)

Figure 6.19 (C) and (D): *see caption on the page number 231.*

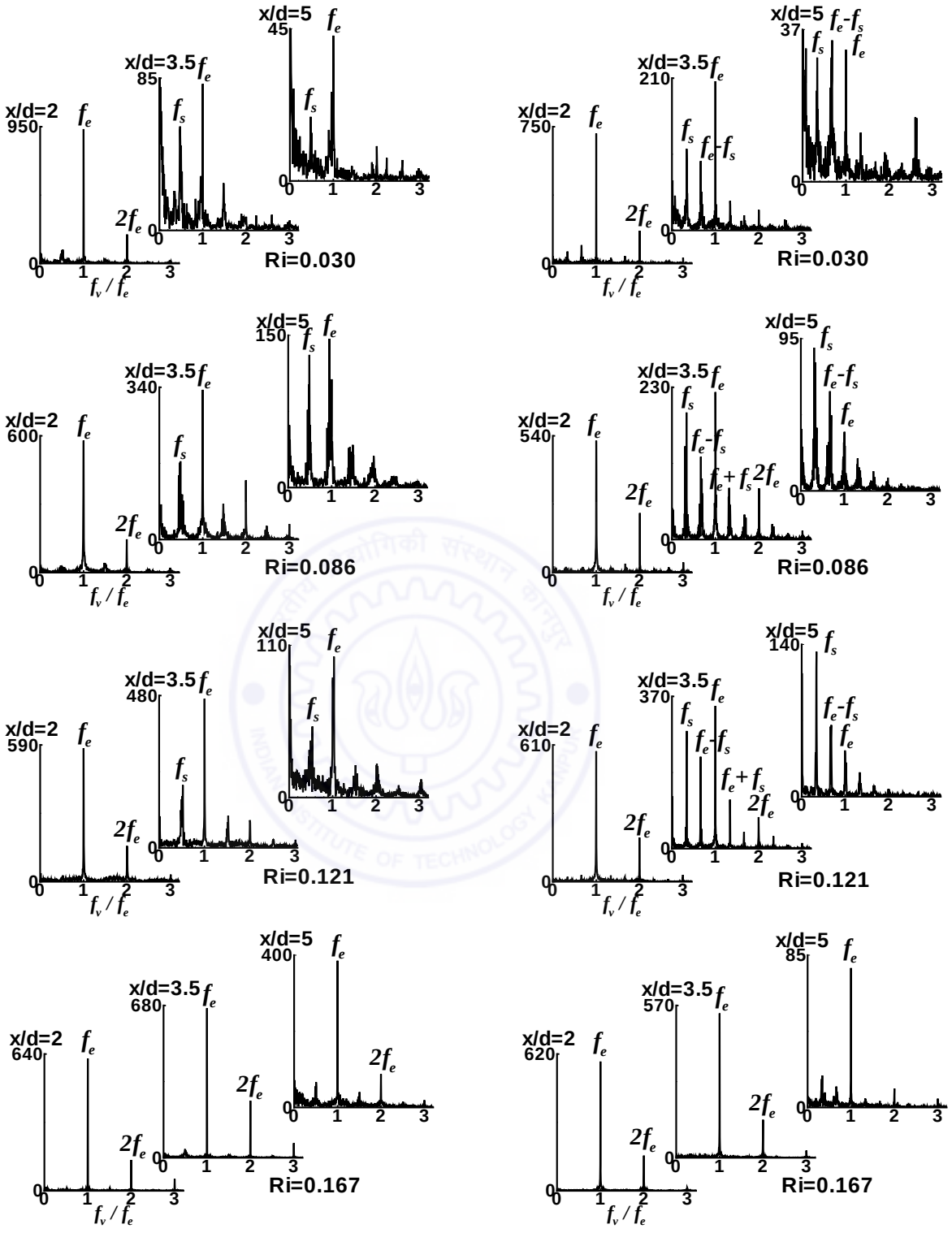

Figure 6.19: Power spectra of light intensity at various stream wise locations (x/d = 2, 3.5 and 5.0) for the oscillating square cylinder at Re = 116. Functional dependence on Richardson number is shown for different excitation frequencies at $a/d = 0.08$: (A) $f_e/f_s = 0$, (B) $f_e/f_s = 1$, (C) $f_e/f_s = 0.5$, (D) $f_e/f_s = 1.5$, (E) $f_e/f_s = 2$, and (F) $f_e/f_s = 3$.

$f_e/3$, $2f_s$, $f_e + f_s$ and $2f_e$ were observed in the C_D spectrum. Zheng and Zhang (2008) related large-amplitude coherent component at $f_e/3$ to the vortex structures repeating every three cycles of the cylinder oscillation. However, the present work clarifies that the presence of $f_e - f_s$ component (Which is theoretically equal to $f_e/3$) in the spectra of near-wake signal is responsible for the flow resemblance after three cycles of the cylinder oscillation.

Figure 6.18 (D) shows large-amplitude spectral peak at the excitation frequency (f_e) for a Richardson number of Ri = 0.078, at $x/d = 2$ location. In contrast to the lower Richardson number (Ri = 0.038), there is no evidence of either natural shedding frequency (f_s) or its combination frequencies i.e. $f_e - f_s$ and $f_e + f_s$. It has been shown later in Section 6.4 that the vortex structures are locked-on with the cylinder oscillation at this location. At the downstream location, $x/d = 3.5$, multiple frequencies are present in the spectrum but the dominant peak occurs at the excitation frequency (f_e). This is also in contrast to lower Richardson number (Ri = 0.038) where dominant peak occurs at the natural shedding frequency (f_s) amongst the multiple frequencies present in the spectrum. At further downstream location, $x/d = 5$, multiple peaks at $f_e - f_s$, f_s and f_e are seen in the power spectra having similar spectral power at $f_e - f_s$ and f_s. It has been shown later in section 6.4 that the vortex structures are not-locked with the cylinder oscillation at the downstream locations, $x/d = 3.5$ and 5. For the higher Richardson number of Ri = 0.124, dominant spectral peak at the excitation frequency (f_e) is observed for all stream wise locations. Smaller peak at twice the excitation frequency ($2f_e$) is also seen due to influence of the vortices from opposite side shear layers. At the downstream locations, $x/d = 3.5$ and 5, extremely small power components at the natural shedding frequency (f_s) and its combination frequencies i.e. $f_e - f_s$ and $f_e + f_s$ are seen in the power spectra. However, no such minor components are seen at $x/d = 2$ location. Therefore, near-wake is quasi locked-on with the cylinder oscillation at $x/d = 3.5$ and 5 locations while it is locked-on with the cylinder motion at $x/d = 2$ location (shown later in section 6.4). At a higher Richardson number of Ri = 0.145, large amplitude clear peak at the excitation frequency (f_e) with smaller peak at $2f_e$ are observed for all stream-wise locations. At this Richardson number, the power spectra for the stationary cylinder shown earlier in Figure 6.18 (A) does not show any clear peak indicating suppression of the vortex shedding process. Therefore, existence of large-amplitude clean peak at the excitation frequency (f_e) shows the re-appearance of vortex structures which follows the periodicity of the excitation frequency (f_e) and are locked-on with the cylinder oscillation. The foregoing discussion shows that with increase in Richardson number, the effect of perturbation on near-wake vortex structures become more pronounced as depicted by the presence of dominant peak at the excitation frequency (f_e) in the power spectra.

Figure 6.19 (D) shows that at a Richardson number of Ri = 0.03, a large-amplitude spectral peak occurs at the excitation frequency (f_e) at $x/d = 2$ location for square cylinder,. Some minor noisy peaks are also observed in the power spectra. Therefore, vortex structures are quasi locked-on with the cylinder oscillation at this location (Shown later in section 6.4). At the downstream location, $x/d = 3.5$, multiple peaks at $f_e - f_s$, f_s, f_e, $2f_s$, $f_e + f_s$ and $2f_e$ are present in the spectrum while at $x/d = 5$ location, multiple peaks at $f_e - f_s$, f_s and f_e are seen in the power spectra. Among these, the dominant peak occurs at f_e and $f_e - f_s$ for $x/d = 3.5$ and 5 locations, respectively. But, the spectral power of natural shedding frequency (f_s) component is also comparable to that of the dominant component at both the locations. Therefore, the vortex structures are not locked-on with the cylinder oscillation at $x/d = 3.5$ and 5 locations. For the higher Richardson numbers of Ri = 0.086 and 0.121, a large-amplitude spectral peak at the excitation frequency (f_e) is observed in the spectra at $x/d = 2$ location. As compared to the lower Richardson number (Ri = 0.03) at this location, small noise peaks are not present in the spectra and near-wake is locked on with the cylinder oscillation. At the downstream location, $x/d = 3.5$, dominant spectral peak at the excitation frequency (f_e) with smaller peak at twice the excitation frequency ($2f_e$) are observed in the power spectra. In addition, small peaks at the natural shedding frequency (f_s) and its combination frequency ($f_e - f_s$) are also seen in the power spectra. Therefore, near-wake is quasi locked-on with the cylinder oscillation at $x/d = 3.5$ location. At further downstream location, $x/d = 5$, multiple frequencies are present in the spectrum but the dominant peak occurs at the excitation frequency (f_e). The vortex structures are not locked-on with the cylinder oscillation at this location. At the higher Richardson number of Ri = 0.167, a large amplitude sharply defined peak at the excitation frequency (f_e) with smaller peak at $2f_e$ are observed for all stream-wise locations. It may be remembered that at this Richardson number, the power spectra for non-oscillating cylinder in Figure 6.19 (A) does not display any clear peak depicting suppression of the vortex shedding process. Therefore, existence of large-amplitude clean peak at the excitation frequency (f_e) show that vortices have reappeared in the near-wake. It has been shown later in section 6.4 that the reappeared structures are completely locked-on with the cylinder motion and follow the periodicity of the excitation frequency (f_e) at all stream-wise locations. The overall behaviour of the power spectra for non-harmonic oscillation ($f_e/f_s = 1.5$) of the circular and square cylinders is almost similar. However, at comparable Richardson numbers, the effect of oscillation on near-wake vortex structures is more pronounced for the square cylinder as compared to the circular cylinder.

Super-harmonic oscillation **($f_e/f_s = 2$)** : Figure 6.18 (E) shows that at a Richardson number of Ri = 0.038 for super-harmonic oscillation ($f_e/f_s = 2$) of the circular cylinder, a

large-amplitude spectral peak occurs at the natural vortex shedding frequency (f_s) for all stream wise locations. At the downstream locations, $x/d = 3.5$ and 5, smaller peaks at the harmonics ($2f_s$) are also observed due to the influence of the vortices from the opposite side shear layers. The existence of peak at f_s indicates almost negligible effect of the cylinder oscillation on the vortex shedding process. It has been shown later in section 6.4 that vortex shedding is not locked-on with the cylinder oscillation for all stream-wise locations. At the higher Richardson number of Ri = 0.078, two large-amplitude peaks of almost equal spectral power occurs at f_e and f_s for $x/d = 2$ location, while a single peak occurs at f_s for $x/d = 3.5$ and 5 locations. The existence of the comparable peaks at f_e and f_s for $x/d = 2$ location indicates a mode competition between the natural vortex shedding and the cylinder oscillation in the formation region. For a higher Richardson number of Ri = 0.124, a dominant spectral peak at the excitation frequency (f_e) is observed for the $x/d = 2$ location. At the downstream locations, $x/d = 3.5$ and 5, multiple peaks including f_e, f_s, $f_e - f_s$ and $f_e + f_s$ are seen in the power spectra. It is to be mentioned that small difference in the f_s and $f_e - f_s$ is highlighted in the spectra. It has been shown later in section 6.4 that near-wake is locked-on and quasi locked-on with the cylinder motion at x/d = 2 and 3.5 locations, respectively and there is no locking with the cylinder oscillation at x/d = 5 location. At a higher Richardson number of Ri = 0.145, large amplitude sharply defined peak at the excitation frequency (f_e) along with smaller peak at $2f_e$ is observed for all stream-wise locations. At this Richardson number, the power spectra for the stationary cylinder in Figure 6.18 (A) does not show any clear peak indicating suppression of the vortex shedding. Therefore, existence of large-amplitude clean peak at the excitation frequency (f_e) shows the re-appearance of vortex structures. These structures are locked-on with the cylinder oscillation at all stream wise locations. The trend in the power spectra shows that with increase in Richardson number, the effect of perturbation become more pronounced in the formation region first and then on all stream wise locations in the near-wake.

Figure 6.19 (E) shows that at the Richardson numbers of Ri = 0.030, 0.086 and 0.121, a large-amplitude spectral peak at the excitation frequency (f_e) along with minor peak at its harmonic ($2f_e$) occur in the spectra at $x/d = 2$ location for square cylinder. At the downstream locations, x/d = 3.5 and 5, a large-amplitude spectral peak at the excitation frequency (f_e) along with smaller peak at the natural shedding frequency (f_s) is observed in the spectra. Some broad band noise is observed in the power spectra at the downstream locations (x/d = 3.5 and 5). At all three Richardson numbers (Ri = 0.03, 0.086 and 0.121), the vortex structures are locked-on with the cylinder oscillation at x/d = 2 location, while not locked at x/d = 3.5 and 5 locations (Section 6.4). At a higher Richardson number of Ri = 0.167, a large amplitude sharply defined peak at the excitation

frequency (f_e) along with smaller peak at its harmonic ($2f_e$) are observed for all stream-wise locations. At this Richardson number, the power spectra for non-oscillating cylinder in Figure 6.19 (A) does not show any clear peak and depicts suppression of the vortex shedding process. The existence of large-amplitude clean peak at the excitation frequency (f_e) show that vortices have reappeared in the near-wake, which are locked-on with the cylinder motion at all stream-wise locations (Section 6.4). The comparison of the power spectra for super-harmonic oscillation ($f_e/f_s = 2$) of the circular and square cylinders shows that the effect of excitation on near-wake vortex structures is more pronounced for the square cylinder as compared to the circular cylinder. However at the highest Richardson numbers, the behaviour of the power spectra is exactly similar for both the cylinders.

Super-harmonic oscillation **($f_e/f_s = 3$)** : Figure 6.18 (F) shows that at the Richardson number of Ri = 0.038 for super-harmonic oscillation ($f_e/f_s = 3$) of the circular cylinder, a large-amplitude spectral peak occurs at the natural vortex shedding frequency (f_s) along with smaller peak at its harmonic ($2f_s$) for $x/d = 2$ and 3.5 locations. However, due to the greater influence of the vortices from the opposite side shear layers at $x/d = 5$ location, the peaks of same spectral power at f_s and $2f_s$ are observed. It has been shown later in section 6.4 that vortex shedding is not locked-on with the cylinder oscillation for all stream-wise locations. At the higher Richardson number of Ri = 0.078, two sharp spectral peaks of comparable spectral power occur at f_s and $f_e/3$ along with smaller peak at f_e for $x/d = 2$ location. At the down stream locations, $x/d = 3.5$ and 5, the dominant peak occurs at f_s in the power spectra. For the higher Richardson number of Ri = 0.124, a dominant spectral peak at the excitation frequency (f_e) along with smaller peak at f_s is observed for $x/d = 2$ location. At the downstream locations, $x/d = 3.5$ and 5, the dominant peak at f_s is seen in the power spectra. It has been shown later in section 6.4 that for both Richardson numbers, Ri = 0.078 and 0.124, the near-wake is quasi locked-on with the cylinder motion at $x/d = 2$ location, and no locking-on with the cylinder oscillation at $x/d = 3.5$ and 5 locations. At a higher Richardson number of Ri = 0.145, large amplitude sharply defined peak at the excitation frequency (f_e) is observed for all stream-wise locations. Small fluctuations are seen in the power spectra at $x/d = 5$ location. At this Richardson number, the power spectra for the stationary cylinder in Figure 6.18 (A) does not show any clear peak indicating suppression of the vortex shedding. Therefore, existence of clear peak at the excitation frequency (f_e) shows the re-appearance of vortex structures. These structures are locked-on with the cylinder oscillation at $x/d = 2$ and 3.5 locations, while quasi locked-on at $x/d = 5$ location (Section 6.4).

Figure 6.19 (F) shows that at the Richardson numbers of Ri = 0.030, 0.086 and 0.121, a large-amplitude spectral peak at the excitation frequency (f_e) along with smaller

peak at its harmonic ($2f_e$) occur in the spectra at $x/d = 2$ location for square cylinder. At the downstream locations, $x/d = 3.5$ and 5, multiple peaks at f_s, $f_e - f_s$ and f_e are present in the spectrum. In addition, minor peaks at $f_e + f_s$ and $2f_e$ are also observed for some cases. Among these dominant components, the peak occurs at f_e and f_s for $x/d = 3.5$ and 5 locations, respectively. At all three Richardson numbers (Ri = 0.030, 0.086 and 0.121), the vortex structures are locked-on with the cylinder oscillation at $x/d = 2$ location, while not locked-on at $x/d = 3.5$ and 5 locations (Section 6.4). At the higher Richardson number of Ri = 0.167, a large amplitude sharply defined peak at the excitation frequency (f_e) is observed for all stream-wise locations. The power spectra for non-oscillating cylinder in Figure 6.19 (A) does not show any clear peak and depicts suppression of the vortex shedding process at this Richardson number. The existence of large-amplitude clean peak at the excitation frequency (f_e) shows that vortices have reappeared in the near-wake, which are locked-on with the cylinder motion at all stream-wise locations (Section 6.4). The comparison of the power spectra for super-harmonic oscillation ($f_e/f_s = 3$) of the circular and square cylinders shows that the effect of excitation on near-wake vortex structures is more pronounced for the square cylinder as compared to the circular cylinder.

The power spectra of the light intensity fluctuations in schlieren images are presented for oscillating circular and square cylinders at three stream-wise locations, $x/d = 2$, 3.5 and 5. Functional dependence on Richardson number is shown at different excitation frequencies for an amplitude ratio, $a/d = 0.08$. The effect of frequency ratio (f_e/f_s), Richardson number (Ri), stream wise location of the near-wake (x/d) and geometry of the cylinder is clearly demonstrated. Depending upon the combination of these parameters, the power spectra contain various frequencies including natural vortex shedding frequency (f_s), imposed excitation frequency (f_e), super-harmonics ($2f_s$ and $2f_e$), sum ($f_e + f_s$) and differences ($f_e - f_s$) of these frequencies. At a higher Richardson number, the power spectra for the stationary cylinder shows a broadband spectra without any clear peak depicting suppression of the vortex shedding. However, excitation of the cylinder at different frequency ratios show a dominant spectral peak at the excitation frequency (f_e) at all stream-wise locations for both circular and square cylinders. This indicates the reappearance of the vortex shedding at this critical Richardson number due to oscillation of the cylinder.

6.3 RMS fluctuations of light intensity

The distribution of stream-wise velocity fluctuations can display the modifications of the wake characteristics due to cylinder oscillation in terms of increase in the intensity of fluctuations and shift in the location of peak fluctuations towards the cylinder base re-

gion. These behaviours can be correlated to increase in the strength of shed vortices and decrease in the extent of vortex formation region, respectively. The rms fluctuation is also dependent other factors such as size of the vortex structures, their interactions and arrangement in the wake. In the present work, as the working fluid is air with Prandtl number of the order of unity, time-dependent fluctuations in light intensity from schlieren images can be correlated to velocity fluctuations. The RMS (mean-removed) fluctuations of light-intensity in the stream-wise direction (x/d) for oscillating circular and square cylinders are presented in Figures 6.20 and 6.21, respectively as a function of frequency ratio. The stream-wise development of fluctuation is presented at a transverse location with maximum value of the peak intensity fluctuations among all transverse locations (from centerline of the cylinder to the transverse extent of the bright wake region). The Reynolds numbers for the case of circular and square cylinders are 105 and 116, respectively. For each frequency ratio i.e. f_e/f_s = 1, 0.5, 1.5, 2, and 3, the rms fluctuation development is presented at different Richardson number (Ri) for two amplitude ratios, a/d = 0.04 and 0.08 and compared with the stationary case, a/d = 0. The rms fluctuations are calculated using a sequence of 3000 images over a time duration of 12 seconds. Figures 6.20 and 6.21 show that rms fluctuations of intensity increases from a small value to a maximum in the stream wise direction, and subsequently reduces in downstream direction for both stationary and oscillating cylinders. The location of the peak fluctuations shift towards the down stream region (i.e. increase in the vortex formation length) with increase in Richardson number. At the highest Richardson number, Ri = 0.145 for the circular and Ri = 0.167 for the square cylinder, the rms fluctuations diminishes to a insignificant value due to the suppression of vortex shedding for the stationary cylinders. However, the plots for the oscillating cylinders at this Richardson number show increase in rms fluctuations to a high level for all excitation frequencies. This indicates the presence of sustained vortex structures as depicted in the visualization images presented earlier in Section 6.1.

Figures 6.20 (A), (C), (D) and (E), respectively show for fundamental (f_e/f_s = 1), 1.5-non-harmonic (f_e/f_s = 1.5), 2-super-harmonic (f_e/f_s = 2) and 3-super-harmonic (f_e/f_s = 3) oscillation of the circular cylinder that at the lowest Richardson number (Ri = 0.038), the peak fluctuations of the oscillating cylinder (both at a/d = 0.04 and 0.08) are of comparable magnitude to that of the stationary cylinder (a/d = 0). However, for f_e/f_s = 1, marginally higher level of fluctuations is seen in the downstream region for the oscillating cylinder and indicates enhanced interactions of the vortices in this region. The corresponding visualization images at a/d = 0.08 in Figures 6.4 (A), 6.11 (A), 6.14 (A) and 6.16 (A), respectively show that the pattern of vortex formation follows the periodicity of the natural vortex shedding frequency. At higher Richardson number, Ri

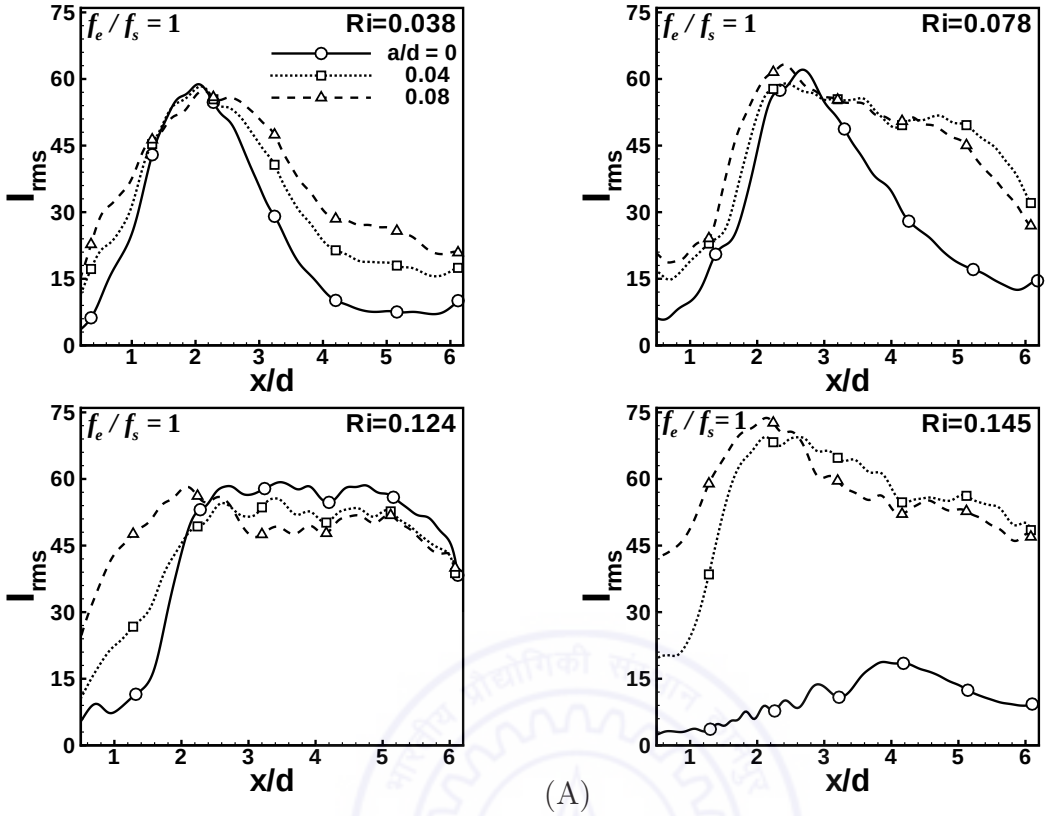

(A)

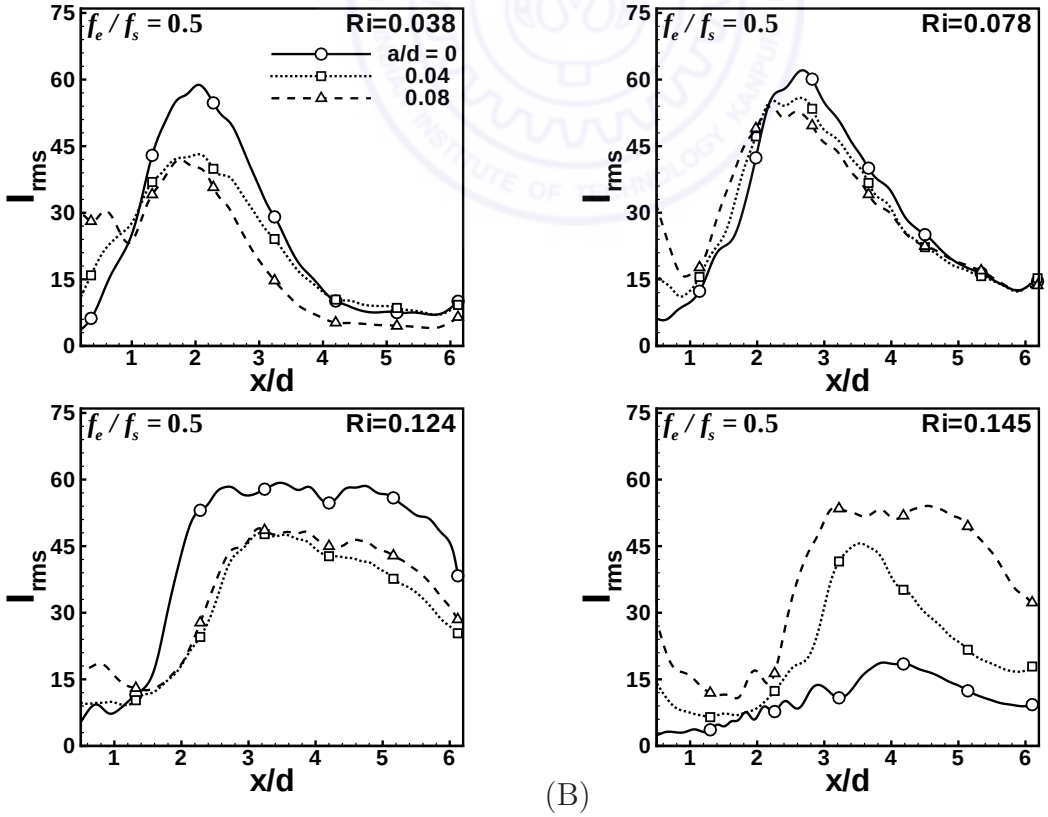

(B)

Figure 6.20 (A) and (B): *see caption on the page number 240.*

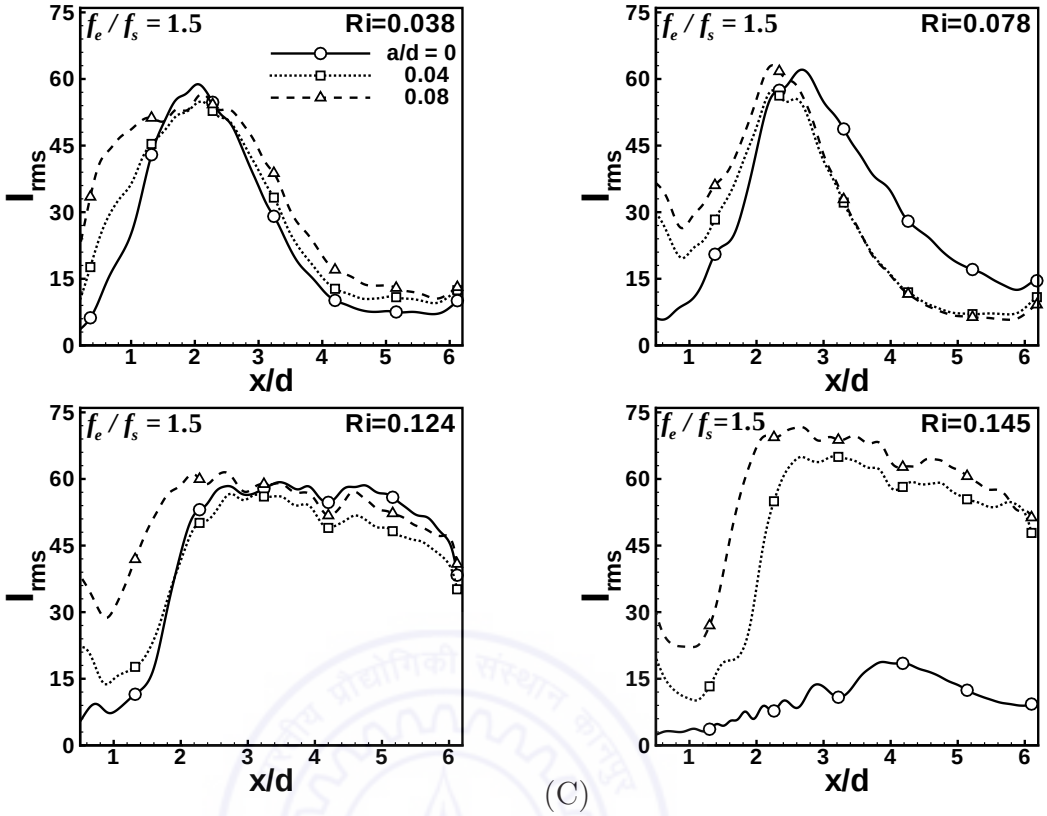

(C)

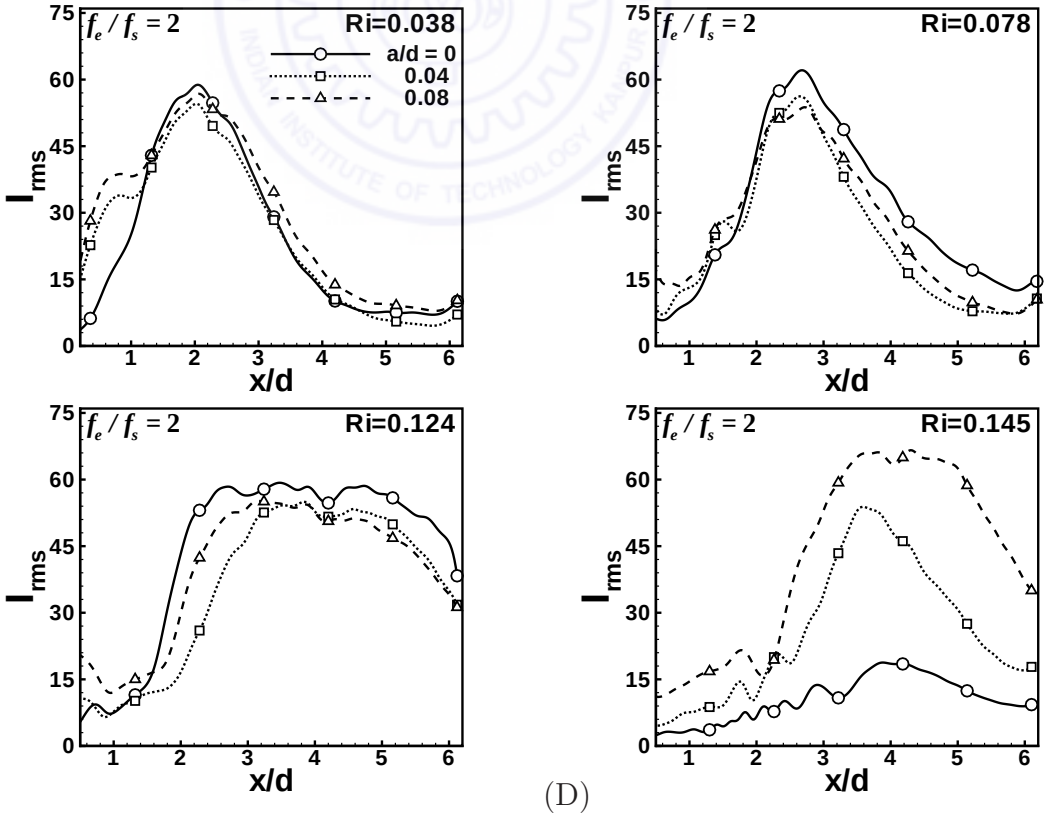

(D)

Figure 6.20 (C) and (D): *see caption on the page number 240.*

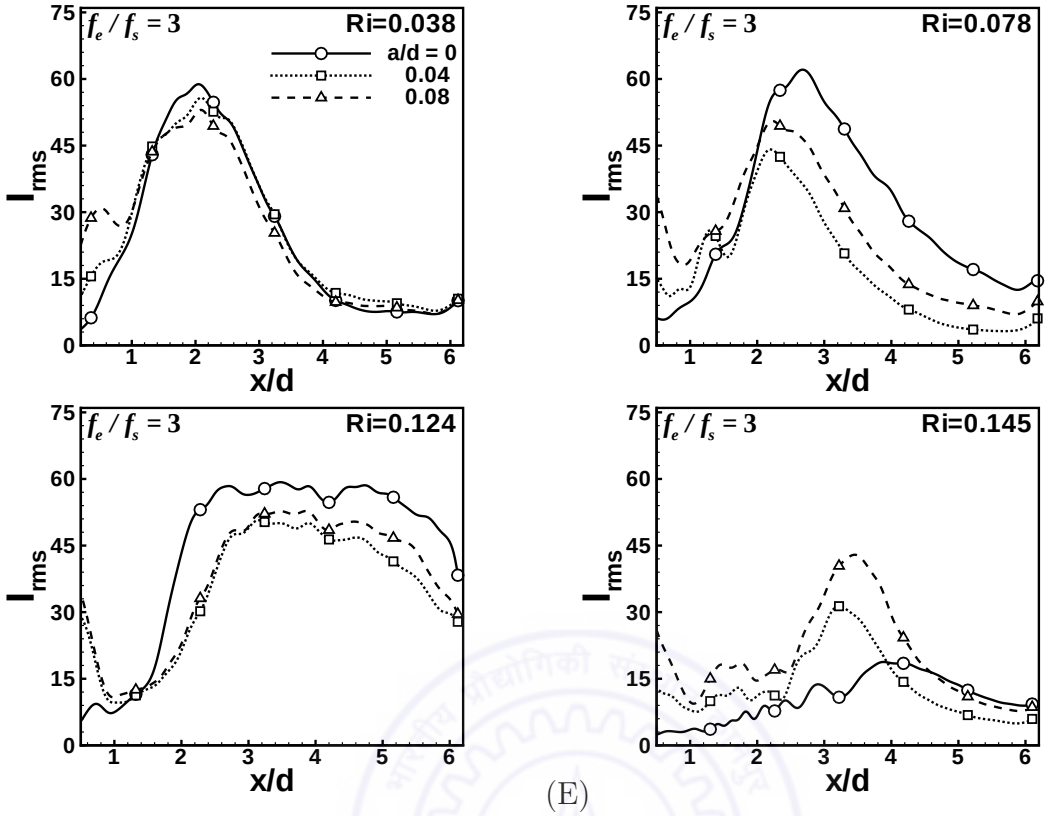

(E)

Figure 6.20: Evolution of the RMS intensity (I_{rms}) in the stream wise direction for oscillating circular cylinder at different Richardson numbers (Ri = 0.038, 0.078, 0.124 and 0.145) and oscillation frequency: (A) $f_e/f_s = 1$, (B) $f_e/f_s = 0.5$, (C) $f_e/f_s = 1.5$, (D) $f_e/f_s = 2$, and (E) $f_e/f_s = 3$. The Reynolds number is set equal to 105.

= 0.078, the peak fluctuations magnitude of the oscillating cylinder is almost similar to that of the stationary cylinder for $f_e/f_s = 1$, 1.5 and 2. However, the level of fluctuations in the downstream region is little higher for $f_e/f_s = 1$ and little lower for $f_e/f_s = 1.5$, 2. The visualization images for $f_e/f_s = 1$ (at $a/d = 0.08$) in Figure 6.4 (B) show stronger vortex structures in the down stream region. However, the images for $f_e/f_s = 1.5$ and 2 in Figures 6.11 (B) and 6.14 (B), respectively show that the formation of vortices in the formation region is regular but the shed vortices show irregularity at the downstream locations. For $f_e/f_s = 3$ at this Richardson number, Ri = 0.078, the level of fluctuations is much lower for the oscillating cylinder (Figures 6.20 (E)). The corresponding visualization images at $a/d = 0.08$ in Figure 6.16 (B) shows that the vortex structures from both sides of the shear layer are not very distinct supporting the trends of rms intensity in Figures 6.20 (E). At a higher Richardson number, Ri = 0.124, the peak fluctuations for the oscillating cylinder (for $f_e/f_s = 1$, 1.5, 2 and 3) are similar to that of the stationary cylinder. For both cases, peak fluctuations are not localized but spreads over a large region due to the presence of comparatively bigger vortex structures. At the highest Richardson number, Ri

= 0.145, rms fluctuations increase to a high level as compared to negligible level (due to the suppression of vortex shedding) for the stationary cylinder. For $f_e/f_s = 1$ and 1.5, the increase in the fluctuations is highest and the location of the peak fluctuations is closer to the cylinder. The visualization images in Figures 6.4 (D) and 6.11 (D), respectively show that very good quality coherent structures reappear in the near-wake, and the roll-up of vortices from the shear layers come closer to the cylinder as compared to Ri= 0.124. For these frequencies, the rate of decrease of fluctuations in downstream direction is lower. In a later section (Section 6.4), it has been shown that spectral coherence between the wake signal and cylinder oscillation signal is very high at all stream wise locations and lock-on (LO) state prevails at all the locations. For $f_e/f_s = 3$, at this Richardson number, the increase in the peak fluctuations is nominal. The corresponding visualization images (at $a/d = 0.08$) in Figure 6.16 (D) shows that the vortex structures are not distinct and merges with the plume without detaching from the shear layer in the downstream region. For sub-harmonic oscillation ($f_e/f_s = 0.5$) of the circular cylinder, Figure 6.20 (B) shows that the level of fluctuations for the oscillating cylinder are lower as compared to that of the stationary cylinder at all Richardson numbers except at the highest Richardson number (Ri = 0.145). This indicates that the strength of the vortices become weaker at $f_e/f_s = 0.5$.

Figures 6.21 (A), (C), (D) and (E), respectively show for fundamental ($f_e/f_s = 1$), 1.5-non-harmonic ($f_e/f_s = 1.5$), 2-super-harmonic ($f_e/f_s = 2$) and 3-super-harmonic ($f_e/f_s = 3$) oscillation of the square cylinder that at all Richardson numbers, the peak fluctuations for the oscillating cylinder is higher as compared to that of the stationary cylinder. This trend is observed for both the amplitude ratios, $a/d = 0.04$ to 0.08 but a small difference between the two fluctuations level is seen. Higher fluctuations level indicates an enhanced vortex activity due to oscillation of the square cylinder. This is in contrast to the case of the circular cylinder in which not much difference in the level of the fluctuations and peak fluctuations is seen (except at the highest Richardson number, Ri = 0.145). Therefore, the effect of oscillation is more pronounced for the square cylinder as compared to the circular cylinder. The corresponding visualization images at $a/d = 0.08$ in the section 6.1 show that distinct and regular vortex structures are formed in the formation region with a periodicity of the excitation frequency. At all Richardson numbers, the location of the peak fluctuations shifts towards the base of the cylinder depicting a decrease in the vortex formation length. Krishnamoorthy *et al.* (2001) observed that for forced transverse oscillations, the shear layers also swings with the cylinder motion and the processes contributing to vortex formation e.g. vortex pairing and coalescence for some excitation conditions are distinctly different than those for a stationary cylinder. Therefore, well accepted definition based on the location of peak

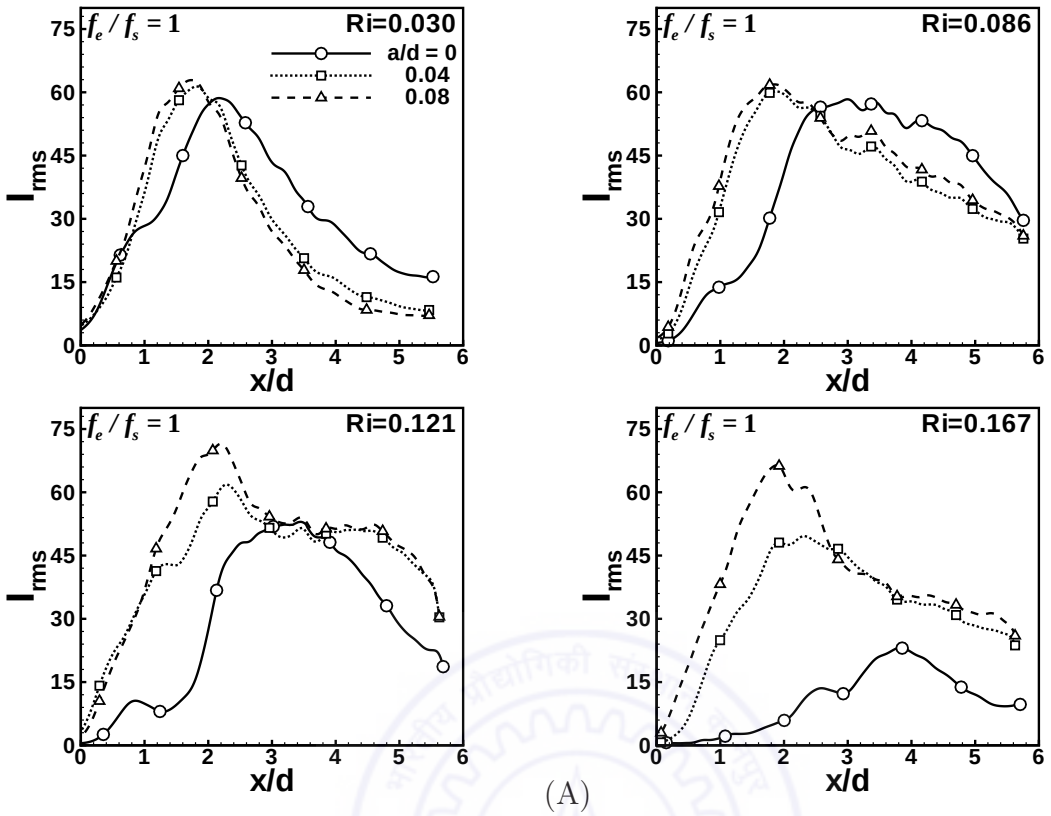

(A)

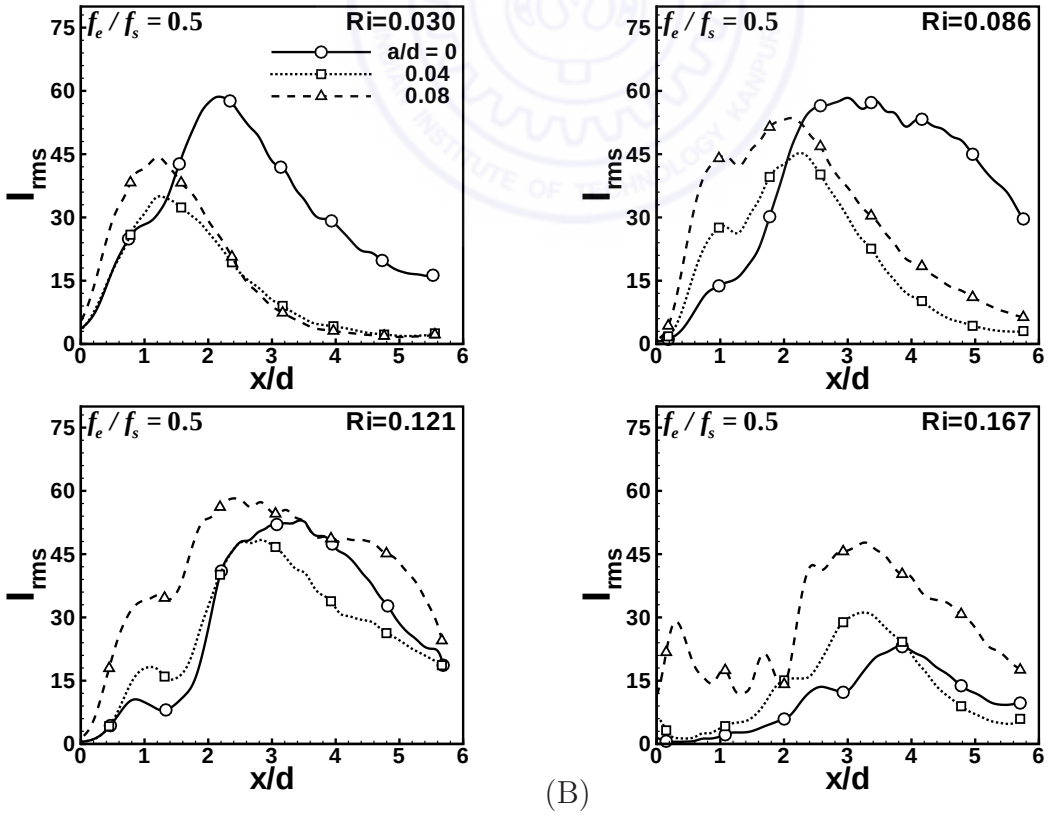

(B)

Figure 6.21 (A) and (B): *see caption on the page number 244.*

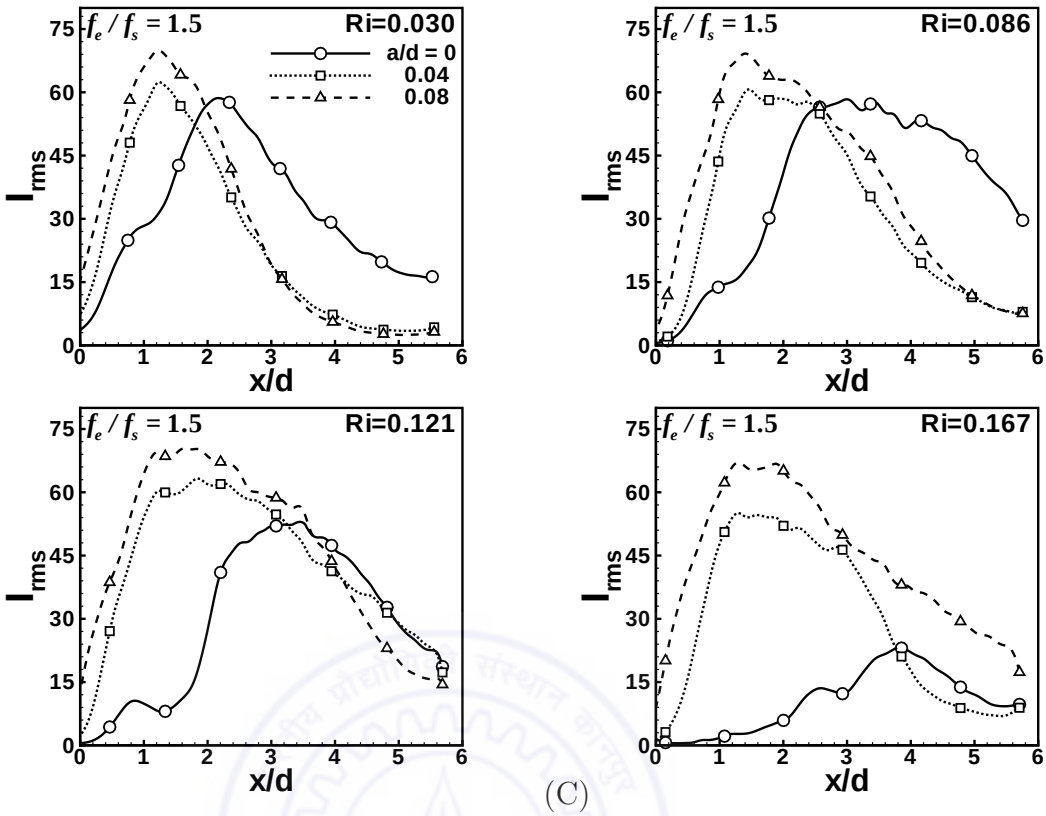

(C)

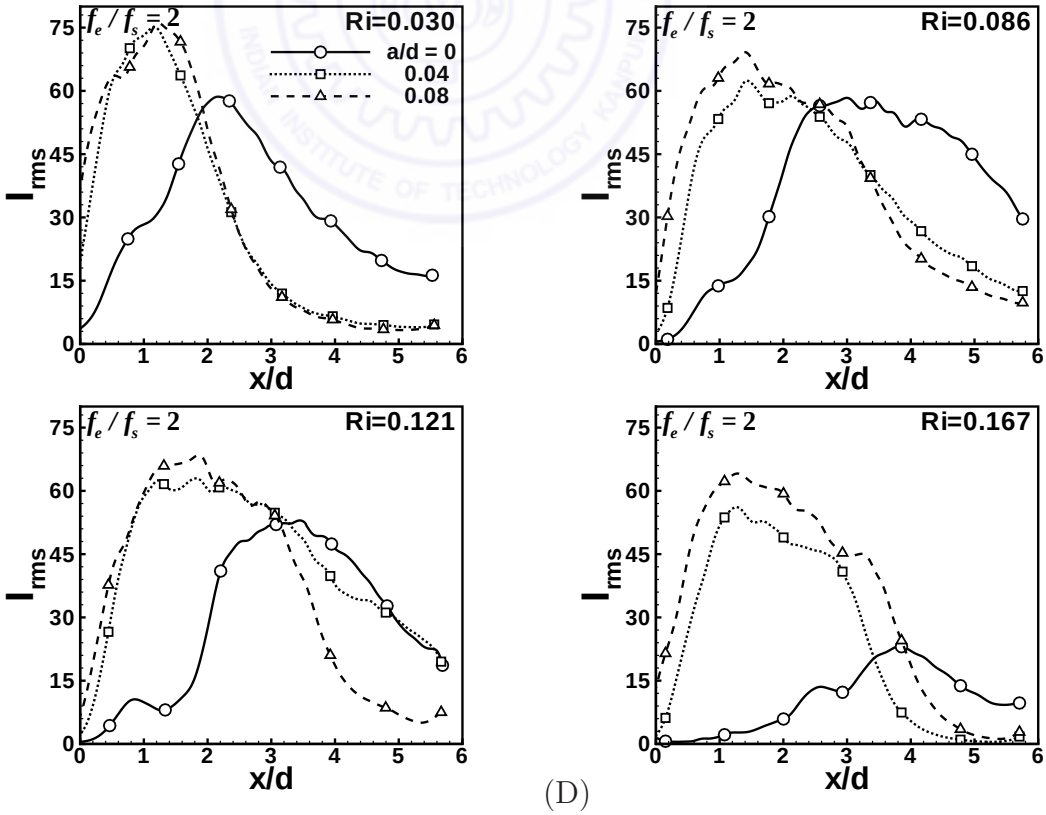

(D)

Figure 6.21 (C) and (D): *see caption on the page number 244.*

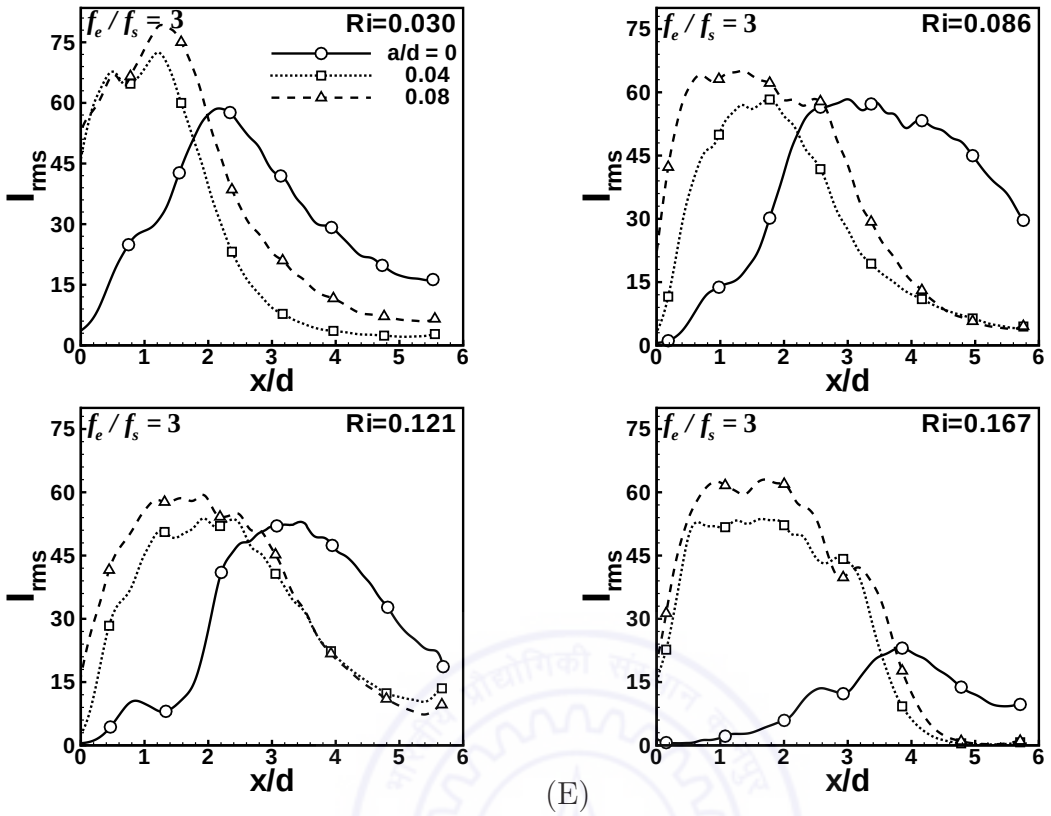

(E)

Figure 6.21: Evolution of the RMS intensity (I_{rms}) in the stream wise direction for oscillating square cylinder at different Richardson numbers (Ri = 0.030, 0.086, 0.121 and 0.167) and oscillation frequency: (A) $f_e/f_s = 1$, (B) $f_e/f_s = 0.5$, (C) $f_e/f_s = 1.5$, (D) $f_e/f_s = 2$, and (E) $f_e/f_s = 3$. The Reynolds number is set equal to 116.

in the stream wise velocity fluctuation at the cylinder centerline for stationary cylinder may not faithfully represent the formation length. Pottebaum and Gharib (2006) also pointed out that the vortex formation length definition holds good for those cases only in which the wake consists of only single vortices, not paired vortices. Therefore, exact estimation of the decrease in the formation length is not reported in the present work. For sub-harmonic oscillation ($f_e/f_s = 0.5$) of the square cylinder, Figures 6.21 (B) shows that the level of fluctuations for the oscillating cylinders are lower as compared to that of the stationary cylinder at the lower Richardson numbers, Ri= 0.030 and 0.086. However, at higher Richardson numbers, Ri= 0.121, fluctuations are marginally higher at a/d = 0.08 as compared to that of stationary cylinder.

The rms fluctuations of light-intensity in the stream-wise direction (x/d) for circular and square cylinders confirm the trends of the vortex structures observed in the visualization images presented earlier in section 6.1. The effect of oscillation on the level of fluctuations, peak fluctuations and location of the peak fluctuations is clearly demonstrated for both the cylinders. The difference in the sensitivity of the near-wake to forced

oscillations for the cylinders of two different geometries is clearly observed. At an elevated heating level, the increase in the fluctuations to a very high level for the oscillating cylinder indicates the reappearance of the vortex shedding in the near-wake, which was suppressed for the stationary cylinder at this Richardson number.

6.4 Synchronization of vortex formation

The most well-known feature of the wake of an oscillating cylinder is the *lock-on* phenomenon also termed as 'phase-locking' or 'synchronization' of vortex formation with the cylinder motion. Many reviews concerning *lock-on* phenomenon are available in the literature. In classical definition, the term *lock-on* is used to convey that vibration of the body causes the inherent vortex shedding frequency (f_s) from the corresponding stationary cylinder to be captured by (or synchronize with) the externally imposed vibration frequency (f_e), (Griffin and Ramberg, 1976). This ultimately results in a single, same characteristic frequency of both the body and the wake. Literature reveals that, for transverse oscillation, *lock-on* is observed when excitation occurs at a frequency close to, or at, the Karman vortex shedding frequency of the stationary cylinder. On the other hand, when f_e is appreciably different from f_s, complex wake patterns containing several frequencies can be produced. In addition, n-superharmonic synchronization and $1/n$-subharmonic synchronization can occur, if f_e is approximately equal to an integer multiple or division of f_s, i.e., when $f_e = nf_s$ or $f_e = f_s/n$ ($n = 1, 2, 3$ . .), (Zheng and Zhang, 2008). Regarding possible criterion for defining *lock-on*, a variety of approaches have been employed in the previous investigations. These include qualitative flow visualization, in which *lock-on* is based on repetition of the vortex shedding patterns in the near-wake region over an integer number of cylinder oscillation periods. Other approach include spectral analysis of single point velocity fluctuations in the near-wake, which is measured at the edge of separating shear layer using a hot-wire or hot-film probe. In numerical studies, spectral analysis of the time histories of lift and/or drag coefficient have been used to identify locked-on states. In addition to power spectra, the phase portraits of the cylinder displacement and unsteady lift coefficient has also been used to postulate locked-on states. Based on above approaches, the investigators have reported bounds of *lock-on* regime in the plane of frequency ratio (f_e/f_s) versus amplitude ratio (a/d). Present study utilizes time series of fluctuating light intensity of the schlieren images to determine vortex shedding frequency. This technique is advantageous compared to single point measurement technique because light intensity signal from different specific locations in the image can be utilized and a global picture of the wake can be studied. Therefore, *lock-on* phenomenon can also be studied as a function of location in the wake i.e. an additional parameter for *lock-on*. In

the present investigation, effect of transverse oscillation on the wake behavior of heated circular and square cylinders have been studied. Both cylinders heated to various levels and subjected to low amplitude transverse oscillation at different excitation frequencies give rise to various types of vortex formation patterns and locked-on states. For a heated cylinder, in addition to frequency ratio (f_e/f_s) and amplitude ratio (a/d), Richardson number (Ri) is also a potential parameter to jointly influence the *lock-on* phenomenon. Therefore, *lock-on* status of vortex shedding with the cylinder motion have been determined as a function of Richardson number (Ri), excitation amplitude (a/d), excitation frequency (f_e/f_s) and stream wise location of the wake (x/d). The results of this parametric study for both circular and square cylinders are discussed in the present section. Multiple representations and criteria have been considered to postulate various types of locked-on states. These include: power spectra of the wake signal from schlieren images; lissajous trajectories of the wake signal versus cylinder oscillation signal; spectral coherence between the wake signal and cylinder oscillation signal at the excitation frequency of the cylinder; and instantaneous patterns of the near-wake vortex structures relative to the cylinder motion from phase-referenced schlieren images. This approach has facilitated the identification of several types of locked-on states of vortex formation in the near-wake and is presented as below.

6.4.1 Overview of locked-on states

In this section, an overview of various locked-on states have been addressed. In essence, the locked-on states of the near-wake with cylinder motion are classified as: (i) no lock-on (NLO), (ii) quasi lock-on (QLO), and (iii) lock-on (LO), following the terminology used by Cetiner and Rockwell (2001). The characteristics of these states have been illustrated below using an example of non-harmonic oscillation ($f_e/f_s = 1.5$; $a/d = 0.08$) of heated circular cylinder at different Richardson numbers, Ri = 0.038, 0.078, 0.124 and 0.145. A total of twelve representative cases are used in the illustration comprising data from three stream-wise locations, $x/d = 2$, 3.5 and 5.0 for each Richardson number. For these cases, the Power spectra of light intensity fluctuation in the schlieren images have been presented earlier in Figure 6.18-D. The occurrence of lock-on (LO) is suggested by a power spectra having large-amplitude sharply defined peak at the excitation frequency (f_e). Besides power spectra, Lissajous trajectories (phase portraits) of the wake signal versus cylinder oscillation signal is also used to analyze the degree of interaction of the near-wake with the cylinder motion. These are presented in Figure 6.22 as a function of Richardson number (Ri= 0.038, 0.078, 0.124 and 0.145) for three stream-wise locations, (a) $x/d = 2.0$, (b) $x/d = 3.5$, and (c) $x/d = 5.0$. Lissajous plots are generated using 3000 images (acquired over 12 seconds duration) encompassing approximately 108-122

cycles (depending on Richardson number) of the cylinder oscillation. The light intensity of the wake signal is plotted on the abscissa and that of cylinder oscillation signal is plotted on the ordinate. Depending upon the degree of congruence between the two signals from cycle to cycle of the cylinder oscillation, these plots demonstrate the degree of phase-locking i.e. no lock-on (NLO), quasi lock-on (QLO), and lock-on (LO) states of vortex formation. In addition to power spectra and Lissajous patterns, spectral coherence between the wake signal and cylinder oscillation signal at the excitation frequency (f_e) of the cylinder is also used to further consolidate the approach of identifying various locked-on states. Its numerical value provides a measure of the degree of correlation between the two signals and an extremely high value (close to one) suggest an indication of lock-on state (LO). In Figure 6.22, the respective lock-on state i.e. NLO, QLO, and LO and corresponding spectral coherence value (in the parenthesis) is mentioned for each case. The phase-referenced schlieren images corresponding to different phases (a-x, Figure 6.10) for three consecutive cycles of cylinder oscillation presented earlier in Figure 6.11-(A-D) as a function of Richardson number clearly displays the visual nature of the locked-on states. These visualization images show instantaneous patterns of the near-wake vortex structures relative to the cylinder motion. The locked-on state is clearly displayed by either repetitive or non-repetitive patterns of the vortex structures over cylinder oscillation cycle(s). The characteristics of the various locked-on states (NLO, QLO, and LO) are discussed as under.

No lock-on **(NLO)** : Limited interaction occurs between the modal fluctuations due to natural instability and the forced cylinder oscillations in no lock-on regime and degree of this interaction varies from almost negligible level to a moderate level. When, the degree of interaction is nearly negligible, the natural vortex shedding is hardly disturbed and power spectra exhibit a dominant peak at the natural shedding frequency (f_s) along with smaller peaks at its super-harmonics. However, for moderate degree of interaction, a mode competition is established between the two oscillations and each of them plays a role in the formation and development of vortices in the near-wake. Therefore, in contrast to a regular, periodic natural vortex shedding, a chaotic nature of the near-wake flow containing aperiodic vortex structures is observed. The power spectra show sharply defined spectral peaks at the natural shedding frequency (f_s) and the excitation frequency (f_e). Besides these, the power spectra also exhibit one and/or other peak(s) at super-harmonics ($2f_s$ and $2f_e$), sum ($f_e + f_s$), and differences ($f_e - f_s$) of these frequencies. For no lock-on state, Lissajous trajectories of the wake signal versus cylinder oscillation signal follow several different paths in successive cycles of the cylinder oscillation and a non-repetitive pattern is observed. The spectral coherence function between the wake signal and cylinder oscillation signal at the excitation frequency (f_e) of the cylinder varies

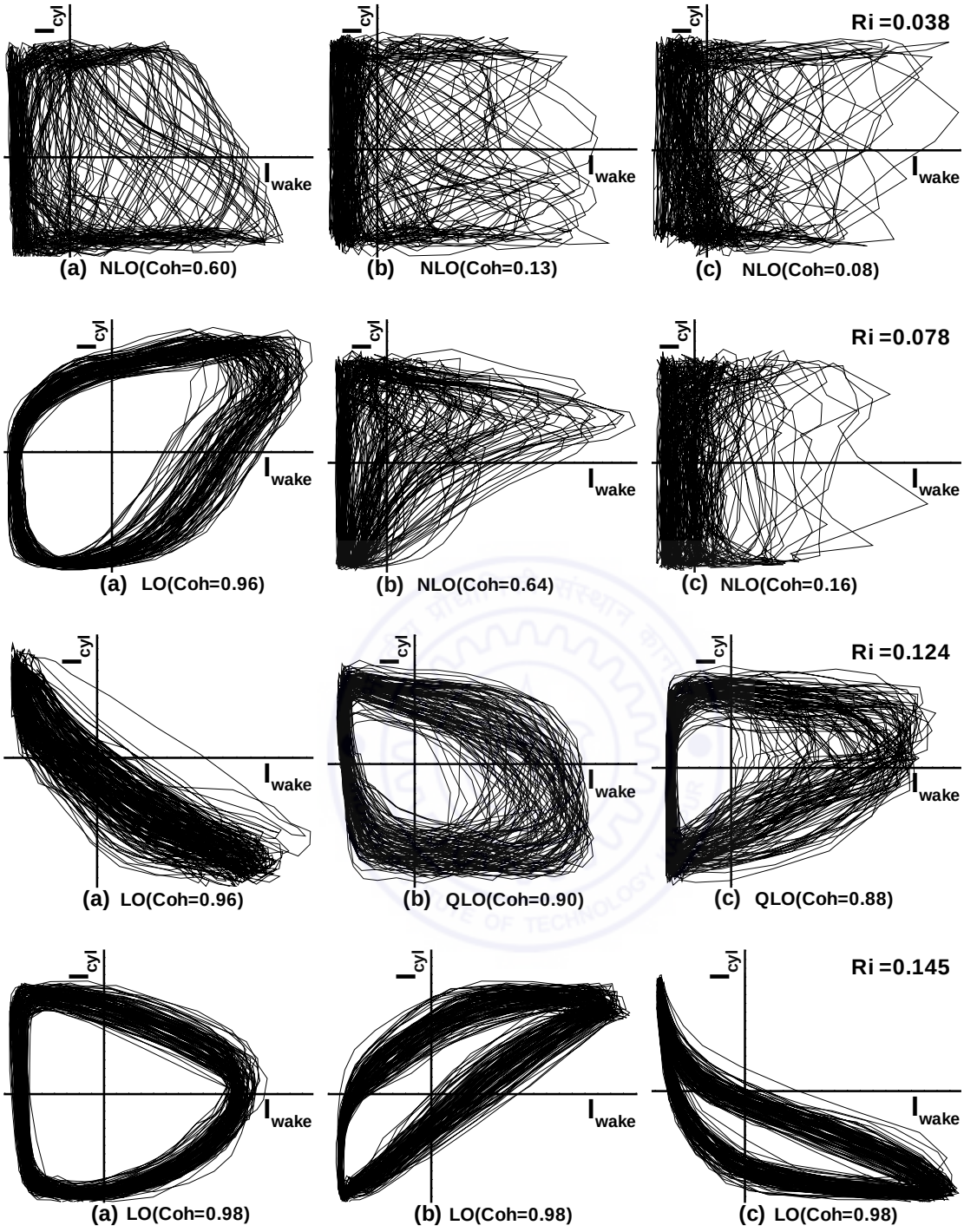

Figure 6.22: Lissajous curves of the wake signal versus cylinder oscillation signal of a circular cylinder ($f_e/f_s = 1.5$; $a/d = 0.08$) as a function of Richardson number (Ri = 0.038, 0.078, 0.124 and 0.145) for three stream-wise locations: (a) $x/d = 2.0$, (b) $x/d = 3.5$ and (c) $x/d = 5.0$. The locked-on states (NLO, QLO and LO) and spectral coherence magnitude between two signals (in the parenthesis) are provided.

from a nearly zero value to a moderately low value. Figure 6.22 shows that out of total twelve representative cases used for describing the locked-on states, five cases are marked

in the category of no lock-on (NLO). These include three cases for Ri = 0.038 comprising data from three stream wise locations i.e. $x/d = 2$, 3.5 and 5.0 and two cases for Ri = 0.078 at two stream wise locations i.e. $x/d = 3.5$ and 5.0. For these cases, Figure 6.18-D shows that multiple frequencies are present in the respective power spectrum and dominant peak occurs either at f_e or at f_s or at $f_e - f_s$. Figure 6.22 shows that Lissajous patterns are non-repetitive and chaotic in nature for these cases. These patterns clearly reflect the presence of multiple frequency components in the wake signal. The numerical value of the spectral coherence function (Coh) ranges between 0.08 to 0.64 for these cases. For the case of Coh = 0.08 (i.e. at Ri = 0.038, $x/d = 5$ location), the dominant peak occurs at the natural shedding frequency (f_s) and for the case of Coh = 0.64 (i.e. at Ri = 0.078, $x/d = 3.5$), the dominant peak occurs at the excitation frequency (f_e) in power spectra plots. This indicates that amplitude of the spectral power at the excitation frequency (f_e) controls the numerical value of the spectral coherence function. Hall and Griffin (1993) defined non lock-on cases as those for which the highest peak in the spectrum occurs at the natural shedding frequency or at a frequency corresponding to neither the perturbation nor the natural shedding frequency. However, the approach adopted here is more restrictive in deciding the lock-on states and utilizes several criteria rather than relying only on the power spectra. Therefore, for the case of Coh = 0.64, although the dominant peak occurs at the excitation frequency (f_e), it is considered as no lock-on state due to the presence of disorderly Lissajous plots, moderately low value of spectral coherence function and irregular vortex structures as evident in Figure 6.11 (B).

Lock-on **(LO)** : A strong interaction occurs between the natural instability oscillations and the forced cylinder oscillations in lock-on regime. As a result, the two oscillations are synchronized and natural vortex shedding adapts its frequency to that of the forced cylinder oscillation. The power spectra of the schlieren signal exhibit large-amplitude sharply defined spectral peak at the excitation frequency (f_e) along with smaller peaks at its super-harmonics. Highly repetitive, nearly overlapping trajectories from cycle to cycle of the cylinder oscillation are observed in the Lissajous plots of the wake signal versus cylinder oscillation signal. The numerical value of the spectral coherence function between the two signals at the excitation frequency (f_e) of the cylinder is extremely high (close to one). Figure 6.22 shows that out of a total of twelve representative cases used for describing the locked-on states, five cases are marked in the category of lock-on (LO). These include two cases for Ri = 0.078 and 0.124 comprising data at $x/d = 2$ location for both the Richardson number and three cases for Ri = 0.145 at three stream wise locations i.e. $x/d = 2$, 3.5 and 5.0. For these cases, Figure 6.18-D shows a large-amplitude sharp spectral peak at the excitation frequency (f_e) along with small peak at its harmonic ($2f_e$) in the respective power spectrum. Figure 6.22 shows that Lissajous trajectories follow well

defined, repetitive path in successive cycles of the cylinder oscillation. The locked-on behaviour persists over entire length of the acquired image data, consisting of approximately 111, 115 and 122 cylinder oscillation cycles at Ri = 0.078, 0.124 and 0.145, respectively. Ideally, the existence of an oval shaped unique limit cycle in the Lissajous plot represents the greatest degree of lock-on with perfect undamped sinusoidal response of the two periodic signals. Due to inherent practical limitations and noise present in the data obtained from the digital images, the intensity of the schlieren image and cylinder image signals do not show accurate sinusoidal behaviour and amplitude of the light intensity signal fluctuates in successive oscillation cycles. Therefore, an unique limit cycle is not obtained in the present Lissajous trajectories. However, highly repetitive character of these trajectories clearly indicate the occurrence of locked-on states. Extremely high numerical value of the spectral coherence function (Coh) ranging from 0.96 to 0.98 consolidate the existence of the locked-on state of vortex formation. It is also to be noted that the presence of small amplitude harmonic ($2f_e$) along with large amplitude dominant peak (f_e) in the power spectra do not affect the cycle-to-cycle periodicity but only shape of the Lissajous curves. Therefore, exactly oval shaped Lissajous curves are not observed. The schlieren images in Figure 6.11 (B), (C) and (D) show that for the locations at which locked-on state of vortex formation occurs, the large scale features of the vortex structures are highly repetitive and consistent in successive cycles of the cylinder oscillation. Hall and Griffin (1993) considered lock-on cases as those in which highest peak in the spectrum occurs at the perturbation frequency or half its value along with the presence of its higher harmonics but complete absence of natural shedding frequency component. The lock-on cases of the present illustrations (which have been identified utilizing several criterion) also display nearly similar behaviour in the power spectra plots.

Quasi lock-on **(QLO)** : This is an intermittent lock-on state, in which the locked-on behaviour exist over a long portion of the acquired image sequence and a non locked-on behaviour during the remaining portion. The near-wake contains a pattern of vortex structures frozen with the cylinder motion for significant duration of the entire time record. The power spectra of the schlieren signal exhibit a dominant peak at the excitation frequency (f_e) along with smaller peaks at its super-harmonics. Minor additional components at the natural shedding frequency (f_s) and its combination frequencies (i.e. $f_e - f_s$ and $f_e + f_s$) are also seen in the power spectra. These components have extremely small spectral power in some cases and are seen like a noise of the power spectra. The presence of minor noisy peaks in the spectra indicates an intermittent interruption in the locked-on behaviour and leads to a quasi locked-on state. The Lissajous plots of the wake signal versus cylinder oscillation signal consists of well-defined trajectories but with less degree of repeatability from cycle to cycle of the cylinder oscillation. The numerical value

of the spectral coherence function between the two signals at the excitation frequency (f_e) of the cylinder is considerably high but less than that observed for the lock-on state. Figure 6.22 shows that out of a total of twelve representative cases used for describing the locked-on states, two cases are marked in the category of quasi lock-on (QLO). These include two cases for Ri = 0.124 at x/d = 3.5 and 5.0 locations. For these cases, Figure 6.18-D, shows that the power spectra consists of a large-amplitude dominant peak at the excitation frequency (f_e), a smaller peak at its harmonic ($2f_e$) and minor noisy peaks at f_s, $f_e - f_s$ and $f_e + f_s$. Figure 6.22 shows that there is a definite decrease in repeatability in the Lissajous trajectories compared to highly repetitive trajectories for the lock-on thus indicating a lower level of lock-on. The numerical value of the spectral coherence function (Coh) for the two cases is 0.90 and 0.88 which is less than that observed for the lock-on state (0.96-0.98).

In the present section, the characteristics of various locked-on states have been explained using illustrative examples. Specific features of the power spectra, Lissajous trajectories, spectral coherence function and near-wake vortex patterns have been discussed in reference to these states. It is observed that highly organized, less organized and unorganized patterns of the Lissajous trajectories are typically associated with the lock-on, quasi lock-on and no lock-on states of the vortex formation, respectively. The degree of organization of these trajectories is reflected in the degree of sharpness of the spectral peaks in the corresponding spectra and the numerical value of the spectral coherence function. The effect of stream wise location (x/d), Richardson number (Ri), amplitude ratio (a/d), frequency ratio (f_e/f_s) and the cylinder geometry on the various locked-on states are presented in the following sections.

6.4.2 Dependence on wake location

The flow in the vortex formation region is considered to be important for overall development of the near-wake flow and physical evolution of the wake. It is believed that this region of the near-wake being close to the cylinder experiences strong effect of the forced oscillations and locks-on with the cylinder motion. Therefore, the effect of stream wise location is studied on the *lock-on* phenomenon in the near-wake closer to the cylinder (near the vortex formation region) and in the near-wake away from the cylinder (beyond the vortex formation region). Literature (e.g. Konstantinidis *et al.* (2003)) reveals that in the near-wake, a region from the base of the cylinder to a location, $x/d \approx 2.0$ is well represented as the vortex formation region. The field of view of the present schlieren images is limited to a stream wise location, $x/d \approx 5.0$. Therefore, the region between x/d = 2 and 5 locations is considered in the study. The numerical value of the spectral

coherence function (Coh) between the wake signal (at a selected location) and the cylinder oscillation signal at the excitation frequency (f_e) of the cylinder represents the degree of correlation between the two signals. This is considered as a direct measure of the degree of lock-on of the near-wake (at that location) with the cylinder oscillation. Figure 6.23 (A) and (B) show the variation of the spectral coherence (Coh) in the stream wise direction (x/d) for a circular cylinder at different Richardson numbers. Functional dependence on the oscillation frequency (f_e/f_s) is shown for two oscillation amplitudes, $a/d = 0.04$ and 0.08. Five frequency ratios (f_e/f_s) for each of the amplitude ratio (a/d) are presented in Figure 6.23 (A) and (B) respectively at four Richardson numbers, Ri = 0.038, 0.078, 0.124 and 0.145. For both the amplitude ratios (a/d) and all frequency ratios (f_e/f_s), the spectral coherence (Coh) continuously decreases in the stream wise direction (x/d) at all Richardson numbers. This indicates that degree of lock-on of the near-wake decreases in the stream wise direction (x/d). Therefore, the degree of lock-on of the near-wake with the cylinder motion closer to the cylinder is higher compared to that away from the cylinder. For some cases, the decrease in Coh is very sharp between $x/d = 2$ and 3.5 locations, while it is nominal between $x/d = 3.5$ and 5 locations. Therefore, locked-on states of vortex formation (i.e. NLO, QLO, and LO) have been identified at three critical stream wise locations (i.e. at $x/d = 2$, 3.5 and 5) and used to describe the overall wake behaviour.

At a frequency ratio, $f_e/f_s = 1$, and Richardson number, Ri = 0.038, the spectral coherence (Coh) value is low ranging from 0.29 to 0.09 at an amplitude ratio, $a/d = 0.04$. However, for the higher amplitude ratio, $a/d = 0.08$, reasonable high values of the Coh in the range of 0.77 to 0.89 are observed. In an experimental study, Koopman (1967) suggested that a critical minimum oscillation amplitude, $a/d = 0.05$ is required for lock-on to occur. Therefore, reasonable high values of the Coh for amplitude ratio, $a/d = 0.08$ can be attributed to the effect of an oscillation amplitude greater than the threshold value required for lock-on (i.e. $a/d = 0.05$). The near-wake is in the state of no lock-on (NLO) for $a/d = 0.04$ and quasi lock-on (QLO) for $a/d = 0.08$ at all stream wise locations. At the higher Richardson numbers, Ri = 0.078 and 0.124, the Coh values are high at all stream wise locations for both amplitude ratios. For these cases, Coh values range from a maximum value of 0.98 to a minimum value of 0.91 depending on the amplitude ratio and stream wise location. Very high values of Coh indicate that significant effect of the perturbation have reached to all stream wise locations and results in lock-on state (LO). At the highest Richardson number, Ri = 0.145, extremely high value of the spectral coherence, Coh = 0.98 is observed for both the amplitude ratios (a/d) indicating the greatest degree of lock-on (LO) at all stream wise locations.

At a frequency ratio, $f_e/f_s = 0.5$ and Richardson numbers, Ri = 0.038 and 0.078, the

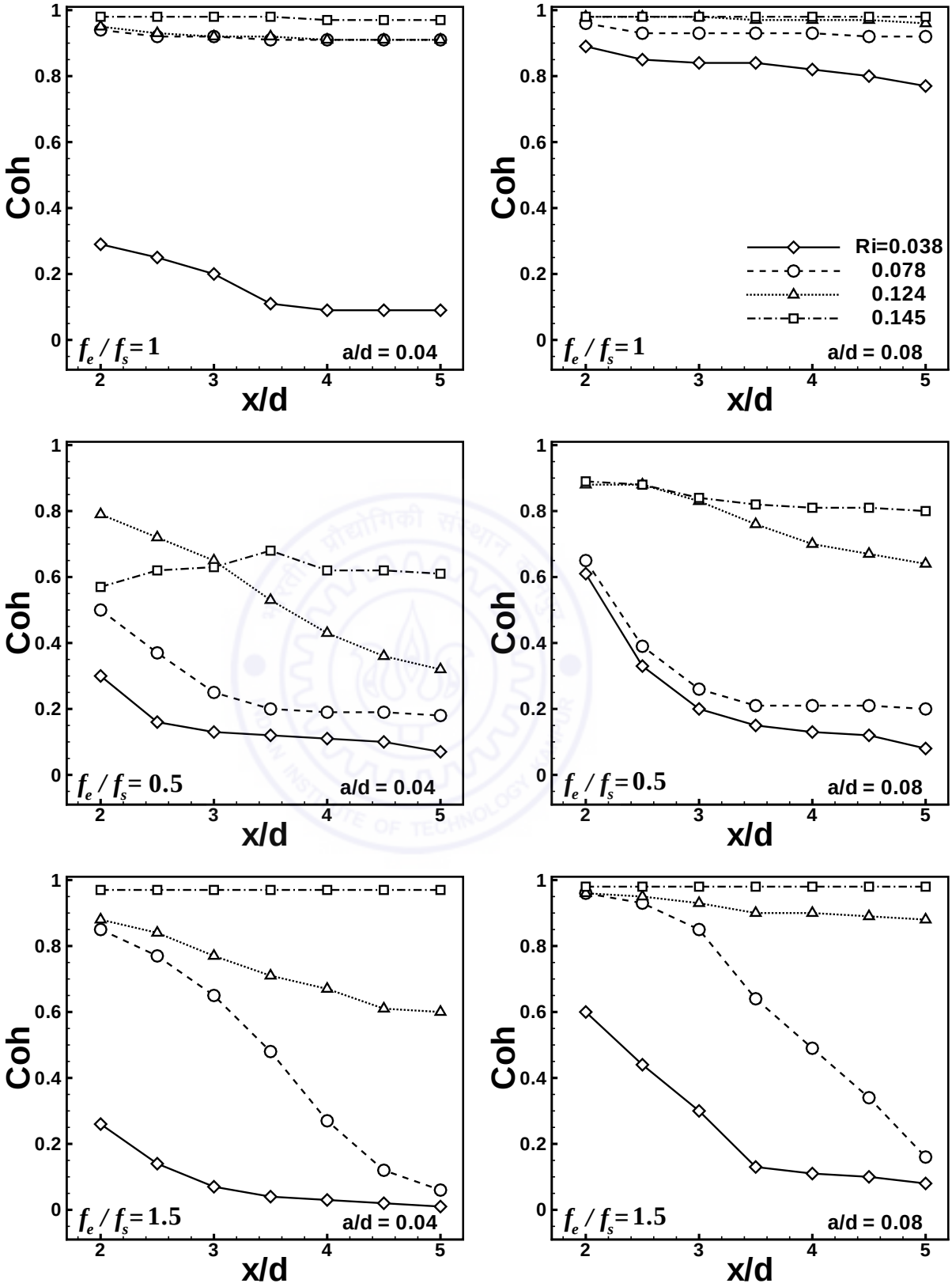

see caption on the next page

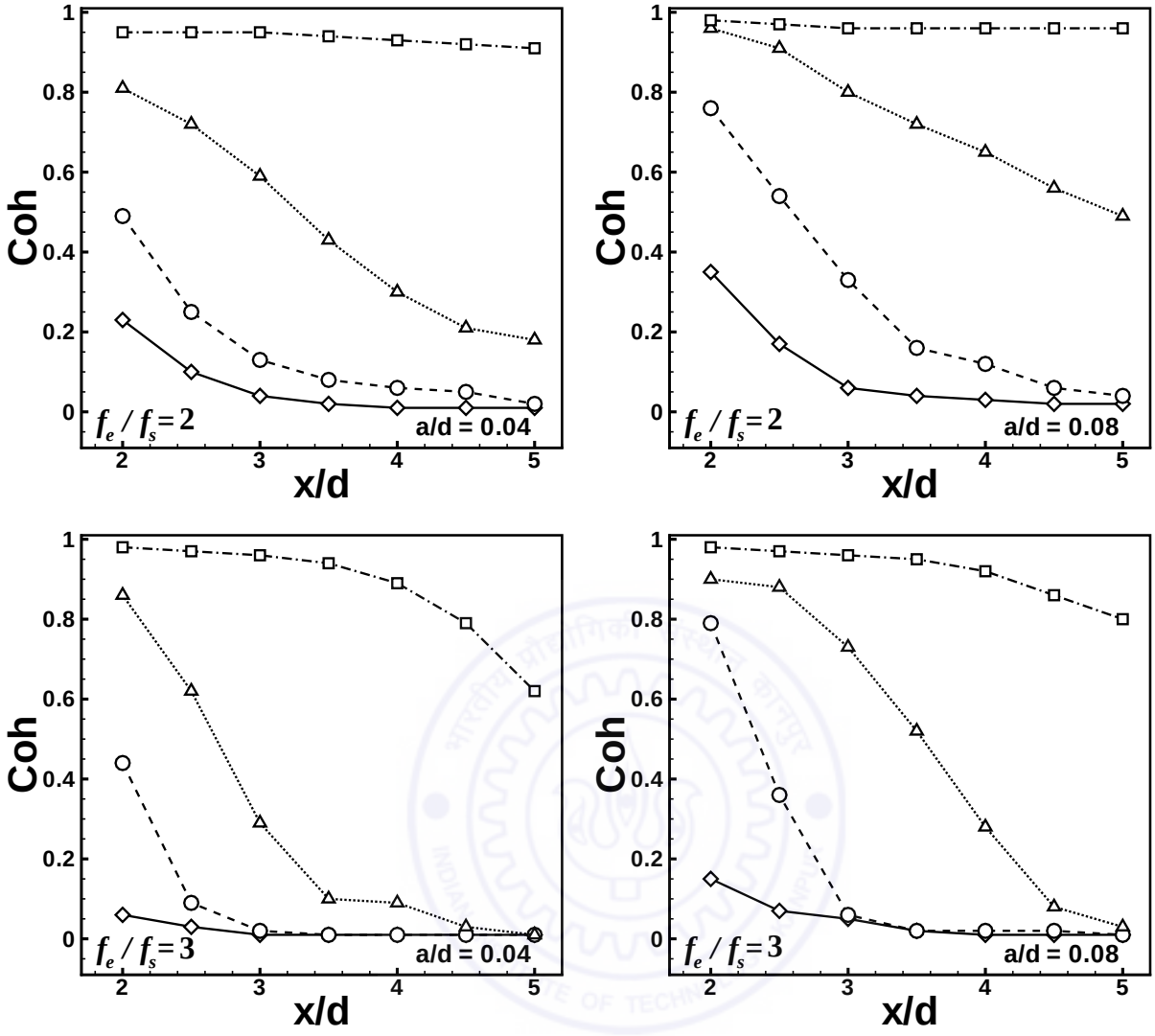

Figure 6.23: Variation of spectral coherence function (Coh) in the stream wise direction (x/d) for a circular cylinder at different Richardson numbers (Ri = 0.038, 0.078, 0.124, 0.145). Functional dependence on the oscillation frequency (f_e/f_s) is shown for two oscillation amplitudes (a/d): (A) $a/d = 0.04$, and (B) $a/d = 0.08$.

Coh values are less than 0.5 for $a/d = 0.04$ and follows a decreasing trend in the stream wise direction. At amplitude ratio, $a/d = 0.08$ the value of spectral coherence at $x/d = 2$ location is higher compared to that at $a/d = 0.04$ but sharply decreases between $x/d = 2$ and 3.5 locations and finally reaches to a minimum value at $x/d = 5$ location. The sharp decrease in the value of Coh between $x/d = 2$ and 3.5 locations indicates a sharp reduction of the effect of cylinder oscillation between these locations. At both Richardson numbers, the near-wake is in the state of no lock-on (NLO) at all stream wise locations for both the amplitude ratios. At a higher Richardson number, Ri = 0.124, the value of Coh

is considerably high at $x/d = 2$ location for both the amplitude ratios and leads to quasi lock-on state (QLO). However, at amplitude ratio, $a/d = 0.04$ there is weak coherence at the downstream locations and at amplitude ratio, $a/d = 0.08$ a certain degree of coherence up to $x/d = 3.5$ location is observed. For $a/d = 0.08$, the near-wake is quasi locked-on and not locked-on with the cylinder motion at $x/d = 3.5$ and 5 locations respectively. However, for $a/d = 0.04$, near-wake is not locked-on with the cylinder motion at both these locations. At the highest Richardson number, Ri = 0.145, considerably high values of the Coh (between 0.89 to 0.80) are observed at amplitude ratio, $a/d = 0.08$ indicating quasi lock-on state at all stream wise locations. However, low values of Coh are observed between $x/d = 2$ and 3.5 locations at amplitude ratio, $a/d = 0.04$. It may be remembered that at Ri = 0.145, there is suppression of vortex shedding for the stationary cylinder with a single steady plume was seen at the center of the cylinder. For the oscillating cylinder, the effect of perturbation at $f_e/f_s = 0.5$ and $a/d = 0.04$ is not sufficiently strong to excite the wave instability.

At a frequency ratio $f_e/f_s = 1.5$, Richardson number, Ri = 0.038 the Coh values are low (< 0.2) for an amplitude ratio, $a/d = 0.04$. For the higher amplitude ratio, $a/d = 0.08$, spectral coherence sharply decreases from a little higher value at $x/d = 2$ location to a very low value at the $x/d = 3.5$ location and finally reduces to a minimum value at $x/d = 5$ location. For both the amplitude ratios, the near-wake is in the state of NLO at all stream wise locations. At a higher Richardson number, Ri = 0.078, the value of the spectral coherence for both the amplitude ratios is quite high at the $x/d = 2$ location (Coh = 0.85 for $a/d = 0.04$ and Coh = 0.96 for $a/d = 0.08$) but decreases to a very low value (Coh ≈ 0.06) at $x/d = 5$ location. At $x/d = 2$ location, the near-wake is in the state of quasi lock-on (QLO) and lock-on (LO) for $a/d = 0.04$ and 0.08, respectively. At higher Richardson number, Ri = 0.124, the value of Coh for both the amplitude ratios is quite high at $x/d = 2$ location and decreases in the stream wise direction. The coherence value is low at the downstream locations, for amplitude ratio, $a/d = 0.04$ while at amplitude ratio, $a/d = 0.08$ good degree of coherence is observed in the downstream region. The near-wake is in the state of QLO, NLO and NLO for $a/d = 0.04$ and LO, QLO and QLO for $a/d = 0.08$ at $x/d = 2$, 3.5 and 5 locations, respectively. At the highest Richardson number, Ri = 0.145, the spectral coherence value is high (Coh = 0.97 and 0.98 for $a/d = 0.04$ and 0.08, respectively) at all locations indicating lock-on (LO) state throughout the near wake region ($x/d < 5$).

At a frequency ratio, $f_e/f_s = 2$, Richardson number (Ri = 0.038) the Coh value is low (Coh < 0.35) for both the amplitude ratios, indicating NLO state at all stream wise locations for both of the amplitude ratios. At higher Richardson number, Ri = 0.078, the value of spectral coherence is higher at $x/d = 2$ location for both amplitude ratios but

sharply decreases to a small value (Coh $\approx$ 0.02) at $x/d = 5$ location. At higher Richardson number, Ri = 0.124, the value of Coh for both the amplitude ratios is quite high at x/d = 2 location (Coh = 0.81 for $a/d = 0.04$ and Coh = 0.96 for $a/d = 0.08$). However, at amplitude ratio, $a/d = 0.04$ the coherence value drops significantly in the stream-wise direction compared to that at amplitude ratio, $a/d = 0.08$. At the highest Richardson number, Ri = 0.145 and for both amplitude ratios high values of Coh ranging from 0.91 to 0.98 are observed indicating the lock-on (LO) state at all stream wise locations.

At a frequency ratio, $f_e/f_s = 3$, and the lowest Richardson number (Ri = 0.038) the Coh values are lowest (Coh < 0.06) amongst all the frequency ratios at this Richardson number. At higher Richardson number, Ri = 0.078, there is sharp decrease in the value of Coh between $x/d = 2$ and 3.5 locations for both amplitude ratios. This indicates that at $f_e/f_s = 3$, the effect of perturbation is confined to a region close to the cylinder and disappears after $x/d = 3.5$ location. At higher Richardson number, Ri = 0.124, spectral coherence sharply decreases from a high value (Coh = 0.86) at $x/d = 2$ location to a low value (Coh = 0.01) at $x/d = 3.5$ location for $a/d = 0.04$. However, at higher amplitude ratio, $a/d = 0.08$, the decrease is less sharp between $x/d = 2$ and 3.5 locations compared to that at $a/d = 0.04$. At higher Richardson number, Ri = 0.145, spectral coherence decreases minimally between $x/d = 2$ and 3.5 locations but sharply decreases between $x/d = 3.5$ and 5 locations for both amplitude ratios. This indicates that at this Richardson number, the near-wake loses its lock-on state after $x/d = 3.5$ location.

The foregoing discussion indicate that locked-on state is dependent on stream wise location of the near-wake. In the near-wake, significant effect of perturbation is felt till $x/d = 2$ location but reduces appreciably in the downstream direction. Therefore, lock-on state is usually observed at $x/d = 2$ location and depending on the experimental conditions, lock-on state may be retained or lost at the downstream locations. Figure 6.23 (A) and (B) indicate that lock-on state in the near-wake closer to the cylinder (near the vortex formation region) does not necessarily result a lock-on state in the near-wake away from the cylinder (beyond the vortex formation region). In view of this, the identification of the locked-on states (i.e. NLO, QLO, and LO) at the three selected locations, $x/d = 2$, 3.5 and 5 in the near-wake have been carried out for all 200 sets of the experiments. These comprise 100 sets for each of the circular and square cylinders based on different conditions of the Richardson number (Ri), frequency ratios (f_e/f_s), and amplitude ratios (a/d). For various sets of the experiments, many combinations of the locked-on states at the three stream wise locations are possible in the near-wake. Based on these combinations, the locked-on state of the near-wake (considering all three locations) is classified into five general types i.e. NLO, QLO(P), QLO(G), LO(P) and LO(G) in the increasing levels of lock-on. The terms 'G' and 'P' in the parenthesis are the symbolic terms used to denote

the global and partial states of the lock-on (LO)/quasi lock-on (QLO) in the near-wake, respectively[1]. LO(G) means that at all three stream wise locations considered here, the near-wake is in the state of lock-on (LO). LO(P) means that near-wake is in the state of (LO) at $x/d = 2$ location (or at $x/d = 2$ and 3.5 locations) but at $x/d = 5$ location near-wake essentially have a lower level of lock-on as compared to that at the $x/d = 2$ location. QLO(G) means that at all three stream-wise location considered here, the near-wake is in the state of quasi lock-on (QLO). QLO(P) means the near wake ($x/d = 2$) is in QLO state and the downstream location ($x/d = 5$) has low level of lock-on i.e. at no lock-on state. NLO in the present categorization simply means that near-wake is in the state of no lock-on (NLO) at all three stream wise locations and the terms 'G' and 'P' have no significance for this category. This is because, no lock-on (NLO) is the lowest level of lock-on and if no lock-on (NLO) state exist at $x/d = 2$ location, then according to the present trend other two locations (i.e. $x/d = 3.5$ and 5) will be in the state of no lock-on (NLO).

Table 6.1 and 6.2 show overview of different lock-on states of the near-wake for the circular and square cylinders, respectively. Both these tables contain 100 entries corresponding to 100 sets of experimental conditions. The effect of frequency ratio (f_e/f_s), amplitude ratio (a/d) and Richardson number (Ri) is clearly visible from these tables. For each frequencies ratio (f_e/f_s), the columnwise entries show the effect of increase in amplitude ratio (a/d) for a constant Richardson number (Ri) and row wise entries show the effect of increase in Richardson number (Ri) for a constant amplitude ratio (a/d). For all entries, spectral coherence (Coh) between the wake signal (at $x/d = 2$) and cylinder oscillation signal is provided in square brackets. For the circular cylinder in Table 6.1, the ranges of numerical value of the spectral coherence function (at $x/d = 2$) for NLO, QLO(P), QLO(G), LO(P) and LO(G) are observed as 0.01-0.71, 0.72-0.90, 0.82-0.90, 0.93-0.99 and 0.94-0.99, respectively. While, for the square cylinder in Table 6.2, the ranges of spectral coherence are 0.25-0.70, 0.75-0.90, 0.85-0.89, 0.92-0.98 and 0.93-0.99 for NLO, QLO(P), QLO(G), LO(P) and LO(G), respectively. The ranges of the Coh values for corresponding locked-on states are similar for both cylinder geometries. The effect of various parameters on the lock-on states of the near-wake have been explained in separate sections in relation to these tables.

[1]These terms are specific to the present study where combined effect of buoyancy and low amplitude forced oscillation is studied in the near-wake flow field limited to a stream wise location, $x/d \approx 5.0$.

Table 6.1: Effect of frequency ratio (f_e/f_s), amplitude ratio (a/d) and Richardson number (Ri) on the locked-on states (NLO, QLO, LO) of the near-wake for a circular cylinder. Spectral coherence function (Coh) between the wake signal (at $x/d = 2$ location) and cylinder oscillation signal is given in the square brackets.

frequency ratio	amplitude ratio	Richardson number (Ri)			
(f_e/f_s)	(a/d)	0.038	0.078	0.124	0.145
1.0	0.02	NLO[0.12]	NLO[0.38]	NLO[0.56]	LO(G)[0.97]
	0.04	NLO[0.29]	LO(G)[0.94]	LO(G)[0.95]	LO(G)[0.98]
	0.06	QLO(G)[0.88]	LO(G)[0.95]	LO(G)[0.98]	LO(G)[0.98]
	0.08	QLO(G)[0.89]	LO(G)[0.96]	LO(G)[0.98]	LO(G)[0.98]
	0.10	LO(P)[0.96]	LO(G)[0.97]	LO(G)[0.98]	LO(G)[0.99]
0.5	0.02	NLO[0.06]	NLO[0.22]	NLO[0.52]	NLO[0.37]
	0.04	NLO[0.30]	NLO[0.50]	QLO(P)[0.79]	NLO[0.57]
	0.06	NLO[0.47]	NLO[0.59]	QLO(P)[0.87]	QLO(G)[0.89]
	0.08	NLO[0.61]	NLO[0.65]	QLO(P)[0.88]	QLO(G)[0.89]
	0.10	NLO[0.68]	NLO[0.71]	QLO(G)[0.90]	QLO(G)[0.90]
1.5	0.02	NLO[0.09]	NLO[0.34]	NLO[0.43]	QLO(G)[0.86]
	0.04	NLO[0.26]	QLO(P)[0.85]	QLO(P)[0.88]	LO(G)[0.97]
	0.06	NLO[0.44]	LO(P)[0.93]	LO(P)[0.95]	LO(G)[0.97]
	0.08	NLO[0.60]	LO(P)[0.96]	LO(P)[0.96]	LO(G)[0.98]
	0.10	QLO(P)[0.73]	LO(P)[0.96]	LO(G)[0.98]	LO(G)[0.99]
2.0	0.02	NLO[0.06]	NLO[0.19]	NLO[0.57]	QLO(G)[0.82]
	0.04	NLO[0.23]	NLO[0.49]	QLO(P)[0.81]	LO(G)[0.95]
	0.06	NLO[0.28]	QLO(P)[0.72]	LO(P)[0.95]	LO(G)[0.96]
	0.08	NLO[0.35]	QLO(P)[0.76]	LO(P)[0.96]	LO(G)[0.98]
	0.10	NLO[0.52]	QLO(P)[0.78]	LO(P)[0.98]	LO(G)[0.99]
3.0	0.02	NLO[0.01]	NLO[0.09]	NLO[0.55]	QLO(P)[0.90]
	0.04	NLO[0.06]	NLO[0.44]	QLO(P)[0.86]	LO(P)[0.98]
	0.06	NLO[0.10]	QLO(P)[0.76]	QLO(P)[0.89]	LO(P)[0.98]
	0.08	NLO[0.15]	QLO(P)[0.79]	QLO(P)[0.90]	LO(P)[0.98]
	0.10	NLO[0.38]	QLO(P)[0.79]	QLO(P)[0.90]	LO(P)[0.99]

Table 6.2: Effect of frequency ratio (f_e/f_s), amplitude ratio (a/d) and Richardson number (Ri) on the locked-on states(NLO, QLO, LO) of the near-wake for a square cylinder. Spectral coherence function (Coh) between the wake signal (at $x/d = 2$ location) and cylinder oscillation signal is given in the square brackets.

frequency ratio	amplitude ratio	Richardson number (Ri)			
(f_e/f_s)	(a/d)	0.030	0.086	0.121	0.167
1.0	0.02	QLO(P)[0.88]	LO(P)[0.92]	LO(P)[0.93]	LO(G)[0.96]
	0.04	LO(P)[0.92]	LO(G)[0.93]	LO(G)[0.95]	LO(G)[0.97]
	0.06	LO(P)[0.94]	LO(G)[0.94]	LO(G)[0.96]	LO(G)[0.98]
	0.08	LO(P)[0.95]	LO(G)[0.96]	LO(G)[0.97]	LO(G)[0.99]
	0.10	LO(P)[0.96]	LO(G)[0.96]	LO(G)[0.98]	LO(G)[0.99]
0.5	0.02	NLO[0.25]	NLO[0.35]	NLO[0.41]	QLO(P)[0.75]
	0.04	NLO[0.40]	NLO[0.58]	QLO(P)[0.79]	QLO(G)[0.89]
	0.06	NLO[0.67]	NLO[0.70]	QLO(G)[0.85]	LO(G)[0.93]
	0.08	QLO(P)[0.80]	QLO(P)[0.81]	QLO(G)[0.88]	LO(G)[0.94]
	0.10	QLO(P)[0.82]	QLO(P)[0.82]	QLO(G)[0.89]	LO(G)[0.96]
1.5	0.02	NLO[0.59]	QLO(P)[0.85]	QLO(P)[0.87]	LO(G)[0.97]
	0.04	QLO(P)[0.82]	LO(P)[0.92]	LO(P)[0.93]	LO(G)[0.98]
	0.06	QLO(P)[0.84]	LO(P)[0.93]	LO(P)[0.93]	LO(G)[0.98]
	0.08	QLO(P)[0.88]	LO(P)[0.94]	LO(P)[0.96]	LO(G)[0.98]
	0.10	QLO(P)[0.90]	LO(P)[0.95]	LO(P)[0.97]	LO(G)[0.98]
2.0	0.02	QLO(P)[0.86]	LO(P)[0.92]	LO(P)[0.93]	LO(G)[0.97]
	0.04	LO(P)[0.93]	LO(P)[0.94]	LO(P)[0.95]	LO(G)[0.98]
	0.06	LO(P)[0.94]	LO(P)[0.95]	LO(P)[0.95]	LO(G)[0.98]
	0.08	LO(P)[0.94]	LO(P)[0.95]	LO(P)[0.96]	LO(G)[0.99]
	0.10	LO(P)[0.95]	LO(P)[0.96]	LO(P)[0.97]	LO(G)[0.99]
3.0	0.02	QLO(P)[0.87]	LO(P)[0.92]	LO(P)[0.92]	LO(G)[0.99]
	0.04	LO(P)[0.92]	LO(P)[0.94]	LO(P)[0.96]	LO(G)[0.99]
	0.06	LO(P)[0.94]	LO(P)[0.96]	LO(P)[0.97]	LO(G)[0.99]
	0.08	LO(P)[0.94]	LO(P)[0.98]	LO(P)[0.98]	LO(G)[0.99]
	0.10	LO(P)[0.95]	LO(P)[0.98]	LO(P)[0.98]	LO(G)[0.99]

6.4.3 Dependence on Richardson number

Synchronisation of vortex structures with the cylinder motion depend on the Richardson number in the near-wake region. The plots at constant f_e/f_s and a/d in Figure 6.23 (A) and (B) show that spectral coherence (Coh) at a stream wise location (x/d) is higher at higher Richardson number indicating a higher degree of lock-on. Table 6.1 and 6.2 shows that at a frequency ratio (f_e/f_s), the locked-on state of the near-wake approaches from a lower level of lock-on to a higher level of lock-on with increase in Richardson number for a constant amplitude ratio (a/d). The spectral coherence correspondingly increases from a negligible value (in the case of NLO) to a extremely high value (in the case of LO(G)). This trend is uniformly observed for all amplitude ratios (a/d) and at all the frequency ratios (f_e/f_s) for both circular and square cylinders. For an unheated cylinder, Koopmann (1967) have reported the limits of the lock-on regime as a function of frequency ratio and amplitude ratio (see Figure 2.11). In the present study, the degree of lock-on has been quantitatively characterized in terms of the spectral coherence (Coh) at $x/d = 2$ location. Therefore, contours of the spectral coherence value (at $x/d = 2$) in amplitude ratio (a/d) versus frequency ratio (f_e/f_s) plane are well suited to show the bounds of the lock-on regime. These are presented in Figures 6.24 and 6.25 for circular and square cylinders, respectively as a function of Richardson number. In these plots, the high gray value shaded regions are the regions of high spectral coherence. The lighter shaded region (Coh between 0.72 and 0.9) and the darker shaded region (Coh greater than 0.91) indicate the approximate envelopes of the quasi lock-on (QLO) and lock-on (LO) states respectively. The region outside the shaded regions is in the state of no lock-on (NLO). For both the cylinders, the area of the shaded regions (i.e. high spectral coherence region) increases with increase in the Richardson number. This indicates that with increase in Richardson number, more conditions of f_e/f_s and a/d are favourable for lock-on to occur in the near-wake.

Figure 6.24 for a circular cylinder shows that at the lowest Richardson number, Ri = 0.038, the envelope of lock-on regime is extremely small and confined to a region enclosing $f_e/f_s = 1$ for $a/d \cong 0.10$. The envelope of quasi lock-on regime is a little larger and encloses one more frequency ratios, $f_e/f_s = 1.5$. At this Richardson number, neither the envelop of quasi lock-on (QLO) nor the lock-on (LO) is able to touch the boundaries of the frequency ratios, $f_e/f_s = 0.5$, 2 and 3. At the higher Richardson number, Ri = 0.078, the envelope of lock-on regime increases in size but confined to a region enclosing two frequencies, $f_e/f_s = 1$ and 1.5, only. The envelope of quasi lock-on regime is wider and encloses two more frequencies, $f_e/f_s = 2$ and 3 but unable to touch the boundaries of $f_e/f_s = 0.5$. At a higher Richardson number, Ri = 0.124, the envelope of lock-on

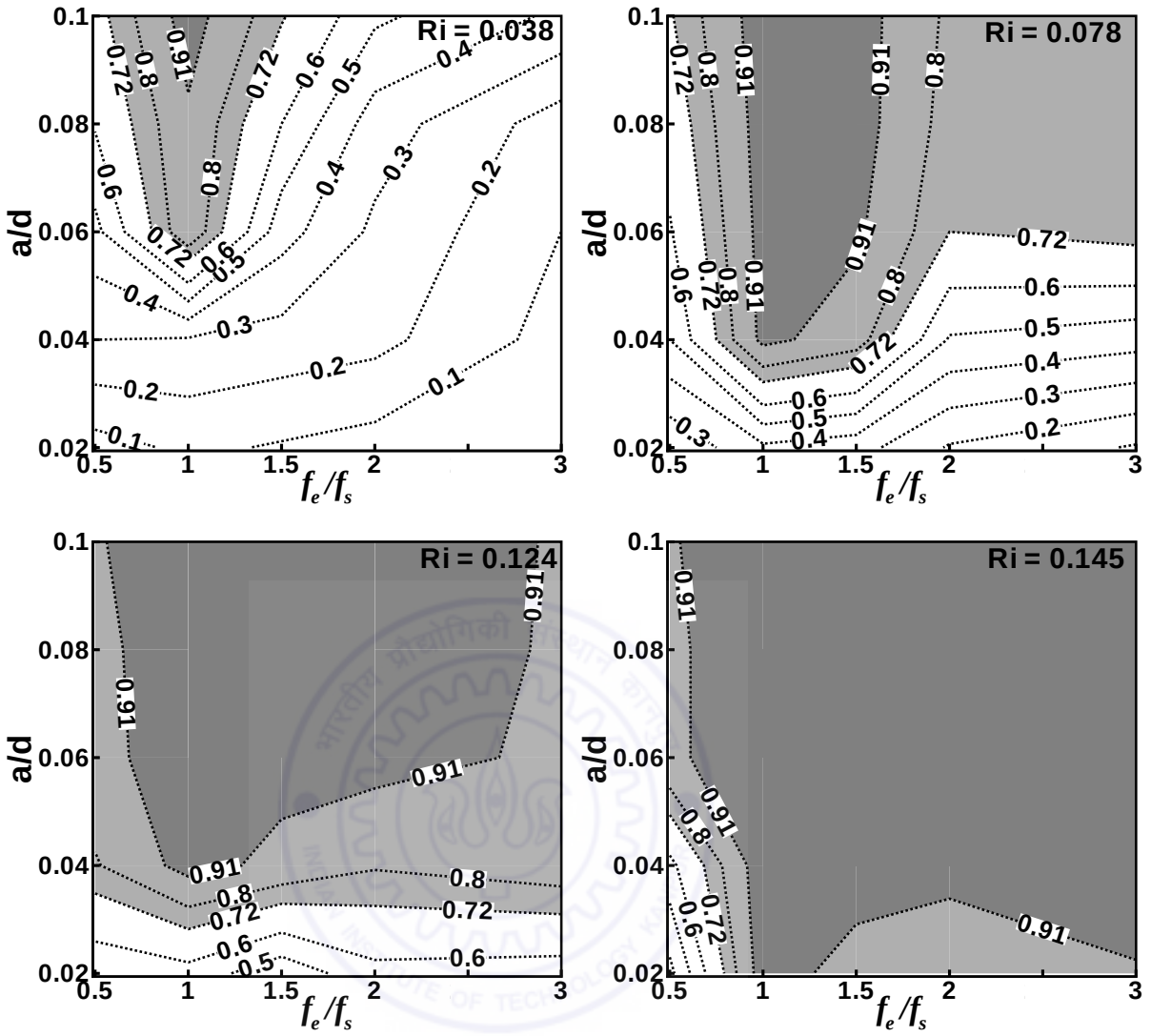

Figure 6.24: Contours of the spectral coherence (at $x/d = 2$ location) in the amplitude ratio (a/d) versus frequency ratio (f_e/f_s) plane of a circular cylinder at different Richardson numbers (Ri = 0.038, 0.078, 0.124, 0.145).

regime increases its area to enclose one more frequency, $f_e/f_s = 2$. At this Richardson number, the envelope of the quasi lock-on regime covers all the frequencies. At the highest Richardson number, Ri = 0.145, almost whole region is enclosed by the envelope of lock-on regime except at $f_e/f_s = 0.5$. For a square cylinder, Figure 6.25 shows that at the lowest Richardson number, Ri = 0.03, the envelope of the lock-on regime covers a large region containing three frequency ratios, $f_e/f_s = 1$, 2 and 3. The envelope of quasi lock-on regime encloses two other frequency ratios, $f_e/f_s = 0.5$ and 1.5 for the higher amplitude ratios and very small region is in the state of NLO (unshaded). At the higher Richardson numbers, Ri = 0.086 and 0.121, the envelope of lock-on regime covers all the frequencies except $f_e/f_s = 0.5$, which is enclosed by the envelope of the quasi lock-on regime. At the

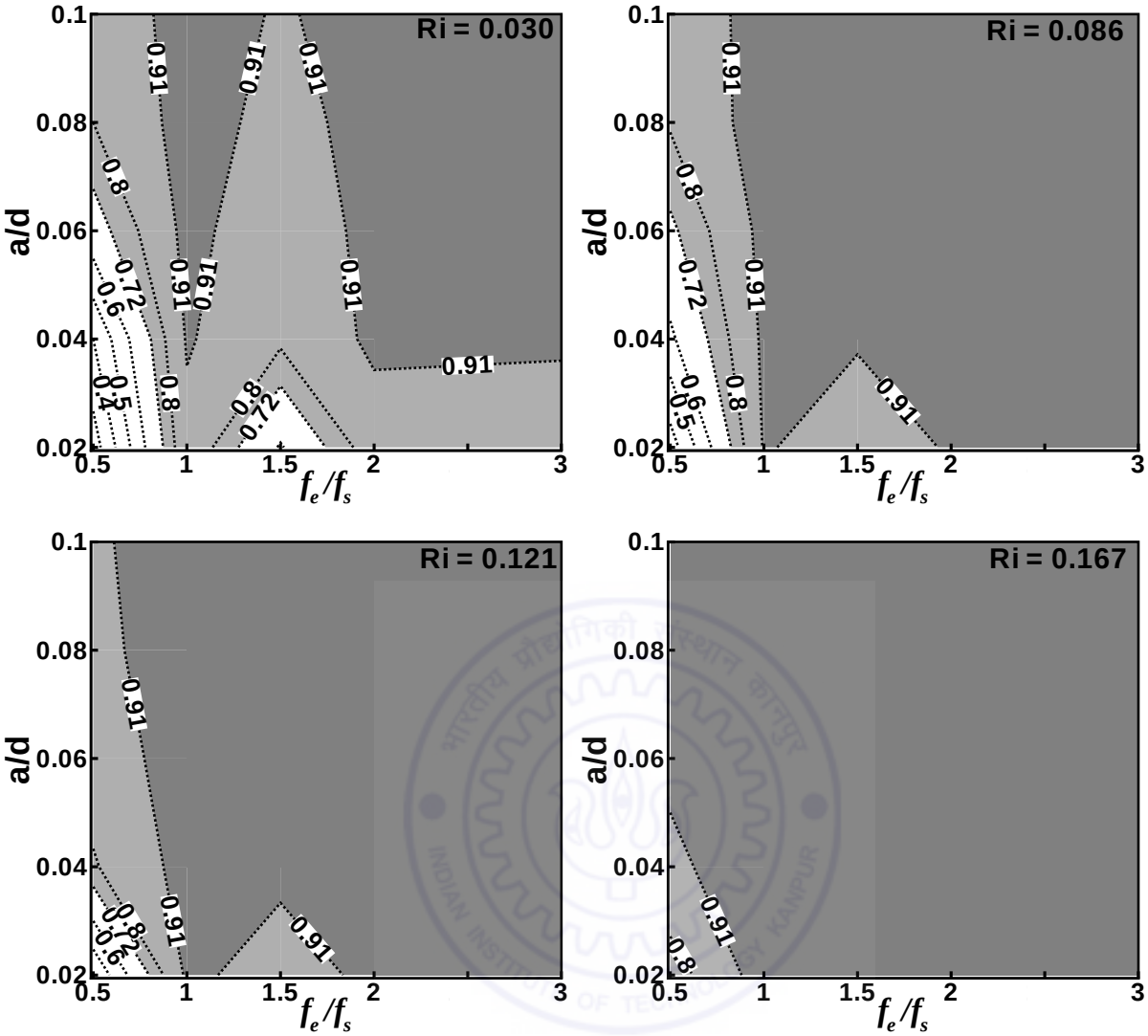

Figure 6.25: Contours of the spectral coherence (at $x/d = 2$ location) in the amplitude ratio (a/d) versus frequency ratio (f_e/f_s) plane of a square cylinder at different Richardson numbers (Ri = 0.038, 0.078, 0.124, 0.145).

highest Richardson number, Ri = 0.167, almost whole region is enclosed by the envelope of lock-on regime. Therefore, at the highest Richardson numbers, almost all frequency ratios (f_e/f_s) and amplitude ratios (a/d) are favourable for lock-on to occur in the near-wake for both the cylinders. The effect of Richardson number on the appearance of Lissajous patterns (Figure 6.22) can provide further insight. At the highest Richardson number, the most organized and persistent patterns of Lissajous trajectories are obtained at all stream wise locations, and at lower Richardson number Lissajous patterns are generally less organized, suggesting a tendency towards lower degree of lock-on.

6.4.4 Dependence on excitation amplitude

Lock-on of vortex shedding with the cylinder motion depends on the amplitude of oscillation in the near-wake. At constant f_e/f_s, a comparison of the plots for $a/d = 0.04$ and 0.08 in Figure 6.23 (A) and (B), respectively show that spectral coherence (Coh) at a stream wise location (x/d) is higher for higher amplitude ratio (a/d) at the same Richardson number (Ri). This indicates that degree of lock-on is higher for higher amplitude ratio (a/d). To show the effect of oscillation amplitude on the locked-on states of the near-wake, the variation of spectral coherence (at $x/d = 2$) with amplitude ratio at different Richardson numbers and frequencies ratios (f_e/f_s =1, 0.5, 1.5, 2 and 3) are presented in Figures 6.26 and 6.27 for the circular cylinder and square cylinders, respectively. The value of spectral coherence for five amplitude ratios, $a/d = 0.02$, 0.04, 0.06, 0.08 and 0.10 is plotted for each Richardson number. The plots show that with increase in amplitude ratio, the value of spectral coherence increases at all the Richardson numbers. This trend is uniformly observed at all the frequency ratios (f_e/f_s).

The plot for circular cylinder in Figure 6.26 for $f_e/f_s = 1$ shows that at the lowest Richardson number (Ri = 0.038), there is a big jump in the value of the spectral coherence from 0.29 to 0.88 for increase in amplitude ratio from $a/d = 0.04$ to 0.06. The corresponding locked-on state of the near-wake switches over from NLO to QLO as shown in Table 6.1. Koopman (1967) have experimentally determined that for transverse oscillation of the circular cylinder, a critical minimum oscillation amplitude, $a/d = 0.05$ is necessary for lock-on to occur in the near-wake. Therefore, remarkable increase in the value of Coh for $a/d = 0.06$ confirms the results of the Koopman (1967) of threshold amplitude ($a/d = 0.05$) for lock-on. It may be noted that the present experiment is performed for mildly heated cylinder (Ri = 0.038, forced convection conditions) compared to unheated cylinder (isothermal flow conditions) in the case of Koopman (1967). At the higher Richardson numbers, Ri = 0.078 and 0.124, similar big jump in the value of Coh takes place in between $a/d = 0.02$ and 0.04 for $f_e/f_s = 1$ and 1.5. The corresponding locked-on state of the near-wake changes from NLO to LO and NLO to QLO for f_e/f_s = 1 and 1.5, respectively (Table 6.1). At all other frequency ratios for these Richardson numbers, spectral coherence continuously increases to a saturated value with a/d. At the highest Richardson number, Ri = 0.145, the value of Coh is considerably high even for the lowest amplitude ratio ($a/d = 0.02$) at all frequency ratios (except $f_e/f_s = 0.5$) indicating a state of lock-on (LO) or quasi lock-on (QLO) (Table 6.1). Therefore, for an increase in Richardson number, the threshold value for lock-on shifts to the lower range of amplitudes. At $f_e/f_s = 0.5$, low values of Coh for $a/d = 0.02$ and 0.04 are observed. For square cylinder in Figure 6.27, the plots at $f_e/f_s = 0.5$ and 1.5 show that spectral

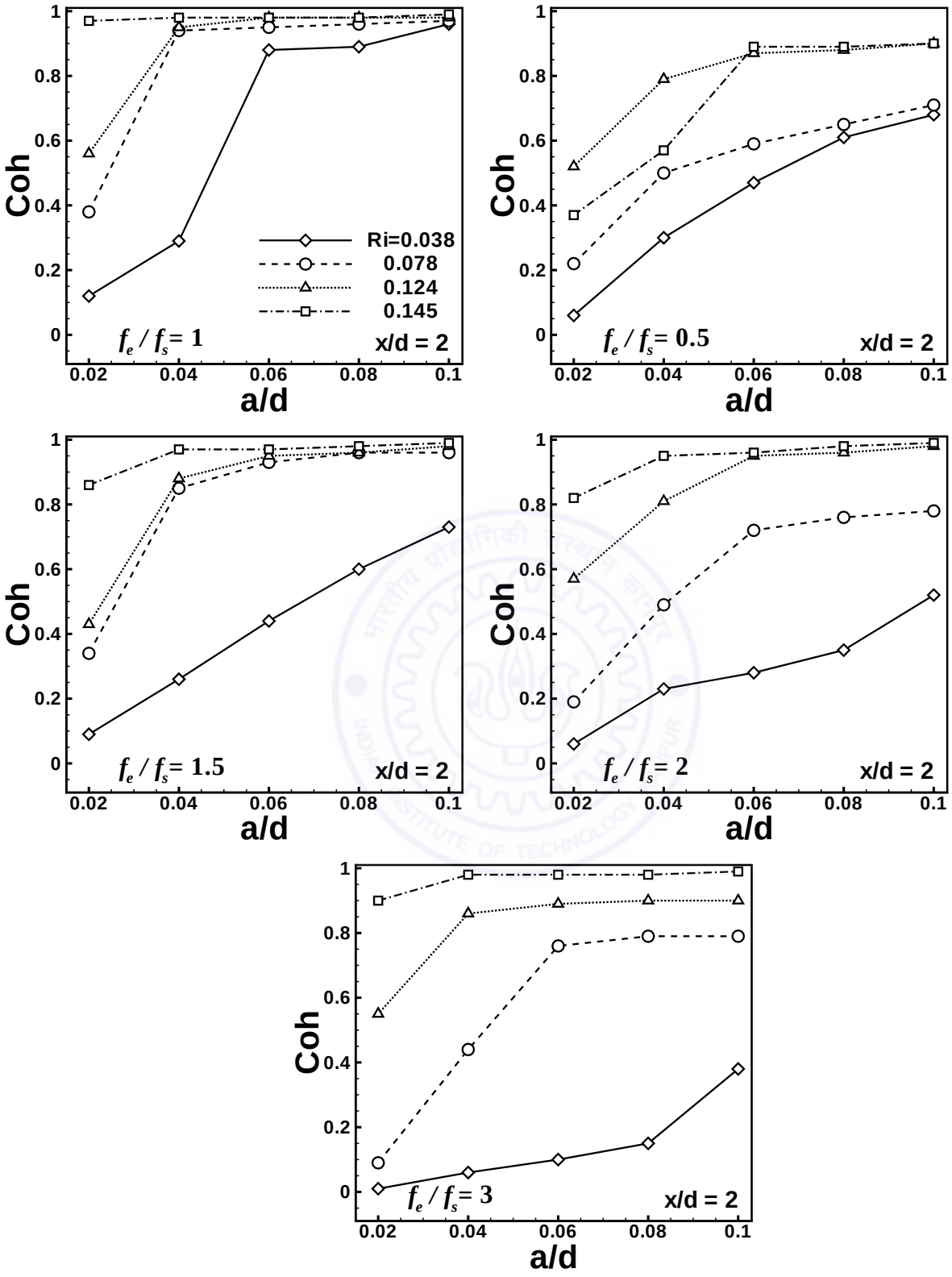

Figure 6.26: Variation of the spectral coherence (at $x/d = 2$ location) with oscillation amplitude (a/d) for a circular cylinder at different Richardson numbers (Ri = 0.038, 0.078, 0.124, 0.145) and oscillation frequency ($f_e/f_s = 1$, 0.5, 1.5, 2 and 3).

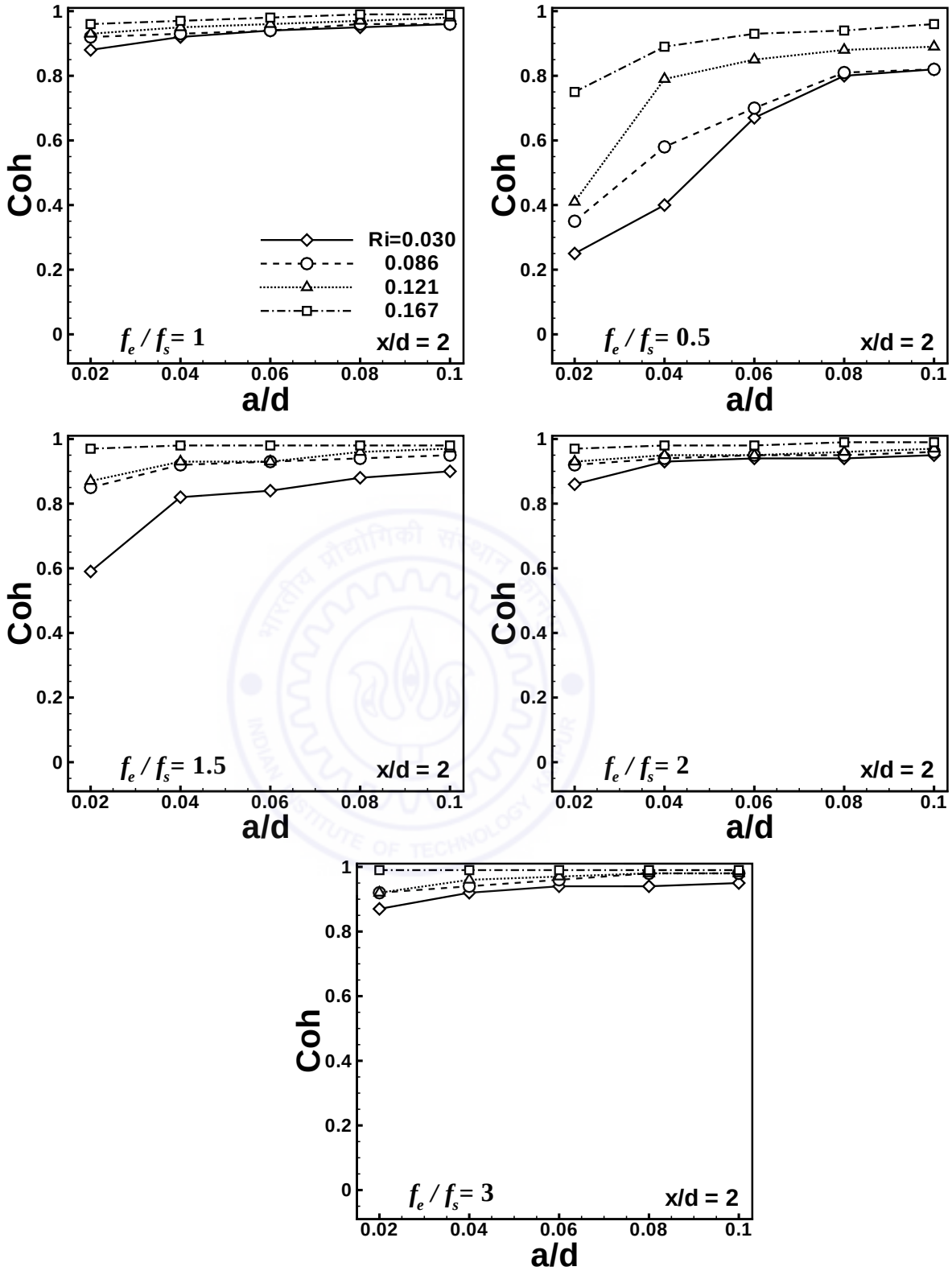

Figure 6.27: Variation of the spectral coherence (at $x/d = 2$ location) with oscillation amplitude (a/d) for a square cylinder at different Richardson numbers (Ri = 0.038, 0.078, 0.124, 0.145) and oscillation frequency (f_e/f_s = 1, 0.5, 1.5, 2 and 3).

coherence increases with a/d and attains a state of LO or QLO at higher amplitudes (Table 6.2). However, at other frequencies, $f_e/f_s = 1$, 2 and 3, quite high values of Coh indicate a state of LO or QLO for all amplitude ratios. The foregoing discussion shows that a critical minimum amplitude exist for lock-on to occur in the near-wake, which is a function of Richardson number, frequency ratio and base geometry of the cylinder.

6.4.5 Dependence on excitation frequency

Lock-on of the vortex structures with the cylinder motion in the near-wake depends on the oscillation frequency. For a circular cylinder, the contours of the spectral coherence (at $x/d = 2$) in Figure 6.24 show that the envelopes of lock-on and quasi lock-on regimes are observed around $f_e/f_s = 1$ at the lowest Richardson number (Ri = 0.038). This indicates that oscillation at the fundamental Strouhal frequency ($f_e/f_s = 1$) provides most favourable conditions for synchronization. With increase in Richardson number, the area of these envelopes increases on both sides of the $f_e/f_s = 1$ and encloses other frequencies in the order of preferences as $f_e/f_s = 1.5$, 2, 3 and 0.5. Sub-harmonic frequency ($f_e/f_s = 0.5$) is last in this order and is enclosed by the envelope of quasi lock-on regime only at the highest Richardson number, Ri = 0.145. This indicates that oscillation at sub-harmonic frequency ($f_e/f_s = 0.5$) provides least favourable conditions for lock-on. For a square cylinder, the contours of the spectral coherence (at $x/d = 2$) in Figure 6.25 show that the envelope of lock-on regime initially develops around three frequency ratios, $f_e/f_s = 1$, 2 and 3 at the lowest Richardson number (Ri = 0.03). With increase in Richardson number, the envelope of lock-on regime increases its area and encloses $f_e/f_s = 1.5$ first and then $f_e/f_s = 0.5$. Therefore, contours of the spectral coherence (at $x/d = 2$) clearly indicates that fundamental Strouhal frequency ($f_e/f_s = 1$) is most favoured frequency, while sub-harmonic frequency ($f_e/f_s = 0.5$) is least favoured frequency for lock-on to occur in the near-wake for the cylinders of both the geometries.

6.4.6 Dependence on cylinder geometry

Lock-on of the vortex shedding with the cylinder oscillation in the near-wake strongly depends on the base geometry of the cylinder. A comparison of the contours of the spectral coherence (at $x/d = 2$) in Figures 6.24 and 6.25 for circular and square cylinders respectively show that at comparable Richardson numbers, the area enclosed by the the envelope of lock-on regime is bigger for the square cylinder as compared to that of the circular cylinder. This indicates higher probability of lock-on of a square cylinder compared to the circular cylinder. At lower Richardson number, the difference between the areas of

envelope of lock-on regime between the two cylinders is significant. However, with increase in Richardson number, the difference in the areas decreases. This indicates that at the lower Richardson number, the presence of sharp corners for a square cylinder contrary to the streamlined structure of a circular cylinder play a important role in disturbing the natural instability for the former case. However, at higher Richardson numbers, the vortices in the near-wake are energized due to addition of the buoyancy forces and the effects of sharp corners is comparatively less significant for lock-on.

6.4.7 Frequency contents of the perturbed wake

The power spectra of the perturbed near-wake for a cylinder subjected to forced oscillations contain a dominant vortex shedding frequency (f_v) and number of other components as a result of nonlinear interactions between the natural vortex shedding and imposed excitation. A graph representing the variation of f_v/f_s versus f_e/f_s is well suited to demonstrate the degree of interactions and *lock-on* behaviour of the near-wake, qualitatively. Previous researchers (e.g. Ongoren and Rockwell (1988a) and Krishnamoorthy *et al.* (2001)) have presented these graphs to show the synchronized behaviour of the near-wake as a function of the excitation frequency (f_e) for unheated cylinders. Although, the earlier discussion have established various locked-on states in the near-wake, quantitatively, it is imperative to show the frequencies of the perturbed near-wake as a function of excitation frequency and the corresponding synchronized behaviour, graphically. Therefore, Figures 6.28 and 6.29 present the variation of non-dimensionalized vortex shedding frequency (f_v) and other components with oscillation frequency ratio (f_e/f_s) for circular and square cylinders respectively as a function of Richardson number. For both the cylinders, the graphs are presented for two amplitude ratios, $a/d = 0.04$ and 0.08. The oscillation frequency ratio (f_e/f_s) is plotted on the abscissa and the vortex shedding frequency ratio (f_v/f_s) along with other components are plotted on the ordinate. In all the plots, solid circle represents the dominant frequency component and hollow circles represent other frequencies in the power spectra of the near-wake. All the components which have 20% spectral power of the dominant frequency or more are included as other frequencies in the plot. For negligible level of interactions, the effect of oscillation frequency on the near-wake is small and perturbed wake frequency, f_v, corresponds to the natural Strouhal frequency, f_s, i.e. f_v/f_s is close to unity. This regime is represented by a horizontal straight line (dotted) in the plot. Seven solid lines passing through the origin, of various slopes, $f_v/f_e = 3$, 2, 1.5, 1, 1/1.5, 1/2 and 1/3 are drawn for identifying the sub-harmonic, non-harmonic and super-harmonic components in the perturbed wake. In these plots, lock-on state (LO) is observed when the dominant frequency lies on a line with a slope of unity ($f_v/f_e = 1$) and other frequencies (if present) fall on the superharmonic

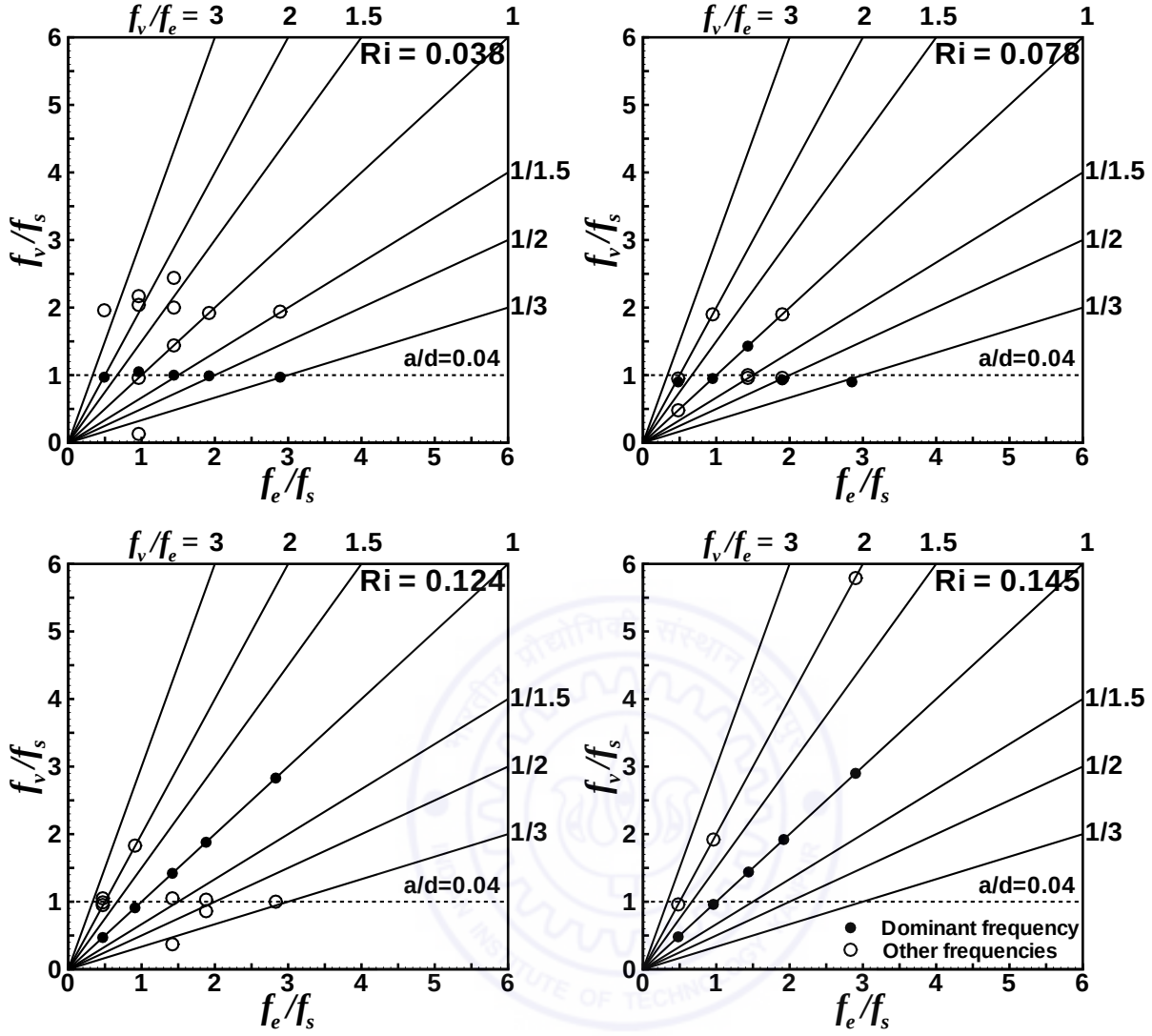

(A)

see caption on the facing page

curves ($f_v/f_e = 2$ and 3). Quasi lock-on state (QLO) can be observed when the dominant frequency lies on a line with a slope of unity and other frequencies fall on the horizontal line ($f_v/f_s = 1$) and/or on the sub-harmonic curves. However, for excitation at $f_e/f_s = 0.5$, the dominant frequency can also fall on the super-harmonic curve, $f_v/f_e = 2$ instead of the curve of unity slope, $f_v/f_e = 1$ for the QLO state. In the case of no lock-on state (NLO), the dominant frequency generally falls on the horizontal line (f_v/f_s) = 1).

Figure 6.28 (A) shows for a circular cylinder at an amplitude ratio of $a/d = 0.04$ that at the lowest Richardson number (Ri = 0.038), the dominant frequency for all frequency ratios falls on the horizontal line ($f_v/f_s = 1$) and displays no lock-on (NLO) behaviour. At the higher Richardson number, Ri = 0.078, the dominant frequency at the frequency ratios, $f_e/f_s = 1$ and 1.5 falls on the line of unity slope ($f_v/f_e = 1$). At $f_e/f_s = 1$, the

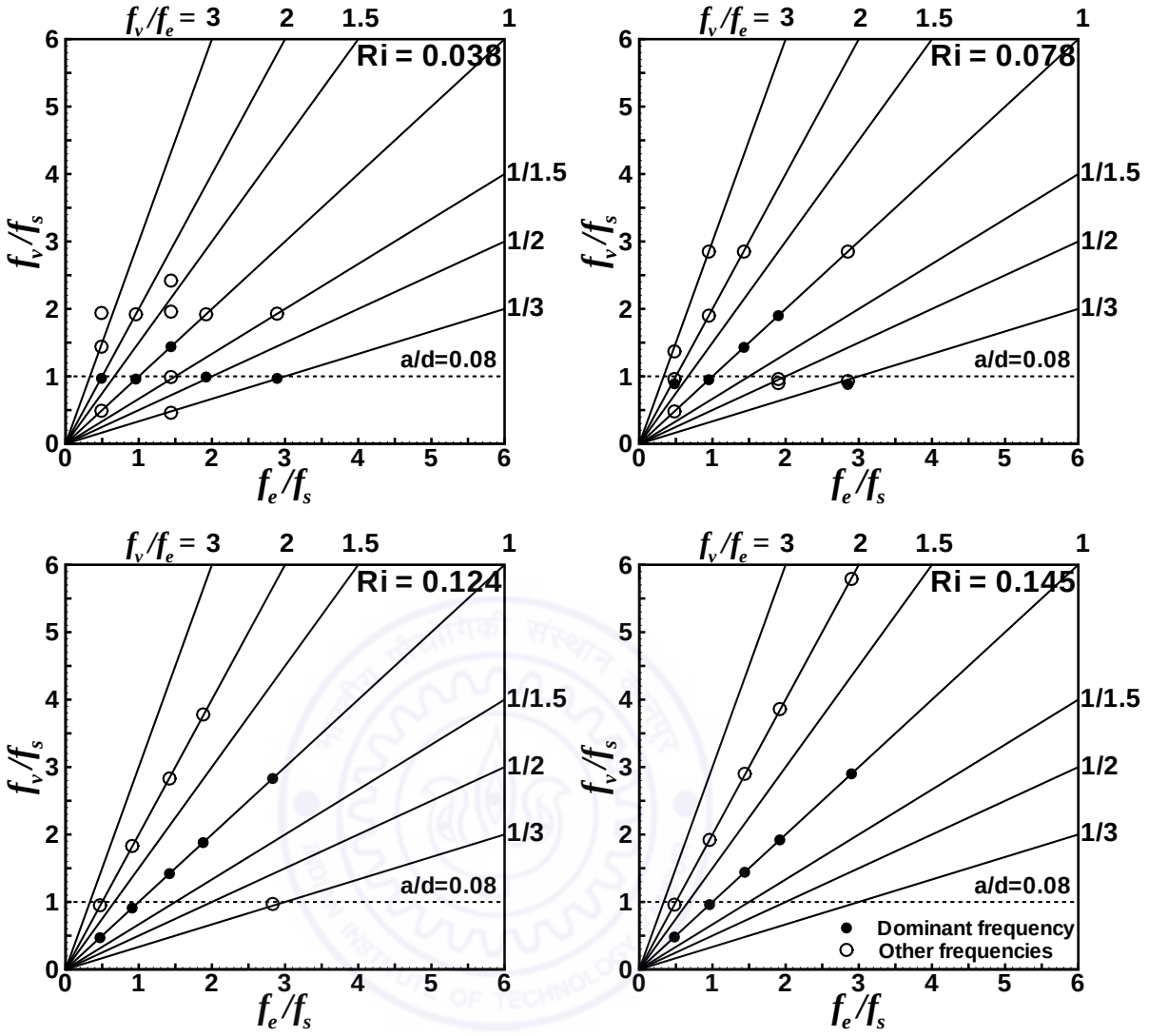

(B)

Figure 6.28: Variation of non-dimensionalized vortex shedding frequency (f_v/f_s) and other components with oscillation frequency ratio (f_e/f_s) for a circular cylinder. Functional dependence on Richardson number is shown. (A) $a/d = 0.04$, and (B) $a/d = 0.08$.

other frequency falls on the super harmonic curve ($f_v/f_e = 2$) and displays lock-on (LO) state, while at $f_e/f_s = 1.5$, the other frequency falls on the horizontal line ($f_v/f_s = 1$) and displays quasi lock-on (QLO) state. At higher Richardson number, Ri = 0.124, the dominant frequency at all frequency ratios falls on the line with a slope unity ($f_v/f_e = 1$). At $f_e/f_s = 1$, the near-wake is in the state of LO and at rest of the frequency ratios, it is in the state of QLO (Table 6.1). At the highest Richardson number (Ri = 0.145), the dominant frequency at all f_e/f_s falls on the line of unity slope and displays LO state for all frequency ratios (except $f_e/f_s = 0.5$). At higher amplitude ratio, $a/d = 0.08$, Figure 6.28 (B) shows that at the lowest Richardson number (Ri = 0.038), the dominant

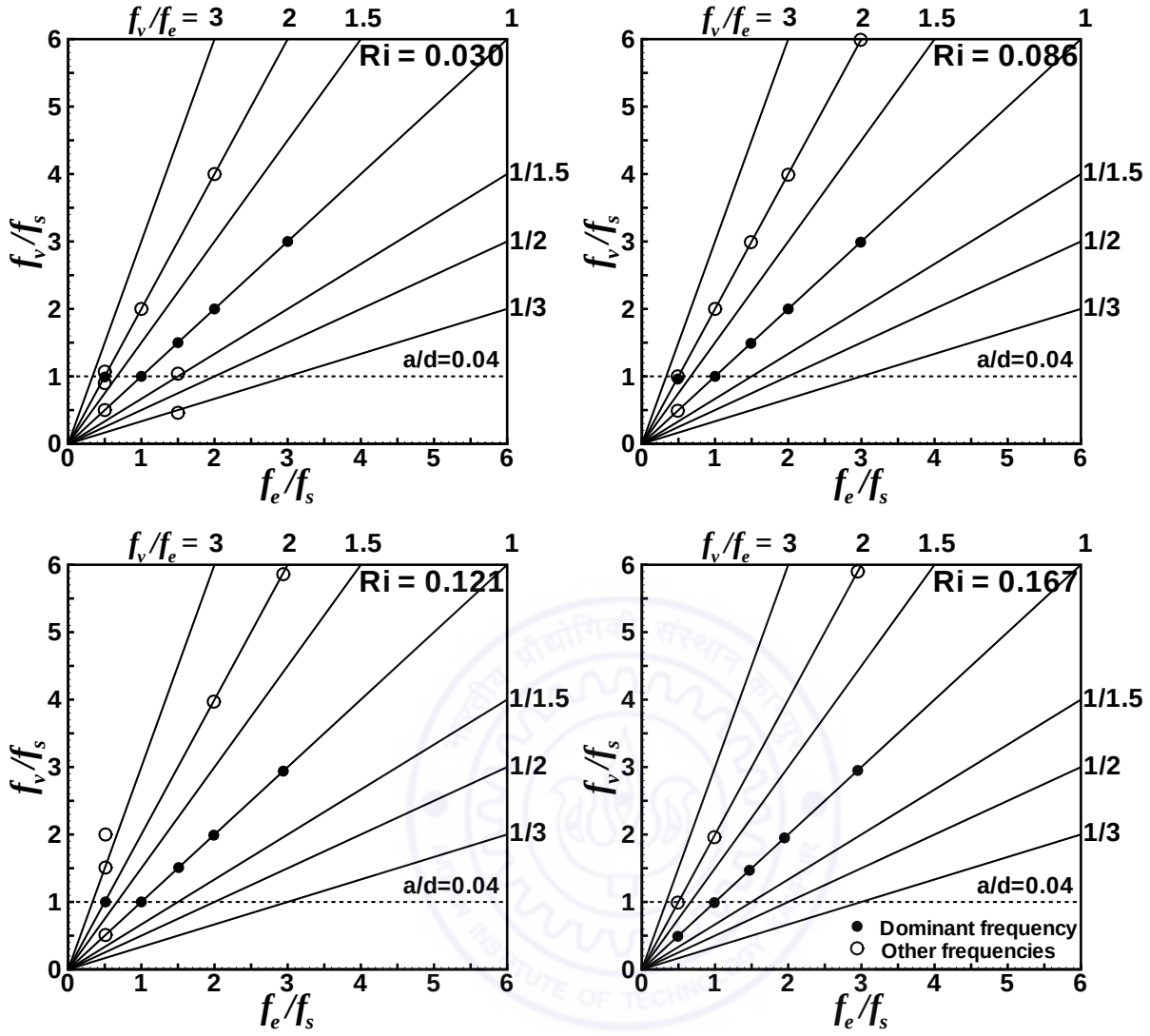

(A)

see caption on the facing page

frequency at $f_e/f_s = 1$ and 1.5 falls on the line of unity slope. Table 6.1 shows that at $f_e/f_s = 1$, the near-wake is in the state of QLO and not LO. This can be attributed to the additional frequency content present in the power spectra of Figure 6.18 (B). At $f_e/f_s = 1.5$, the near-wake is in the state of NLO and not QLO. This is due to the presence of comparable peaks at f_e and f_s in the power spectra in Figure 6.18 (D). At Ri = 0.078, the dominant frequency at the frequency ratios, $f_e/f_s = 1$, 1.5 and 2 fall on the line of unity slope and displays LO, LO and QLO states, respectively. At $f_e/f_s = 3$, two components of comparable spectral power at $f_e/3$ and f_s along with smaller peak at f_e are present as seen in the power spectra in Figure 6.18 (F). Therefore, near-wake is in the state of QLO and not NLO. At higher Richardson numbers, Ri = 0.124 and 0.145, the dominant frequency at all frequency ratios falls on the line with a slope unity and displays either

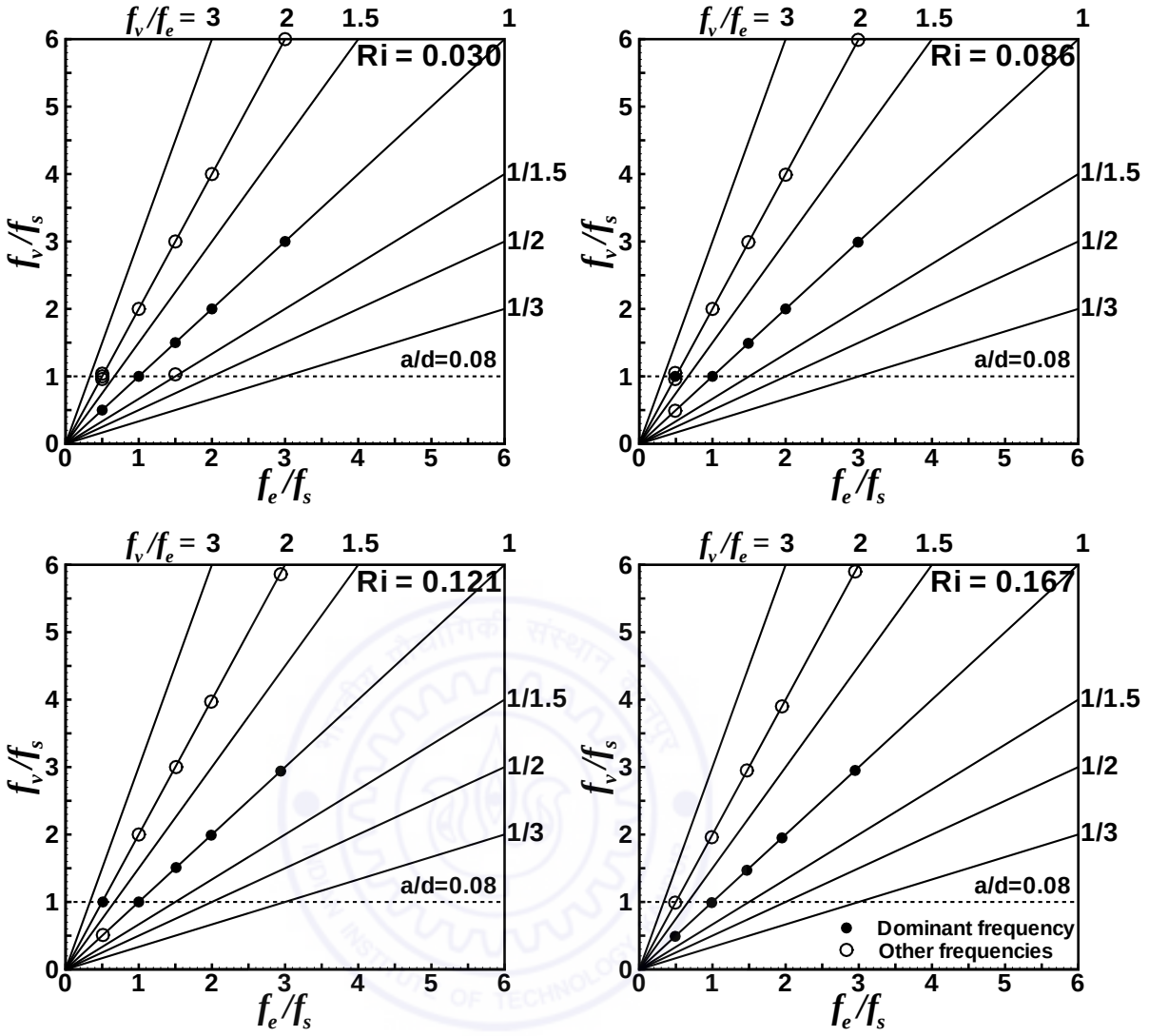

(B)

Figure 6.29: Variation of non-dimensionalized vortex shedding frequency (f_v/f_s) and other components with oscillation frequency ratio (f_e/f_s) for a square cylinder. Functional dependence on Richardson number is shown: (A) $a/d = 0.04$, and (B) $a/d = 0.08$.

LO or QLO states as presented in Table 6.1.

Figure 6.29 (A) shows for a square cylinder at an amplitude ratio of $a/d = 0.04$ that at the lower Richardson numbers, Ri = 0.03 and 0.086, the dominant frequency at all frequency ratios (except $f_e/f_s = 0.5$) falls on the line of unity slope. At $f_e/f_s = 0.5$, the dominant frequency falls on the horizontal line ($f_v/f_s = 1$) for both Richardson numbers and displays NLO state. At $f_e/f_s = 1$, 2 and 3, the near-wake is in the state of LO for both Richardson numbers. At $f_e/f_s = 1.5$, the near-wake is in the state of QLO and LO for Ri = 0.03 and 0.086, respectively. At higher Richardson numbers, Ri = 0.121 and 0.167, the dominant frequencies at $f_e/f_s = 1$, 1.5, 2 and 3 fall on the line with a unity

slope and displays LO state. At $f_e/f_s = 0.5$, the dominant frequency falls on the curve, $f_v/f_e = 2$ for Ri = 0.121, while it falls on the on the curve, $f_v/f_e = 1$ for Ri = 0.167. The near-wake is in the state of QLO for both Richardson numbers at $f_e/f_s = 0.5$. At higher amplitude ratio, $a/d = 0.08$, Figure 6.29 (B) shows that at the lowest Richardson number (Ri = 0.03), the dominant frequency at all frequency ratios falls on the line of unity slope ($f_v/f_e = 1$). At $f_e/f_s = 1$, 2 and 3, the near-wake is in the state of LO, while at $f_e/f_s = 0.5$ and 1.5, the near-wake is in the state of QLO. At the higher Richardson numbers, Ri = 0.086 and 0.121, the dominant frequency at all frequency ratios (except $f_e/f_s = 0.5$) falls on the curve, $f_v/f_e = 1$ and displays state of LO. At $f_e/f_s = 0.5$, the dominant frequency falls on the super-harmonic curve, $f_v/f_e = 2$ and displays QLO state for both Richardson numbers. At highest Richardson number, Ri = 0.167, the dominant frequencies at all frequency ratios fall on the line with a unity slope along with other frequencies falling on super-harmonic curve and display LO state.

6.5 Summary

This chapter reports the wake characteristics of circular and square cylinders under joint influence of buoyancy and forced oscillations in the transverse direction to mean flow. The Reynolds number is set at around Re = 100 for a wide range of buoyancy (Richardson number) and oscillation parameters (i.e. frequency and amplitude of oscillation). The frequency of oscillation is set at multiples of the natural vortex shedding frequency i.e. $f_e/f_s = 0.5$, 1, 1.5, 2 and 3. The oscillation amplitude (a/d) is varied from 0.02 to 0.10 in a small step of 0.02. Some key observations from this chapter are summarised below.

Vortex shedding reappears for the oscillating cylinders (both circular and square) at critical Richardson number for suppression of vortex shedding for the stationary cylinder. At all oscillation frequency ratios (f_e/f_s), the formation and shedding of the reappeared structures follows the periodicity of the excitation frequency (f_e) and exactly similar structures are repeated in subsequent oscillation cycles. However, the shape and size of the reappeared structures are different at different frequency ratios (f_e/f_s).

The vortex formation is periodic with the excitation frequency (f_e) and two vortices are alternatively formed from either side of the cylinder during one oscillation cycle at fundamental excitation ($f_e/f_s = 1$), for both the cylinders. The formation of vortices is periodic with the natural shedding frequency (f_s) and four vortices (two from each side shear layer) are formed from the cylinder during one oscillation cycle at sub-harmonic oscillation ($f_e/f_s = 0.5$) for both the cylinders. At 1.5-non-harmonic, 2-super-harmonic and 3-super-harmonic oscillation, the periodicity of vortex formation is a joint function of

the cylinder geometry and Richardson number. At the lowest Richardson number, for the circular cylinder, one vortex from each shear layer is formed for every 1.5 cycles, 2 cycles and 3 cycles of the cylinder oscillation at $f_e/f_s = 1.5$, 2 and 3, respectively (i.e. periodic with f_s). However, for the square cylinder at all three frequency ratios, one vortex from each shear layer is formed for every oscillation cycle (i.e. periodic with f_e). This indicates more pronounced effect of oscillation for the square cylinder compared to the circular cylinder. At higher Richardson numbers, the vortices are periodic at excitation frequency (f_e) for both the cylinders indicating regularizing effect of buoyancy on the formation of vortices. However, for both the cylinders, the detached vortices show irregularity due to decreased influence of buoyancy in the down stream region leading to loss of coherency.

The power spectra show the presence of a single or multiple frequencies depending on the excitation frequency ratio (f_e/f_s), Richardson number (Ri), stream wise location of the near-wake (x/d) and geometry of the cylinder. The observed frequencies include natural vortex shedding frequency (f_s), excitation frequency (f_e), super-harmonics ($2f_s$ and $2f_e$), sum ($f_e + f_s$) and differences ($f_e - f_s$) of these frequencies.

RMS fluctuations of the light intensity for an oscillating cylinder is a function of the frequency ratio, Richardson number, and geometry of the cylinder. At critical Richardson number, the fluctuations level is very high at all frequency ratios as compared to insignificant value for the stationary cylinder and indicates the presence of sustained vortex structures. The level of fluctuations along with the peak fluctuations for the oscillating square cylinder is higher compared to the stationary cylinder at these excitation frequencies. For square cylinder, the location of the peak fluctuations shifts towards the base of the cylinder indicating a decrease in the vortex formation length. At $f_e/f_s = 0.5$, for both the cylinders, the level of fluctuations for the oscillating cylinders are lower compared to that of the stationary cylinders indicating the presence of weaker vortices.

The lock-on of vortex shedding with the cylinder oscillation is a function of stream wise location of the wake (x/d), Richardson number (Ri), amplitude ratio (a/d), frequency ratio (f_e/f_s), and base geometry of the cylinder. Several criterion e.g. power spectra, Lissajous trajectories, spectral coherence function, and instantaneous patterns of the near-wake vortex structures have been utilized to postulate the locked-on behaviour. Spectral coherence has been used as a quantitative measure of the degree of lock-on of the shed vortices with the cylinder motion. Various types of locked-on states of vortex formation e.g. no lock-on (NLO), quasi lock-on (QLO), and lock-on (LO) have been identified. The variation of the spectral coherence (Coh) in the stream-wise direction (x/d) shows a decreasing trend and indicating lower degree of lock-on in the stream-wise region. The locked-on state of the near-wake is categorized into five general types i.e. NLO, QLO(P),

QLO(G), LO(P) and LO(G) in the increasing levels of lock-on. Spectral coherence (Coh) at a stream-wise location (x/d) is higher at higher Richardson number indicating a higher degree of lock-on. The contours of the spectral coherence show increase in regions of high spectral coherence with increase in Richardson number. The spectral coherence magnitude also increases with increase in amplitude ratio indicating higher degree of lock-on for higher amplitude ratios. A critical minimum amplitude exists for lock-on to occur in the near-wake and is a function of Richardson number, frequency ratio, and base geometry of the cylinder.

The envelope of lock-on regime indicates that fundamental Strouhal frequency ($f_e/f_s = 1$) is the most favoured frequency and sub-harmonic frequency ($f_e/f_s = 0.5$) is the least favoured frequency for occurrence of lock-on in the near-wake for cylinders of both the geometries. At comparable Richardson numbers, the area enclosed by the envelope of lock-on regime in the contours of the spectral coherence is larger for the square cylinder as compared to that of the circular cylinder indicating that square cylinder provides more favourable condition for lock-on to occur as compared to the circular cylinder. The variation of non-dimensionalized frequency of the perturbed wake (f_v/f_s) with oscillation frequency ratio (f_e/f_s) demonstrate the locked-on states of the near-wake, graphically. Functional dependence of lock-on on the Richardson number, amplitude ratio, and cylinder geometry is clearly observed.

Chapter 7

Conclusions and Scope for Future Work

The present work reports an experimental study on flow past heated stationary and oscillatory cylinders (both circular and square). Internally heated circular and square cylinders maintained at constant temperature are configured inside vertical test cell in aided buoyancy configuration. Laser schlieren-interferometry configured with a high-speed camera is used for flow imaging. The flow behavior is examined at Reynolds numbers near Re = 100. Richardson number is varied to cover both forced and mixed convection regimes in the range of 0.025-0.314. The oscillation frequencies are set equal to multiples of the natural vortex shedding frequency i.e. f_e/f_s = 0.5, 1, 1.5, 2 and 3. The oscillation amplitude (a/d) is varied from 0.02 to 0.1 in a small step of 0.02. Quantitative flow field statistics are obtained from the gray scale value of the fluctuating light intensity of the schlieren images. Phase-referenced schlieren images, RMS fluctuations, power spectra, cross spectra, phase shift, Strouhal number, vortex formation length, convection velocity, and coherence function results are reported for detailed quantitative characterization of wake dynamics. The main observations from this study can be broadly summarized in two parts as follows:

7.1 Effect of buoyancy

1. Control of vortex shedding behind circular and square cylinders can be realized by heating the cylinder. The similarities in schlieren visualization images, vortex formation lengths, time traces and power spectra between the two geometries indicate that both cylinders experience similar flow mechanisms for the suppression of instability.

2. The Strouhal number is a function of both Reynolds number and Richardson num-

ber. It is higher at higher Reynolds numbers and slowly increases with an increase in Richardson number. Beyond a certain critical Richardson number, the vortex shedding abruptly ceases and Strouhal number falls to zero. The critical Richardson number is Reynolds number dependent and a linear relationship between the two is observed.

3. The cylinder surface temperature (T_w) provides best estimate of instability characteristics in the mixed convection regime for calculation of fluid properties in a vertical flow configuration. This observation is in contrast to the horizontal mean flow configuration in the forced convection regime, where an effective temperature based on initiation of vortex shedding successfully characterizes the wake instability.

4. Instantaneous visualization images show that the shape, size and time-dependent movement of vortex structures are altered with increase in Richardson number. Before suppression of vortex shedding, the regular vortex structures are transformed to thin elongated structures of slender shape with minimal interaction between the vortices from opposite sides of the wake centerline. These patterns are subsequently replaced by a single plume-like structure slowly oscillating in the transverse direction which finally becomes steady during suppression.

5. The vortex formation length increases with an increase in Richardson number for both cylinders approaching an asymptotic value. Similar values of the asymptotic formation length at similar Reynolds numbers for heated circular and square cylinders indicate similarity in the instability mechanisms of two geometries.

6. RMS fluctuations of light intensity is high for sub-critical Richardson numbers due to regular vortex shedding. The fluctuations increase to a maximum in the streamwise direction upto vortex formation length and subsequently reduces in the downstream region. RMS fluctuations is higher inside the shear layers and reduces towards the cylinder centerline. The fluctuation level diminishes due to lower interactions between the vortices of opposite shear layer before suppression of vortex shedding leading to a insignificant value at complete suppression of vortex shedding.

7. The power spectra show a clear dominant frequency inside the shear layer and frequency doubled harmonic at the central region of the wake. At elevated Richardson number, the harmonic mode disappears and only fundamental mode prevails at all locations indicating minimal interaction between the vortices and modification of vortex shape to slender structures. At vortex suppression, the spectra show absence of any clear peak and there is a broadband spectra indicating an overall suppression of unsteadiness.

8. The time-averaged streamwise velocity profiles across the wake show a decrease in velocity deficit with an increase in Richardson number. This trend continues till the velocity deficit disappears and the velocity profile is close to uniform. At this point, the buoyancy forces add enough momentum to cancel the momentum deficit due to cylinder blockage. With subsequent increase in Richardson number, the velocity inside the wake exceeds that of the free stream velocity due to additive effect of buoyancy in an aided flow configuration.

9. The convection velocity of vortex structures is a function of Richardson number and streamwise location. It increases in the streamwise direction for all Richardson numbers. With increase in Richardson number, the instant of vortex detachment from the cylinder is delayed but structures attain similar asymptotic speeds. The convection velocity at a given streamwise location is however lower for a higher Richardson number. Phase shift of vortex structures between two streamwise locations increases with an increase in Richardson number. This increase in phase shift is attributed to the momentum provided by the aided buoyancy due to heating.

7.2 Joint effect of buoyancy and oscillation

1. Vortex shedding reappears due to oscillation of both circular and square cylinders at critical Richardson number for suppression of vortex shedding of the stationary cylinder. The shape and size of the vortex structures are different at different oscillation frequency ratios (f_e/f_s).

2. The vortex formation is periodic with the excitation frequency (f_e) and two vortices are alternatively formed from either side of the cylinder during one oscillation cycle at fundamental oscillation ($f_e/f_s = 1$), and all Richardson number for both circular and square cylinders.

3. The formation of vortices is periodic with the natural shedding frequency (f_s) and four vortices (two from each side shear layer) are formed from the cylinder during one oscillation cycle at sub-harmonic oscillation ($f_e/f_s = 0.5$) for both the cylinders.

4. The periodicity of vortex formation is a joint function of cylinder geometry and Richardson number at 1.5-non-harmonic, 2-super-harmonic and 3-super-harmonic oscillation. One vortex from each shear layer is formed for every 1.5 cycles, 2 cycles and 3 cycles of the cylinder oscillation at $f_e/f_s = 1.5$, 2 and 3 respectively (i.e. periodic with f_s) at the lowest Richardson number for the circular cylinder. However, for the square cylinder at all three frequency ratios, one vortex from each

shear layer is formed for every oscillation cycle (i.e. periodic with f_e). This indicates more sensitiveness to the oscillation for the square cylinder compared to the circular cylinder. At higher Richardson numbers, the formation of vortices is periodic with the excitation frequency (f_e) for both the cylinders. This indicates that buoyancy regularizes the formation of vortices. The detached vortices show irregularity and loss of coherency in down stream region for both cylinders due to weakening of the buoyancy force.

5. The power spectra show the presence of single or multiple frequencies depending on the oscillation frequency ratio, Richardson number, stream wise location of the near-wake and geometry of the cylinder. The observed frequencies include natural vortex shedding frequency (f_s), excitation frequency (f_e), super-harmonics ($2f_s$ and $2f_e$), sum ($f_e + f_s$) and differences ($f_e - f_s$) of these frequencies. At critical Richardson number, the power spectra for the oscillating cylinders at all frequency ratios show a dominant spectral peak at the excitation frequency (f_e) as opposed to a broadband spectra without any clear peak for the stationary cylinders indicating the reappearance of vortex shedding.

6. RMS fluctuations of the light intensity for an oscillating cylinder is a function of the oscillation frequency ratio, Richardson number, and geometry of the cylinder. At critical Richardson number, the fluctuation level is very high due to the presence of regular vortex structures at all frequency ratios as compared to insignificant value for the stationary cylinder. The level of fluctuations for the oscillating cylinder is lower as compared to that of the stationary cylinder indicating the presence of weaker vortices at $f_e/f_s = 0.5$, for both the cylinders.

7. The lock-on of vortex shedding with the cylinder oscillation is a function of stream wise location of the wake, Richardson number, amplitude ratio, frequency ratio, and base geometry of the cylinder. Several criterion e.g. power spectra, Lissajous trajectories, spectral coherence function, and instantaneous patterns of the near-wake vortex structures have been utilized to postulate the locked-on behaviour. Spectral coherence has been used as a quantitative measure of the degree of lock-on of the shed vortices with the cylinder motion. Various types of locked-on states of vortex formation e.g. no lock-on (NLO), quasi lock-on (QLO), and lock-on (LO) have been identified.

8. The variation of the spectral coherence in the stream-wise direction shows a decreasing trend indicating lower degree of lock-on in the downstream region. The contours of the spectral coherence indicate that the regions of high spectral coherence increases with increase in the Richardson number.

9. The spectral coherence increases with increase in amplitude ratio indicating higher degree of lock-on at higher amplitude ratios. A critical minimum amplitude exists for lock-on to occur in the near-wake, which is a function of Richardson number, frequency ratio, and base geometry of the cylinder.

10. The contours of spectral coherence indicate that fundamental Strouhal frequency ($f_e/f_s = 1$) is the most favoured frequency and the sub-harmonic excitation, $f_e/f_s = 0.5$ is the least favoured frequency for occurrence of lock-on in the near-wake of both cylinder geometries.

11. The area enclosed by the envelope of lock-on regime in the contours of the spectral coherence is larger for the square cylinder as compared to that of the circular cylinder at comparable Richardson numbers. This indicates that square cylinder provides more favourable condition for lock-on compared to the circular cylinder

12. The variation of non-dimensional frequency of the perturbed wake (f_v/f_s) with oscillation frequency ratio (f_e/f_s) graphically demonstrate the locked-on states of the near-wake. Functional dependence of lock-on with Richardson number, amplitude ratio, and cylinder geometry is clearly observed.

7.3 Future work

The present study has shown many interesting flow physics related to bluff body flows. However, it has opened up many possibilities for extending the present work. Based on the detailed literature survey carried out here and results obtained from the present experimental study, the following scope for future work is proposed.

1. The present study is carried out for heated stationary and oscillating bluff body flows in aided-buoyancy configuration, where the buoyancy force is added to the flow inertia. The addition of buoyancy force, cylinder surface motion and flow inertia at an angle to each other is expected to have strong influence on the wake dynamics. Therefore, it is proposed to carry out detailed experimental study on oscillation of cylinder at an angle to the mean flow.

2. The present study has reported detailed study on synchronization between near wake with transverse oscillation of circular and square cylinders. Limited experimental results on in-line oscillation case have also been reported. Detailed quantitative analysis related to vortex dynamics and lock-on phenomena need to be carried out.

3. Feedback of cylinder heating and oscillation with the coherent structures present in the wake is expected to be useful for flow control applications i.e. drag reduction and mixing/heat transfer enhancement etc. Therefore, the present work need to be extended for detailed study on influence of feedback between heated oscillating cylinders with the wake motion.

References

[1] Adrian, R. J., (1991), Particle imaging techniques for experimental fluid mechanics, *Annu. Rev. Fluid Mech.*, Vol. 23, pp. 261-304.

[2] Al-Mdallal, Q. M., Lawrence, K.P. and Kocabiyik, S., (2007), Forced streamwise oscillations of a circular cylinder: Locked-on modes and resulting fluid forces, *J. Fluids and Structures*, Vol. 23, pp. 681-701.

[3] Anderson, R. C. and Milton, J. E., (1989), A large aperture inexpensive interferometer for routine flow measurements, In: Instrumentation in aerospace simulation facilities, ICIASF'89 record, International congress on, IEEE pp. 394-399.

[4] Antonia, R. A. and Rajagopalan, S., (1990), Determination of drag of a circular cylinder, *AIAA Journal*, Vol. 28(10), pp. 1833-1834.

[5] Badr, H. M.,(1984), Laminar combined convection from a horizontal cylinder-parallel and contra flow regimes, *Int. J. Heat Mass Transfer*, Vol.27 (1), pp.15-27.

[6] Bearman, P. W., (1971), Corrections for the effect of ambient temperature drift on Hotwire measurements in incompressible flows, *DISA Information*, No. 11.

[7] Bearman, P. W., (1997), Near wake flows behind two-and three-dimensional bluff bodies, *J. Wind Engg. Ind. Aerodyn.*, Vol. 69-71, pp. 33-54.

[8] Ben-yakar, A. and Hanson, R. K., (2002), Ultra-fast-framing schlieren system for studies of the time evolution of jets in supersonic crossflows, *Experiments in fluids*, Vol. 32, pp. 652-666.

[9] Blackburn, H. M. and Henderson, R. D., (1999), A study of two-dimensional flow past an oscillating cylinder, *J. Fluid Mech.*, Vol. 385, pp. 255-286.

[10] Brackenridge, J. B. and Peterka, J., (1967), Criteria for quantitative schlieren interferometry, *Applied optics*, Vol. 6(4), pp. 731-735.

[11] Bruun, H. H., (1995), *Hot-wire Anemometry, Principles and Signal analysis*, Oxford University Press, New York.

[12] Carberry, J., Sheridan, J. and Rockwell D., (2001), Forces and wake modes of an oscillating cylinder, *J. Fluids and Structures*, Vol. 15, pp. 523-532.

[13] Cetiner, O. and Rockwell, D., (2001), Streamwise oscillations of a cylinder in a steady current. Part 1. locked-on states of vortex formation and loading, *J. Fluid Mech.*, Vol. 427, pp. 1-28.

[14] Chang, K. S. and Sa, J.Y., (1990), The effect of buoyancy on the vortex shedding in the near wake of a circular cylinder, *J. Fluid Mech.*, Vol. 220, pp. 253-266.

[15] Davis, R. W. and Moore, E. F., (1982), A numerical study of vortex shedding from rectangles, *J. Fluid Mech.*, Vol. 116, pp. 475-506.

[16] Dalziel, S. B., Hughes, G.O. and Sutherland B. R., (2000), Whole-field density measurement by synthetic schlieren, *Expts. Fluids*, Vol. 28, pp. 322-335.

[17] Dumouchel, F., Lecordier, J. C., and Paranthoen, P., (1998), The effective Reynolds number of a heated cylinder, *Int. J.Heat Mass Transfer*, Vol.41 (12), pp. 1787-1794.

[18] Farinotti, S., Beghuin, D. and Joannes, L., (2005), Real-time Phase shift schlieren, *Optical Engineering*, Vol 44(8), pp. 083603 (1-4).

[19] Franke, R., Rodi, W. and Schönung, B., (1990), Numerical calculation of laminar vortex-shedding flow past cylinders, *J. Wind Engg. Ind. Aerodyn.*, Vol. 35, pp. 237-257.

[20] Gad-el-hak, M., (2000), *Flow control: passive, active, and reactive flow management*, Cambridge university press, United Kingdom.

[21] Gau, C., Wu, J.M. and Liang C.Y., (1999), Heat transfer enhancement and vortex flow structure over a heated cylinder oscillating in the crossflow direction, *J. Heat Transfer*, Vol.121, pp. 789-795.

[22] Gau C., Wu, S.X., Su, H. S., (2001), Synchronization of vortex shedding and heat transfer enhancement over a heated cylinder oscillating with small amplitude in streamwise direction, *J. Heat Transfer*, Vol.123, pp. 1139-1148.

[23] Gayhart, E. L., and Prescott, R., (1949), Interference phenomenon in schlieren system, *J. Opt. Soc. Am.*, Vol. 39, pp. 546-550.

[24] Gerrard, J. H.,(1966), The mechanics of the formation region of vortices behind bluff bodies, *J. Fluid Mech*, Vol. 25, pp. 401-413.

[25] Goldmeer, J. S., Urban D. L. and Yuan, Z. G., (2001), Measurement of gas-phase temperatures in flames with a point- diffraction interferometer, *Applied optics* , Vol. 40(27), pp. 4816-4823.

[26] Goldstein, R. J., (1996), *Fluid Mechanics Measurements*, Taylor and Francis, New York.

[27] Griffin, O. M. and Votaw, C. W., (1972), The vortex in the wake of a vibrating cylinder, *J.Fluid Mech.*, Vol. 51(1), pp. 31-48.

[28] Griffin, O. M. and Ramberg, E., (1974), The vortex-street Wakes of vibrating cylinders, *J. Fluid Mech.*, Vol. 66(3), pp. 553-576.

[29] Griffin, O. M. and Ramberg, S. E., (1976), Vortex shedding from a cylinder vibrating in line with an incident uniform flow, *J. Fluid Mech.*, Vol. 75, Part 2, pp. 257-271.

[30] Griffin, O. M. and Hall, M. S., (1991), Review- Vortex shedding lock-on and flow control in bluff body wakes, *Transactions ASME J. Fluids Engg.*, Vol. 113, pp. 526-537.

[31] Griffin, O. M., (1995), A note on bluff body vortex formation, *J. Fluid Mech.*, Vol. 284, pp. 217-224.

[32] Gu, W., Chyu, C. and Rockwell, D., (1994), Timing of vortex formation from an oscillating cylinder, *Phys. Fluids*, Vol. 6, No.11, pp. 3677-3682.

[33] Guilmineau, E. and Queutey, P., (2002), A numerical simulation of vortex shedding fro an oscillating circular cylinder, *J. Fluids and Structures* , Vol. 16(6), pp. 773-794.

[34] Hall, M. S. and Griffin, O. M., (1993), Vortex shedding and lock-on in a perturbed flow, *Transactions ASME J. Fluids Engg.*, Vol. 115, pp. 283-291.

[35] Hatanka, K. and Kawahara, M., (1995), A numerical study of vortex shedding around a heated/cooled cylinder by three- step Taylor-Galerkin method,*Int. J. Numerical Methods in Fluids* , Vol.21, pp.857-867.

[36] Henderson, R., (1997), Nonlinear dynamics and pattern formation in turbulent wake transition, *J. Fluid Mech.*, Vol. 352, pp. 65-112.

[37] Jain, P. C. and Lohar, B.L., (1979), Unsteady mixed convection heat transfer from a horizontal circular cylinder, *Trans. of ASME, J. Heat transfer*, Vol. 101, pp.126-131.

[38] joannes, L., Dubois, F. and Legros, J. C., (2003), Phase shifting schlieren: high-resolution quantative schlieren that uses the phase-shifting technique principle, *Applied Optics*, Vol 42(25), pp. 5046-5053.

[39] Kay, S. M., 1988, *Modern Spectral Estimation: Theory and Application*, Prentice Hall International, Englewood Cliffs, New Jersey.

[40] Keane, R. D. and Adrian, R. J., (1990), Optimization of particle image velocimeters. Part I: Double-pulsed system, *Meas. Sci. Technol.*, Vol. 1, pp. 1202-1215.

[41] Keane, R. D. and Adrian, R. J., (1992), Theory of cross-correlation analysis of PIV images, *Appl. Sci. Research*, Vol. 49, pp. 191-215.

[42] Kelkar, K. M. and Patankar, S. V., (1992), Numerical prediction of vortex shedding behind a square cylinder, *Int. J. for numerical methods in fluids*, Vol.14, pp. 327-341.

[43] Kim, W., Yoo, J. Y. and Sung, J., (2006), Dynamics of vortex lock-on in a perturbed cylinder wake, *Phy. Fluids*,Vol. 18, pp 074103 (1-22).

[44] Konstantinidis, E., Balabani, S. and Yianneskis, M., (2003), The effect of flow perturbations on the near wake characteristics of a circular cylinder, *J. Fluids and Structures*, Vol. 18, pp. 367-386.

[45] Koopmann, G.H., (1997), The vortex wakes of vibrating cylinders at low Reynolds numbers, *J. Fluid Mech.*, vol. 28(3), pp. 501-512.

[46] Krishnamoorthy, S., Price, S. J. and Paidoussis, M. P., (2001), Cross-flow past an oscillating circular cylinder: synchronization phenomena in the near wake, *J. Fluids and Structures*, Vol. 15, pp. 955-980.

[47] Lecordier, J. C., Hamma, L. and Paranthoen, P., (1991), The Control of vortex shedding behind heated circular cylinders at low Reynolds numbers, *Experiments in Fluids*, Vol. 10, pp. 224-229.

[48] Lecordier, J. C., Browne, L. W. B., Masson, S., Le,Dumouchel, F. and Paranthoen, P., (2000), Control of vortex shedding by thermal effect at low Reynolds Numbers, *exper. Thermal and Fluid Science*, Vol. 21, pp. 227-237.

[49] Lin, C. and Hsieh, S. C., (2003), Convection velocity of vortex structures in the near wake of a circular cylinder,*J. Engg. Mechanics*,Vol. 129(10), pp. 1108-1118.

[50] Lu, X. Y. and Dalton, C., (1996), Calculation of the timing of vortex formation from an oscillating cylinder, *J. Fluids and Structures* , Vol. 10, pp. 527-541.

[51] Luo, S. C., Chew, Y. T. and Ng, Y. T., (2003), Characteristics of square cylinder wake transition flow, *Phys Fluids*, Vol. 15 (9), pp. 2549-2559.

[52] Maas, W. J. P. M., Rindt, C. C. M. and Van Steenhoven, A. A., (2003), The influence of heat on the 3D-transition of the von Karman vortex street. *Int J. Heat Mass Transfer*, Vol. 46, pp. 3069-3081

[53] Meier, G. E. A., (2002), Computerized background-oriented schlieren, *Expts. Fluids*, Vol. 33, pp. 181-187.

[54] Merkin, J. H., (1977), Mixed convection from a horizontal circular cylinder *J. Heat Mass Transfer*, Vol. 20, pp. 73-77.

[55] Michaux-Leblond, N. and Belorgey, M., (1997) , Near wake behavior of a heated circular cylinder: Viscosity-Buoyancy Duality, *Expt. Thermal and Fluid Sc.*, Vol. 15, pp. 91-100.

[56] Minewitsch, S., Franke R., Rodi W., (1994), Numerical investigation of laminar vortex-shedding flow past a square cylinder oscillating in line with the mean flow, *J.Fluids and Structures*, Vol. 8, pp. 787-802.

[57] Mori Y., Hijkata K., Nobuhara, (1986), A fundamental study of symmetrical vortex generation behind a cylinder by wake heating or by splitter plate or mesh, *J. Heat and Mass transfer*, Vol. 29(8), pp. 1193-1201.

[58] Muralidhar K., (2001) Temperature field measurement in buoyancy-driven flows using interferometric tomography, *Annual Review of Heat Transfer*, Vol.12, pp. 265-376.

[59] Nishihara, T., Kaneko, S. and Watanabe, T., (2005), Characteristics of fluid dynamic forces acting on a circular cylinder oscillated in the streawise direction and its wake patterns, *J. Fluids and Structures*, Vol. 20, pp. 505-518.

[60] Nobari, M. R. H. and Naderan, H., (2006), A numerical study of flow past a cylinder with cross flow and inline oscillation, *Computers and Fluids*, Vol. 35, pp. 393-415.

[61] Noto, K., Ishida, H. and Matsumoto, R., (1985), A breakdown of the Karman vortex street due to natural convection, *Flow Visualization III*, pp. 348-352, Springer, New York.

[62] Okajima, A., (1982), Strouhal numbers of rectangular cylinders, *J. Fluid Mech.*, Vol. 123, pp. 379-398.

[63] Ongoren, A. and Rockwell, D., (1988a), Flow structure from an oscillating cylinder Part 1. Mechanisms of phase shift and recovery in the near wake, *J. Fluid Mech.*, Vol. 191, pp. 197-223.

[64] Ongoren, A. and Rockwell, D., (1988b), Flow structure from an oscillating cylinder, part 2. Mode competition in the near wake, *J. Fluid Mech.*, Vol. 191, pp. 225-245.

[65] Oosthuizen, P. H. and Madan, S., (1971), The effect of flow direction on combined convective heat transfer from cylinders to air, *Trans. ASME C: J. Heat Transfer*, Vol. 93, pp. 240-242.

[66] Oosthuizen, P. H. and Naylor, D., (1999), *An Introduction to Convective Heat Transfer Analysis*, WCB/McGraw-Hill, New York.

[67] Oppenheim, A. K., Urtiew, P.A. and WeinBerg, F.J.,(1966), On the use of laser light sources in schlieren interferometer systems, *Proc. Roy. Soc. A* , Vol.291 , pp. 279-290.

[68] Park, H. G. and Gharib, M., (2001), Experimental study of heat convection from stationary and oscillating circular cylinder in cross flow, *J. Heat Transfer*, Vol. 123, pp. 51-62.

[69] Patnaik, B. S. V., Narayana, P.A. A. and Seetharamu, K. N., (1999), Numerical simulation of vortex shedding past a circular cylinder under the influence of buoyancy, *Int. J. of Heat and Mass transfer*, Vol. 42, pp. 3495-3507.

[70] Perry, A. E., (1982), *Hot-Wire Anemometry*, Oxford University Press, USA.

[71] Perry, A. E., Chong, M. S. and Lim, T. T., (1982), The vortex shedding process behind two dimensional bluff bodies, *J. Fluid Mech.*, Vol. 116, pp. 77-90.

[72] Placzek, A., Sigrist, J.F. and Hamdouni, A. (2009), Numerical simulation of an oscillating cylinder in a cross-flow at low Reynolds number: Forced and free oscillations, *Computers and Fluids*, Vol. 38, pp. 80-100.

[73] Pottebaum, T. S. and Gharib, M., (2006), Using oscillations to enhance heat transfer for a circular cylinder, *J. Heat and Mass Transfer*, Vol. 49, pp. 3190-3210.

[74] Raj Kumar, Kaura, S. K., Sharma, A. K., Chhachhia, D. P. and Agarwal, A.K.,(2007), Knife-edge diffraction pattern as an interference phenomenon: An experimental reality, *optics and laser tech.*, Vol. 39, pp. 256-261.

[75] Richardson, P. D., (1967), The estimation of the temperature profile in a laminar boundary layer with a schlieren method, *Int. J. heat mass transfer*, Vol. 8, pp. 557-566.

[76] Richard, H. and Raffel, M., (2001), Principle and applications of the background oriented schlieren (BOS) method, *Meas. Sci.and Tech.*, Vol. 12, pp. 1576-1585.

[77] Robichaux, J., Balachandar, S. and Vanka, S.P., (1999), Three-dimensional Floquet instability of the wake of a square cylinder, *Physics of fluids*, Vol.11(3), pp. 560-578.

[78] Roshko, A., (1993), Perspectives on bluff body aerodynamics, *J. Wind Engg. Ind. Aerodyn.*, Vol. 49, pp. 79-100.

[79] Saha, A. K., Biswas, G. and Muralidhar, K., (2003), Three dimensional study of flow past a square cylinder at low Reynolds numbers, *Int. J. heat and fluid flow*, Vol. 24, pp. 54-66.

[80] Schlichting, H., (1979), *Boundary-layer theory*, Mcgraw-Hill Publisher, U.S.A.

[81] Schumm, M., Berger, E. and MonkeWitz, P. A., (1994), Self-excited oscillations in the wake of two-dimensional bluff bodies and their control, *J. Fluids Mech.*, Vol. 271, pp.17-53.

[82] Settles, G.S., (2001), *Schlieren and Shadowgraph Techniques: visualizing phenomenon in transparent media*, Springer Publication, New York.

[83] Sharma, A. and Eswaran,V., (2004), Effect of adding and opposing buoyancy on the heat and fluid flow across a square cylinder at Re=100 , *Numerical Heat transfer,Part A*, Vol. 45, pp. 601-624.

[84] Shi, J.-M., Gerlach, D. and Breuer, M., (2004), Heating effects on steady and unsteady horizontal laminar flow of air past a circular cylinder, *Phy. of Fluids*, Vol. 16(12), pp. 4331-4345.

[85] Singh, S., Biswas G. and Mukhopadhyay, A., (1998), Effect of thermal buoyancy on the flow through a vertical channel with a built-in circular cylinder, *Numerical Heat transfer*, Vol. 34, pp. 769-789.

[86] Smith, K.M. and Dutton, J.C., (1999), A procedure for turbulent structure convection velocity measurements using time-correlated images, *Experiments in fluids*, Vol. 27, pp. 244-250.

[87] Sohankar, A., Norberg, C. and Davidson, L., (1998), Low-Reynolds-number flow around a square cylinder at incidence: Study of blockage, onset of vortex shedding and outlet boundary condition, *Int. J. Numer. Meth. Fluids*, Vol. 26, pp. 39-56.

[88] Sohankar, A., Norberg, C. and Davidson, L., (1999), Simulation of three-dimensional flow around a square cylinder at moderate Reynolds numbers, *Physics of fluids*, Vol. 11, No. 2, pp. 288-306.

[89] Stricker, J. and Rosenblatt, F., (2003), Heterodyne schlieren system, *Optics letters*, Vol. 28(16), pp. 1427-1429.

[90] Stricker, J. and Rosenblatt, F., (2005), Performance analysis of heterodyne schlieren system, *Experiments in fluids*, Vol. 39, pp. 564-572.

[91] Strykowski, P. J.and Sreenivasan, K. R., (1990), On the formation and suppression of vortex shedding at low Reynolds numbers, *J. Fluids Mech.*, Vol. 218, pp. 71-107.

[92] Tanda, G. and Devia, F., (1998), Application of a schlieren technique to heat transfer measurements in free-convection, *Experiments in fluids*, Vol. 24, pp. 285-290.

[93] Tanida, Y., Okajima, A. and Watanabe, Y., (1973), Stability of a circular cylinder oscillating in uniform flow or in a wake, *J. Fluid Mech.*, Vol. 61(4), pp. 769-784.

[94] Temple, E. B.,(1957), Quantitative measurement of gas density by means of light interference in schlieren system, *J. Opt. Soc. Am.*, Vol. 47 (1), pp. 91-100.

[95] Tokumaru, P. T. and Dimotakis, P. E., (1995), Image correlation velocimetry, *Experiments in fluids*, Vol. 19, pp. 1-15.

[96] Vit, T., Ren, M., Travnicek, Z., Marsik, F. and Rindt, C.C.M., (2007), The influence of temperature gradient on the Strouhal Reynolds number relationship for water and air, *Experimental Thermal and Fluid Science*, Vol. 31, pp. 751-760.

[97] Wang, A. B., Travnicek, Z. and Chia, K. C., (2000), On the relationship of effective Reynolds number and Strouhal number for the laminar vortex shedding of a heated circular cylinder, *Physics of Fluids*, Vol. 12 (6), pp. 1401-1410.

[98] Williamson, C. H. K., (1988), The existence of two stages in the transition to three-dimensionality of a cylinder wake, *Phys. Fluids*, Vol. 31, pp. 3165-3168.

[99] Williamson, C. H. K., (1989), Oblique and parallel modes of vortex shedding in the wake of a circular cylinder at Low Reynolds numbers, *J. Fluid Mech.*, Vol. 206, pp. 579-627.

[100] Williamson, C. H. K., (1997), Advances in our understanding of vortex dynamics in bluff body wakes, *J. Wind Eng. Ind. Aerodyn.*, Vol. 69-71, pp. 3-32.

[101] Williamson, C. H. K. and Roshko, A., (1988), vortex formation in the wake of an oscilltaing cylinder, *J. Fluids and Structures*, Vol. 2, pp. 355-381.

[102] Wu, J., Sheridan, J., Soria, J. and Welsh, M.C., (1994), An experimental investigation of streamwise vortices in the wake of a bluff body, *J. Fluids and Structures*, Vol. 8, pp. 621-625.

[103] Xu, S.J, Zhou, Y. and Wang M. H., (2006), A symmetric binary-vortex street behind a longitudinally oscillating cylinder, *J. Fluids Mech.*, Vol. 556, pp. 27-43.

[104] Yildirim, B. S. and Agarwal, A. K., (2005), Full-field measurements of self-excited oscillations in momentum-dominated helium jets, *Experiments in fluids*, Vol. 38, pp. 161-173.

[105] Yu, M. H., Monkewitz, P. A., (1990), The effect of nonuniform density on the absolute instability of two-dimensional inertial jets and wakes, *Phys. Fluids A 2(7)*, pp. 1175-1181.

[106] Zdravkovich, M. M., (1982), Modification of vortex shedding in the synchronization range, *Trans. ASME J. Fluids Engg.*, Vol. 104, pp. 513-517.

[107] Zdravkovich, M. M., (1997), *Flow around Circular Cylinders, vol 1: Fundamentals*, Oxford University Press, New York.

[108] Zheng, Z.C., and Zhang N., (2008), Frequency effects on lift and drag for flow past an oscillating cylinder, *J. Fluids and Structures*, Vol. 24, pp. 382-399.

[109] Zhong, S. and Squire, L. C., (1995), An interferometric study of organized structures in wakes of circular cylinders, *Experiments in Fluids*, Vol. 20, pp. 91-99.

[110] Zhou, Y. and Antonia, R. A., (1992), Convection velocity measurements in a cylinder wake, *Experiments in fluids*, Vol. 13, pp. 63-70.

भारतीय प्रौद्योगिकी संस्थान कानपुर
INDIAN INSTITUTE OF TECHNOLOGY KANPUR

Appendix A

Circular Cylinder Wake: Influence of Buoyancy and In-line Oscillation

Experiments are performed to study the flow structures over a heated circular cylinder subjected to forced oscillations in the streamwise (inline) direction. Inline oscillation of a cylinder in steady uniform flow is distinctly different from transverse oscillation case. The perturbation produced by the forced oscillation is symmetric, while natural occurring mode of vortex formation is antisymmetric for inline oscillation. Literature reveal that there is a competition between these two modes of vortex formation. Most of the studies on oscillating cylinder have focused on an isothermal fluid in which no temperature difference is maintained between the body and the ambient. However, the present work aims at characterization of the wake of a circular cylinder under combined influence of buoyancy and forced in-line oscillations. The electrically heated cylinder is mounted in a vertical airflow facility such that the buoyancy aids to the inertia of the main flow. The Reynolds number (Re) is set equal to 104 and four different heating levels with Richardson number, Ri = 0.027, 0.058, 0.108, and 0.144 are used. For a particular Richardson number, initial experiments were performed without oscillating the cylinder. Subsequently, the experiments were performed with the cylinder oscillating at different frequencies in the multiples of natural vortex shedding frequency, i.e. at f_e/f_s = 1, 1.5 and 2 corresponding to fundamental, non-harmonic and super-harmonic frequencies respectively. The oscillation amplitude (a/d) is varied from 0.02 to 0.10 in a small step of 0.02. Small oscillation amplitudes are selected to simulate self induced oscillation present in practical applications. Laser schlieren-interferometry is used for flow visualization and quantitative analysis of flow structures. Results obtained from the present study are presented in the following sequence: (a) Phase-referenced visualization images and (b) Power spectra.

A.1 Phase-referenced visualization images

Phase-referenced visualization images have been used to present the dynamical characteristics of the vortex structures, relative to the cylinder motion. In the present section, instantaneous schlieren images for stationary circular cylinder as a function of Richardson number have been presented first as a reference case for comparison with the oscillating cylinder results. Subsequently, phase-referenced schlieren images have been presented for different excitation frequencies as a function of Richardson number and at an oscillation amplitude, $a/d = 0.08$.

A.1.1 Stationary cylinder ($f_e/f_s = 0$)

Figure A.1 shows the time sequence of schlieren images as a function of Richardson number for a stationary circular cylinder. At a given Richardson number, the visualization images are separated by a time interval of one eighth of the time period of vortex shedding. Figure A.1 (A) shows the alternate vortex shedding at Ri = 0.027. This is due to growth of small disturbances in shear layer and dominant frequency is the natural vortex shedding frequency (f_s). Figure A.1 (B) shows the vortex shedding at a higher temperature (Ri = 0.058). Compared to Figure A.1 (A), there is distinct and regular vortex shedding in Figure A.1 (B). Figure A.1 (C) shows schlieren images at cylinder temperature of 63°C (Ri = 0.108). The detached shear layer arising from the vortex shedding process is more elongated at this Richardson number. Figure A.1 (D) shows the schlieren images at cylinder temperature of 77°C (Ri = 0.144) where, two shear layers have merged into one leading to a single steady plume. The schlieren images depict the suppression of vortex shedding at this temperature and the wake degenerates into a steady plume.

A.1.2 Fundamental oscillation ($f_e/f_s = 1$)

The images are presented corresponding to different phases (a-h) during one oscillation cycle for the oscillating cylinder case as shown in Figure A.2. Figure A.3 show the sequence of phase-referenced schlieren images as a function of Richardson number for inline oscillating circular cylinder. For each Richardson number, the cylinder is oscillated at the corresponding vortex shedding frequency (i.e. $f_e/f_s = 1$) of the stationary cylinder. The amplitude of oscillation is fixed at 0.08 times the diameter of the cylinder (i.e. $a/d = 0.08$). The time interval between two consecutive images in the sequence is equal to one eighth of the time period of cylinder oscillation; The first image in the sequence (marked as 'a') corresponds to the maximum downward position of the cylinder whereas image marked

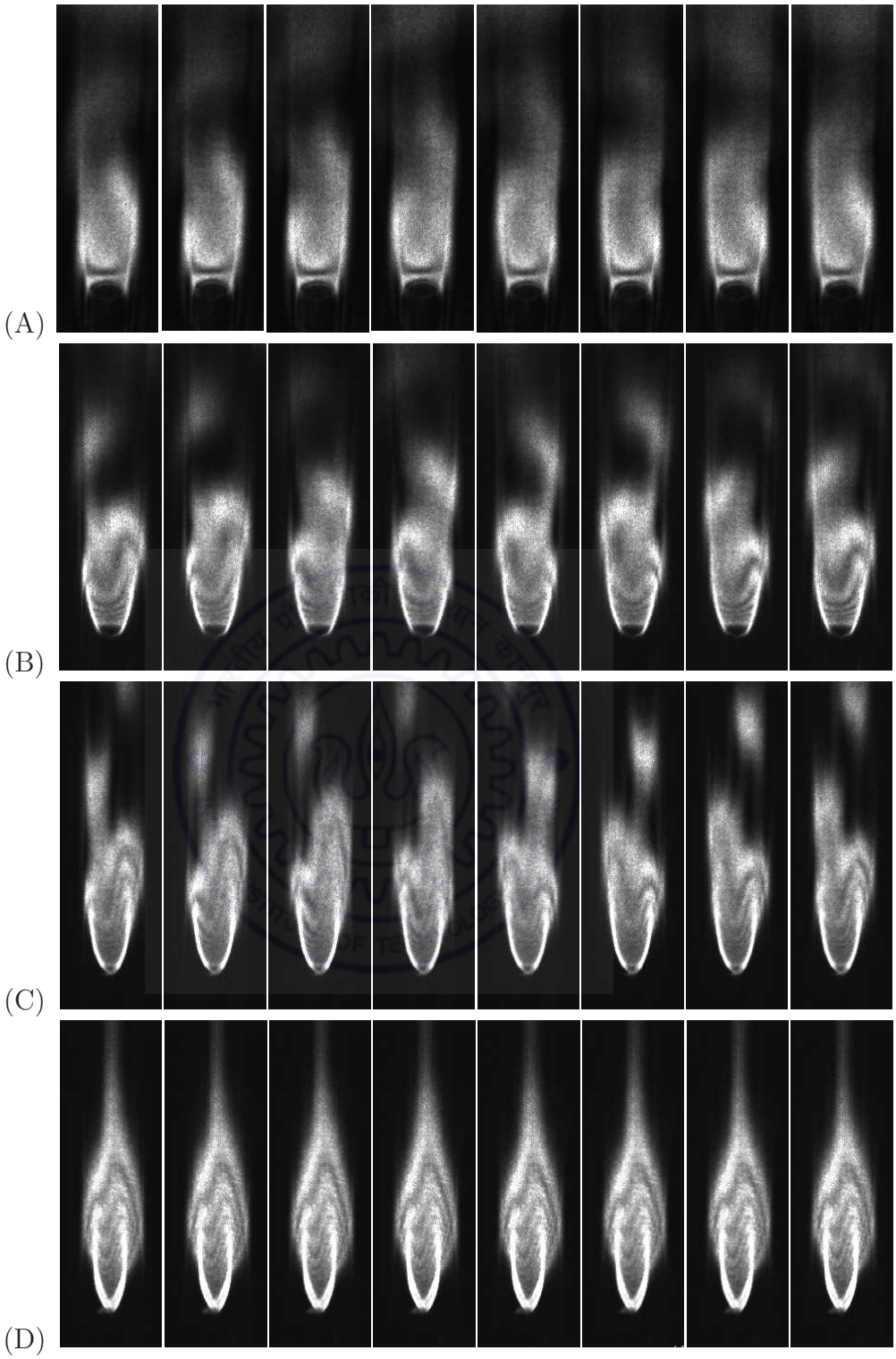

Figure A.1: Time sequences of instantaneous schlieren images for a stationary circular cylinder separated by a time interval of one eighth of the time period of vortex shedding at Re=104 for different Richardson number: (A) Ri=0.027, (B) Ri=0.058, (C) Ri=0.108, and (D) Ri=0.144. For Ri $\geq$ 0.144, images show steady state.

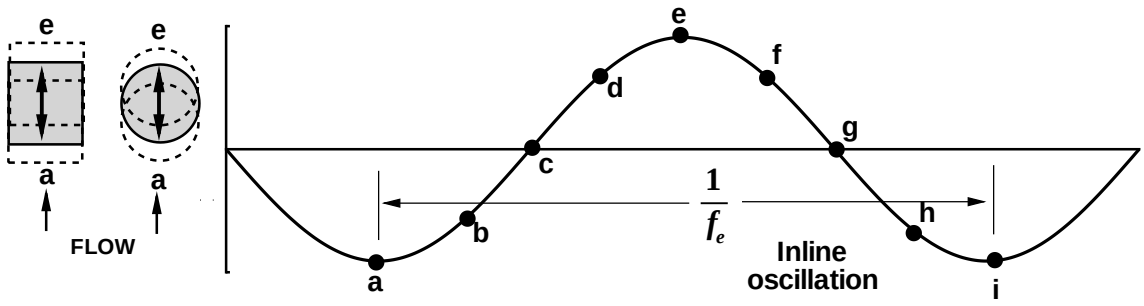

Figure A.2: Different phases (a-i) during one oscillation cycle of inline oscillation of circular and square cylinders.

as 'e' corresponds to the maximum upward position of the cylinder (see Figure A.2). The sequence of images for perturbed flow show two different types of vortex shedding i.e. symmetric and antisymmetric. For symmetric type, the vortex shedding from right and left side of the cylinder occurs and grows simultaneously. For antisymmetric type, the vortex shedding from opposite sides of the cylinder occurs and grows alternatively.

Figure A.3 (A) shows the instantaneous schlieren images for oscillating cylinder at a cylinder surface temperature of 34°C (Ri = 0.027). In Figure A.3(A), wake mode shows the antisymmetric shedding, but the symmetric shedding is also observed at later times. These two shedding modes switch abruptly from one mode to other with each mode persisting over finite number of cycles. The mode switching is observed in a long continuous sequence composed of many number of cycles. These two modes of shedding with mode competition were also observed by Ongoren and Rockwell (1988b) for the circular cylinder oscillating at fundamental Strouhal frequency. The present schlieren visualization images confirm the same patterns of vortex formation. This mode switching can be attributed to competition between the natural vortex shedding and symmetrical perturbation given at same Strouhal frequency. Figure A.3 (B) show the instantaneous schlieren images for oscillating cylinder at a surface temperature of 45°C (Ri = 0.058). Here the vortex patterns are antisymmetrical for the total recorded sequence but a small difference in phase of the vortices between two sides is observed at down stream locations. In Figure A.3 (C) for a surface temperature at 63°C (Ri = 0.108), the instantaneous schlieren images also show the antisymmetric patterns as observed for a surface temperature of 45°C (Ri = 0.058). This shows that at higher Richardson number, the inline perturbation regularizes the alternate vortex shedding. Figure A.3 (D) shows the instantaneous schlieren images for oscillating cylinder at a surface temperature of 77°C (Ri = 0.144). The vortex structures have antisymmetric patterns. Stationary cylinder at same Richardson number in Figure A.1 (D) shows that due to buoyancy both sides shear layers have merged into single

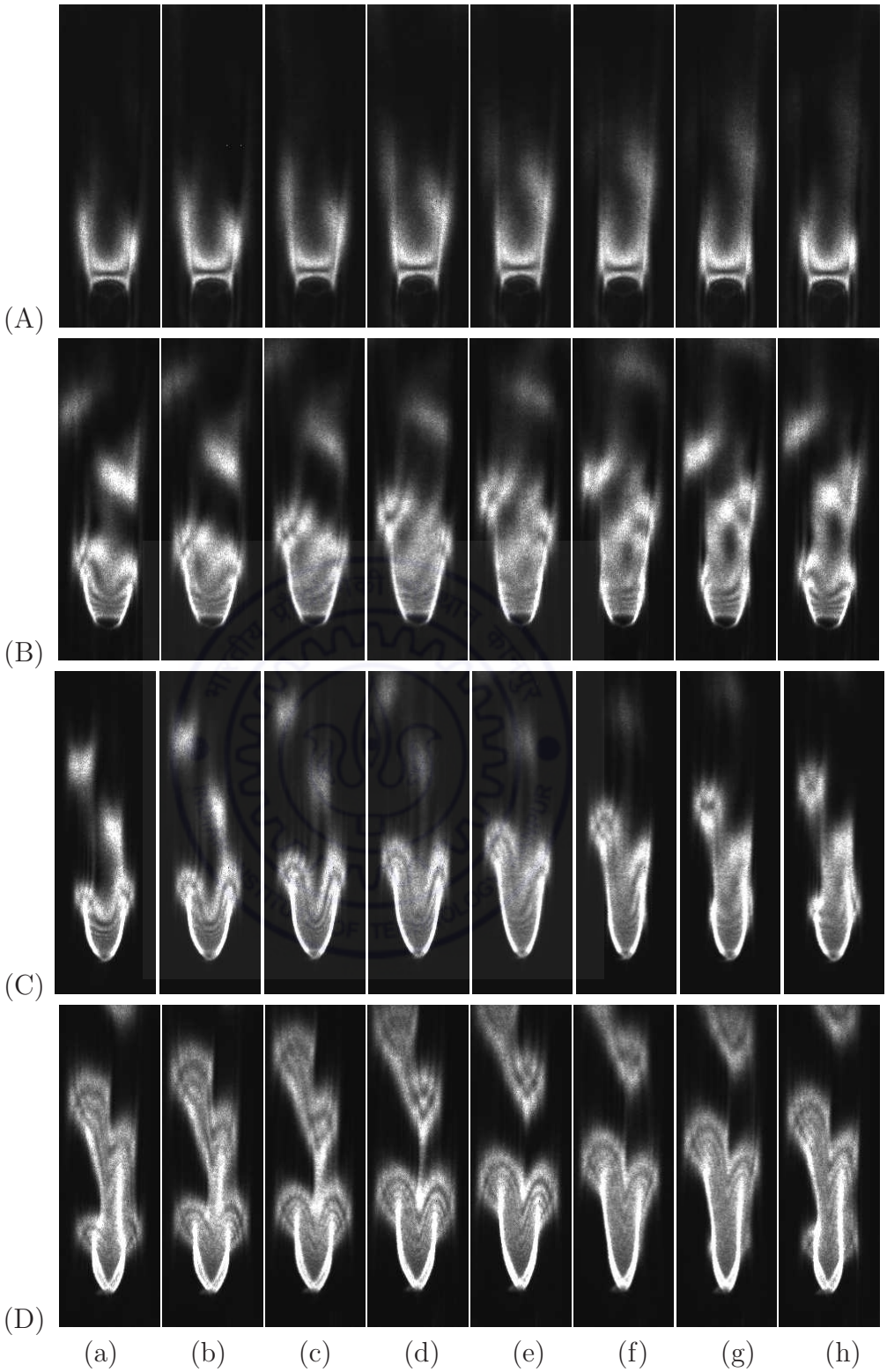

Figure A.3: Phase-referenced schlieren images for a circular cylinder corresponding to different phases (a-h) of cylinder oscillation (Figure A.2) at fundamental Strouhal frequency ($f_e/f_s = 1$) and amplitude, $a/d = 0.08$ as a function of Richardson number: (A) Ri=0.027, (B) Ri=0.058, (C) Ri=0.108, and (D) Ri=0.144.

steady plume and vortex shedding have disappeared. But the inline oscillating cylinder shows a clear vortex shedding. The re-appearance of vortex structures can be attributed to the additional energy imparted to wake by small amplitude inline oscillations of the cylinder.

A.1.3 Non-harmonic oscillation ($f_e/f_s = 1.5$)

Figure A.4 show the sequence of phase-referenced schlieren images for inline oscillating circular cylinder as a function of Richardson number at non-harmonic (1.5 times) of the fundamental Strouhal frequency (i.e. $f_e/f_s = 1.5$) for an amplitude ratio, $a/d = 0.08$. For each Richardson number, the images are presented corresponding to different phases (a-h) during one oscillation cycle as shown in Figure A.2. The time interval between two consecutive images in the sequence is equal to one eighth of the time period of cylinder oscillation. The first image in the sequence (marked as 'a') corresponds to the maximum downward position of the cylinder whereas image marked as 'e' corresponds to the maximum upward position of the cylinder (see Figure A.2).

Figure A.4 (A) shows the instantaneous schlieren images for oscillating cylinder at a cylinder surface temperature of 34°C (Ri = 0.027). In Figures A.4 (A) wake mode shows the symmetric shedding. This shedding mode persisted over long continuous sequence composed of many number of cycles. The mode switching is not observed. In Figure A.4 (B), at a cylinder surface temperature of 45°C (Ri = 0.058), wake also shows the symmetric shedding. At cylinder surface temperature of 63°C i.e. Ri = 0.108 (Figure A.4 (C)) and 77°C i.e. Ri = 0.144 (Figure A.4 (D)), the vortex structures are completely symmetrical. The structures form both sides start growing at the same instant, shed at the same instant and travel together.

A.1.4 Super-harmonic oscillation ($f_e/f_s = 2$)

A schematic diagram representing different phases (a-q) during two successive cycles of inline super-harmonic oscillation of the cylinder is shown in Figure A.5. Figure A.6 show the sequence of phase-referenced schlieren images for inline oscillating circular cylinder as a function of Richardson number at super-harmonic (2 times) of the natural vortex shedding frequency (i.e. $f_e/f_s = 2$) at an amplitude ratio, $a/d = 0.08$. At this excitation frequency, phase-referencing is extended over two successive cycles of the cylinder oscillation with eight evenly spaced phases during each oscillation cycle. The images corresponding to different phases (a-p) for two consecutive cycles of the cylinder oscillation are presented in two rows i.e. the images in first and second row corresponds to phases (a-h) of the

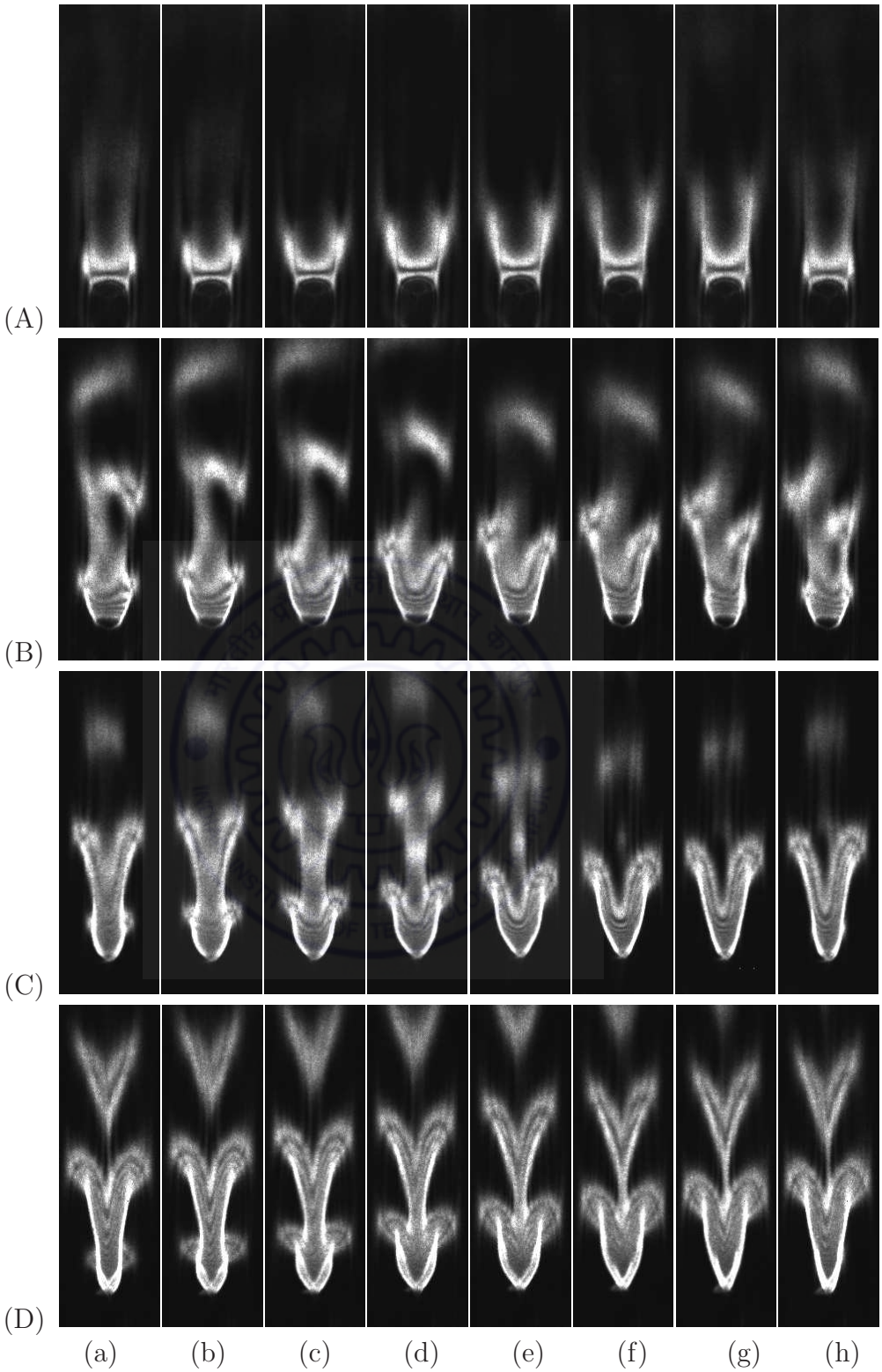

Figure A.4: Phase-referenced schlieren images for a circular cylinder corresponding to different phases (a-h) of cylinder oscillation (Figure A.2) at non-harmonic frequency (f_e/f_s = 1.5) and amplitude, a/d = 0.08 as a function of Richardson number: (A) Ri=0.027, (B) Ri=0.058, (C) Ri=0.108, and (D) Ri=0.144.

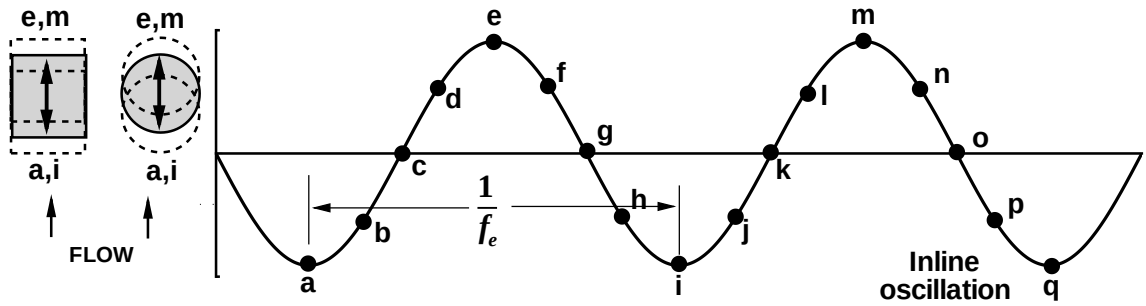

Figure A.5: Different phases (a-q) during two consecutive cycles of inline oscillation of circular and square cylinders.

first cycle and phases (i-p) of the second cycle, respectively. In each row, the images in the sequence are separated by a time interval of one-eighth of the time period of cylinder oscillation. First image of the sequence in each row (marked as 'a' and 'i') corresponds to the maximum downward position of the cylinder whereas images marked as 'e' and 'm' corresponds to the maximum upward position of the cylinder (see Figure A.5).

The sequence of images in Figure A.6 show alternate vortex shedding for all Richardson number considered. However, the size, shape and period of the vortex structures are different than the alternate pattern of vortex shedding observed in a stationary cylinder. For Ri = 0.144, vortex shedding was suppressed for the stationary cylinder (Figure A.1 (D)). With harmonic oscillations, the wake is transformed from a steady plume to the alternate vortex shedding (Figure A.6 (D)). Careful examination of the images shows that two vortices are shed during each cycle of cylinder oscillation. The near wake is arranged into alternating pairs of vortices from different sides with each pair consisting of two vortices of opposite sign. The images at corresponding phases in two consecutive cycles look like mirror images.

A.2 Power spectra

The power spectra of the fluctuating light intensity are shown in Figures A.7 and A.8 for Ri = 0.058 and 0.144, respectively at different frequency ratios, $f_e/f_s = 0$, 1, 1.5, and 2 at the amplitude ratio, $a/d = 0.08$. Three stream-wise locations, namely $x/d = 2$, 3.5 and 5 in the near-wake region are considered at a transverse location $y/d = 0.7$. Total 1250 images acquired over 5 seconds at a rate of 250 frames per second are used for calculation of the power spectra. For all locations, the light intensity is averaged over 4×4 pixels to minimize the pixel level noise.

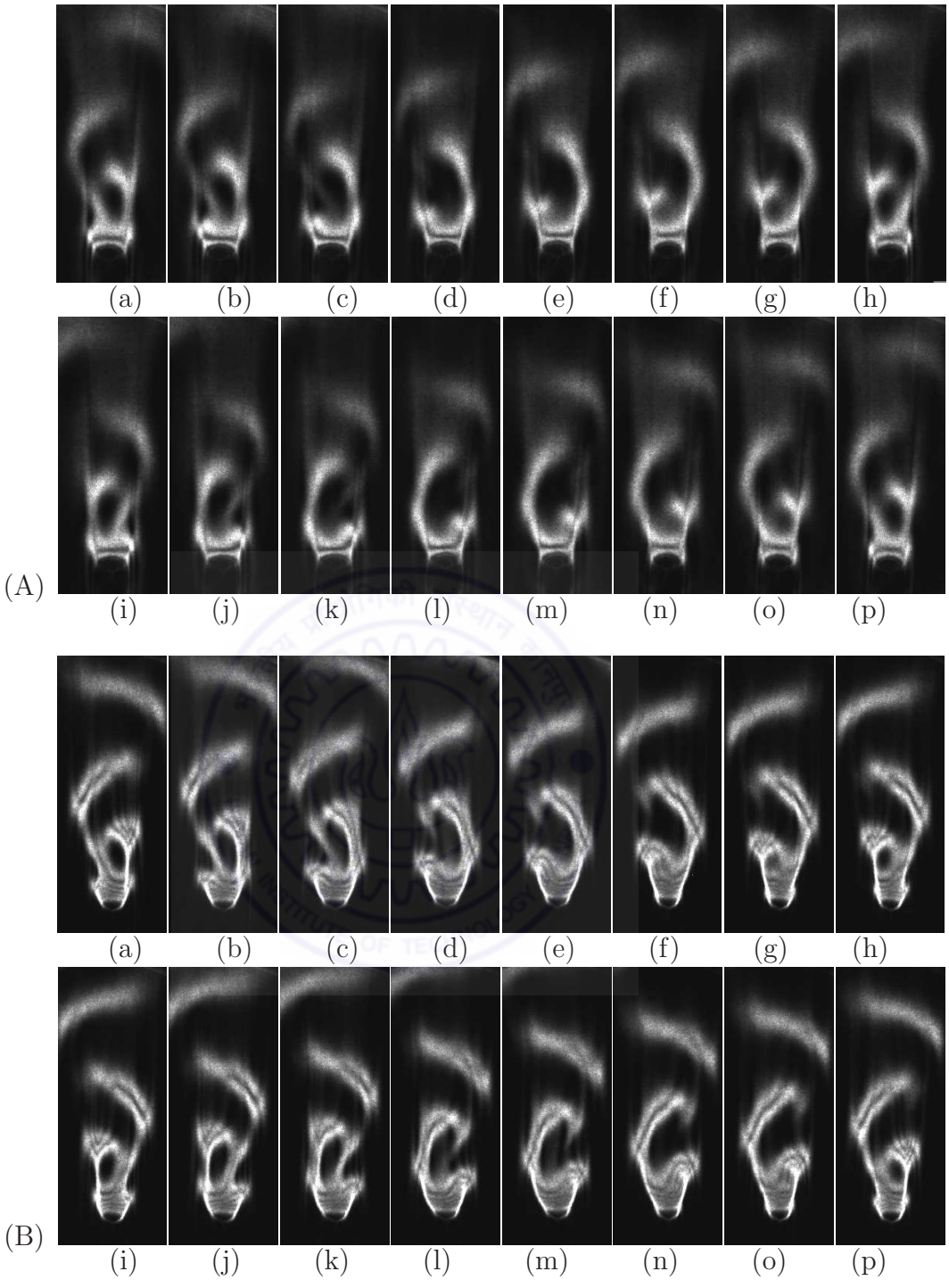

see caption on the next page

In Figure A.7 (A) the spectral peak is dominant at vortex shedding frequency for all streamwise locations (x/d = 2, 3.5 and 5). The presence of harmonics can be attributed to the interaction between vortices from opposite side of the shear layer. Figure A.7 (B) for fundamental oscillation, $f_e/f_s = 1$, shows stronger peak at fundamental frequency compared to the stationary case. The harmonics are also more energized possibly due to

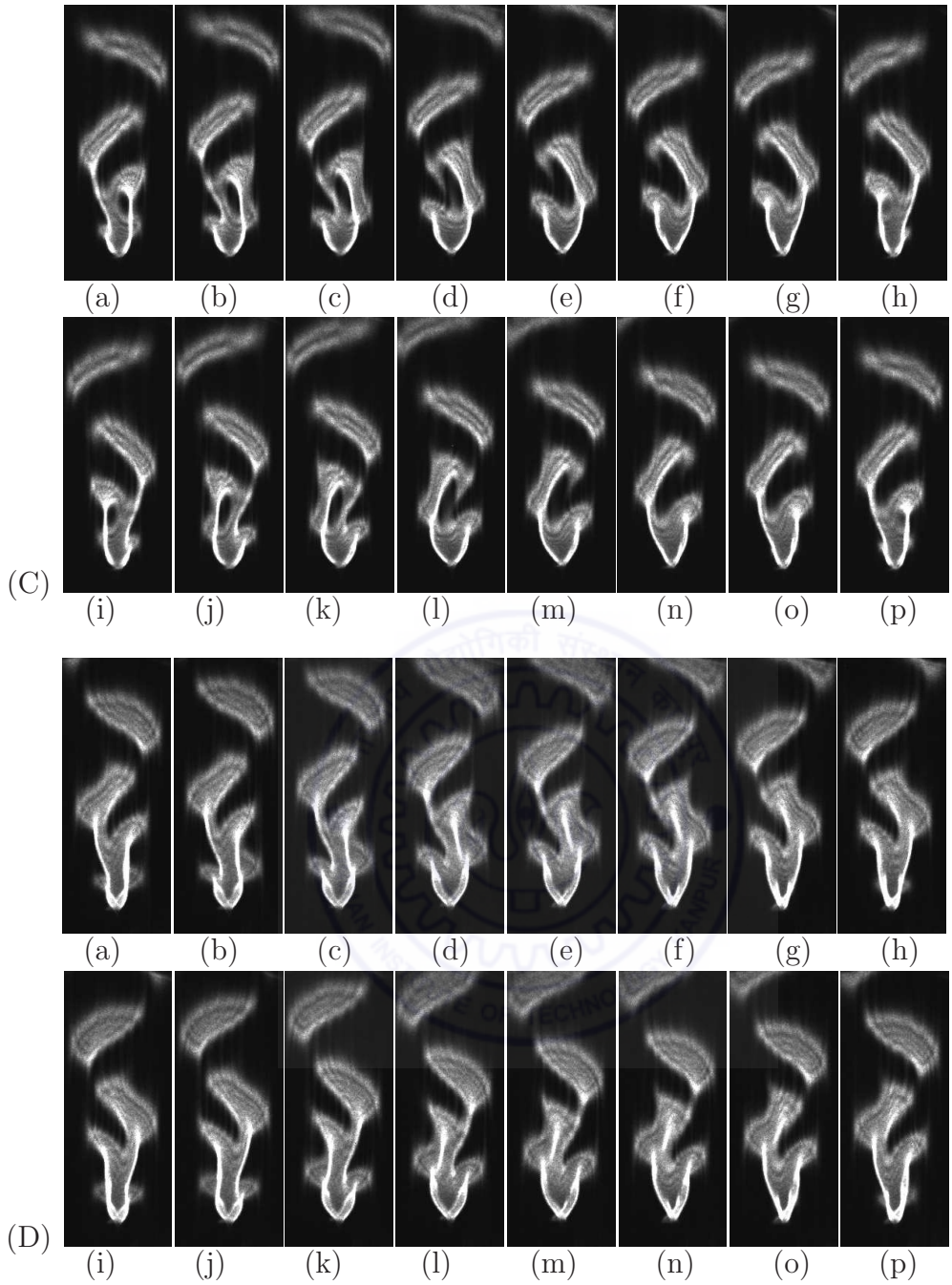

Figure A.6: Phase-referenced schlieren images for a circular cylinder corresponding to different phases (a-p) of cylinder oscillation (Figure A.5) as a function of Richardson number: (A) Ri=0.027, (B) Ri=0.058, (C) Ri=0.108, and (D) Ri=0.144. The cylinder is oscillating at super-harmonic of the Strouhal frequency ($f_e/f_s = 2$) and amplitude ratio, $a/d = 0.08$.

greater interaction between the opposite shear layers. In Figure A.7 (C) for $f_e/f_s = 1.5$, at $x/d = 2$, the peak is at cylinder oscillation frequency. At down stream locations (x/d = 3.5 and 5), the peak is at the vortex shedding frequency of the stationary cylinder and smaller peaks at $f_e/f_s = 1.5$ with its harmonics are also present. This indicates that wake

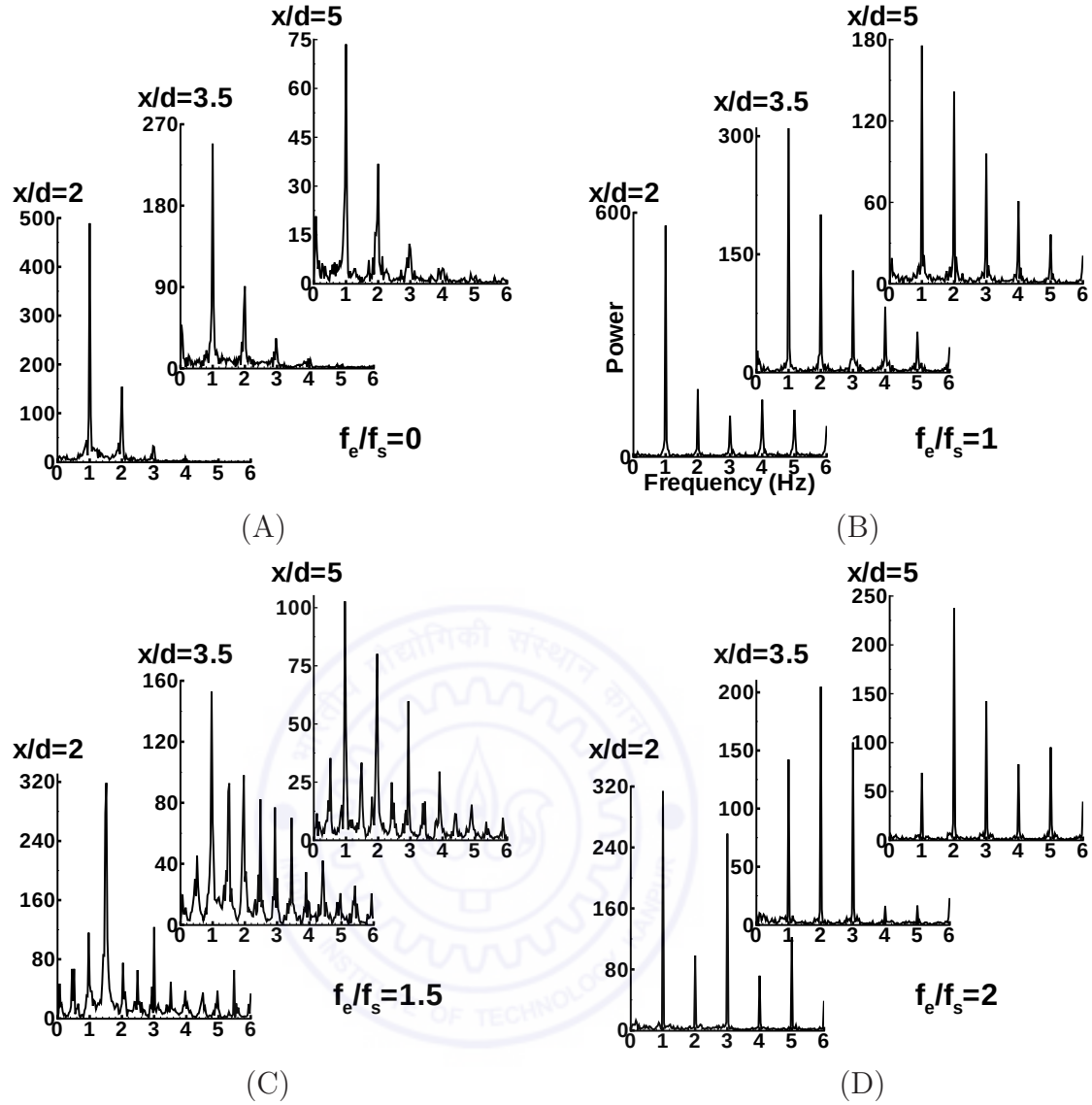

Figure A.7: Power spectra of light intensity at various streamwise locations (x/d = 2, 3.5 and 5.0) for the oscillating circular cylinder for Ri = 0.058 at different excitation frequencies: (A) $f_e/f_s = 0$, (B) $f_e/f_s = 1$, (C) $f_e/f_s = 1.5$, and (D) $f_e/f_s = 2$. The amplitude of oscillation is set at $a/d = 0.08$.

is synchronized at $x/d = 2$ location. However, at $x/d = 3.5$ and 5, there is a competition between cylinder oscillation frequency and vortex shedding frequency. Therefore lock on of the wake is limited to the near region of the cylinder. In Figure A.7 (D) at $f_e/f_s = 2$, the peak is seen at twice the Strouhal frequency at $x/d = 3.5$ and 5. This is due to lock on of the wake with cylinder oscillation.

In Figure A.8 (A), the broadband spectra show that at this temperature the vortex shedding is suppressed for stationary cylinder. But in Figure A.8 (B), the clean peak is at vortex shedding frequency with small amplitude harmonics present for all streamwise

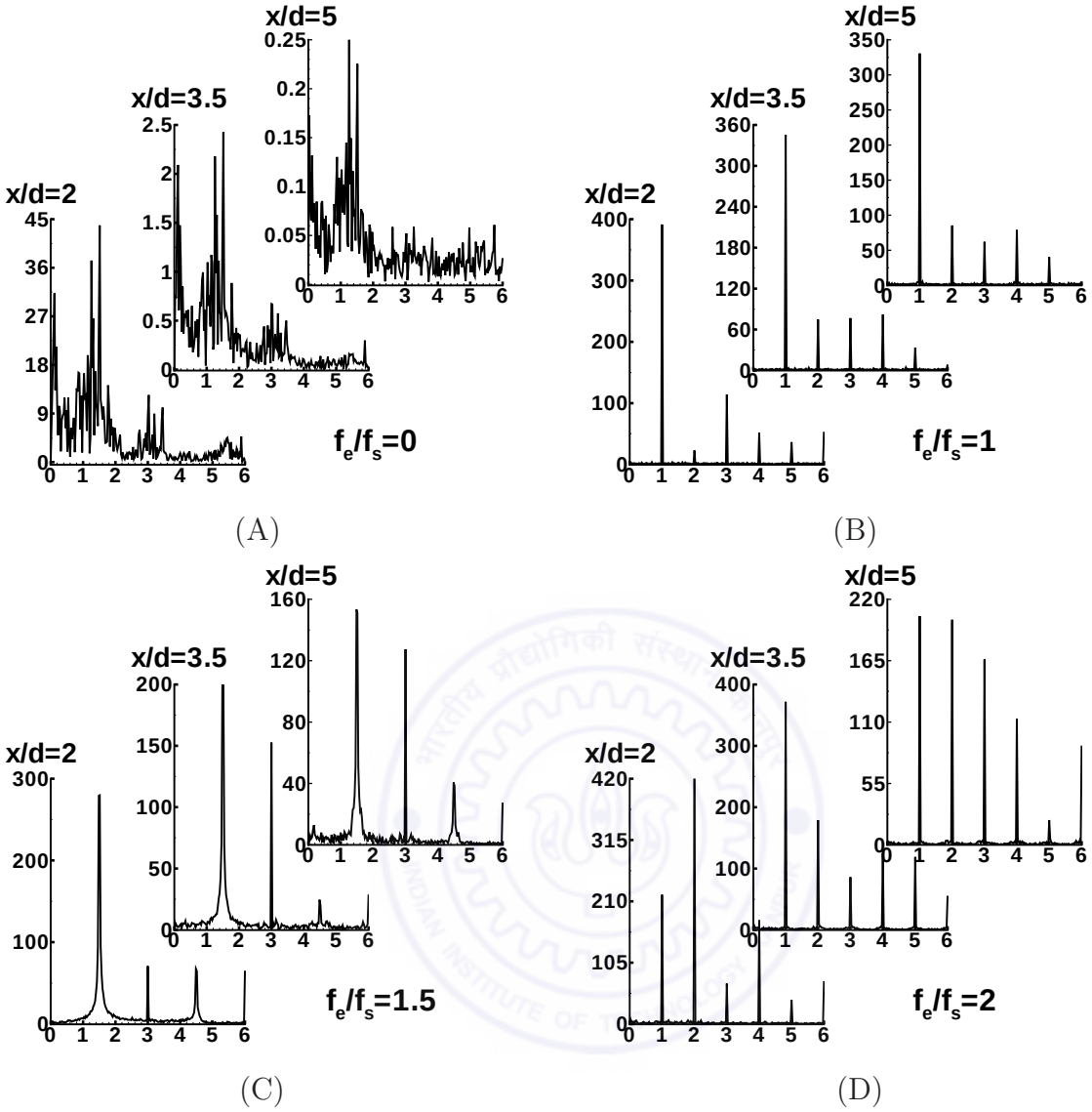

Figure A.8: Power spectra of light intensity at various streamwise locations (x/d = 2, 3.5 and 5.0) for the oscillating circular cylinder for Ri = 0.144 at different excitation frequencies: (A) $f_e/f_s = 0$, (B) $f_e/f_s = 1$, (C) $f_e/f_s = 1.5$, and (D) $f_e/f_s = 2$. The amplitude of oscillation is set at $a/d = 0.08$.

locations (x/d = 2, 3.5 and 5). In Figure A.8 (C), a clear peak is observed at cylinder oscillation frequency with presence of comparable magnitude harmonics at locations x/d = 3.5 and 5. In Figure A.8 (D) at $f_e/f_s = 2$, a clear peak is seen at twice the Strouhal frequency at x/d = 2 indicating lock on of the wake with cylinder oscillation. There is presence of some spectral energy at vortex shedding frequency indicating competition between two modes.

A.3 Summary

The present study investigates the effect of buoyancy on wake instability of heated circular cylinder oscillating in streamwise direction. The frequency of oscillation is kept at f_e/f_s = 0, 1, 1.5 and 2. The amplitude of oscillation is varied between 0.02-0.10 times the diameter of the circular cylinder. Temporally resolved schlieren imaging have been used as a tool for qualitative flow visualization and quantitative measurements of dynamic behaviors of vortical structures. The instantaneous visualization images and power spectra are presented and discussed. The effect of buoyancy due to heating leads to disappearance of vortex shedding after a critical value of Richardson number. However, the inline oscillation of the circular cylinder initiates the appearance of vortex structures. The patterns of vortex formation are either symmetrical or anti-symmetrical, which depend on the oscillation frequency. For anti-symmetric shedding patterns, the size, shape and period of vortex structures are different compared to that of stationary cylinder. Overall, the combined effect of buoyancy and inline oscillation of circular cylinder influences the wake instability.

भारतीय प्रौद्योगिकी संस्थान कानपुर
INDIAN INSTITUTE OF TECHNOLOGY KANPUR